CAMBRIDGE MONOGRAPHS ON PHYSICS

GENERAL EDITORS

N. FEATHER, F.R.S.
Professor of Natural Philosophy in the University of Edinburgh

D. SHOENBERG, PH.D.
Fellow of Gonville and Caius College, Cambridge

ELECTRON OPTICS

ELECTRON OPTICS

S/C

BY

O. KLEMPERER, Ph.D.

Assistant Professor and Reader
Imperial College, University of London

SECOND EDITION

CAMBRIDGE
AT THE UNIVERSITY PRESS
1953

catlog

PUBLISHED BY
THE SYNDICS OF THE CAMBRIDGE UNIVERSITY PRESS

London Office: Bentley House, N.W. 1
American Branch: New York

Agents for Canada: Macmillan

First edition, 1939
Second edition, 1953

CHECKED

K67GE

JAMMU & KASHMIR UNIVERSITY
LIBRARY
No. 12548
Date 7.7.55
SRINAGAR

ALLAMA IQBAL LIBRARY
12548

Printed in Great Britain at the University Press, Cambridge
(Brooke Crutchley, University Printer)

GENERAL PREFACE

The Cambridge Physical Tracts, out of which this series of Monographs has developed, were planned and originally published in a period when book production was a fairly rapid process. Unfortunately, that is no longer so, and to meet the new situation a change of title and a slight change of emphasis have been decided on. The major aim of the series will still be the presentation of the results of recent research, but individual volumes will be somewhat more substantial, and more comprehensive in scope, than were the volumes of the older series. This will be true, in many cases, of new editions of the Tracts, as these are re-published in the expanded series, and it will be true in most cases of the Monographs which have been written since the War or are still to be written.

The aim will be that the series as a whole shall remain representative of the entire field of pure physics, but it will occasion no surprise if, during the next few years, the subject of nuclear physics claims a large share of attention. Only in this way can justice be done to the enormous advances in this field of research over the War years.

N. F.
D. S.

CONTENTS

AUTHOR'S PREFACE *page* xi

CHAPTER I

Historical Introduction: The Fundamental Principles of Electron Optics

1.1. Historical development, p. 1. **1.2.** Variation principles and the refractive index of an electron, p. 2. **1.3.** Image formation by collinear projection, p. 10. **1.4.** The physical problem of image formation, p. 12.

CHAPTER II

The Cardinal Points of an Electron Lens

2.1. Location of cardinal points by ray tracing with a sliding target, p. 16. **2.2.** Geometrical relations between object- and image-space, p. 18. **2.3.** Practical methods for locating cardinal points, p. 21.

CHAPTER III

Field Plotting and Ray Tracing

3.1. Potential distribution and Laplace's equation, p. 25. **3.2.** Experimental field plotting, p. 28. **3.3.** Ray tracing by Snell's law, p. 34. **3.4.** Circle method and parabola method, p. 38. **3.5.** Ray tracing by integration of the equations of motion of the electron, p. 43. **3.6.** Automatic ray-tracing machines, p. 45. **3.7.** Fields and electrodes, p. 47.

CHAPTER IV

Some Electrostatic Electron Lenses

4.1. General properties, p. 49. **4.2.** Symmetrical two-tube lenses, p. 50. **4.3.** Various two-electrode lenses, p. 56. **4.4.** The single aperture, p. 60. **4.5.** Multielectrode lenses, p. 63. **4.6.** Saddle-field lenses, p. 64. **4.7.** Gauze lenses, p. 72. **4.8.** Electron mirrors, p. 73.

CHAPTER V

Magnetic Electron Lenses

5.1. Electron path in homogeneous magnetic fields, p. 79. **5.2.** Paraxial rays in inhomogeneous magnetic fields of circular symmetry. The thin lens, p. 84. **5.3.** Focal length and image rotation of thick magnetic lenses, p. 88. **5.4.** Practical lens design, p. 94. **5.5.** Determination of magnetic field distributions, p. 111. **5.6.** Ray tracing through magnetic lenses, p. 115. **5.7.** Combined electrostatic and magnetic lenses, p. 120.

CHAPTER VI

Lens Errors: Geometrical Aberrations

6.1. Classification of aberrations, p. 122. **6.2.** Deviations from circular symmetry, p. 124. **6.3.** Spherical aberration, p. 129. **6.4.** Spherical aberration: measuring methods and results, p. 136. **6.5.** Correction of spherical aberration, p. 148. **6.6.** Field aberrations: coma, p. 155. **6.7.** Field curvature and astigmatism, p. 159. **6.8.** Distortion, p. 164. **6.9.** Anisotropic aberrations, p. 169.

CHAPTER VII

Electronic Aberrations

7.1. Chromatic aberration, p. 172. **7.2.** The use of chromatic aberration in electron lens spectrometers, p. 177. **7.3.** Relativistic aberration, p. 189. **7.4.** Space charge error, p. 191. **7.5.** Diffraction error, p. 192. **7.6.** Combination of aberrations, p. 196.

CHAPTER VIII

Electron Optics and Space Charge

8.1. Spreading of a homogeneous, homocentric beam, p. 199. **8.2.** Focus spread and focus shift. Space charge equivalent lens, p. 207. **8.3.** Aberrations of the space-charge-equivalent lens. Beam spreading under extreme conditions, p. 210. **8.4.** Space charge in interaction with electrodes and electron lenses, p. 216. **8.5.** Space charge and positive ions, p. 219. **8.6.** Balancing of space charge pressure by external fields, p. 222. **8.7.** Use of the electrolytic trough for field plotting in presence of space charges, p. 225. **8.8.** Minimum in the potential distribution along the beam. The virtual cathode, p. 229.

CHAPTER IX

Emission Systems

9.1. The acceleration of the emitted electrons, p. 237. **9.2.** Fields and electron orbits in emission systems. Cross-over formation, p. 241. **9.3.** Optical approach to emission systems, p. 247. **9.4.** Aberrations in emission systems, p. 251. **9.5.** Beam intensity modulation, p. 259. **9.6.** Design of triode systems, p. 264. **9.7.** Multielectrode systems, p. 275.

CHAPTER X

Electron Lenses and Emission Systems with Line Focus

10.1. Focusing by two-dimensional fields. Terminology, p. 282. **10.2.** Field plotting and ray tracing. Computational mapping, p. 283. **10.3.** 'Two-dimensional' electrostatic line-focus lenses, p. 289. **10.4.** Some practical lenses with line focus, p. 292. **10.5.** Space charge effects in ribbon-shaped beams, p. 300. **10.6.** Emission systems with line focus, p. 302. **10.7.** Some practical line-focus emission systems, p. 306. **10.8.** Magnetic lenses with line focus, p. 314.

CHAPTER XI

Deflecting Fields

11.1. Optical approach, p. 320. **11.2.** Homogeneous weak deflecting fields, p. 321. **11.3.** Practical electrostatic deflexion systems, p. 325. **11.4.** Practical magnetic deflexion systems, p. 332. **11.5.** Focusing deflexion in electrostatic fields, p. 336. **11.6.** Focusing deflexion in magnetic fields, p. 344. **11.7.** Superposition of electrostatic and magnetic fields, p. 356. **11.8.** Deflexion errors, p. 363. **11.9.** Deflexion-focusing errors, monochromatic linewidth and field correction, p. 367. **11.10.** Dispersion, resolving power and collecting power of focusing deflexion fields, p. 373.

CHAPTER XII

Application of Electron Optics in Industry and Research

12.1. Introduction, p. 380. **12.2.** Cathode ray oscillographs, p. 381. **12.3.** Television, p. 385. **12.4.** Photo-multipliers, p. 393. **12.5.** Image tubes, p. 396. **12.6.** Electron microscopes, p. 401. **12.7.** Electron spectrometers, p. 408. **12.8.** Electron accelerators, p. 418. **12.9.** Electron optics in thermionic valves, p. 427. **12.10.** More applications of electron optics, p. 433.

APPENDIX: Tables 438

BIBLIOGRAPHY: A. List of General Works 443
B. Special References 443

INDEX 461

PLATES

Tobacco mosaic virus, shadowed with palladium *facing* p. 407

Aluminium oxide replica of aluminium surface, etched with hydrochloric acid and deformed *facing* p. 408

AUTHOR'S PREFACE

The aim of this monograph is to give a concise account of the most important principles, methods and applications of geometrical electron optics. The monograph represents a second edition of a relatively small tract which was written in 1938 when the subject of electron optics was still at an early stage of development. Less than 100 references were quoted in this first edition, and about 100 pages appeared to be adequate for presenting an account of the most essential knowledge of those days. In the meantime the subject has greatly expanded. In order to give a balanced account of the present state of development it seemed necessary to select from the great wealth of the available literature about 500 papers for reference and to expand the volume to about 450 pages which this new edition comprises.

The present book is intended to serve a twofold purpose: first, to introduce the student to a specialized subject, and secondly, to present the research worker or the designer of electron optical gear with all the basic principles and the most essential quantitative information on the subject and to be a guide to that literature where all available details can be found. The two purposes are complementary, since the specialized parts of the book which will be needed by the designer serve as illustrations of the more general expositions which are addressed to the student. The expert will find many items which have been described in patent specifications only, and various other items which have not been published at all in the literature.

Selection, arrangement and presentation of the material have been made according to the personal experience of the author, who has worked for 11 years in charge of electron optical developments in industry and who has spent another 20 years at various universities engaged in teaching and research on electron physics. The book is concerned primarily with the experimental aspect of the subject. It should be intelligible both to the advanced student of general physics and to the research worker who has not specialized either in geometrical optics or in electron physics.

The first five chapters give an outline of principles and facts

about electron lenses. Similar expositions may be found in other books on electron optics (cf. 'List of General Works' in the bibliography at the end of this book). Chapters VI–XI differ from the usual presentation. Lens errors (Chapters VI and VII) are discussed here from an essentially experimental point of view. Chapters VIII, IX and X expound the subject of 'Space charge and electron optics', 'Emission systems' and of 'Electron lenses and emission systems with line focus'. To the author's knowledge these subjects have so far not been reviewed adequately elsewhere. Chapter XI gives an account of the deflecting fields; this includes a discussion of focusing deflexion, a rapidly developing subject which is of much interest in the spectrometry of corpuscular rays. Finally, Chapter XII contains a short survey of important applications of electron optics in industry and in research. The system of rationalized m.k.s. units has been adopted throughout the book.

O. K.

ACKNOWLEDGEMENTS

The author has much pleasure in thanking his friends and colleagues, Mr N. C. Barford, Dr M. Blackman and Dr H. H. Hopkins who have read various parts of the manuscript, and Dr W. Weinstein who has read the proofs. They all have made valuable suggestions for improvements.

Thanks are due to the following authors, publishers and learned bodies for permission to reproduce figures from books and journals. *Arch. Elektrotech.* for figs. 5.8, 5.9, 6.13, 6.22; *Ark. Mat. Art. Fys.* (Stockholm), 11.14; Barth, *Ann. Phys.* 9.7; Dr C. S. Bull and the Controller of Her Majesty's Stationery Office, 10.20; Controller, H.M.S.O., 10.7, 10.8, 10.9, 10.10, 10.11; the Clarendon Press and Dr V. E. Cosslett, 5.7, 10.17, 11.16; Messrs Chapman and Hall and Dr B. Lovell, 10.19; *Elect. Comm.* 4.3; *Fiat Rev. German Sci. Elect.* 12.6, 12.7, 12.8; Professor L. M. Field, 9.14; *J. Appl. Phys.* and Messrs J. Hillier and E. Ramberg, 3.2, 5.14, 6.2; *J. Brit. Inst. Radio Engrs* and Dr H. Moss, 9.9, 9.10; *J. Instn Elect. Engrs*, 9.8, 9.13, 12.2, 12.22, 12.23; *J. R. Micr. Soc.*, Dr D. G. Drummond, Mr H. L. Nixon and the Rothamsted Experimental Station, 12.13, 12.14; *Naturwissenschaften*, 7.4; *Optik*, 6.17, 6.18, 7.5, 9.16; L. Marton, 5.7; G. A. Morton, 9.17; J. R. Pierce, 3.2; Dr J. H. Reisner, 5.14; Dr A. Sommer, 12.5; Professor K. Spangenberg, 4.3; Springer Verlag, 12.12; Dr J. S. Thorp, 10.14; John Wiley and Sons Inc., 3.2, 6.13, 6.14, 6.24, 11.15, 12.9, 10.18; *Z. Phys.* 6.7, 6.9, 9.6; *Z. tech. Phys.* 11.17.

O. K.

CHAPTER I

HISTORICAL INTRODUCTION. THE FUNDAMENTAL PRINCIPLES OF ELECTRON OPTICS

1.1. Historical development

Electron optics is a relatively new field of science, although neither the method, nor the subject which is attacked by the method, is new. The method is that of geometrical optics, which was developed by several generations of physicists. Before the advent of electron optics, the motion of electrons had been studied in many experimental and theoretical investigations; but in all these either the ballistic or the electrodynamical viewpoint was adopted.

The birth of the subject of electron optics may be said to have occurred in 1926, when H. Busch showed that the action of a short axially symmetrical magnetic field on electron rays was similar to that of a glass lens on light rays. In 1931 and 1932, C. J. Davisson and C. J. Calbick, and independently E. Brüche and H. Johannson, recognized that axially symmetrical electrostatic fields could also be used as 'electron lenses'. The use of electron lenses for the projection of extended electron images was developed, first by M. Knoll and E. Ruska (1931), who worked mainly with magnetic lenses, then by E. Brüche and his collaborators (1934), who worked mainly with electrostatic lenses and subsequently by many others. Up to 1939, electron optics experienced a rapid development, induced by a strong industrial need. Large companies which were especially interested in building up and producing a television technique of electronics employed considerable staffs of scientific workers who were engaged to an appreciable extent with fundamental research on electron optics. Thus the research laboratories of Electric and Musical Industries in England, of the R.C.A. in U.S.A., of Telefunken and A.E.G. in Germany, and of Philips in Holland, have played a prominent part in the early development of electron optical science.

A detailed study of electron optical problems has also been taken up in connexion with electron microscopes of great magnification. The first working model of such an instrument was built by Knoll and Ruska (1932*a*). Then the technical development of the electron microscope was taken up by industrial firms; first in the field were Siemens and A.E.G. in Germany, Radio Corporation and General Electric in U.S.A. and Metropolitan Vickers in England.

During the 1939–45 war, electron optics again received strong stimulation through practical requirements. Thus, new types of cathode-ray tubes were developed for Radar purposes and image-converter tubes were developed for infra-red vision. Most important, however, was the evolution of klystron and magnetron tubes for production of high-frequency electromagnetic waves. The need for improvement of these tubes stimulated the development of electron optics in the region of great space-charge densities.

The most recent growth of electron optics has been stimulated by the demands of nuclear physics. Investigation of nuclear energy levels required the development of electron spectrometers of great resolving and collecting power, and the recently emerging technique of particle acceleration by betatrons, synchrotrons, etc., favoured the development of electron optics in the relativistic region of highest electron velocities.

1.2. Variation principles and the refractive index of an electron*

The fundamental theory of electron optics is based on Hamilton's conceptions of the identity of the optical description of the path of a light ray through refractive media and the mechanical description of the motion of a mass point through a potential field. These general conceptions were presented as early as 1828–37; they originally started from a comparison of Fermat's principle of least time (about 1650) as applied to the path of a light ray, with Maupertuis's principle of least action (1744) as applied to any mechanical movement.

For conservative forces, the action a is given by the line integral of the momentum p of the particle along its path s between two

* A reader who is primarily interested in the practical aspect of electron optics may omit §§ 1.2–1.4 and continue his perusal from § 2.1.

points P and P', namely, by

$$a = \int_P^{P'} p \, \mathrm{d}s. \tag{1.1}$$

For an electron, the momentum is given by

$$p = m u_{el},$$

where u_{el} is the velocity of the electron. According to Maupertuis's principle, the action integral must be a minimum, i.e. its variation must vanish. In this case the electron proceeds along a line of least action, and the number of Joule seconds (compare with the everyday term 'number of man-hours') is a minimum.

On the other hand, the time of transit for a light ray travelling from a point P to a point P' can be expressed by

$$t = \int_P^{P'} (\bar{N}/c) \, \mathrm{d}s, \tag{1.2}$$

where the refractive index, $\bar{N}$, is usually defined as

$$\bar{N} = c/u_{ph}, \tag{1.3}$$

i.e. as the ratio of the velocity *in vacuo*, c, and the phase velocity u_{ph}, of the light wave. According to Fermat's principle, expression (1.2) must be a minimum, i.e. its variation must vanish. In other words, the ray proceeds along a line of 'fastest arrival'.

Hamilton developed his theory from the close relationship between wave and particle that follows from the comparison of (1.1) and (1.2), but he did not, of course, know the concept of an electron. The subject of electron motion did not come into existence until 60 years later (J. J. Thomson, W. Kaufmann, 1897), and yet another 30 years had to elapse before the development of the optics of electron rays was started.

A comparison of Fermat's and Maupertuis's principles suggests that the path of the electron is identical with the path of a wave if

$$\bar{N} \propto u_{el},$$

i.e. if the refractive index of a medium is assumed to be proportional to the electron velocity. In another way a definition of the refractive index for the electron is derived from the relation between its phase velocity and particle velocity

$$u_{ph} \times u_{el} = c^2, \tag{1.4}$$

which was established in 1924 by De Broglie. It is convenient (cf. Zworykin *et al.* 1945) to define a dimensionless refractive index by combining (1.4) with (1.3) which leads to

$$\bar{N} = u_{el}/c. \tag{1.5}$$

In practice it is useful to express the refractive index of an electrostatic field by the electron energy in electron-volts. There, the potential V is connected with the velocity of an electron of mass m and charge* $-e$ by the principle of conservation of energy which can be written

$$\tfrac{1}{2}m u_{el}^2 - eV = 0, \tag{1.6}$$

if $u_{el} = 0$ for $V = 0$. Substitution for u_{el} in (1.5) from (1.6) yields

$$\bar{N} = k_1 \sqrt{V}, \tag{1.7}$$

where $k_1 = (1/c)\sqrt{(2e/m)} = 1{\cdot}978 \times 10^{-3}$ [sec./m.] is a constant. Since the presence of constants does not change the significance of the variation principles, (1.1) and (1.2), the constant k_1 may be disregarded and a practical refractive index of the electron may be expressed directly in electron-volts, namely, by

$$N = \bar{N}/k_1 = \sqrt{V}. \tag{1.8}$$

Care has to be taken in the labelling of the zero voltage level. For problems connected with cathode-ray tubes for instance, it is quite usual to assume the cathode potential as the zero level. If the cathode is actually connected to earth, the voltage V of any equipotential as measured against earth potential leads very approximately to the right refractive index $\sqrt{V}$. Greater accuracy, however, would be obtained if the cathode potential were taken not as zero but as $V_c = V_{em}$, i.e. equal to the emission energy of the electron which, for an oxide cathode, is of the order of 0·1 eV. For electrons from a radioactive source, the emission energy V_{em} is considerable. If the source is at earth potential, the refractive index at any equipotential is given by

$$N = \sqrt{(V + V_{em})}, \tag{1.9}$$

* Note the negative sign: in the greater part of electron optical literature and throughout this book the symbol e is used for the absolute value of the electronic charge.

where V is the voltage difference of the equipotential as measured against earth potential.*

(1·8) may be illustrated by the elementary example shown in fig. 1.1. There, a beam travelling through a medium with a refractive

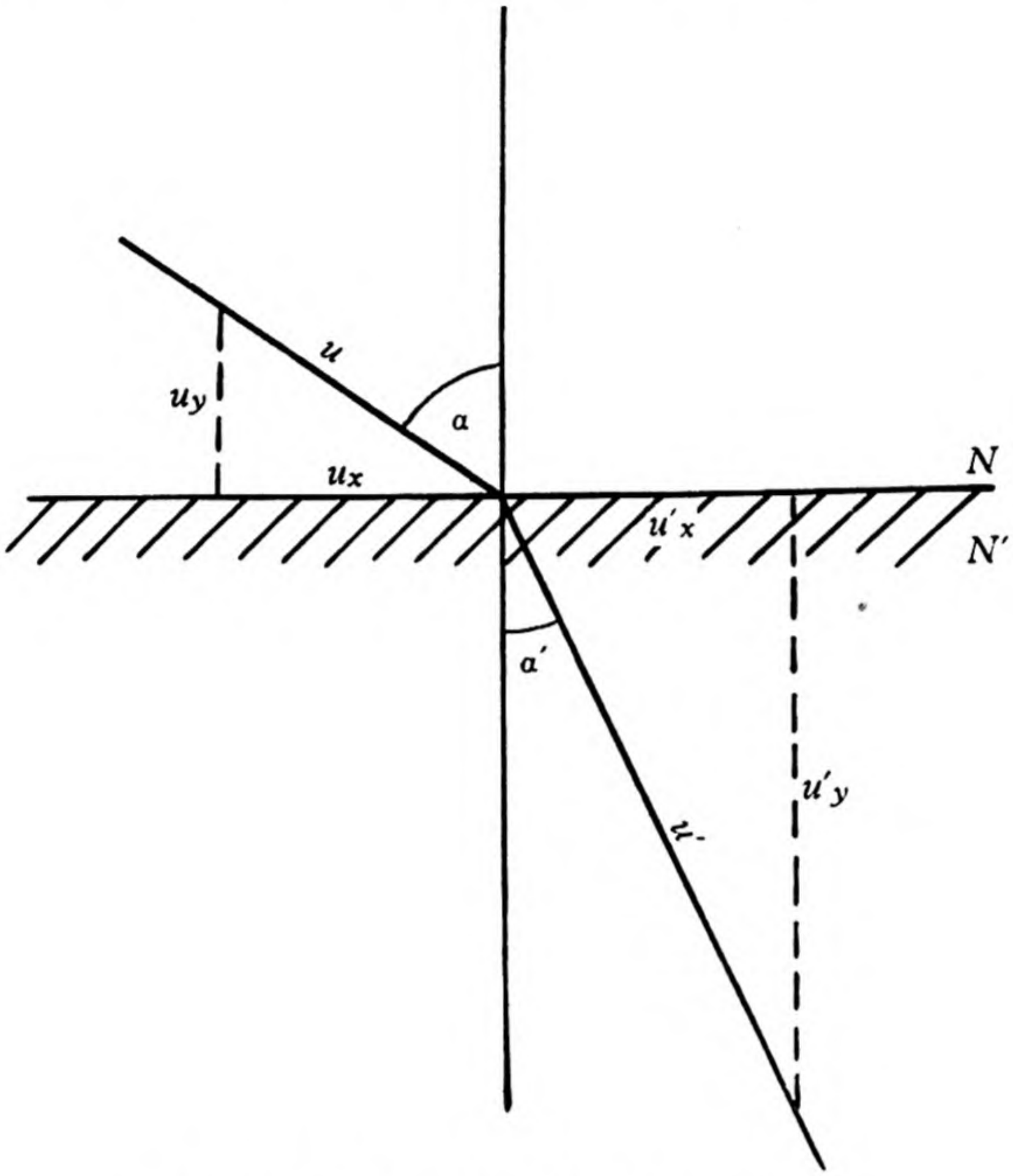

Fig. 1.1. Refraction of an electron beam.

index N passes into another medium with a refractive index N'. The angle of incidence α and the angle of refraction α' are connected by Snell's law:

$$N \sin \alpha = N' \sin \alpha'. \qquad (1.10)$$

This optical law may be interpreted mechanically in the way which Newton used to explain the refraction of light at a glass surface.

* In electron diffraction theory, the refractive index of a crystal is usually written as

$$N = \sqrt{E/(E - W_i)},$$

where E is the kinetic energy of the electron in vacuo and W_i is the 'internal potential' of the crystal. In our notation the potential outside the crystal with respect to the electron source is $V_0 = E/e$, hence $W_i = e(V_0 - V_i)$ and

$$N = N_0/N_i = \sqrt{(V_0/V_i)}.$$

Suppose an electron travelling with uniform speed u through a space of constant potential V passes a potential step into a space with another homogeneous potential V', so that the path of the electron suddenly changes its direction. Assuming, as in fig. 1.1, that the potential V' is greater (positively) than V, the normal velocity component of the electron u_y is increased and the electron is accelerated. The tangential component u_x remains unchanged, so that $u_x = u'_x$. Now, according to (1.6) the velocity of the electron is proportional to the square root of the potential. Moreover,

$$\sin\alpha = u_x/u,$$

$$\sin\alpha' = u'_x/u'.$$

Therefore

$$\frac{\sqrt{V}}{\sqrt{V'}} = \frac{\sin\alpha'}{\sin\alpha}. \qquad (1.11)$$

Comparison of (1.11) and (1.10) leads again to the fundamental equation, (1.8).

For high electron velocities (1.8) becomes inaccurate because of the relativistic increase of the mass of the particle. According to (1.1), a suitable definition of the refractive index of high-speed electrons is given by the momentum $p = m u_{el}$. In order to conform with the definition of the refractive index $\bar{N}$ given by (1.5), the momentum may be divided by $p_0 = m_0 c$, where m_0 is the rest-mass of the electron and c the velocity of light *in vacuo*.

It is often convenient to express the momentum of the electron by the product $B_e r_e e$, where r_e is the radius of curvature of the electron path in a field of flux density B_e. The refractive index is then

$$\bar{N} = \frac{p}{p_0} = \frac{eB_e r_e}{m_0 c} = 0{\cdot}586 \times 10^3 B_e r_e = 1{\cdot}978 \times 10^{-3} V_r^{\frac{1}{2}} \qquad (1.12)$$

The expression $B_e r_e = p/e$ is called the 'electron-momentum' or the 'magnetic rigidity' of the electron ray.*

$$V_r = V[1 + eV/(2mc^2)] = V(1 + 0{\cdot}978 \times 10^{-6} V), \qquad (1.13)$$

is the relativistically corrected electron voltage, hence the last part of (1.12) becomes identical with (1.7) for small electron velocities.

* The electron momentum is very frequently denoted in the literature by the letters $H\rho$. Here, the use of $B_e r_e$ has been adopted since the letter ρ was reserved for the space charge density, and B was preferred to H since the deflexion of an electron is effected by the flux density B rather than by the field H.

One principal difference between the great majority of light-optical and electron-optical refractions should be mentioned. Light rays are generally refracted by a finite number of refracting surfaces where the refractive index changes suddenly, whereas in electron-optical arrangements the refractive index changes continuously along the path of the electron. However, this difference is not an important obstacle in the application of practical light-optical methods to electron-optical problems. It is always possible to divide the range of continuously changing potential into a finite number of steps of an assumed constant potential corresponding to a finite number of sheets, each of constant refractive index. It can, for instance, be shown that the path of an electron may be traced through an electrostatic electron lens by a repeated application of Snell's law. In this case, a theoretical splitting up of the continuously varying field into a finite number of steps is sufficient to obtain results of high accuracy.

The magnitudes of refractive indices with which we have frequently to deal in electrostatic lens systems would never occur in glass optics. For instance, in an electron microscope, electrons may be emitted from the cathode with 0·1 eV, but they reach the screen with 100 keV. The corresponding ratio

$$\frac{N}{N'} = \sqrt{\frac{10^5}{0{\cdot}1}} = 10^3 \tag{1.14}$$

would be quite unheard of in glass optics, since the highest refractive indices occurring in commercial glass lenses are below $N = 2$.

The optical description of the motion of an electron in a magnetic field is not as obvious as it is in an electrostatic field. In the presence of magnetic fields, Maupertuis's principle ceases to be applicable since the force on the electron is non-conservative, i.e. it cannot be expressed as the derivative of the potential energy of the electron in this field. The magnetic flux density B exerts a force at right angles to the electron velocity u and so has no effect upon the kinetic energy. Schwarzschild (1903) has formulated a variation principle according to which the expression

$$\int_P^{P'} (p - eA\cos\gamma)\,\mathrm{d}s \tag{1.15}$$

has to become a minimum. A is the magnetic vector potential defined* by the vector equation

$$B = \operatorname{curl} A, \tag{1.16}$$

and γ is the angle between A and the path element ds. Comparing Schwarzschild's and Fermat's principles, it appears that the refractive index in the magnetic field is given by

$$\bar{N} = \frac{e}{m_0 c}\left[\sqrt{\left(\frac{2V}{e/m}\right)} - A\cos\gamma\right]. \tag{1.19}$$

Again, since only relative values matter, one can take

$$\begin{aligned} N &= \sqrt{V} - \sqrt{(e/2m)}\, A\cos\gamma \\ &= \sqrt{V} - 2{\cdot}966 \times 10^5 A\cos\gamma, \end{aligned} \tag{1.20}$$

where V is measured in volts and A in Webers/metre. According to (1.20), N depends upon $A\cos\gamma$, i.e. the scalar product of the vectors A and ds. Thus N depends not only on the position, but also upon

* The mathematical definition of the vector potential may be found in text-books on vector theory. A physical picture for the distribution of the vector potential A in a magnetic field in which the flux density B is known (say, from search-coil measurements) can be gained from the fact that A is related to B in the same way as B is related to the generating current density i. Thus the B-lines may be represented by electric currents. The magnetic lines of flux density produced by these currents will show the direction and magnitude of A.

The determination of numerical values for A is complicated. In order to show how particular numerical values for A may be determined from a simple flux-density distribution, (1.16) may be written in cylindrical coordinates (z, r, ϕ) as follows:

$$\left.\begin{aligned} B_z &= \frac{1}{r}\left[\frac{\partial(rA_\phi)}{\partial r} - \frac{\partial A_r}{\partial \phi}\right], \\ B_r &= \frac{1}{r}\frac{\partial A_z}{\partial \phi} - \frac{\partial A_\phi}{\partial z}, \\ B_\phi &= \frac{\partial A_r}{\partial z} - \frac{\partial A_z}{\partial r}. \end{aligned}\right\} \tag{1.17}$$

Thus for the homogeneous field $B_z = \text{const.}$, (1.17) can yield

$$A = A_\phi = \tfrac{1}{2}B_z r. \tag{1.18}$$

In this case, the numerical value of the vector potential equals half the electron-momentum value of an electron rotating about the z-axis (cf. $B_e r_e$-values, Appendix, table A.4). Further explanations will be given in Chapters V and X.

the direction of the motion of the electron. Under the influence of the magnetic field, the electron performs a spiralling motion in space so that the optical analogy appears to be rather complicated. (For a full discussion of the refractive index in the magnetic field, cf. Glaser (1933*a*, 1951), Opatowski (1944) and Ehrenberg and Siday (1949).)

For electron motion in magnetic fields we have no general, simple scalar potential which can easily be visualized by obvious analogies such as that of a little ball rolling on a curved surface. However, it will be pointed out in Chapter V that for axially symmetrical arrangements the problem can generally be reduced to a two-dimensional one by tracing the movement of the electron in a meridional plane which rotates, together with the electron, round the axis of its spiralling motion. In this meridional plane there can be defined a 'meridional potential' which is easily derived from the vector potential of the magnetic field. It will be explained that the electron is refracted at the equipotentials of this meridional potential in essentially the same manner as at the equipotentials of the electrostatic field.

Discussing the electron-optical problem under the most general conditions, we may ask whether the refractive index defined by (1.20) fully covers all contributions to the refraction of the electron beam in an electromagnetic field. The answer may readily be derived from Maxwell's equations from which the following integral form can be obtained:

$$F = e\,(\operatorname{grad} V - [u \times \operatorname{curl} A] - \partial A/\partial t), \qquad (1.21)$$

where F is the total force acting on the electron. This is the well-known Lorentz equation which is particularly convenient for electron-optical considerations, as it shows clearly the sort of potentials acting on the charge of the electron. The force F is composed of three parts. The first is the Coulomb force or electrostatic force due to the action of the electrostatic potential. The second part is the Lorentz force or the electrokinetic force due to the motion of the electron in a stationary magnetic potential field, while the third part is Faraday's electrotonic force due to the retardation of potentials or to the finite velocity of propagation of the fields caused by rapidly moving charges. Since we shall consider here stationary conditions

only, the electrotonic forces may be ignored, and the refractive index for the electron beam can be obtained by superposition of the electrostatic and the magnetostatic effects as in (1.20).

1.3. Image formation by collinear projection

At this stage it may be asked whether there is any advantage in discussing the action of potentials on electrons from the optical point of view, since at first sight, such a discussion might appear to be no more than a modern analogy for talking about an old problem. To take a simple example, there is certainly not much point in speaking of refractive indices instead of electric potentials, nor is there any advantage in calling a homogeneous electric or magnetic deflecting field an 'electric prism' or a 'magnetic prism'.

The advantages of the optical approach as compared with the ballistic or with the electrodynamic treatment of electron motion become evident when we deal with axially symmetric fields. Every electric or magnetic field of circular symmetry has the properties of a lens (cf. Chapters III and V), i.e. it can project an optical image. This implies that we can obtain important parts of the electron path by considering two regions outside the particular refracting fields, the 'object space' and the 'image space'. A knowledge of only six points of the field, i.e. of the 'cardinal points' of the lens (which may be obtained, for example, by simple experimental procedure), is sufficient for predicting the paths of the electrons after their passage through even the most complicated electric and magnetic fields.

Object and image space are quite generally connected by a mathematical relationship of three linear equations (cf. Drude, 1925). This collinear relationship reduces to a relatively simple form in the case of circular symmetry. There, we need investigate the image formation only in a meridional section. Taking y and z as the radial and the axial coordinates respectively, we have the following relations between the object space (y, z) and the image space (y', z'):

$$\left.\begin{aligned} z' &= \frac{az+b}{cz+d}, \\ y' &= \frac{ey}{cz+d}. \end{aligned}\right\} \tag{1.22}$$

The five constants a, b, c, d, e determine the relative positions of the six cardinal points. The plane $cz+d=0$ of the object space is, according to (1.22), conjugate to an infinitely distant plane in the image space. It is called the focal plane and cuts the axis in the focus F. Similarly, a focus F' is defined in the image space. By placing the origins of the z and z' coordinates at the foci F and F' respectively, new axial coordinates

$$x = z + \frac{d}{c},$$

$$x' = z' - \frac{a}{c}$$

are obtained. Moreover, if we introduce the abbreviations

$$\left.\begin{aligned} f &= e/c, \\ ff' &= \frac{cb-ad}{c^2}, \end{aligned}\right\} \tag{1.23}$$

we obtain

$$xx' = ff', \tag{1.24}$$

and

$$\frac{y'}{y} = \frac{f}{x} = \frac{x'}{f'}. \tag{1.25}$$

f and f' are called the focal lengths in the object and in the image space respectively, (1.24) is Newton's lens equation and the ratio y'/y is called the magnification. For all points of the plane $x=f$ of the object space to which the plane $x'=f'$ in the image space is conjugate, this ratio is unity according to (1.25). These planes are called principal planes. Every ray passes these two planes at equal radial distances from the axis. Consequently if a ray intersects the axis at x and again at x' making the angles Θ and Θ' with it in object and image space respectively,

$$\frac{\tan\Theta'}{\tan\Theta} = \frac{x+f}{x'+f'}$$

or from (1.24)

$$= \frac{f+x}{f'+ff'/x} = \frac{f+x}{f'(x+f)} = \frac{x}{f'}, \tag{1.26}$$

and from (1.25)

$$fy\tan\Theta = f'y'\tan\Theta'. \tag{1.27}$$

The conjugate points on the axis for which $\Theta=\Theta'$ are called the nodal points; they are the third pair of cardinal points in addition

to the foci and to the principal points. The necessity for considering the general type of object-image relation is given by the fact that all electron lenses are fundamentally 'thick lenses'. A full discussion of the use of the cardinal points in the construction of optical paths and of their determination in practice will be found in Chapter II.

1.4. The physical problem of image formation

It is a very important fact that (1.27), which is derived from purely mathematical principles, can be applied in physics to paraxial rays

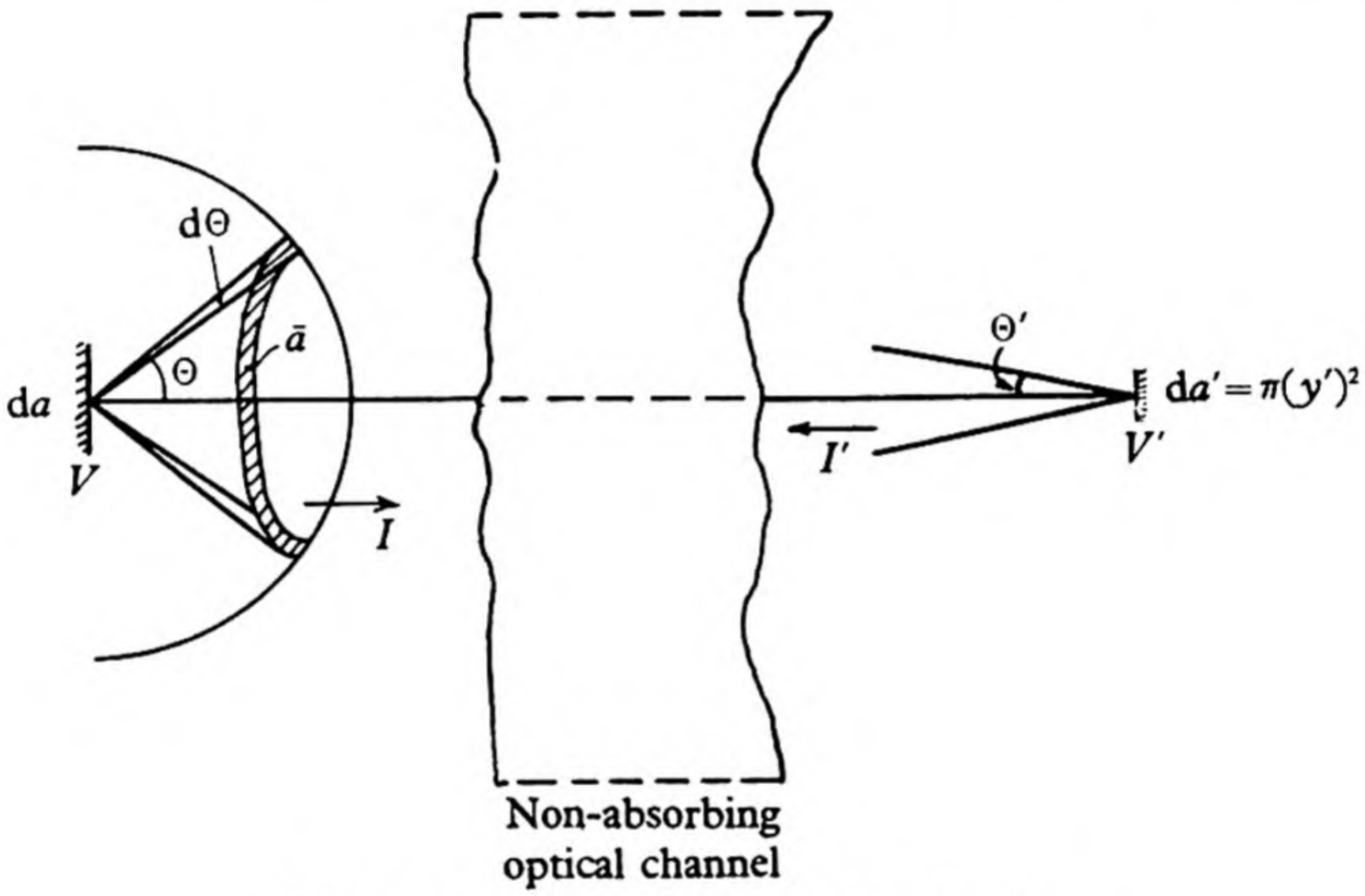

Fig. 1.2. Derivation of Abbe's sine law.

only, i.e. only to rays which are close to the axis and make with it a very small angle Θ. For wide beams, the image formation for an element of area is no longer collinear. A correct point-by-point imaging of objects of any size by widely diverging beams is physically impossible. This statement applies to electron optics in the same sense as it applies to light optics, as can be shown in various ways. We shall present here a thermodynamical discussion of the electron optical problem which only slightly differs from the usual treatment for electromagnetic rays found in standard optical text-books (cf. Drude, 1925).

Let (cf. fig. 1.2) da and da' be two surface elements of equal physical properties. da' may represent the optical image of da formed by a bundle of rays which are symmetrical to the normal to

da and have an angle of semi-aperture Θ in the object space and Θ' in the image space. Now the total emission by da within the bundle under consideration must fall upon da', and inversely da' must radiate upon da since the rays denote the path of the energy flow. Both surfaces are considered to be originally at the same temperature, and no difference in temperature between da and da' can arise because of the radiation. Hence the flow of energy $VI(\Theta)$ [Watts] emitted from da must be equal to the flow of energy $V'I'(\Theta')$ received back from da', i.e.

$$VI(\Theta) = V'I'(\Theta'), \tag{1.28}$$

where V and V' are the potentials and $I(\Theta)$ and $I'(\Theta')$ the electron currents at the source and at the image surface respectively.

According to Lambert's law the emission density in any direction is proportional to the cosine of the angle Θ with the normal, and it is given by

$$i_\Theta = \frac{i_{em}}{\pi}\cos\Theta, \tag{1.29}$$

where i_{em} is the total emission per unit area into the hemisphere. Hence, the emission from the area da into the angular interval between Θ and $\Theta + \mathrm{d}\Theta$, i.e. towards a ring area $\bar{a} = 2\pi\sin\Theta\,\mathrm{d}\Theta$ on the unit sphere, is given by

$$\mathrm{d}I(\Theta) = i_\Theta\,\mathrm{d}a\,\bar{a} = \frac{i_{em}}{\pi}\cos\Theta\,\mathrm{d}a\,2\pi\sin\Theta\,\mathrm{d}\Theta. \tag{1.30}$$

The emission from a circular area of radius y ($\mathrm{d}a = \pi y^2$) into the full cone of semi-vertical angle Θ is obtained by integration of (1.30), namely,

$$I(\Theta) = \int_0^\Theta \mathrm{d}I(\Theta) = i_{em}\,\pi y^2\sin^2\Theta, \tag{1.31}$$

and a corresponding expression

$$I'(\Theta') = i_{em}\,\pi(y')^2\sin^2\Theta' \tag{1.32}$$

is obtained for the emission from the image. The emission density i_{em} is the same in both cases, since both surfaces are identical and of the same temperature. Substituting now (1.31) and (1.32) into (1.28) and bearing in mind that according to (1.8) the refractive

index is given by $N = \sqrt{V}$, one obtains

$$Ny \sin \Theta = N'y' \sin \Theta'. \tag{1.33}$$

This is the well-known sine law. It was derived from thermodynamical principles first by Clausius (1863) and later found independently and discussed extensively by Helmholtz (1873). The full importance of this law in optics, especially in the theory of lens errors, was realized by Abbe (1873), and it is generally quoted under his name in the literature. The general validity of Abbe's sine law in electron optics is emphasized here by the presentation of a thermodynamical derivation based on general principles and not requiring any special assumptions on the shape of refracting surfaces, etc.

In electron optics, just as in glass optics, Abbe's sine law implies that the image formation for an element area can be collinear for narrow bundles of rays with small aperture Θ only. Now, since

$$\sin \Theta = \Theta - \frac{\Theta^3}{3!} + \frac{\Theta^5}{5!} - \cdots, \tag{1.34}$$

(1.33) may be reduced by neglecting higher order terms to

$$Ny\Theta = N'y'\Theta'. \tag{1.35}$$

This is called Lagrange's law. A comparison of (1.35) with (1.27) leads to the conclusion that

$$\frac{f}{f'} = \frac{N}{N'}. \tag{1.36}$$

Moreover, according to this comparison of (1.35) with (1.27) the collinear projection provides a satisfactory approximation to the physical image formation if Θ is small so that $\sin \Theta \approx \tan \Theta \approx \Theta$, i.e. if $\sin \Theta$ is approximated accurately enough by the first term of (1.34). The treatment based on this approximation is called 'Gaussian optics' after its originator. Alternatively, it is called 'first-order theory' as distinguished from a more rigorous 'third-order theory' which attempts to include the second term of the sine series (1.34).

The explanations given in the last two sections illustrate the essential character of the optical method for the study of electron

orbits. It is seen that the optical method consists in the investigation of systems of rays, i.e. of a 'collective' of paths. Optical properties apply to this collective, e.g. to foci, to principal planes, etc., while mechanical properties apply to individual paths.

It is, however, immaterial how the optical properties of a system are derived, whether with the help of optical or ballistic or electrodynamic or thermodynamic methods, and in the following chapters we shall make use of all available methods in a complementary manner and according to best convenience.

CHAPTER II

THE CARDINAL POINTS OF AN ELECTRON LENS

2.1. Location of cardinal points by ray tracing with a sliding target

A true optical image is formed if every point of the image space corresponds to a conjugate point of the object space. Straight lines, connecting two points, are in the ideal case reproduced as straight lines, and planes are reproduced as planes. According to § 1.3, such image formation can be effected near the axis of a refracting system of circular symmetry. There, the relationship between object and

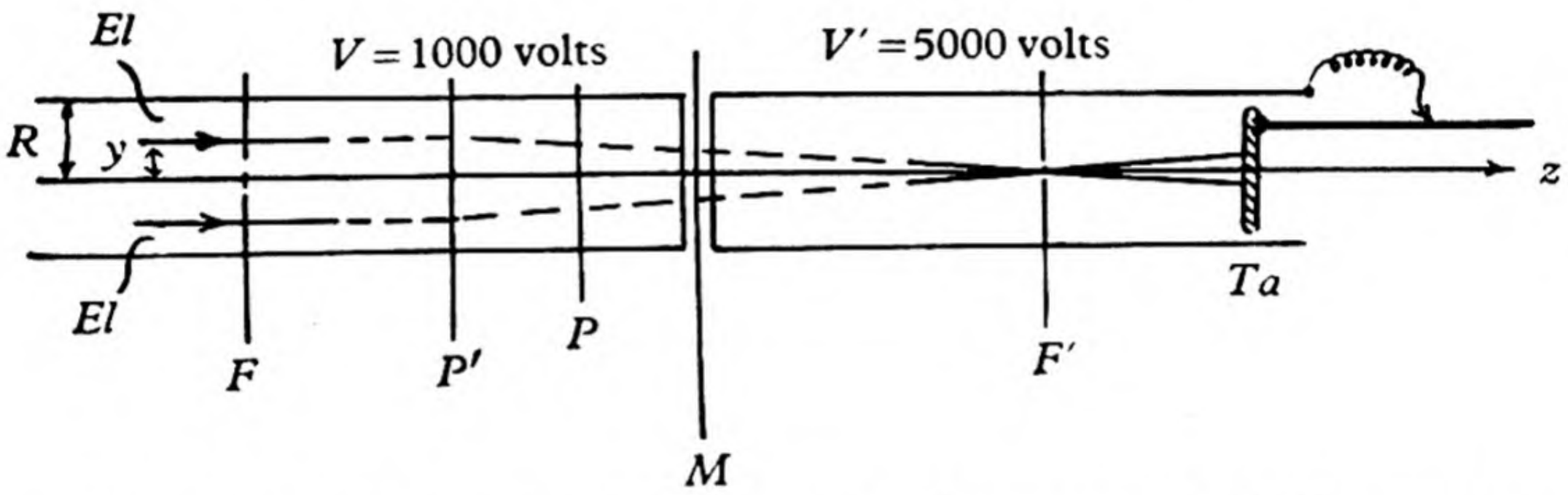

Fig. 2.1. Investigation of an electron lens by means of a sliding target.

image space can be defined completely by the location of six points. These are the two focal points, the two principal points and the two nodal points. We shall start with an explanation of these points in the case of the simplest electron lens. We shall also discuss how these points can be located experimentally and how the knowledge of their position can be used for practical purposes.

The simplest arrangement acting as an electron lens consists of two coaxial metal tubes which are kept at different electrostatic potentials. In fig. 2.1 are shown two tubes of equal diameter, the left at the lower electric potential V, the right at a higher potential V'. In order to specify a concrete example, we shall assume that $V = 1000$ volts and $V' = 5000$ volts. Both tubes lie symmetrically about an ideal plane, the so-called midplane of the system, cutting the axis of circular symmetry (the z-axis) at the point M. By

a special arrangement, which will not be described at the moment, electron beams *El*, travelling exactly parallel to the z-axis, are transmitted through the tubes. These electrons are gradually accelerated from the lower potential V to the higher potential V', and in passing through the electric field they are also gradually deflected. The path of the beams can be investigated by means of a small target *Ta* which is covered with fluorescent substance. This target is kept at the potential V' of the second tube and can be moved along the axis of the tube. All points where the electron beams hit the target are visible by fluorescence, so that the distances of the beam from the z-axis can be everywhere determined. To avoid disturbances of the field of the lens, the target should be kept outside the lens, i.e. in the field-free space where the electrons travel along perfectly straight lines. The path of the beams inside the lens is actually curved. The straight, broken lines drawn in fig. 2.1 are obtained by extrapolation of the measured parts of the paths.

It will be noticed that the electron beams intersect at one point, the focus F'. Extrapolating the straight part of a traced electron beam backwards until it cuts the prolongation of the original parallel beam one finds the principal plane, which intersects the axis in the principal point P'. Assuming parallel beams starting from the high-voltage side of the lens (i.e. coming from the right side of fig. 2.1), the electrons would be decelerated and focused at a point F. The intersection of the extrapolated original parallel beam and the extrapolated final direction would show the other principal point P. Thus, by this simple experiment, there can be found four cardinal points, P, P' and F, F', of the electron lens. The two remaining points are the nodal points K and K'. They lie in the same direction as the principal points with reference to the respective focal points, but are shifted by the difference between the numerical values of the two focal lengths, thus

$$\left.\begin{aligned} KF &= PF + |\,P'F' - PF\,| = P'F', \\ K'F' &= PF. \end{aligned}\right\} \tag{2.1}$$

Therefore if the focal points and the principal points are obtained experimentally, the nodal points can be located by an easy procedure. For a general estimate of the position of the cardinal points

it may be helpful to notice that for all two-electrode lenses, both principal points lie on the same side of the midplane, namely, at the low-voltage side where the refractive index is small. The principal points as well as the nodal points are crossed over with respect to their appropriate focal points.

2.2. Geometrical relations between object- and image-space

The location of the cardinal points for any axially symmetrical electric field is of the greatest practical importance. Their position controls the size and position of the electron image of any source of electron rays. This may be explained by means of fig. 2.2. There, F and F' are the two focal points, P and P' the two principal points and JB the electron source. At J' there can be detected (for instance, by means of the sliding fluorescent target) a sharp electron image. In the example of fig. 2.2 this image $J'B'$ is found to be slightly reduced in comparison with the object JB. By the following simple construction this image can be found graphically. A beam, parallel to the z-axis drawn through a point B of the object, is refracted at the principal plane through P' so as to pass through the focus F'. Another beam emerging from B and travelling through the focus F is refracted at the principal plane through P and leaves the lens in a direction parallel to the axis. The two rays intersect at B', where the image is formed.

The general lens formulae which were derived in Chapter I from the collinear relationship can be obtained here at once geometrically from fig. 2.2. Taking $FJ = x$ and $J'F' = x'$ as object and image distances, measured from the foci, and taking $FP = f$ and $F'P' = f'$ as the focal lengths of the system and $JB = y$ and $J'B' = y'$ as object and image size, it can be seen from fig. 2.2 that the following relation holds for the lateral magnification y'/y:

$$\frac{y'}{y} = \frac{f}{x} = \frac{x'}{f'}, \tag{2.2}$$

from which Newton's formula

$$xx' = ff' \tag{2.3}$$

is derived. Moreover, taking $s = f + x$ and $s' = f' + x'$ as the object and image distances from the appropriate principal points, there

follows from (2.3)
$$(s-f)(s'-f') = ff'$$
or
$$\frac{f}{s}+\frac{f'}{s'} = 1. \tag{2.4}$$

The angular magnification or ratio of conjugate divergences is defined as the ratio of the two angles which two conjugate beams make with the axis. The angles may be so small that their tangents are substantially equal to their radian measure. In fig. 2.3 object and image points are represented by J and J', and the two conjugated divergences are Θ and Θ'.

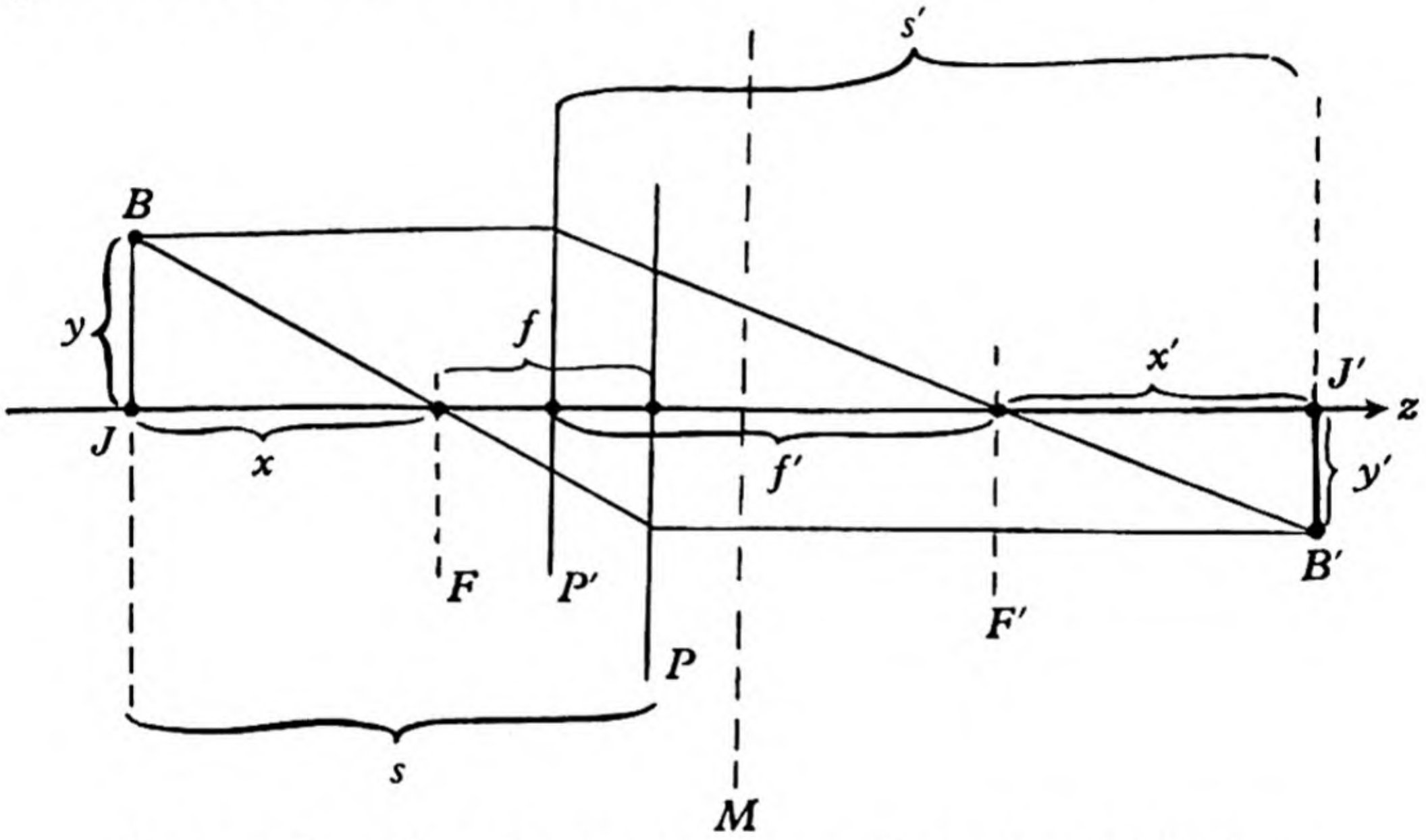

Fig. 2.2. Location of an optical image. Lateral magnification.

From fig. 2.3 it follows immediately (cf. (1.26))
$$\frac{\Theta'}{\Theta} = \frac{JP}{J'P'} = \frac{s}{s'} = \frac{f+x}{f'+x'}, \tag{2.5}$$
and using (2.3)
$$\frac{\Theta'}{\Theta} = \frac{x}{f'}. \tag{2.6}$$

The angular magnification Θ'/Θ and the lateral magnification y'/y are connected by Lagrange's law which, according to (1.35) and (1.8), can be written
$$\Theta y\sqrt{V} = \Theta' y'\sqrt{V'}. \tag{2.7}$$

Combining (2.7) with (2.6) and replacing there x by $(y/y')f$ from (2.2) leads to the relation (cf. also (1.36) and (1.7))
$$\frac{f}{f'} = \sqrt{\frac{V}{V'}}. \tag{2.8}$$

The ratio of the two focal lengths of the electron lens is equal to the square root of the ratio of the voltages at the electrodes.

The principal planes are defined as planes of unit lateral magnification, i.e. a ray arriving at one of the principal planes at a given distance from the axis will leave the other principal plane at the same axial distance. Nodal planes, that is, planes perpendicular to the axis through the nodal points, are correspondingly defined as planes of unit angular magnification, i.e. a ray passing one of these planes at an angle Θ to the axis, passes the other nodal plane with the same inclination $\Theta' = \Theta$. Thus from Lagrange's law (2.7) it follows that the lateral magnification in the nodal planes is given by $y'/y = \sqrt{V}/\sqrt{V'}$, or combining this result with (2.2) and (2.8) the expression (2.1) for locating the nodal points is proved. The location of the nodal points is of practical interest for the determination of the lateral magnification. Since the angular magnification in the nodal points is unity, $\tan\Theta' = \tan\Theta$ or

$$\frac{y'}{K'J'} = \frac{y}{KJ}. \tag{2·9}$$

Hence the lateral magnification is equal to the ratio of the nodal distances for any conjugate object and image.

Electron lenses are generally 'thick' lenses, since the field produced by the one electrode penetrates appreciably into the other electrode, so that the region of varying refractive index extends over a distance which is considerable in comparison with the focal length of the lens. However, for many practical considerations it is a useful fact that there can always be found a 'thin equivalent lens', i.e. an infinitely thin lens that will produce an image of the same size and in the same place as the image produced by the thick lens. The distances b and b' of the object and image from this thin equivalent lens depend on the magnification and on the refractive indices (Hess, 1934); they are given by:

$$\frac{y'}{y} = \frac{b'}{b}\sqrt{\frac{V}{V'}}. \tag{2.10}$$

The position of the thin equivalent lens E is indicated in fig. 2.3. It may be noticed, however, that this position is not fixed, but changes with the position of the object and image. The thin equi-

valent lens always lies between the two principal planes P and P', it moves gradually from P' to P as the object J moves gradually from an infinite distance to the focus F (corresponding to a movement of the image J' from the focus F' to infinity). If the object J and the image J' are connected by straight lines with any point E of the thin equivalent lens (see fig. 2.3), the ratio of the object and image distances gives the correct angular magnification

$$\frac{\Theta}{\Theta'} = \frac{b'}{b}. \tag{2.11}$$

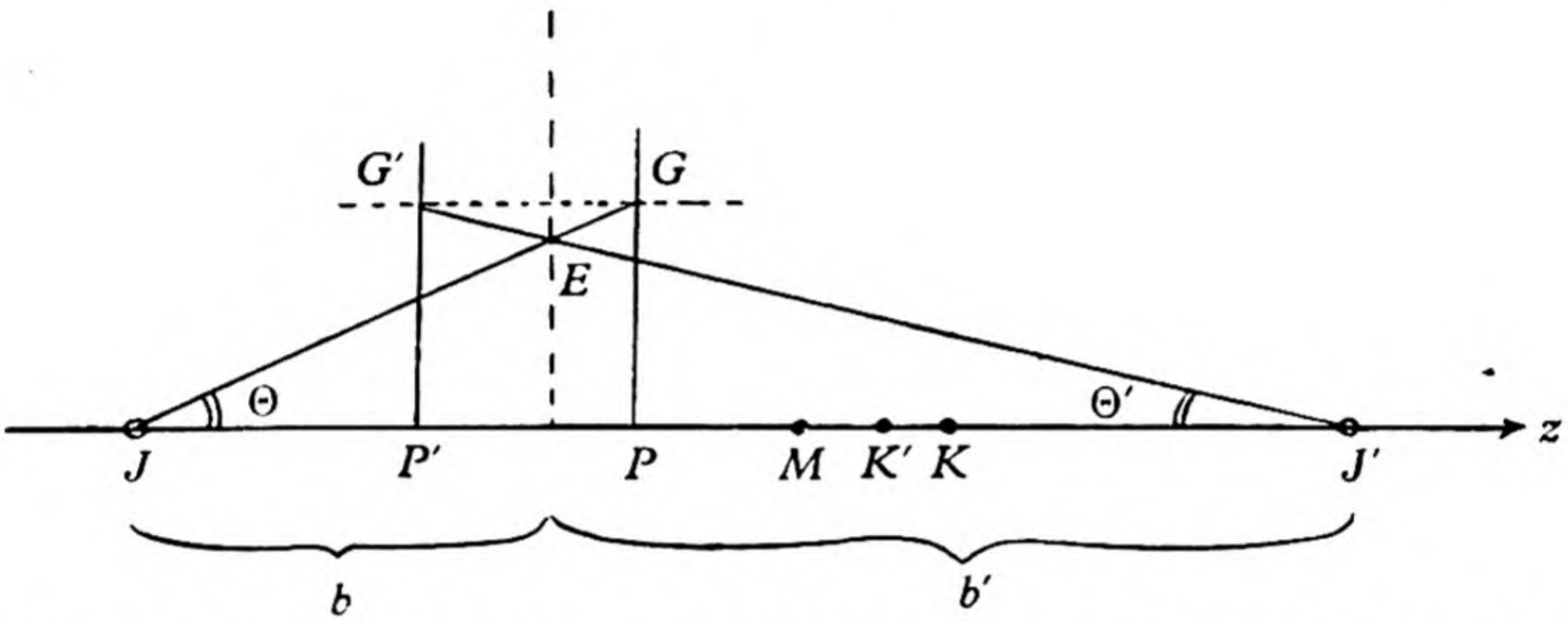

Fig. 2.3. Divergence of a beam. Angular magnification. Thin equivalent lens.

This can be seen by introducing Lagrange's equation (2.7) in (2.10). Combining (2.5) with (2.11) one obtains an expression for locating the thin equivalent lens

$$\frac{b}{b'} = \frac{s}{s'}. \tag{2.12}$$

The position of the thin equivalent lens divides the object-image distance JJ' in the ratio $JP/J'P'$, which is given by the distances of object and image from their appropriate principal planes.

2.3. Practical methods for locating cardinal points

The theory of the location of cardinal points presented so far applies in the same way to electron lenses and to glass lenses. The technique of measuring the positions of these points, however, is substantially different in the two cases. In electron optics special experimental methods are required, since the measurements have to be taken in evacuated tubes and special precautions are necessary to avoid the occurrence of spurious electric or magnetic fields which easily would modify the path of charged particles.

The accurate, but rather elaborate, method by Klemperer and Wright (1939) is a direct application of the electron pencil tracing already mentioned at the beginning of this chapter. A series of initially parallel, very narrow pencils (diam. $\approx 0{\cdot}1$ mm.) emerges through the fine holes of a 'pepperpot-diaphragm', and then passes through the electron lens under investigation. The pencils are detected with a sliding fluorescent target. This target may be made from glass covered with Willemite (1 mg./cm.^{2}) shielded by a fine wire gauze. The fluorescent spots are observed from the back of the target, and their mutual distances are measured by a scale in the eyepiece of a calibrated microscope of large object-to-objective distance.

A more rapid but less accurate method for the location of the cardinal points has been described by Epstein (1936). Lateral magnifications have to be measured at two different object and image distances. A wire mesh 'illuminated' with electrons may be used as a suitable object; suppose the mesh is arranged at a distance p from the midplane. The image can be found by means of the sliding fluorescent target; let it be distant q from the midplane. Using again the same notation as above, we obtain

$$\left.\begin{aligned} p &= JM = x + MF = \frac{y}{y'} f + MF, \\ q &= J'M = x' + MF' = \frac{y'}{y} f' + MF'. \end{aligned}\right\} \tag{2.13}$$

If p_1, q_1 and y_1, y_1' correspond to one position of the object, p_2, q_2 and y_2, y_2' to another position of the object, it follows that

$$f = \frac{p_1 - p_2}{\dfrac{y_1}{y_1'} - \dfrac{y_2}{y_2'}}, \tag{2.14}$$

$$MF = \left(p_1 \frac{y_1'}{y_1} - p_2 \frac{y_2'}{y_2}\right) \Big/ \left(\frac{y_1'}{y_1} - \frac{y_2'}{y_2}\right). \tag{2.15}$$

The conjugate values of f' and MF' are obtained if in (2.14) and (2.15) the experimental values of p, y and y' are interchanged with those of q, y' and y. Since, however, the image has to be measured with paraxial rays only, the depth of focus is very large, and

therefore the accuracy of locating the image and of measuring the distance q is low.

Klemperer and Wright (1939) pointed out that Epstein's method may be easily modified by replacing lateral by angular magnifications using Lagrange's law (2.7). In (2.14) and (2.15) therefore, every ratio of y/y' has to be replaced by $\frac{\Theta'}{\Theta}\sqrt{\frac{V'}{V}}$. The required

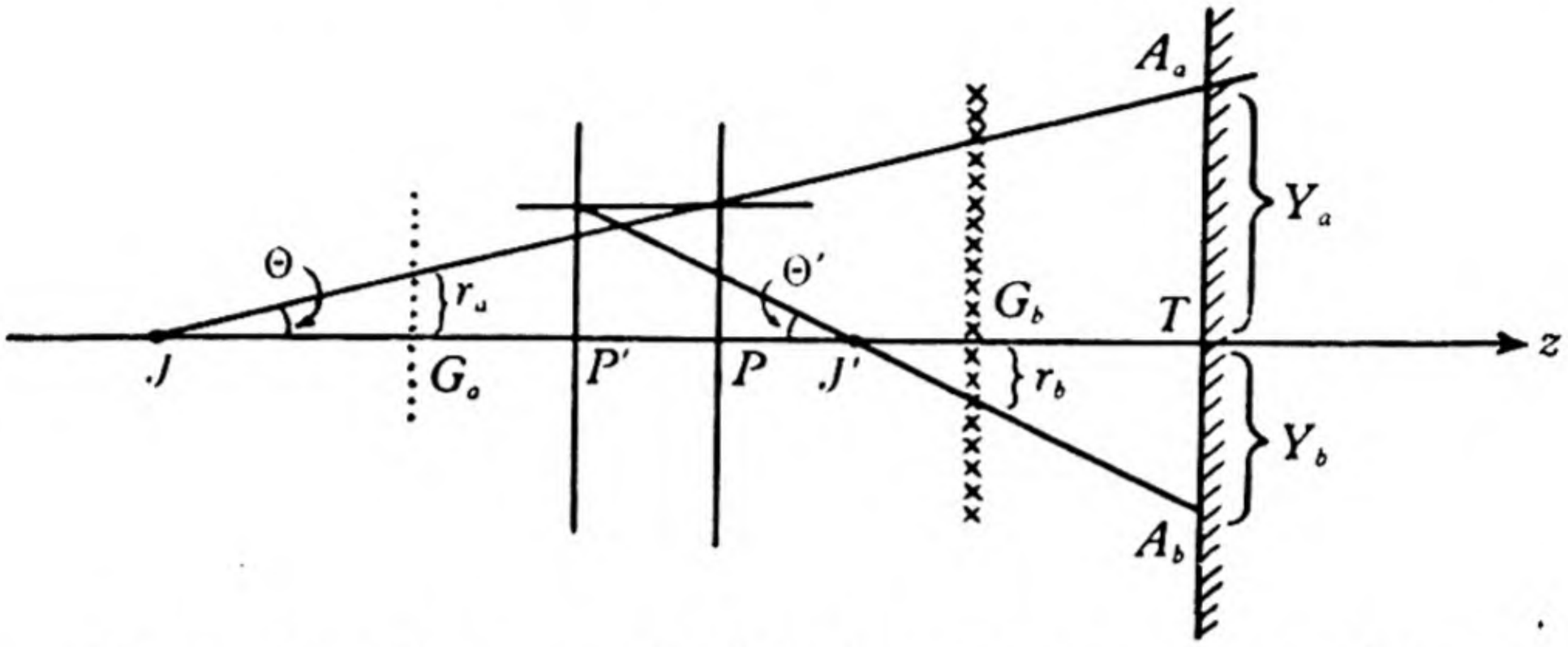

Fig. 2.4(*a*). Shadow method for location of cardinal points.

pairs of values of p, q, Θ and Θ' are found experimentally by tracing divergent pencils emitted from a point-source object (see Chapter IX) and focused to a point image.

This line of attack has been followed up by Spangenberg and Field (1942*a*, *b*) and by other workers (cf. Heise and Rang, 1949). They measured the angular magnification by their ingenious 'shadow method', which has the great advantage of avoiding the need of parts which have to be moved relative to one another in the vacuum. The method is illustrated in fig. 2.4(*a*). A cone of rays of fixed semi-vertical angle Θ is emitted from a point source J and detected by a fluorescent target T, both in fixed position. At the object and at the image side respectively there are wire grids G_a and G_b, each casting a shadow on the target. Both these measuring grids consist of parallel equidistant wires at right angles to the axis. The wires of G_a are arranged in a perpendicular direction to those of G_b, so that their shadows on the target can be distinguished from one another as shown in fig. 2.4(*b*).

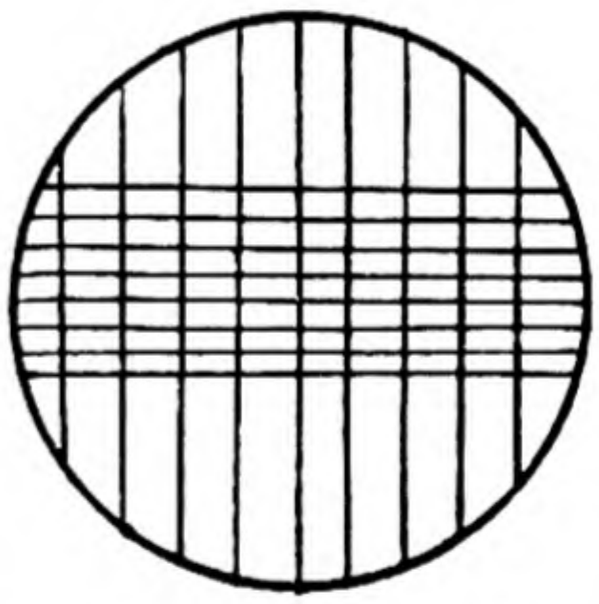

Fig. 2.4(*b*). Shadows of measuring grids G_a and G_b on target.

The radius of the illuminated area on the target is Y_a if no voltage

difference is applied to the lens electrodes; it changes into Y_b if a voltage difference is applied. The radii of the beam at G_a and G_b are r_a and r_b respectively; they can be determined by counting the number of wire shadows in the image at the target. Now if the positions of the points G_a, G_b and T at which the two grids and the target respectively intercept the axis (z) are known, the angles of divergence of the beam at the object J and at the image J' are given by

$$\left.\begin{aligned} \Theta &= \frac{r_a}{JG_a} = \frac{Y_a}{JT}, \\ \Theta' &= \frac{Y_b - r_b}{G_bT} = \frac{Y_b}{J'T}. \end{aligned}\right\} \tag{2.16}$$

These equations are sufficient for the determination (i) of the angular magnification Θ'/Θ and (ii) of object and image positions J and J' respectively, i.e. of p and q. Two measurements have to be taken at two different positions of J giving p_1, p_2 and q_1, q_2 also:

$$\frac{y'_1}{y_1} = \frac{\Theta_1}{\Theta'_1}\sqrt{\frac{V_1}{V'_1}},$$

and

$$\frac{y'_2}{y_2} = \frac{\Theta_2}{\Theta'_2}\sqrt{\frac{V_2}{V'_2}}.$$

These six values for p_1, p_2, y_1, y_2, y'_1 and y'_2 can be substituted into (2.14) and (2.15) leading to the determination of the cardinal points.

A special case of practical importance is met in electron microscopy where lenses are operated under extreme conditions of high magnification, say $y'/y = 10^2$ to 10^3. There the object distance is very nearly equal to the focal length and the image distance s' is relatively so large that, with sufficient accuracy, it equals the mid-image distance q or the distance x' of the image from the focus, namely

$$s' \simeq q \simeq x'.$$

Moreover, the refractive index is generally the same in the object space and in the image space. Hence, using (2.8) and (2.13) one obtains

$$f = f' \simeq \frac{q}{y'/y} \simeq \frac{q}{(y'/y)+1}. \tag{2.17}$$

In this way, the focal lengths of microscope lenses are obtained in practice (Dosse, 1941; Liebmann, 1952*a*) by measuring, with an object of known size y, the image size y' and the image distance q from the centre of the lens.

CHAPTER III

FIELD PLOTTING AND RAY TRACING

3.1. Potential distribution and Laplace's equation

The equipotentials are the refracting surfaces of electrostatic electron optics. They correspond to the material refracting surfaces of glass lenses in ordinary optics. The electric field E is given in terms of the potential V by the general relation

$$E = -\operatorname{grad} V,$$

and the direction of the field is always perpendicular to the equipotentials.

A rough sketch of the field plot can be obtained in the following way: First, some equipotentials in the neighbourhood of the electrodes can be drawn parallel to the electrode surfaces. Then an equipotential between two electrodes can be drawn bisecting everywhere the angle between the conductive surfaces. Moreover, after drawing some field lines at right angles through the above equipotentials, the rest of the equipotential lines may be filled in duly regarding the conservation principle of flux, so that

$$\Phi = \epsilon \frac{\Delta V}{\Delta s} \Delta a = \text{const.}, \tag{3.1}$$

where Φ is the flux through a tube bounded by two field lines, ϵ is the dielectric constant, ΔV is the potential increment between two successive equipotentials of distance Δs at the cross-sectional area Δa of the tube. In two-dimensional fields, for instance, the area Δa is proportional to the distance Δb of the field lines bounding the tube. In fields of circular symmetry, however, $a \propto r \Delta b$, where r is the mean distance of the elementary volume $\Delta a \Delta s$ from the axis of symmetry.

More exact methods for the determination of potential distributions follow from the theory of the electrostatic field (see, for instance, Weber, 1950). The potential distribution in space is entirely defined by the geometry and the potentials of the electrodes. Neglecting space charges, the potential distribution can be

completely calculated from Laplace's differential equation

$$\nabla^2 V = 0. \tag{3.2}$$

But, although this theoretical possibility is very interesting in principle, an integration of (3.2) under the proper conditions as given by geometry and potentials of the electrodes is generally very complicated. In the majority of practically important cases, experimental methods have to be used.

Though the analytical calculation of the potential distribution for a given electrode configuration from Laplace's equation is impracticable in many cases, complete numerical computation can always be performed. For instance, Laplace's equation (3.2) may be written in cylindrical coordinates (r, z) as follows:

$$\frac{\partial^2 V}{\partial r^2} + \frac{1}{r}\frac{\partial V}{\partial r} + \frac{\partial^2 V}{\partial z^2} = 0. \tag{3.3}$$

For the purpose of a numerical solution (3.3) may now be replaced by a system of difference equations. There, the values of V can be determined at the points of a square net of finite mesh length. For example, at any point P_0 of this net the potential V_0 can be expressed in terms of the potentials V_1, V_2, V_3 and V_4 of the four neighbouring mesh points P_1, P_2, P_3 and P_4. This follows from an expansion in Taylor series for the potentials of these points, namely,

$$\left.\begin{aligned} V_1 &= V_0 + g\frac{\partial V}{\partial r} + \frac{g^2}{2}\frac{\partial^2 V}{\partial r^2} + \cdots, \\ V_3 &= V_0 - g\frac{\partial V}{\partial r} + \frac{g^2}{2}\frac{\partial^2 V}{\partial r^2} - \cdots, \\ V_2 &= V_0 + g\frac{\partial V}{\partial z} + \frac{g^2}{2}\frac{\partial^2 V}{\partial z^2} + \cdots, \\ V_4 &= V_0 - g\frac{\partial V}{\partial z} + \cdots, \end{aligned}\right\} \tag{3.4}$$

where g is the length of the meshes. From (3.4) we obtain

$$V_1 + V_2 + V_3 + V_4 - 4V_0 = g^2\left(\frac{\partial^2 V}{\partial r^2} + \frac{\partial^2 V}{\partial z^2}\right). \tag{3.5}$$

The right-hand side of this equation can, with the help of (3.3), be replaced by

$$-\frac{g^2}{r_0}\frac{\partial V}{\partial r}, \tag{3.6}$$

where r_0 is the distance of point P_0 from the z-axis. Moreover, with the difference of the first two equations of (3.4) substituted into (3.6), (3.5) can be written

$$V_1\frac{1-g}{2r_0}+V_3\frac{1+g}{2r_0}+V_2+V_4-4V_0=0. \tag{3.7}$$

Hence the potential V_0 at any point P_0 of the net can be calculated if the potential of the surrounding four net points are known.

In practice, boundary conditions must be given by, say, the potentials of the electrodes of the electron lens. Arbitrary V-values are assumed first at all points of intersection of a network covering the axial plane between the electrodes. These values are then adjusted systematically and repeatedly in accordance with the requirement that the value at every point must equal the mean of the values of the four equidistant nearby net points given by (3.7). This, in a nutshell, is the principle of the so-called relaxation method. Its exposition in this section may serve to convey a picture of the physical meaning of Laplace's equation.

The actual application of the relaxation method is no quick process. In particular, the process of adjusting the various values of the points of a network to bring them gradually into agreement with the given values at the electrodes is quite laborious and cannot be followed up here. Reference may be made to the papers by Christopherson and Southwell (1938), and of Fox (1947, 1948), and to a book by Southwell (1946). The special application of the relaxation method to the determination of the potential distribution of an electron optical two-tube lens has been described in detail by Motz and Klanfer (1946). The application of the relaxation method to two-dimensional fields, which is certainly much simpler on account of the simpler structure of Laplace's equation in two dimensions, will be discussed in detail in § 10.2 of this book.

Another very important conclusion can be drawn from the validity of Laplace's equation throughout the lens field, namely, that the potential on the axis uniquely determines the potential distribution outside it. An integral solution of (3.2) leads to the power series

$$V(r,z)=V_0(z)-\frac{r^2}{2^2}\frac{d^2V_0(z)}{dz^2}+\frac{r^4}{2^2 4^2}\frac{d^4V_0(z)}{dz^4}\cdots, \tag{3.8}$$

Hence, for the determination of a lens field, a measurement of the field $V_0(z)$ along the axis only should be sufficient, the rest being obtainable by calculation.

This fixation of the potential distribution in space by the axial potential distribution brings out a fundamental difference between ordinary optics and electron optics which complicates the process of computing electron lenses. In light optics, the curvatures and refractive indices of lenses can be selected independently and so, for instance, by skilful choice, lens errors can be compensated. On the other hand, in electron optics, the radii of the refracting surfaces seem to be already determined by the change of refractive index along the axis. Referring to the practical problem, however, it will be pointed out in § 3.7 that insignificant variations of the axial potential can yield decisive changes in the potential distribution outside it. Hence from the practical point of view of obtaining reliable results for ray tracing the axial potential distribution should be used for paraxial tracing only. For zonal and marginal ray tracing, a measurement of the whole potential field is always advisable.

3.2. Experimental field plotting

The electrolytic trough. Experimental methods for the determination of potential distributions in electron lenses are in the majority of practical cases very much preferable to calculations and computations whenever the necessary apparatus is available. The method of the electrolytic trough is of the greatest practical value. This method had been used to investigate general electrostatic problems a long time before any electron optical research was started. It is based on the perfect physical analogy between the propagation of electric currents through electrolytes and the spreading of the lines of force through an electrostatic field. Details about electrolytic troughs have been given, for instance, by Zworykin *et al.* (1945), by Ertaud (1946), by Willoughby (1946), by Musson-Genon (1947) and by Hutter (1947*b*).

The general features of the method are shown by fig. 3.1. *G* represents a large box or glass trough which is filled with a weakly conducting liquid. For instance, a solution of copper sulphate in distilled water (about 10 mg./l.) or sometimes clear tap water is used

as electrolyte. In the present example, T_1, T_2 and T_3 represent three electrodes of an electron lens; they are tubes, cut along their axes and fixed in such a way that the axis of the lens coincides with the surface of the liquid. An alternating-current source Q is connected to two large, variable precision resistances A and B, used as a potentiometer for the adjustment of a given potential at a probe P, the tip of which is just dipping into the surface of the liquid. A current-detecting device D will indicate that no current is taken

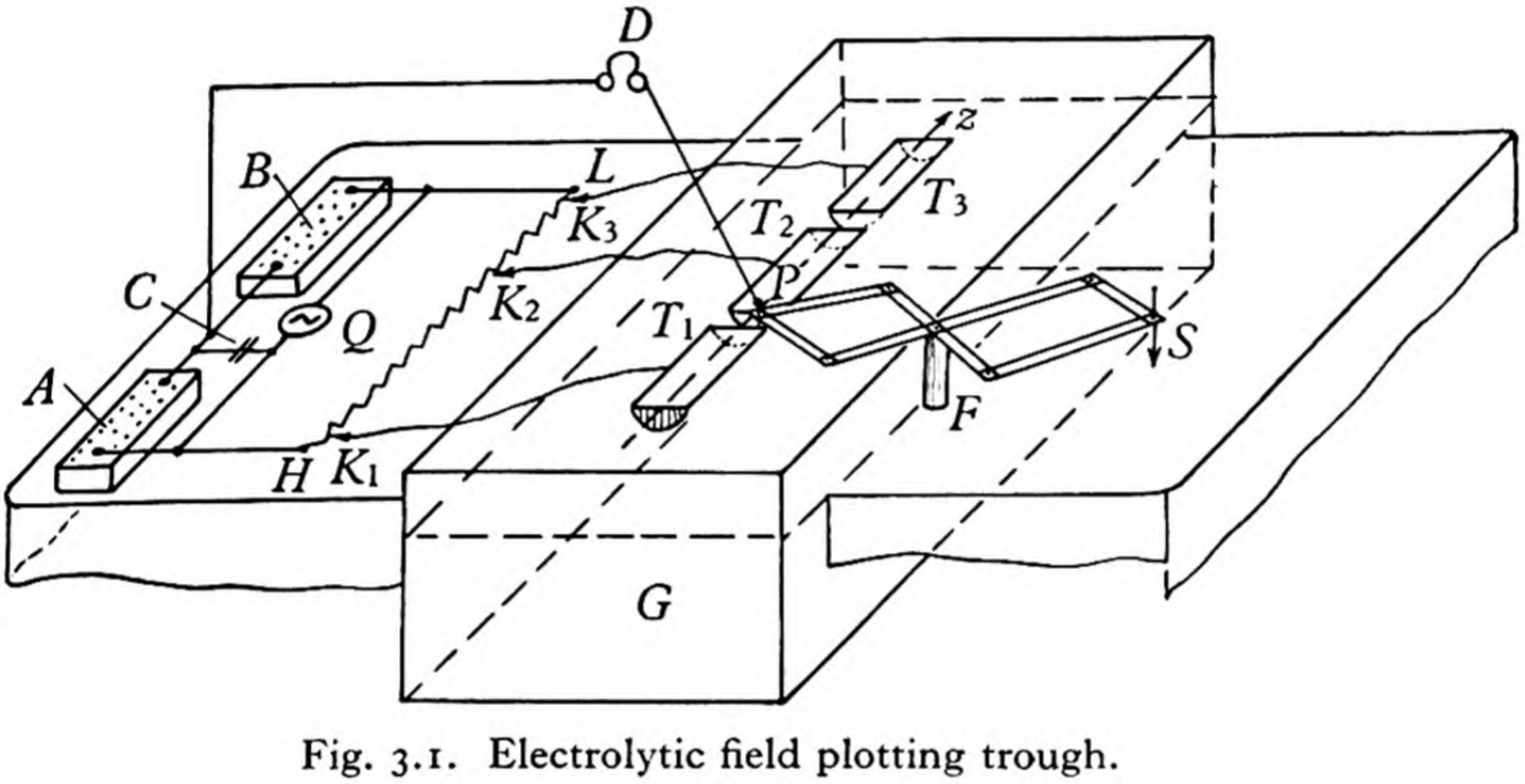

Fig. 3.1. Electrolytic field plotting trough.

by the probe as soon as its tip is in the particular equipotential line which corresponds to the adjustment of the ratio of the resistances A and B.

The source Q is also connected to the ends H and L of a potentiometer supplying any desired voltage to the electrodes T_1, T_2 and T_3 through the sliding contacts K_1, K_2 and K_3. To set up any desired potential at an electrode T, this electrode may be touched with the probe of preadjusted potential, and the corresponding contact K may be adjusted to zero current in the detector D.

To avoid electrolysis, the source Q should supply alternating current. A valve oscillator of 400–1000 cyc./sec. is convenient. Headphones are suitable for the detecting device D. In order to avoid disturbances due to a shift of the phase angle, it is often necessary to balance the capacity of the electrodes by a small variable condenser C which can be switched in parallel with either of the resistances A or B. The probe may be carried by a pantograph attached to the side of the trough and moving about the pivot F.

This pantograph transmits the motion of the probe to a plotting pencil *S* which moves over a drawing board. The probe is fixed in an earthed metal barrel and it is connected by a screened flexible lead to the headphones.

The accuracy of electrolytic field plotting is limited mainly by electrolytic polarization and by the surface tension of the liquid producing a meniscus. According to Einstein (1951) the errors in the relative potential measurements can be reduced to 0·2 %.

The method of field plotting described can be applied to any electrode system possessing a plane of symmetry that can be placed in the surface of the liquid. In systems of circular symmetry, such a plane is given by any meridional plane, i.e. a plane which includes the axis. The reason for placing the liquid level in such a position is that in electron lenses all electric field vectors lie in meridional planes only. There are no field components tangential to a conductor. Analogously, in the electrolytic trough, there cannot exist any current vectors crossing meridional planes.

The wedge trough. A particular technical development of the method of electrolytic field plotting was initiated by the conclusion that an insulating plane may be placed in any meridional plane of the electrode arrangement. Manifold and Nicoll (1938) proposed the important design of the wedge trough, which implies an appreciable practical simplification. Such a trough is shown in fig. 3.2. There, a thin wedge of electrolyte is realized by a tilted trough containing electrolyte resting on a plane, insulating bottom. The thin edge of the wedge represents the axis of the electrode system. The bottom of the trough may be made from glass so that a coordinate system can be placed beneath it and seen from above. The tilt of the trough may be varied by foot screws. By their adjustment, the edge of the wedge can be moved into any desired position with respect to the electrodes. In order to obtain reliable plots, it is absolutely necessary for the liquid forming the wedge to have perfect contact with the glass bottom. The edge of the wedge must be really straight. To avoid disturbing effects of surface tension, the glass surface may be wiped perpendicularly to the edge with a fine abrasive (Klemperer, 1944*a*). Moreover, capillary effects are relatively less disturbing if large-size troughs can be employed.

If the angle of the wedge is small, the electrodes used need not

be surfaces of revolution but can be replaced by strips of plane metal sheet, bent to the shape of a longitudinal section of the actual electrode. For instance, a two-tube lens is simply represented by two flat strips of metal placed in the liquid in a direction parallel to the thin edge (tube axis) of the wedge.

Electrolytic field plotting can also be applied to finding a potential distribution that is modified by the neighbourhood of an intense electron beam. According to Pierce (1940*a*) and Samuel (1945), the edge of the beam may be represented by a strip of insulator in the

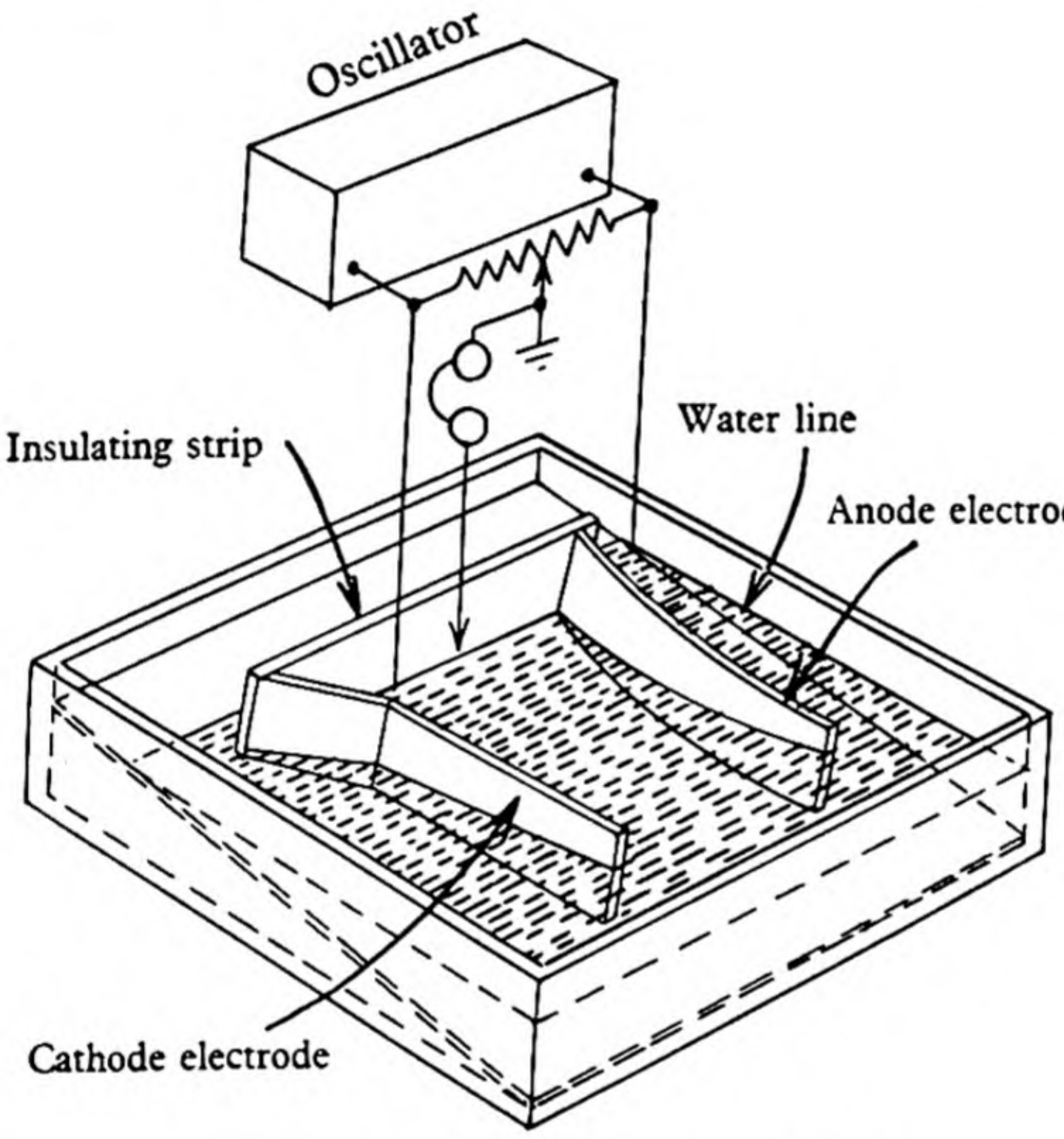

Fig. 3.2. Electrolytic wedge trough.

electrolyte (see fig. 3.2). Since there can be no current flow normal to the insulator this ensures that the field at the edge of the beam normal to the beam surface will be zero. Field plotting in the presence of space charges will be fully discussed in § 8.9.

Labelling of the equipotentials. In fig. 3.3 there is shown an actual potential plot of the symmetrical two-tube lens. The equipotentials are marked as a percentage of the total potential difference between the two electrodes. For instance, if the bridge resistances are equal ($A = B$ in fig. 3.1) the probe is at the 50 % equipotential, or if $A/B = 1/9$, the probe is at the 10 % equipotential, etc. In this way one obtains a very general diagram, and the potential plot can easily

be interpreted for all varieties of voltages or voltage ratios at the electrodes, since it is evident that the shape of the equipotentials does not change if the voltage at either of the two electrodes is altered. For instance, the two tubes may have the potentials $V = 1000$ V. and $V' = 5000$ V. In this case the 10 % equipotential would be at

$$1000 + \tfrac{10}{100}(5000 - 1000) = 1400 \text{ V}.$$

In another example, the same two tubes may be at $V = 500$ V. and $V' = 20{,}000$ V.; then the 10 % equipotential would be at 2450 V. The 1400 V. equipotential of the first example would be in exactly the same place as the 2450 V. equipotential of the second example.

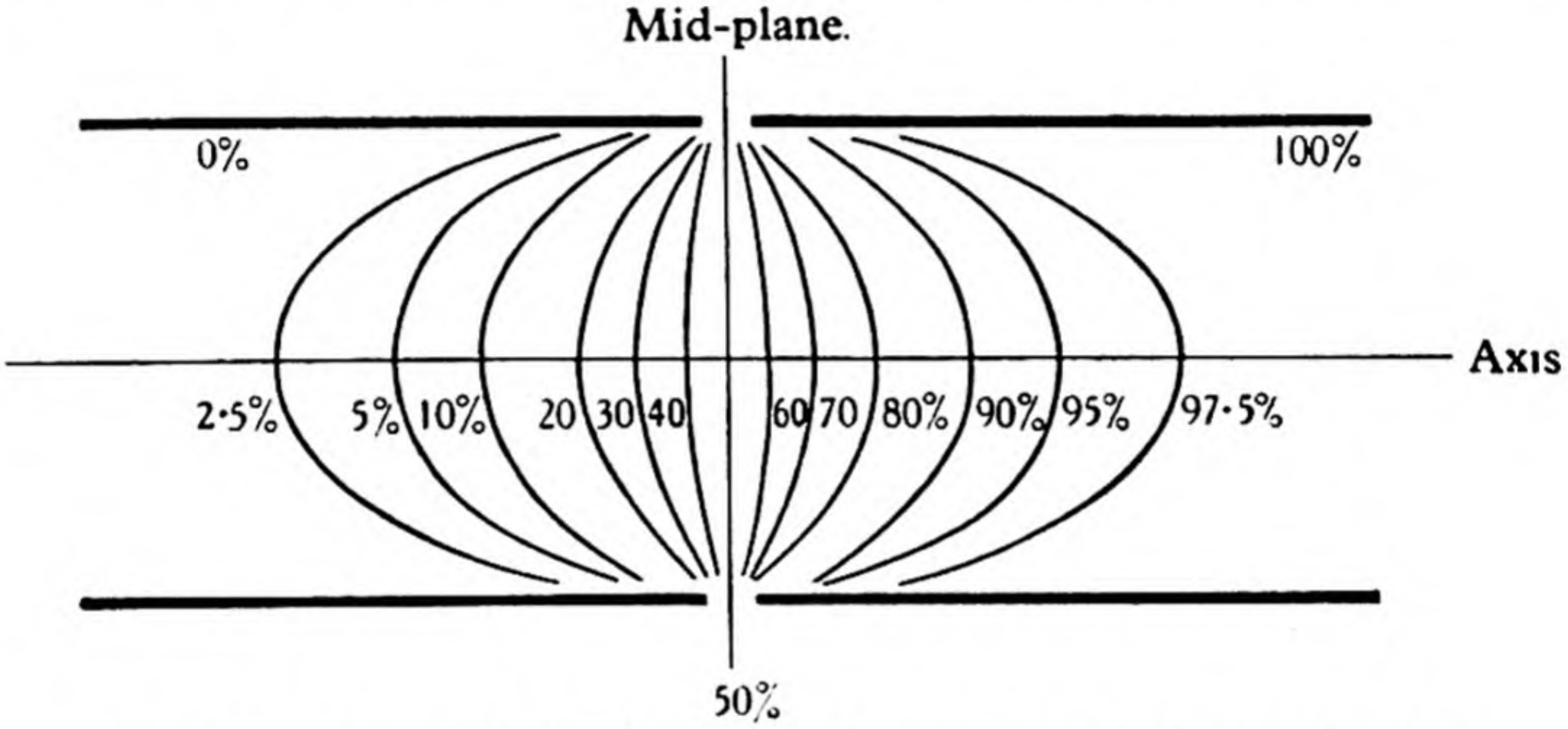

Fig. 3.3. Potential distribution in the symmetrical two-tube lens.

The equipotentials in fig. 3.3 are given in steps of 10 % between 10 and 90 %, and to show the spreading of the field into the tubes, extra equipotentials are plotted at 2·5, 5, 95 and 97·5 %. One can see that the whole figure is perfectly symmetrical with respect to the midplane. Moreover, the potential gradient is greatest at the midplane, where the equipotentials are closest together, and it decays slowly towards the outer ends of the tubes, the 90 % equipotential having a distance of about one tube radius from the midplane and the 97·5 % equipotential being twice as far from that plane.

It is advisable to measure every geometrical distance in terms of the tube radius R as a unit, so that it is easy to transfer the results of a field plot to electron lenses of any size. In order to obtain good accuracy in plotting the equipotentials, the model of the electrodes should be made as large as the size of the trough allows. Other metal parts and insulators should, however, be sufficiently removed

in order to avoid disturbances. It has been explained that insulators, such as the glass wall of the trough, act as mirrors towards the equipotentials. On the other hand, conductor surfaces are equipotentials. If, for example, in order to avoid external disturbances, the ends of the tubes in the electrolytic trough are closed by metal sheets, kept at the tube potential, these sheets must be sufficiently far away from the midplane in order to avoid any influence on the equipotentials to be investigated. According to practical experience, a plane sheet perpendicular to the axis and at a distance of three tube radii from the midplane would not modify markedly the shape or position of the 95 % equipotential.

When a part of the whole potential plot has to be investigated with increased accuracy, metal sheets could be shaped exactly like a natural equipotential measured in the electrolytic trough, and could be introduced in the trough. For example, the midplane was found to coincide exactly with the 50 % equipotential. Therefore, a plane metal sheet could be connected to the end H of the bridge-resistance A instead of one of the two tubes of the lens of fig. 3.3. The probe would then measure the same equipotentials in the other tube as given in fig. 3.3, but the designation of the equipotential would no longer be given by the ratio $A/(A+B)$ of the resistances but in the present example by $50+100A/2(A+B)$ %. Generally, two metal sheets replacing the equipotentials of n and m % may be connected to the ends of the resistances A and B. The right designation of any measured equipotential is then given by

$$n+\frac{m-nA}{100\,(A+B)}. \tag{3.9}$$

By this artifice of replacing two equipotentials by metal sheets, a relatively small fraction of the whole field could be investigated separately on a scale enlarged as much as the dimensions of the electrolytic trough would allow, and plots of considerable accuracy could be obtained, even with small troughs.

Resistor network. For the purpose of field plotting, the continuous distribution of the conducting medium of the electrolytic trough can be replaced by a network of discrete resistance units connecting a square array of studs. The electrodes of the electron-optical system are simulated by short-circuiting corresponding

studs. The operation of the network can be seen from Kirchhoff's law

$$\Sigma I_n = 0.$$

The currents I_n, with $n = 1, 2, 3, 4$, towards any stud O are given by

$$I_n = \frac{V_n - V_0}{\Omega}, \tag{3.10}$$

where V_n are the potentials of the four studs adjoining the stud O of the potential V_0 and where Ω is the value of the resistance units. If all these units are equal, one obtains

$$\Sigma V_n - 4V_0 = 0. \tag{3.11}$$

This equation describes a two-dimensional field, as will be seen later on in Chapter X. It is identical with (10.4). Such a two-dimensional network analogue has been described first by Hogan (1943). On the other hand, Packh (1947) and Liebmann (1949*b*) have shown the application of the network method to three-dimensional potential distributions of circular symmetry. There, the resistances have to be graded logarithmically in the radial direction. Liebmann (1950*a*) has shown experimentally that with a graded network a high degree of accuracy (10^{-3} to 10^{-4}) can be obtained, which compares favourably with that of the best wedge troughs. However, he used large arrays of precision resistances with 20 and 60 meshes in radial and in axial direction respectively; in addition, his board was surrounded by an 'infinity strip' network for moving the reflecting boundary farther away from the axis. In this version, the need for some 3000 accurate resistors makes the expense prohibitive for the ordinary laboratory.

3.3. Ray tracing by Snell's law

After having obtained an exact potential plot of the investigated electron lens with all the values of the equipotentials calculated in volts, the path of any electron could be traced in principle immediately from Snell's law. The spaces between the equipotentials V_1 and V_2, V_2 and V_3, V_3 and V_4, etc., are assumed to be media of constant refractive indices $N_1 = \sqrt{V_1}$, $N_2 = \sqrt{V_2}$, $N_3 = \sqrt{V_3}$, etc. The angle of incidence α_1 of the electron at the first equipotential V_1 may be measured with a protractor. The corresponding angle of

refraction α_1' may be calculated with Snell's law (1.10) and plotted with the protractor at the other side of the equipotential. The path of the electron between the equipotentials V_1 and V_2 is drawn as a straight line. The same procedure is applied for the angles α_2 and α_2' at the equipotential V_2, and so on.

For practical purposes the tracing procedure by Snell's law is simplified if a field plot with geometrical progression of voltages of

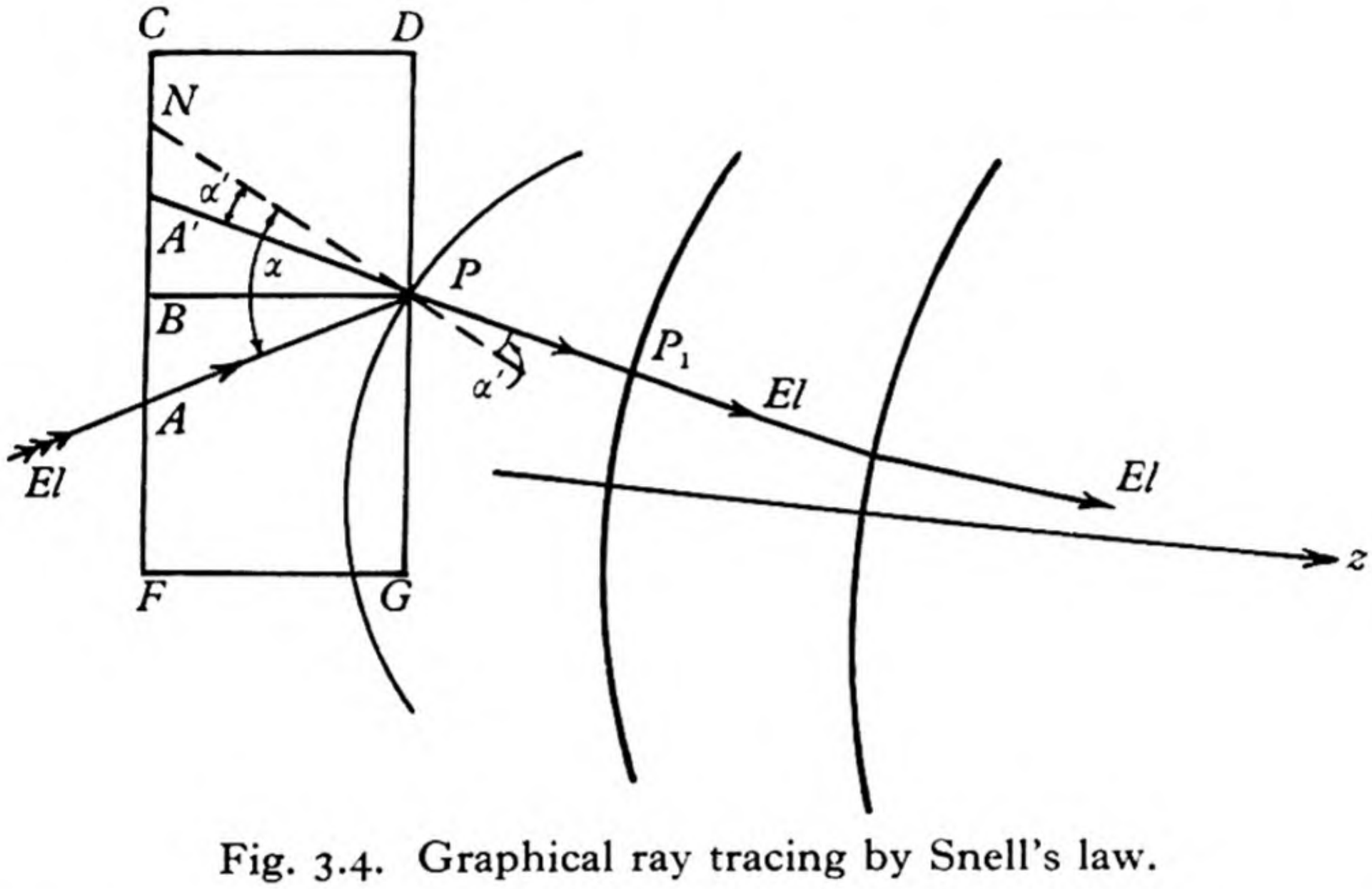

Fig. 3.4. Graphical ray tracing by Snell's law.

the equipotentials is available. There, the ratio of refractive indices is the same for each step, i.e.

$$\sqrt{\frac{V_1}{V_2}} = \sqrt{\frac{V_2}{V_3}} = \sqrt{\frac{V_3}{V_4}} \cdots = \sqrt{\frac{V_n}{V_{n+1}}}. \tag{3.12}$$

To find the refracted rays, it is convenient to make a stencil from paper, or celluloid, etc., as shown by $CDGF$ in fig. 3.4. One edge CF of the stencil is marked by the points A, A' and N, so that

$$\frac{NA}{NA'} = \sqrt{\frac{V_{n+1}}{V_n}}.$$

A line BP is drawn on the stencil as the perpendicular bisector to AA' (Bloch, 1936; Jacob, 1938). For ray tracing, the template is laid on the field plot so that the bisector passes through the point of incidence P. Moreover, point A is placed on the incident ray El and N on the normal to the equipotential through P. Then $A'P$ gives the direction of the refracted ray PP_1. This is easily proved from the

sine formula of trigonometry:

$$\frac{NA}{\sin NPA} = \frac{NP}{\sin PAA'} = \frac{NP}{\sin PA'N} = \frac{NA'}{\sin NPA'}. \qquad (3.13)$$

The sines in the second and third item are equal, since, according to construction, $\sphericalangle PAA' =. \sphericalangle PA'A = 180° - PA'N$. Thus

$$\frac{NA}{\sin \alpha} = \frac{NA'}{\sin \alpha'}$$

follows from the first and last item.

The main source of error in the graphical method of tracing with Snell's law is the difficulty in finding the exact directions of the normals of the equipotentials which are needed to plot the angles α and α'. The errors are cumulative, so that after a number of steps the result of tracing might deviate considerably from the true electron path. However, the method is useful in practice, yielding preliminary information quickly.

A certain ambiguity is experienced when the path of an electron has to be traced near the cathode from which it has been emitted with negligible velocity. It is known that the electron travels initially along a field line, i.e. at right angles to the cathode surface and to other equipotentials which are very close to the cathode. However, as soon as the electron gathers momentum, the radius of curvature r_e becomes greater than the radius r_E of the field line. According to a practical rule by Rajchman (1938) the initial path may be plotted with $r_e \approx 3r_E$ until ray tracing can be started by plotting refractions according to Snell's law.

Trigonometrical ray tracing. A highly accurate procedure derived from Snell's law is the method of trigonometrical ray tracing which is quite commonly used in glass optics. It is based on the following four computing formulae, which are quite old and probably date back to the eighteenth century:

$$\sin \alpha = \sin \Theta \frac{(l+r)}{r}, \qquad (3.14)$$

$$N' \sin \alpha' = N \sin \alpha, \qquad (3.15)$$

$$\Theta' = \alpha' - \alpha + \Theta, \qquad (3.16)$$

$$l' = \frac{r \sin \alpha'}{\sin \Theta'} - r. \qquad (3.17)$$

To elucidate these formulae, we might explain that in ray tracing the initial data available are (see fig. 3.5)

Θ = the angle between the initial beam and the axis,

l = the distance from the refracting surface of the intersection of initial beam and axis,

r = radius of curvature of the refracting surface which is assumed to be of spherical shape, and

N/N' = the ratio of refractive indices at both sides of the refracting surface.

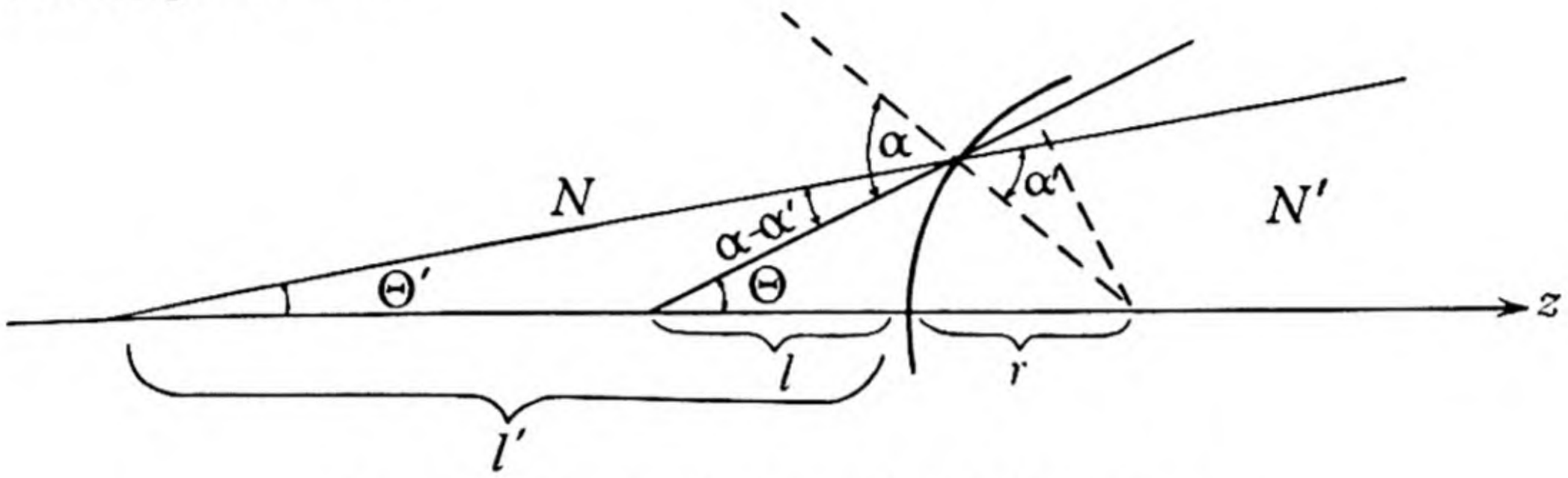

Fig. 3.5. Refraction on spherical surface.

The equation (3.14) is obvious from inspection of fig. 3.5. It enables $\sin\alpha$ to be calculated, and then from (3.15) (Snell's law) $\sin\alpha'$ is obtained. From (3.16), which is again obvious from fig. 3.5, there is calculated Θ', the angle of the refracted ray. From (3.17) it is then possible to calculate the distance l' from the refracting surface to the point of intersection of the refracted beam and the axis. (3.17) can again be derived from fig. 3.5, or may be obtained from (3.14) by interchanging dashed and undashed symbols. If the ray has to be traced through two refracting surfaces, then Θ_1' and l_1' of the first surface are equal to Θ_2 and $l_2 + d$ of the second surface, where d is the separation between the two successive surfaces, but for the ratio N_2/N_2' (where $N_2 = N_1'$), the index N_2' has to be given and the radius of curvature r_2 has to be given as well. Numerical examples to explain the use of trigonometrical ray tracing in glass optics can be found in the appropriate literature, and the books by Hardy and Perrin (1932, p. 38), or by Conrady (1929, pp. 17 and 51), may be referred to.

The application of the ray-tracing method to electrostatic lenses has been described by Klemperer and Wright (1939). In their method, the continuously varying electric field of the lens is

assumed to be subdivided into a finite number $n+1$ of uniform fields bounded by n equipotential surfaces. A lens modified in this way will differ from the actual electron lens, but the difference will decrease as n increases. On the other hand, the amount of work involved in the ray-tracing procedure makes it advisable to keep the value of n as small as compatible with the required accuracy. In practice it has been found convenient to subdivide an electron lens into about ten or twenty steps of equal refraction. If N and N' are the refractive indices at the two sides of an equipotential surface, N_1 being the initial refractive index and N'_n the final refractive index, then the ratio N/N' for each surface is given by

$$\frac{N}{N'} = \sqrt[n+1]{\frac{N_1}{N'_n}} = \sqrt[n+1]{\left(\frac{V_1}{V'_n}\right)^{\frac{1}{2}}}, \tag{3.18}$$

since N is proportional to the square root of the voltage V. The required subdivision of the potentials can be obtained practically by plotting $\log V$ against the axis coordinate and by subdividing $\log V$ into the adopted number of equidistant steps.

Although the computing formulae (3.14)–(3.17) apply only to spherical surfaces, it is noticed at once by inspection of fig. 3.3 that the equipotentials are generally not spherical. In that case, the compromise of using only the central portions of the equipotentials as spherical to a first order of accuracy has proved to be successful. The radii of the central portions of the equipotentials can be measured with the help of a series of templates which are fitted to the experimentally determined surfaces. From a curve of these radii against the axis coordinate the radii at the required points can be interpolated and the computing formulae can be readily applied.

3.4. Circle method and parabola method

Of great importance for electron ray tracing is the 'circle method'. This is originally based on some calculations by Heath (1887), who discussed the refraction of light through media of varying density. He showed by optical methods that the product of refractive index and curvature of the ray is at any moment proportional to the gradient of refractive index in normal direction to the ray.

We prefer to give the dynamical derivation of Heath's theorem. The centrifugal force of the electron is balanced by the centripetal

force that is produced by the normal field vector $E_\perp$:

$$\frac{mu^2}{r_e} = -eE_\perp. \tag{3.19}$$

With the energy equation

$$\frac{mu^2}{2} = eV,$$

we obtain the radius of curvature

$$r_e = \frac{-2V}{E_\perp}. \tag{3.20}$$

This equation is equivalent to Heath's result. E may be taken as the potential difference $(V_n - V_{n+1})$ between two equipotentials divided by their perpendicular distance p. To obtain $E_\perp$, the field component normal to the orbit, $(V_n - V_{n+1})/p$ is multiplied by the cosine of the angle which the equipotential makes with the orbit. This equals the sine of α, the angle of incidence. The potential V may be taken as the mean of the two equipotentials or nearly enough as that of either one of them. With $E_\perp = \frac{V_n - V_{n+1}}{p} \sin\alpha$, it follows from (3.20) that

$$2r_e \sin\alpha = 4p/(k-1) = b, \tag{3.21}$$

where $k = V_n/V_{n+1}$ is a constant if the equipotentials are drawn again (cf. (3.12)) in geometrical progression of the voltages.

Equation (3.21) may be used for a graphical application of the circle method (cf. Salinger, 1937; Jacob, 1938). This is shown in fig. 3.6 (*a*). For finding the centre of curvature of the electron orbit, the length b of the parameter in (3.21) is plotted on the normal to the equipotential, starting at the point of incidence P of the electron. At the end of b (i.e. at T) a perpendicular is erected which is intersected at Q by a circle of radius $2r_e$, centre P. Bisecting PQ gives the centre O of the electron orbit of radius r_e.

There are regions in the field plot in which the radius of curvature of the electron path r_e becomes so great that ordinary compasses can no longer be used for the graphical construction. Surprisingly large errors would, however, be encountered if the paths were replaced by straight lines. It is advisable to use the following approximation shown in fig. 3.6 (*b*). The straight continuation of

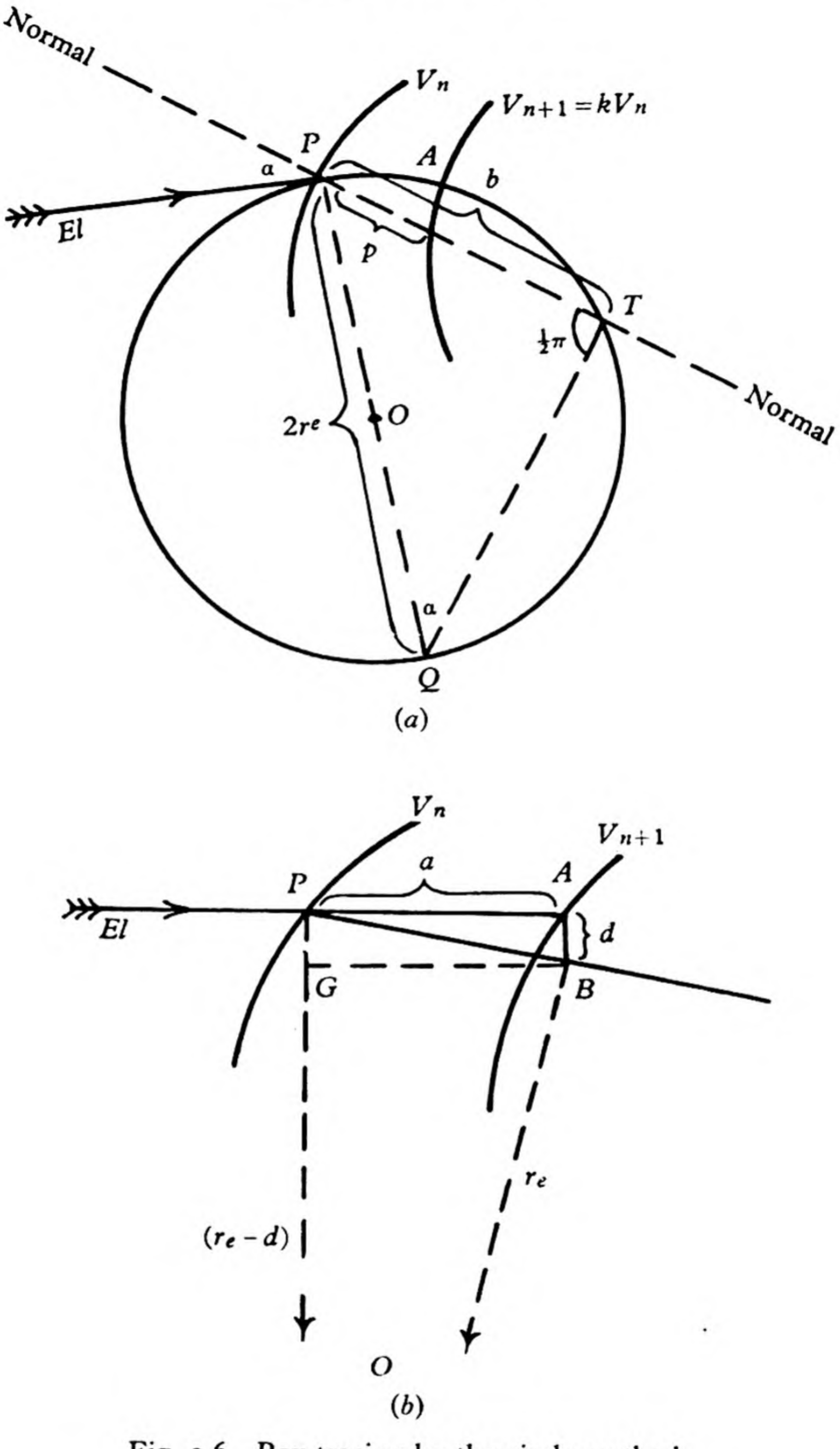

Fig. 3.6. Ray tracing by the circle method.

the path *El* from the equipotential line V_n to the equipotential line V_{n+1} is drawn of length $PA = a$. At the point A where a reaches V_{n+1} a short distance AB is plotted at right angles to a, to the side that is easily guessed from the voltages and shapes of the two equi-

potentials. The length of this perpendicular is given to a reasonable degree of accuracy by

$$AB = d \approx \frac{a^2}{2r_e}, \tag{3.22}$$

and the curved electron ray will pass through B. For $2r_e \gg AB$, the approximate relation (3.22) is easily verified since a is the height of the right-angled triangle BOG inscribed in the circle of radius r_e with the base r_e. A straight line connecting the middle of a to the point B gives well enough the direction of the ray leaving the equipotential V_{n+1}.

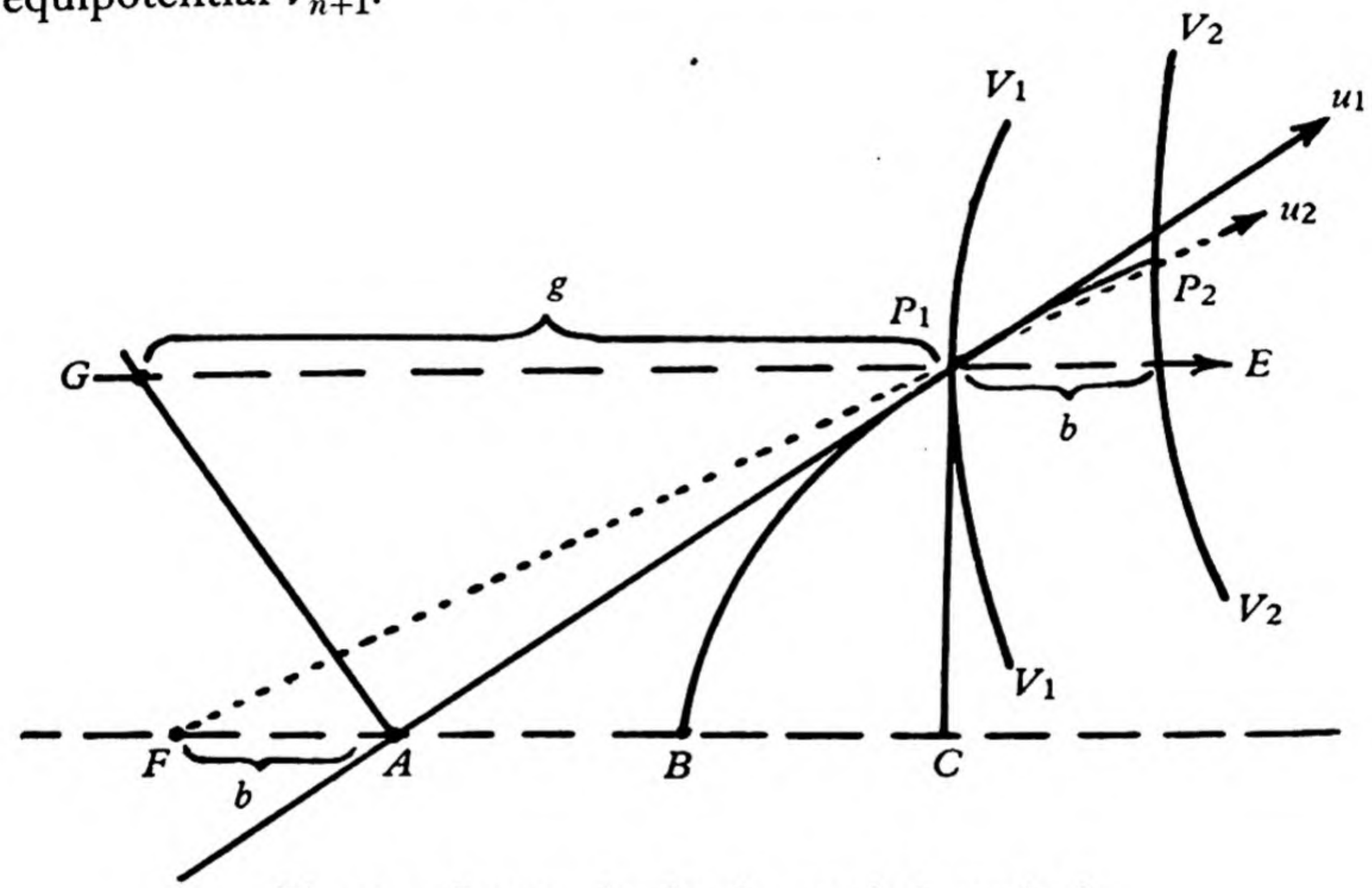

Fig. 3.7. Ray tracing by the parabola method.

The circle method is most useful for large angles of incidence, particularly when the electron crosses the equipotential at a grazing angle. On the other hand, the application of the proper graphical method is often not feasible for paraxial rays because for these rays the radii of curvature are very large. It may be mentioned that this difficulty is overcome in a computational equivalent to the graphical circle method which has been developed by Spangenberg and Field (1942*a*). On the other hand, rays of small curvature can be traced with fair accuracy by the graphical 'parabola method' as described originally by Hepp (1939) and modified by Zworykin and Morton (1940). It will be explained now with the help of fig. 3.7 how the electron path between two equipotentials can be replaced by the osculating parabola.

Let V_1 and V_2 be two equipotentials of relatively small curvature. The distance between these equipotentials is b, so that the field is given by

$$E = \frac{V_2 - V_1}{b} \cdot \cdot \tag{3.23}$$

An electron of velocity u_1 meets the equipotential V_1 at the point P_1 at an angle of incidence $\Theta = \sphericalangle(E, u_1)$. Hence the component of u_1 at right angles to the equipotential V_1 is

$$u_\perp = u_1 \cos \Theta. \tag{3.24}$$

If the electron had fallen through a homogeneous potential field E the component $u_\perp$ would have been zero at the vertex B of a parabolic path, the potential V_B at B being given by the energy equation

$$eV_B = \frac{mu_\perp^2}{2}. \tag{3.25}$$

Now, u_1 is the tangent to the parabolic path, the axis of which is parallel to the field E. Since the subtangent (AC) of a parabola is always bisected by its vertex (B), the length of this subtangent, obtained from (3.23)–(3.25), is

$$AC = 2\left(\frac{V_B}{E}\right) = \frac{b}{V_2 - V_1} \frac{(u_1 \cos \Theta)^2}{e/m}$$

$$= \frac{2V_1 b \cos^2 \Theta}{V_2 - V_1}. \tag{3.26}$$

The point A can therefore be located by the following simple construction: draw the field line E perpendicular to V_1 at P_1, intersecting the equipotential V_2 at a distance b from P_1. Produce field line E back from point P_1 to the point G, such that

$$P_1 G = g = \frac{2V_1 b}{V_2 - V_1}. \tag{3.27}$$

Drop a perpendicular from G to the produced line of u_1 (incident beam) intersecting this in the point A. Now draw $AF\,(=b)$ parallel to the field line E; and the straight line from F through P_1 is the velocity vector u_2 intersecting the equipotential V_2 in P_2. The electron path between P_1 and P_2 would be an arc of a parabola, since (3.27) follows from (3.26) when g is projected on to AP_1 and AP_1

is projected again on to AC. Moreover, FP_2 would be near enough a tangent to the parabola at P_2 since the subtangent to FP_2 is again bisected by the vertex B.

3.5. Ray tracing by integration of the equations of motion of the electron

A great variety of methods has been proposed which are all based on various ways of integrating of the equations of motion of the electron:

$$\left.\begin{aligned} m\frac{\mathrm{d}^2z}{\mathrm{d}t^2} &= e\frac{\partial V}{\partial z}, \\ m\frac{\mathrm{d}^2r}{\mathrm{d}t^2} &= e\frac{\partial V}{\partial r}. \end{aligned}\right\} \tag{3.28}$$

A differential equation for the electron orbit can be derived by elimination of t from (3.28). In the paraxial region $(dr/dz)^2 \ll 1$, moreover, the first two terms of the power series (3.8) can be substituted for $V(r, z)$. This leads to the 'electrostatic paraxial ray equation':

$$\frac{\mathrm{d}^2r}{\mathrm{d}z^2}+\frac{1}{2V_0(z)}\frac{\mathrm{d}V_0(z)}{\mathrm{d}z}\frac{\mathrm{d}r}{\mathrm{d}z}+\frac{1}{4V_0(z)}\left(\frac{\mathrm{d}^2V_0(z)}{\mathrm{d}z^2}\right)r=0. \tag{3.29}$$

The focal length of a lens can be obtained from (3.29), which may be written

$$-\frac{\mathrm{d}^2V}{\mathrm{d}z^2}\times\frac{r}{4}=\frac{1}{2}\frac{\mathrm{d}V}{\mathrm{d}z}\frac{\mathrm{d}r}{\mathrm{d}z}+V\frac{\mathrm{d}^2r}{\mathrm{d}z^2}=V^{\frac{1}{2}}\frac{\mathrm{d}}{\mathrm{d}z}\left(\frac{\mathrm{d}r}{\mathrm{d}z}V^{\frac{1}{2}}\right); \tag{3.30}$$

integration gives

$$\left[\frac{\mathrm{d}r}{\mathrm{d}z}V^{\frac{1}{2}}\right]_{z_1}^{z_2}=-\frac{1}{4}\int_{z_1}^{z_2}\frac{r}{V^{\frac{1}{2}}}\frac{\mathrm{d}^2V}{\mathrm{d}z^2}\,\mathrm{d}z, \tag{3.31}$$

taking parallel incident rays, $(\mathrm{d}r/\mathrm{d}z)_{z_1} = \tan\Theta = 0$,

$$-\left(\frac{\mathrm{d}r}{\mathrm{d}z}\right)_{z_2}=-\frac{1}{4(V^{\frac{1}{2}})_{z_2}}\int_{z_1}^{z_2}\frac{r}{V^{\frac{1}{2}}}\frac{\mathrm{d}^2V}{\mathrm{d}z^2}\,\mathrm{d}z. \tag{3.32}$$

This equation can be solved by successive approximation only. For a thin lens, however, $r \approx$ const. for the path of the electron within the lens and

$$-\left(\frac{\mathrm{d}r}{\mathrm{d}z}\right)_{z_2}=\tan\Theta'=\frac{r}{f'},$$

where f' is the focal length and r the aperture of the incident ray.

The power of the thin lens is then

$$\frac{1}{f'} = \frac{1}{4\sqrt{V'}} \int_{-\infty}^{+\infty} \frac{\mathrm{d}^2 V}{\mathrm{d}z^2} \frac{\mathrm{d}z}{\sqrt{V}},$$

where V' is the potential in the image space.

Applying partial integration and with

$$\frac{\mathrm{d}V}{\mathrm{d}z} = 0$$

for the integration limits on either side of the lens, i.e. for constant potential in the object and in the image space,

$$\frac{1}{f'} = \frac{1}{8\sqrt{V'}} \int_{-\infty}^{+\infty} \left(\frac{\mathrm{d}V}{\mathrm{d}z}\right)^2 \frac{\mathrm{d}z}{V^{\frac{3}{2}}}. \tag{3·33}$$

This is known as the 'electrostatic thin-lens formula' of Scherzer (1933). Applied to ordinary thick electrostatic lenses the result of (3·33) would present a very rough approximation only of the true focal length, and higher terms of the solution of (3.32) would have to be included.

Numerical ray tracing. The various methods of ray tracing which make direct use of the equations of motion are distinguished by the way in which these equations (3.28) or the ray equation (3.30) can be integrated. It is generally not possible to give analytical solutions for the complicated fields of actual electron lenses; hence very often the equations have to be integrated by computational or numerical methods. The following examples may show the way in which the problems of numerical ray tracing have been attacked.

Maloff and Epstein (1934, 1938) divided the lens field into intervals (Δz) in which

$$\frac{1}{2V_0}\frac{\mathrm{d}V_0}{\mathrm{d}z} \quad \text{and} \quad \frac{1}{4V_0}\frac{\mathrm{d}^2 V_0}{\mathrm{d}z^2}$$

were assumed to be constants. These constants could be substituted into the paraxial ray equation (3.29) leading to an expression of r as a function of z which could be calculated for every step.

Gans (1937) replaced the $V_0(z)$ curve, representing the potential along the axis of the lens, by a polygon of straight lines, so that $\mathrm{d}^2V/\mathrm{d}z^2$ vanished for each section. In this way the paraxial ray equation (3.29) was reduced to the first two terms only which again

could be integrated to give $r = f(z)$ for each section. The method gives only approximate results, but it could be much improved by approximating the $V_0(z)$ curve rather by a sequence of parabolic arcs, and Recknagel (1936) has worked out a step-by-step integration of (3.29) on this principle.

Of further interest is the method by Spangenberg and Field (1942*a*), who made use of the property of the electron paths of being orthogonal to the lines of constant action. The action function as given by (1.1) was developed from the known potential V_0 as a power series of r. There has been published a number of other numerical ray tracing methods based on the paraxial ray equation (3.29). We can only mention the papers by Picht (1932), by Dosse (1941), by Ramberg (1942) and by Burfoot (1952). More methods of this kind have been worked out for ray tracing in magnetic lenses. They will be treated in Chapter V, and they could be adapted for use in electrostatic fields without difficulty.

The accuracy of all these methods depends on the size of the integration interval Δz. However, even by choosing very small Δz, one cannot expect to obtain information beyond the range of the first-order theory from methods which are based on the paraxial equation. For tracing lens aberrations, one has to use methods for numerical integration of the general equations of motion (3.28). For this purpose, the experimental values of $V(r, z)$ and its derivatives $\partial V/\partial z$ and $\partial V/\partial r$ have to be tabulated for suitable intervals of Δz and Δr for the region through which the ray passes. Different methods of zonal ray tracing are distinguished again by the ways in which the integration of the equations of motion is carried out. We refer in this connexion to the papers by Goddard (1944), Goddard and Klemperer (1944), Motz and Klanfer (1946*b*) and Liebmann (1949*b*). We have, however, no space to discuss the numerical integration processes; the procedures are long and complicated, and the reader who wants to apply them must study the details in the relevant literature.

3.6. Automatic ray-tracing machines

Such devices have only recently gained practical importance: in all cases the apparatus is complicated and could not be produced quickly without much previous experience. The earliest two

automatic ray-tracing machines are due to Gabor (1937) and to Langmuir (1937*a*, 1950); they are both based on the circle method described in § 3.4, and they work on the following principles: Both potential and potential gradient are measured simultaneously by probes dipping into an electrolytic trough and rigidly connected to a small carriage which guides a pencil drawing the electron path. The carriage is automatically steered by an electric motor. The steering angle is adjusted in the following way. The probe is split

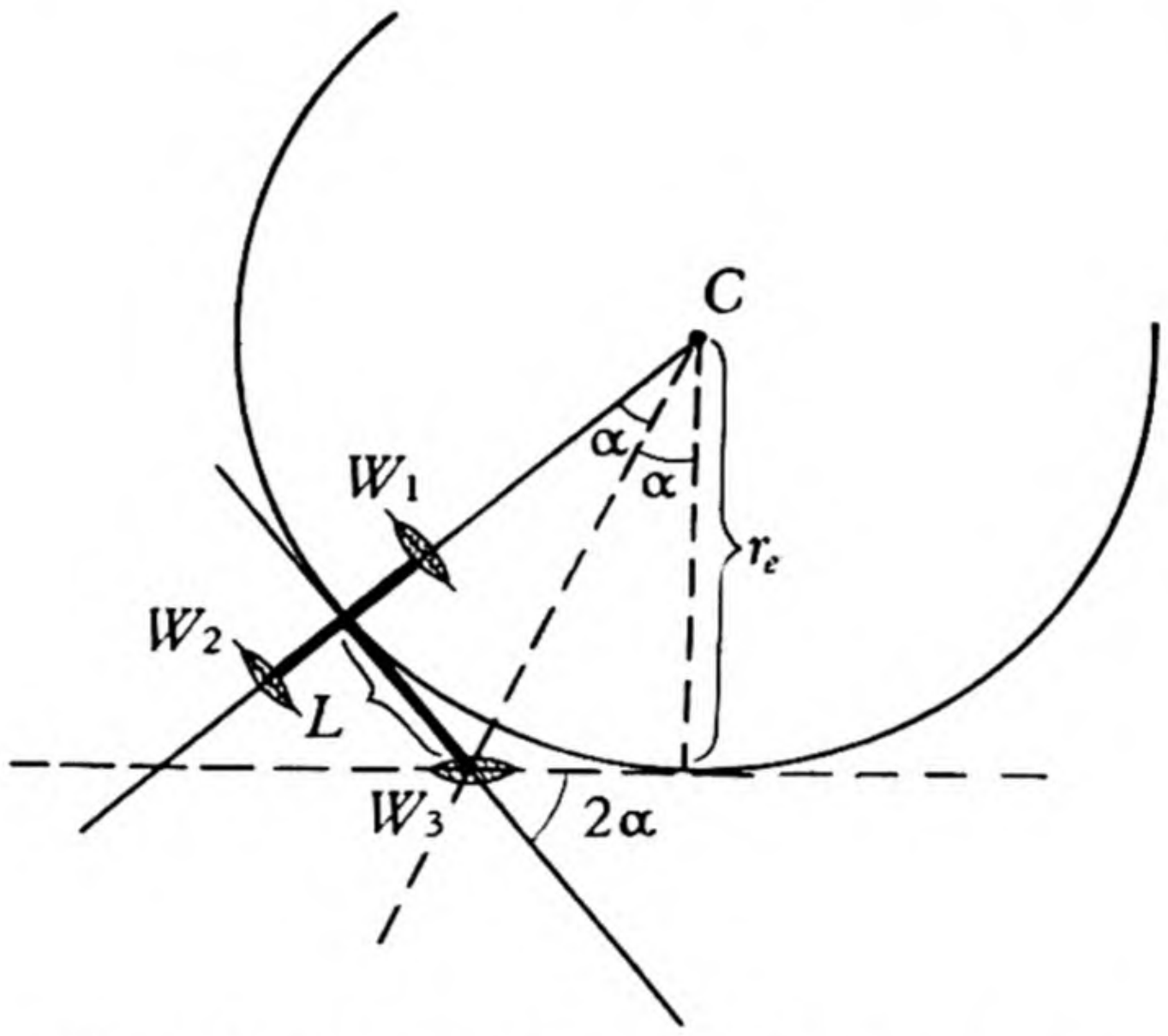

Fig. 3.8. Automatic ray tracing apparatus.

up into two wires arranged so that the line joining them is perpendicular to the electron path. Thus it measures not only the potential difference V of the particular point relative to the origin of the electron (for instance, the cathode), but also the field component $E_\perp$ in the direction normal to the trajectory, namely, $E_\perp = -\Delta V/\Delta r$, where ΔV and Δr are the voltage difference and the distance respectively of the two wires of the split probe which is always kept at right angles to the path. Now the steering angle ($= 2\alpha$), i.e. the angle included by the two axles of the carriage, has to be adjusted at each point in order to produce the path with the radius of curvature r_e as given by (3.20). As can be seen in fig. 3.8, this path will be followed, if the two planes which are defined by the rims of the wheels W_1, W_2 and W_3 are kept parallel to the tangents of the path. In this case, the locus for the centre C of the circle with the radius r_e is the intersection of: (1) the prolongation

of the axle of the wheels W_1 and W_2 which is rigidly connected with the carriage, and (2) the bisecting line of the angle between the planes parallel to the wheels which passes through the pivot of the wheel W_3 which is steered. Under these conditions it follows immediately that $r_e = L\cot\alpha$ if L is the distance between the pivot and the fixed axle. The necessary control of steering is achieved by applying both V and ΔV to a special circuit, the so-called 'tangential bridge', which is arranged to show balance when the ratio of the two voltages is given by

$$\frac{V}{\Delta V} = \frac{L}{2\Delta r}\cot\alpha. \tag{3·34}$$

Very good accuracy of ray tracing has been obtained by using a differential analyser set up for the direct integration of the equation of motion of the electron. Again, differential analysers are relatively complicated machines; they are, however, readily available in some mathematical laboratories. Blewett (1948) used such an analyser for ray tracing in two-dimensional fields. Sander, Oatley and Yates (1949, 1952) worked out a completely automatic precision method for ray tracing through circular symmetrical systems. The differential analyser was used to integrate the equations of motion of an electron, the components of acceleration of which were constantly determined by automatic probe measurements in the electrolytic trough. The accelerations following from the axial and radial components of the electric field were measured by the voltages between three suitably placed probes mounted on a movable carriage. The voltages were amplified and converted into proportional rotations for feeding the analyser, and this was done by means of self-balancing linear potentiometers, embodying conventional follow-up servo-mechanisms. The rotations were each fed into a pair of integrators. The double integrals of the accelerations then gave the displacements which were fed back to the probe carriage. In this way the system was continuously integrating the equations of motion and the probes were moving along an electron path.

3.7. Fields and electrodes

The preceding paragraphs presented a choice of a relatively large number of methods by which the electron path can be traced through any given system of electrodes. The inverse problem given

by the task of finding the electrode system which produces a desired electron path is incomparably more difficult.

Mathematical methods may help in a few very simple cases. At first sight, the problem seems simplified by the fact that the potential on the axis uniquely determines the distribution outside it (cf. § 3.1). However, Berz (1950) has shown how the rigorous mathematical concept of a function differs from its practical meaning, so that if the potential on the axis is known within finite but arbitrary limits the potential problem still admits an infinity of solutions.

For practical purposes methods of trial and error have to be adopted. In this way Balachowsky (1946) proposed a graphical method based on Laplace's equation. Hutter (1947*b*) attacked the problem experimentally by using in his electrolytic trough six probes, each connected to a vacuum tube voltmeter and arranged along a desired equipotential line. He then tried to modify the shape, arrangement and potential of his electrodes until all indicators were balanced simultaneously.

If a particular electrostatic field has to be produced, the absolutely correct electrode shapes for which the appropriate boundary conditions are satisfied exactly are unique. There is, however, an infinity of quite dissimilar electrode shapes by which the boundary conditions can be satisfied to a good approximation. An approximate solution may be better in a practical sense than an exact solution, for the approximate solution may allow a certain amount of adjustment of the electrode shapes to meet exigencies of construction. For the purpose of practical lens design it is often useful to choose for a start the best obtainable simple type of lens the properties of which are well known. Such a lens might fulfil the practical requirements to some extent. The electrodes of this lens and their potentials may then be changed in such a way as to improve the result. A certain store of knowledge of the properties of such simple lens types is very convenient for this purpose and will be presented in the next chapter.

CHAPTER IV

SOME ELECTROSTATIC ELECTRON LENSES

4.1. General properties

According to the considerations of Chapter III it is clear that the optical properties of an electrostatic lens are fixed by voltage ratios, the absolute value of the potentials at the electrodes being unimportant. Usually, all electrode potentials are measured with respect to a zero level at which the electron ray considered would have zero velocity; the ratio of these electrode potentials alone fixes the position of the cardinal points. For instance, in (3.18) the ratio of refractive indices which is responsible for the angle of refraction at each equipotential is given by V_1/V'_n, so that, for example, the cardinal points drawn in fig. 2.2 would be in exactly the same position whether the potentials at the two tubes were 0·1 and 0·5 V. or 10 and 50 kV. respectively.

It is convenient to measure all geometrical lengths of electrostatic lenses in terms of the radius of one of the electrodes. For instance, the symmetrical two-tube lens of fig. 2.1 with the voltage ratio $V'/V = 5$ has two mid-focal lengths: $MF = 5{\cdot}4R$ and $MF' = 4{\cdot}7R$. Thus, if the radius of the tube were 2 cm., these mid-focal lengths would be 10·8 and 9·4 cm. respectively, or with tubes twice this radius, the mid-focal lengths would be twice as large.

The principal planes of the two-tube lens in fig. 2.2 are crossed over with respect to their corresponding foci. It can be shown from the paraxial ray equation (3.29) that the principal planes are crossed over in every electrostatic lens. The foci of all electrostatic lenses are moved towards the mid-plane if the voltage ratio is increased. A lens may be strong enough to make initially parallel rays cross the axis inside the lens field, so that a real focus is formed before the rays leave the lens. If after passing this focus the rays are still exposed to the lens field, it is quite possible that they are made convergent again to reach a second or even a third focus. Alternatively, after crossing over, the rays would leave the lens as a divergent bundle. However, it can be shown (for instance, from the paraxial ray equation (3.29)) that there exist no proper diverging

electron lenses with negative focal length, provided that the lens electrodes are arranged outside the beam and that the lens field is bounded by a field free space at the entrance side and at the exit side of the beam.

4.2. Symmetrical two-tube lenses

Experimental values (Klemperer, unpublished) for the two mid-focal lengths of the symmetrical two-tube lens, measured in tube

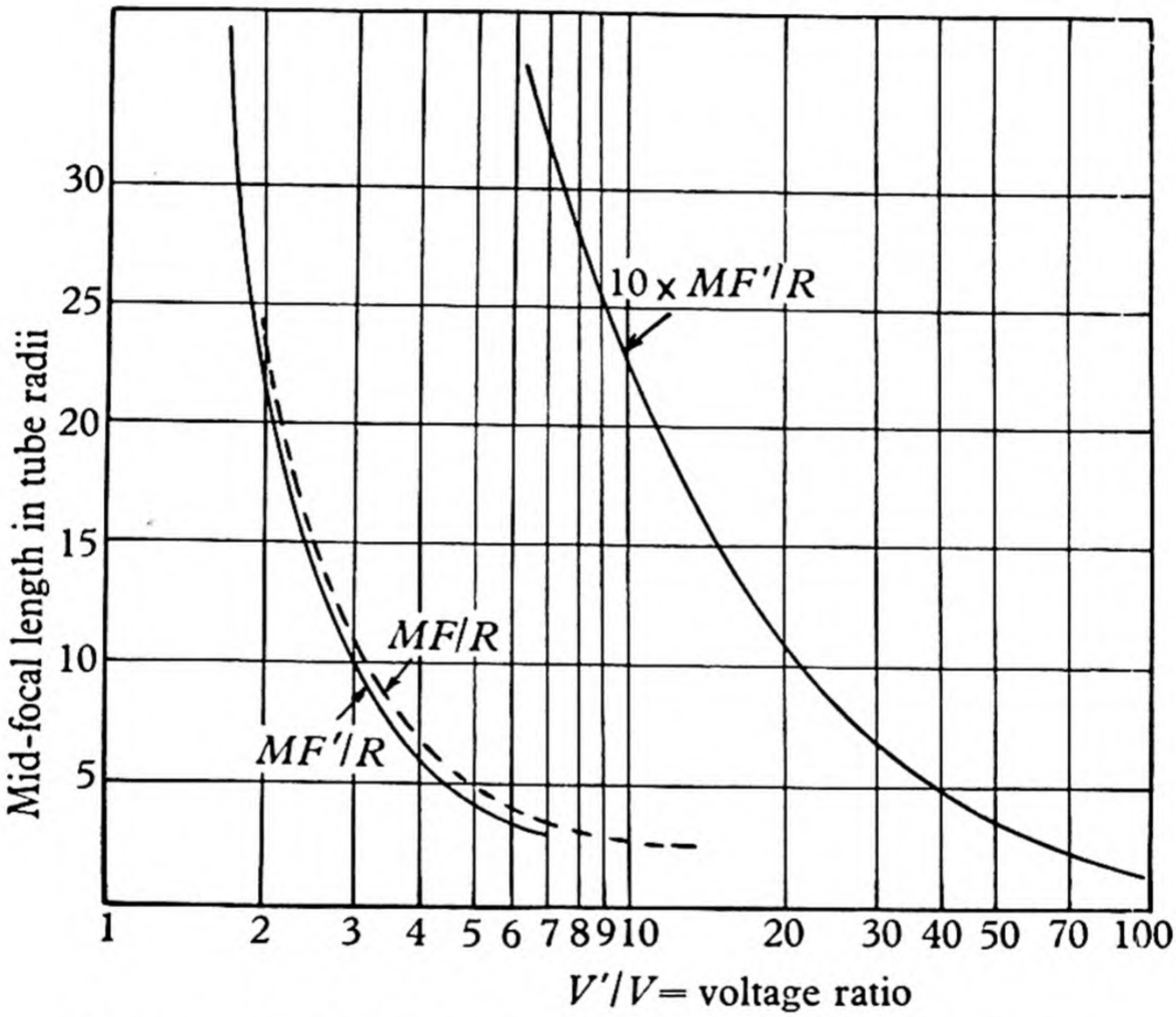

Fig. 4.1. Mid-focal lengths of the symmetrical two-tube lens.

radii, are plotted in fig. 4.1 as a function of the voltage ratio. The meaning of the symbols MF, R, etc., is again the same as in figs. 2.1 and 2.2. The broken curve, denoted by MF/R, belongs to the focus F obtained when parallel rays are decelerated. The solid curves give the mid-focal distances MF'/R for the focus F' of parallel beams accelerated by this lens. The left-hand solid curve in fig. 4.1 covers mid-focal lengths between 2·5 and 30R, the right-hand curve plotted over the same abscissa, with 10 times enlarged ordinate

values, covers mid-focal lengths between 0·3 and 4 tube radii and reaches up to a voltage ratio of 100.

The distances of the two corresponding principal planes from the mid-plane, as a function of the voltage ratio, are shown in fig. 4.2, the broken curve corresponding to the principal plane P in fig. 2.2, and the solid curve corresponding to P'. The position of the principal planes changes relatively little with the voltage ratio. Mid-focal lengths for the accelerated beam are slightly shorter than those for the decelerated beam. However, the focal length at the high-

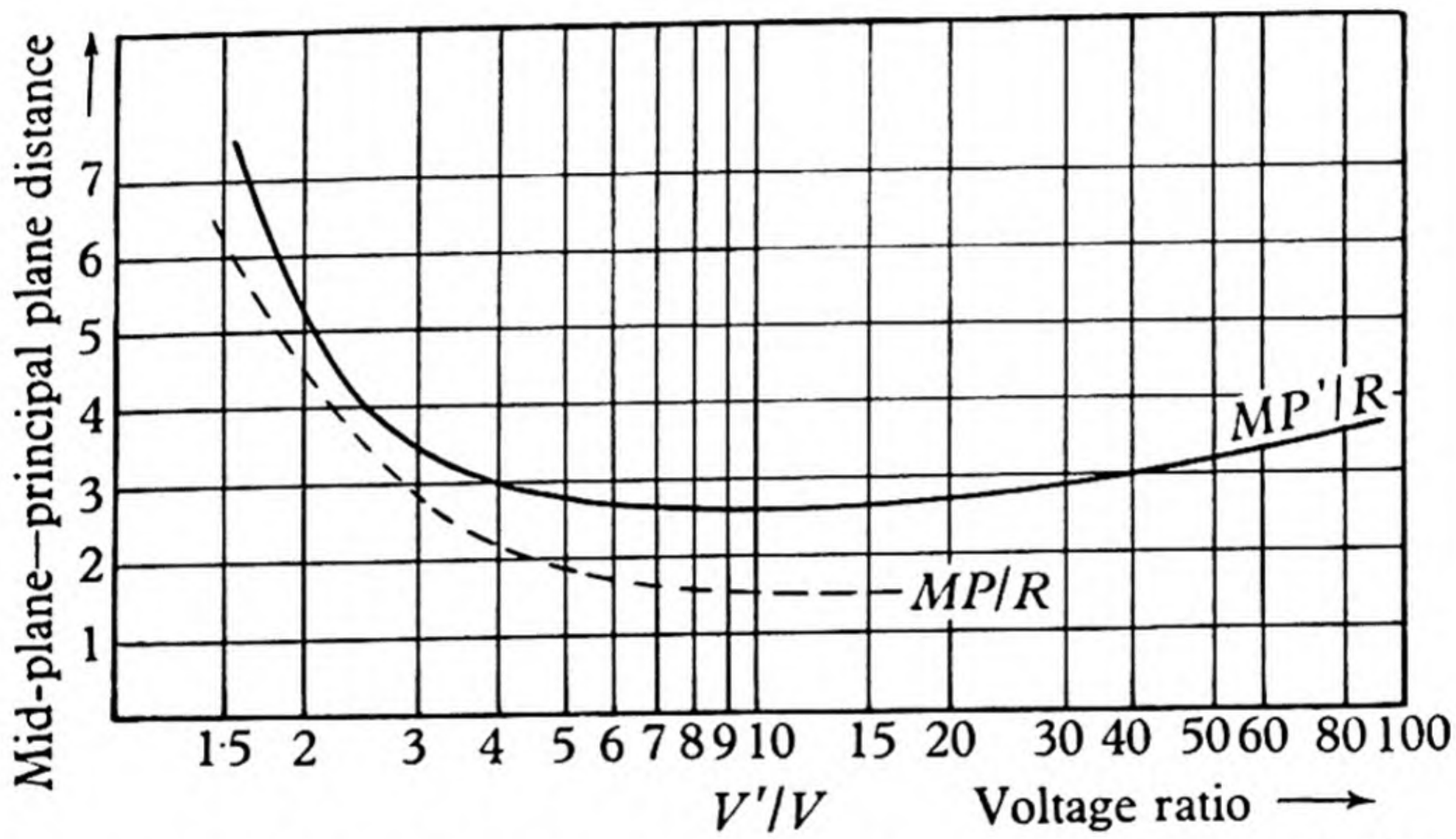

Fig. 4.2. Position of principal planes of the symmetrical two-tube lens.

voltage side $f' = MF' + MP'$ is always appreciably longer than the focal length at the low-voltage side $f = MF - MP$. The symmetrical two-tube lens has been studied by numerous investigators. We mention the experimental investigations by Nicoll (1938*a*), Klemperer and Wright (1939) and Spangenberg and Field (1942*a*) and

TABLE I. *Symmetrical two-tube lens: theoretical values* (Goddard, 1946)

Focal lengths (PF, $P'F'$) and mid-plane to principal plane distances (MP, MP') expressed in tube radii (R) for various voltage ratios (V'/V).

V'/V	2	3	5	7	10
MP/R	4·22	2·74	2·04	1·83	1·75
$f = PF/R$	21·61	7·98	3·44	2·26	3·31
MP'/R	5·00	3·55	2·93	2·76	2·62
$f' = P'F'/R$	30·56	13·82	7·71	5·98	4·95

the theoretical investigations by Gray (1939), Plass (1942), Hutter (1945*a*) and Goddard (1946*a*). The latter author substitutes a theoretical axial potential distribution obtained by Bertram (1940) into the paraxial ray equation (3.29), and by using a development by Picht (1939) he arrives at the numerical values given in Table I. These values, which are obtained by entirely theoretical methods, are within a few per cent identical with the values taken from figs. 4.1 and 4.2, which have been measured by the author with the 'pepperpot method' (cf. § 2.3).

Since the two-tube lens always makes the electron beam more convergent, it is a positive lens, and this is true whether it accelerates or decelerates the electrons. Ray-tracing results show that the two-tube lens can be considered as consisting of two 'semi-lenses', a positive one, having equipotentials convex towards the lower potential side, and a negative one, making the beam more divergent, having the equipotentials concave towards the lower potential side. As can be seen from fig. 3.3 of Chapter III, the mid-plane separates the two semi-lenses. The power of the positive semi-lens is always greater than that of the negative semi-lens, so that its effect predominates in the resulting full lens. In fig. 4.4 (*b*) there are shown the paths of the two characteristic parallel beams decelerated and accelerated. The glass-optical analogies of the semi-lenses are also shown in fig. 4.4 (*a*) as convex and concave lenses. The voltage ratios of the two semi-lenses could be defined as the voltage ratio between the mid-plane and the first of the tubes, and as the voltage ratio between the other tube and the mid-plane. The values of these voltage ratios are

$$\left(\frac{V'-V}{2}+V\right)\Big/V=\frac{V'+V}{2V} \tag{4.1}$$

for the positive semi-lens, and

$$\frac{2V'}{V'+V} \tag{4.2}$$

for the negative one. Thus the voltage ratio of the positive semi-lens increases without limit as a linear function of the total voltage ratio V'/V, but the voltage ratio of the negative semi-lens, being always smaller than that of the positive one, approaches the value 2 as an upper limit as the total voltage ratio is increased indefinitely. If the

electrons are accelerated and sufficiently high-voltage ratios are applied, the electrons cross over very close to the mid-plane, and a beam would leave the lens more divergent than it entered. If the voltage ratios are still higher, for instance, of the order of 1000, it could happen that the beam crossed over early in the first semi-lens and left the lens converging, thus crossing over finally a second time (Nicoll, 1938*a*).

The positions of the nodal points of the electron lens, which are important for a discussion of the magnification, can be calculated from the data of figs. 4.1 and 4.2 by means of (2.1). In this way it is found that both the nodal points usually lie on the high-voltage side of the mid-plane and are crossed over with respect to their corresponding focal points. The position of the nodal points changes but slightly with the voltage ratio.

The fact that the two nodal points are on the high-voltage side suggests that the magnification y'/y of an image y' produced on the high-voltage side would be smaller than a magnification calculated as the ratio q/p of mid-image to mid-object distance. As these two distances are always easy to measure, it is of some practical interest to know the order of magnitude of a figure $\frac{p}{q}\frac{y}{y'}$ which indicates how much smaller the actual magnification is than the ratio of q and p. Using (2.2) and (2.13) we have

$$\frac{p}{q}\frac{y'}{y} = \frac{(x+MF)}{(x'+MF')}\frac{f}{x} = \frac{x+MF}{f'+\dfrac{xMF'}{f}} = \frac{x+MF}{MF'+MP'+\dfrac{xMF'}{MF-MP}}. \tag{4·3}$$

But substituting practical values for f, f', MF and MF' (dashed indices represent high-voltage side), it can be recognized that $\frac{p}{q}\frac{y'}{y}$ lies generally round 70 %, tending to slightly smaller values when either the voltage ratio or the object distance is decreased.

The approximate constancy of $\frac{p}{q}\frac{y'}{y}$ involves, for instance, the following curious result. If the values of p and q are given, an image can be obtained by using either large or small tubes. If large tubes are used the voltage ratio has to be relatively higher, but the mid-

object distance as measured in tube radii (p/R) becomes relatively smaller. However, for a given p and q the magnification can scarcely be varied by changing the size of the tubes, although this change may include very large corresponding changes of the ratio of refractive indices of object and image space. These facts are conveniently shown by a practically useful type of diagram represented

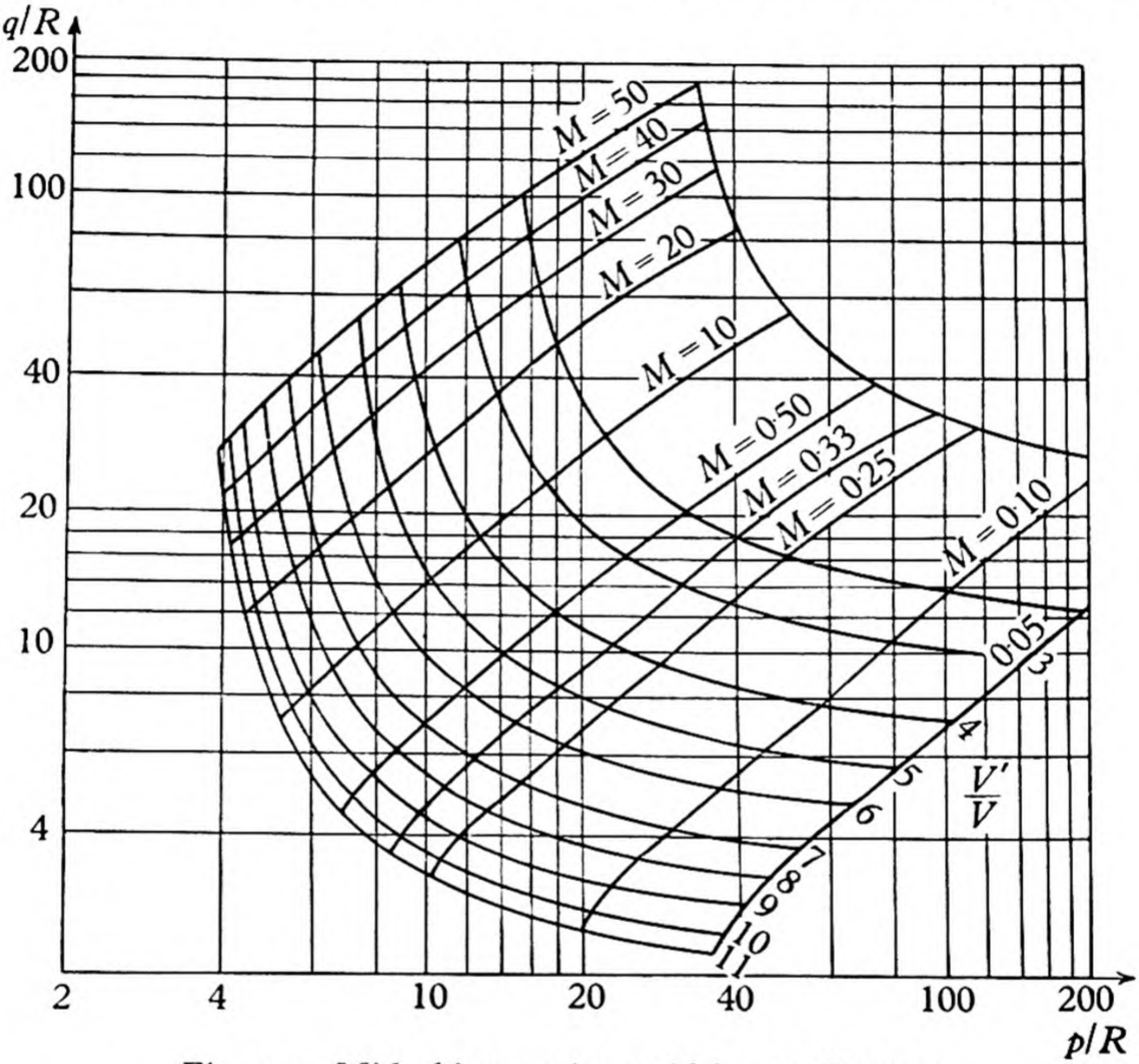

Fig. 4.3. Mid-object against mid-image distances for symmetrical two-tube lens.

by fig. 4.3 which is due to Spangenberg and Field (1943). The coordinates give mid-object and mid-image distances, and two families of curves are shown which are characterized by given parameters V'/V (voltage ratio) and $M = \dfrac{y'}{y}$ (magnification) respectively.

In the two-tube lens discussed so far it was understood that the gap between the tubes was to be small in comparison with the tube radius. In the field plot of fig. 3.3, for instance, the gap was chosen to be $2g = 0{\cdot}2R$, the tube ends being $g = 0{\cdot}1R$ apart from the mid-plane.

Due to the fact that the potential $V(z)$ near the mid-plane is approximately a linear function of the axial coordinate z, the gap width has practically no influence on the lens characteristics as long as the gap is small. The effect of large gap width is demonstrated by Table II. There the influence of gap width $2g$ is shown for three different electrode spacings. The voltage ratios V'/V are set to obtain a given focal length $P'F'$, which in one example is $6R$, in the other example $12R$. The increase in voltage ratio with gap width is plausible since increase of gap width produces an extension of a quasi-homogeneous field inserted between the two semi-lenses. Moreover, it is of interest that with increasing gap width, the mid-plane-nodal point distances and thus the magnifications appear to decrease slightly. This can be seen by substituting the figures of Table II into $MK = MF - P'F'$ and the corresponding equation for MK' which follow from (2.1) and (2.9). Tube lenses with increased gap width have to be shielded carefully to avoid disturbances through the large gap by spurious external electric fields. However, these lenses are of practical importance, because the application of large voltage differences often requires large gaps in order to avoid a breakdown by spark discharges.

TABLE II. *Gap width, voltage ratio, and mid-focal lengths of symmetrical two-tube lens* (Spangenberg and Field, 1943)

$2g$	$P'F' = 6R$			$P'F' = 12R$		
	V'/V	MF'/R	MF/R	V'/V	MF'/R	MF/R
$0{\cdot}2R$	8·0	3·0	4·4	3·5	7·4	8·8
$1{\cdot}0R$	9·0	3·0	4·0	3·9	7·5	8·2
$2{\cdot}0R$	12·0	3·3	3·1	6·4	9·0	6·9

For very high voltages at the electrodes, i.e. high energies of the electron rays, the focal length of the two-tube lens is increased owing to a relativistic increase in electron mass. Hansen and Webster (1936) calculated for electrons approaching the velocity of light the following relation between mid-object distance p and mid-image distance q:

$$\frac{1+\gamma}{p} + \frac{1-\gamma}{q} = 3\gamma^2\zeta, \tag{4.4}$$

where γ and ζ are the following functions of the potentials V and V' at the lens electrodes and of the field $\partial V_0/\partial z$ along the axis:

$$\gamma = \frac{V'/V - 1}{V'/V + 1}, \quad \zeta = \int_{-\infty}^{+\infty} \left(\frac{\partial V_0/\partial z}{V' - V}\right)^2 \mathrm{d}z.$$

The latter integral has been solved for the two-tube lens by Kirkpatrick and Beckerley (1936), who found

$$\zeta = \frac{1}{R}\left[2{\cdot}06 + 1{\cdot}50\left(\frac{g}{R}\right)^2\right],$$

where g is again the half gap width between the tubes. For large voltage ratios, $\gamma \to 1$, consequently the value of $1/p + 1/q$ obtained from (4.4) is found to exceed the corresponding $1/p + 1/q$ for relatively slow electrons by a factor 4. Thus the values of the mid-focal distances plotted in fig. 4.1, etc., would have to be increased by several hundred per cent as the speed of the electron ray approaches light velocity.

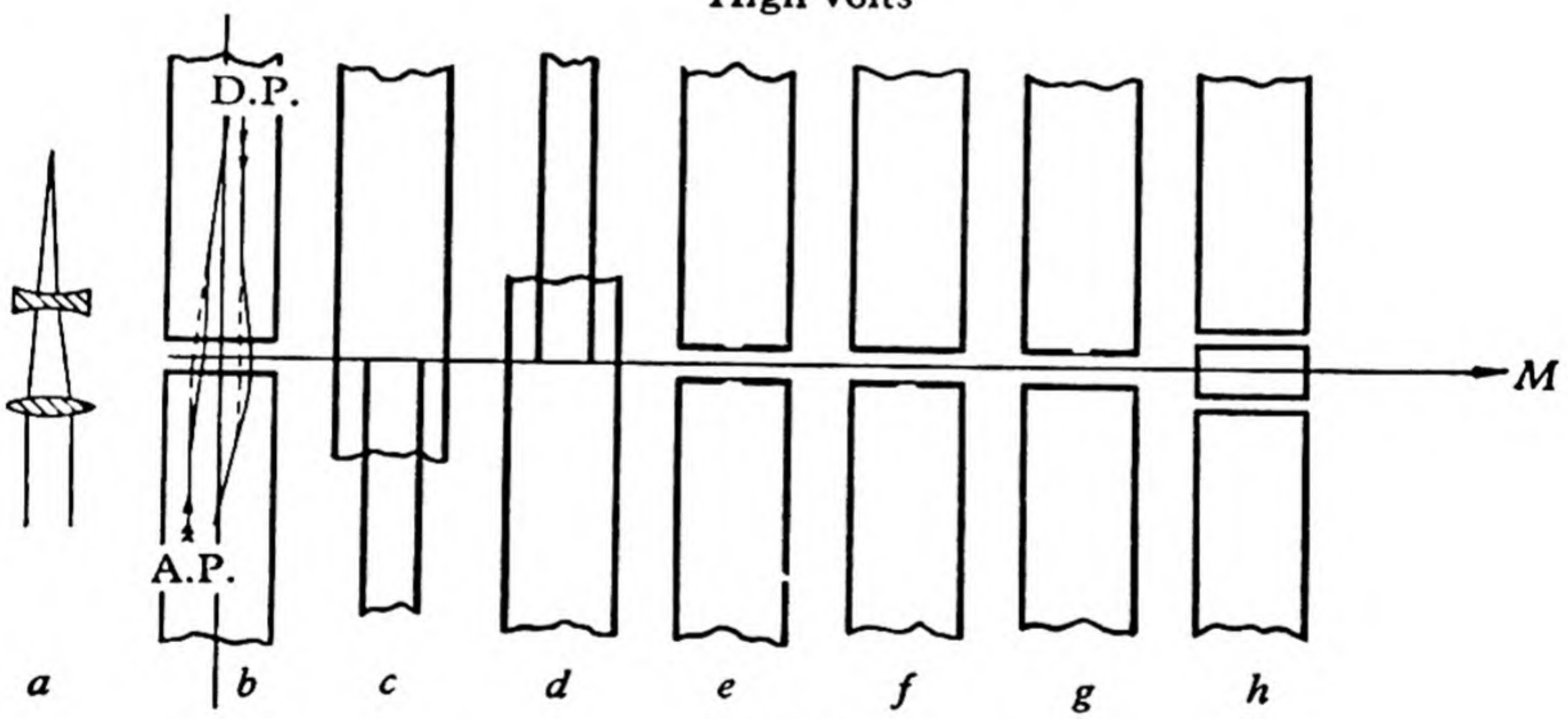

Fig. 4.4. Some simple electrostatic electron lenses.

4·3. Various two-electrode lenses

The position of the cardinal points can be slightly varied if the shape of the electrodes of the electron lens is changed. There exists a very large variety of shapes, and we have to confine ourselves to mentioning just a few simple types in order to explain the principal characteristics and possibilities. In fig. 4.4 (b)–(g) are shown six examples of two-electrode lenses produced by combinations of

cylindrical tubes and straight diaphragms. The straight line M, drawn through all the lenses, coincides in each case with the mid-plane. Only in lenses (*b*) and (*e*) does the mid-plane represent a plane of symmetry; in the other cases it is a rather arbitrary plane of reference. It is always practically convenient to take the radius R of the *largest* electrode as a unit of length, since this radius is limited by the size of the evacuated glass tube containing the electron lens. In Table III are given the data concerning mid-focal lengths and the distances between the principal points and the mid-point, the plain symbols corresponding again to the decelerated parallel beam D.P., the dashed ones to the accelerated parallel beam A.P. It can be seen that the given values are markedly different, although the same voltage ratio ($V'/V = 5$) was taken in all cases.

TABLE III. *Experimental data concerning the location of foci F and F′ and principal points P and P′*

Lens (fig. 4·4)	Electrodes, radius		$V'/V = 5$				Potential at M (%)
	At low volts	At high volts	MF	MF'	MP	MP'	
b	Tube, R	Tube, R	4·8	4·4	2·0	2·9	50
c	Tube, $\frac{1}{2}R'$	Tube, R'	2·6	3·2	0·1	1·0	31
d	Tube, R	Tube, $\frac{1}{2}R$	4·3	3·4	1·5	2·3	69
e	Diaphragm, $\frac{1}{4}R$	Diaphragm, $\frac{1}{4}R$	1·5	1·4	0·4	0·9	50
f	Diaphragm, $\frac{1}{4}R'$	Tube, R'	2·4	2·9	1·3	0·5	13
g	Tube, R	Diaphragm, $\frac{1}{4}R$	4·4	3·2	1·9	2·6	87

In order to understand the results, we may consider again that any one of these electron lenses can be thought of as consisting of two semi-lenses which are separated by the mid-plane. A large decrease in focal length would then be expected if the smaller electrode is on the low-voltage side. The smaller electrode would then correspond to the positive semi-lens (fig. 4.4(*a*)), which always overpowers the negative semi-lens, as was pointed out at the beginning of this chapter. The results obtained with lenses 4.4(*c*) and 4.4(*f*) support this expectation qualitatively, although the decrease in focal length is rather less than proportional to the decrease in electrode radius. Moreover, if the smaller electrode is at the high-voltage side, it corresponds to a negative semi-lens, which, according to the above

considerations, should not greatly affect the focal length of the complete lens. The results show, however, that even here the focal length of the complete lens is appreciably decreased in comparison with the symmetrical two-tube lens. The reason for this reduction of focal length with diminishing dimensions of the high-voltage electrode becomes obvious when a field plot of an unsymmetrical arrangement* is inspected. The mid-plane then no longer coincides with any equipotential. The 50 % equipotential has become concave towards the smaller electrode and has penetrated appreciably into the larger electrode.

The axial coordinate at which the curvature of the equipotentials changes its sign is generally not far away from the mid-point. The potential at the mid-point is more removed from 50 % the greater the difference between the sizes of the two electrodes. In the last column of Table III are noted the actual potential values at the mid-point of the lens. It can be seen that in all cases the voltage ratio of the semi-lens in the smaller tube is decreased and the voltage ratio of the semi-lens in the larger tube is correspondingly increased with respect to the voltage ratios of the semi-lenses in the symmetrical two-tube lens (see (4.1) and (4.2)). Thus, if the dimensions of the electrode at the high-voltage side are reduced, the decrease of focal length and the shifting of the principal points of the complete lens can be understood to be caused by increasing voltage ratio of the positive semi-lens which is contained in the larger tube. From the point of view of magnification it may be expected that an image at the high-voltage side will generally be more magnified if the smaller electrode is on that side.

The lens types represented by fig. 4.4 (*c*)–(*g*) have found wide application in cathode-ray tubes (cf. Epstein, 1936). The good electric shielding of the lenses 4.4 (*c*) and (*d*), with the larger tube overlapping the smaller one, is a practical merit (cf. §6.2). In particular, the lens of fig. 4.4 (*c*) has been frequently employed as a focusing lens in television tubes, the wider tube being formed by the metallized glass neck into which the smaller tube protrudes as the end of the electron gun (cf. fig. 12.1). By using a greater diameter for the second tube, fouling of the beam is avoided when it is scanned by deflecting fields.

* Equipotentials of an unsymmetrical two-tube lens are drawn in fig. 12.1.

Numerical data for two examples of unsymmetrical two-tube lenses are shown in Table IV. There, the ratio of tube radii is 2/3 and 3/2 respectively, one lens having the larger tube at the high-voltage side ($R'/R = 1{\cdot}5$), the other lens having the larger tube at the low side ($R'/R = 1/1{\cdot}5$); in both cases focal lengths and mid-focal distances are measured in units of the large tube radius.

TABLE IV. *Focal lengths and mid-focal distances of unsymmetrical two-tube lenses* (Spangenberg and Field, 1943)

V'/V	Lens of fig. 4.4(*c*) $R'/R = 1{\cdot}5$			Lens of fig. 4.4(*d*) $R'/R = 1/1{\cdot}5$		
	$P'F'/R'$	MF'/R'	MF/R'	$P'F'/R$	MF'/R	MF/R
2	35	33	−24	16·5	12·3	−19·4
3	11·2	9·5	− 7·9	11·8	8·0	− 9·4
5	6·5	3·9	− 4·3	8·2	5·0	− 6·6
7	4·9	2·4	− 3·1	6·3	3·3	− 5·2
10	3·8	1·6	− 2·4	4·8	2·2	− 4·2
13	3·3	1·3	− 2·1	4·3	1·7	− 3·6

TABLE V. *Focal lengths and mid-focal distances of symmetrical two-diaphragm lenses* (Spangenberg and Field, 1943)

V'/V	Gap $= 2R_A$			Gap $= 6R_A$		
	$P'F'/R_A$	MF'/R_A	MF/R_A	$P'F'/R_A$	MF'/R_A	MF/R_A
2	38	33·0	−34·0	17·5	13·0	−15·5
3	17·6	13·4	−15·0	12·0	7·5	−11·0
5	8·8	5·6	− 9·2	6·1	2·5	− 6·5
7	6·5	3·6	− 8·4	4·7	0·9	− 5·5
10	5·3	2·0	− 8·0	3·7	−0·1	− 4·9
13	5·0	1·4	− 7·8	3·1	−0·7	− 4·7

Numerical data for symmetrical two-diaphragm lenses as shown in fig. 4.4(*e*) have been published by Polotovski (1934) and by Spangenberg and Field (1943). Two examples are given in Table V. The two lenses are distinguished by the distances between the diaphragms, i.e. the 'gap' which is taken as two aperture radii and six aperture radii respectively. Focal lengths and mid-focal distances are also measured in units of aperture radii. The tubes which are terminated by the diaphragms are assumed to be large in comparison with the aperture. In this case the value of the tube radius

hardly influences the electron-optical characteristics of the lens. The real function of the tubes consists in providing support for the diaphragms and in the electrostatic shielding of the lens from spurious fields. If the diaphragms are separated by a sufficiently large gap, the power of the lens can be calculated to some approximation as the resultant of a combination of two single apertures (cf. Cosslett, 1946*b*).

4.4. The single aperture

A plane diaphragm may be placed between two plane conductors A and B of different potentials V_A and V_B. Two electric fields will be produced at the two sides of the diaphragm, namely,

$$E = \frac{V_A - V_C}{a} \quad \text{and} \quad E' = \frac{V_C - V_B}{b},$$

where V_C is the potential of the central diaphragm and a and b are its two distances from the external conductors. Now, a small circular aperture may be made in the central diaphragm. Equipotentials will bulge through the aperture, with the stronger field penetrating into the region of the weaker field. This field penetration through an aperture has been studied by Glaser and Henneberg (1935) theoretically and in the field plotting trough. Detailed computations of field distributions about apertured diaphragms of finite thickness have been published by Liebmann (1948*a*).

Two essentially different potential distributions can be distinguished according to the senses of the two fields E and E', which may be in the same or in opposite directions. Examples of such potential distributions are shown in fig. 4.5 (*a*) and (*b*). If the fields are in the same direction the potential distribution will have no maxima or minima. The equipotentials may penetrate through the aperture to a considerable extent but none of them cross, just one singular equipotential being observed reaching the diaphragm C at right angles. On the other hand, if the fields E and E' are in opposite directions, the potential distribution no longer slopes monotonically but a potential saddle is formed. The saddle-shaped field is like a pass over a mountain, the greatest height of the pass being the saddle point which lies on the axis. But even this saddle point may be flanked on both sides by still greater heights.

The saddle point always lies at the side of the weaker field; let its distance s from the centre of the aperture be measured in terms of the aperture radius R and tabulated as a function of the ratio of the weaker field to the stronger field. Taking $E' > E$ the following five values may be given as an example:

s/R	0	0·2	0·5	1	3
E/E'	1	0·6	0·29	0·16	0·01

Here E and E' again correspond to the field strengths on either side of the diaphragm in the case when the aperture is closed.

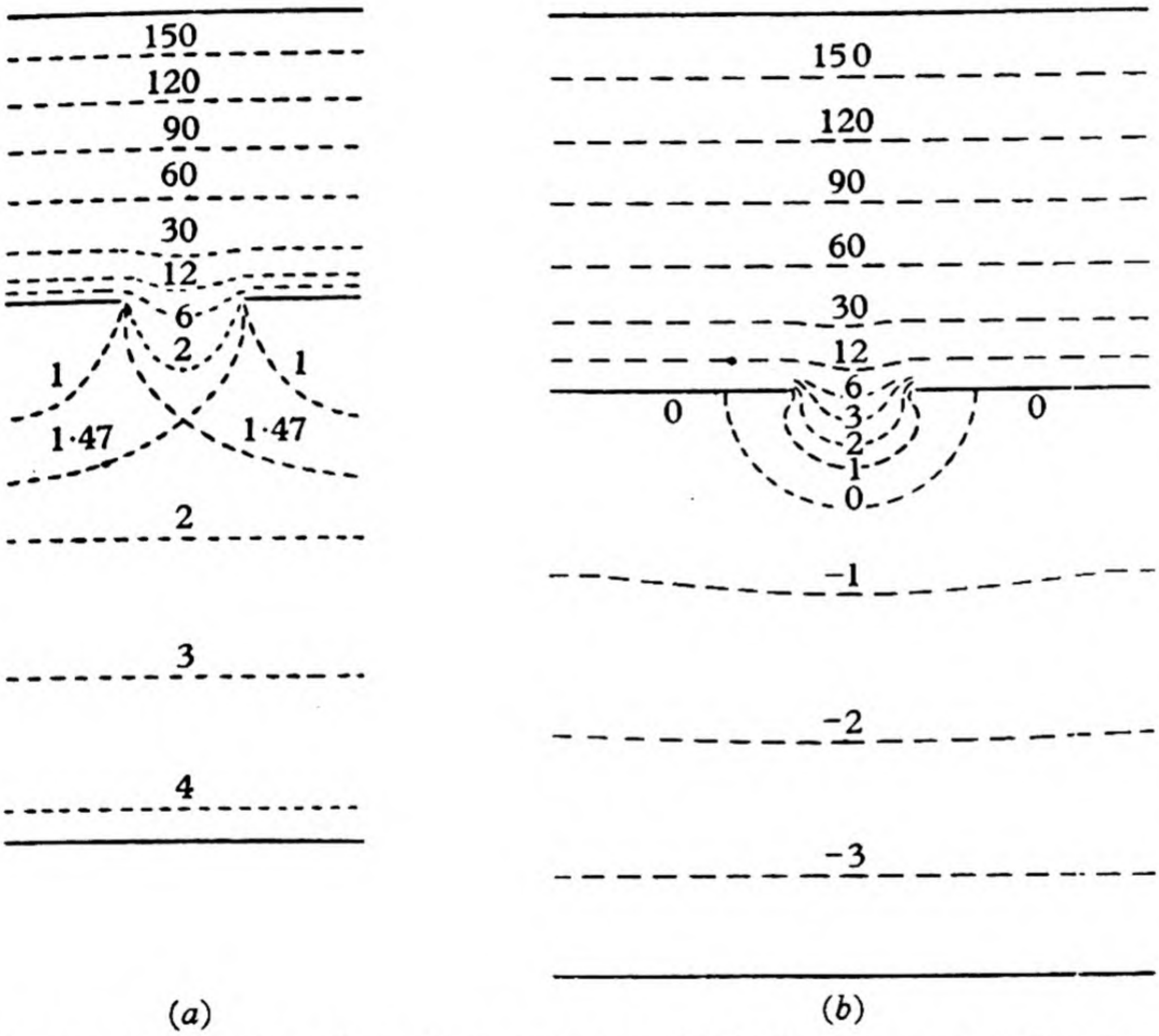

Fig. 4.5. Penetration through an aperture: (*a*) fields in opposite directions; (*b*) fields in the same direction.

The potential distribution at a single aperture cannot be considered to be a complete electron lens because it is not bounded by spaces of constant refractive index. Thus lens formulae like (2.8) cannot be applied directly. However, the study of the focusing properties of the aperture is sufficiently interesting for the understanding of various aperture lenses and of emission systems (cf. Chapter IX) in which apertured diaphragms are incorporated as

elementary units. Moreover, the apertured thin diaphragm is of particular historical interest. It was used in the earliest electrostatic electron lenses, and its focal length was given very early by Davisson and Calbick (1931). Its focusing properties were studied experimentally when it was arranged between a cathode and a fluorescent screen. If the fields at either side of the aperture are small in comparison with the ratio V_C/R (= aperture potential/aperture radius) a formula for the focal length can easily be derived. The axial velocity component near the diaphragm is given by the energy equation

$$u_z = \sqrt{\left(2\frac{e}{m}V_C\right)}. \tag{4.5}$$

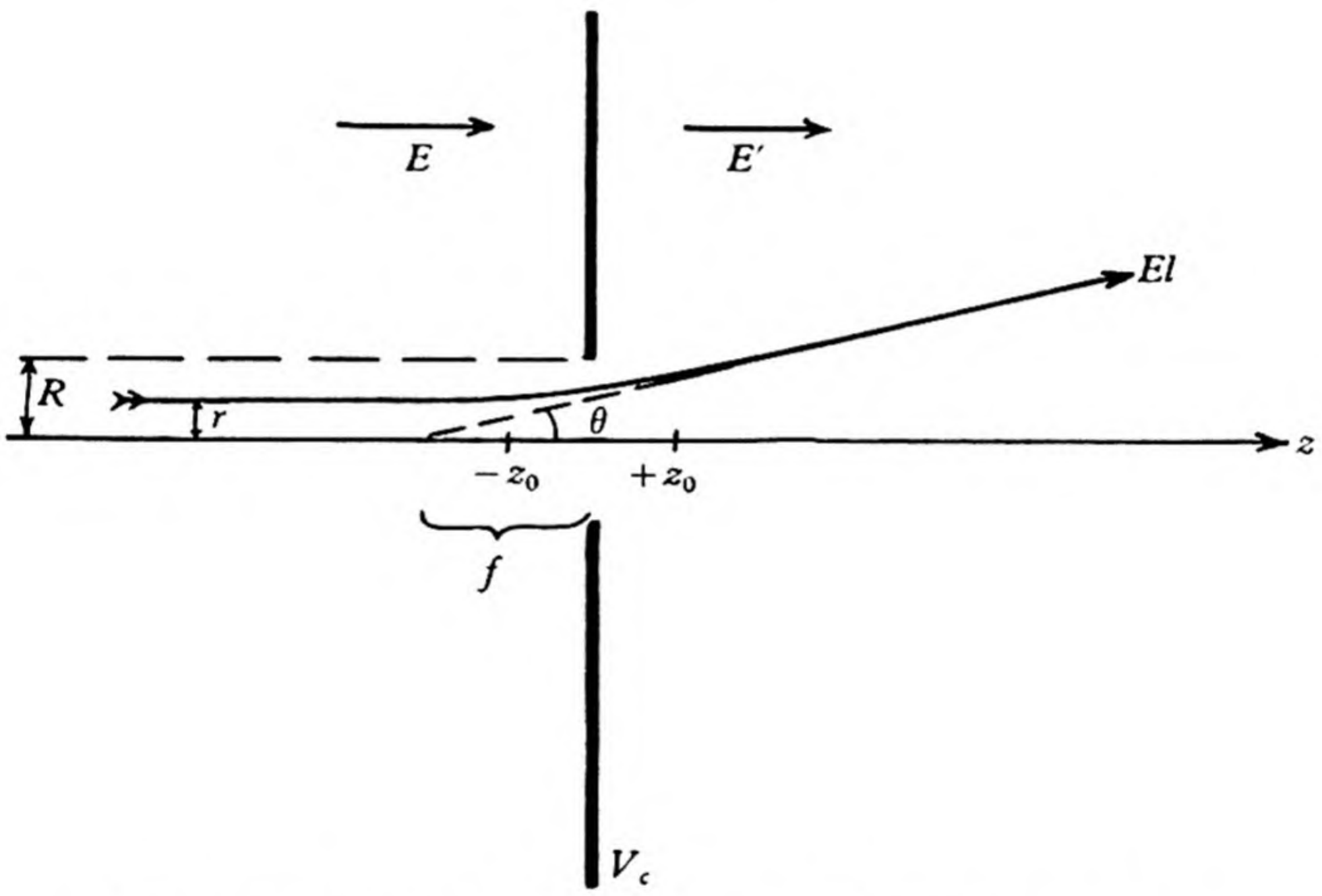

Fig. 4.6. Derivation of Davisson and Calbick's formula.

The radial component of velocity is given by the momentum which the electron acquires in the field of the aperture

$$mu_r = -\int_{-t_0}^{+t_0} eE_r \,\mathrm{d}t,$$

or replacing $\mathrm{d}t = \mathrm{d}z/u_z$,

$$u_r = -\frac{e}{mu_z}\int_{-z_0}^{+z_0} E_r \,\mathrm{d}z, \tag{4.6}$$

where the limits $\pm z_0$ are assumed to be the short distances from the aperture centre over which the radial field E_r extends. The integral

of (4.6) can be replaced with the help of Gauss's law according to which the surface integral over the normal component of flux density ϵE is equal to the enclosed charge. Consider a cylinder symmetric and coaxial with the aperture and extending from $-z_0$ to $+z_0$. As the cylinder contains no charge we have

$$2\pi r \int_{-z_0}^{+z_0} \epsilon E_r \,\mathrm{d}z + \pi r^2 \epsilon (E' - E) = 0.$$

Therefore
$$\int_{-z_0}^{+z_0} E_r \,\mathrm{d}z = \frac{r}{2}(E' - E). \tag{4.7}$$

From (4.5), (4.6) and (4.7) we obtain

$$\frac{r}{4}\frac{(E' - E)}{V_C} = \frac{u_r}{u_z} = \tan\Theta = \frac{r}{f},$$

where Θ is the angle through which the ray, initially parallel to the axis, is deflected (cf. fig. 4.6) and f is the focal length. Thus

$$f = \frac{4V_C}{E' - E}, \tag{4.8}$$

which is the well-known formula of Davisson and Calbick. It should be noted that the result is only an approximation applying to paraxial rays ($u_r \ll u_z$) in thin lenses ($z_0 \ll R$). Both focal lengths of this lens are equal. The aperture diverges the rays, i.e. $f < 0$ if $E' < E$ as assumed in fig. 4.6.

4.5. Multielectrode lenses

The electron lenses which have been discussed in §§ 4.2 and 4.3 are two-electrode lenses. This implies that the potential of the object space is different from that of the image space. The two-electrode lenses are analogous therefore to glass optical immersion lenses. Multielectrode lenses belong to the same class if the potential of any intermediate electrode ranges between the potentials of the two adjacent electrodes. For example, in fig. 4.4 (*h*) is shown a three-tube lens in which the potential of the intermediate tube V_2 is variable and lies between the potentials of the first and of the last tube ($V_1 < V_2 < V_3$). It will be observed that the focal lengths of such three-tube lenses are somewhat larger than the focal lengths of the corresponding two-tube lens with the voltage ratio V_3/V_1. As a

development from the three-tube lens, still more small intermediate tubes can be inserted between the two external tubes. In this way the 'lens chain' is obtained, by which electrons may be accelerated or decelerated with a relatively small focusing action. The extreme case of a lens chain is an insulating tube sprayed with a very thin metal layer. The resistance of this layer is large enough to maintain a linear potential drop from one end of the tube to the other. Such an arrangement produces a very nearly homogeneous field; it has actually been used to accelerate electrons without focusing them (Farnsworth, 1934), so that the focal length has in this case become infinite.

4.6. Saddle-field lenses

A completely new situation arises if the voltage of the intermediate electrode of a three-electrode lens is adjusted to be outside the range V_1 to V_3. Lenses belonging to this class of multielectrode lenses are called 'saddle-field lenses', because the potential distribution becomes saddle-shaped, as shown in the field plot of fig. 4.5 (*a*).

The focal length of a saddle-field lens is shortened gradually as the voltage V_2 of the intermediate electrode either increases beyond V_3 or decreases below V_1. Thus the focal length of the lens can be controlled within a very large range by varying V_2 for any constant value of V_3/V_1. A case of practical interest arises if $V_3 = V_1$. The equivalent electron lens is then surrounded by media of the same refractive indices at both sides, and corresponds to an isolated glass lens, so that in the literature it is often called an 'einzel' lens (i.e. single lens). Since the voltages at both sides of the lens are equal ($V = V'$) the two focal lengths f and f' of the lens must be equal too (cf. (2.8)), and the two nodal points K and K' must coincide with the two principal points P and P' (cf. (2.1)). The electron velocity outside the einzel lens is given by the potential V_0 of the two outer electrodes. Inside the lens, the electron is initially accelerated or decelerated according to the choice of the potential V_i of the inner electrode, but in both cases a converging lens is obtained. The electron while passing through the lens, however, travels much nearer to the axis when $(V_i - V_0) > 0$, than when $(V_i - V_o) < 0$. On the other hand, it is easier to obtain short focal

lengths by applying negative voltage $(V_i - V_o) < 0$ than by applying positive voltage $(V_i - V_o) > 0$ to the einzel lens.

The particular case of an einzel lens with $V_i = 0$ is of practical importance. There, the inner lens electrode is simply brought up to cathode potential, while the outer electrodes may be connected to the anode of the system from which the electrons are emitted. Thus only one voltage is applied to such a lens and it is frequently

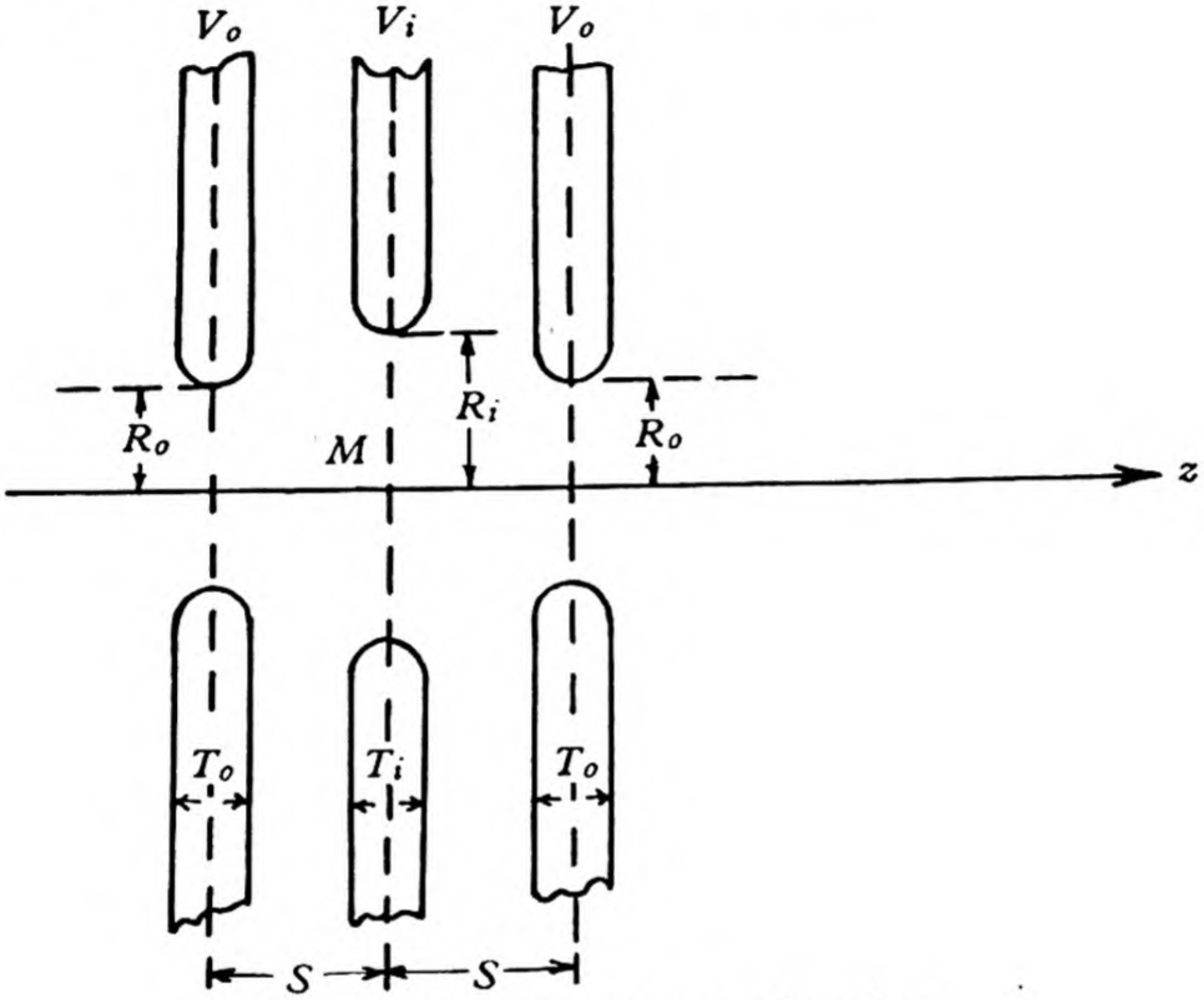

Fig. 4.7. Three-diaphragm einzel lens.

called a 'univoltage' or 'unipotential' lens.* Moreover, as the voltage ratio V_o/V_i of the univoltage lens is always infinite, the positions of its cardinal points will be independent of the applied voltage provided the electron velocities are not excessive so that the relativistic increase of the electron mass is negligible.

The fact that the focal length of the univoltage lens does not depend on the applied voltage is of considerable technical interest. Fluctuations of the voltage source are not disturbing. It is even possible to project sharp images with a univoltage lens that is operated with an alternating voltage. On the other hand, the focal length depends largely on the dimensions of the intermediate

* Epstein (1936) uses the general term 'univoltage' lenses for all einzel lenses.

electrode. If a univoltage lens is used in an apparatus where a given focal length is required, the dimensions of the electrodes must be adjusted with sufficient precision.

The two basic types of the einzel lens are the three-tube einzel lens (fig. 4.4 (*h*)) and the three-diaphragm einzel lens consisting of three plane, apertured diaphragms (fig. 4.7).

The saddle-shaped potential distributions of a short and of a long symmetrical three-tube einzel lens are presented in figs. 4.8 (*a*) and 4.8 (*b*) respectively. In order to show the equipotentials on a sufficiently large scale, only one quadrant of the whole field plot is drawn in each of these two figures. The diagrams are symmetrical about the mid-plane M and about the axis of rotational symmetry z. L_i represents one-half of the intermediate tube and L_o one of the two external tubes. Near the intersection of the mid-plane and the z-axis, the equipotentials are symmetrical hyperbolae. The asymptotes are two singular equipotentials which cross on the axis; they represent cones which are coaxial with the lens axis, having a semi-vertical angle $\gamma = 54{\cdot}6°$. This angle is indicated in figs. 4.8 (*a*) and 4.8 (*b*), and it is remarkable that it does not depend on the shape of the electrode. The shape of the equipotentials can be found from measurements in the field-plotting trough, but since the potential gradient near the saddle point (i.e. near the point where the equipotentials cross over) is relatively small, it is generally difficult to determine the field there by experimental methods. Fortunately it is possible to calculate the saddle field as a particular integral of Laplace's equation (cf. Brüche and Scherzer, 1934).

The great influence of the intermediate tube length L_i on the power of three-tube einzel lenses is demonstrated by fig. 4.9. There, three curves for the mid-focal lengths are given as functions of the intermediate tube length L_i (Klemperer, unpublished). The radii of all three tubes are equal and the spacings between the tubes are small in all cases (gap = 0·1 tube-radii). Inscriptions to each curve are the voltage ratios $V_i/V_o = 0{\cdot}5$, 0·2 and 0 respectively, representing constant parameters. In every case the electrons are initially decelerated inside the lens since $(V_i - V_o) < 0$. The curve $V_i/V_o = 0$ belongs to the series of univoltage lenses.

Exact measurements about the cardinal points of a few selected three-tube univoltage lenses have been published by Liebmann

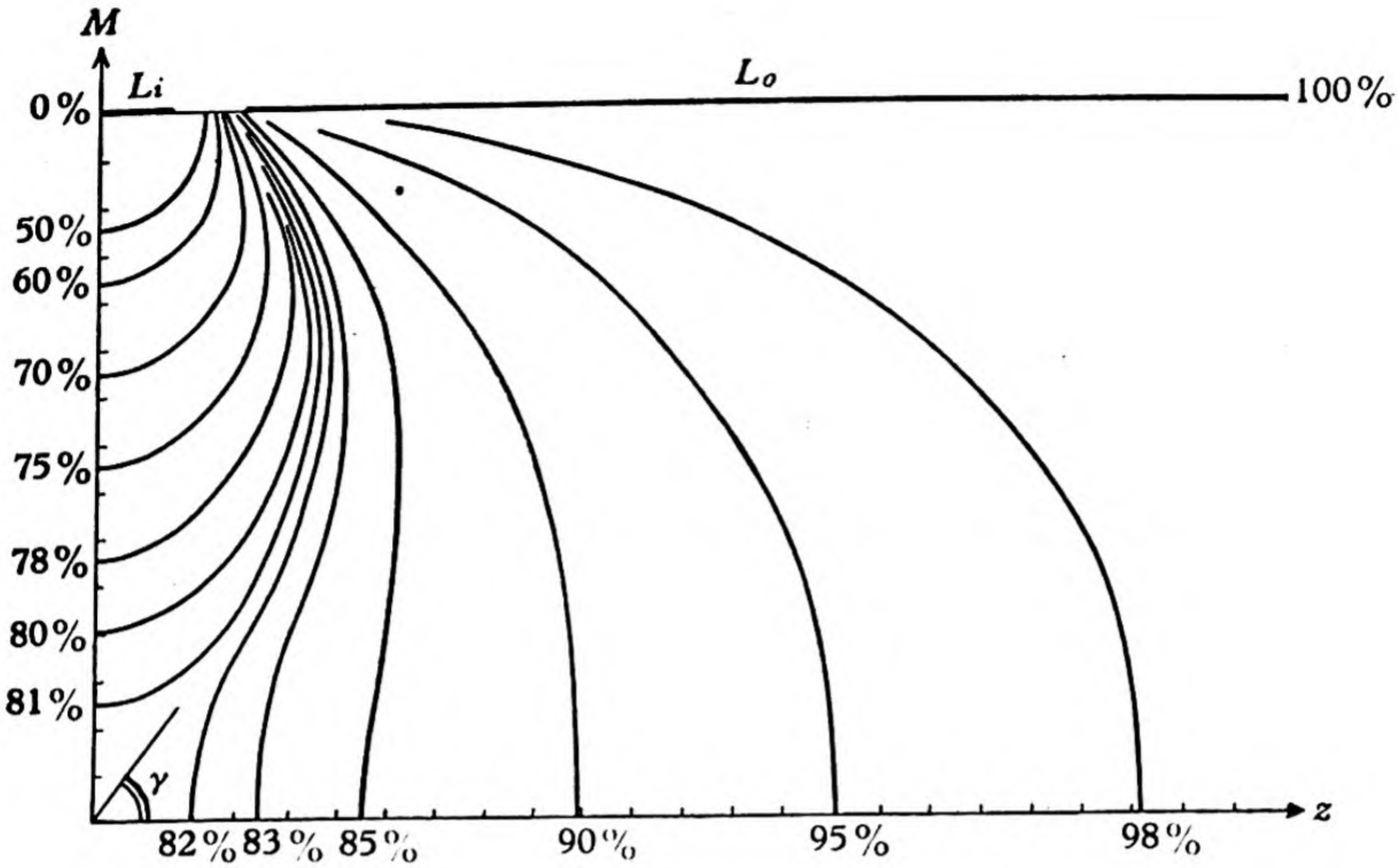

(*a*)

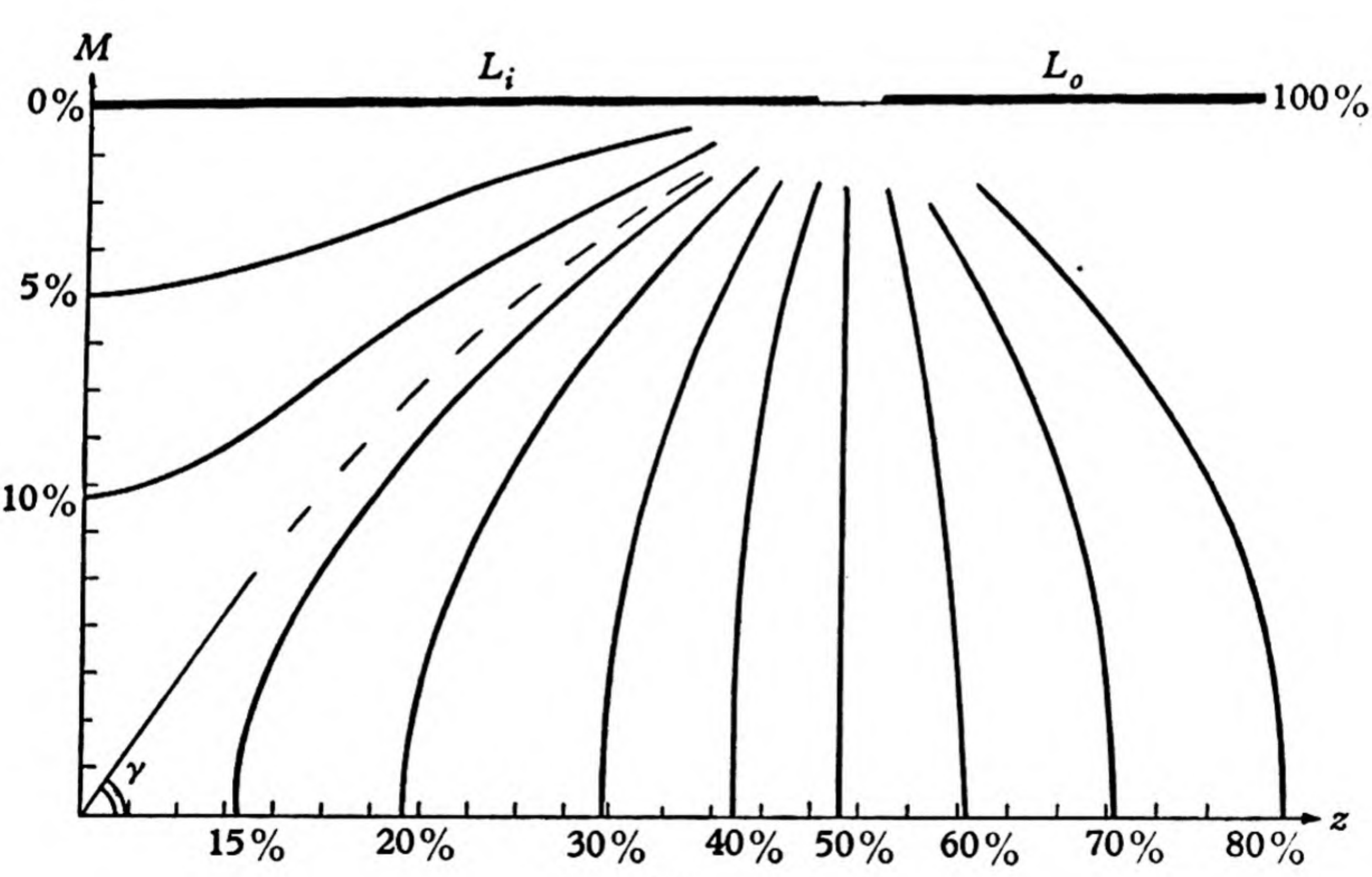

(*b*)

Fig. 4.8. Symmetrical saddle-shaped potential distribution: (*a*) of a short three-tube einzel lens; (*b*) of a long three-tube einzel lens.

(1949*a*). He found, for instance, the focal lengths for tube lenses with three tubes of equal radius R, and with intermediate tube length $L_i = 0{\cdot}68R$, to be $f = 6{\cdot}20R$ (and $3{\cdot}84R$) for tube spacings $0{\cdot}26R$ (and $0{\cdot}76R$ respectively). Again, for tube spacings equal to one tube-radius, he found focal lengths $f = 1{\cdot}94R$ (and $1{\cdot}72R$) with $L_i = 1{\cdot}44R$ (and $2R$ respectively). The distances between the mid-plane and

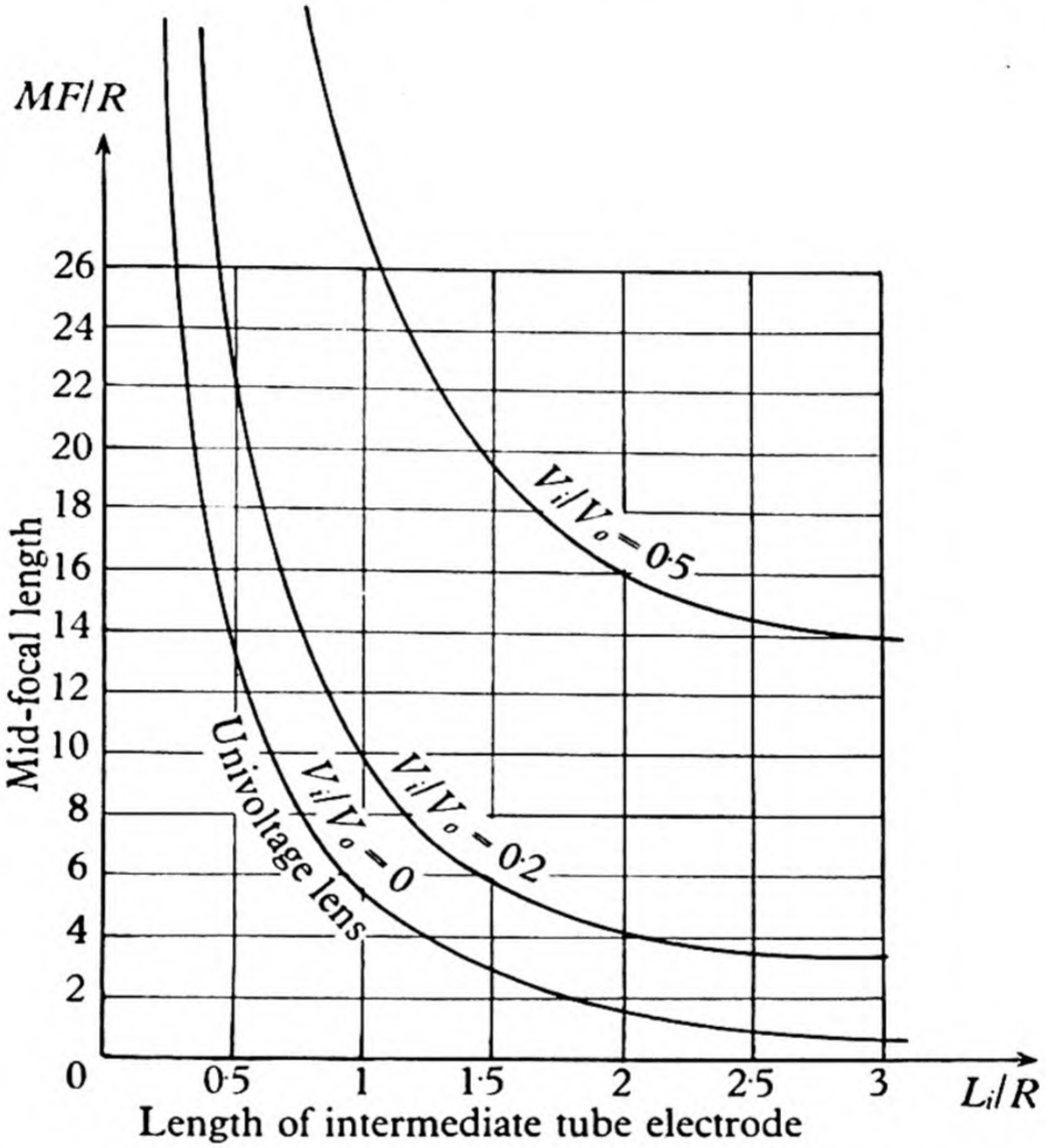

Fig. 4.9. Mid-focal lengths of three-tube einzel lenses.

each of the principal planes were found for all the above lenses to be $MP = 0{\cdot}2R$ within the accuracy of the measurement, with P and F lying on opposite sides of M.

Some investigations on three-tube einzel lenses have been published also in a paper by Gobrecht (1941) which, however, is mainly concerned with the errors of this lens (cf. Chapter VI). A paper by Iams (1939) deals with the application of a univoltage lens of three tubes of unequal radius to the focusing of electrons in cathode-ray tubes.

Three-diaphragm einzel lenses consisting of three plane, apertured diaphrams (cf. fig. 4.7) have been studied originally by Brüche and his collaborators (cf. Brüche and Scherzer, 1934). Their properties depend on the radii R_o of the outer apertures, the radius R_i of the inner aperture, the thickness T of the diaphragms and on their mutual spacings S. Chancon (1947) investigated the einzel lens of fig. 4.7 by ray tracing and found some useful empirical relations for the location of the foci F and of the principal points P. The focal length $f = PF$ appears to be a simple function of the potential $\bar{V}_i$ in the centre of the inner diaphragm, i.e. of the potential saddle which can be determined from a potential plot, namely,

$$f = 6{\cdot}5\,\frac{V_o - \bar{V}_i}{V_o - V_i}\,S, \tag{4.9}$$

where V_o and V_i are again the potentials of the outer and of the inner diaphragms respectively. Relation (4.9) appears to hold within an accuracy of $\mp 5\%$ for $0{\cdot}02 < \dfrac{V_o - \bar{V}_i}{V_o - V_i} < 0{\cdot}4$. The influence of the thickness T of either of the diaphragms is negligible if $T < \frac{1}{10}S$. The distance between principal point P and mid-plane M is given by the empirical relation

$$MP = 0{\cdot}06RS/(R_o + T). \tag{4.10}$$

The mid-plane is located between focus and principal point.

Regenstreif (1951*a*) derived formulae for the potentials at the centres of the apertures in the inner diaphragm ($\bar{V}_i$) and in either of the outer diaphragms ($\bar{V}_o$), namely

$$\bar{V}_i = V_i + (V_o - V_i)\Big/\left[1 + \frac{S}{R_i}\tan^{-1}\frac{S}{R_i}\right] \tag{4.11}$$

$$\bar{V}_0 = V_i + (V_o - V_i)\left[1 - \frac{R_o/2R_i}{1 + \dfrac{R_i}{S}\tan^{-1}\dfrac{S}{R_i}}\right] \tag{4.12}$$

when the thickness T of the diaphragms is again negligible. Regenstreif found that the optical properties of any einzel lens are fixed by the single characteristic parameter

$$x = \bar{V}_i/\bar{V}_o. \tag{4.13}$$

Moreover, he showed that the field along the axis can be approximated by an analytic function, represented by three parabolic arcs joined at the points of inflexion. For this field, the paraxial ray equation can be integrated and the cardinal points of the lens can be found. For instance the focal length is given by the simple formula

$$f = \frac{3}{8}\frac{x}{(1-x)^2}S. \qquad (4.14)$$

Of some technical importance is the question of finding lenses of shortest possible focal length for use in electron microscopes, and (4.9) and (4.14) might lead to the conclusion that the least f should be obtained just with the shortest spacing S between the diaphragms which can be used without the danger of sparking. Bachman and Ramo (1943*b*) had already noticed a distinct minimum of focal length as a function of either the inner aperture radius R_i or of the voltage ratio V_i/V_o. This minimum has been confirmed by calculations of Bruck and Romani (1944) and it is explained by the fact that the rays will continue to be refracted after passing through the focus (§ 4.1). In effect, on decreasing R_i or V_i to very small values, the principal point moves towards the electron source more rapidly than the focus. The problem of this 'ultra-focal' refraction will be fully treated in the discussion of the strong magnetic lenses (§§ 5.3, 5.6 and 5.9).

The location of foci and principal points for very small R_i/S and for very small or negative values of V_i/V_o has been investigated by various methods theoretically and experimentally. For instance, Regenstreif (1951*a*) has calculated many examples of electron trajectories through einzel lenses with the characteristic parameter x of (4.13) varying as much as $10^{-10} < x < 1$, and the periodical character of the focal length can be clearly recognized. E.g., minima occur at $x = 5{\cdot}8 \times 10^{-2}$ ($f_{\min} = 0{\cdot}7S$), at $x = 7{\cdot}6 \times 10^{-4}$ and 9×10^{-5}. Between the minima, the focus recedes to infinity at $x = 1$, $7{\cdot}1 \times 10^{-3}$ and $8{\cdot}2 \times 10^{-5}$, while the initially parallel ray is focused at the centre of the outer aperture at $x = 0{\cdot}2$, $2{\cdot}3 \times 10^{-3}$ and $2{\cdot}9 \times 10^{-5}$.

Location of principal points and foci for very small or negative values of V_i have been measured systematically by Rang (1948) and by Heise and Rang (1949) with particular regard to einzel lenses

with large thickness T_i of the inner diaphragm. The large experimental material for f as a function of V_i, S, T_o, T_i, R_o and R_i can be divided into several regions which are classified by the fact that the electron orbits may cross the lens axis once, twice or even three times respectively. The first region shows characteristic minima and the second region shows characteristic maxima for the focal length as a function of the voltage ratio.

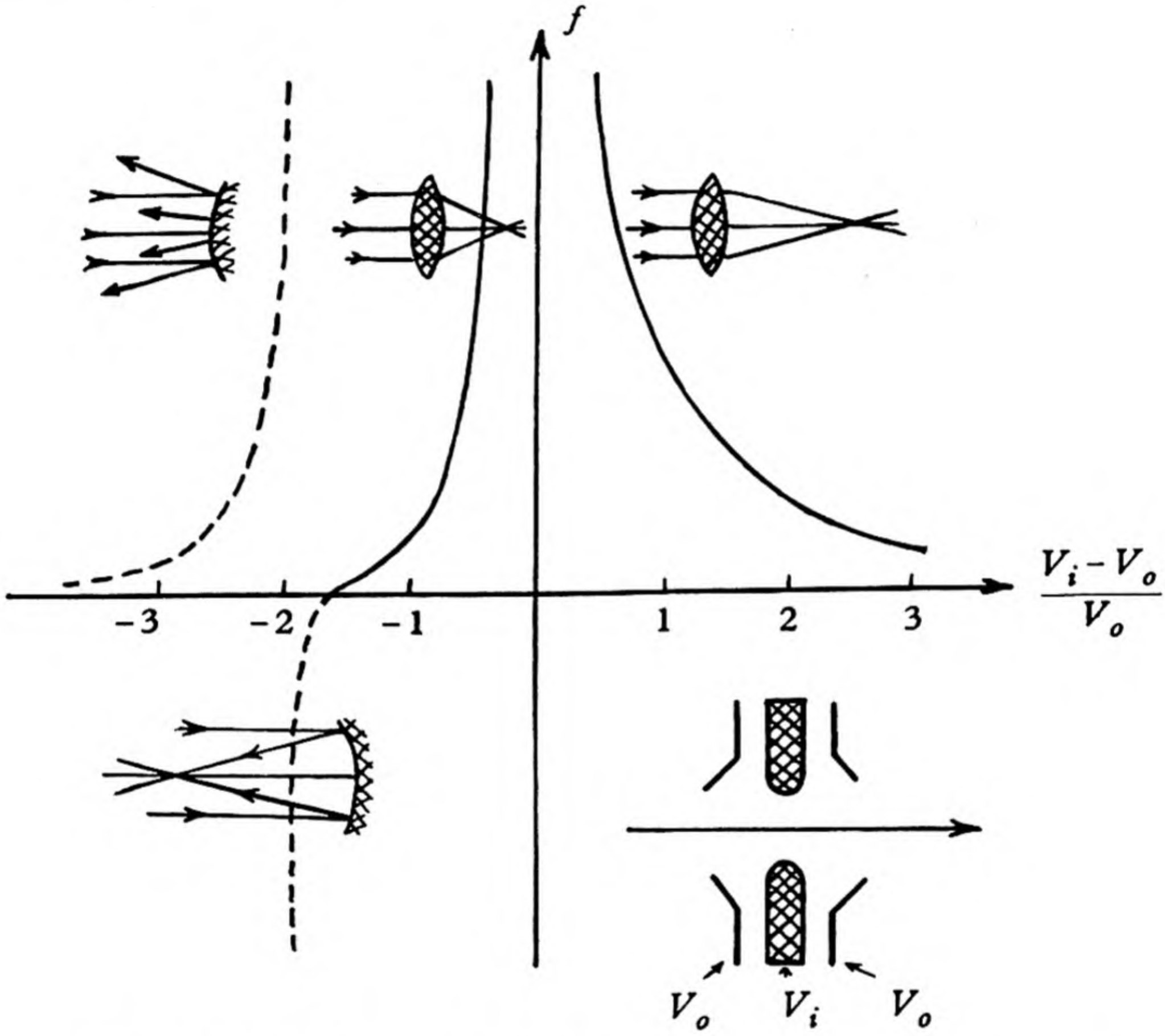

Fig. 4.10. Foca llengths of three-diaphragm einzel lens ——, and of electron mirror – – – –.

Apart from the simple three-diaphragm lenses with plane, apertured diaphragms, other types of three-diaphragm einzel lenses with specially shaped electrodes have received detailed treatment in the literature. Here, we refer to the discussion of lenses with hyperbolic field structure by Rudenberg (1948) and to the papers by Ramberg (1942) and by Liebmann (1949*a*). The latter authors investigated a lens with an inner diaphragm which was tapered towards its relatively wide aperture. We also mention the thoroughly investigated lens type shown in fig. 4.10 (cf. Johannson

and Scherzer, 1933), where the two external diaphragms are extended outwards in the shape of coaxial cones. The whole range of focal lengths of this einzel lens is shown in the figure. The focal lengths increase to infinity with decreasing positive value of $(V_i - V_o)/V_o$. Then for increasing negative values of this voltage ratio, the focal length decreases rapidly until the lens blocks the transit to the incident rays and changes into an electron mirror as will be discussed in § 4.8.

A point of great general interest is the behaviour of einzel lenses towards fast electrons in the relativistic region. Laplume (1947) calculated the focal length f of a three-diaphragm univoltage lens ($V_i = 0$) as a function of the energy V_o of the incident electrons. The following values may be quoted:

V_0 in MeV.	0	0·3	1	2	5	10	∞
f/S	1·28	1·33	1·38	1·36	1·28	1·20	1·06

where S is again the distance between the median planes of two consecutive electrodes. It can be seen that the focal length f of the univoltage lens reaches a distinct maximum in the region of 1 MeV.

4.7. Gauze lenses

In the earliest development of electrostatic electron lenses, shaped metallic wire gauzes or screens were used to represent the refracting surfaces. Knoll and Ruska (1932*a*) used a spherical condenser consisting of two concentric spheres at different potentials and provided with wire gauze windows. They also discussed the use of other lenses of similar kind made of two closely spaced parallel wire screens at different potentials dividing the space into two equipotential regions and thus simulating the glass surfaces of light lenses. In all cases, however, disturbances are produced by a certain amount of field penetration through the meshes of the gauze. Each aperture of the gauze acts as a separate little 'facet-lens', the focal length of which could be estimated in the way explained in § 4.4. Gauze lenses with relatively small field non-uniformities are produced if gauze screens are made to the shape of an equipotential of an electrode arrangement and inserted in place of this equipotential. For instance, it is practicable to replace the midplane of the symmetrical two-tube lens by a plane wire gauze. In this way the two semi-lenses discussed in § 4.2 could be separated

by inserting a plane gauze in place of the mid-plane. By application of different potentials to this mid-plane gauze, the focal lengths of the two semi-lenses could then be controlled independently. Moreover, by omitting either of the tubes, each of these semi-lenses could be obtained separately. If the gauze is at the higher potential, the focal length of the tube-gauze lens is appreciably shorter than that of the two-tube lens (cf. Table I, p. 51). This applies particularly to relatively low voltage ratios, as can be seen from the experimental values (Klemperer, unpublished) in Table VI. On the other hand, if the gauze is at the lower potential, a diverging electron lens is obtained. This is a remarkable result, since ordinary electron lenses are always converging lenses.

TABLE VI. *Tube-gauze lens: focal lengths ($P'F'$) and midplane to principal plane distance (MP') expressed in terms of the tube radius (R) for various voltage ratios V'/V*

V'/V	1·5	2	3
$P'F'/R$	8·7	5·5	3·7
MP'/R	1·0	1·0	1·0

Einzel lenses with gauze screens have been investigated by Knoll and Weichardt (1938) and by Liebmann (1949*a*). In a three-aperture einzel lens the inner diaphragm may be replaced by a plane gauze. There, a converging lens is obtained if the potential of the gauze is positive with respect to the outer diaphragms ($V_i > V_o$). A diverging lens is obtained if the potential of the gauze is made negative with respect to the outer diaphragms ($V_i < V_o$). The principal planes of such lenses are not crossed; thus the mid-focal distances are greater than the focal lengths.

Gauze lenses are not suitable for the production of sharp foci or for the projection of high-quality optical images. Foci and images will always be impaired by the inevitable non-uniformity of the field in the gauze. It is, however, not unlikely that gauze lenses will find some application in electron multipliers or electron accelerators (cf. Gabor, 1947) in which sharp foci are not required.

4.8. Electron mirrors

If the potential of the intermediate electrode in a saddle-field lens is gradually made more and more negative, the path of the electrons

will finally be blocked and all those moving up the potential mountain will be returned. At first the marginal electrons are returned, but when the inner electrode becomes still more negative, the axial electrons are also reflected. In this way the einzel lens can be used to modulate the intensity of an electron beam. The lens behaves as if closed by an iris diaphragm when the negative voltage V_i is increased.*

If the electrons emitted by any extended object are projected backwards by such a reflecting, axially symmetrical field, a marvellous phenomenon can be observed. Under certain conditions, the reflected electrons form a real image. This was predicted theoretically by W. Henneberg and A. Recknagel (1935*a*) and was verified later by G. Hottenroth (1936). The arrangement acts as a mirror. By changing the voltage at the negative electrode, different equipotentials can be chosen to act as reflectors. Thus the focal length and the principal plane of the mirror can be varied. In fig. 4.10 two broken curves show the focal length of the electron mirror produced by the electrode arrangement of a three-aperture lens. This focal length at first increases with decreasing negative bias; then suddenly it assumes negative values, which means that the mirror reflects the electrons like a concave glass optical mirror.

For strongly negative potentials V_i, of the inner electrode, the mirror becomes periodically 'concave' and 'convex'. According to Regenstreif (1951*b*) the mirror can again be characterized by the function x of (4.13). According to his calculations, a three-diaphragm mirror (fig. 4.7) is convex for $-2 < x < -0{\cdot}5$, plane for $x = -0{\cdot}5$, concave for $-0{\cdot}5 < x < -7{\cdot}1 \times 10^{-3}$, plane for $x = -7{\cdot}1 \times 10^{-3}$, convex for $-7{\cdot}1 \times 10^{-3} < x < -8{\cdot}2 \times 10^{-5}$, etc.

A simple type of electron mirror is produced by the electric field between two tubes. Electron reflexion by such a two-tube mirror is shown in fig. 4.11. At the moment of reflexion, the axial velocity component of the electron is reduced to zero. Thus the reflecting equipotential is very nearly at cathode potential, and it is often called the 'zero equipotential'. In fig. 4.11 the electron is reflected at the mid-plane of the lens. Since the potential of the mid-plane

* In Gaussian optics, all electrons should have equal axial velocities independent of their axial distance. Thus either all electrons should be transmitted or reflected simultaneously. The finite slope of any actual modulator characteristic is due to lens errors.

is $\frac{1}{2}(V_1+V_2)$, i.e. half-way between the potential of the electrodes, the cathode potential must have been half-way between the electrode potentials, and $V_2 = -V_1$.

For the present purpose it is again suitable to label the equipotentials as in fig. 3.3 in terms of percentages of the total potential difference. If V_1 is taken as a positive voltage and V_2 as a negative voltage with respect to the cathode, the zero equipotential of the electron mirror is equivalent to the equipotential labelled

$$V_C = \frac{100}{(1-V_1/V_2)}\,\%. \qquad (4.15)$$

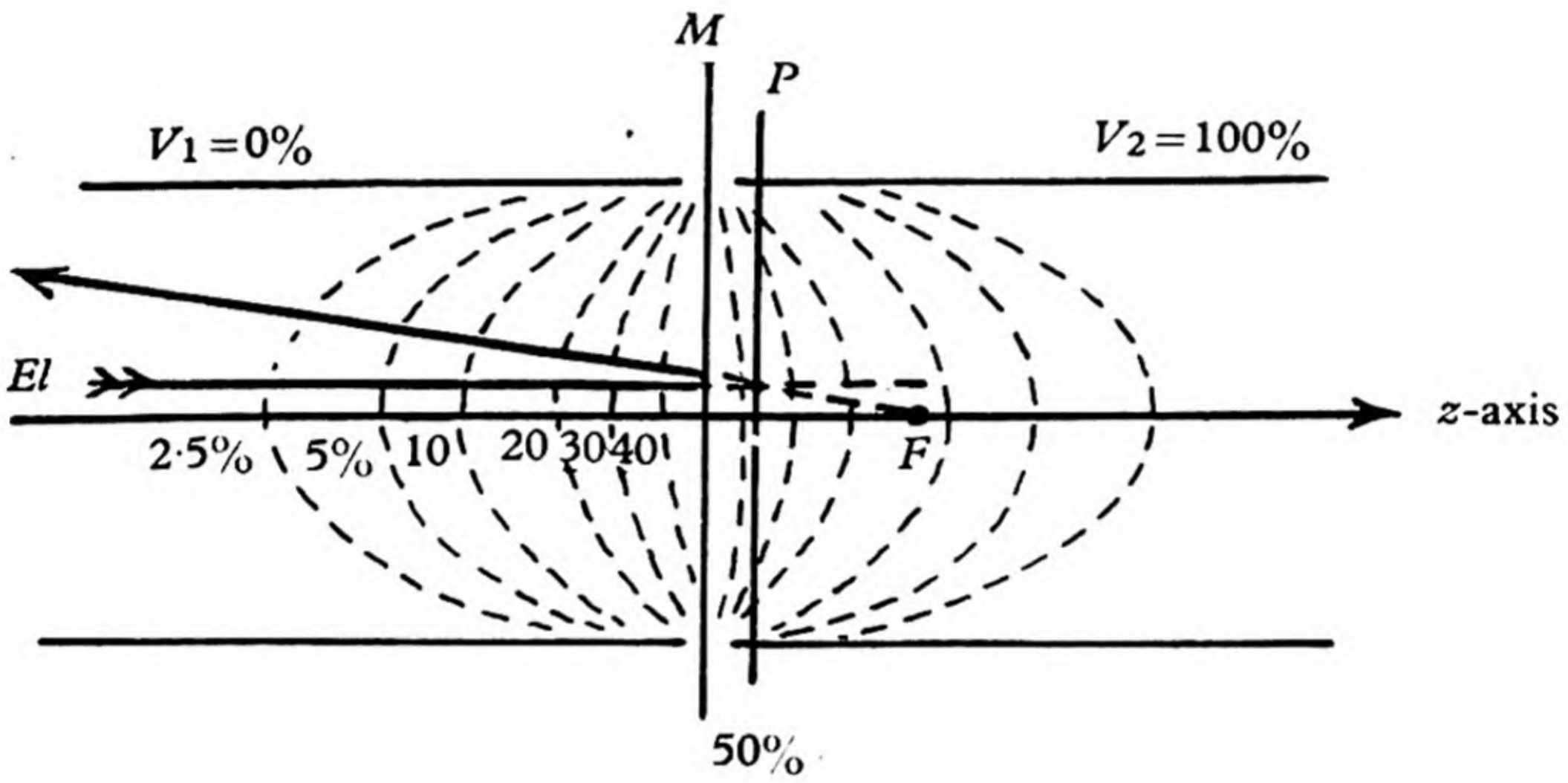

Fig. 4.11. Two-tube electron mirror: measurement of focus and principal plane.

Some of these equipotentials are shown in fig. 4.11 with the proper designation. Focal point F and principal plane P can be measured in the way described in § 2.1, by tracing initially parallel electron pencils. The pencils are made visible by a sliding fluorescent target before and after having passed the reflecting field. Such a target, however, has to be traversed by the incident beam. Klemperer (unpublished) used a target made from a fine metal gauze, the wires of which were coated with a thin layer of fluorescent material. The pencils passing through the meshes grazed the fluorescent wires and thus became visible. The target was then moved along the z-axis and the semi-apertures of the incident and of the emerging pencil were measured as a function of the z-coordinate with a microscope viewing 'through' the lens, i.e. against the direction of the incident beam. Focus F and principal plane P

were traced by finding the extrapolated intersections of the emerging pencil with the axis and with the extrapolated incident pencil respectively. Table VII shows the results. In all cases, the electron mirror acts like an optical mirror in combination with an optical lens, the lens being represented by the field which is passed before and after the reflexion. The mirror converges the electron rays, until the voltage ratio reaches $-0{\cdot}412$; for still more negative values of V_2 the mirror diverges the rays. At $V_C/V_1 = -0{\cdot}412$ the field behaves for paraxial rays like a plane mirror.

TABLE VII. *Cardinal points of two-tube electron mirror*

Mirror ...	Converging			Plane	Diverging	
V_2/V_1 ...	$-0{\cdot}2$	$-0{\cdot}25$	$-0{\cdot}35$	$-0{\cdot}412$	$-0{\cdot}50$	$-1{\cdot}0$
Reflecting equipotential:						
% ...	17	21	27	29·5	34	50
at ...	$+0{\cdot}66R$	$+0{\cdot}56R$	$+0{\cdot}44R$	$+0{\cdot}40R$	$+0{\cdot}30R$	0
MF/R	$-0{\cdot}3$	$-0{\cdot}9$	$-3{\cdot}2$	∞	$+3$	$+0{\cdot}8$
MP/R	$+1{\cdot}1$	$+0{\cdot}9$	$+1{\cdot}1$	∞	$+0{\cdot}5$	$+0{\cdot}2$

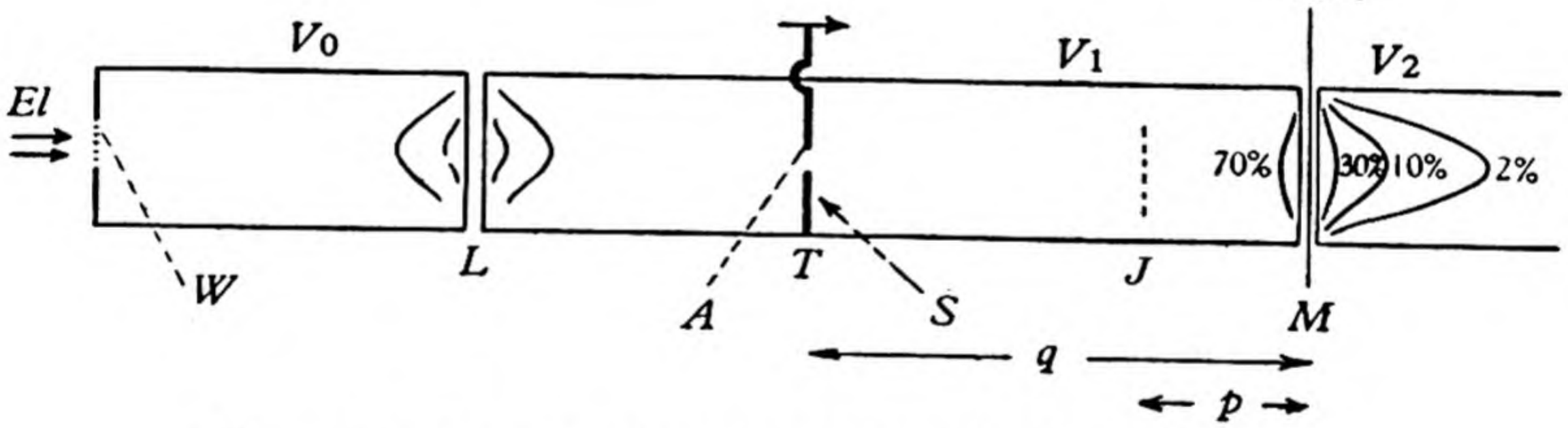

Fig. 4.12. Investigation of the two-tube electron mirror.

Mid-object and mid-image distances and magnifications by the two-tube electron mirror have been measured by Nicoll (1938*a*). The scheme of his measuring apparatus is shown in fig. 4.12. There, the electron beam *El* illuminates the wire gauze object *W* and the electron lens *L*, consisting of two tubes with the voltages V_0 and V_1, projects an electron image *J* of the gauze. The position of the image *J* depends on the voltage ratio of the lens, and can be calculated according to the data given in figs. 4.1 and 4.2; the position of principal planes and focal points of the lens *L* is known as a function of this voltage ratio V_1/V_0. The image *J* serves as an object for the

electron mirror M which is formed by the electric field produced by the two tubes with the voltages V_1 and V_2. The mirror M projects the electrons emitted from the 'mirror-object' J into a 'mirror-image' which can be detected with a fluorescent screen S on the

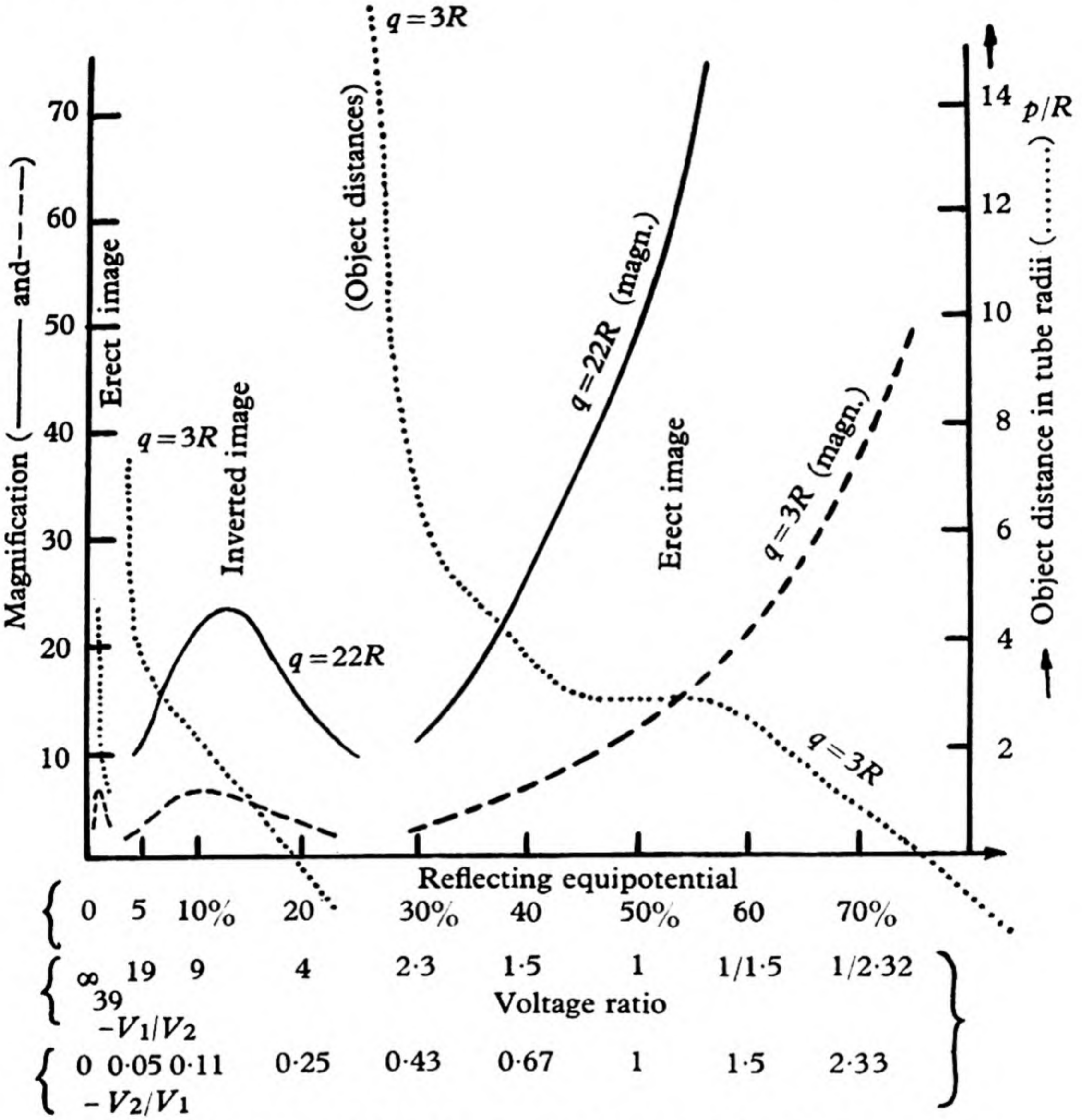

Fig. 4.13. Magnification by the two-tube mirror.

movable target T. The pictures at the fluorescent screen are observed by looking 'through' the electron mirror. The target contains a small aperture A in its centre which is sufficient to let through the electrons coming from W and forming the mirror-object J, but is narrow enough to cut out only a very small central fraction of the image produced by the mirror.

In fig. 4.13, object distances and magnifications are plotted as functions of the voltage ratios $(-V_1/V_2)$. The corresponding re-

flecting equipotentials are noted according to (4.15). For obtaining the curves shown in the figure, the target T was fixed consecutively at two different mid-image distances q. The broken curves correspond to $q = 3R$ and the solid curves to $q = 22R$, R being the radius of the tube electrodes. In the measurements, fixed values of the voltage ratio V_1/V_2 of the electron mirror were arranged, so that by varying the voltage ratio V_1/V_0 of the lens L, the position of J was controlled, i.e. the mirror-object distance $p = MJ$ was varied until the image at the screen S on the target T appeared to be in focus. Then the magnification could be measured as plotted in the diagram.

When the value of V_1/V_2 is gradually changed from $-\frac{1}{3}$ to $-1{\cdot}5$, the surface where the reflexion takes place gradually changes from the 75 to the 40 % equipotential. Within this range of V_1/V_2 the mirror object is virtual for the two fixed image distances and the mirror projects an erect image. The mirror reduces the convergence of the incident electron beams and thus acts like a convex glass mirror.

If the reflecting surface changes from the 40 to the 30 % equipotential, corresponding to a decrease of V_1/V_2 to $-2{\cdot}5$, the distance of the mirror object from the mid-plane increases to infinity whilst the magnification decreases. Proceeding to still smaller values of the reflecting equipotential, the mirror will project an inverted image corresponding to a real mirror object. If these values are still further decreased, the object again moves off to infinity. At $V_1/V_2 \approx -20$ (5 % equipotential), the field between reflecting equipotential and fluorescent screen is powerful enough to converge the beams again after a first cross-over, so that an intermediate image is produced, and at the fluorescent screen a second image is detected. With still larger values of $(-V_1/V_2)$ this process is repeated as the beam crosses over more and more times until finally space charge in the low-velocity region of the mirror and increased aberrations prevent the formation of a well-defined image.

All the pictures produced by the electron mirror show a surprisingly good definition. Thus it seems possible that the mirror might be applied as a useful element of construction of electron-optical apparatus. Moreover, there are distinct possibilities of using the mirror even for improving the performance of electron lenses, with a view to correcting the errors of distortion and of chromatic aberration (cf. Chapters VI and VII).

CHAPTER V

MAGNETIC ELECTRON LENSES

5.1. Electron path in homogeneous magnetic fields

In a magnetic field the electron is accelerated in a perpendicular direction both to the field vector and to its own velocity. A static magnetic field does not change the kinetic energy of the electron but only changes the curvature of its path. Equating the magnetic force to the centrifugal force of the electron one obtains

$$euB_z = \frac{mu^2}{r_e}, \tag{5.1}$$

$-e$ and m being charge and mass of the electron respectively, u its linear velocity, B_z the flux density of the magnetic field at right angles to the velocity u and r_e the radius of curvature of the path.

If the electron moves parallel to the direction of a homogeneous magnetic field, it is not influenced and travels along a straight line. If it moves in a direction perpendicular to the homogeneous field, its path is a circle. The time t_L required to traverse a complete circle, i.e. the period of the circular movement, is given by $u = 2\pi r_e/t_L$. Thus the angular frequency of rotation is

$$\frac{2\pi}{t_L} = 2\pi\nu_L = \omega_L = \frac{eB_z}{m}; \tag{5.2}$$

ν_L is the 'Larmor frequency', which only depends upon the magnetic flux density but is independent of the electron velocity* and of the radius of the electron path.

If the electron moves through the homogeneous magnetic field in a direction making an angle Θ with the lines of force, the velocity

* In the relativistic region, the Larmor frequency decreases with increasing electron velocity due to the increase in electron mass m. Substituting in (5.2) for m from the relativistic equation

$$mc^2 = e(V_0 + V),$$

we obtain

$$\omega_L = Bc^2/(V_0 + V), \tag{5.3}$$

where V is the kinetic energy of the electron expressed in electronvolts and $V_0 = 511 \times 10^3$ eV. is its rest energy.

u can be imagined to be split up into two components. The first component

$$u_z = u\cos\Theta$$

is parallel to the field and is not influenced by the field. The action of the field on the other component

$$u_y = u\sin\Theta,$$

which is perpendicular to the field, will not depend on the existence of the first component. Thus the projection of the electron path on a plane perpendicular to the lines of force must be a circle, and the path of the electron itself must be a spiral lying in the wall of a cylinder. It is useful to note that the electron will follow the spiral path moving forward in the sense of a right-hand corkscrew if u_z and B_z have the same direction.

The pitch of the spiral path may be obtained by considering the distance z_f which the electron moves in longitudinal direction while performing just one circle with the Larmor frequency:

$$z_f = u_z t_L = (u\cos\Theta)\frac{2\pi}{B_z}\frac{m}{e}. \tag{5.4}$$

Suppose a number of electrons of given velocity u cross any given line of force at a point J at a number of different inclinations Θ, which may be assumed to be so small that $\cos\Theta \approx 1$. All these electrons will again cross the same line of force at another common point J', because the component perpendicular to the line of force performs just one full revolution within the Larmor period t_L given by (5.2).

Using in (5.4) $mu/e = B_e r_e$ for the electron momentum (cf. § 1.2), we obtain

$$JJ' = z_f \approx \frac{2\pi}{B_2} B_e r_e. \tag{5.5}$$

Thus it appears that a homogeneous magnetic field is able to produce an electron optical picture of unit magnification within a distance z_n from the object, z_n being equal either to z_f as given by (5.5) or to a multiple of z_f. z_n is perfectly defined by the ratio of the electron velocity u and the flux density B_z of the magnetic field. The focal length of the homogeneous field is always infinite; thus optically it does not represent a simple lens but it belongs to the telescopic systems.

It may seem difficult to understand the motion of the electron in a magnetic field from an optical point of view. The difficulty is due to the fact that the refractive index of the beam is not a simple function of its coordinates only but, as follows from the above considerations, it also depends on the direction of the beam. Such a refractive index has already been specified in (1.20). Now Störmer (1933) and Dosse (1936) have shown that the problem of the refraction of electrons in all magnetic fields of circular symmetry can be attacked in a much simplified way by considering two-dimensional motion of the electron in two separate planes. The two planes are:

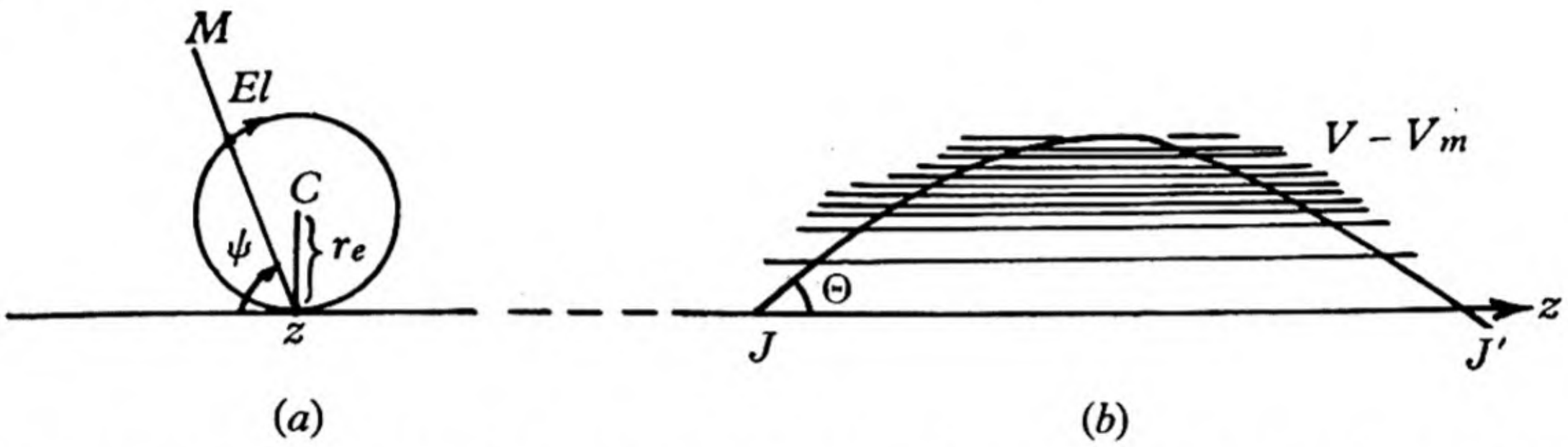

Fig. 5.1. Motion of an electron in a homogeneous magnetic field: (*a*) path in the equatorial plane; (*b*) path in the rotating meridional plane.

(1) An 'equatorial' plane at right angles to the axis of circular symmetry, moving with the longitudinal speed u_z of the electron.

(2) The 'meridional' plane rotating with the electron about the line of force that passes through the object point and the image point.

This line may be considered as the axis of the system.

The electron path in the rotating meridional plane and in the equatorial plane is shown in fig. 5.1. In the equatorial plane, the electron *El* moves along a circle, starting from *J*. (5.1) and (5.2) describes this circular motion about the centre *C* in terms of the radius of curvature r_e and of the angular velocity $\mathrm{d}\alpha/\mathrm{d}t = \omega_L$, i.e. the Larmor frequency.

We may also describe the electron motion in the homogeneous field with respect to the z-axis through *J*. The distance of the electron from this axis, i.e. the radius vector r, corresponds to the ordinate of the electron in the meridional plane *M*. The vector r always lies in this rotating meridional plane including an angle $\psi = \frac{1}{2}\alpha$ with the initial position of the plane. Using (5.2),

the angular velocity of the meridional plane is given by

$$\frac{\mathrm{d}\psi}{\mathrm{d}t} = \frac{e}{m}\frac{B_z}{2}. \tag{5.6}$$

On the other hand, the angular momentum of the electron with respect to the axis is

$$p_\psi = mru_\psi, \tag{5.7}$$

where u_ψ is the tangential velocity component. The magnetic force is

$$F_\psi = eu_r B_z, \tag{5.8}$$

where u_r is the radial velocity component. Now the change in angular momentum equals the moment of forces, i.e.

$$\frac{\mathrm{d}p_\psi}{\mathrm{d}t} = rF_\psi. \tag{5.9}$$

(5.9) with (5.7) and (5.8) gives

$$\int_{(1)}^{(2)} \mathrm{d}(mru_\psi) = \int_{(1)}^{(2)} eB_z r\,\mathrm{d}r,$$

or

$$(mru_\psi)_1 - (mru_\psi)_2 = \frac{e}{2\pi}[(B_z\pi r^2)_1 - (B_z\pi r^2)_2]. \tag{5.10}$$

(5.10) shows that the angular momentum of an electron proceeding from a position (1) to a position (2) changes proportionally to the magnetic flux which passes between the two coaxial circles drawn through the initial and the final positions respectively. We now use Stokes's equation

$$\int \mathrm{curl}\, A\,.\,\mathrm{d}a = \oint A\,.\,\mathrm{d}s, \tag{5.11}$$

A being the vector potential defined by $B = \mathrm{curl}\, A$. (5.11) shows that the integral over the scalar product of B and the surface element $\mathrm{d}a$ (i.e. over the product of the normal component B_z with $\mathrm{d}a$) equals the line integral over the vector potential by the line elements $\mathrm{d}s$ which form the boundary enclosing the surface. Since in the homogeneous field B_z is constant over this surface and perpendicular to it everywhere,

$$B_z\pi r^2 = A_\psi 2\pi r, \tag{5.12}$$

A_ψ being the only component of A that can exist in the homogeneous field. Substituting (5.12) into (5.10) and dropping the index of A gives

$$r(mu_\psi - eA) = C. \tag{5.13}$$

Since C is constant, (5.13) expresses the conservation of total angular momentum of the electron. The constant C vanishes if the electron starts on the axis or crosses the axis where $r = 0$ and $u_\psi = 0$. Thus $C = 0$ for all but for 'skew' rays. Thus for the axial rays (5.13) yields

$$mu_\psi = eA,$$

or

$$\frac{mu_\psi^2}{2} = \frac{e^2}{m}\frac{A^2}{2}. \tag{5.14}$$

Now the total velocity u is composed of the tangential velocity vector u_ψ and of the velocity vector u_m in the meridional plane, i.e.

$$u^2 = u_\psi^2 + u_m^2,$$

or

$$\frac{mu^2}{2} = \frac{mu_\psi^2}{2} + \frac{mu_m^2}{2} = eV,$$

where V is the constant electron energy in electron-volts. Substituting (5.14) gives

$$\frac{mu_m^2}{2} = e\left(V - \frac{e}{2m}A^2\right). \tag{5.15}$$

(5.15) is equivalent to an 'energy equation of the electron in the meridional plane'. The term in brackets is called the 'equivalent electrostatic potential' or the 'meridional potential' V_m. The integration constant in A was chosen so that on the axis $A = 0$. Thus on the axis this potential V_m equals V, and off the axis it decreases. In this way, V_m is comparable to the electrostatic potential in a saddle-field lens with a negative voltage $(V_i - V_o)$ at the inner electrode with respect to the outer electrode (cf. Chapter IV).

A 'meridional refractive index' N_m may thus be defined by

$$N_m^2 = V_m = V - \frac{e}{2m}A^2. \tag{5.16}$$

By means of (5.16) any electron ray can be traced through the meridional plane according to Snell's law.

To obtain numerical values of N_m in a field of given flux density B_z, the value for A given by (5.12) may be substituted in (5.16). In particular, when dealing with homogeneous fields, one has $B_z = \text{const.}$, and $N_m = c_1 + c_2 r$, where c_1 and c_2 are constant. Consequently, in homogeneous fields the lines of constant meridional

refractive index are straight lines parallel to the axis with the value of N_m growing linearly with the distance from the axis. Such lines of constant N_m are drawn, for example, in fig. 5.1, and an electron passing through the refracting field in the meridional plane is seen to describe a path of the shape of a sine curve. In a gravitational model, the electron moving away from the axis would have to climb up a potential mountain, reaching its maximum 'height' at its greatest distance from the axis.

5.2. Paraxial rays in inhomogeneous magnetic fields of circular symmetry. The thin lens

The treatment of the electron motion in the rotating meridional plane which has just been given for the case of a homogeneous field also applies to the paraxial region of an inhomogeneous magnetic field of circular symmetry. For relatively small distances r, from the axis, the axial component of the flux density B_z may be considered to be independent of r. In this case also, the speed of rotation of the electron, given by (5.6), is independent of r, and rays of different aperture travelling at any time in a given rotating meridional plane will remain in this plane. Again, the integration of (5.9) leads to (5.10) and (5.12) only as long as B_z is considered to be independent of r.

The condition of constancy of B_z for paraxial rays at any given value of z may be illustrated by developing the magnetic scalar potential V_H into a power series, as given by (3.8) for the electrostatic potential V. Substitution of

$$B_z = -\mu \frac{\partial V}{\partial z}$$

into (3.8) leads to the following power series:

$$B_z(r,z) = B_z - \frac{r^2}{4}\frac{\mathrm{d}^2 B_z}{\mathrm{d}z^2} + \frac{r^4}{64}\frac{\mathrm{d}^4 B_z}{\mathrm{d}z^4}. \qquad (5.17)$$

(5.17) shows the above restrictive condition to be fulfilled for small r for which the higher terms can be neglected. Moreover, substituting $B_z(r, z)$ of (5.17) into Stokes's equation (5.11) gives the series

$$A_\psi = \frac{r}{2}B_z - \frac{r^3}{16}\frac{\mathrm{d}^2 B_z}{\mathrm{d}z^2} + \frac{r^5}{384}\frac{\mathrm{d}^4 B_z}{\mathrm{d}z^4}. \qquad (5{\cdot}18)$$

(5.18) becomes identical with (5.12) if r is small enough to allow higher terms to be neglected. Again, in inhomogeneous fields of circular symmetry A_ψ is the only existing component of A so that the index ψ may be dropped.

The constant C in (5.13) now vanishes not only for all axial rays as in § 5.1, but in addition it vanishes also for all electrons which start in a field-free space where $u_\psi = 0$ and $A = 0$. The field-free space is the object space from which a complete paraxial image can be projected by the magnetic lens into the image space. The meridional refractive index N_m is again given by (5.16). Since however, B_z, now a function of z, reaches a maximum somewhere in the lens, the lines of constant meridional refractive index in the inhomogeneous field are curved.

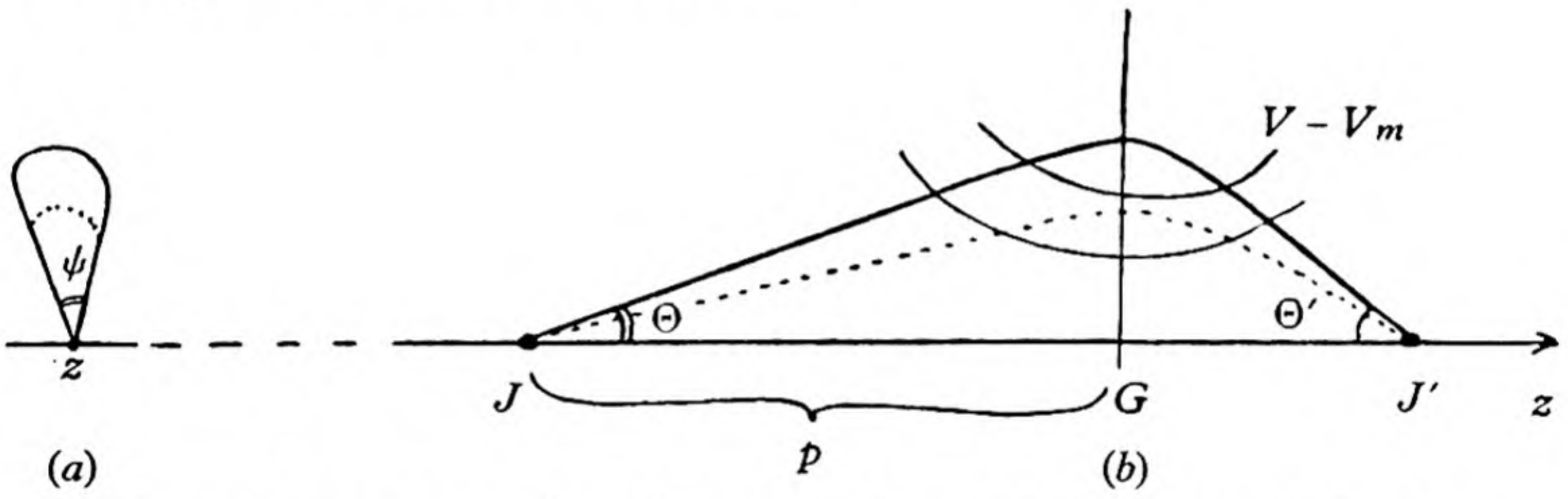

Fig. 5.2. Focusing action of magnetic lens: (*a*) electron path in the equatorial plane; (*b*) electron path in the rotating meridional plane.

The focusing action of an inhomogeneous field of circular symmetry is shown in fig. 5.2. There, two different electron paths are drawn starting at the same point J on the axis with different angles Θ. These paths are seen in the equatorial plane (fig. 5.2 (*a*)) and in the rotating meridional plane (fig. 5.2 (*b*)). Any electron starting on the axis at a point J travels along a substantially straight path until it gradually enters the magnetic field. This field extends round an equatorial plane G and decays rapidly in both directions along the z-axis. To give an impression of the shape of the lines of constant meridional refractive index N_m, two such lines are drawn in fig. 5.2 (*b*). The electrons are deflected gradually in the field and then proceed to the substantially field-free space where they travel along straight lines; eventually they intersect the axis at J'.

For a given mid-object distance $JG = p$, the position of the image does not depend on the slope angle Θ as long as Θ is small. The

meridional plane through which the electron travels is of course stationary while the electron moves through the field-free space. While the electron passes the magnetic lens, the meridional plane rotates through the angle ψ which is shown in fig. 5.2(*a*). This angle of rotation is given by the integral of (5.6)

$$\psi = \int_{z_1}^{z_2} \frac{e}{m} \frac{B_z}{2} \mathrm{d}t.$$

Replacing $\mathrm{d}t$ by $\mathrm{d}z/u_z$ and again introducing the energy $V = mu^2/2e$ one obtains

$$\psi = \sqrt{\frac{e}{8mV}} \int_{z_1}^{z_2} B_z \mathrm{d}z = \frac{1{\cdot}48 \times 10^5}{\sqrt{V}} \int_{z_1}^{z_2} B_z \mathrm{d}z$$

$$= \frac{1}{2B_e r_e} \int_{z_1}^{z_2} B_z \mathrm{d}z \quad \text{[radians]}. \tag{5.19}$$

In the last part of (5.19), $B_e r_e$ is used again as a convenient measure for the momentum of the electron (cf. § 1.2 and Table A. 4), and thus this last part is relativistically correct for highest electron speeds. ψ increases clockwise on looking in the direction of B_z, if the electron travels in the direction of B_z. According to (5.19) the rotation ψ between two points z_1, z_2 on the axis is proportional to the magnetic potential difference $V_H = \int_{z_1}^{z_2} \frac{B_z}{\mu} \mathrm{d}z$ between these points. If object and image are located at z_1 and z_2 respectively, ψ represents the relative rotation of the image.

The study of the electron motion in the rotating meridional plane allows one to visualize all geometrical properties of the complicated spiral path of an electron through inhomogeneous magnetic fields. The lens properties of such fields which are responsible for image formation and which have already been mentioned in this section can easily be derived from the equations of motion:

$$m \frac{\mathrm{d}^2 r}{\mathrm{d}t^2} = -eB_z u_\psi + \frac{mu_\psi^2}{r}$$

$$= -eB_z r \frac{\mathrm{d}\psi}{\mathrm{d}t} + mr \left(\frac{\mathrm{d}\psi}{\mathrm{d}t}\right)^2. \tag{5.20}$$

It is understood that (5.20) refers to the radial acceleration (r = radius vector) in the equatorial plane. With respect to the z-axis, the magnetic force ($-eB_z u_\psi$) is no longer balanced by the

centrifugal force mu^2_ψ/r. Now (5.6) which, as we pointed out, applies to paraxial rays in any field of circular symmetry, may be substituted into (5.20) giving

$$m\frac{\mathrm{d}^2r}{\mathrm{d}t^2} = -\frac{er^2}{4m}B_z^2;$$

or, again with $\mathrm{d}t = \mathrm{d}z/u_z$ and $mu_z^2 = 2eV$,

$$\frac{\mathrm{d}^2r}{\mathrm{d}z^2} = -\frac{e}{8m}\frac{B_z^2 r}{V}. \tag{5.21}$$

This is the 'paraxial magnetic-ray equation' (corresponding to the electrostatic equation (3.29)); it shows the lens properties of the inhomogeneous circular-symmetrical field, since the radial acceleration appears to be proportional to the value of the aperture r. Integration of (5.21) gives

$$\left(\frac{\mathrm{d}r}{\mathrm{d}z}\right)_1 - \left(\frac{\mathrm{d}r}{\mathrm{d}z}\right)_2 = \frac{e}{8mV}\int_{-\infty}^{+\infty} rB_z^2\,\mathrm{d}z. \tag{5.22}$$

(5.22) immediately leads to the focal length of the lens, if this lens is so short that the beam aperture r is substantially a constant in the lens field, i.e. if $r = r_0 = \text{const.}$, where $B \neq 0$. With this restriction and taking $\mathrm{d}r/\mathrm{d}z$ as the slope of the ray in the field-free object space (1) and image space (2) respectively, it follows for parallel incident rays that

$$\left(\frac{\mathrm{d}r}{\mathrm{d}z}\right)_1 = \tan\Theta' = 0,$$

and

$$\left(\frac{\mathrm{d}r}{\mathrm{d}z}\right)_2 = \tan\Theta = \frac{r}{f}.$$

Therefore

$$\frac{1}{f} = \frac{e}{8mV}\int_{-\infty}^{+\infty} B_z^2\,\mathrm{d}z = \frac{2{\cdot}20\times 10^{10}}{V}\int_{-\infty}^{+\infty} B_z^2\,\mathrm{d}z$$

$$= \frac{1}{(2B_e r_e)^2}\int_{-\infty}^{+\infty} B_z^2\,\mathrm{d}z, \tag{5.23}$$

the last part of (5.23) again being relativistically correct for very great electron speeds. (5.23) is the famous 'short-lens formula' derived by Busch (1926) in his historic first paper on electron optics (cf. Chapter I).

5·3. Focal length and image rotation of thick magnetic lenses

Axially symmetrical magnetic fields can be produced by ordinary electric coils (air coils), by iron-shielded coils or by permanent magnets. The formulae of § 5.1 find approximate application for the limiting case of very long coils only. On the other hand § 5.2, and in particular Busch's equation (5.23), apply to paraxial rays in very short fields only. There, the geometrical extension of the lens field along the axis should be negligibly small in comparison with the focal length and with object and image distances. Most frequently met with in practice, however, is the intermediate case of the thick lens, for which, so far, no simple theoretical formulae have been derived.

For practical purposes, the focal length of the thick lens can be well estimated with the help of an empirical formula:

$$f = G\frac{V}{(nI)^2} = \frac{G}{7{\cdot}20}\left(\frac{B_e r_e}{\mu n I}\right)^2, \tag{5.24}$$

where V is the energy of the electron in electron-volts for which, at high energies, should be used the relativistically corrected value V_r of (1.13), nI is the number of ampere-turns of the coil, and G is an empirical factor called 'coil-form factor'. The second expression in (5.24) contains $B_e r_e$ as a measure of the electron momentum and $\mu = 1{\cdot}26 \times 10^{-6}$, the permeability of space; it is relativistically correct for highest electron energies.

Various definitions have been given for a coil-form factor by Ruska (1934*b*), Klemperer (1935), Deutsch, Elliot and Evans (1944), Cosslett (1946*b*) and others. The coil-form factor G in (5.24) is a constant of the value G_0 for a given air coil, if practically the whole lens field is contained between object plane and image plane, i.e. if the field does not spread substantially beyond this interval. Empirical values of the form factor G_0 for all kinds of air coils of different shapes are found within the limits

$$97R < G_0 < 110R, \tag{5.25}$$

where R is the mean radius of the coil. The values of G_0 are found to be the smaller the more concentrated the field towards the mid-plane. This may be explained in the following way: The total

magnetic potential difference generated by the coil equals the number of ampere-turns, namely,

$$V_H = nI.$$

A certain fraction of this potential difference extends along the lens axis between object position z_1 and image position z_2 and is given by

$$^{z_2}_{z_1}V_H = n\frac{I}{2}(1-\beta) = \frac{1}{\mu}\int_{z_1}^{z_2} B_z \mathrm{d}z, \qquad (5.26)$$

where β is usually a small correction term which accounts for the 'ultrafocal field' on the axis. For, given $^{z_2}_{z_1}V_H$, however, the integral $\int_{z_1}^{z_2} B_z^2 \mathrm{d}z$ in Busch's equation (5.23) will be the larger the narrower the B_z distribution. The narrowest physically possible B_z distribution of all air coils belongs to the single wire loop.* Its G_0 value is calculated from (5.23) and (5.24) to be

$$G_0 = 97R,$$

where R is its radius (cf. Deutsch, Elliot and Evans, 1944).

If either the object plane or the image plane are so close to the lens (say, less than five coil radii from the end of the coil) that the field outside the interval between these planes cannot be disregarded, then β in (5.26) is no longer negligible and the value of the empirical form factor G in (5.24) exceeds its lower limit G_0.*

Again, Busch's formula applies exactly to a thin lens only. It would be unsuitable for calculating the G value, even of a single wire loop, excepting when applied in the case where its focal length is really large in comparison with the thickness of the lens field. For thick lenses, the focal length f_{Busch} calculated from (5.23) is nearly always much smaller than the actual focal length f. This may be illustrated by some results obtained by Siday (1942) with a solenoid of a few layers of wire (see Table VIII). According to Siday, f_{Busch}, f and MP depend relatively little upon R, the coil radius if the coil is relatively long, i.e. if the coil length-to-diameter ratio ($= L/R$) cannot be neglected. The figures of Table VIII are valid for $0{\cdot}5 < L/R < 1$.

* The large reduction of G effected by iron shielding the coil will be discussed in §5.5.

If very thick lenses are used in practice, generally object or image (or both) are so deeply immersed into the field of the coil that the ultra-focal field is of the same order of magnitude as the focusing field. In this case, it is difficult to determine a focal length. For instance, in the limiting case of a solenoid with a homogeneous field one obtains a 'telescopic' system with principal planes at infinity (§ 5.1) and no finite focal length can be defined. Hence, (5.24) is of no use for the description of very thick lenses. It is yet of practical interest to compare the number of ampere-turns which, as a function of length and diameter of a coil, is sufficient for the projection of an electron image with a given electron voltage at a given distance.

TABLE VIII. *True focal length f and the focal length* f_{Busch} *calculated from the axial field distribution* (5.23)

MP = distances between midplane and principal plane; $2L$ = length of coil.

f/L	1·92	2·38	2·87	5·36	10·35
MP/L	0·165	0·13	0·11	0·08	0·06
f_{Busch}/f	0·78	0·86	0·87	0·93	0·97

The practically important case of a thick lens in symmetrical position with respect to object and image has been discussed by Graham and Klemperer (1952). Let the object to image distance be given by

$$z_f = k\left(\frac{B_e r_e}{\mu n I}\right)^m, \tag{5.27}$$

where k and m are parameters which depend on the diameter and on the thickness of the lens. For a thin lens with $L \ll z_f = 4f$, (5.27) and (5.24) yield

$$m = 2 \quad \text{and} \quad k = 0{\cdot}56 G_0 = 54 R_0,$$

where R_0 is the radius of the wire loop. For a solenoid, the flux density of the homogeneous field is given by the well-known formula

$$B = \frac{\mu n I}{2L_s}, \tag{5.28}$$

which by substitution into (5.5) yields

$$m = 1 \quad \text{and} \quad k = 4\pi L_s,$$

where $2L_s$ is the length of the solenoid.

When the coil length is increased from zero to infinity (wire loop to solenoid) the parameters of (5.27) gradually change between the limits

$$2 \geqslant m \geqslant 1$$

$$54R_0 \geqslant k \geqslant 12{\cdot}6L_s,$$

where $R_0 \ll z_f \ll L_s$. The diameter of the wire loop ($2R_0$) should be small and the length of the solenoid ($2L_s$) should be large in comparison with the object to image distance z_f. According to experimental results by Witcher (1941), the length of a solenoid should be about 1·5 times greater than the object-to-image distance in order to have within 1 % a homogeneous field along the path of rays between object and image.

A useful approach for obtaining practical formulae for the focal lengths of thick lenses is based on the possibility of an empirical representation of the experimental field distribution (cf. § 5.5) by an analytical formula. The flux-density distribution along the axis of a circular current (single wire loop) can be calculated with Ampere's law to be

$$B_z = B_0 \Big/ \left[1 + \left(\frac{z}{R_0}\right)^2\right]^{\eta}, \tag{5.29}$$

where B_0 is the maximum flux density in the centre, R_0 is the radius of the loop and $\eta = \frac{3}{2}$ is a constant. The electron optical theory of this case has been studied in detail by Wallauschek and Bergmann (1935). Glaser (1941*b*) proposed* to represent the field of any magnetic lens by (5.29), taking for the R_0 the following empirical value:

$$R_0 = \frac{h}{\sqrt{\{(2)^{1/\eta} - 1\}}}, \tag{5·30}$$

where $2h$ is the half-maximum width of the experimental distribution of flux density (cf. for instance, fig. 5.7), while η is obtained by a process of curve fitting. If (5.29) is substituted in the paraxial ray equation (5.21) it can be integrated exactly. For the particular case $\eta = 1$ and thus $R_0 = h$, Glaser obtained for the focal length

$$PF = f = \frac{h}{\sin\left[\pi/\sqrt{(1 + K^2)}\right]}, \tag{5·31}$$

* Different analytical representations of the field distribution in magnetic lenses have been proposed by Ramberg (1942), by Lenz (1951*a*, 1952) and by Grivet (1952).

and for the midfocal length

$$MF = \frac{h}{\tan\left[\pi/\sqrt{(1+K^2)}\right]}, \tag{5·32}$$

where

$$K^2 = \left(\frac{hB_0}{2B_e r_e}\right)^2 = \frac{2{\cdot}2\times 10^{10}(hB_0)^2}{V(1+10^{-6}V)}. \tag{5·33}$$

K is a dimensionless parameter which is called the 'lens-strength parameter' or 'excitation parameter'. Comparison with (5.24) shows that K is roughly proportional to G/f (cf. Ments and Le Poole, 1947). For low field values, i.e. for $K\to 0$, Glaser's formula (5·31) agrees with Busch's thin-lens equation (5.23), both leading to the focal length

$$f\approx 2h/(\pi K^2), \tag{5·34}$$

i.e. in the region of low field values, the power of the lens is proportional to K^2.

Equation (5.29) has fairly wide application to air coils as well as to the iron-shielded lenses which will be described in the next section. Asymmetrical fields can be represented by combining two halves of curves with identical B_0 but with different h values. The above case of $\eta = 1$ fits well to magnetic microscope lenses which are worked near the saturation of the iron shield (cf. Dosse (1941) and Ruska (1944). The case η being an integer $\geqslant 1$ has been investigated by Swartholm (1942). The limiting case $\eta\to\infty$ has been tested by Siegbahn (1943). There, (5.29) reduces to

$$B_z(z) = B_0 \exp\left[-(z\sqrt{(\log_e 2)}/h)^2\right]. \tag{5·35}$$

This equation gives a good analytic representation of actual field distributions of shielded lenses when a relatively low flux density passes through the iron shield of the lens, i.e. for conditions far from saturation. For instance, it is in good agreement with experimental results obtained with the large lenses of Beta-ray spectrometers.

Closest approximation to the experimental fields of microscope lenses is obtained by an empirical modification of (5.29) which is due to Glaser (1950). There, the exponent η is still unity, but the half-maximum width $2h$ and the field strength parameter K of (5.30)–(5.32) are multiplied by a new factor which is derived from the curvature $(\mathrm{d}^2B/\mathrm{d}z^2)$ of the empirical curve at the maximum.

Another way, perhaps more useful in practice, of improving Glaser's field representation (5.29) is due to Lenz (1950). He gave a formula for calculating the exponent η of (5.29) and (5.30) in such a manner that the actual field distribution and its analytical representation not only agree with respect to maximum flux value B_0 and to the half-maximum width $2h$ but also cover the same range of magnetic potential difference

$$\int_{-\infty}^{+\infty} (B/\mu)\,\mathrm{d}z.$$

The focal length PF given by (5.31) is always larger than the mid-focal length MF given by (5.32). In agreement with experimental results, the principal planes are always crossed over. The principal plane to mid-plane distance increases according to equation (5.32) with increasing parameter K of (5.33).

The image rotation by a thick lens is given by (5.19). For large lenses of Beta spectrometers this rotation is conveniently calculated after Siegbahn (1942) by substitution of (5.35) for $B(z)$ into (5.19); there, the integration has to be taken from the object point z_1 to the image point z_2. The image rotation of microscope lenses is calculated after Ments and Le Poole (1947) according to the following convenient formula (cf. (5.24)):

$$\psi = 0{\cdot}19nI/\sqrt{\{V(1+10^{-6}V)\}}. \qquad (5.35a)$$

The angles of rotation generally are somewhere between 0 and 180° and the limiting cases are: (i) The short lens with $\psi \to 0$, i.e. with negligible rotation, leading to an inverted image as in the case of the glass lens. (ii) The solenoid with $\psi = 180°$ yielding an erect image. The rotation by lenses of given focal length, is the larger the more the field extends along the axis. Thus, the image rotation is always larger for an air coil than for an iron-shielded coil of the same focal length.

Magnetic lenses without image rotation can be obtained by using a pair of similar coils traversed by the same current in opposite directions. The electrons pass in succession two fields of opposite directions, and the rotation in the first field is eliminated by an opposite rotation produced in the second field (Stabenow, 1935; Becker and Wallraff, 1940*b*). Such rotation-free lenses, however, are not often met in practice: (i) since they need a multiple of the

number of ampere-turns of the ordinary lens, (ii) since they are much more sensitive to misalignment, (iii) since they have very much greater aberrations (cf. Chapter VI) than the corresponding single coils.

Of some principal interest is the possibility of producing magnetic lenses of negative focal length. Graham (1949) and Hubert (1951) have shown that a 'paraxial baffle coil', i.e. a very small coil arranged coaxially with an electron beam so as to intercept paraxial rays, will diverge the zonal and marginal rays of this beam. The diverged rays of the beam remain substantially homocentric; thus the paraxial baffle coil acts as a lens of negative focal length. The beam-diverging properties of the baffle coil may be recognized by considering the refractive index (see (1.20)) which is expected to have a minimum at the conductor, since the distribution of the vector potential has a maximum there. An idea of the distribution of the vector potential outside a coil may be obtained from the well-known distribution for the single wire loop (cf. Smythe, 1939).

5.4. Practical lens design

If a magnetic lens is required for any electron-optical apparatus, three conditions are generally given at the outset: namely, the lens has to focus electrons of a certain velocity, these electrons have to be focused from a given object point into a given image point, and a certain fraction of the total electron emission from the object has to be focused into the image.

The first two conditions involve the electron energy V and the focal length f, for which (5.24) yields the necessary number of ampere-turns nI. The fraction of the emission which is focused into the image is called 'collecting power' of the lens. Assuming an isotropically radiating point source on the lens axis, the collecting power can be measured by the solid angle subtended at the source by all focused rays. The request for a certain collecting power at a given object distance establishes a lower limit for the inner coil radius R_i. Another limit for R_i is usually given by the diameter of the neck of the vacuum tube or by the pole-pieces of a magnet over which the coil has to fit.

Now, for given nI and R_i, coil length ($2L$), outer-coil radius (R_o) and wire thickness ($2r$) have to be determined. The wire thickness

clearly depends upon the voltage which is available for energizing the coil. Again, outer-coil radius and length of the coil depend on the total number of turns n_c, on the radius r of the wire and on the thickness x of the insulation of the wire. If further insulation, say between the layers of the wire, etc., may be neglected it follows from geometry that

$$(R_o - R_i)\,2L = n_c(2r+2x)^2. \tag{5·36}$$

After introducing the mean coil radius R_c by the relation

$$R_o - R_i = 2(R_c - R_i)$$

(5·36) may be written

$$n_c = L\frac{(R_c-R_i)}{(r+x)^2}. \tag{5·37}$$

On the other hand, n_c is also given by the required number of ampere-turns, since a certain current density i is desirable in the copper wire. If i is chosen too large, the coil will run hot; if it is chosen too small, the coil becomes unnecessarily bulky and material is wasted. A practical figure for i may be 2–3 amp./mm.^{2} if coils are used in air without particular cooling. The larger densities may be chosen for coils with a larger surface-to-ampere-turn ratio. With suitable air blow or running water-cooling, i may of course be increased beyond the stated limits. The number of turns following from a fixed i may be written

$$n_c = \frac{nI}{\pi r^2 i}. \tag{5·38}$$

In a third way, the number of turns n_c depends on the voltage V_c which is available for energizing the coil. This can be seen in the following way:

$$n_c = \frac{l_w}{2\pi R_c}, \tag{5·39}$$

where l_w is the total length of the wire. Now l_w may be replaced by Ω_c/Ω_m, the ratio of the electrical resistance of the whole coil to the resistance per unit length. On the other hand, the given voltage V_c requires

$$\Omega_c = \frac{V_c}{i\pi r^2}.$$

Moreover, the resistance per unit length of wire is given by the

specific resistance $\Omega_0 = \Omega_m \pi r^2$. With these three substitutions, (5·39) becomes

$$n_c = \frac{V_c}{2\pi i \Omega_0 R_c}. \tag{5.40}$$

With (5·37), (5·38) and (5.40), the wire radius r and the outer coil radius R_o may be calculated from a given R_i, L and nI. For practical purposes a step-by-step approximation allows this in the easiest way. For this purpose we introduce two auxiliary quantities a and b. By substitution of (5·38) into (5·37):

$$\frac{r^2(R_c - R_i)}{(r+x)^2} = \frac{nI}{i\pi L} = b. \tag{5.41}$$

By substitution of (5·38) into (5.40)

$$\frac{r^2}{R_c} = \frac{2nI\Omega_0}{V_c} = a. \tag{5·42}$$

Now the first approximation R_c' of the mean coil radius R_c is obtained by neglect of x against r in (5.41). Thus

$$R_c' = R_i + b. \tag{5.41}'$$

This may be substituted into (5.42) giving the first approximation for the wire radius

$$r' = \sqrt{(aR_c')}. \tag{5.42}'$$

Again r' in (5.41) yields a second approximation for the mean coil radius

$$R_c'' = R_i + b\left[1 + \frac{2x}{r'}\right], \tag{5.41}''$$

and with R_c'' in (5.42)′ a second approximation is obtained for the wire radius

$$r'' = \sqrt{(aR_c'')} = \sqrt{a}\left\{R_i + b\left[1 + \frac{2x}{\sqrt{a}\,(R_i+b)^{\frac{1}{2}}}\right]\right\}^{\frac{1}{2}}. \tag{5.42}''$$

Taking for instance, copper with $\Omega_0 = 1{\cdot}7 \times 10^{-8}$ [$\Omega \times$ m.] and taking an average coil size allowing a current density $i = 2{\cdot}5 \times 10^6$ amp./m.^{2}, we have in m.k.s. units

$$a = 3{\cdot}4 \times 10^{-8}\frac{nI}{V_c}, \tag{5·43}$$

$$b = 1{\cdot}3 \times 10^{-7}\frac{nI}{L}. \tag{5·44}$$

These values and the given value of R_i substituted first in $(5.41)'$ and $(5.42)'$ and taken in $(5.41)''$ and $(5.42)''$ give first and second approximation values for R_c and r respectively. The second approximations are generally sufficiently near to the first ones that no further approximations are needed. In particular, since available wire gauges are graded in relatively coarse steps, only a nearest convenient gauge can be chosen anyway.

The preceding formulae allow the calculation of the outer-coil radius and wire thickness if the inner-coil radius (R_i), the coil lengths ($2L$) and the number of ampere-turns are given. The further question now arises, whether—by suitable choice of the coil length—it may be possible to minimize the number of ampere-turns, of electrical power and also of the weight of copper wire required for producing a lens of given power.

Apparently, a given number of ampere-turns is employed with the best efficiency if the flux along the axis is all concentrated between object and image. Hence, the dimensionless factor

$$\frac{B_e r_e}{\mu n I} \tag{5·45}$$

has been termed 'focusing efficiency' (Graham, 1949); under given geometrical conditions, it indicates the number of ampere-turns required to focus rays of a given momentum ($B_e r_e$). Most efficient of all air coils is the single wire loop, but its diameter should be chosen as small as possible in comparison with object to image distance.

Values of the focusing efficiency as a function of coil length, coil radius and of object-to-image distance can be found in the papers by Graham (1949) and by Graham and Klemperer (1952). Very short coils seem to be wasteful, since the required ampere-turns have to be wound in very many layers. Hence the mean radius of a very short coil becomes very large with subsequent large spreading of the lens field outside the object-to-image-range. On the other hand, a very long coil will again suffer from the disadvantage of widely spread field regions, particularly when the coil extends beyond the object-to-image distance.

Calculations and experiments on the optimum efficiency of powerful air coils placed symmetrically between object and image

have been carried out by Graham (1949). Minimum weight of copper wire and least consumption of electrical energy are required if the coil length ($2L$) is chosen of the order of half the object to image distance ($2s$). The optimum for L/s is not critical, its exact

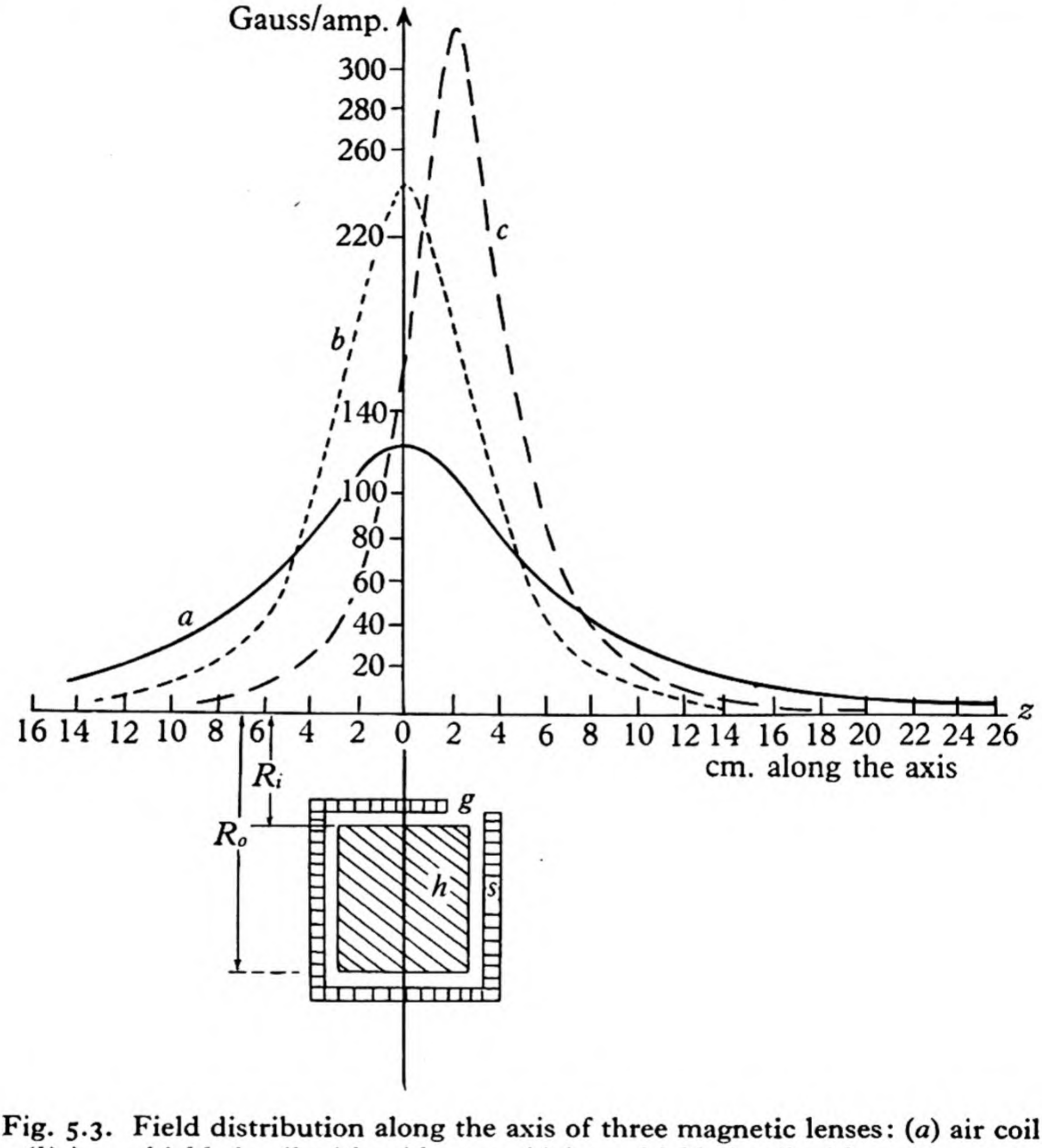

Fig. 5.3. Field distribution along the axis of three magnetic lenses: (*a*) air coil; (*b*) iron shielded coil with wide gap; (*c*) iron shielded coil with narrow gap.

value depends of course on the required aperture R_i of the coil and on the momentum of the electrons which have to be focused.

Great economy in electrical energy is gained by shrouding the coil with material of high permeability. The scheme of an iron-shielded coil is shown in a meridional section in fig. 5.3. The coil *h* (produced by rotation of the rectangle *h* about the axis *z*) has the

inner and outer radii R_i and R_o. The mild iron shield s completely surrounds the coil leaving only a relatively small annular gap g. The total flux passing through the iron has to cross this gap. It produces an intense stray field by which the electrons are focused.

The axial component of flux density along the axis of the lens is plotted as curve c in fig. 5.3. The relevant figures of flux density have been obtained with a coil of 1550 turns and with an iron shield 5 mm. thick leaving a gap of 2 cm. The coil dimensions, length $2L = 15$ cm., inner and outer radii $R_i = 5$ cm. and $R_o = 12$ cm., are indicated in the figure. For $I = 1$ amp., B_z reaches a maximum of 320×10^{-4} Webers/m.^{2} in the middle of the gap. For the coil of fig. 5.3, the gap width of 2 cm. presents an optimum; maximum flux density in the middle of the gap decreases for wide gaps as well as for smaller gaps. If the gap is enlarged to 6 cm. (i.e. if the whole *inner* iron cylinder is omitted) the maximum is decreased to 240×10^{-4} Webers/m.^{2}/amp., the corresponding axial flux density distribution being shown in curve (b). Curve (a) applies to the 'air coil', the iron shield being omitted completely. The centre of the coil is chosen in each case as origin of the coordinates. The width of the flux-density distribution of an air coil is always reduced by the application of an iron shield. For example, in the two cases of curves (a) and (b) the field decays to 10 % of its maximum value within distances of about two mean coil radii and within about one mean coil radius respectively.

Axial components of flux density along the radii of the above lenses are shown in fig. 5.4. The curves a, b, c again belong to the air coil, the iron coil with wide gap and to the iron coil with small gap, respectively, as given in fig. 5.3. Curves a and b are measured along a radius from the centre of the coil. For curve c the measurements are taken from the middle of the gap which is displaced from the centre of the coil. All curves show increasing values of flux density with increase in radius. Curve d shows the radial distribution of the iron coil with the large gap at some distance from the centre of the coil. This curve shows the remarkable decrease of field for the peripheral regions.

The focal lengths of the magnetic lenses of fig. 5.3 as a function of the coil current and of the focused electron velocities can be calculated by means of the formula for thick lenses (5.24). The value

of the coil-form factor G may be determined by the measurement of one focal length with a known electron velocity at a given coil current provided the number of turns of the coil is known. In this way, for instance, with object and image, each at a distance of six mean coil radii from the mid-plane the following values have been

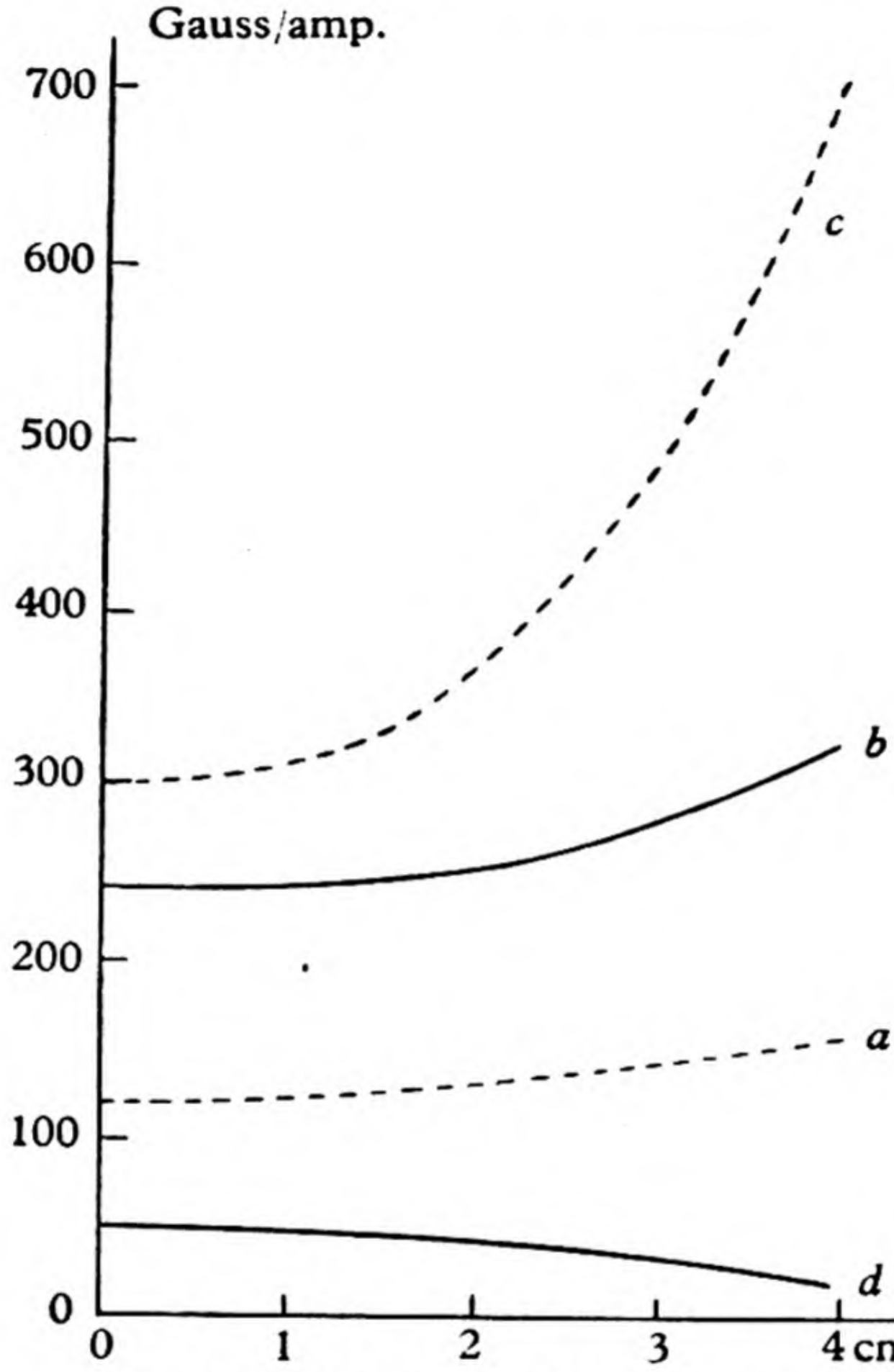

Fig. 5.4. Radial field distributions in magnetic lenses.

obtained: for the air coil of fig. 5.3, $G = 9 = 106R$, where R is the mean coil-radius; for the corresponding iron-shielded coil (2 cm. gap) $G = 2{\cdot}4$ [m.k.s.]. An increase of the latter value due to saturation of the iron shield sets in very gradually and slowly. For instance, when the iron-shielded coil with 2 cm. gap reaches a maximum flux density of 0·1 Weber/m.^{2} on the axis, G is increased by 5 % in comparison with its value at low-coil currents. On the other hand, for the same shielded coil with 6 cm. gap the increase of G is only of the order of 1 % at the above flux density. The magnetic lenses of figs. 5.3 and 5.4 have been used in a spectrometer for focusing electrons up to 1·5 MeV (cf. Klemperer, 1935).

A very large air coil for focusing 16 MeV. electrons within an object-to-image distance of 1·06 m. has been used in a spectrometer by Graham and Klemperer (1952); the coil was 88 cm. long with inner and outer radius of 9·4 and 23 cm. respectively; it had 4600 turns of rectangular (2·5 × 5 mm.) copper strip weighing $\frac{3}{4}$ ton. Up to 45 amp. could be passed continuously through the coil, the dissipated heat energy of 16 kW. being carried away by forced water-cooling. Electrons of about equally large energy have been focused by Cosslett (1940*a*) with the help of heavy iron-shielding. There, the

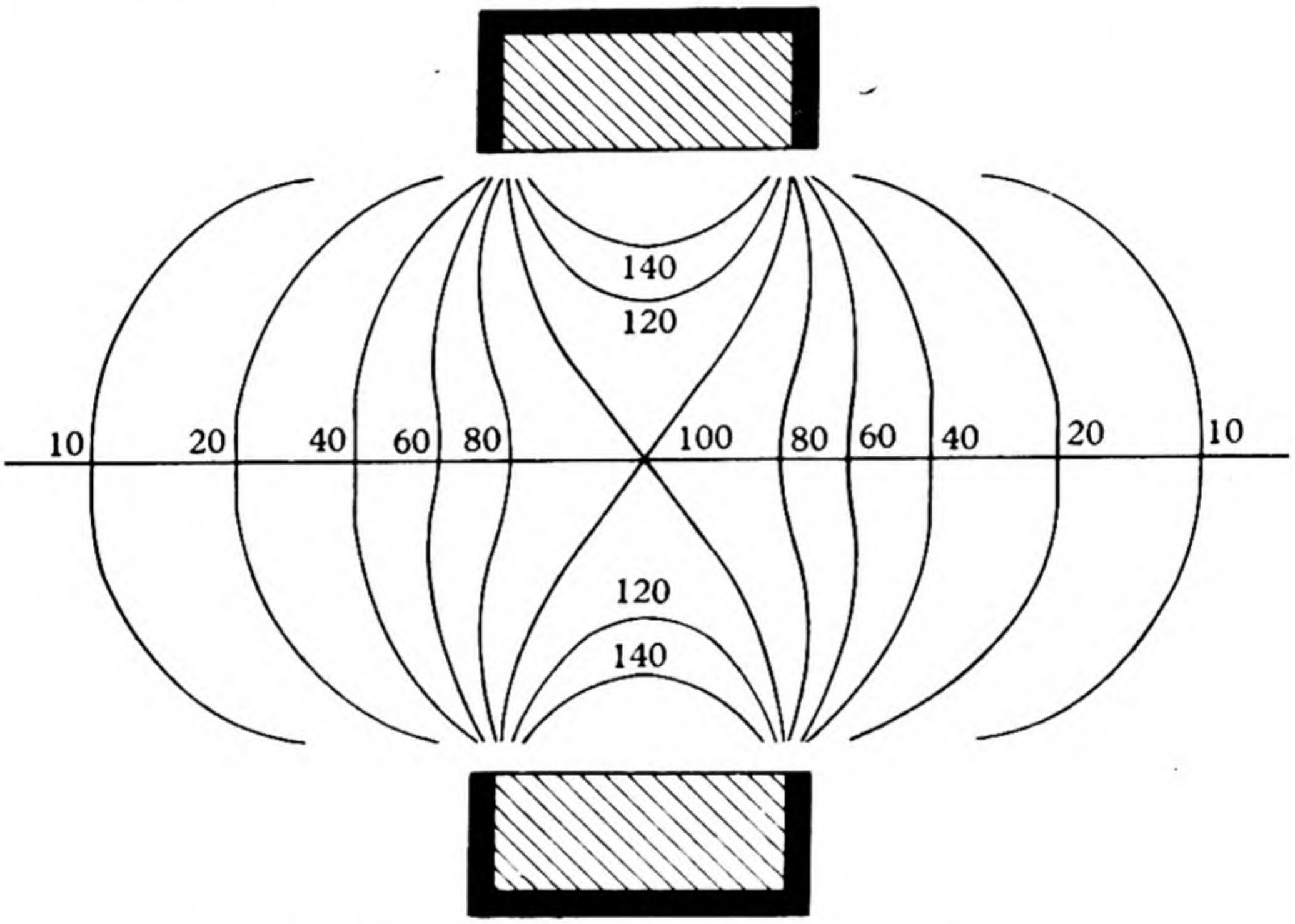

Fig. 5.5. Contour lines of axial components of flux density in iron shielded coil.

relatively short lens was formed in the gap of a large yoke magnet, between hollow, cylindrical pole-pieces, inside which the electrons travelled. The maximum attainable flux density was of the order of 1 Weber/m.^{2}. The focal length was about 15 times shorter than that of the energizing (unshielded) coils. The collecting power of Cosslett's lens, however, was relatively small, since the object-to-image distance was nearly 1·5 m. and the bore of the pole-pieces was only 5 cm.

As a further example for practical lens design (used in the image converter (fig. 5.19) and in the pick-up tube (fig. 12.2)), we describe here a relatively weak iron-shielded lens (cf. figs. 5.5 and 5.6, 5.17

and 5.18). The coil has 1500 turns of fine wire, it has an inner and outer radius of 58 and 75 mm. respectively and is shielded by 4 mm. iron sheet. The shape of the shield is shown in fig. 5.5. This figure also contains a map of contour lines of the axial component of flux density. The similarity of these contour lines to

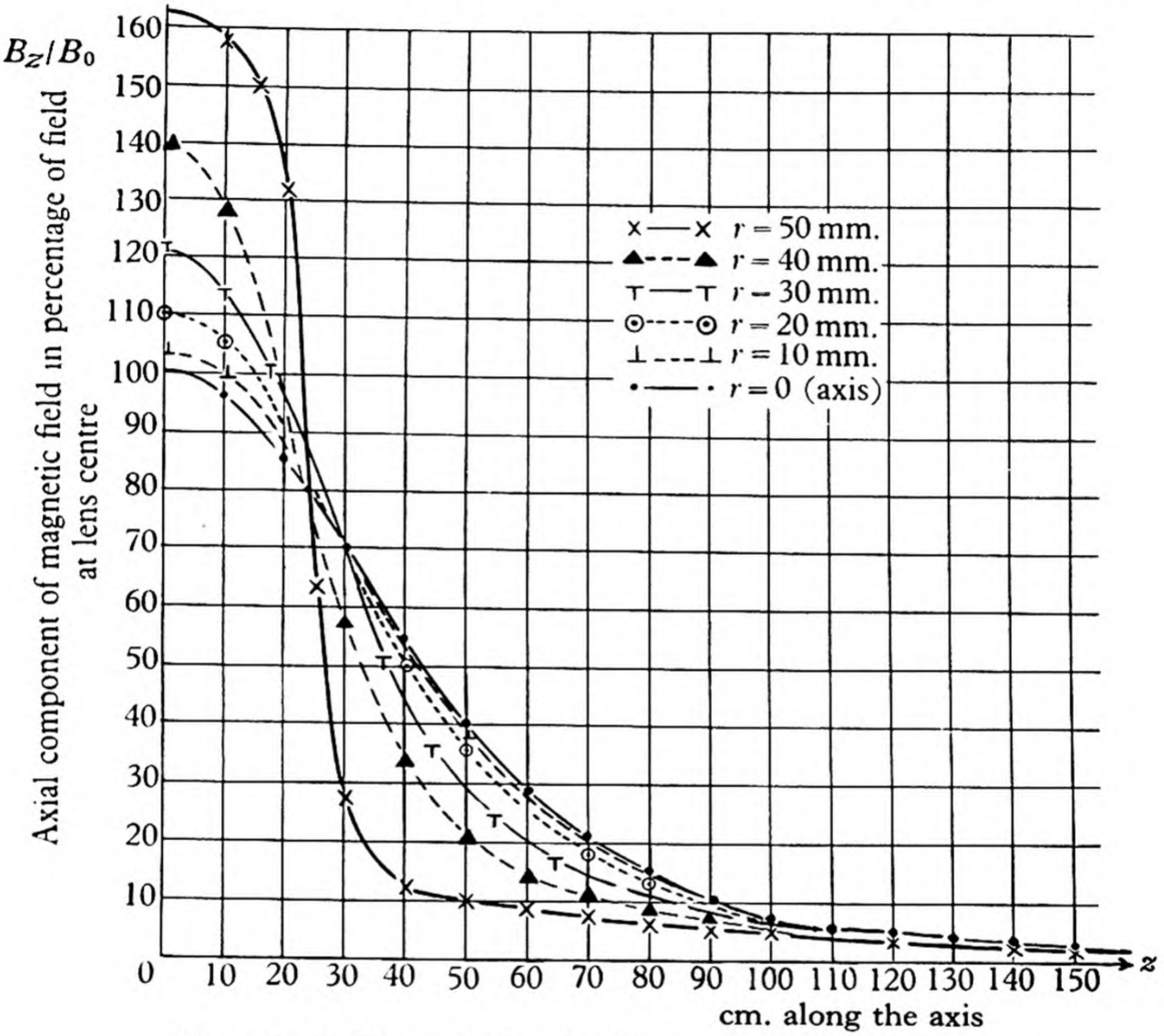

Fig. 5.6. Field distribution in the magnetic lens of fig. 5.5.

the equipotential lines in a symmetrical electrostatic saddle-field lens is seen on comparison with fig. 4.8. The figures given against the contour lines indicate the axial component of flux density with respect to that at the centre of the lens as 100 %. The usual graphical representation of the same flux distribution is given in fig. 5.6. There, the axial components of flux density are plotted against the axial z-coordinate along the axis and along lines parallel to the axis and in various distances from it. The flux density in the centre is again taken as $B_0 = 100$ %. The batch of curves of fig. 5.6 covers

the whole lens field by a network of flux-density values; it is a very convenient representation of the lens for the purpose of ray tracing, as will be seen in the next section.

Of quite a particular design are the magnetic electron lenses that are used in electron microscopes. Strongest possible fields have to be concentrated within the shortest space along the axis in order to obtain smallest possible focal lengths. Microscope objectives are produced by powerful coils (order of 5×10^3 ampere-turns) which are shielded by iron excepting for a small gap between pole-pieces. Microscope projector lenses are of similar design. The requirements for the two types, however, are rather different: the rays pass right through the projector lens, whereas in the objective, the rays effectively originate from an object which is near the focal point (cf. § 12.6). Fig. 5.7, for instance, shows the construction and flux-density distribution curve of an objective lens described by Marton and Hutter (1944). The gap is only 1 mm. wide, while the half-maximum width ($2h$) of the flux density distribution curve amounts to 2 mm.

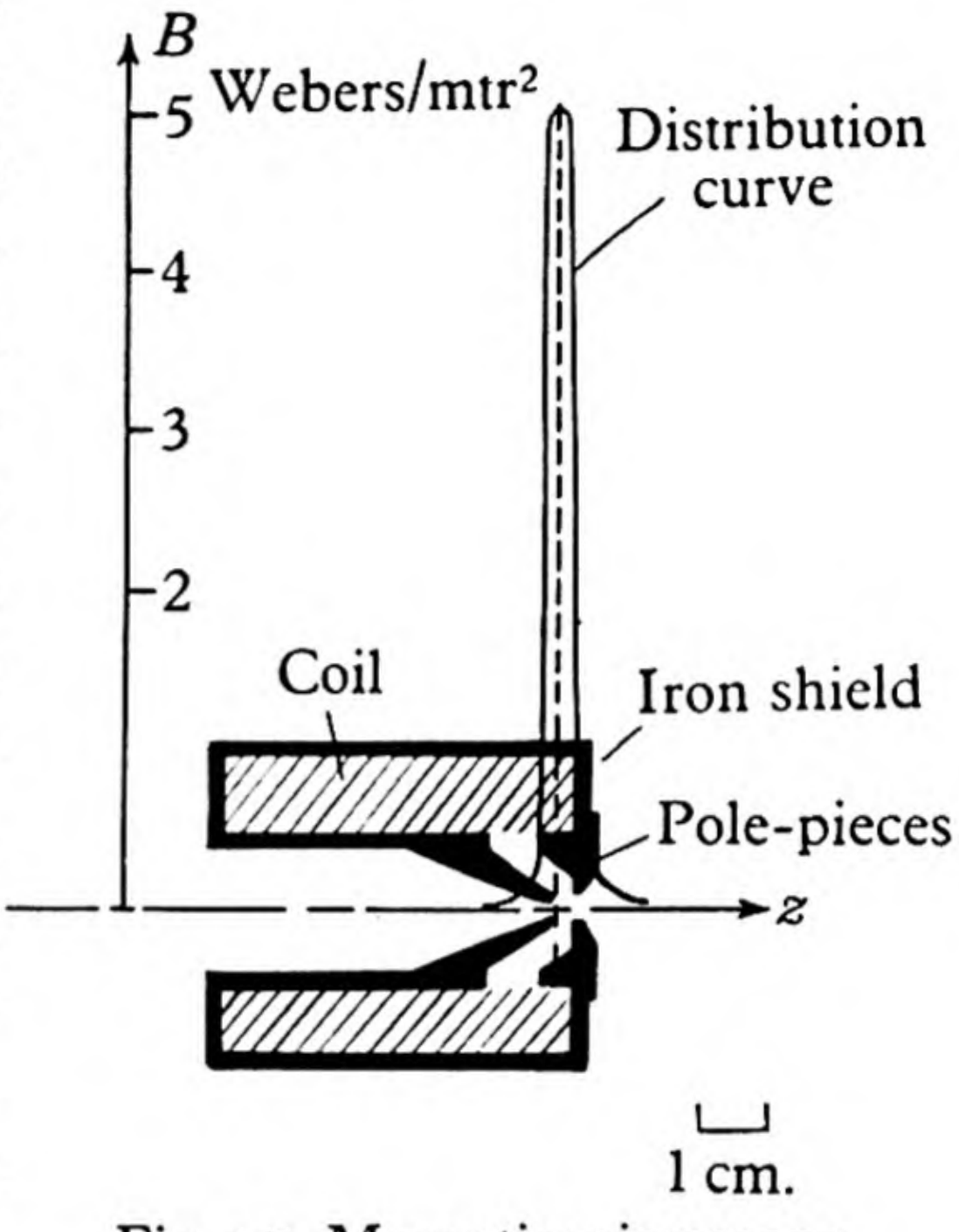

Fig. 5.7. Magnetic microscope objective lens with flux density distribution.

With the view of obtaining shortest focal lengths, pole-pieces of small diameter with small gaps are used. A scaling down of the geometrical dimensions of the pole-pieces may result in a proportional reduction of the focal length, but only outside the saturation region of the iron. For sufficiently small coil currents, the form factor G of a microscope objective is, according to Ruska (1934*b*), of the order of magnitude of that of a single wire loop (cf. § 5.3) if the radius of the loop corresponds with the clear inner radius of the objective. According to ray tracing results by Liebmann and Grad (1951) this form factor can be estimated within 10 % to be

$$G = 70\,(RS)^{\frac{1}{2}},$$

where R is the bore radius of the pole pieces and S is their separation. However, with the largest currents used in practice the iron is sometimes so much saturated that G has increased to a multiple of its original value.

The objective lenses of electron microscopes are always sufficiently strong to have their focus substantially inside the lens field. Hence it is important to have the field concentrated within the shortest possible distance. This is explained by fig. 5.8 which is an

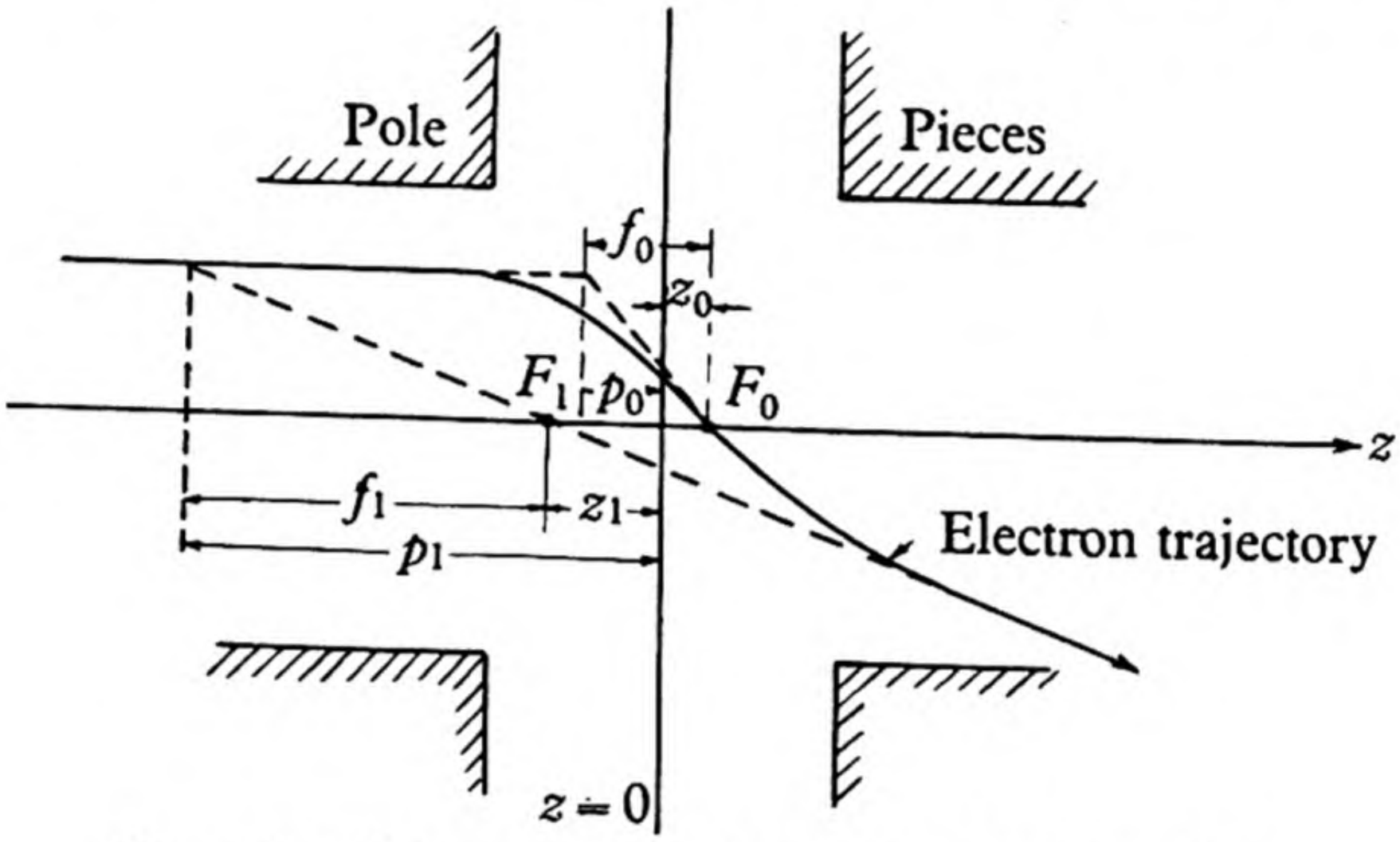

Fig. 5.8. Electron path and effective focal length in a microscope projection lens.

exact ray tracing diagram due to Liebmann and Grad (1951). The real focus F_0 is found at the distance z_0 from the mid-plane ($z = 0$), the principal plane is seen at the distance $-p_0$, so that the real focal length is $f_0 = p_0 + z_0$. After passing F_0, the trajectories are again converged by the ultrafocal field. Hence, the virtual focus F_1 which is produced as the intersection of the emerging straight part of the trajectory with the z-axis is found at the distance $-z_1$ from the midplane. The virtual principal plane, i.e. the plane of the intersection of the produced incident and emerging rays is found at a distance $-p_1$ from the mid-plane. Hence $f_1 = p_1 - z_1$ is the effective focal length, which, according to (2.2), controls the magnification obtained by the objective.

With increasing coil current, the mid-focal distance (z_0) gradually decreases while the ultrafocal field increases in intensity and extension. Hence, the effective focal length f_1 first decreases, then passes through a minimum at a given optimum number of ampere turns.

For extremely high fields, the iron becomes progressively less effective in concentrating the magnetic lines of induction. Eventually, the maximum field strength on the axis ceases to increase with current; instead, the field distribution along the axis broadens. Since, however, the focal length of the objective is short enough for the focal point to lie inside the magnetic field, the broadening of the field distribution will cause an additional increase of the ultra-focal part of the field. This tends to increase the effective focal length as the coil current is increased beyond a certain limit. For this reason, steels of highest magnetic saturation fields are best suited for shielding of microscope lenses. This has been illustrated, e.g., by results of Rakhimov and Sushkin (1948) who, for instance, found Permendur to be superior to Armco iron.

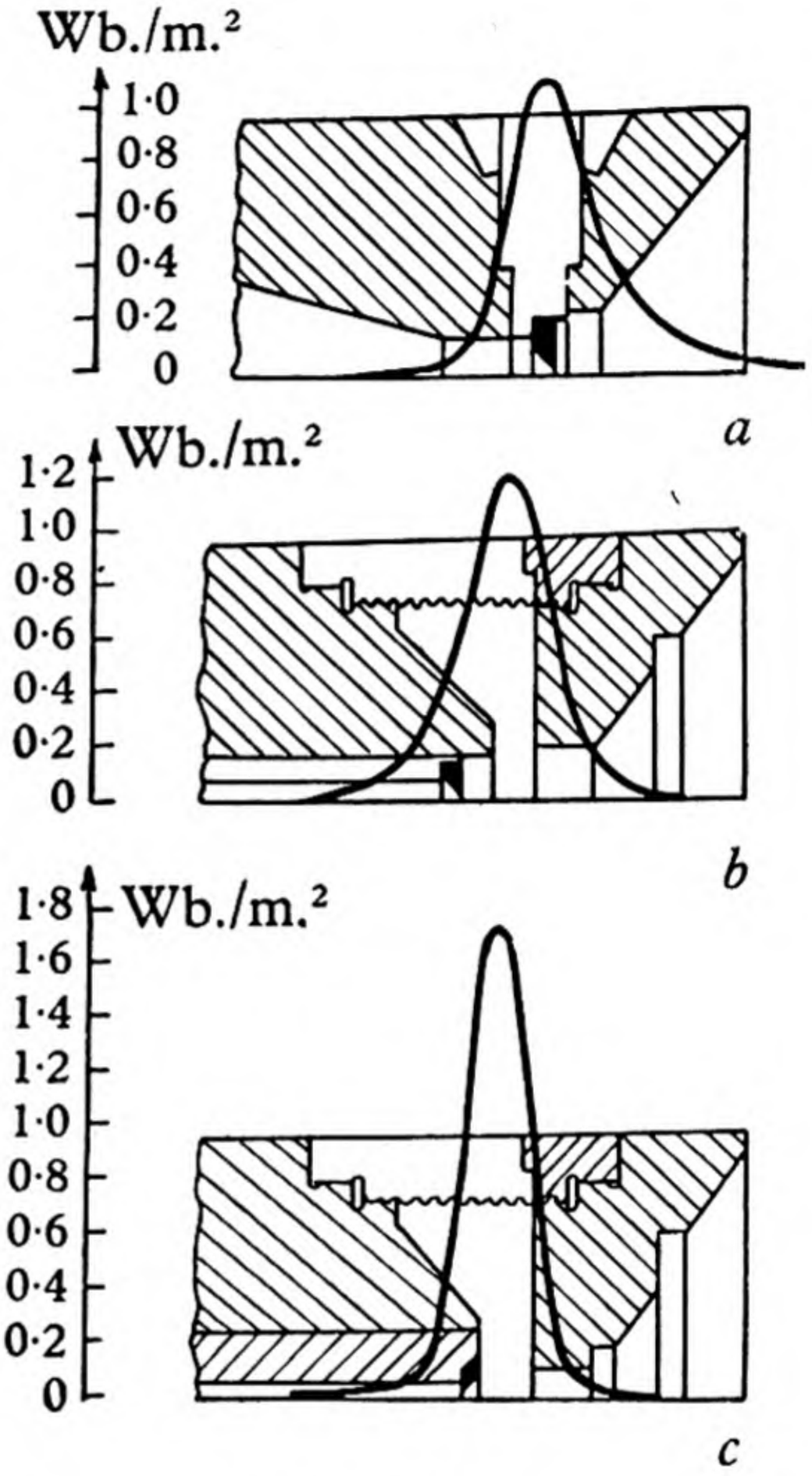

Fig. 5.9. Shape of pole pieces of objective lens and flux density distribution.

The geometry of the pole-pieces is of major importance from the point of view of obtaining shortest focal lengths. Ruska (1934*b*), for instance, experimentally investigated lenses with different ratios of pole-piece gap S to bore radius R. For his 60 kV. microscope objective he found the optimum to be of the order of $S/R \approx \frac{3}{2}$. The optimum size and shape for the pole-pieces has later on again been studied by Ruska (1944). The magnetic resistance offered to the flux by the iron part of the circuit should be small compared to that offered by the gap. At the same time, the cross-sectional area of the gap should be large enough for the field on the axis in the centre of the gap to attain the largest possible values. These requirements led Ruska (1944) to pole-piece designs of the general character as shown in fig. 5.9. The pole-piece tips are ground off flat to a

diameter considerably greater than their free opening. In this manner, saturation effects in the pole-piece tips are reduced to a minimum. The two pole-pieces need not be symmetrical, they generally are of different shape and cross-section. Even the cylindrical channels in the two pole-pieces are sometimes made with different bore radius.

Microscope lenses with symmetrical pole-pieces have been studied by Liebmann and Grad (1951) and by Liebmann (1952*a*, *b*). There, the fields were mapped with the resistance network analogue described below (§ 5.5) and the electron rays were traced by numerical methods (§ 5.6). The geometry of the symmetrical lenses is completely characterized by the ratio S/R of pole-piece spacing over pole-piece bore radius. The minimum focal length was found to decrease with decreasing S/R until magnetic saturation becomes substantial. An optimum R for minimum focal length, however, was found as a function of the field in the saturation region. Moreover, relatively large values of S/R may be required with a view to avoiding excessive lens aberration (cf. Chapter VI).

Practical projector lenses are usually designed with a gap-to-bore ratio between the limits $2 < S/R < 4$. The lower limit is observed in order to avoid pronounced saturation. The upper limit is given by the need to keep the beam sufficiently far from the pole-pieces to avoid the appearance of higher order aberrations. The shortest possible focal lengths are generally required for microscope objectives of high magnification. The performance of the objective depends, as was shown, to some extent on the position of the object in the lens field. However, it has been found (Lenz (1950), Liebmann (1952*b*)) that the shortest obtainable focal length is proportional to V_r/B_p where V_r is the relativistically corrected accelerating voltage (1.13) and B_p is the flux density in the parallel part of the pole-piece gap, the maximum possible value of which is known for each kind of iron used. For given values of V_r and B_p the shortest possible focal length can be represented as an empirically known function of S/R.

Due to recent great improvements in the manufacture of magnet steels, permanent magnetic lenses have become a practical proposition. Alloys with remanences of the order of 1–1·5 Webers/m.^{2} have been obtained (cf. ref. 'Steels', 1940, 1945, 1947). The sim-

plest permanent lenses are set up by tubular, cylindrical pieces of magnetic material through which the electrons travel.

The field set up by a tubular permanent magnet is qualitatively different from the field of a solenoid. The permanent magnet of

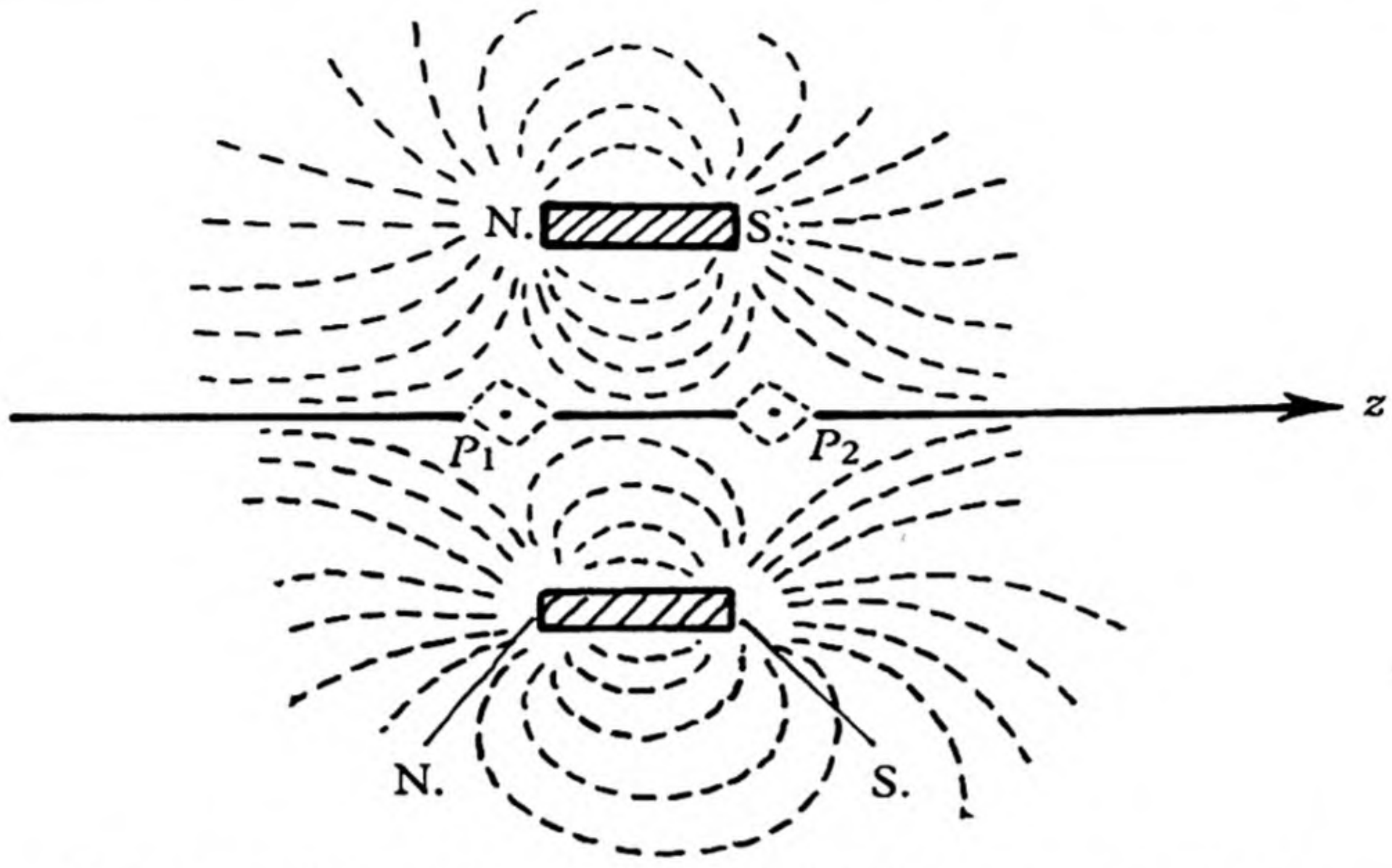

Fig. 5.10. Lines of force of a cylindrical permanent magnet.

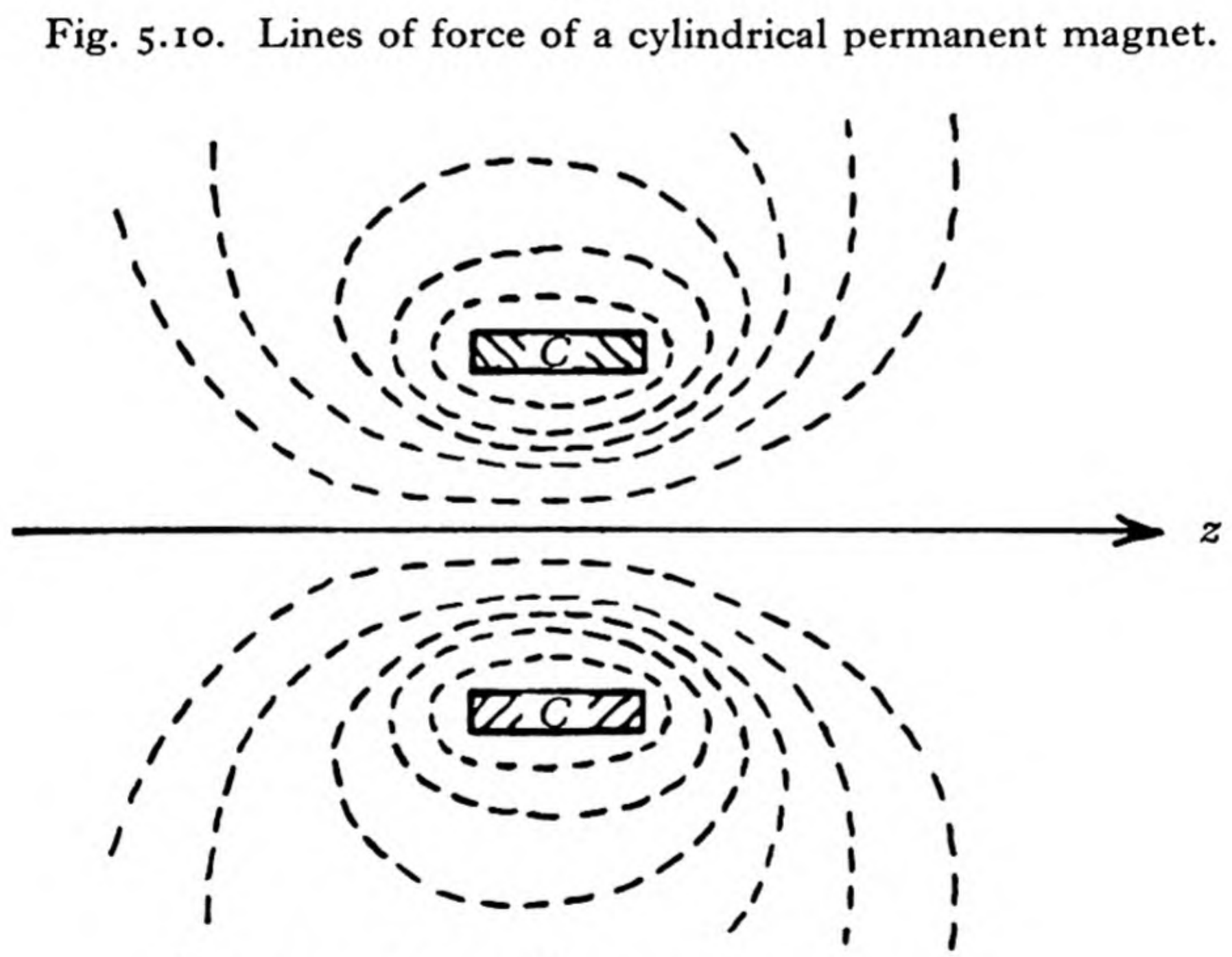

Fig. 5.11. Lines of force of a current coil.

fig. 5.10, with z being its axis of circular symmetry, has the circular poles N. and S. to which all the lines of force converge. On the other hand, the solenoid coil C of fig. 5.11 sets up closed lines of force which encircle the coil. In fig. 5.12 are shown distributions of flux densities along the axes of the two lenses, both being reduced

to the same maximum B_0. While the flux density along the axis of the coil gradually decays from the maximum to infinity, the flux density along the axis of the permanent magnet decays more rapidly, becomes zero at the two points P_1 and P_2, where it reverses its direction. Electron optically, this implies a reversal of the sense of rotation of the rotating meridional plane at P_1 and P_2, resulting in a relatively small image rotation produced by the permanent lens.

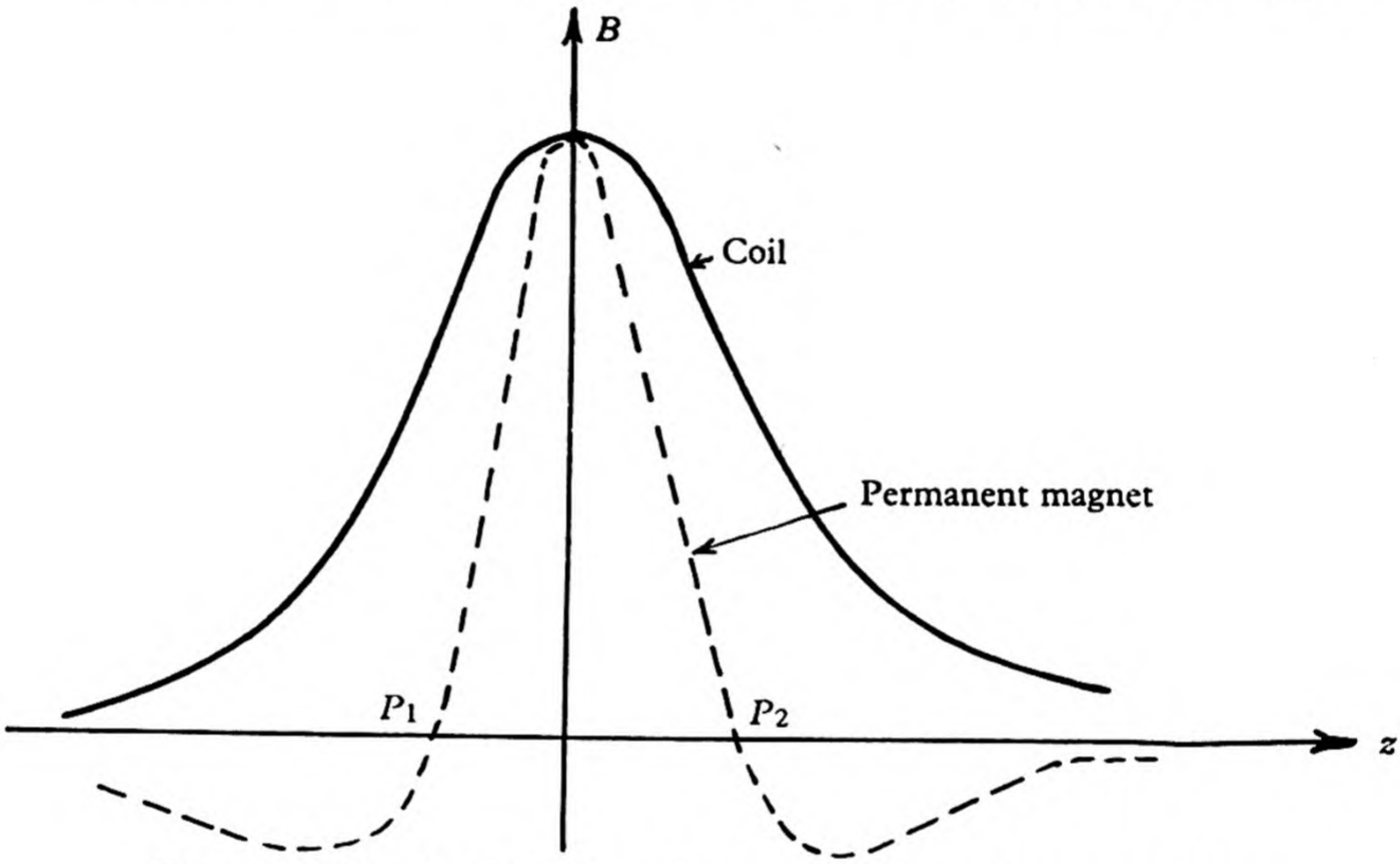

Fig. 5.12. Flux densities along the axes of magnetic lenses produced by a current coil and by a permanent magnet.

The points P_1 and P_2 are clearly seen in the lines-of-force picture of fig. 5.10.

Fields set up by the modern permanent magnetic lenses are surprisingly strong. For instance, a cylinder 40 mm. long of 40 mm. diameter and 8 mm. wall thickness may easily retain a magneto-motive force of 10^3 ampere-turns between its end-faces, producing a maximum flux density of 4 Webers/m.^{2} in the centre of the cylinder.

If permanent magnetic lenses are used for the sharp focusing of electron images, a control of focal length is desirable. Such control has been obtained with the help of magnetic shunts. Two kinds of shunts have been used, these are shown in fig. 5.13. In both cases the flat circular disks D_1 and D_2 made from mild steel, are attached

to the permanent magnetic cylinders A. If the shunt is used outside the magnet as in fig. 5.13 (a), these disks D_1 and D_2 extend outside the cylinder A. In this case, the shunt is a cylinder C made from

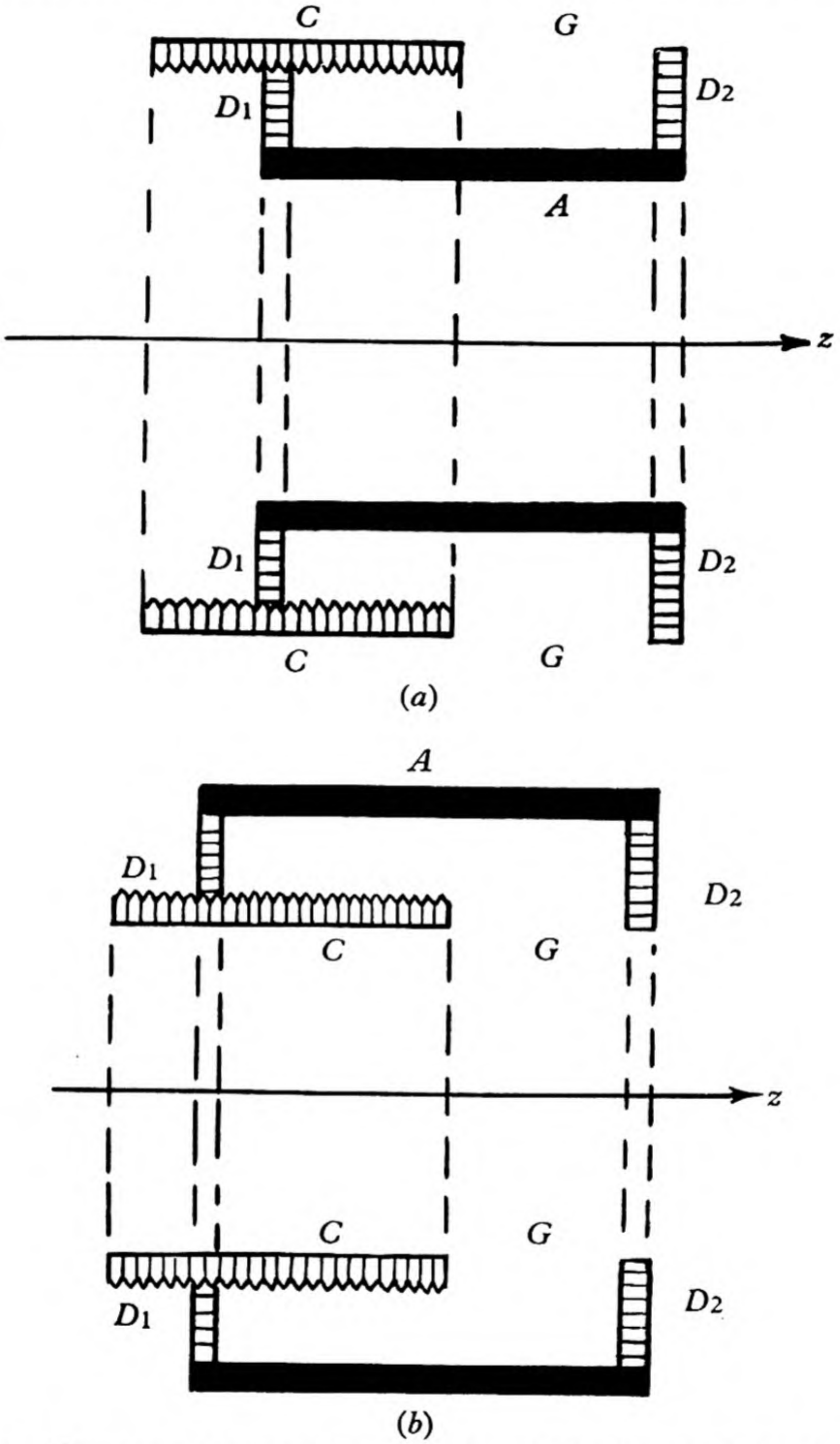

Fig. 5.13. Permanent magnet lenses: (a) outside shunt; (b) inside shunt.

mild steel with a screw thread on its inside so that it may be screwed over the disk D_1 in order to close up the magnetic gap G towards D_2. On the other hand, the shunt may be used inside the permanent magnet as shown in fig. 5.13 (b). There, the mild steel cylinder C is

threaded outside and screwed through the inner aperture of D_1 in order to close the gap G. The magnetic lens in fig. 5.13 (*b*) is formed by the stray field in the gap, while in fig. 5.13 (*a*) the lens field originates directly from the poles of the permanent magnetic cylinder.

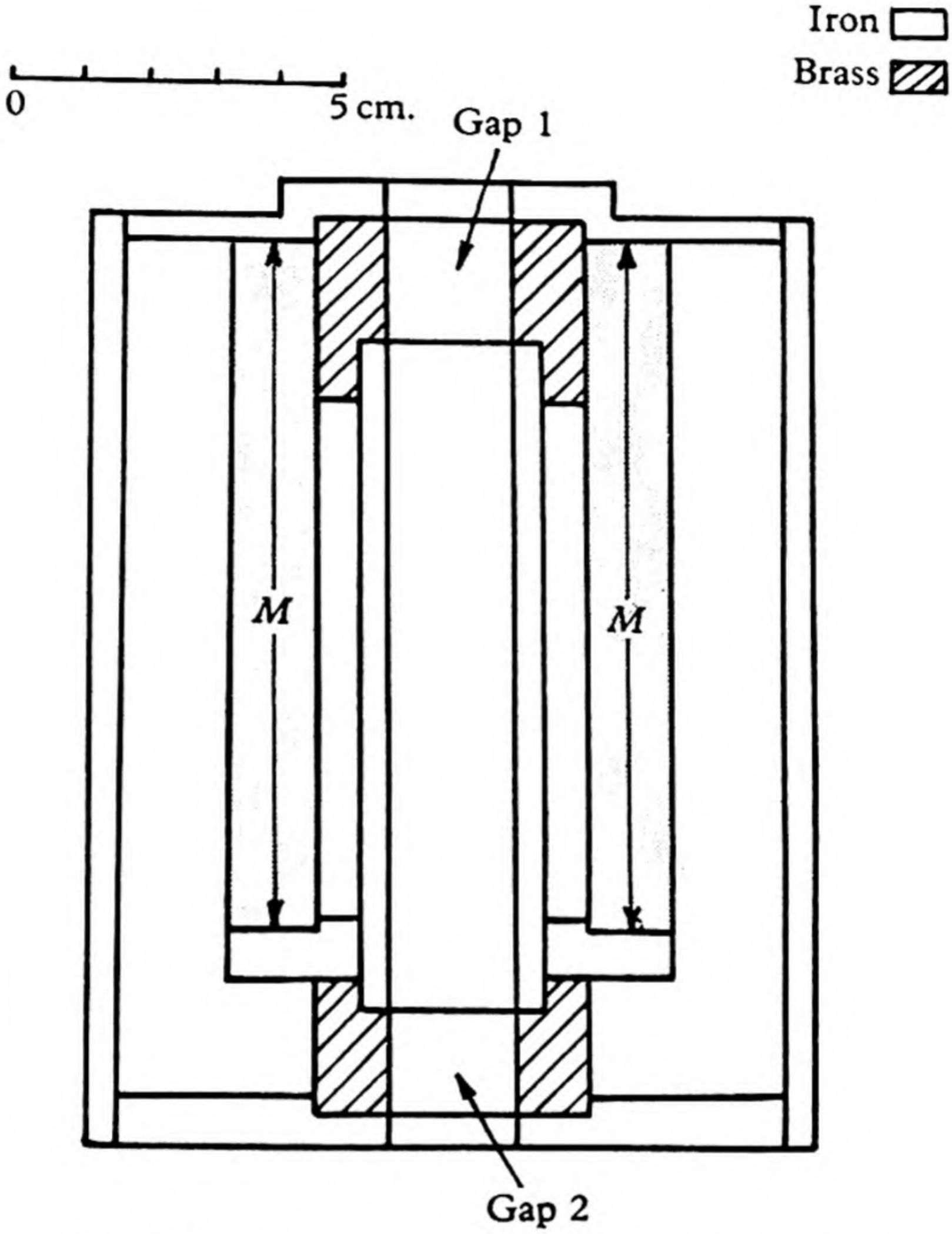

Fig. 5.14. Permanent magnetic microscope objective and projector lens.

Some permanent magnetic lenses for television tubes have been described by Hadfield (1950). The application of permanent magnetic lenses to electron microscopes has led to relatively cheap, small instruments. Von Borries *et al.* (1940) have described an experimental instrument for 50 keV. in which objective coil and projector coil were replaced by about a dozen bar magnets each. 7·5 and 2·7 mm. focal lengths respectively were obtained in these lenses. Reisner and Dornfield (1950) have described a small commercial R.C.A. microscope, and Reisner (1951) has given details about its lens system, the cross-section of which is shown in fig. 5.14. Four

rectangular parallelepipeds *M* (two are visible in the figure), made from 'Alnico V' and ground to shape, are placed symmetrically about the axis and attached to mild steel pole-pieces of circular symmetry. There are two magnetic gaps filled with brass spacers. The fields of the two electron lenses formed by these gaps are in opposition hence the image rotation is small. An outside shell of mild steel which reduces stray fields to a minimum is sensibly a surface of constant magnetic potential. Potential differences of 1000 and 700 ampere-turns can be measured across the objective lens (gap 1) and across the projection lens (gap 2) respectively. In some models, the gap separation of the objective lens can be adjusted. Though the focal length is hardly affected by such adjustment, the principal planes of the lens are shifted by it, and in this way image focusing on the target is attained. Magnifications between 1500 and 6000 are reached. The stability of Alnico is great, and lens assemblies have been in use for years without apparent loss in field strength.

5.5. Determination of magnetic field distributions

An exact calculation of magnetic lens fields by integration over the field components of the current elements is possible for air coils only. For every lens field, however, there can be used computational methods. For example, Hesse (1950) has shown how field distributions in magnetic lenses can be obtained by a relaxation method.

Most important are direct determinations of the flux-density distribution. Nearly all direct measurements in magnetic lenses have been made with search coils. For the investigation of iron-free lenses, the e.m.f. at the search coil may be measured when the current of the lens coil is reversed. If the lenses contain iron, care must be taken to prevent errors from hysteresis effects; the search coil has to be brought into position, then snatched out of the field.

In the measurement of field distributions in microscope lenses, the main practical difficulty lies in the small physical dimensions of the field to be investigated. Thus, Dosse (1941) used a search coil with 100 turns of 0·02 mm. wire whose outer diameter and length were only 0·4 mm. The position of the coil along the lens

axis is measured with a microscope and a micrometer joined rigidly to the coil.

In the measurement of fields of larger lenses much time can be saved by rotating or oscillating the search coils. Kohaut (1937) and Cole (1938) used rotating coils. Langer and Scott (1950) refined this method to measure fields accurately down to 1/100 Gauss. Klemperer and Miller (1939) have used the search coil oscillator shown in fig. 5.15. The small search coil *C* performs a reciprocating rotation by 180°, the movement being coupled by a shaft *S* to

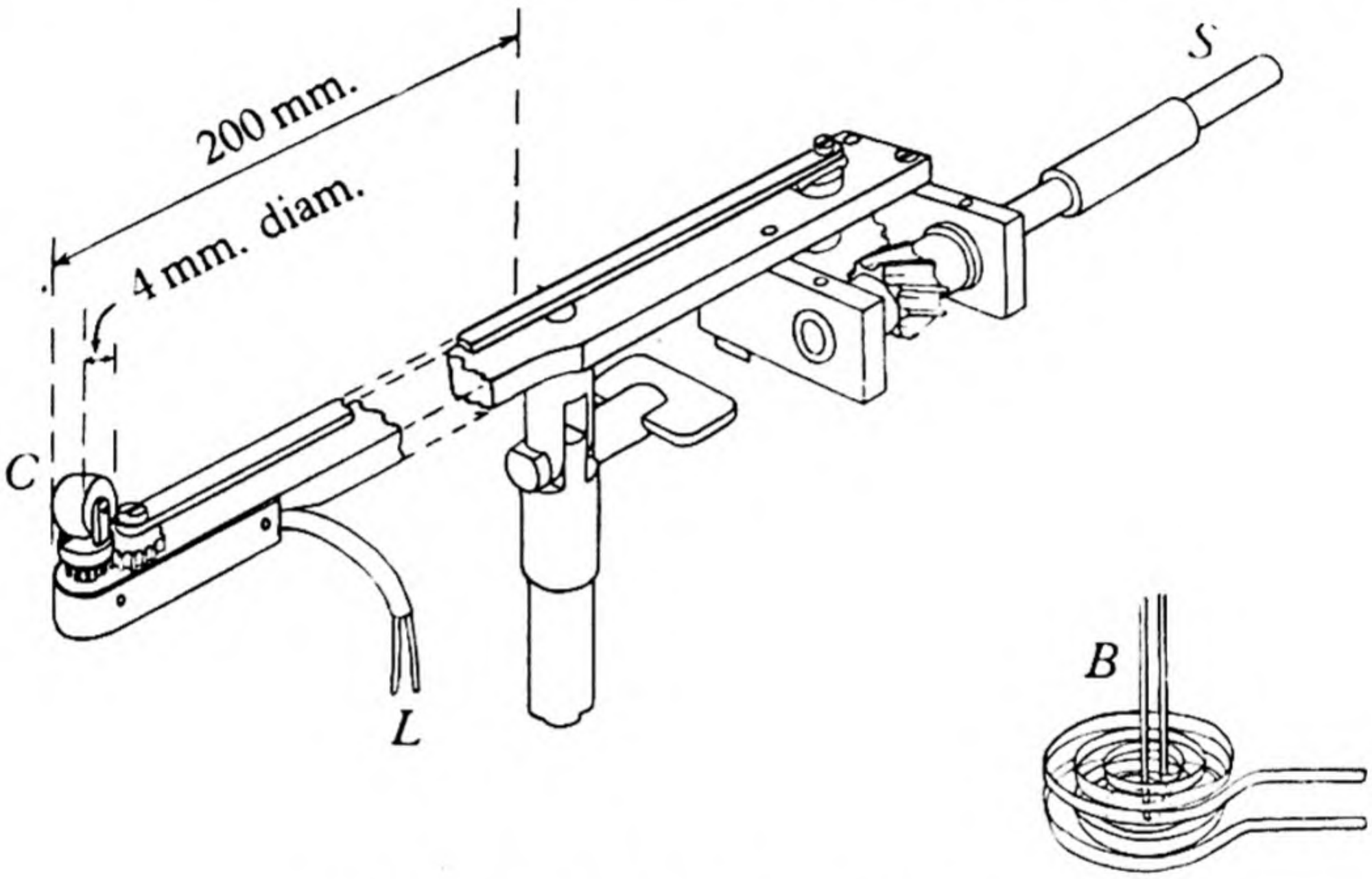

Fig. 5.15. Search coil oscillator.

a synchronous motor. The alternating current induced to the oscillating search coil is conducted through two hair-spring spirals *B* (not shown in the main figure) and through the stationary leads *L* to a 10 cyc./sec. resonance amplifier.

The flux density measured by a search coil is strictly correct only when the field can be considered to be homogeneous over the area of the search coil. Correction formulae for inhomogeneous fields have been derived by Goddard and Klemperer (1944). Instead of applying such corrections, it is, however, more convenient to use search coils of smallest possible area and to increase the level of output current by sufficient amplification. Another method for overcoming the effects of local field inhomogeneity is due to Brown and Sweer (1945) and to Williamson (1947), who used the 'flux ball', which is a spherical search coil wound in co-axial layers of

cylindrical windings, each layer having different length and diameter. Sweer showed by calculation that for this shape, the total flux is proportional to the field in the centre of the coil.

In an alternative method, developed by Sandor (1941), the effects of field inhomogeneity are overcome, and still larger output currents are obtained by the use of a series of large coaxial search coils of very gradually varying diameter. The integral flux in axial direction is measured, and the flux density as a function of the radial distance from the axis is obtained from the difference in search-coil currents and search-coil areas respectively.

Particularly suitable for measuring the field in small microscope lenses is the magnetic field balance described by Ments and Le Poole (1947). It consists essentially of a very long coil evenly wound on a non-magnetic bar which is suspended horizontally so that its axis coincides with the lens axis. The coil winding has somewhere a point of reversal, so that it acts like two solenoids in opposition. The external poles of these two solenoids are far outside the lens field so that no force is exerted on them. The two internal poles are of equal sign, and they coincide with the point of reversal. Hence an axial force is exerted on the coil by the field of the lens, this force being proportional to the axial flux density of the lens at the point of reversal. The force is indicated by a small horizontal displacement of the bar which is read by a microscope.

Of general interest is an experimental method for mapping distributions of the magnetic vector potential $A_\psi(r, z)$ produced by circular symmetrical current-carrying conductors and iron of arbitrary shape. According to Liebmann (1950*c*) these distributions can be determined with the help of a resistor network as described in § 3.2. Any stud 0 of the network is joined to its four neighbour studs 1, 2, 3 and 4 by resistances R_1, R_2, R_3 and R_4, the values of which are functions of the three radial coordinates r_0 ($= r_1 = r_3$), r_2 and r_4 of the respective studs. In distinction to the previously (Chapter III) described network, all studs are now connected to a common potential by a fifth resistance R_5, the magnitude of R_5 being proportional to the radial coordinate r_0. A current proportional to the current density flowing through the conductor (magnet coil) is fed into the studs at all positions occupied by this conductor. If iron is present, the network must be open-circuited along the

boundaries of the iron in order to fulfil the condition for infinite permeability requiring that the normal derivative $\partial A_\psi/\partial n$ should vanish. Moreover, the values of the resistances R_5 have to be adjusted along this boundary. The network represents the operator

$$\left[\frac{\partial^2}{\partial z^2}+\frac{\partial^2}{\partial r^2}+\frac{1}{r}\frac{\partial}{\partial r}-\frac{1}{r^2}\right],$$

which, applied to the vector potential A_ψ, is proportional to the generating current density. It can be seen that the application of

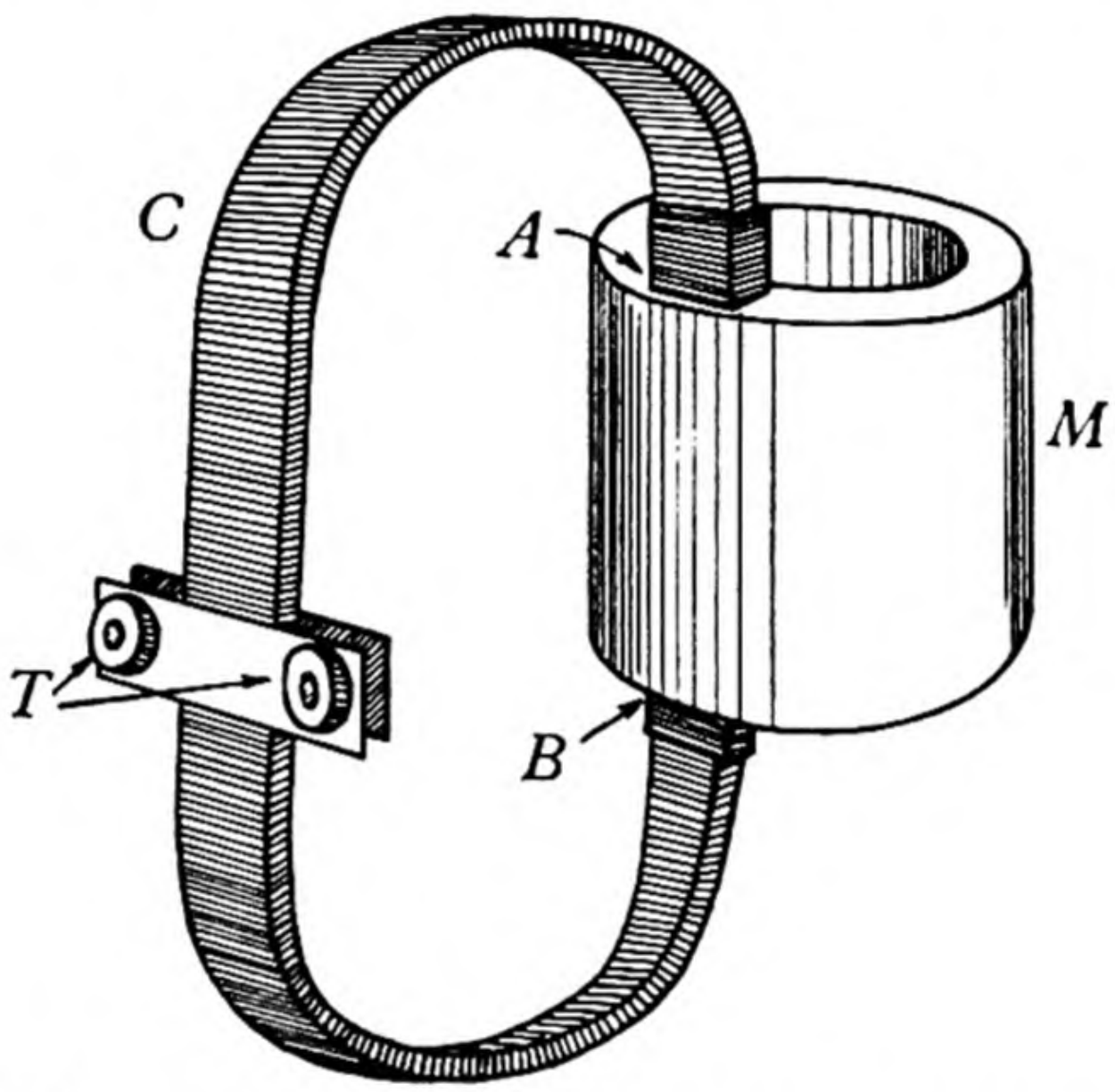

Fig. 5.16. Magnetic potentiometer and permanent magnetic lens.

the resistor network method for magnetic field plotting is complicated and needs elaborate apparatus, but apparently good accuracy has been obtained in its results. For details we have to refer to the original literature.

Relatively simple is the application of the electrolytic trough for magnetic field plotting in iron-shielded coils. Due to the large value of the permeability of the iron shell compared with that of free space, the pole-faces may be regarded as being at uniform magnetic potentials V_H and V'_H, and they may be represented by metal electrodes in the electrolytic trough (Chapter III). Such electrodes could even be used to give approximate representation of the whole magnetic shell, if the two halves of the shell are assumed to be separated by a double-layer plane producing the difference of potential nI. The equipotentials measured in the trough correspond with surfaces of equal magnetic scalar potential.

If for a shielded coil the magnetic resistance of the iron part of the magnetic circuit is negligibly small in comparison with the resistance across the gap, the magnetic potential difference across the gap is near enough given by $V_H - V'_H = nI$, i.e. by the number of ampere-turns of the energizing coil. Generally, however, the magnetic potential difference between the pole-pieces has to be obtained by measurement with a small magnetic potentiometer, for instance. Such a potentiometer is shown in fig. 5.16. It consists of a long, narrow coil C made by winding wire in opposite directions in two layers upon a flexible non-magnetic strip of material. The terminals T of the coil have to be connected with a ballistic galvanometer. The ends A and B of the potentiometer are first set to the points between which the magnetic potential has to be measured, e.g. to the end-faces of the tubular permanent magnetic lens M shown in the figure, then withdrawn and set tightly against each other. The ballistic deflexion produced by this action is proportional to the magnetic potential difference; it may be calibrated in units of ampere-turns with an air coil in the usual manner.

5.6. Ray tracing through magnetic lenses

According to the explanations of §§ 5.1 and 5.2, axial rays may be traced through the refracting field in the rotating meridional plane, if the refractive index $N_m(r, z)$ is known as a function of the co-ordinates r and z. The vector potential $A(r, z)$ in (5.16) cannot be measured directly; but it has been pointed out in § 5.2 how far the special case of circular symmetry A is related to the flux. Apply Stokes's law (5.11) over a disk of radius r_0, set normal to the axial component of flux density B_z. The boundary of the disk is of the length $2\pi r_0$ and it encloses an area πr^2; hence

$$\oint A \,\mathrm{d}s = 2\pi r_0 A = \int_0^{r_0} 2\pi r B_z \,\mathrm{d}r = \Phi, \tag{5.46}$$

where Φ is the total flux through the considered disk. Using (5.16), the meridional refractive index in any field of circular symmetry is given by

$$N_m^2 = V_m(r, z) = V - \frac{e}{2m}\left(\frac{\Phi}{2\pi r}\right)^2 = V - 2{\cdot}25 \times 10^9 \frac{\Phi^2}{r^2}, \tag{5.47}$$

where V is the initial electron energy in electron-volts which stays constant throughout the lens. Φ is the total flux through the circular area of radius r, which may be obtained either by direct measurements with a set of axial coils of various diameters, or according to (5.46) by integrating the flux-density distribution curves as given for instance in fig. 5.6. However, ray tracing through a meridional field plot cannot yield results of great accuracy for the reason that the rays cut the equipotentials at small angles, especially near the maximum elongation from the axis, where the ray meets a refracting equipotential under a grazing angle (cf. figs. 5.1 and 5.2).

Siday (1942) has used for tracing the integral (5.22) of the paraxial ray equation. If not only the integrals $\int_{z_1}^{z_2} B_z^2 \mathrm{d}z$, taken between two points z_1 and z_2 on the axis, but also the initial values of r and $\mathrm{d}r/\mathrm{d}z$ are known, the rest of the ray can be traced. Other methods based on the paraxial equation of motion, but distinguished by the way in which this equation is integrated, have been described by Goddard and Klemperer (1944), by Cosslett (1946*b*) and by Liebmann (1949*b*).

So far, only a computational method by Goddard and Klemperer (1944) allows accurate tracing of paraxial and marginal rays through experimentally known magnetic fields. This method starts from the equations of motion:

$$\left.\begin{aligned} \frac{\mathrm{d}^2 z}{\mathrm{d}t^2} &= -\left(\frac{e}{m}\right)^2 A \frac{\partial A}{\partial z}, \\ \frac{\mathrm{d}^2 r}{\mathrm{d}t^2} &= -\left(\frac{e}{m}\right)^2 A \frac{\partial A}{\partial r}, \\ \frac{\mathrm{d}\psi}{\mathrm{d}t} &= \frac{e}{m}\frac{A}{r}. \end{aligned}\right\} \tag{5.48}$$

The following steps are taken in the procedure of computation:

(i) the vector potential $A(r, z)$ has to be obtained which, according to (5.46), is given by

$$A(r, z) = \frac{\mathrm{I}}{r_0}\int_0^{r_0} rB(r, z)\,\mathrm{d}r. \tag{5.49}$$

The values of $B(r, z)$ in (5.49) may be taken from an experimental

plot (such as shown, for instance, in fig. 5.6) and integrated numerically. A whole lattice of A values may be obtained.

(ii) The derivatives $\partial A/\partial r$ and $\partial A/\partial z$ are computed by numerical differentiation and two new lattices are constructed for these values.

(iii) With the aid of these three lattices the equations of motion (5.48) are integrated simultaneously using a step-by-step method.

Results of the various steps are conveniently put down in a table which may contain the following columns:

The time interval t, say in units of 10^{-9} sec.,

$$\frac{d^2z}{dt^2},\ \frac{dz}{dt},\ z;\quad \frac{d^2r}{dt^2},\ \frac{dr}{dt},\ r;\quad \frac{d\psi}{dt}$$

and

$$W=\left(\frac{dr}{dt}\right)^2+\left(\frac{dz}{dt}\right)^2+r^2\left(\frac{d\psi}{dt}\right)^2.$$

The start of the table is given by the initial velocity components and coordinates of the given ray. The last column serves as a very convenient check; it contains the values for the energy W of the electron which should be constant in view of the energy equation. Thus a direct measure of the accuracy of the path is available for every step.

This computational method is quick and accurate, but only an operator who is skilled in the art can perform the necessary steps in computation. We have refrained from describing the mathematical details of the method which may be studied in the original paper. The method is of particular interest in so far as its procedure forms in every way a counterpart to the experimental electron-ray tracing method with the fluorescent target. Figs. 5.17 and 5.18 show, for example, the path of initially parallel electrons through the lens field given by figs. 5.5 and 5.6. The good agreement of the computed orbits with the experimental path may be recognized.

The experimental ray tracing with a sliding, fluorescent target differs for magnetic lenses in essential points from the corresponding procedure for electrostatic lenses which has been described in detail in Chapter III. In electrostatic lenses (restricting our attention to non-skew rays) the electron path is a plane curve; thus for tracing the path only two coordinates (y and z) need to be measured. In the case of the magnetic lens, however, owing to the gyro-action of the field, the path is a twisted curve and it is necessary to

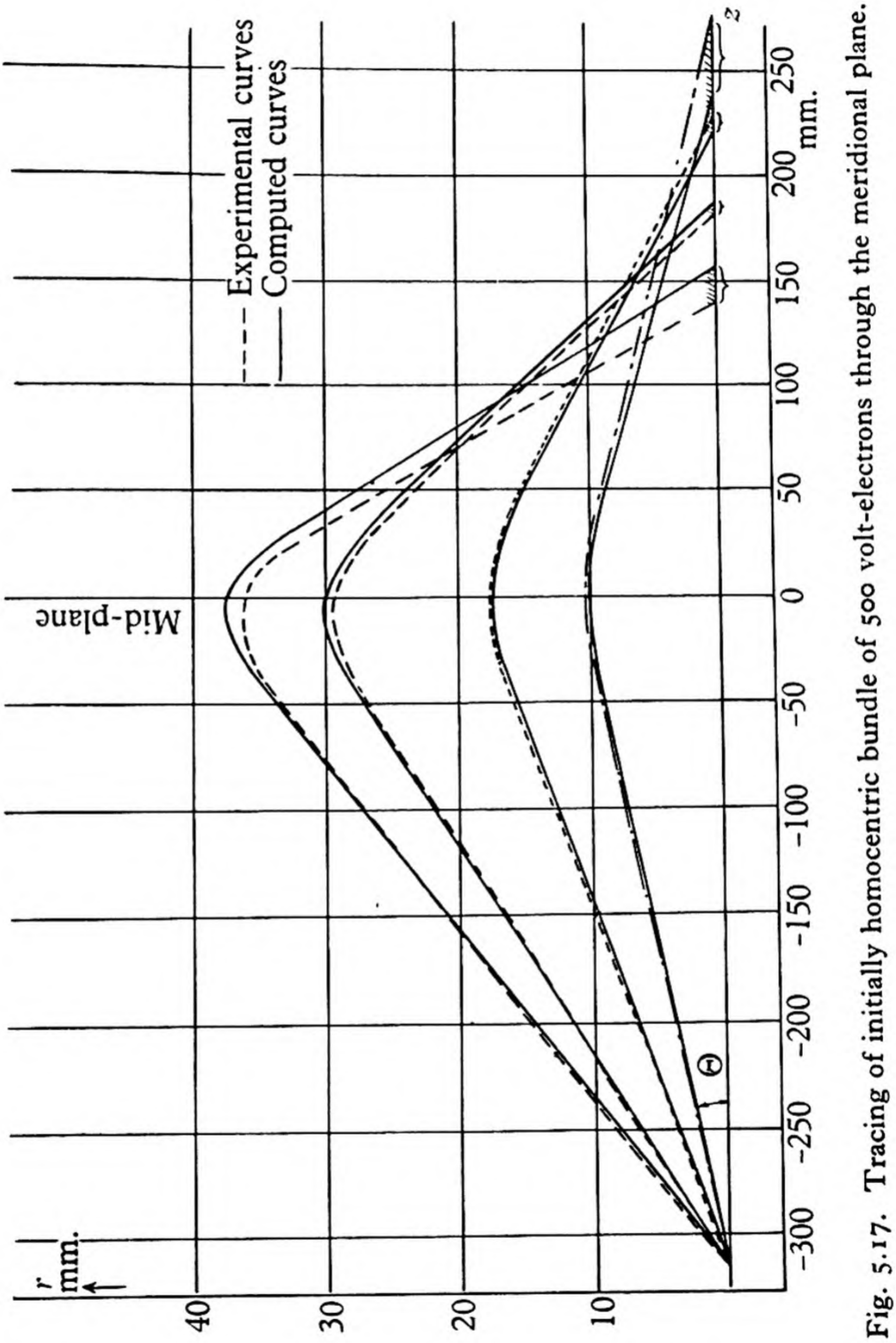

Fig. 5.17. Tracing of initially homocentric bundle of 500 volt-electrons through the meridional plane.

measure three coordinates, viz. x and y, normal to the z-axis, and the distance z along the axis itself. For this purpose a cross-scale providing a metric in the xy-plane may be arranged in the eyepiece of the measuring microscope with which the sliding target is observed. The z-coordinate is measured by a pointer attached to the moving system of the target. A second difference arises from the fact that the path can only be measured outside the electrostatic lens, since a fluorescent target placed inside the lens would disturb the electric field distribution. In the case of the magnetic lens,

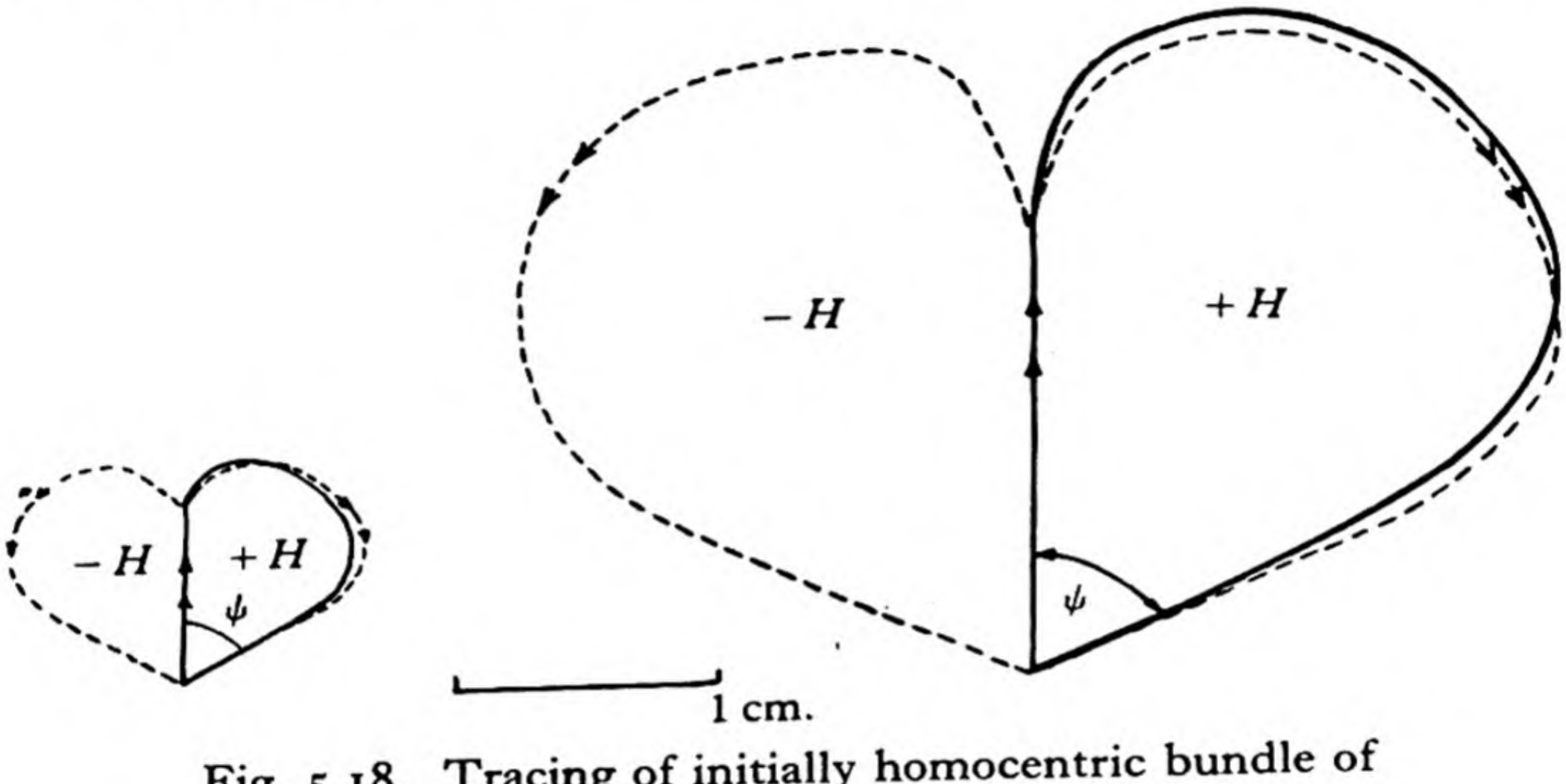

Fig. 5.18. Tracing of initially homocentric bundle of 500 volt-electrons through the equatorial plane.

however, there is no disturbance and the target can be moved through the whole field of the lens, thus allowing the full path to be traced.

Tracing of single rays with a sliding fluorescent target becomes impracticable for the important case of electron-microscope lenses, the dimensions of these lenses being too small for an application of the procedure. These lenses have been investigated experimentally by measuring magnifications and object and image distances. According to Ruska (1944) a thin metal foil with an aperture of the order of 0·1 mm., illuminated from the back by the electron beam, may serve as an object. This foil is mounted over the end of a small tube, lowered by a pulley into the lens structure in order to change the object position. A fine celluloid window bearing a few particles of metal dust of colloidal dispersion covers the aperture of the metal foil. This dust serves as an indicator for a sharp focus when the image is observed on a fluorescent screen. The magnification is

obtained by a measurement of the diameter of the image of the foil aperture, the diameter of the foil aperture itself being known from measurements under a light microscope. The determination of the cardinal points of larger magnetic lenses does not need further explanation; the methods are quite analogous to those discussed in detail for electrostatic lenses (cf. Chapters II and III).

5.7. Combined electrostatic and magnetic lenses

These lenses are constituted by any superimposition of electric and magnetic fields of circular symmetry. Only in very simple cases (e.g. superposition of homogeneous fields) can the effects of the two fields be separated completely. In general, the combined effect of the fields on the electron has to be considered at each point in space. In this way rays may be traced using the refractive index in the rotating meridional plane (cf. Sandor, 1941), given by

$$N_m^2 = V_0 - 2{\cdot}25 \times 10^9 \frac{\Phi^2}{r^2} + V_1. \tag{5.50}$$

(5.50) follows from (5.47) by addition of the local electric potential V_1. If the computational method by Goddard and Klemperer (1944) is to be used for ray tracing, the equations of motion to be integrated are of the following form:

$$\left.\begin{aligned} \frac{\mathrm{d}^2 z}{\mathrm{d}t^2} &= \frac{e}{m}\frac{\partial V}{\partial z} - \left(\frac{e}{m}\right)^2 A \frac{\partial A}{\partial z}, \\ \frac{\mathrm{d}^2 r}{\mathrm{d}t^2} &= \frac{e}{m}\frac{\partial V}{\partial r} - \left(\frac{e}{m}\right)^2 A \frac{\partial A}{\partial r}, \\ \frac{\mathrm{d}\psi}{\mathrm{d}t} &= \frac{e}{m}\frac{A}{r}, \end{aligned}\right\} \tag{5.51}$$

which follow from (5.48) by addition of the electrostatic acceleration (cf. Glaser and Lammel, 1941; also Cosslett, 1946*b*). The focal length of a thin combined lens is obtained by integration of the paraxial ray equation of a combined field. According to Zworykin *et al.* (1945) it is given by

$$\frac{1}{f'} = \left(\frac{V_0}{V_0'}\right)^{\frac{1}{4}} \int_z^{z'} \left[\frac{3}{16}\left(\frac{1}{V}\frac{\mathrm{d}V}{\mathrm{d}z}\right)^2 + 2{\cdot}20 \times 10^{10}\frac{B_z^2}{V}\right] \mathrm{d}z, \tag{5.52}$$

where V is the variable potential inside the lens, V_0 and V_0' are the potentials of object and image space respectively and z and z' are the

axial coordinates of object and image. Thus the lens power $1/f'$ in the image space is simply the sum of the lens powers of the component fields. For $V_0 = V_0' = V$, (5.52) reduces to Busch's thin-lens formula, (5.23), while for $B = 0$ it reduces to an expression which is equivalent to Scherzer's thin-lens formula, (3.33). The

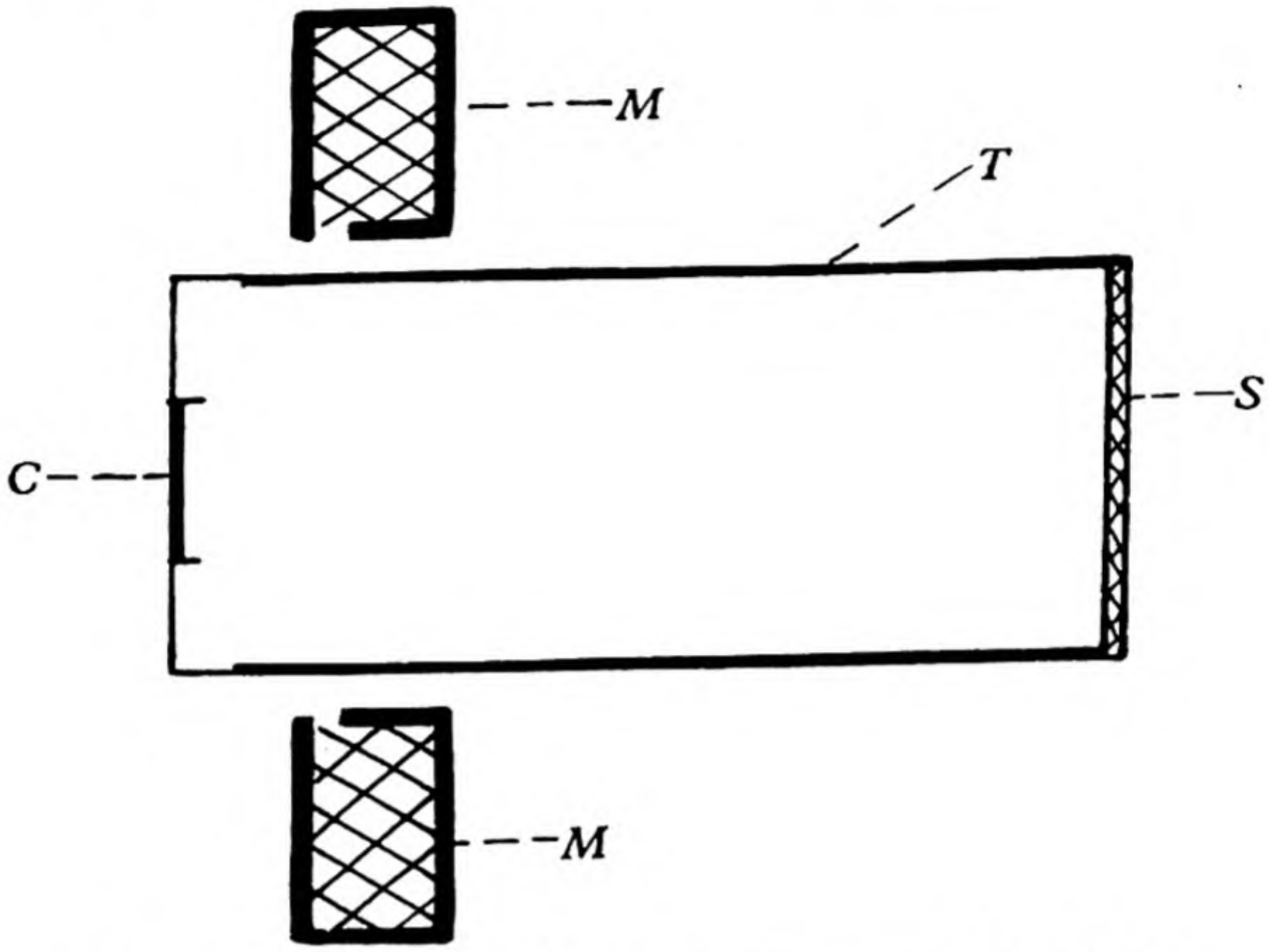

Fig. 5.19. Electrostatic-magnetic image converter.

rotation of the image by the combined lens is again given by (5.19), where $\sqrt{V}$ now, as a variable, is written under the integral sign.

Combined electric and magnetic lenses have found widespread application whenever the slow electron emission of a thermionic or photoelectric cathode is accelerated and magnetically focused at the same time. For example, fig. 5.19 shows a combined lens used in the image converter of a television pick-up tube which will be discussed in Chapter XII. There, a flat cathode C is surrounded by a guard ring which curves the equipotentials in such a way that the emitted electrons are accelerated towards the axis. The cylindrical tube T and the target S are at a common positive potential. A magnetic field produced by the iron-clad coil M is superimposed on the whole arrangement.

CHAPTER VI

LENS ERRORS: GEOMETRICAL ABERRATIONS

6.1. Classification of aberrations

The laws of Gaussian optics interpreting the behaviour of paraxial beams in electron lenses, which were developed in Chapter II, are valid only if certain restricting conditions are fulfilled. Any deviation of the real image from the ideal, perfect picture, due to lack of fulfilment of these restricting conditions, is termed an 'aberration' of the image. The radius vector, which can be drawn from any ideal picture point to the corresponding point of intersection of the actual ray with the Gaussian image plane, gives the value of the aberration which may be ascribed to every imaging ray. The total aberration of a ray may be regarded as the vector sum of a number of independent constituent aberrations. Each constituent aberration is due to the lack of fulfilment of particular conditions which are listed in Table IX. The errors (1) and (2) of Table IX are purely geometrical, the errors (3)–(5) depend on properties of the electron beam, and will be discussed in the next chapter under the title 'Electronic errors'.

TABLE IX. *Classification of aberrations*

Condition	Error
1. No deviation from circular symmetry	1. Adjustment error
2. Imaging aperture and image field must be relatively small	2. Geometric-optical error
3. Electron speed must be homogeneous	3. Chromatic error
4. Current density must be small	4. Space charge error
5. Picture element and imaging aperture must be large in comparison with the wave-length of the electron	5. Diffraction error

The survey presented in Table IX may be further extended by giving the usual classification of the components of the geometric optical error (2). It has been pointed out in Chapters I and II that the application of Gaussian optics is restricted to paraxial rays. Gaussian optics is valid only if the rays are so close to the axis that

terms of higher order than the first in the expansion of the sine of their slope angles (cf. (1.34)) can be neglected. However, in practically useful electron optical systems, the apertures are generally so large that paraxial rays constitute but a small fraction of the image-forming rays.

In 1885 L. Seidel extended the first-order theory by developing a trigonometrical analysis and by including the third-order term in the sine expansion (cf. Born, 1933). In this third-order theory a series of five correction terms is applied to the first-order theory. These five terms, which characterize five independent lens errors, can also be developed in a completely different way starting from Hamilton's characteristic functions (cf. Synge, 1937; Rogowski, 1937). In this way it can be shown for the isotropic media of glass optics as well as for electrostatic electron optics that just these five and no more third-order aberrations can exist.

For anisotropic refraction, however, which occurs in magnetic fields, Glaser (1933*c*) has shown that eight independent third-order errors have to be assumed. We thus give the complete list of third-order geometric optical aberrations as follows:

2.1. Spherical aberration (= axial or aperture error).
2.2. Coma.
2.3. Field curvature.
2.4. Astigmatism.
2.5. Distortion.
2.6. Spiral distortion.
2.7. Anisotropic coma.
2.8. Anisotropic astigmatism.

Although the mathematical theories supply a logical basis for classifying the lens errors, they have so far been of little practical assistance for the design of corrected electron-optical instruments. The only systematic way of improving the correction of electron lenses is to begin by measuring the lens errors separately, either by direct methods or by tracing the rays through plots of equipotentials. Then for electrostatic lenses, the arrangement and the shape of electrodes, for magnetic lenses the arrangement of the current conductors and the shape of the iron shielding have to be altered with the view of improving correction. In the following we shall not attempt to expound the general mathematical treatment of

aberrations. Rather we will try to give some physical explanations, discussing the useful formulae for each error separately, and we will describe the important experimental methods for the detection and measurement of the aberrations.

6.2. Deviations from circular symmetry

Consequences and effects of such deviations are easily noticed. For instance distortions are seen in a focused spot or in the electron picture. The causes of the asymmetry are sometimes very difficult to detect. They may be given for instance by a misalignment, or by lack of circular symmetry of the lens electrodes. In electron-microscope objectives even traces of dust and dirt have frequently been observed causing serious field asymmetries. In magnetic lenses, deviations from circular symmetry are often due to a lack of homogeneity of the magnetic material of the pole-pieces. Disturbances by spurious electric or magnetic fields are quite common causes of small deviations from circular symmetry, and the ways and means of avoiding them will be discussed below.

Small deviations from circular symmetry of the electrodes of electrostatic lenses are often very troublesome. If, for instance, a symmetrical two-tube lens (cf. § 4.2) is used for focusing a spot in a cathode-ray tube, variations in tube diameter near the mid-plane may be less than 1 %; but they will still cause a distortion of the spot, which in this case is not round but of elliptical shape. The circular symmetry of relatively large electrostatic lens electrodes is tested in practice, for instance, with the help of a wedge gauge, i.e. a piece of metal sheet cut to triangular shape, the sides of the triangle having a slope of about 1 : 20. The depth to which the wedge gauge can be lowered into the lens electrode will change according to the asymmetry. Microscopic testing is necessary for small lens electrodes or small magnetic pole-pieces.

The smallest deviations from circular symmetry have been found to be very serious in case of magnetic lenses of electron microscopes. According to Glaser (1943) the ultimate limits of resolving power of practical instruments used to depend on the degree of circular symmetry to which magnetic lenses could be made. Machining tolerances of the order of 200 Å. have been quoted for high-quality magnetic electron-microscope objectives (Le Poole, 1948; Marton,

1950), and a similar degree of accuracy (10^{-4} diameter) has been proved necessary for electrostatic electron-microscope objectives (Bertein, 1948*b*; Rang, 1949). Under these circumstances the asymmetry error is not likely to be overcome by achieving ultimate accuracy of mechanical operation but rather by application of compensating elements which can be adjusted to reduce the field asymmetry to zero. A full discussion of such elements will be given at the end of this section.

A lens of perfect circular symmetry may show serious adjustment troubles if it is only slightly tilted against the axis of the optical system. The image will be shifted in radial direction and also out of the Gaussian plane. In addition, even for a paraxial object the image might be affected by field errors (cf. §§ 6.7–6.9). The tilted lens corresponds to an untilted lens with an object of a distance $s\epsilon$ off the axis, where s is the object distance and ϵ the angle of tilt.

Alignment errors will also occur when the lenses in an assembly are not strictly coaxial. Such errors can often be traced by simple tests. If, for instance, in a magnetic electron microscope the lens axes of objective and projector do not coincide, a change in objective current will cause the image to rotate about some point outside the image field. The relative lens positions may then be adjusted until rotation occurs about the centre of the image field.

Inhomogeneity of magnetic material, already mentioned as a serious cause of lens asymmetry, has to be avoided by the use of mild steel of special choice for all pole-pieces or shields of electromagnetic electron lenses. In the manufacture of permanent magnetic lenses (§ 5.4), the inhomogeneities of an alloy of high remanence often cannot be avoided. The asymmetries, however, can be smoothed out sufficiently when the permanent magnets are used with suitable pole-pieces made from permeable material such as mild steel.

Spurious magnetic fields are sometimes troublesome in electrostatic lenses if magnetic material is used in the electrode structure. For instance, nickel is very commonly used for electrodes in electronic engineering owing to its excellent properties in the evacuated tubes. If, however, a local discharge or spark has accidentally passed between two nickel electrodes, a spurious permanent magnetization is set up and distortions in the electron image are

observed. The magnetization of the nickel electrodes is driven off by eddy-current heating or baking of the electrodes at sufficiently high temperature.

It need not be emphasized that all external disturbing fields have to be shielded off carefully from any electron lens. Spurious external electrostatic fields may easily penetrate through the gaps between electrodes unless these gaps are carefully protected. These fields may be set up, for instance, by charges on the wall of a glass tube enclosing the electron-optical arrangement or from the mechanical supports of the lens electrodes. Such supports consist of insulating material or of a conductor which may be at a potential different from that of a neighbouring lens electrode. The gaps between the electrodes have to be shielded either by an overlapping lens electrode or by a specially designed 'penetration shield' connected to a lens electrode.

External spurious magnetic fields, as, for instance, the earth's magnetic field, can be shielded off sufficiently by a shield of well annealed Mu-metal of about 0·5–1 mm. thickness. As an alternative, 'Helmholtz coils' may be used for compensation ('degaussing') of the spurious, external fields if these spurious fields are homogeneous enough. Helmholtz coils are two equal short coils placed co-axially and at a distance apart equal to one coil radius R. Near the axis, half-way between the two coils, is set up a very homogeneous field of flux density

$$B = (4/5)^{\frac{3}{2}}\,\mu nI/R = 0{\cdot}9 \times 10^{-6} nI/R.$$

For example, to compensate the total earth-magnetic field of $0{\cdot}54 \times 10^{-4}$ Wb./m.^{2} in the centre of two Helmholtz coils of 1 m. radius, 60 ampere-turns would be required for each coil. If field homogeneity is required in an annular zone rather than in a volume near the centre, the mutual distance of the coils has to be reduced. Craig (1947) has investigated the field homogeneity between the coils as a function of their mutual distance, and detailed information can be found in his paper. For instance, in an annular volume between $0{\cdot}3R$ and $0{\cdot}5R$, extending $\pm 0{\cdot}2R$ from the mid-plane between the coils, homogeneity within $\pm 2\,\%$ is obtained with a mutual distance of the coils of $0{\cdot}84R$.

The use of rectangular degaussing coils is convenient if the

earth's field has to be compensated over an elongated cylindrical volume. In particular, the 'bent-head' or 'tail-up' type of rectangular coils as drawn perspectively in fig. 6.1 produces a homogeneous field over a relatively large volume. The proportions of such coils have been investigated by Harris (1934) and by Lyddane and Ruark (1939). If the width ($2A$) of each coil equals 3·5 times the distance ($2B$) between them, and the distance (C) of the bent-up head from the z-axis equals 1·25 times the distance R of the rectangular part from the z-axis, then the region in which the field

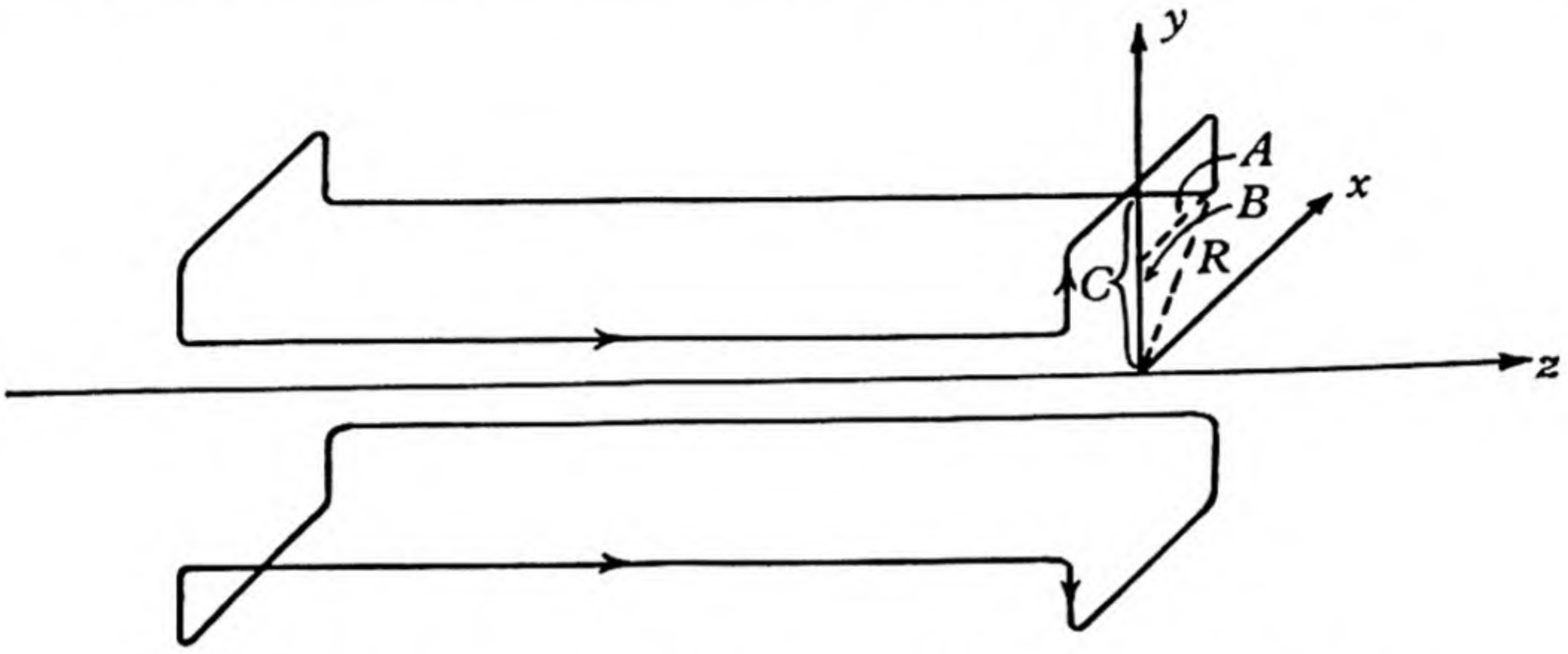

Fig. 6.1. Coils for producing a uniform magnetic field.

deviates less than 1 % from the value at the centre encloses a cylinder of about 0·05R radius and of 1·4L length where $2L$ is the coil length of the rectangular part.

An arrangement of three long, rectangular coils for the production of very homogeneous fields has been recommended by Haynes and Wedding (1951). The planes of these coils are parallel, and their sizes and spacings are defined by a circular cylinder, the axis of which lies in the plane of the mid-coil. The two outer coils are spaced by $\pm 45°$ from the mid-coil on the surface of the cylinder.

Whenever a complete elimination of the causes of errors in circular symmetry of the lens proves to be difficult, the use of compensating devices is of great practical importance. This was recognized first by Bertein (1947, 1948*a*). Hillier and Ramberg (1947) corrected commercial magnetic microscope objectives in a practical way as shown by fig. 6.2. They arranged eight iron screws C in the non-magnetic metal spacers A of the pole-pieces B of the objective. The positions of these screws could be adjusted systematically until the microscope image was free from asymmetry errors.

For an electrostatic correction of the asymmetry error, an arrangement of four electrodes is sufficient in principle. There, opposite electrodes are connected electrically and the two pairs thus formed are on adjustable potentials of opposite sign with respect to the anode potential. The whole arrangement is symmetrical about the lens axis, but it has to be turned bodily into the right azimuthal position in order to oppose the asymmetry of the bundle of rays due to the astigmatism in the objective lens.

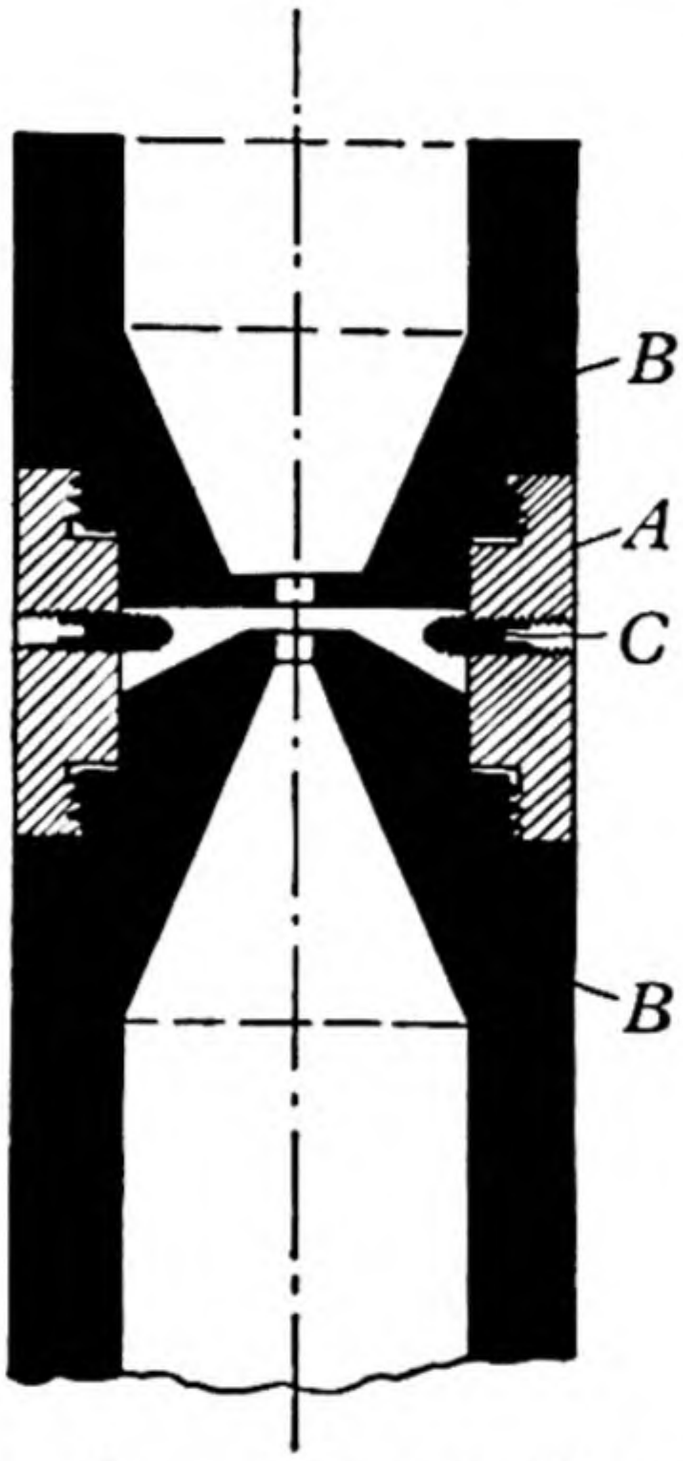

Fig. 6.2. Cross-section of microscope objective pole-pieces, provided with compensating screws.

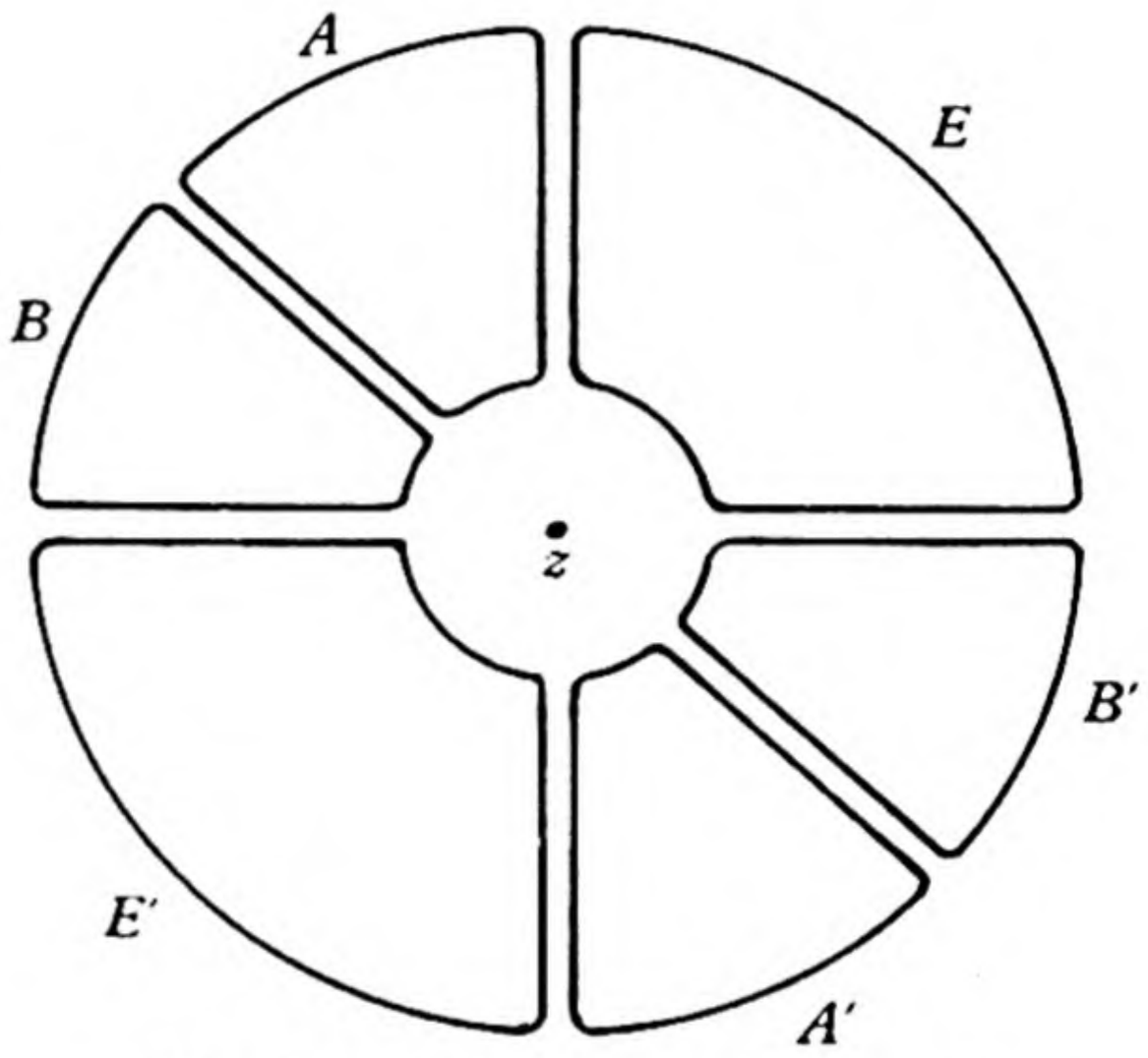

Fig. 6.3. Stigmator electrodes.

In commercial microscopes a six-electrode 'stigmator' described by Rang (1949) and shown in fig. 6.3 is used in the following way: The two electrodes E and E' are permanently earthed, i.e. they are connected to anode potential. Referring to the remaining four electrodes, A is connected electrically to A' and B is connected electrically to B', each pair being charged by a separate potentiometer either above (+) or below (−) earth (= anode) potential. The two potentiometers are linked by mechanical gearing in such a way that complete azimuthal rotation of the correcting field can be performed by a single knob while the stigmator electrodes remain in their fixed position. The absolute potential values of the pairs

AA' and BB' are controlled by another linked potentiometer pair. All stigmator electrodes are arranged symmetrically about the axis z which should strictly coincide with the lens axis. Strict alignment of the two axes during the operation of the stigmator is effected by means of a cross-slide on which the stigmator is mounted. The possibility of a quick and easy adjustment of the stigmator is a great asset, since the asymmetry of a microscope objective is often subject to daily uncontrollable changes which may require frequent readjustment.

The asymmetry error is often recognized from the effect that an image point is drawn out into a small line. Hence, in the literature, this error is frequently referred to as 'astigmatism'. It should, however, not be confused with the third-order geometric-optical error of astigmatism which, as distinct from the asymmetry error, occurs only off the axis, and which is fully discussed in § 6.7.

6.3. Spherical aberration

The axial error, called spherical aberration, occurs if rays emitted from a point object on the axis do not recombine to form a point image. The case of parallel incident rays (i.e. object at infinity) which is of principal interest is illustrated in fig. 6.4. There is shown a symmetrical two-tube lens with the axis z and with the mid-plane M. Two pairs of parallel rays are drawn, the zonal rays (1) and (3) which are travelling at a 'medium' distance y_1 from the axis and the 'marginal' rays (2) and (4) at a relatively large distance y_2 from the axis. Paraxial rays (not drawn in the figure) would be focused in the paraxial focus F. For a lens with spherical aberration, the focus F_1 of the zonal rays and the focus F_2 of the marginal rays are found to be different from the paraxial focus F. The distances of FF_1 and FF_2 are called the longitudinal spherical aberrations of the rays (1), (3) and (2), (4) respectively. If, as in the given example, the focal distance decreases with increasing aperture of the beam, the sense of the aberration is conventionally called positive. As a rule of experience, the spherical aberration of electron lenses is generally positive.

The spherical aberration for a given semi-aperture y changes with the voltage ratio of the lens. This is illustrated by fig. 6.5, where the mid-focal lengths of symmetrical two-tube lenses

decelerating parallel rays, are plotted against the voltage ratio. The parameters of the different curves correspond to the different semi-apertures of the rays entering the lens, as noted in the figure.

From fig. 6.5 data can be taken for drawing the conventional type of aberration curve, as shown in fig. 6.6, in which, for a given voltage

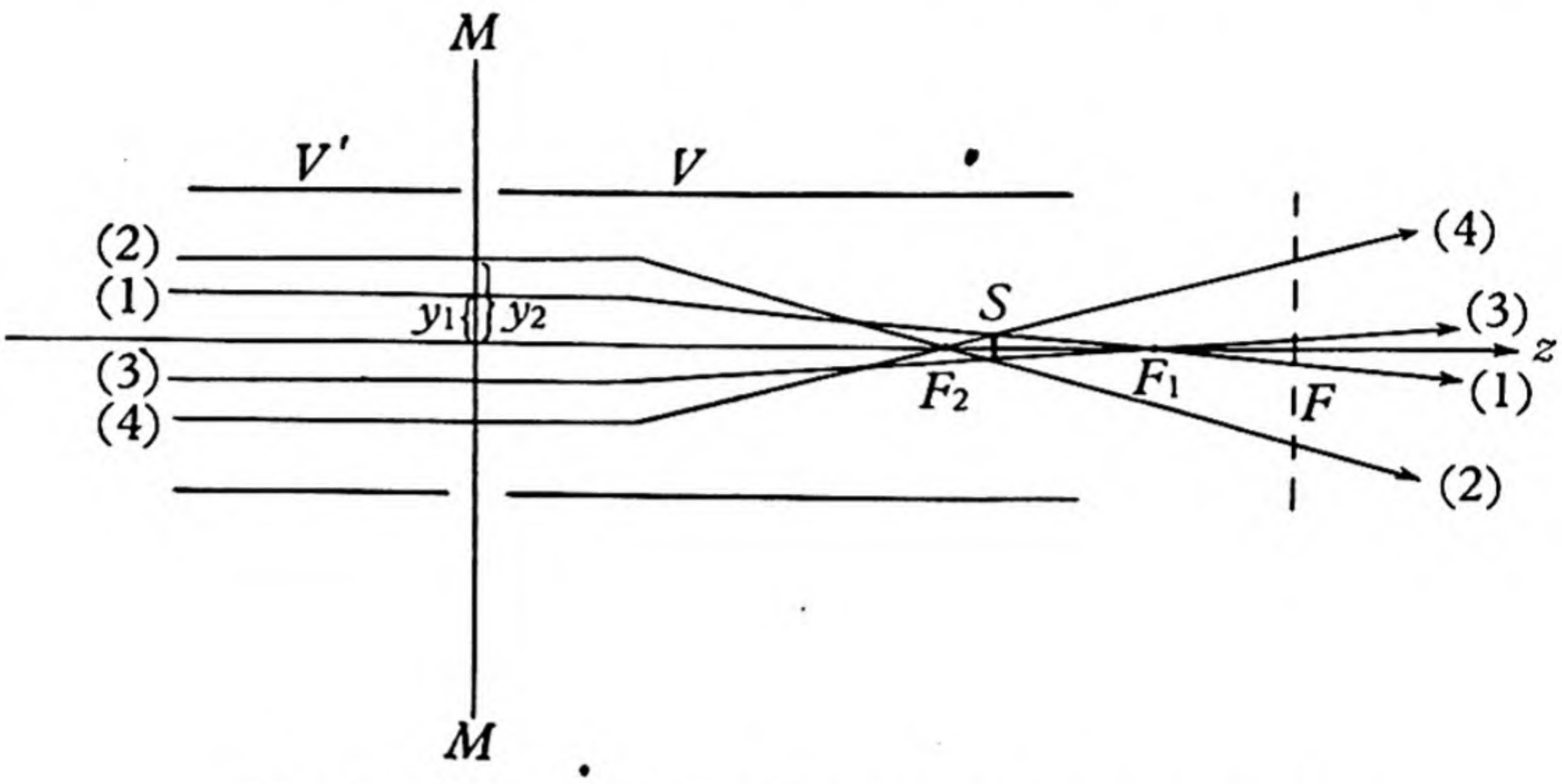

Fig. 6.4(*a*). Initially parallel rays focused by a lens with spherical aberration.

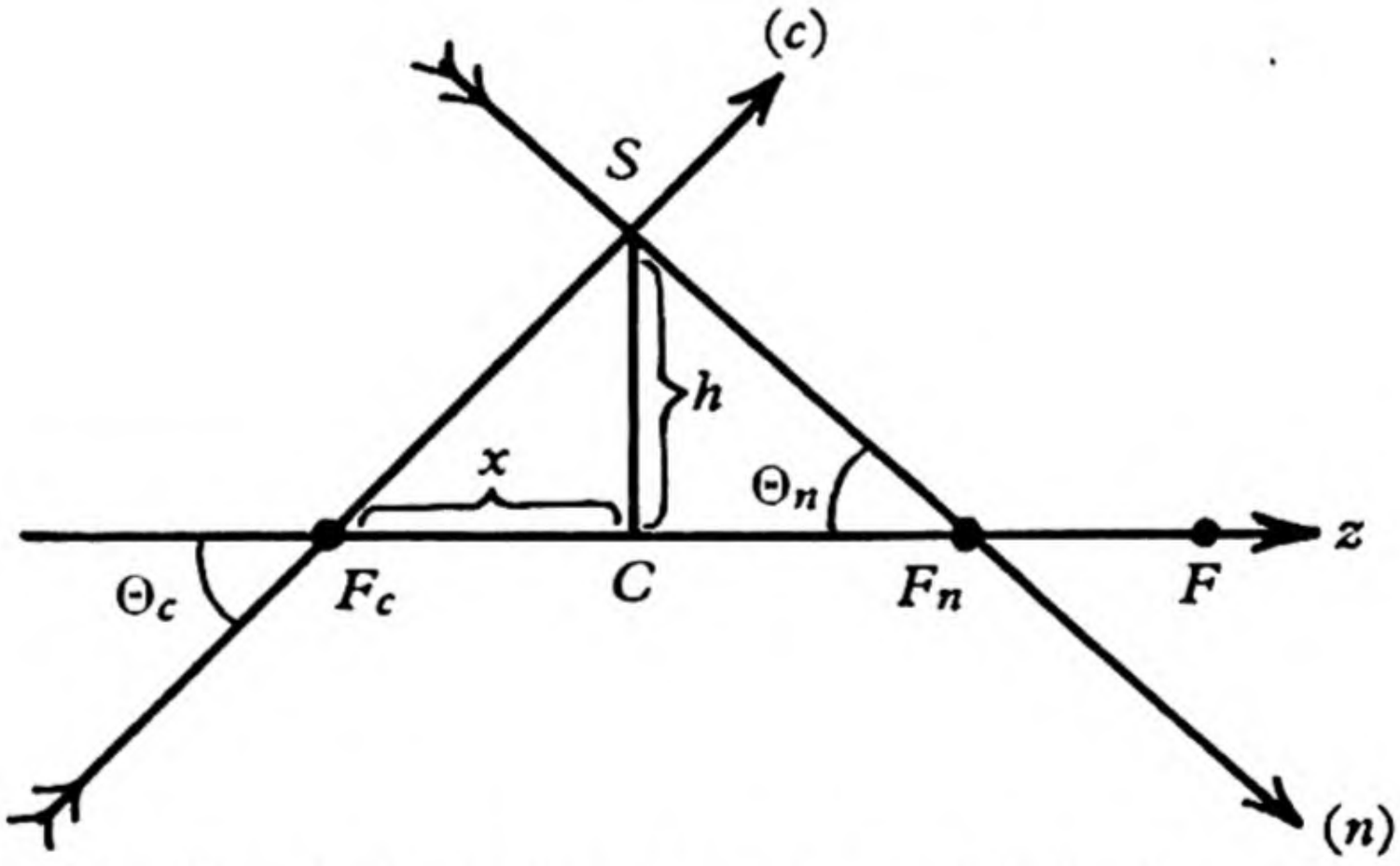

Fig. 6.4(*b*). Spherical aberration and disk of confusion.

ratio as parameter, the mid-focal lengths are plotted against the semi-apertures of the rays. The two solid curves illustrate the spherical aberration of the symmetrical two-tube lens decelerating parallel rays; they refer to the voltage ratios 5 and 15. The corresponding curves for the same lens accelerating parallel rays are plotted as broken lines. It appears that the lens is of a much better quality if the parallel rays are at the low-voltage side.

Curve	*a*	*b*	*c*	*d*	*e*	*f*
Semi-aperture in tube radii	0·08	0·16	0·24	0·32	0·40	0·63

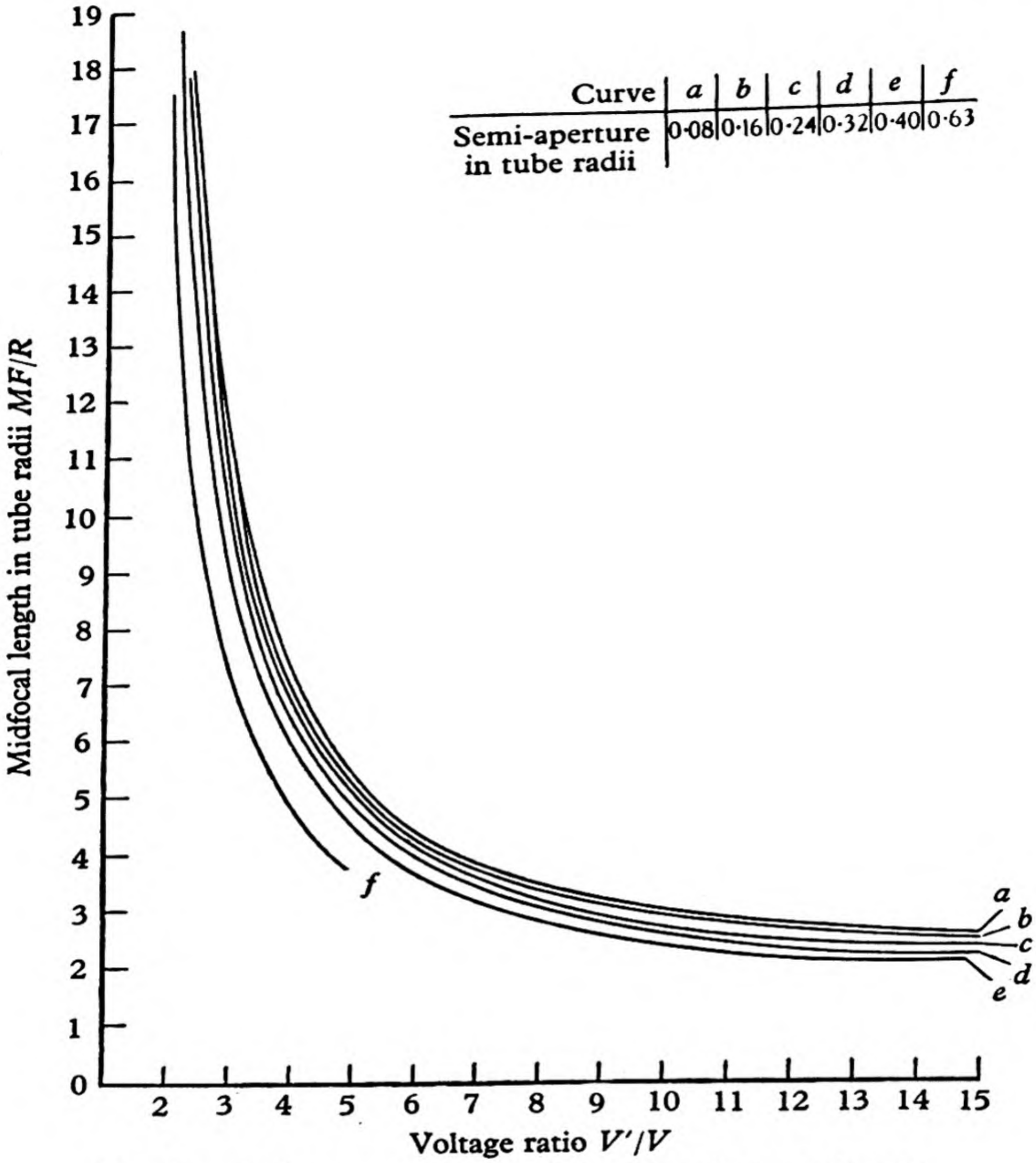

Fig. 6.5. Voltage ratio and mid-focal length for different semi-apertures (symm. two-tube lenses, D.P.).

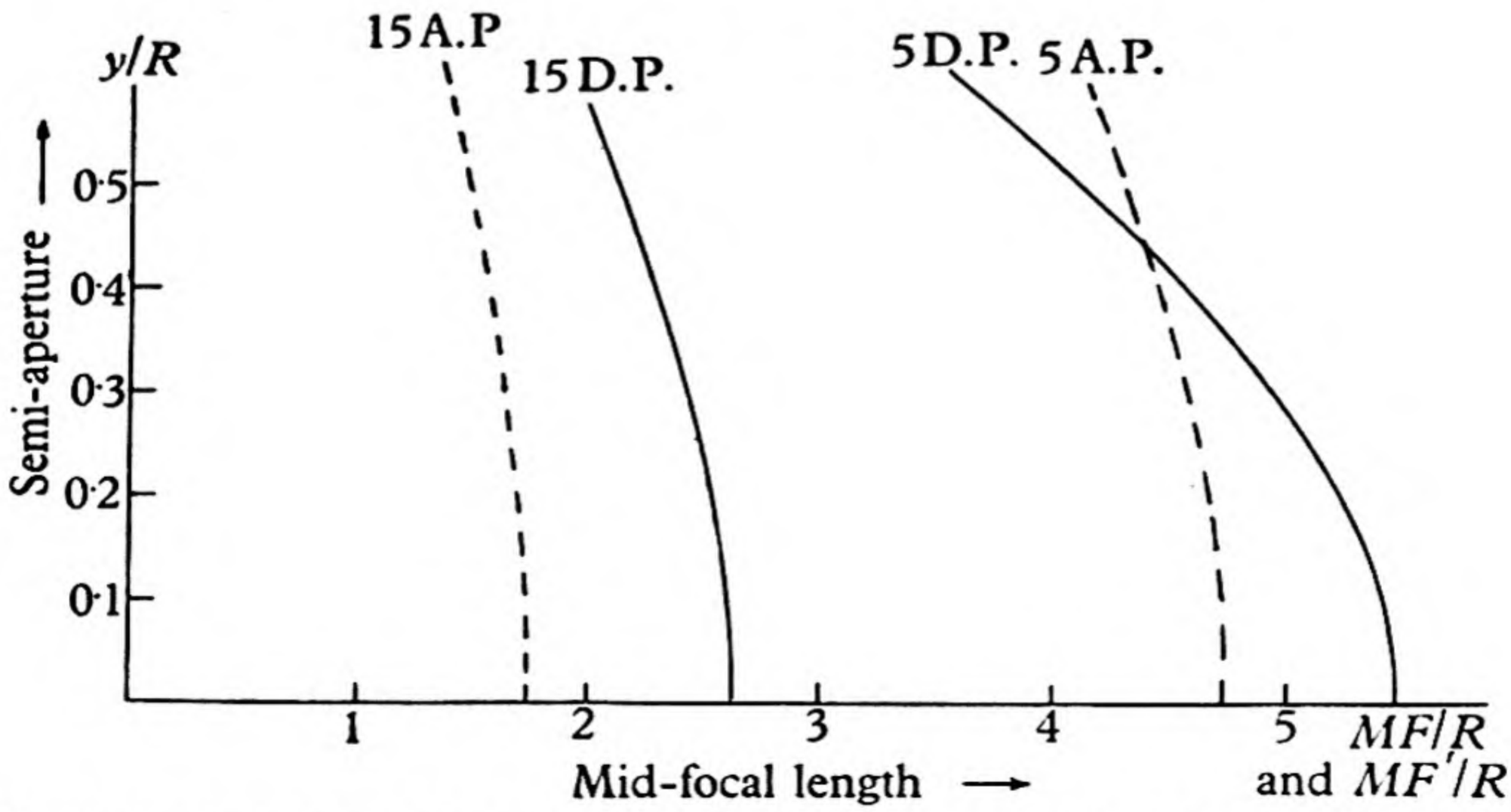

Fig. 6.6. Spherical aberration curves for symmetrical two-tube lenses.

The aberration for finite object or image distances is often, but not always, found to be intermediate between the two extreme cases of infinite distances. Quite generally it is of the same order of magnitude for all object positions. To obtain accurate results for any particular case, special measurements with the proper object and image distances have to be performed.

For a finite object distance s', the longitudinal aberration $\Delta J = JJ_n$ is defined by the distance of the paraxial image J from the zonal image J_n. In order to plot the aberration ΔJ of the divergent beam in accordance with the diagram shown in fig. 6.5, the location of the aperture, which is changing in size along the ray, has to be specified. This aperture (y) may conveniently be taken either at the principal plane (y_p) or at the thin equivalent lens (y_L). In these positions the apertures are connected, according to § 2.2, by the slope angle Θ of the ray at the image side:

$$\tan \Theta_n \approx \Theta_n = \frac{(y_p)_n}{s_n} = \frac{(y_L)_n}{b_n},$$

where $s_n = PJ_n$ is the distance between principal plane P and image point J_n of the nth ray with the aperture $(y_p)_n$, and where $b_n = LJ_n$ is the image distance from the thin equivalent lens L.

In practical aberration diagrams the apertures y_L are plotted only if the position of the principal plane of the lens is not known. In this case, however, the longitudinal aberrations ΔF_n (change in focal distance) or ΔJ_n (change in image distance) are preferably plotted against Θ_n.

Aberration coefficients. The longitudinal aberrations ΔF or ΔJ respectively may be expressed in the form of a power series either of the linear aperture y or of the angular aperture Θ. Thus

$$\left.\begin{aligned} \Delta J &= c_2 y^2 + c_4 y^4 + c_6 y^6 + \dots \\ &= a_2 \Theta^2 + a_4 \Theta^4 + a_6 \Theta^6 + \dots . \end{aligned}\right\} \tag{6.1}$$

The odd power terms of these power series vanish, since naturally ΔJ has the same value for $+\Theta$ and for $-\Theta$ corresponding to rays on either side of the axis. Thus ΔJ is a symmetrical function of Θ.

Neglecting the higher terms in (6.1) one obtains

$$\Delta J = cy^2 = C_s \Theta^2; \tag{6.2}$$

the factors c and C_s are called 'primary aberration coefficients'. Relations (6.2) hold for all real lenses to a certain approximation. They approximate the aberration curves, such as are given in fig. 6.6, by parabolae. The magnitude of c or C_s respectively is representative for all apertures of rays belonging to a given object position; it characterizes the quality of a given lens.

The representation of ΔJ by cy^2 is of course not quite equivalent to that by $C_s\Theta^2$. It can be shown, for instance, that, if all the higher terms c_4, c_6, ..., etc., in (6.1) strictly vanish, the first coefficient a_2 alone of the angular power series will describe the full aberration curve to some approximation only. For example, for the special case $c_4 = 0$, $c_6 = 0$, etc., the following relations are easily calculated:

$$\left.\begin{aligned} a_2 &= \quad c_2 s_0^2, \\ a_4 &= -c_2^2 s_0, \end{aligned}\right\} \tag{6.3}$$

where s_0 is the paraxial image distance. The difference between $c_2 y^2$ and $a_2\Theta^2$, however, is generally of small order only.

From the general theory of third-order lens aberrations the so-called 'Seidel term' S_1 is derived as a characteristic for the spherical aberration (Born, 1933; Rogowski, 1937). Since S_1 is frequently used to present experimental results, its connexion with the longitudinal spherical aberration ΔJ is of interest. This may be written as

$$S_1 = 2N\Theta^2\Delta J, \tag{6.4}$$

where N is the refractive index. Comparison of (6.4) with Lagrange's law (1.35) suggests that the magnitude of S_1 remains unchanged when the longitudinal aberration ΔJ is projected by an aberration-free lens system into another image space. In this way S_1 is proportional to a quantity which may be termed an 'aberration invariant' (Conrady, 1929, p. 44).

Instead of observing the longitudinal aberrations ΔJ, it is often convenient to observe the distances Δr of the rays (h in fig. 6.4 b) from the axis (z) in the Gaussian plane. Δr is called 'transverse aberration' and it is given by

$$\Delta r = \Delta J \tan\Theta. \tag{6.5}$$

Using (6.1) or (6.2) respectively, (6.5) can be written

$$\begin{aligned} \Delta r &= a_2\Theta^3 + a_4\Theta^5 + \ldots \\ &= C_s\Theta^3. \end{aligned} \tag{6.5a}$$

The optical quality of a lens is judged by the ratio of its aberration coefficient C_s to its paraxial focal length f. Thus the following dimensionless aberration coefficient is often used:

$$\frac{C_s}{f} = \frac{\Delta J}{f\Theta^2} = \frac{\Delta r}{f\Theta^3}. \tag{6.6}$$

If the lens under investigation is used for projecting an object point with the high magnification y'/y on to a relatively distant image plane, the radius $\Delta r'$ of the circle of confusion at the image side leads to an aberration coefficient at the object side, given by

$$C_s = \frac{\Delta r'}{\Theta^3}\frac{y}{y'} = \frac{\Delta J'}{\Theta^2}\frac{y}{y'}. \tag{6.6a}$$

Since the magnification is large, the object is placed very near to the focus and the rays leaving the lens are nearly parallel. (6.6*a*) is frequently used to characterize the aberration of microscope objectives.

Disk of least confusion. For practical purposes the quantitative effect of the spherical aberration on the quality of any image point is most important. In the presence of spherical aberration, a perfectly sharp focus of a wide bundle of rays becomes impossible, since every zone of the bundle produces a different focal point.

The rays of a bundle of electrons focused by a lens with spherical aberration may be received on a sliding fluorescent target which is arranged so as to be always perpendicular to the optical axis. If the target is gradually moved along the axis, the radius of the fluorescent circle marking the cross-section of the bundle is found to pass through a minimum at a place which is some distance in front of the paraxial focus F. This minimum diameter corresponds to the best possible focus. The disk of electrons formed at this best focus is called the disk of least confusion.

Take, for instance, the rays (2) and (4) in fig. 6.4 (*a*), which represent the wall of a cylinder, since this diagram shows an axial cross-section. This cylinder surrounds a bundle of parallel rays of electrons. As shown in fig. 6.4 (*a*), and in an enlarged scale in fig. 6.4 (*b*), the rays are focused and reach a minimum cross-section at the point C, CS being the radius of the disk of least confusion. The rays passing the periphery of the disk of least confusion are focused

on the axis at F_c and at F_n respectively, and they intersect the axis at the angles Θ_c and Θ_n. The spherical aberration FF_n of a ray (n) may again be assumed to be proportional to the square of the angular semi-aperture Θ as given in (6.2). The neglect of higher-order terms actually has little influence upon the result of the following calculation of the disk of least confusion.

The distance of the focus F_n from the centre C of the disk of least confusion is given by

$$\begin{aligned} CF_n &= F_cF - F_nF - F_cC \\ &= C_s(\Theta_c^2 - \Theta_n^2) - x, \end{aligned} \tag{6.7}$$

if $F_cC = x$. The radius h of the disk of least confusion is

$$\begin{aligned} CS = h = x\Theta_c &= CF_n\Theta_n \\ &= C_s[(\Theta_c^2 - \Theta_n^2) - x]\,\Theta_n. \end{aligned} \tag{6.8}$$

From the third and the last term of this equation one obtains, by adding $x\Theta_n$,

$$x(\Theta_c + \Theta_n) = C_s(\Theta_c^2 - \Theta_n^2)\,\Theta_n$$

or

$$x = C_s\Theta_n(\Theta_c - \Theta_n),$$

and with (6.8)

$$h = C_s(\Theta_n\Theta_c^2 - \Theta_c\Theta_n^2). \tag{6.9}$$

In order to find the maximum value of h if Θ_n is varied, (6.9) may be differentiated with respect to Θ_n and then put equal to zero:

$$\frac{dh}{d\Theta_n} = C_s(\Theta_c^2 - 2\Theta_c\Theta_n) = 0$$

or

$$\Theta_c = 2\Theta_n.$$

Putting this value in (6.9) one finds

$$h_{\max.} = \frac{C_s}{4}\Theta_c^3. \tag{6.10}$$

Comparing (6.10) with (6.5*a*) it appears that the radius of the disk of least confusion is only a quarter of the radius of the transverse aberration Δr_c of the ray (c) in the Gaussian image plane.*

Addition of spherical aberrations of two lenses. This is of considerable practical importance, since many electron optical instruments

* Some authors define the aberration coefficient by $h_{\max.}$, i.e. by the radius of the disk of least confusion. This value would amount to one-quarter of the coefficient C_s in (6.6).

are made up of two-lens systems (e.g. emission system and focusing lens in the cathode-ray tube, or objective and projection lens in the electron microscope). First an intermediate image is formed between the two systems. Then a final image is produced which suffers from aberration contributions of both systems. The aberration coefficient C_s of the combination can be calculated from the coefficients C_{s1} and C_{s2} of the two systems (cf. Liebmann, 1949) to be approximately

$$\frac{C_s}{f} = \frac{C_{s1}f_2^2 + C_{s2}(D-f_1)^2}{(f_1+f_2-D)^2}, \tag{6.11}$$

where f is the focal length of the combination and f_1 and f_2 are the focal lengths of the two lens systems which are spaced within the distance D.

6.4. Spherical aberration: measuring methods and results

Since spherical aberration is of fundamental importance in limiting the performance of every electron-optical device, a great amount of work has been spent on its exact investigation. The tests which have been employed in these investigations may be divided into three groups: 'pepperpot' methods, 'shadow' methods and the remaining other methods.

The *pepperpot method* is well known in glass optics under the name of 'Hartmann test'. It has been introduced into electron optics by Epstein (1936). A modification of Epstein's method by Klemperer and Wright (1939), which uses a sliding fluorescent target to trace the path of the electron pencils, has already been described above in Chapter II (cf. fig. 2.1). The electron pencils emerge through the fine apertures of a pepperpot-like diaphragm intercepting a wide homocentric electron beam. The pepperpot apertures may be arranged as a series of concentric equidistant circles, and a movable flap may cover all but one circle which is left free at a time for passing a batch of pencils through the lens, travelling on a circular cylinder coaxially with the electron lens. Tracing of the foci of the circles of pencils of various radii leads immediately to aberration curves as given in fig. 6.6.

For the accuracy of the pepperpot method it is essential that the pepperpot holes defining the thickness of the pencils Δy be small in

comparison with the radii of the circles, i.e. the semi-apertures y of the pencils. For relatively large electron lenses pepperpot diaphragms with mechanically produced apertures have proved satisfactory. However, for electron-microscopic objectives which are of the order of a millimetre in diameter, different means have to be used for producing sufficiently narrow zones ($\Delta y \ll 1$ mm.) of pencils. Mahl and Recknagel (1944) have utilized for their aberration measurements the zones of electron rays which are produced by diffraction of a very fine pencil through a thin aluminium foil. The foil was arranged in the object plane of a microscope objective. Debye-Scherrer diffraction rings were taken on a photographic

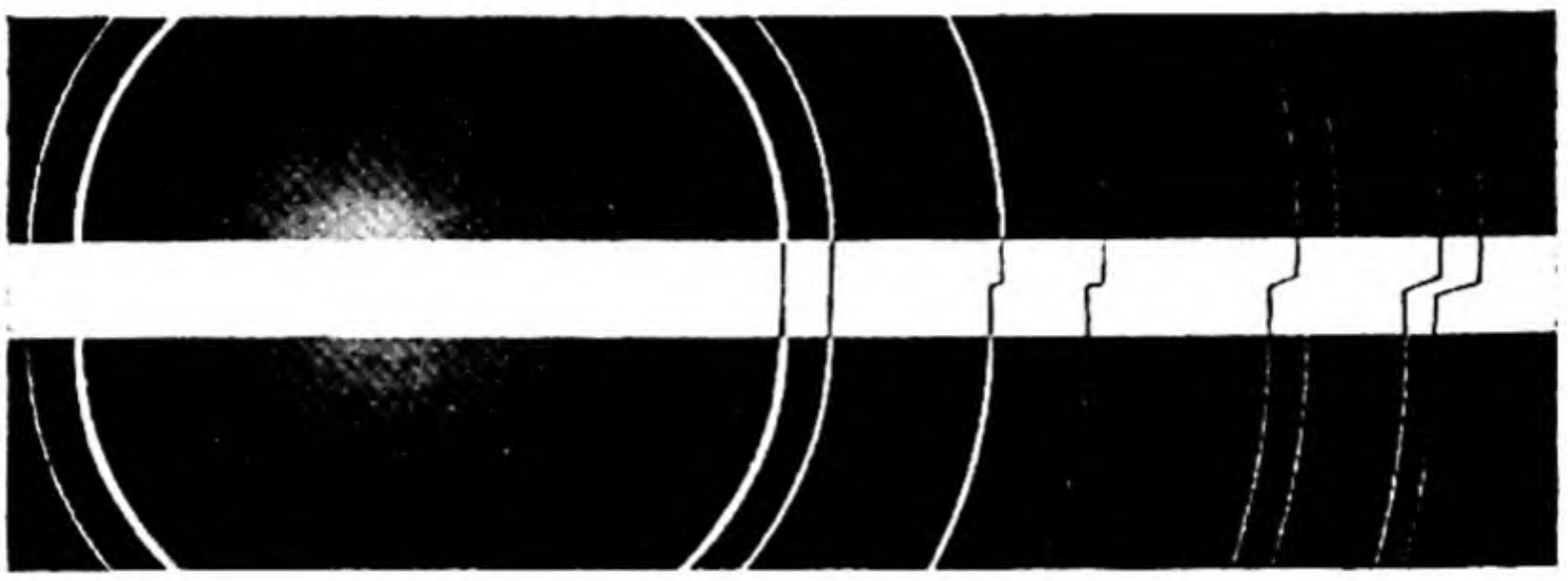

Fig. 6.7. Aberration measurement from the distortion of a diffraction pattern.

plate in a large distance behind the objective. A comparison of the radii of these rings without lens and with lens gives quantitative information on the aberration of the objective. Diffraction patterns of a 50 kV. beam are shown in fig. 6.7. The picture above is taken without lens, and below with the saddle-field lens of an electrostatic electron microscope. Owing to the shorter focal length of the more marginal lens zones, the radii of the larger diffraction rings appear to be more contracted by the lens action than those of the smaller rings.

Shadow methods. These are related to the 'knife-edge test' of glass optics. In some early investigations on electron shadowgraphs, Boersch (1939) observed that spherical aberration does not lead to diffusion but to distortion. In fig. 6.8 (*a*) K may represent a straight 'knife-edge' placed at right angles to the axis z of a lens with the principal plane P. A parallel bundle of rays limited by K crosses P with the semi-aperture y_p travelling at right angles to the straight edge. The limiting ray shown in the figure is refracted through the focus F_1 and meets the target T with the semi-aperture

$y_T + \Delta y_T$. If the lens were free of aberration, all rays would be refracted through the paraxial focus F, and Δy_T would vanish.

Now, the radial semi-aperture of the limiting rays which is increasing along the straight edge may be given in the principal plane as $r_p = \sqrt{(y_p^2 + x_p^2)}$, where x is the coordinate parallel to the straight edge. Since the aberration is increasing with the aperture, the shadow of the edge on the target will be curved convex towards

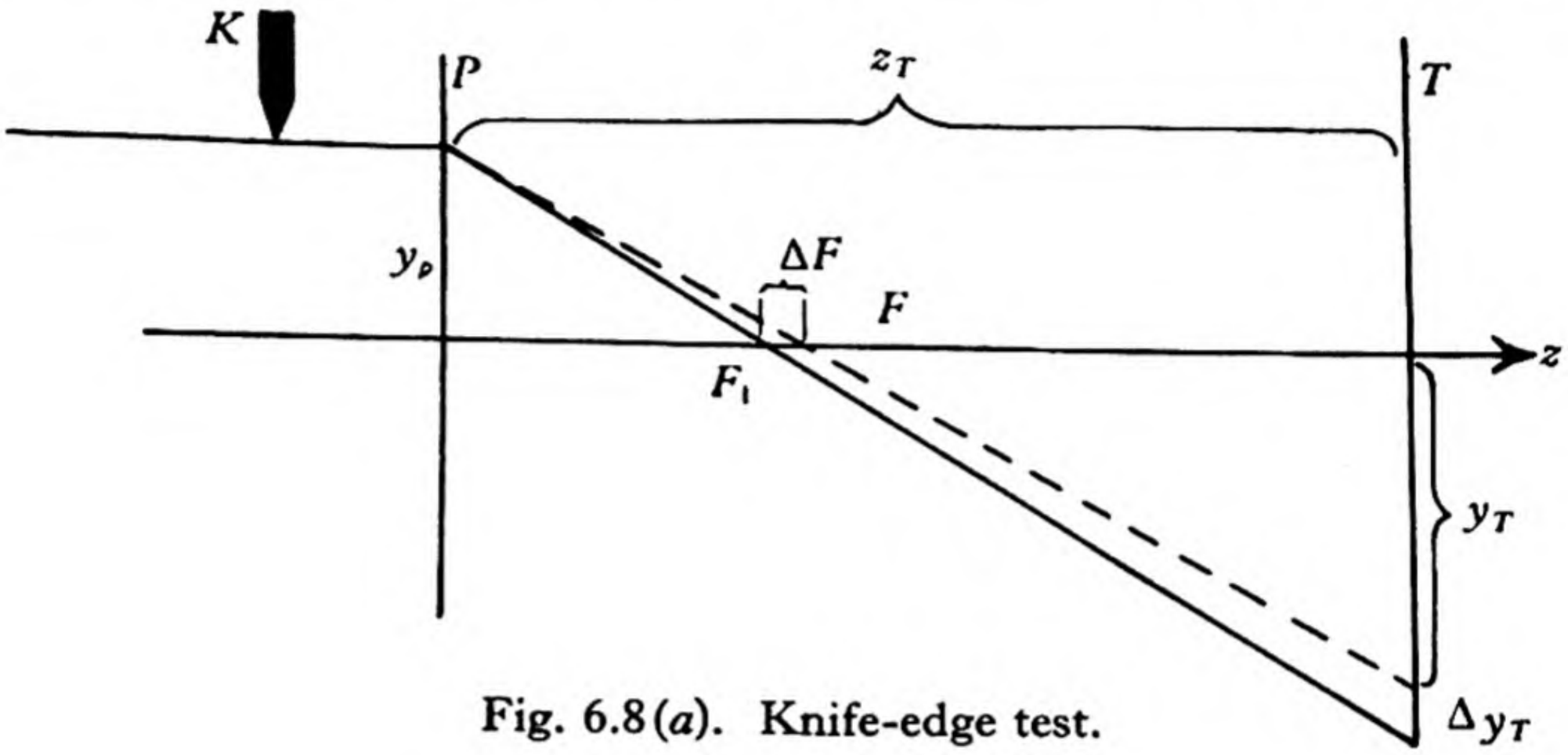

Fig. 6.8(*a*). Knife-edge test.

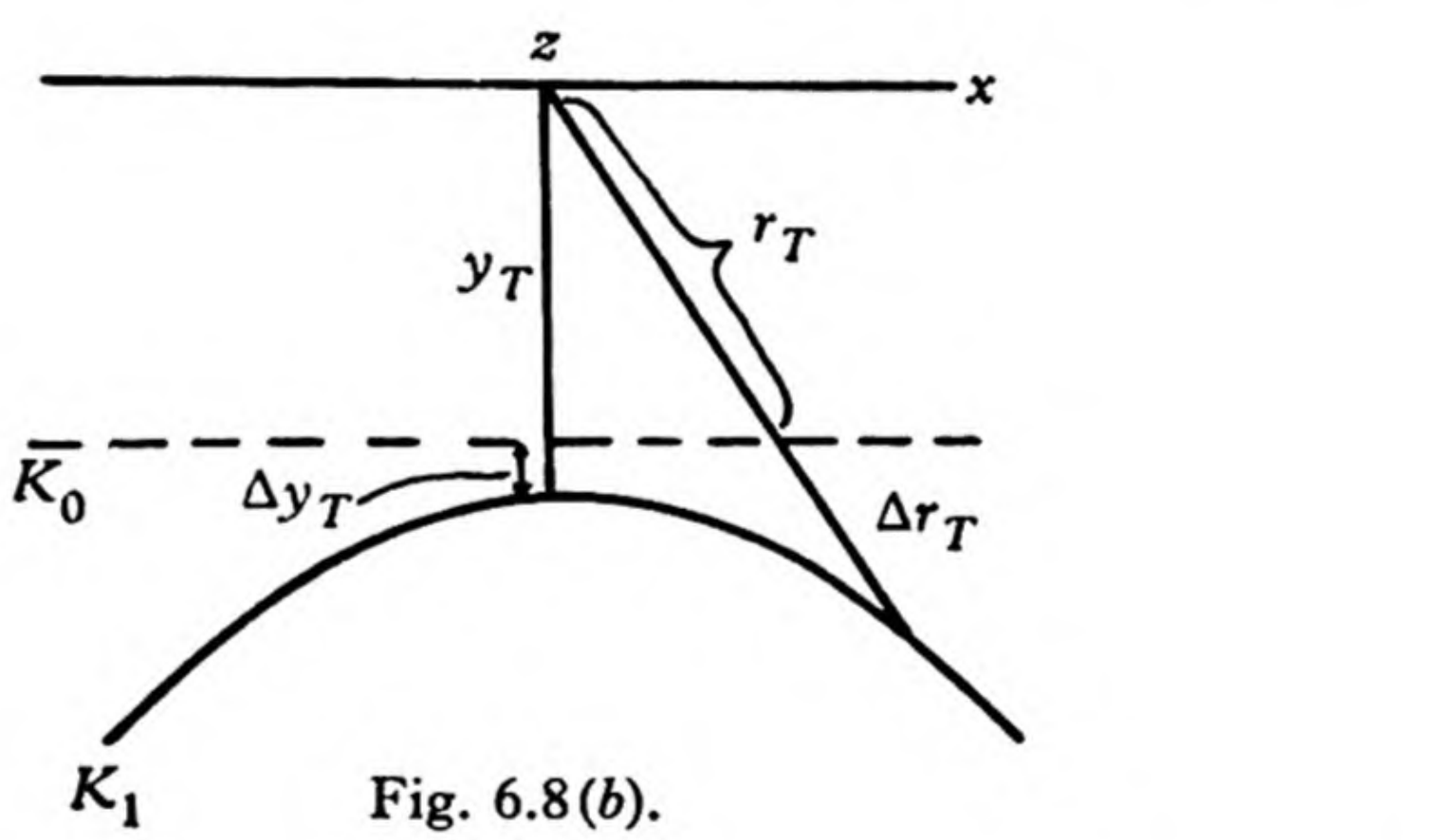

Fig. 6.8(*b*).

the z-axis as shown in fig. 6.8(*b*). If the longitudinal aberration is small and the target distance z_T is large in comparison with the focal length ($\Delta F \ll f \ll z_T$), the radial displacement of the curved shadow edge K_1 from the straight 'Gaussian' shadow edge K_0 can be calculated (cf. Liebmann, 1949*a*) to be

$$\Delta r_T = z_T \left(\frac{r_p}{f}\right)^3 \frac{C_s}{f}, \tag{6.12}$$

where C_s is the aberration coefficient defined by (6.6). Assuming a square-law relationship (6.2) for the spherical aberration, it can be

proved that the distorted shadow edge is a parabola, the origin of which is displaced by an amount given by (6.12), so that C_s can be determined from the shadow-graph if f is known from other measurements.

Spangenberg and Field (1942*a*, *b*) used for the measurement of spherical aberration a shadow method which has been described here (§ 2.3). As shown in fig. 2.4 two grids consisting of equidistant parallel wires are placed in front of and behind the lens. As above, from the known positions and dimensions of the grids and by measuring the magnifications of the shadows, the projection centres J and J' and hence the positions of the cardinal points are determined. For an investigation of the spherical aberration the position of J' has to be determined as a function of the angle of convergence Θ'. Since, owing to aberration, the centres of the paraxial projection (J') are nearer to the second grid than those of the marginal projection, the shadow of the grid would show a 'pin-cushion' distortion, i.e. the shadows of the wires shown in fig. 2.4 (*b*) as straight lines would now appear to be convex towards the axis.

Heise (1949) used the shadow method for some exact aberration measurements of electrostatic microscope objectives of about 5 mm. focal length. The shadow casting grid wires were of 0·03 mm. diameter only and were adjusted within 5×10^{-3} mm.

An interesting adaptation of the shadow method for the investigation of magnetic electron-microscope objectives of a few millimetres focal length is due to Dosse (1941). He observed the shadow of a spider's thread of 10^{-3} mm. The thread was mounted in a long tubular object holder and passed step by step along and across the axis of the small objective, keeping it always perpendicular to the axis. Fig. 6.9 shows the shadow image of the spider thread in three parallel positions on the same photographic plate. The aberration coefficient is calculated (i) from the distances of the shadows as marked in fig. 6.9 by d_0 at the centre, and by d_1 at the semi-aperture r; (ii) from the magnification at the centre which for fig. 6.9 was $y/y' = 6400$. Spherical aberration again leads to a distortion but not to a diffusion of the shadow image.

The shadow method is not altogether satisfactory in electron optics, since the shape of the shadow edge is so easily changed by even the slightest spurious surface charges at the knife-edge. Such

charges may be caused by insulating surface contaminations or by secondary emission. Moreover, if the aberration does not follow the pure square-law equation (6.2), i.e. if the higher terms in (6.1) are not negligible, the interpretation of the shadow-graph becomes rather complicated.

Other methods. The 'tilt-method' by Seeliger (1948) is a most direct method for the measuring of transverse aberration Δr. A point image is projected in the Gaussian plane by a very narrow pencil which originates from a point object on the axis. The distance Δr of the point image from the axis is measured as a function

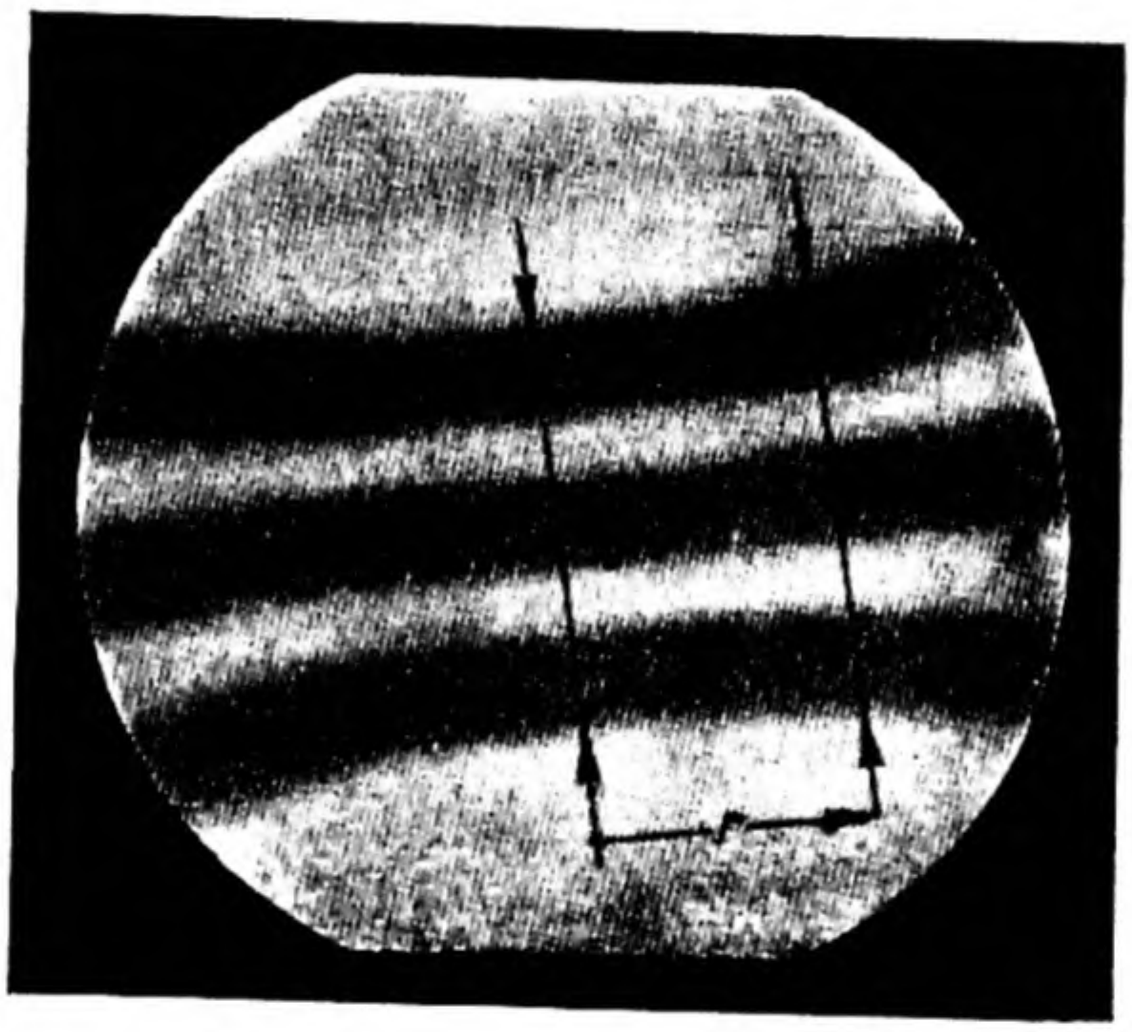

Fig. 6.9. Determination of spherical aberration of microscope objectives from the distortion of the shadow of a cobweb thread.

of the tilt Θ of the pencil in the object space against the lens axis. It is clear that the method requires a particular electron source of negligible diameter and aberration. Moreover, the emission of this source has to be projected into a vary narrow cone, the axis of which has to be tilted by an exactly adjustable amount. The tilt angle Θ between cone axis and lens axis is varied between 0 and 5°. By plotting the displacement Δr of the image point in the Gaussian plane against Θ, a parabola of higher order is obtained, the analysis of which allows the determination of the aberration coefficients $a_2, a_4, \ldots$ in (6.1). The method has yielded so far the most accurate results about spherical aberration of microscope objectives.

A useful qualitative aberration test has been described by Klemperer (1951). In presence of aberration, a focus of rays appears as a spot surrounded by a discrete halo ring, if a diaphragm with a fine

circular aperture is placed across the electron beam in front of the focus. The geometry of rays forming the halo is shown by fig. 6.10. o, ..., o represents the axis beam. (1), (2), ..., (6) are rays which initially are equidistant and parallel to the axis, P is the principal plane of the lens. The marginal rays (6) are focused first, the paraxial rays (1) are focused last. A diaphragm D with a narrow circular aperture is fixed at right angles to the axis in a plane containing the

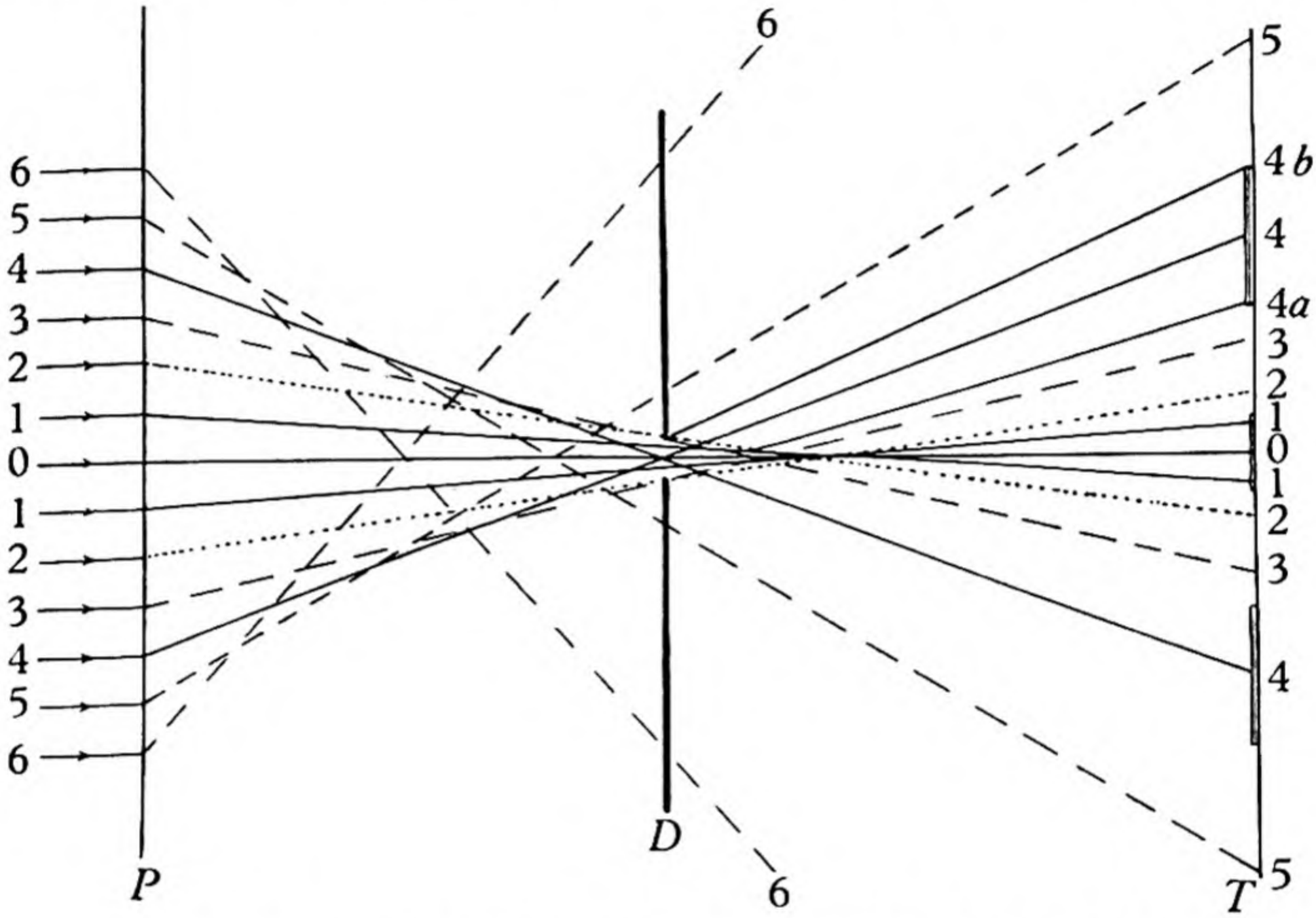

Fig. 6.10. Halo formation in presence of aberration.

focus of the zonal rays (4). At some distance from the diaphragm D on the fluorescent target T, two discrete groups of rays are intercepted which have passed the aperture in D:

(i) A paraxial group forming a spot.

(ii) A zonal group surrounding ray (4) and producing the picture of an annular ring on the target.

The two regions on the target illuminated by electron rays are marked in the cross-sectional fig. 6·10 by double lines parallel to the target. The rays (2) and (4) are intercepted by the diaphragm so that a dark zone is left between ring and spot. Also rays (5) and (6) are intercepted so that the space outside the bright ring is dark again.

Fig. 6.11 (*a*) shows the picture at the target near the minimum diameter of the electron beam, a spot being surrounded by a halo. This pattern belongs to an electron lens with simple positive

spherical aberration, e.g. to a symmetrical two-tube lens. The other pattern, fig. 6.11 (*b*), has been taken with a saddle-field lens containing a space charge near the axis as will be described in Chapter VIII. This lens shows positive aberration for marginal rays but negative aberration for zonal rays. Consequently two separate halo rings are discovered by a halo test as shown in fig. 6.11 (*b*). The smaller ring is produced by zonal rays with negative aberration, the larger one by marginal rays with positive aberration.

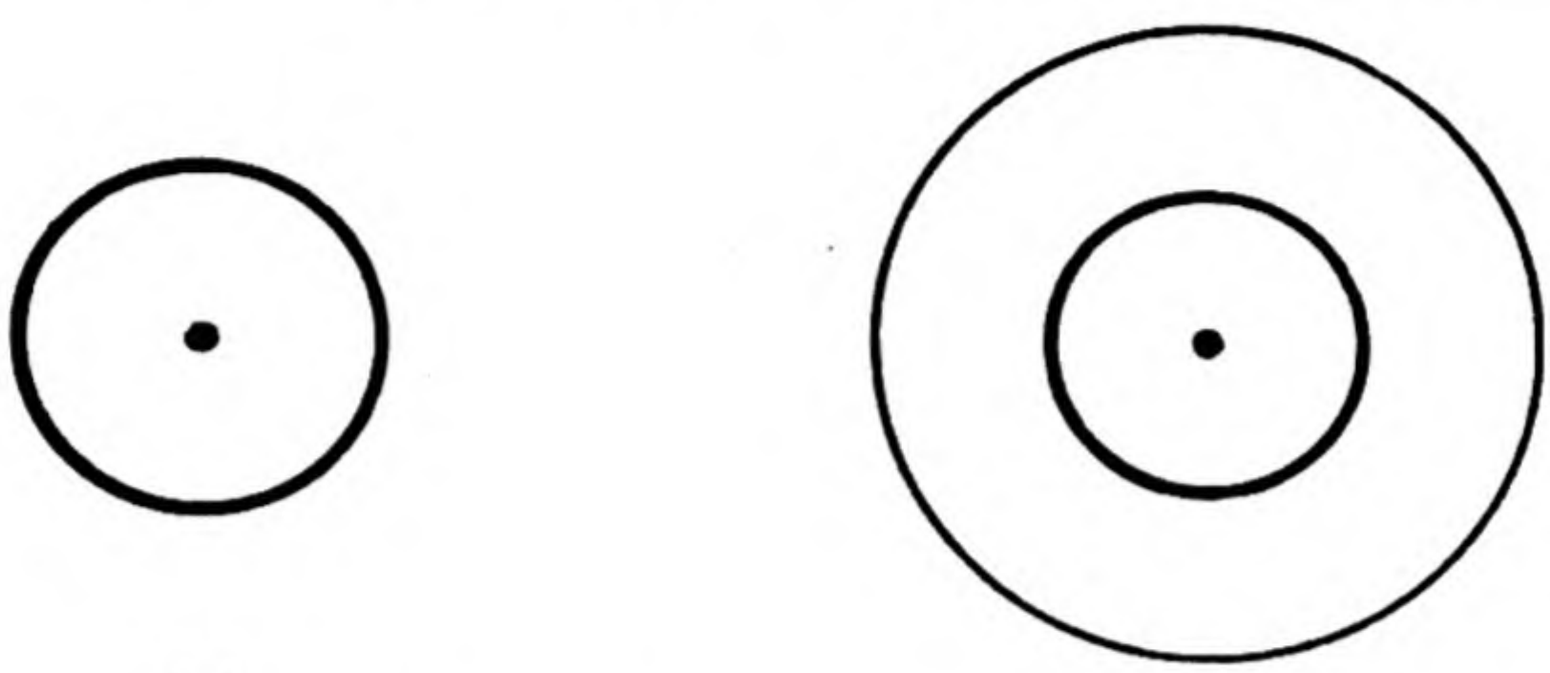

(*a*) (*b*)

Fig. 6.11. Single halo (*a*) and double halo (*b*).

Spherical aberration of electrostatic lenses. A wide range of results is available on the aberration of symmetrical two-tube lenses. Values of the coefficient C_s of (6.2) measured in units of a tube radius R are plotted in fig. 6.12 against the voltage ratio V'/V. The curves are derived from measurements by Klemperer (unpublished) such as recorded by figs. 6.5 and 6.6. in §6.3. A.P. and D.P. refer to parallel rays accelerated and decelerated respectively. These curves refer to the longitudinal spherical aberration ΔF for relatively small angles Θ. For large Θ the higher coefficient a_4 in (6.1) has to be taken into account. Measurements on the symmetrical two-tube lens lead to $a_4 = -a_2/f_0$, where f_0 is the paraxial focal length, since (cf. (6.3)) the longitudinal aberration of this lens is found to increase fairly accurately with the square of the aperture y.

The spherical aberration of asymmetrical two-tube lenses has been investigated by Gundert (1939, 1941). He measured the coefficient C_s in units of the radius R' of the large tube as a function of the ratio of the tube radii R'/R. As a result C_s/R' is found to pass through a distinct minimum at $R' = R$. A reduction of the radius of the high-voltage electrode has a smaller adverse effect than the reduction of the radius of the low-voltage electrode.

Spherical aberration of large, weak electrical saddle-field lenses has been investigated by Gobrecht (1941) and by Klemperer (1942*a*). Initially accelerating saddle fields have very much less spherical

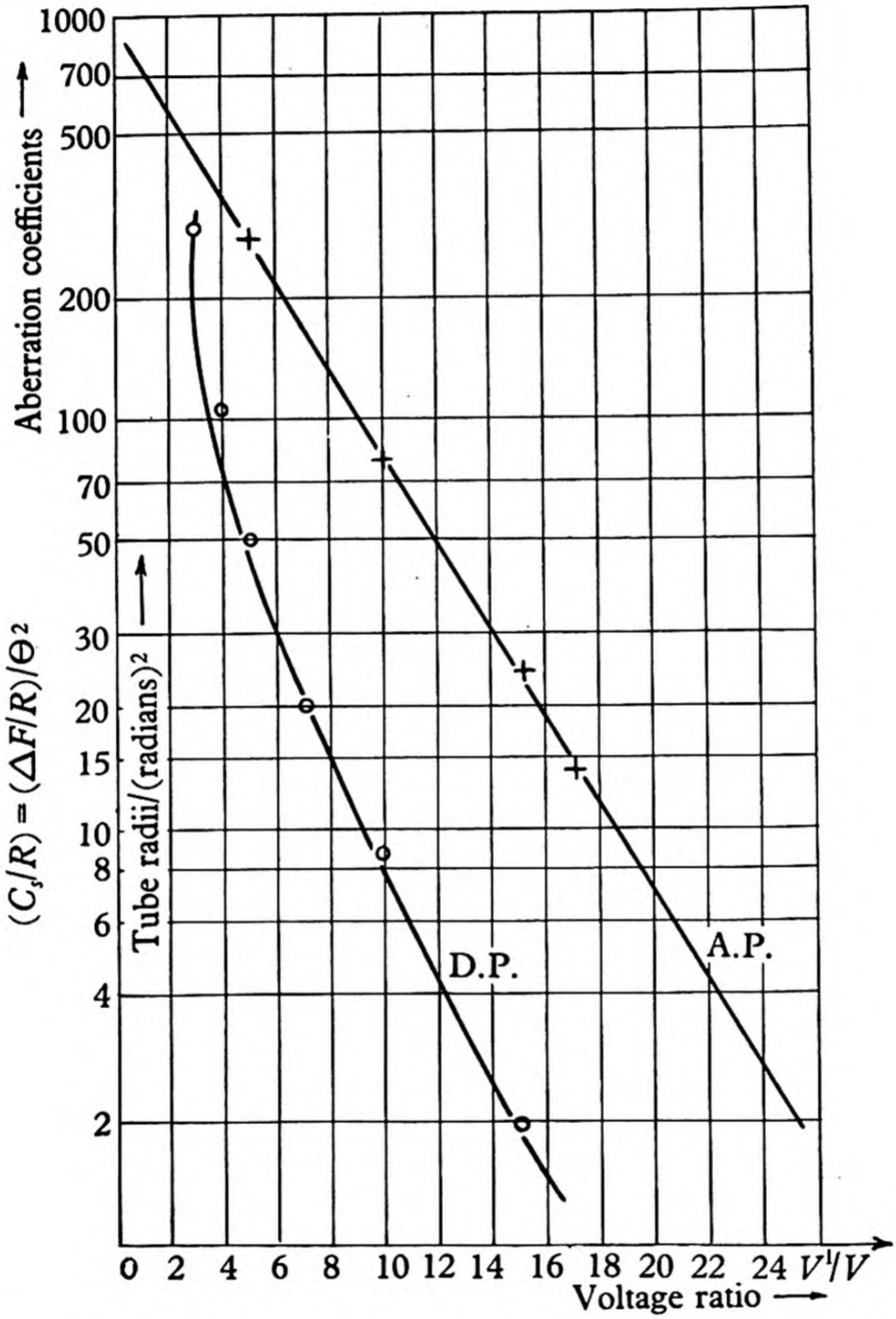

Fig. 6.12. Spherical aberration coefficients of the symmetrical two-tube lens.

aberration than the initially decelerating ones. However, the latter type is used nearly exclusively for practical reasons. The aberration largely depends upon size and shape of the electrodes. The following

results of Gobrecht referring to three-tube einzel lenses are of practical interest:

(1) When the ratio of radii (R_i/R_o) of inner and outer tubes is varied, the aberration measured in units of the larger radius is found to reach a minimum for equal tube radii ($R_i = R_o$).

(2) For given object and image position, and for a given total length of the lens, the aberration coefficient decreases with increasing tube radius. The rate of decrease in aberration with increasing tube radius is rapid for short lenses, but it is rather small for total lengths of the lens tubes greater than one tube radius.

(3) Aberration decreases with increasing total length of the lens. It depends, however, not only upon the total length but also upon the ratio of the lengths of inner and outer tubes separately. Minimum aberration is obtained if the outer electrodes take about 30 % of the total length.

(4) The aberration increases with increasing focal length of the lens, but it decreases with increasing image distance.

The dimensionless spherical aberration coefficient of electrostatic univoltage lenses is represented approximately, according to Liebmann (1949*a*), over a wide range of modifications of lens design or lens potentials by the following empirical formula:

$$C_s/f = K(f/R_i)^2,$$

where f/R_i is the focal length expressed in terms of the radius of the inner tube. K is a constant which depends upon the shape of the electrodes; K is of the order of 2·5 for plain-tube lenses, but it is increased, to about 5, if diaphragms are introduced in the tube electrodes.

It will be pointed out in §8.5 that many initially decelerating three-tube saddle-field lenses suffer from disturbances by space charge and should therefore be used for focusing rays of relatively small intensity only. Three-diaphragm saddle-field lenses are comparatively free from space-charge errors. With such lenses, small spherical aberration is obtained when their field is relatively extended in the axial direction. Best results are obtained with three-diaphragm lenses when the apertures are smaller than their mutual distances and when the radial extension of the diaphragms is

relatively large. A convex curvature of the outer diaphragm towards the saddle field has been found to be advantageous in some cases.

The small, strong three-diaphragm einzel lenses are of great importance for electrostatic electron microscopes and have thus been investigated in detail. Chancon (1947) showed from field-plotting and ray-tracing studies that the dimensionless aberration coefficient C_s/f (6.6) hardly depends upon diaphragm spacings, aperture diameters and electrode shape or thickness. A reduction of the focal length, however, nearly always leads to a reduction of C_s/f. This focal length may, according to § 4.6, be decreased by scaling down the geometrical dimensions or by increasing the applied voltages. The shortest obtainable focal length is eventually reached when sparking limits the field that can be maintained between inner and outer diaphragms. Up to about 200 kV./cm. can practically be applied to the lens electrodes. Surfaces which stand highest fields lead to einzel lenses of shortest focal length, and hence to a reduction of the aberration of the electrostatic-microscope objective. Practical lenses have therefore electrodes with highly polished and well-rounded surfaces. Their general design for avoiding disruptive discharges has been explained in § 4.6.

Einzel lenses with focal lengths of a few millimetres have been found to have aberration coefficients of the order of $C_s/f = 10$. The first precision measurements on such lenses are due to Mahl and Recknagel (1944). Moreover, Heise (1949) succeeded in measuring position and shape of principal surfaces and focal surfaces, and he found a distinct minimum of the aberration coefficient C_s/f at an optimum voltage ratio for which simultaneously a minimum focal length was experienced. This optimum voltage ratio is a function of the geometrical lens parameters (cf. R, T and S in fig. 4.7). Eventually, Seeliger (1948) determined with his tilt method the values of primary and secondary aberration coefficients (cf. (6.1)). For his best lenses these coefficients were within the limits $3 < a_2/f < 10$ and $30 < a_4/f < 80$ respectively.

Spherical aberration of magnetic lenses. This aberration is generally found to be smaller than the aberration of an electric lens of comparable focal length. Large weak lenses formed by iron-free coils of a few layers of wire have been investigated by Becker and Wallraff (1938, 1940*b*). They found the aberration coefficient to

decrease with increasing length ($2L$) of the coil according to the empirical relation

$$C_s/f \sim L^{-0.4}. \tag{6.13}$$

The length-to-diameter ratio (L/R) of the coils was varied in Becker and Wallraff's experiments between 0·1 and 5. The focal length f was kept between R and $2R$, R being the mean coil radius. For instance, $C_s/f = 3{\cdot}0$ is found for an air coil with $L/R = 0{\cdot}13$ and $f/R = 1{\cdot}6$. This applies to initially parallel beams.

Relatively much larger C_s values are obtained for diverging beams. Graham and Klemperer (1952) measured aberration coefficients of monolayered coils for symmetrical object and image positions and presented the C_s-values in terms of the object to image distance z_f as a function of the coil radius R and of the coil length $2L$. They found for instance $C_s = 9z_f$ for $R = 0{\cdot}1z_f$ and $2L = 0{\cdot}1z_f$. The C_s/z_f values decrease rapidly with increasing L/z_f and with decreasing z_f/R. For $L \gg R$, the field approaches homogeneity. In the homogeneous field the longitudinal aberration depends on the cosine of the initial semi-aperture Θ of the ray, since according to § 5.1, the distance between object and image point is given by

$$z_\Theta = z_f \cos\Theta.$$

Hence

$$\Delta J = z_f - z_\Theta = z_f(1-\cos\Theta) = z_f\left[1-\left(1-\frac{\Theta^2}{2!}+\frac{\Theta^4}{4!}\dots\right)\right]$$

$$\approx z_f\frac{\Theta^2}{2}. \tag{6.14}$$

With (6.6), the aberration coefficient is found to be

$$C_s = z_f/2. \tag{6.15}$$

The spherical aberration of an iron-shielded coil is appreciably larger than that of the corresponding air coil. Becker and Wallraff (1938) investigated this aberration as a function of the width of the gap in the shield. Their curves for a coil of inner radius $R = 4$ cm. and length $2L = 6{\cdot}5$ cm. are reproduced in fig. 6.13. The dimensions of coil and iron shield are large enough to avoid the saturation region of the iron at the used number of ampere-turns. The aberration is least for the smallest gap width; however, the current to obtain the given focal length is excessively large at the smallest gap widths

(cf. § 5.4). The aberration reaches a maximum at about 1 cm. gap width and then continuously decreases with larger gap widths, while the current to produce the given focal length reaches a minimum at about 4 cm. gap width.

Iron-shielded lenses of shortest possible focal length are of great interest for use in electron microscopes. Their aberration has therefore been studied in great detail. The coefficient C_s/f has been found to decrease with increasing lens power. The lens power is

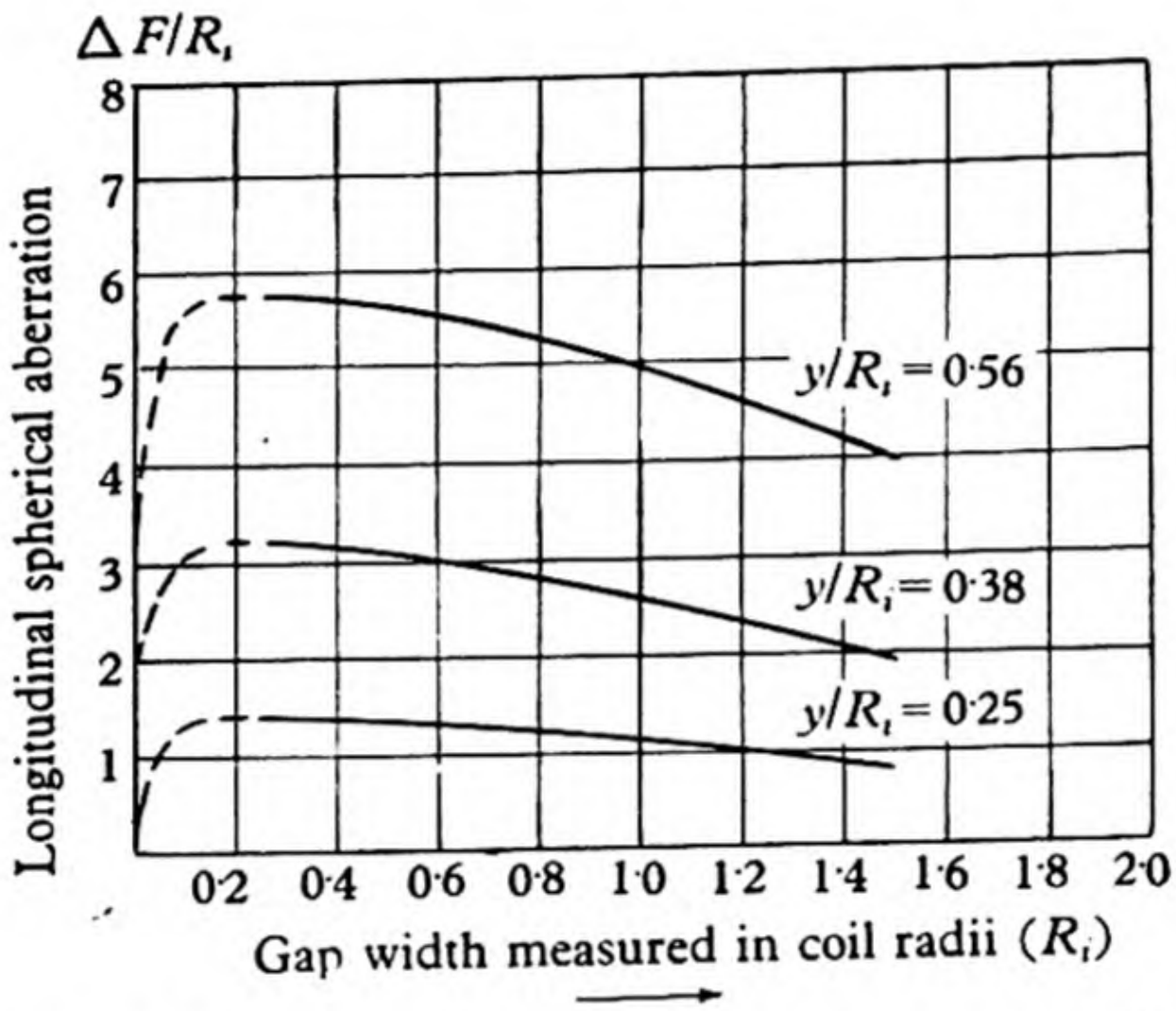

Fig. 6.13. Variation of spherical aberration with width of gap of iron shielded coil for three different apertures of rays.

increased by increasing the field strength and reducing the lens dimensions. The limits set to both these procedures by the saturation properties of the iron have been discussed in § 5.4. Aberration coefficients of magnetic-microscope objectives have been measured by Ruska (1934*b*), Ardenne (1939*b*), Dosse (1941) and Liebmann (1946). These authors agree about an optimum result. The smallest obtainable aberration coefficients are found to be about

$$C_s/f \approx 0{\cdot}8$$

for lenses between 1 and 2 mm. focal length. Magnetic lenses can be made of shorter focal length than electrostatic lenses. But even if lenses of equal focal length are compared magnetic-microscope objectives are superior to the electric ones.

The decrease in aberration with focal length is also borne out by the fact that C_s/f values of magnetic-microscope objectives are

several times smaller than the corresponding coefficients of large, weak magnetic lenses. The iron-shielded lens specified by figs. 5.6 and 5.17, for instance, has an aberration coefficient

$$C_s/f = 2{\cdot}4,$$

though compared with other lenses of similar focal length it is of a fairly good quality.

6.5. Correction of spherical aberration

The large positive spherical aberration experienced for all electron lenses is not unexpected. For instance, all magnetic lenses must suffer from the cosine effect which has been shown (cf. (6.14)) to shorten the focal length of marginal rays in homogeneous fields. Lenses of finite thickness would suffer from an additional shortening of the marginal rays focal length, since the marginal fields in such lenses are always stronger than the paraxial fields. Again, electrostatic lenses will suffer from aberration for a similar reason that the marginal fields are always too strong.

In all investigations concerned with the search for lenses of least aberration, the theory has given some valuable lead. First, it has been shown that smallest aberration coefficients are likely to be found with lenses of smallest focal length. For instance, Ramberg (1942) studied by means of analytical methods the variation of aberration of various lens types as a function of the lens power. For his calculations he used analytical distributions which approximate closely the actual experimental field. Some of Ramberg's results are shown in the graph of fig. 6.14. Abscissae are the refractive powers ($2R/f$), where R is the inner radius of the electrode in case of an electric lens or of the iron shield in case of a magnetic lens. f is the focal length. Ordinates are the aberration coefficients C_s (cf. (6.2)) expressed in diameters $2R$.

At any given focal length, accelerating and decelerating symmetrical two-tube lenses (A.P. and D.P.) show the smallest and the largest aberrations respectively of all investigated types. Some results on two different symmetrical decelerating saddle-field lenses are included in the diagram. One of these saddle-field lenses contains three relatively thin diaphragms, the other three rather thick electrodes. The results, however, are almost identical. The curve for the

magnetic lens in fig. 6.14 refers to the idealized case of a set of cylindrical pole-pieces of infinitely great permeability at very small axial distance, but it is actually quite comparable with the lens shown in fig. 5.3 (*c*). The theoretical results of fig. 6.14 are in good

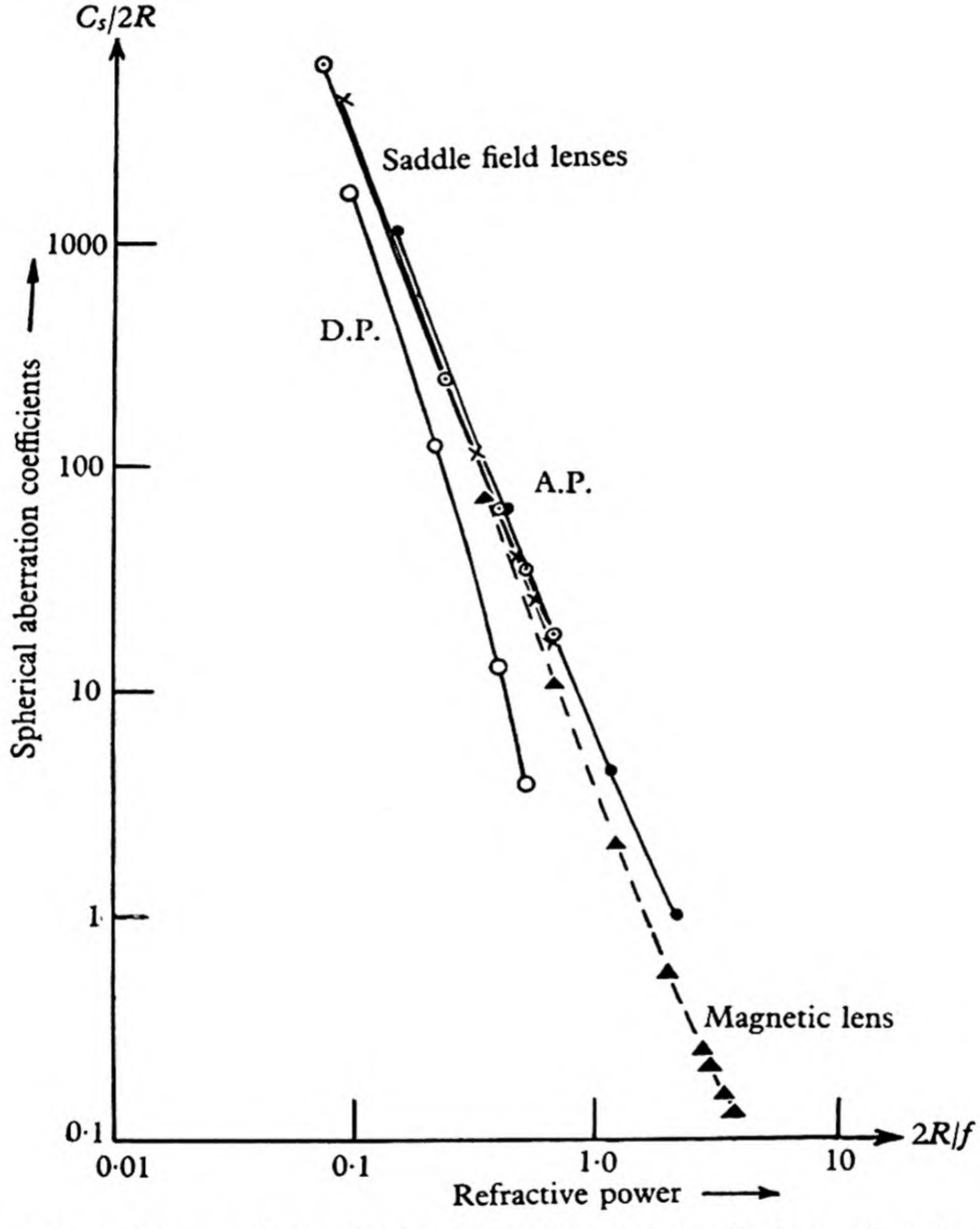

Fig. 6.14. Comparison of spherical aberration coefficients of various electron lenses calculated by Ramberg (1942).

agreement with the experimental values given in the last section (§6.4). For all equipotential lenses, the aberration decreases with increasing lens power $1/f$, and from the slope of the curves in fig. 6.14 the approximate relation is derived:

$$C_s/f \sim f^{1.7}. \tag{6.16}$$

The question then arises how lenses of a given focal length may be corrected. Analytical expressions for electric potentials or magnetic flux densities along the axis have been derived for lenses of least aberration. For example, Scherzer (1936) and Rebsch and Schneider (1937) recommended for weak, thin electric or magnetic lenses a decay of electric potential or of flux density respectively proportional to $\exp(-\text{const.}\, z)$ along the z-axis. Scherzer (1936) even proposed a complicated electrode structure for producing a lens of extremely small aberration, which has, however, never been realized in practice.

Practical progress in the design of large magnetic lenses for electron spectrometers is due to a suggestion by Glaser (1940*a*), who was first to discuss the merits of a 'dip-field distribution'. The flux density in a magnetic lens off the axis can be developed as a series

$$B_z(y,z) = B_z(z) - \frac{y^2}{4}\frac{\partial^2 B_z(z)}{\partial z^2} + \ldots. \qquad (6.17)$$

It follows from this equation that if we require a decrease in field with increasing aperture y, then $\partial^2 B(z)/\partial z^2$ should be positive. Consequently, if we desire to reduce positive aberration, the axial distribution of flux density should not be, as in figs. 5.3 and 5.7, bell-shaped or concave towards the axis but rather convex towards the axis as shown in fig. 6.15. Siegbahn (1946) succeeded in producing these particular fields in a large iron-shielded lens which is shown here diagrammatically in fig. 6.16. There the coil C is placed in an iron cylinder F of 60 cm. length, and has internal and external radii of 10 and 16 cm. respectively. The iron end-pieces E_1 and E_2 are 5 cm. thick having pole-pieces with apertures A_1 and A_2 of 1·4 cm. radius. Object and image are placed at these apertures where the flux density B_z is largest. Towards the middle, B_z decreases to within a few per cent of its value near the apertures.

Reasoning along similar lines, Quade and Halliday (1948) have used a segmented air coil. This consists essentially of two short individual coils which are arranged sufficiently far away from the mid-plane to produce a dip in flux density near the mid-plane. However, for reducing spherical aberration the latter arrangement is less effective than Siegbahn's iron-shielded lens (fig. 6.16). The field of the segmented air coils in this particular arrangement

decreased substantially before reaching object and image planes. For best correction, object and image have to be placed in the respective mid-planes of each coil. There, however, the coils have to be spaced so far apart that a relatively very high power consumption is required for energizing the field. A powerful dip-field arrangement of this kind has been described by Agnew and Anderson (1949); it was made up of two coils of 74 cm. diameter, their centres spaced within 96 cm. These coils consumed 10 kW. for focusing 2 MeV. electrons. An application of the dip-field principle for reducing the aberration of microscope lenses has been discussed by Marton and Bol (1947), but the result promises little practical advantage.

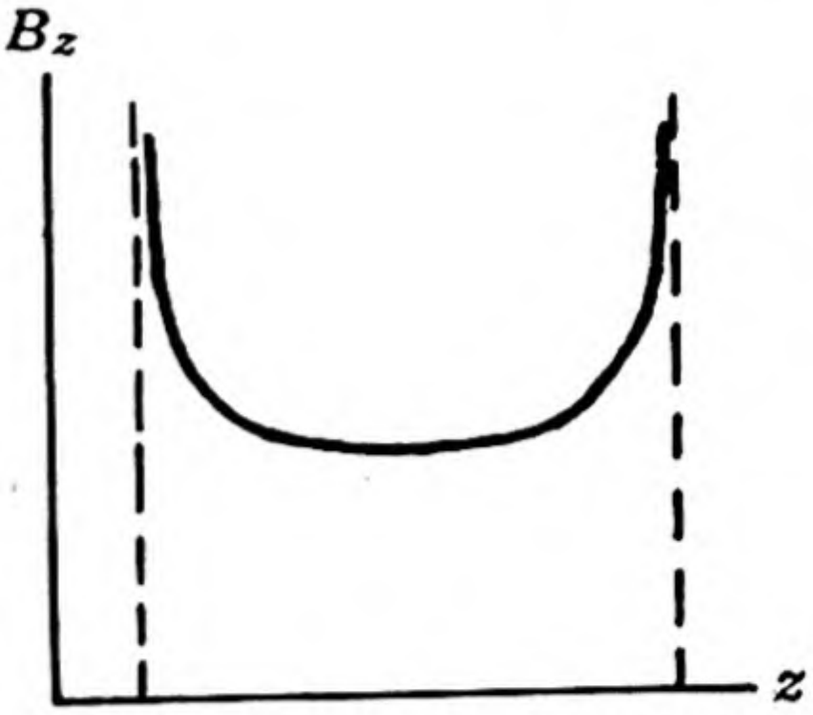

Fig. 6.15. Dip-field with no spherical aberration.

A practically useful approach to the correction of microscope objectives is due to Glaser (1941 *a*). He applied an approximate formula by Scherzer (1936) for the calculation of aberrations produced by bell-shaped magnetic-flux density distributions as

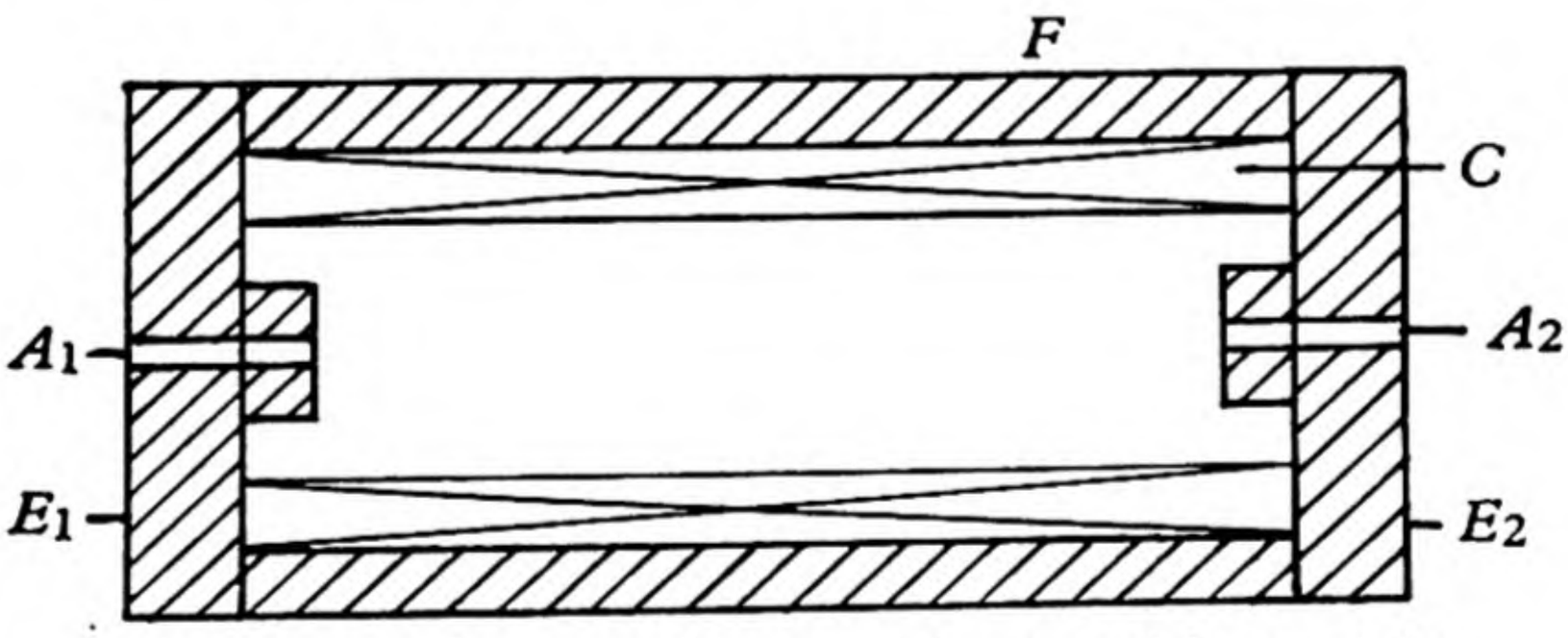

Fig. 6.16. Corrected lens with closed iron ends.

represented by (5.29). In particular, he recommended the use of asymmetrical distributions (combinations of two bell-shaped halves, cf. fig. 5.9) and he found the aberration to be the smaller, the steeper the side of the field on which the object is located. On the other hand, Dosse (1941) found for symmetrical bell-shaped distributions a minimum value for the aberration coefficient C_s for an optimum half-maximum width $2h$ of the distribution curve. These values are

$$(C_s)_{\text{min.}} = 3{\cdot}5 \times 10^6 (V)^{\frac{1}{2}}/B_0, \tag{6·18}$$

$$h_{\text{opt.}} = 10{\cdot}8 \times 10^6 (V)^{\frac{1}{2}}/B_0, \tag{6·19}$$

while a different $h_{\text{opt.}} = 6 \times 10^6 (V)^{\frac{1}{2}}/B_0$ exists for obtaining a minimum focal length

$$f_{\text{min.}} = 8{\cdot}5 \times 10^6 (V)^{\frac{1}{2}}/B_0, \tag{6.20}$$

where the beam voltage V, the maximum flux density B_0 and the lengths h, C_s and f are all measured in m.k.s. units. Liebmann (1951) derived from his field mapping and ray tracing investigations (cf. § 5.4) a practical optimum for the ratio of pole-piece spacing over bore radius to be about $S/R = 2$.

On the whole correction of aberration has made little headway by changing the geometry of pole-pieces or electrodes. Scherzer (1947, 1949*b*), however, discussed new possibilities of correcting spherical aberration. His proposals concern: (1) The use of high-frequency fields to vary the relative refractive power of marginal and axial fields during the transit of the electrons. (2) Placing of metal films into the ray path. (3) Insertion of axial electrodes. (4) Insertion of a cloud of free electrons. (5) Use of electron mirrors. (6) Giving up circular symmetry.

The first two of these proposals have not been seriously tested yet by experiments. Attempts to overcome aberration by application of axial electrodes in electrostatic or in magnetic lenses are not new. Such 'coaxial lenses' have been described first by McGregor-Morris and Mines (1925) and by Nicoll (1938*b*). An electrostatic coaxial lens may consist, for instance, of a straight cylindrical wire in the axis surrounded by some annular electrodes, say, for instance, by two tubes. Potential is applied to the wire in order to provide increased acceleration of the paraxial electrons towards the axis and thus to decrease the paraxial focal length until it equals the zonal or even marginal focal length. In the coaxial magnetic lens, a straight conductor is mounted in the axis, and current is passed through this conductor by flat strips connected radially to both ends of the conductor. When the electron flow through the conductor is in the same direction as that in the electron beam, a converging coaxial force is produced upon the electrons which is inversely proportional to their distance from the axis of the conductor. Evidently it is not possible to utilize a complete annular aperture in these lenses, since the wire must be supported, and the support will interfere with the beam. Also the supports must be arranged

in field-free zones so that the lens field is not disturbed in its circular symmetry. Gabor (1946) first suggested a practicable three-electrode arrangement for such coaxial lenses. Dungey and Hull (1947) have shown by extensive numerical calculations that in such an arrangement, having a focal length of 3 mm. at 60 kV., zones of an angular range of $0{\cdot}09 \pm 0{\cdot}006$ radian can be corrected to have an error of less than 10^{-7} radian. Annular focusing correction of a magnetic lens has been obtained by Hubert (1951) by placing a diverging air coil on the axis of symmetry at the centre of the field, i.e. he used the paraxial baffle coil arrangement mentioned in § 5·3. Control of aberrations by space charges (cf. Chapter VIII) has not been successful so far. This will be more fully discussed in § 7.4 and in §§ 8.4–8.5.

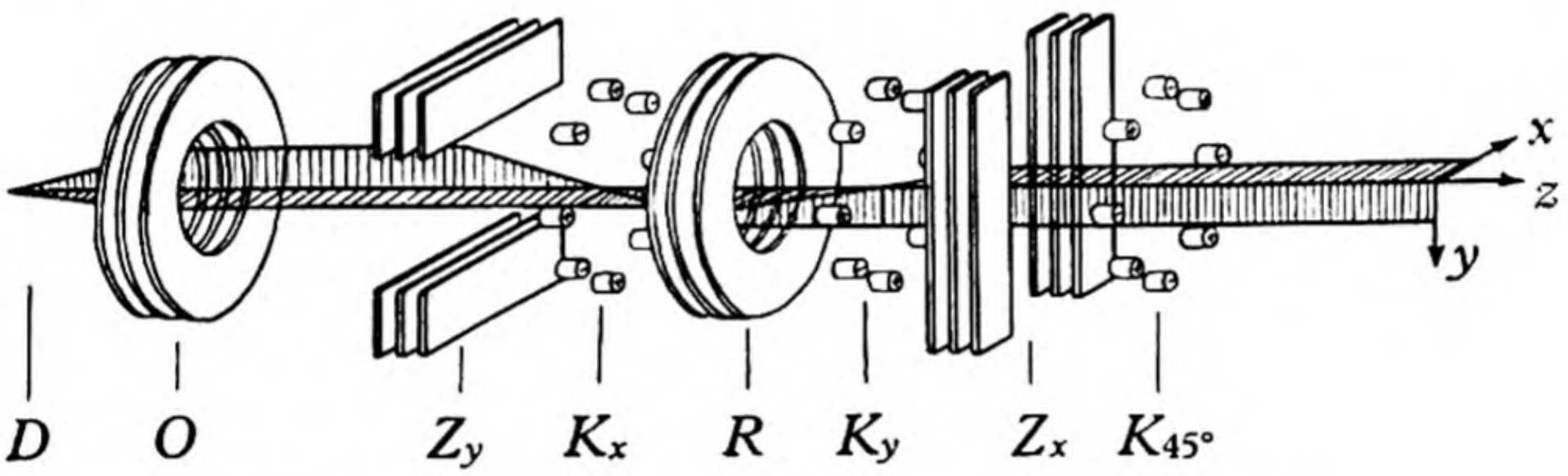

Fig. 6.17. Astigmatic system for correction of spherical aberration.

Ramberg (1949) studied the possibility of inserting a correcting electron mirror into the electron microscope. He calculated the proper concave shape for the mirror electrodes, but found that for an effective correction of the usual microscope objectives the dimensions of the mirror would have to be unreasonably small (of the order of 0·1 mm.). On the other hand, the correction of electron lenses of larger focal length by means of electron mirrors still appears a hopeful task, especially since some of these mirrors have been found experimentally to show large negative aberration.

Scherzer's proposal to give up circular symmetry seems to show the best promises. Seeliger (1949, 1951) has started in this connexion experiments to correct the aberration with a pair of crossed line focus lenses (cf. Chapter X), as illustrated by the perspective drawing of fig. 6.17. There, fast electrons coming from the axial object point *D* are made nearly parallel by the electrostatic microscope objective *O* and enter a system which consists of the two

line-focus lenses Z_x and Z_y and of an ordinary lens R of circular symmetry. By this system, the image of the point D is first split up into two line-foci and then combined again at infinity. At the two line-foci there are arranged two stigmators K_x and K_y respectively. The stigmators are the correcting units described in §6.2 (cf. fig. 6.3) and discussed in more detail below. By suitable choice of the stigmator voltages, Seeliger found it possible to correct most of the third-order aberration. The remaining aberration in the 45° direction was small and could be corrected by a further stigmator $K_{45°}$. Eventually, only fifth-order aberration remained. This could be demonstrated by means of the tilt method which we described in §6.4. Seeliger could also show that the quality of a highly magnified image projected at a relatively large distance from the system as not affected by the formation of the intermediate astigmatic images, and that the use of stigmators at the line foci resulted in some improvement of the image definition. Hence, the new method can be expected to lead ultimately to a substantial improvement of the resolving power of the electron microscope.

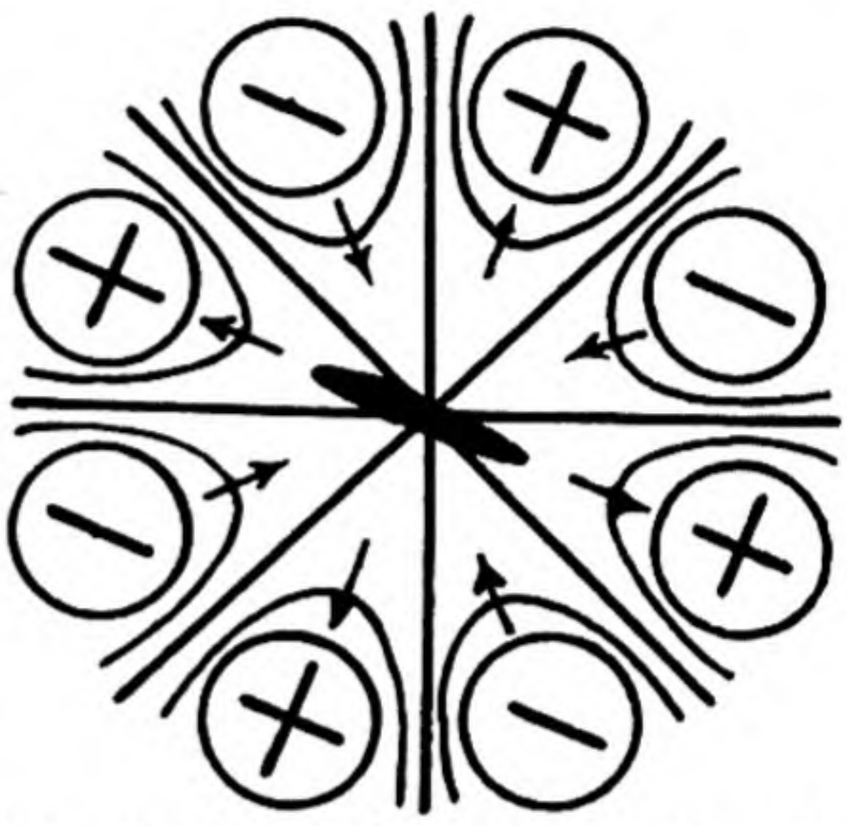

Fig. 6.18. Stigmator action for correction of spherical aberration.

The correcting action of the stigmator as required for the compensation of the spherical aberration is explained by fig. 6.18. There are eight alternately charged electrodes arranged symmetrically about the z-axis which here extends at right angles to the plane of the drawing. The potential V and the field E_r in the stigmator are given by

$$\left.\begin{aligned} V &= \quad kr^4 \cos 4\psi, \\ E_r &= -4kr^3 \cos 4\psi, \end{aligned}\right\} \tag{6.21}$$

where k is a constant, r is the radial distance from the z-axis and ψ the azimuth angle. The force on the electron in radial direction changes sign four times when ψ is continuously increased from 0 to 2π. For a suitable potential difference of the + and − electrodes, a given third-order aberration (a_2) is cancelled in the xz-plane, i.e. for $\psi = 0$, and in the yz-plane, i.e. for $\psi = 90°$, while it is doubled

in the two orthogonal sections $\psi = 45°$ and $135°$. In order to cancel the aberration for all azimuth angles simultaneously, stigmators have to be arranged in the planes of the astigmatic intermediate images, i.e. in the planes of the line foci at K_x and K_y of fig. 6.17.

In fig. 6.18 there is shown inside the stigmator a line-focus which is parallel to the x-axis. The forces on the electron beam which are proportional to the third power of the distance of the electron from the axis are indicated by arrows. However, the fields which are directed inwards are not effective, because there are no rays in the regions where the inward fields are acting. Hence, the stigmator of fig. 6.18, which corresponds to K_x in fig. 6.17, corrects the aberration in x-direction without deflecting the electrons in y-direction. Analogously the stigmator K_y in fig. 6.17 is adjusted to correct the aberration in y-direction.

Calculation still shows the existence of a remaining error in the $\psi = 45°$ and $135°$ directions; this, however, can be compensated by a third stigmator ($K_{45°}$ in fig. 6.17). For theoretical reasons third-order spherical aberration is completely corrected as soon as its compensation is complete in the two perpendicular directions (x and y) and in one other direction.

6.6 Field aberrations: coma

If points lying off the axis are reproduced by rays of large semi-aperture, a lens error called coma causes an asymmetrical deformation of the individual image points to a comet-like appearance. The coma is usually determined as the distance of the focus of the marginal pair of rays from the principal ray. To illustrate this, in fig. 6.19 parallel rays are shown crossing the axis at an angle Θ. If the lens were perfect, all the beams would be focused at the point E which lies in the plane intersecting the axis z at the focus F. If the lens suffers from coma only, the rays close to the principal ray (1) will be focused at E, but rays with larger semi-aperture will be focused at a different point C in the image plane FE, the zonal variation CE being a function of the semi-aperture of the beam. On the other hand, spherical aberration would cause a shift of the marginal focus along the central beam, say to a point C'. If both coma and spherical aberration are present, the intersection of the marginal beams can happen anywhere off the central beam and

off the focal plane. Thus in a picture a general lack of definition would result, and the blurring would increase with increasing distance from the axis.

The simplest condition for the absence of coma is due to Abbe. For large apertures, Lagrange's equation (1.35) has to be replaced by Abbe's sine law (1.33), according to which the lateral magnification y'/y should be a constant for all zones if $\sin\theta'/\sin\theta$ is

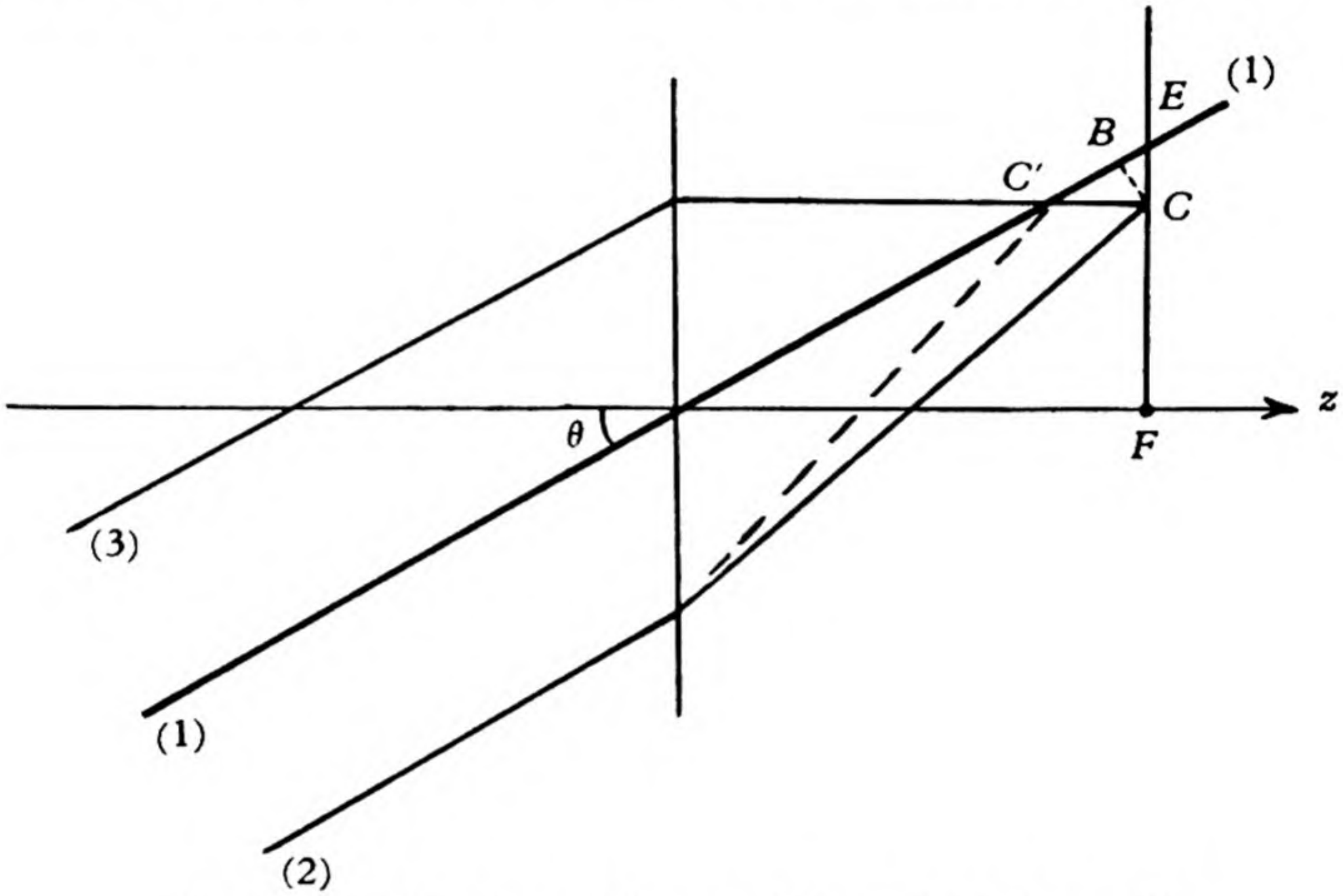

Fig. 6.19. Thin lens with coma (C), and thin lens with spherical aberration (C').

a constant. For an infinitely distant object $\sin\theta'$ is proportional to the height y of the incident rays, so that $y/\sin\theta$ should be constant for incident parallel rays and should be identical with the focal length PF of the system

$$\frac{y}{\sin\theta} = PF. \tag{6.22}$$

In a Gaussian system, each of a bundle of parallel incident rays (if continued) intersects the corresponding emergent ray in a plane. This is commonly known as the principal plane. According to (6.22), however, this is no longer true for large apertures. For a lens which is free from coma and spherical aberration, these intersections should take place on a spherical surface, the radius of curvature of this 'principal surface' being the focal length. If no other aberrations were present, the deviation of the principal surface

from the spherical shape would reveal coma. In the case of a lens suffering also from spherical aberration the coma could be found by subtracting the spherical aberration from the paraxial focal length along the various rays. This is shown in fig. 6.20. There, $\bar{P}_n$, a spherical surface of radius f_0 about the centre F_0, represents the principal surface of a coma-free lens with the focal length f_0 and with the focus F_0. On the other hand, P_0 would represent the principal plane according to the first-order theory, while P_n may be the actual principal surface of a lens which suffers from coma. All three surfaces (P_n, P_0 and $\bar{P}_n$) cut the lens axis (z) at z_0.

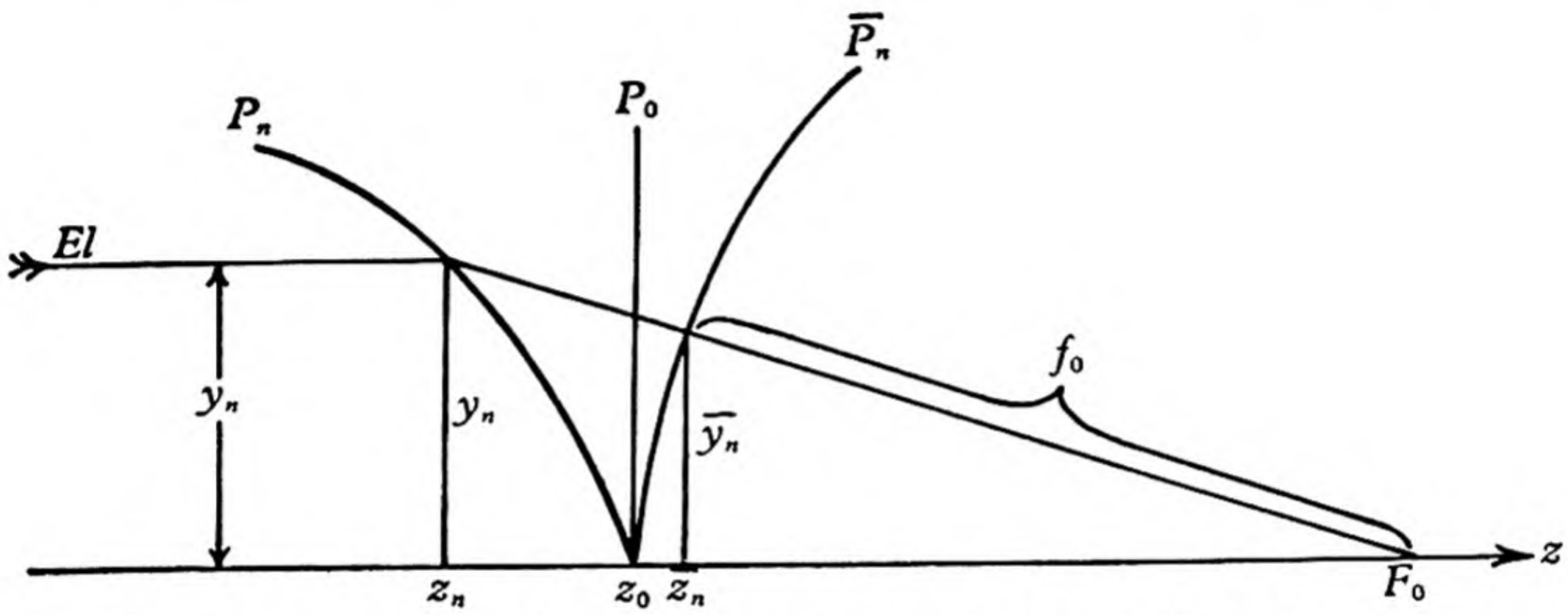

Fig. 6.20. Coma and the curvature of the principal surface.

The electron ray *El* which is initially parallel to the z-axis is, in the absence of spherical aberration, focused through the paraxial focus F_0. The intersection of the direction of the ray at the focus F_0 and of its initial direction leads to a point with the coordinates (y_n, z_n) on the principal surface P_n. On the other hand, the direction of the ray at the focus F_0 cuts the ideal principal surface within the distance f_0 from F_0 at a point with the coordinates $(\bar{y}_n, \bar{z}_n)$.

Now, the coma may be expressed either by

$$\Delta y_n = y_n - \bar{y}_n, \tag{6.23}$$

or by

$$\Delta z_n = z_n - \bar{z}_n. \tag{6.24}$$

For the ideal principal surface $\bar{P}_n$ one would obtain

$$z_0 - \bar{z}_n \approx \bar{y}_n^2 / 2f_0. \tag{6.25}$$

(6.25) follows from geometry, since $z_0 - \bar{z}_n$ represents the deviation of a circle of radius f_0 from its tangent. For the representation of

the actual principal curve there is frequently used an expression similar to (6.25), namely,

$$z_n - z_0 = \frac{y_n^2}{f_0}\left(\frac{C_T}{f_0} - \frac{1}{2}\right), \tag{6.26}$$

where C_T is called the coma coefficient which is proportional to the coma and vanishes for coma-free lenses.

If a lens suffers from spherical aberration, the focus of a ray of semi-aperture y_n is shifted by ΔF_n (cf. § 6.3). For a lens with spherical aberration and coma, the change in focal length Δf_n is composed of the shift in focus (ΔF_n) and of the deviation of the principal surface from its ideal shape ($-\Delta z_n$), hence

$$\Delta f_n = f_n - f_0 \approx \Delta F_n - \Delta z_n - \Delta \bar{z}_n, \tag{6.27}$$

but since, according to (6.2),

$$\Delta F_n = C_s(y_n/f_0)^2,$$

(6.26) with (6.27) yield

$$\Delta f_n = \frac{y_n^2}{f_0^2}(C_s - C_T). \tag{6.28}$$

This zonal difference in focal lengths causes a zonal difference in magnification which owing to (6.28) is proportional to $(C_s - C_T)$.

There are few experimental results on foci and principal surfaces which are sufficiently accurate for a determination of Δf_n. Heise (1949) published curves for principal surfaces and focal surfaces (location of F_n against y_n) of some microscope-objective einzel lenses as a function of the voltage ratio. The results represented by these curves appear to be suitable for precise evaluation which, however, has not been given by this author. Apparently, C_T is always smaller than C_s, but both coefficients are of the same order of magnitude. Liebmann (1949*a*) gave some experimental results on the coma of weak electrostatic univoltage lenses, the coefficients are obtained with $\pm 20\,\%$ accuracy, and for the various lenses they range between $2 < C_T/f_0 < 14$. The coma of magnetic microscope lenses has been determined from field plotting and ray tracing investigations by Liebmann and Grad (1951). It was found to increase with increasing ratio S/R of pole-piece spacing over bore radius (cf. § 5.4). Compared with the spherical aberration, its influence becomes more pronounced with increasing lens excitation.

6.7. Field curvature and astigmatism

A most serious lens error in electron optics is the curvature of field. It causes the image of a plane object to be formed upon a curved surface instead of the usually desired flat image plane. When astigmatism is also present, there will exist two curved image surfaces, corresponding to the sagittal and the tangential or meridional foci. This may be illustrated in the following introductory manner. Take as object a wheel with its axle lying in the axis of the lens system. The rim of the wheel will be projected sharply on to the

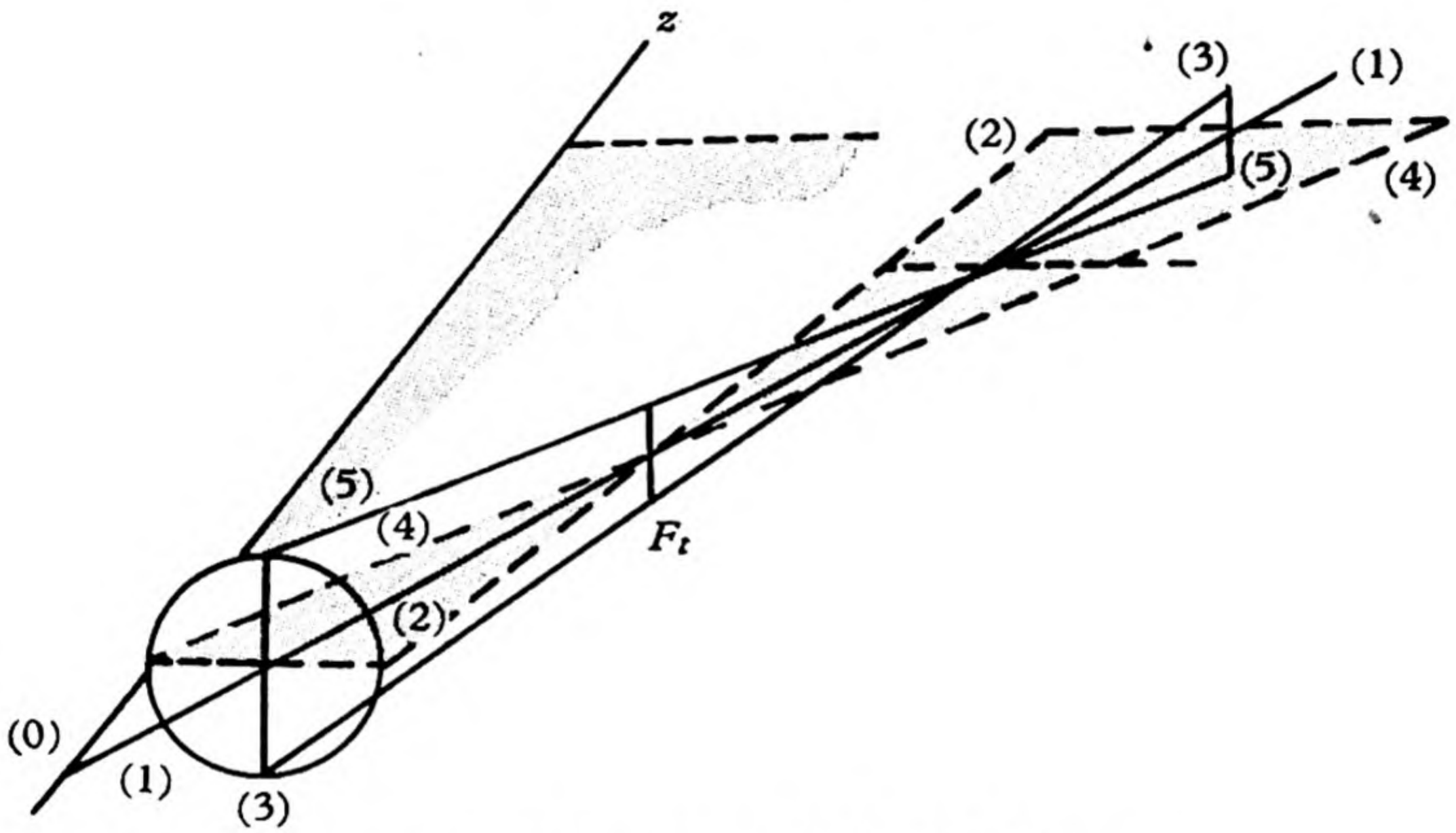

Fig. 6.21. Astigmatism of a bundle of rays.

tangential image surface, whilst the spokes of the wheel will appear to be focused sharply in the sagittal image surface. More exact explanations may be given by means of fig. 6.21, where z is the lens axis and (1) is the central ray of a bundle of rays crossing the axis at O. The two tangential beams (2) and (4) and the two sagittal beams (3) and (5) are also shown. These pairs of beams indicate that the whole bundle of rays has two longitudinally separated constrictions, the tangential or primary focus F_t and the sagittal or secondary focus F_s. In the absence of coma the two constrictions become sharp focal lines. Nowhere along the central ray exists a point focus; the nearest approach to it is about midway between the two astigmatic foci, in a disk of least confusion.

The four image surfaces crossing the axis at the Gaussian image point are shown in fig. 6.22. G is a section through the Gaussian image plane in which the paraxial rays are focused. T and S represent the tangential and the sagittal image surface respectively and D is the surface of least confusion. There is also shown one central ray 00 (which intersects the z-axis) and a bundle of rays 1, 2, 3

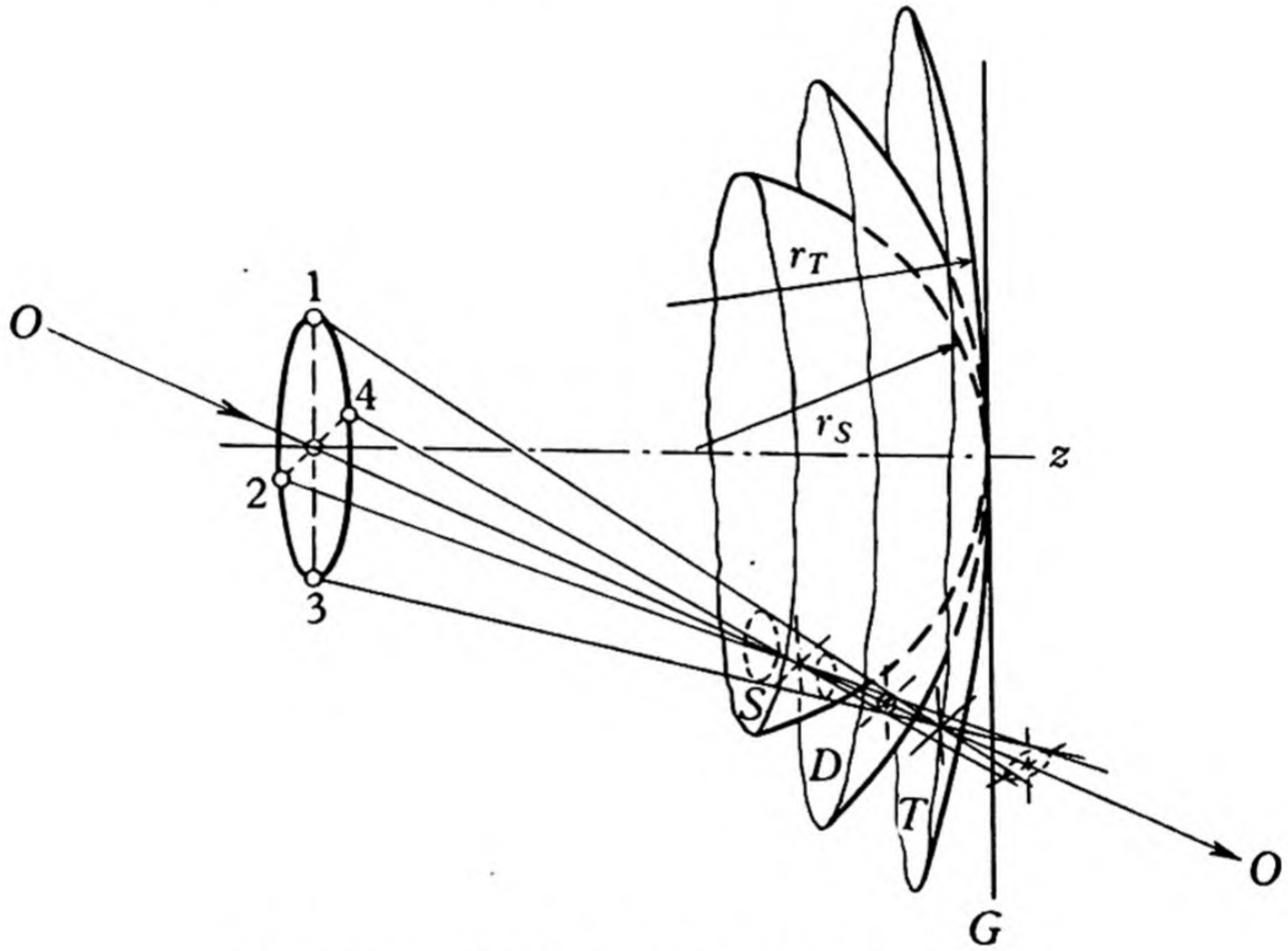

Fig. 6.22. Field curvature and astigmatism: tangential and sagittal image surfaces.

and 4 passing through apertures of a pepperpot diaphragm on a circle about the axis. In all actual electron lenses the image surfaces are strongly curved; they all are concave towards the lens.

Some measure of the astigmatism is given by the radii of curvature r_T and r_S of the tangential and of the sagittal surface near the axis. In experimental investigations, for instance, let the image of a flat cathode serving as an object be projected by a lens on to a movable target. If the cathode contains a pattern of concentric circles and of radial lines, the target positions in which sharp images of circular zones of the cathode appear can be measured as a function of the mean zone radii. In this way, the tangential image surface is located by observation of the circular pattern, and the sagittal surface is located by observation of the radial pattern.

More accurate measurements are obtained if a point object is moved across a flat object plane and its images are located point by point on a movable target. The images of the point object will appear as two short lines projected into mutually perpendicular (tangential and radial) directions with an intermediate disk of least confusion. If the astigmatism of a lens is measured in this way by observing the images of a point object off the axis, the divergent rays emerging from the point object are usually confined within a given aperture. For example, as seen in fig. 6.22, the rays may emerge through pepperpot holes arranged in concentric circles so that coaxial cones of pencils are formed just as in the measurement of spherical aberration. Now, however, the cones are not coaxial with the lens. The axis of the cones, i.e. the principal ray, intersects the lens axis in the lens centre (thick lenses in a nodal point). Usually, the deviations Δz_S and Δz_T of the tangential and of the sagittal surfaces respectively from the Gaussian plane are plotted against the slope angle of the principal ray. Such measurements can be taken for cones of different apertures of rays from the object point.

Morton and Ramberg (1936) applied the method of location of the image of a large, flat cathode for the investigation of a symmetrical two-tube lens. They used a photo-cathode to which a light-optical image was projected. The electron optical pictures, however, were so strongly curved that only a minute axial part of them could be obtained on a flat screen. The axial radii of curvature for the tangential and for the sagittal image surfaces were found to be $r_T = R/23$ and $r_S = R/13$ respectively, where R is the radius of the tubular lens electrodes.

Some measurements by Johannson (1933, '1934*a*) on the large field curvature of two-diaphragm objectives will be discussed in connexion with the field curvature of emission systems (§ 9.4).

Exact measurements on three-tube einzel lenses have been taken by Gobrecht (1942) with a point source off the axis. The tangential image surface was found to have stronger curvature than the sagittal. The magnitude of the field curvature can be judged from the fact that the image deviation Δz from the Gaussian plane for a given slope angle of the principal ray is about 5–7 times greater for electrostatic einzel lenses than for uncorrected spherical glass lenses of similar focal length in light optics. The image

deviation decreases with the focal length of the lens; moreover, it becomes smaller the longer the inner lens tube, and the larger the tube radius R. For instance, for an inclination of 7° of the principal ray, for a focal length of $f = 2{\cdot}6R$ and with both outer lens tubes having a length $L_0 = 0{\cdot}9R$, deviations of the tangential image surfaces $\Delta z_T = 1R$ and $= 2{\cdot}2R$ have been observed for inner lens tubes of lengths $L_i = 2{\cdot}1R$ and $= 0{\cdot}9R$ respectively. The image distance in the quoted example was of the order of $4R$. Generally, the image deviations slightly decrease with increasing image distance. The image curvature does not depend on the aperture of the cone of rays from the object point.

Becker and Wallraff (1939, 1940*a*, *c*) investigated the astigmatism of various magnetic lenses with a point source off the axis. Again, the tangential image surface had the greater curvature in all cases. And quite generally, the longer the lens, the smaller the curvature of the image field. For air coils this curvature was found to increase greatly with the focal length ($\propto f^2$ or f^3). Compared with the electrostatic tube lenses the field curvature of the air coils is small. Becker and Wallraff quote, for instance, for the radius of curvature $r_D = R/3{\cdot}6$ for the mean image surface of an air coil of inner radius $R = 5{\cdot}6$ cm. of semi-length $L = 0{\cdot}18R$ and focal length $f = 1{\cdot}5R$.

Iron-shielded coils show, according to Becker and Wallraff (1940*c*), much greater field curvature than air coils. The field curvature depends upon the width of the gap in the iron shield. It is smallest for very narrow and very wide gaps and reaches a maximum for approximately the same gap widths as those for which maximum spherical aberration is observed (cf. fig. 6.13).

The problem of correcting field curvature can be attacked with the help of the so called Petzval theorem which was introduced in glass optics about a hundred years ago. If the system consists of a number of media, of refractive indices $N_0, N_1, N_2, \ldots$, having spherical faces whose radii of curvature are $r_0, r_1, r_2, \ldots$, the Petzval curvature of the image is

$$\frac{1}{r_P} = -\sum_j \frac{1}{r_j}\left(\frac{1}{N_{j-1}} - \frac{1}{N_j}\right). \tag{6.29}$$

The Petzval surface is in general slightly less curved than either the sagittal or the tangential surface. If these two surfaces coincide,

they also coincide with the Petzval surface, and the field will then be flat, if the Petzval curvature vanishes. For electron-optical purposes the Petzval theorem has been formulated in a convenient form by Klemperer and Wright (1939). The field of an electrostatic lens may be subdivided as indicated in Chapter III in such a way that the ratio of the square roots of subsequent equipotentials $\sqrt{(V_j/V'_j)}$ is a constant (see (3.12)). If V'_n is the voltage of the last equipotential and r_j is the radius of curvature of the jth equipotential, the radius of curvature r_P of the image surface is given by

$$\frac{1}{r_P} = \sqrt{V'_n}\left(1 - \sqrt{\frac{V_j}{V'_j}}\right)\Sigma\frac{1}{(V_j)^{\frac{1}{2}}\,r_j}. \tag{6.30}$$

Take both an image field and an equipotential concave towards the cathode. Then, the value of $1/r_P$ and that of $1/(V_j)^{\frac{1}{2}}\,r_j$ are assumed to have the same sign if an electron passing the equipotential surface is decelerated.*

The extreme difficulty of trying to flatten the image field may be realized from a consideration of (6.30). If, for instance, a two-tube lens is used to project the electrons from a flat cathode on to a flat screen, the electrons are accelerated in passing the equipotentials of the lens, and these are convex towards the cathode at the low-potential side of the mid-plane (see fig. 3.3), i.e. so long as V_j is small. It therefore follows that the first semi-lens will produce a large part of the sum $\Sigma(V_j)^{-\frac{1}{2}}\,r_j^{-1}$. However, when the curvature of the equipotential has changed sign (in the second semi-lens), the electrons have already gained so much velocity that there are only a few equipotentials with opposite sign contributing to the sum in (6.30), and V_j is so large that the terms $1/(V_j)^{\frac{1}{2}}\,r_j$ are small. Hence $1/r_P$ will be a large sum giving r_P as a small radius corresponding to a steeply rounded field concave towards the cathode.

Some theoretical discussion of the Petzval curvature of electron lenses can be found in the papers by Glaser (1935) and by Goddard (1946*b*). A useful expression for the Petzval curvature of purely

* In glass optics, a field curvature concave towards the object is conventionally defined to be positive. Assuming the object in air, a glass surface, however, concave towards this object, has, according to the usual conventions, a negative sign of curvature.

magnetic lenses is derived in the latter paper

$$\frac{1}{r_P} = -\frac{e}{4m} V^{\frac{3}{2}} \int_{-\infty}^{+\infty} B_z^2 \mathrm{d}z, \tag{6.31}$$

where e/m is the charge to mass ratio, V the constant electric potential (electron-volts) in the lens and B_z the axial magnetic flux density along the axis. Since the integrand is always positive, it follows that $1/r_P > 0$. Thus the Petzval field curvature of a purely magnetic lens cannot be eliminated. Combining (6.31) with Busch's lens formula (5.23), the field curvature of a thin lens is found to be

$$\frac{1}{r_P} = -\frac{2}{f\sqrt{V}}, \tag{6.32}$$

i.e. the radius of curvature of the image surface is proportional to the focal length of the lens and to the electron velocity.

6.8. Distortion

This error is again of major importance in electron optics. It is somewhat different from the other four isotropic errors in so far as it has no effect upon the sharpness of the image; it only detracts from its faithfulness. Distortion merely displaces the image points towards or away from the optical axis. According to Seidel's third-order approximation (cf. §6.1) the amount of displacement $\Delta r'$ is calculated to be proportional to the cube of the distance r of the object point from the axis. In the paraxial part of the image, the magnification y'/y is fixed by Lagrange's law (1.35). Thus, the distortion is described by

$$\Delta r' = C_d \frac{y'}{y} r^3, \tag{6.33}$$

where the constant C_d is called the distortion coefficient and $\Delta r'$ is the distance of the actual marginal image point from its ideal position as given by the magnification y'/y calculated from Lagrange's law.

On the other hand, in practical distortion measurements the marginal magnification r'/r is directly compared with the paraxial magnification y'/y, and the following dimensionless distortion factor is found in the experimental literature:

$$D_d = \frac{r'}{r}\frac{y}{y'} - 1. \tag{6.34}$$

This factor is generally measured as a function of the slope angle of the principal rays. But since $r = y$ and $\Delta r' = r' - y'$, it would be expected that

$$D_d = C_d r^2, \tag{6.35}$$

If the distances of the actual image points from the axis are greater than the distances of the ideal image points, the outer parts of the image are on too large a scale, the factor D_d in (6.34) is positive and the distortion is called 'pin-cushion distortion'. This is explained by fig. 6.23 (*a*). There, a broken line indicates the Gaussian image of a square-pattern, the solid line shows the

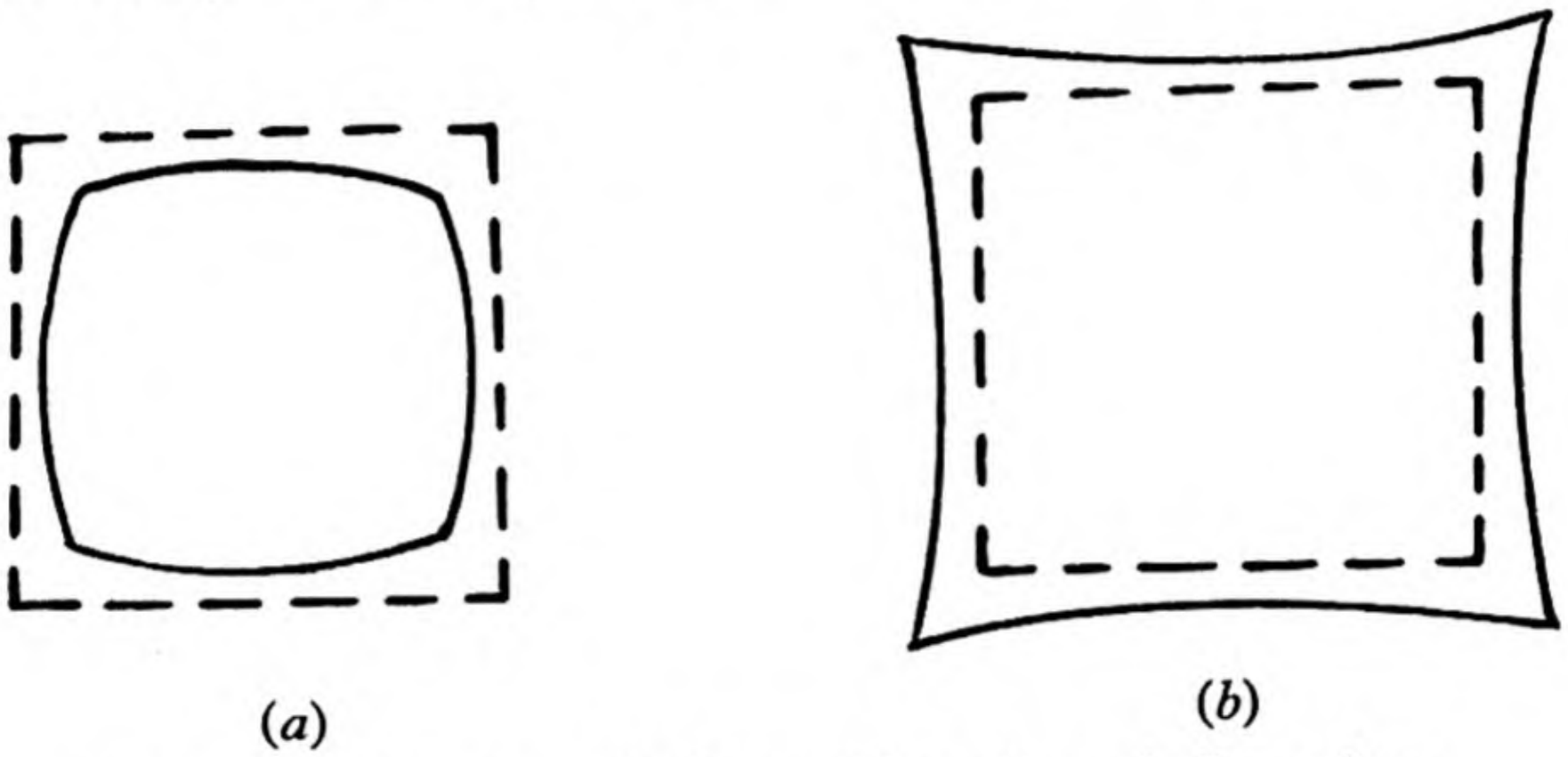

(*a*) (*b*)

Fig. 6.23. Barrel- and pin-cushion-shaped distortion.

stretched, actual image. If, on the other hand, the outer parts of the image are on too small a circle, the distortion factor D_d is negative and so-called 'barrel distortion' will occur. This is illustrated by fig. 6.23 (*b*), the Gaussian image again being indicated by a broken line.

Becker and Wallraff (1940 *a*, *c*) compared the distortion of various weak magnetic lenses for a given object distance and for a fixed focal length. For instance, with an air coil of the mean radius $R = 75$ mm., of the axial width $2L = 20$ mm. and of the focal length $f = 100$ mm., they found a distortion coefficient

$$C_d = 3{\cdot}6 \times 10^{-4} (\text{mm.}^{-2}).$$

The cube law equation (6.33) for the displacement was found to hold well for all air coils. However, for iron-shielded coils the displacement $\Delta r'$ was found to increase with a higher power of the axial distance, namely, with $r^{3{\cdot}5}$ to $r^{3{\cdot}7}$. C_d was found to have a slightly higher value for iron-shielded coils than for air coils. Varying the gap of the iron shield, a maximum of C_d was reached at those

gap widths at which, according to §§ 6.3 and 6.7, maximum spherical aberration and maximum field curvature have been observed. For a lens of 100 mm. focal length, shielded by 4 mm. thick iron and having a gap width near that value which results in a maximum distortion, Becker and Wallraff measured $C_d = 5 \times 10^{-4}$ mm.$^{-2}$. There, the factor D_d was found to increase rapidly with the slope angle of the principal rays. For example, D_d values of $-0{\cdot}4$ and $-0{\cdot}8$ were found for slope angles of 13 and 17° respectively.

Distortion can be rather troublesome in microscope projection lenses, since these lenses have to focus rays of relatively large distances from the axis. Hence, much attention has been drawn to the distortion error of strong electrostatic einzel lenses. Jacob and Mulvey (1949) measured the distortion of strong symmetrical einzel lenses with three apertures of equal radius R as a function of the spacing S and of the thickness T_i of the intermediate aperture (cf. fig. 4.7). They found the parabolic law equation (6.35) to hold up to nearly $r = 0{\cdot}5R$, and they found pin-cushion distortion mainly for small values of T_i/R but barrel distortion for large values of T_i/R. For $T_i/R = 1{\cdot}5$, where with decreasing spacing S the distortion is found to change over from barrel to pin-cushion, a corrected lens is obtained at $S \approx 2R$.

Rang (1948) and Heise (1949) measured the distortion error of various einzel lenses as a function of the voltage ratio V_i/V_o in the neighbourhood of the focal-length minimum which has been discussed in § 4.6. As long as f decreases with decreasing V_i/V_0, the distortion is found to be positive (pin-cushion), but for f increasing again with further decreasing V_i/V_o, the distortion is found to be negative. At the minimum focal length a distortion-free lens is obtained. It is of particular interest that the region of vanishing distortion coincides with the region of minimum spherical aberration which is also reached at minimum focal length. Of practical importance is the distortion-free univoltage lens (i.e. the einzel lens with $V_i = 0$). After the above experience this lens can be found by varying the radius R_i of the intermediate electrode until the focal-length minimum is reached just at the voltage ratio $V_i/V_o = 0$.

All field aberrations affecting an image point off the axis depend upon the part of the lens field that is utilized for image projection. For example, field aberrations can be changed by shifting an

aperture stop along the axis. This effect is very pronounced in the case of distortion. In glass optics, distortion is known to be a function of the effective position of the aperture plane. This is the plane in which the principal rays of the imaging pencils intersect the axis. As explained by fig. 6.24 (*a*), barrel-shaped distortion results if the aperture plane is in front of a thin lens. With this very

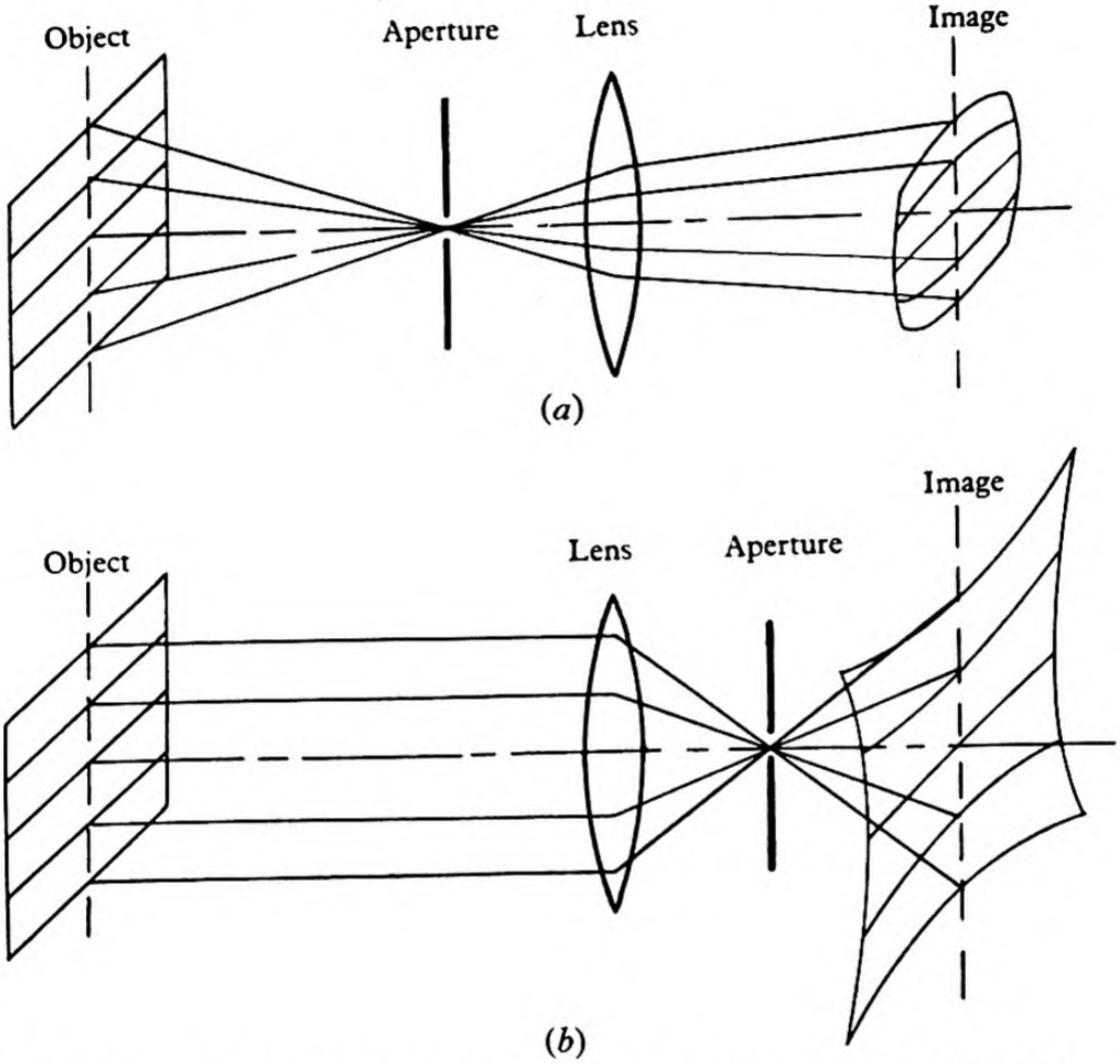

Fig. 6.24. Effect of aperture position on character of distortion.

same lens pin-cushion distortion can be produced as shown in fig. 6.24 (*b*) if the aperture plane is shifted behind the lens.

An example for correcting the distortion of an electron lens has been described by Morton and Ramberg (1936). A two-tube lens was used in an image converter (cf. § 12.5) for projecting a picture of a flat photoelectric cathode on a flat fluorescent screen. The resulting strong pin-cushion distortion could be cured by curving the cathode surface concave towards the lens. In this way the principal rays from the cathode were slightly converged so that their intersection with the axis was shifted, in the direction of the cathode, closer to the effective centre of the lens until an undistorted image resulted.

Independent of the proper distortion error just discussed is a distortion-like displacement of image points from their Gaussian position which is observed when the aperture of rays is sufficiently small but spherical aberration is sufficiently large. A variation of focal length with aperture will appear as a differential shift of each image point as the outer pencils are more strongly refracted than those nearer to the axis. Hence the magnification of the outer zones is increased. However, no confusion of the individual image points is noticed owing to the great depth of focus of the narrow pencils. This aberration distortion has been discussed in § 6.4 in connexion with the shadow method for the measurement of spherical aberration. Though the causes of true distortion and of spherical aberration distortion are quite different, the effects are similar in both cases. A comparison of (6.12) with (6.33) shows that in both cases the radial displacement increases with the cube of the distance from the axis. For relatively thin lenses spherical aberration alone is responsible for nearly all the distortion of the image.

Spherical aberration distortion plays some part in projection lenses of electron microscopes. There the image produced by an objective constitutes the 'object'. The area of this object is large compared with the area of the projector lens, but the individual pencils utilized in the projector lens have an extremely small angular aperture of the order of 10^{-5} radian. None of the third-order aberrations appears as an observable diffusion of the image. According to Liebmann (1952*a*) the pincushion aberration distortion of a projector lens drops steeply with increasing lens excitation, it vanishes in the region of minimum focal length (§ 5.4), and for strongest excitations it changes into barrel distortion. Hence, in principle, all projector lenses can be operated free from aberration distortion. According to Hillier (1946) the aberration distortion can be reduced to negligible proportions by the use of pole-pieces with a double gap. The two gaps have to act as two lenses of about equal focal length, with the second lens being placed at the focal point of the first one. The second lens effects additional focusing with spherical aberration, but as the rays in it are crossed over with respect to the first lens, the distortion due to the first lens can be balanced.

6.9. Anisotropic aberrations

Magnetic electron lenses show three anisotropic errors in addition to the five isotropic errors which we have just discussed. The general theory of these anisotropic errors has been worked out by Glaser (1933*b*). For the case of a magnetic microscope objective Glaser and Lammel (1943) have given some quantitative expressions for all eight errors which they derived from the bell-shaped analytical distribution curve of the lens field which we discussed in § 5·3·

The anisotropic distortion is often called rotational distortion or spiral distortion. It results in tangential displacement of the real

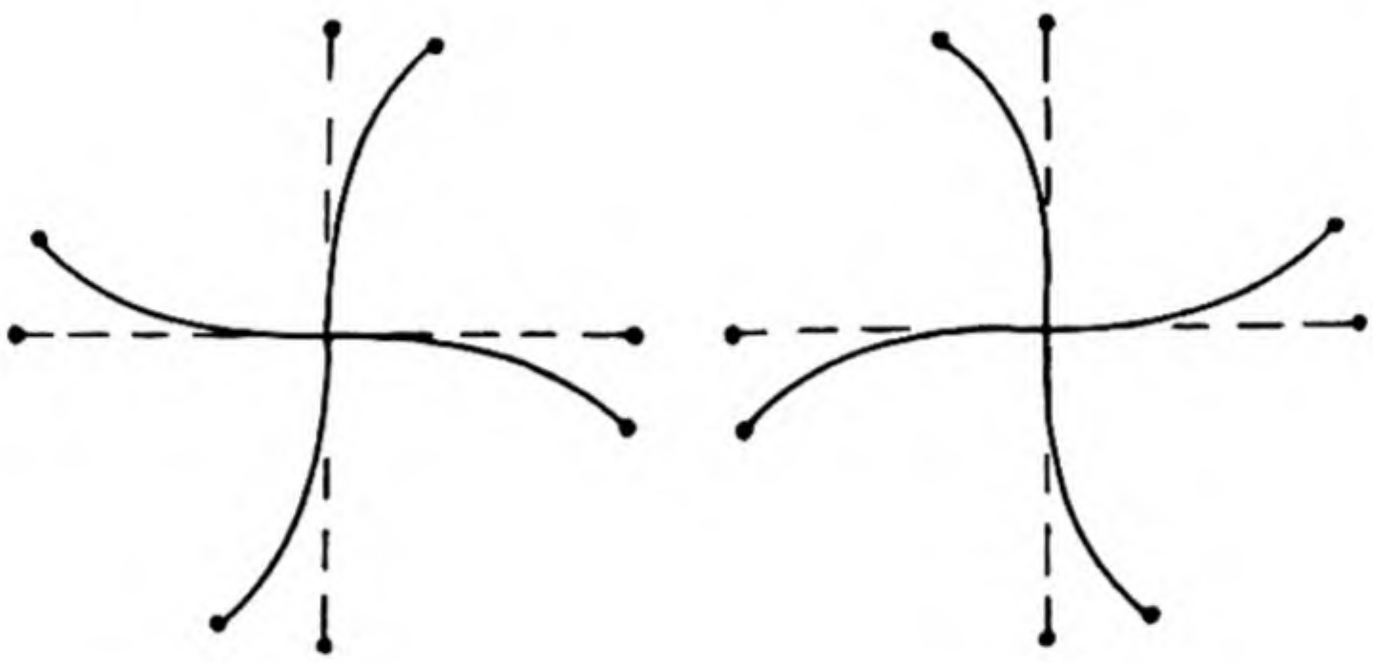

(*a*) (*b*)

Fig. 6.25. Spiral distortion.

image point from the ideal image point which generally increases with the cube of the axial distance of the point. In § 5.2 we have discussed the rotation of the image by a magnetic lens. In the case of spiral distortion, the angle of rotation (ψ in (5.19)) is no longer independent of the radial distance of the image point from the axis. The effect of spiral distortion is seen in fig. 6.25, which shows the images of a cross of two mutually perpendicular lines. The broken lines represent Gaussian images while the solid lines show the actual distorted images; these are shaped like spirals from which the name of the aberration is derived. The image of fig. 6.25*a* changes into the image of fig. 6.25*b* when the current through the lens is reversed. The lateral shift of the image point reverses sign with the direction of the magnetic field.

A coefficient C_x of spiral distortion is usually defined by the increment $\Delta\psi$ in rotation of the image point namely

$$\Delta\psi = C_x r^2, \tag{6.36}$$

where r is the distance of the object point from the axis. (6.36) leads to the following expression for the lateral displacement of the image point

$$r'\Delta\psi = C_x(y'/y)r^3, \tag{6.37}$$

where r' is the distance of the image point from the axis and y'/y is the magnification. (6.37) is quite analogous to the radial displacement (6.33).

Liebmann (1952*a*) found that the coefficient C_x of a microscope projector lens increases with increasing lens excitation but decreases with increasing ratio S/R of pole-piece spacing over bore radius.

According to Becker and Wallraff (1940*b*), spiral distortion is not greater for large, weak iron-shielded lenses than for air coils. Spiral distortion can be avoided, in principle, by using two equal magnetic lenses in opposition forming the rotation-free lens type described in § 5.3. However, this type of lens suffers to such an extent from other lens errors that it is useless for most practical purposes. On the other hand, it appears feasible to improve spiral distortion by decreasing the strength of the marginal part of a lens field in comparison to its axial part. For instance, the use of coaxial coils of different radius with their fields in opposition has been recommended.

Anisotropic coma occurs when not only the whole image is rotated round the axis of the lens but every single element of the picture is also rotated round its proper centre. There results an asymmetrical deformation of the individual image elements to a comet-like appearance. The tail of the comet is not, however, radially directed as with isotropic coma, but lies in a direction perpendicular to the radial coordinate.

Anisotropic astigmatism causes a marginal object point to be projected in a line focus which is inclined at an angle of 45° to the radial coordinate. The image surface where these line foci are sharp is generally curved. Therefore, a general confusion will result in the image plane, especially in the marginal zones.

The last two anisotropic errors have so far been unimportant, and no quantitative experimental investigations have been made about them. However, Diels and Wendt (1937) demonstrated the existence of all eight third-order errors in a magnetic lens by investigating the image of an electron-point source.

In spite of the occurrence of the anisotropic errors, magnetic lenses are often found to be superior to the best electrostatic lenses. Magnetic lenses can be made with shorter focal length than electrostatic lenses. But even if lenses of equal focal length are compared, magnetic lenses can be superior with respect to every one of the five isotropic errors. The disadvantage of anisotropic errors in magnetic lenses is not serious enough to reverse the general judgement.

CHAPTER VII

ELECTRONIC ABERRATIONS

In addition to the geometrical lens errors studied in the previous chapter, some other kinds of errors occur in the electron-optical image formation. These errors are not primarily caused by properties of the lens field, but they are rather produced by some properties of the particular electron beams. Unavoidable inhomogeneities in electron velocity will lead to chromatic aberration. The mutual repulsion of the electrons in sufficiently intense beams will lead to a space-charge error. The de Broglie wave-length of the electron will lead to a diffraction error.

7.1. Chromatic aberration

So far, the electron beams passing through electron lenses have been assumed to consist of electrons of strictly homogeneous velocity. This simplifying assumption, however, is never fulfilled exactly. Electron rays start from a cathode. There, the original range of emission velocities always covers a certain band. The relative band width as compared with the actual electron velocity is, of course, narrowed down as the electron rays are accelerated. But there are more sources of inhomogeneities of electron velocities. For instance, there may be small fluctuations in the accelerating voltage. Or, for example in electron microscopy, inelastic scattering of the electron rays at the atoms of the object leads to a 'straggling' of velocities.

Chromatic aberration in light optics arises from the fact that light of different colour (wave-length) is refracted to a different degree, leading to a glass lens of shorter focal length for blue light than for red. For electrons, the wave-length changes inversely with the velocity. An increase in velocity (shorter wave-length) results in electron optics in a reduced refractive power of the lens. In addition to this, the magnification and also (for magnetic lenses) the rotation will be different for electrons of different velocities.

The small change in focal length caused by a small change ΔV in electron energy (electron-volts) is called the longitudinal chro-

matic aberration Δf_{cr}. Values of Δf_{cr} for given lenses may be read directly from the curves of focal length of mid-focal length as a function of voltage; such curves have been presented in Chapter IV. A lateral chromatic aberration in the Gaussian plane is defined quite analogously to the lateral spherical aberration (cf. Chapter VI) by

$$\Delta r_{cr} = \Delta f_{cr} \Theta, \tag{7.1}$$

where Θ is the slope angle of the ray. Again, in front of the paraxial focus, a disk of least confusion is formed by rays with chromatic aberration.

Chromatic aberration coefficients. In some early papers, the relative variation in focal length $\Delta f_{cr}/f$ is simply taken as equal to the relative variation in $\Delta V/V$. However, Glaser (1940*b*) introduced a proportionality coefficient by writing

$$\Delta f_{cr} = C_{cr}\left(\frac{2\Delta B}{B} - \frac{\Delta V}{V}\right); \tag{7.2}$$

C_{cr} is called the coefficient of chromatic aberration. $\Delta B/B$ is the relative change of magnetic flux density in the lens due to fluctuations of the energizing current. V is the arithmetical mean of electron energies in the object space and in the image space. C_{cr} is frequently measured in terms of the focal length f of the lens. $C_{cr}/f = 1$ applies for weak magnetic lenses. For the strong magnetic objectives of electron microscopes, C_{cr}/f has been found to come down to a value of about 0·7. However, C_{cr}/f seems to depend little upon the shape of the field. When Dosse (1941) investigated for magnetic microscope lenses C_{cr} as a function of h, where $2h$ is the half-maximum width of the magnetic field distribution (cf. § 5·3), he found the minimum of C_{cr} and the minimum of f to occur at the same value of h. (The minimum of spherical aberration was found to occur at a different h-value! (cf. 6.5).) Liebmann (1952*b*) confirmed a minimum of C_{cr} to occur simultaneously with the minimum of f under the same conditions for V_r, B_p and S/R as stated in § 5.4.

C_{cr}/f is larger for electrostatic than for magnetic lenses. In electrostatic lenses, $\Delta V/V$ changes along the electron path, where V is the local value of the electron energy. Indeed, $\Delta V/V$ is much larger in regions of low voltages V than in other parts of the lens with high voltage. Changes in $\Delta V/V$ are to some extent responsible for the relatively large values of C_{cr}/f (cf. Bachman and Ramo, 1943*a*).

Ramberg (1942) found $C_{cr}/f \approx 2$ for all weak electrostatic lenses. With increasing lens power C_{cr}/f is found to decrease in initially accelerating saddle-field lenses only. In all other types of electrostatic lenses, however, C_{cr}/f increases with increasing lens power.

Decelerating two-electrode lenses have the least chromatic aberration coefficients, accelerating two-electrode lenses the largest ones. Initially decelerating saddle-field lenses are intermediate between the latter and the former types. For saddle-field lenses of electron microscopes in which the centre electrode is connected to the cathode, C_{cr}/f is found to be of the order of 4.

A correction of chromatic aberration is not easy, since all ordinary electron lenses have chromatic errors of the same sign. Though electron mirrors have chromatic errors of the opposite sign, their application for chromatic correction meets, according to Ramberg (1949), with serious difficulties (cf. also § 6.5). A focusing method free from chromatic aberration which is of some fundamental interest has been indicated by Gabor (1951). There, however, the axis of the optical system cannot be straight, but it has to be of helical shape. The image projection in this case is obtained by deflexion focusing, such as will be studied in detail in §§ 11.5 and 11.6. There it will be shown that the electrons perform oscillations about the curvilinear axis. Electrons with greater velocities travel along wider circles, and, in case of electrostatic deflexion, they travel nearer to the negative condenser plate so that they are slowed down. Conditions can be chosen under which the period of the above oscillations becomes, within limits, independent of the initial velocity. Hence, the design of systems in which the chromatic focusing error vanishes appears to be possible.

Practical effects of chromatic aberration. These effects will now be discussed for some practically important examples. There are, for instance, two important kinds of chromatic error occurring in electron microscopes. The first kind arises either from fluctuations in the driving voltage, or from fluctuations in the energizing coil currents of the magnetic lenses. This kind of chromatic aberration is eliminated in practice by the use of carefully designed voltage and current stabilizers respectively. In high-resolution microscopes stabilization tolerances of 0·01–0·001 % are required both for voltages and for currents.

The other kind of chromatic error appearing in electron microscopes arises from energy losses of the electrons in the object. This, however, does not seem to affect the resolution; it even appears to increase the contrast in the picture. Different intensities in the picture are produced by elastic and inelastic scattering of the electrons by the different thicknesses of the object. There, a certain fraction of the electrons is scattered outside the physical aperture of the objective. These scattered electrons no longer contribute to the density of the picture elements. A relatively large amount of the electrons, however, is scattered in small angles still remaining inside the physical aperture. Many of these electrons have suffered a noticeable loss of velocity in the scattering process. Now the chromatic aberration of the objective is beneficial in so far as slightly slowed down electrons will no longer be focused on the photographic plate but somewhat nearer to the objective. On the other hand, the chromatic aberration is large enough not to interfere with the definition of the image; it merely produces a slightly darker border around it.

An important source of velocity variations is given by the unavoidable distribution of emission velocities of the electrons leaving the cathode. In case of a thermionic cathode, the velocities are distributed according to the Maxwellian law. If $n(V)\,\mathrm{d}V$ is the fraction of electrons emitted with an initial kinetic energy between eV and $e(V+\mathrm{d}V)$, we have

$$n(V)\,\mathrm{d}V = \left(\frac{e}{kT}\right)^2 \exp\left(-\frac{eV}{kT}\right)\mathrm{d}V, \qquad (7{\cdot}3)$$

where k is Boltzmann's constant (cf. appendix, Table A.3) and T is the absolute temperature of the cathode. This distribution has a maximum at

$$V_m = \frac{kT}{e} = \frac{T}{11{,}600} \quad [\mathrm{eV.}]. \qquad (7{\cdot}4)$$

For example, for a tungsten cathode with $T = 2900°$, $V_m = 0{\cdot}25$ V. Or for an oxide cathode with $T = 1{,}000°$, $V_m = 0{\cdot}1$ V. Taking V_m for the voltage variation ΔV in (7.1) and (7.2) and assuming an electron-microscope objective with $f \approx 3$ mm., with an angular aperture $\Theta \approx 10^{-3}$ and with 50 kV. electron rays, the chromatic disk of confusion is calculated to be below 1 Å., i.e. negligibly small.

It is otherwise, however, in the case of the chromatic error of an

electron gun. There the upper limit of current density that can be focused into a spot is set by the velocity distribution of thermionic emission. The spot is an electron-optical image of a cross-over of rays or of the cathode itself. Thus the radius y' of the spot may be calculated from the radius y of the object (cross-over or cathode surface) by application of Abbe's sine law (1.33) which by squaring leads to

$$\left(\frac{y}{y'}\right)^2 = \frac{(N')^2 \sin^2 \Theta'}{N^2 \sin^2 \Theta}, \tag{7.5}$$

N and N' being the refractive indices and Θ and Θ' the corresponding angular semi-apertures of the beam at the cathode and at the spot respectively. We now multiply y^2 and $(y')^2$ with πI, where I is the emission current which is conserved from the cathode to the target. Then, the left-hand side of (7.5) gives i'/i, the ratio of current densities at cathode and target respectively. At the right-hand side of this equation the squared refractive indices may be replaced by the voltages of the beam according to (1.8). Thus

$$\frac{i'}{i} = \frac{V_A + V_{em}}{V_{em}} \frac{\sin^2 \Theta'}{\sin^2 \Theta}.$$

Now the maximum angular aperture of the emission is given by electrons which leave the cathode surface tangentially, so that $\Theta = \frac{1}{2}\pi$, hence

$$i' = i(V_A/V_{em} + 1) \sin^2 \Theta'. \tag{7.6}$$

This important equation was derived first by Langmuir (1937*b*). According to it, the current density i' in the spot depends on the ratio of anode voltage V_A to the energy V_{em} which corresponds to the effective band-width of thermionic emission velocities. Moreover, i' is proportional to the emission density i and to the squared sine of the angular semi-aperture Θ' of the beam at the spot. It may be concluded that the chromatic aberration is one of the most important limiting factors for the performance of cathode-ray tubes (cf. §§ 9.4 and 12.3).

The chromatic aberration due to the range of emission velocities is even larger for electron-optical arrangements employing photocathodes. While the band-width of the thermionic cathode is practically of the order $\Delta V \approx 0{\cdot}1$ eV., that of a photocathode is at least 0·5 eV. Photocathodes have to be used in the technically important image converters which will be described in § 12.5.

In these instruments a light-optical image is converted by a photocathode into an electron emission image which is projected by an electron lens system on to a fluorescent target. In order to keep the chromatic aberration of an image converter within practicable limits the voltage V_A at the target has to be sufficiently high. For example, for $V_A = 5\,\mathrm{kV}$, $\Delta V/V_A \approx 10^{-4}$. The maximum angular aperture at the cathode is again $\Theta = \frac{1}{2}\pi$, due to the occurrence of tangential emission.

It should be noted, however, that the chromatic error depends very much upon the projecting electron optics. This has been calculated by Henneberg and Recknagel (1935*b*), who have compared the performances of three technically important cases of image converters. Assuming unit magnification they found the following expressions for the disks of least confusion:

(i) $\Delta r = 4l\left(\frac{\Delta V}{V_A}\right)^{\frac{1}{2}}$ for a homogeneous electric field projecting the photoelectrons on to the target.

(ii) $\Delta r = 2l\frac{\Delta V}{V_A}$ for superimposed homogeneous electrostatic and magnetic fields.

(iii) $\Delta r = \frac{2}{3}l\frac{\Delta V}{V_A}$ for a short magnetic field, the electrons being accelerated by a potential rising linearly up to the lens.

In all three cases, l represents the distance between cathode and target. In practice l can be kept very much shorter in case (i) than in cases (ii) or (iii). However, assuming a given l the least disturbance by chromatic aberration occurs in the converter employing the short magnetic lens.

7.2. The use of chromatic aberration in electron-lens spectrometers

The chromatic aberration as a desirable property of electron-optical systems has found an important use for the purpose of sorting electron velocities in 'lens spectrometers'. A first model of this device has been described by Klemperer (1935), and a detailed discussion of it has been published by Deutsch, Elliot and Evans (1944). Spectrometers which utilize the chromatic aberration of solenoidal focusing have been described by Tricker (1924) and by Witcher (1941).

In order to utilize chromatic aberration for separating different electron velocities, an annular slot is set up near the mid-plane of an electron lens, and a small electron source is arranged on the lens axis. Rays of a given velocity will be focused into a small spot which forms the electron-optical image of the source within a given distance from it. Hence rays of a given velocity can be collected by a small aperture subtending the area of the spot. Rays of greater or of smaller velocity are focused on the axis in greater or smaller distances from the source respectively. In the plane of the collecting aperture, however, the rays of these different velocities are spread over annular disks of confusion and are not able to enter the selecting aperture.

In other words, a lens of given focal length with chromatic aberration, collecting hollow, coaxial cones of rays into a paraxial aperture, will select a small interval of momenta between p and $(p+\mathrm{d}p)$. The value of the collected momentum p depends on the power of the lens. The selected p can be varied, say in case of a magnetic lens, by varying the coil current. Hence the number of selected electrons as a function of the coil current provides the momentum spectrum or velocity spectrum of the investigated electron source, and in this way a simple electron lens can be used as an electron spectrometer.

A scheme for such a simple lens spectrometer is shown in fig. 7.1. A cone of electrons emitted from a source S enters through an aperture A. A ring baffle B arranged in the mid-plane of a magnetic lens coils L selects the external part of this cone of rays which is focused by the lens on to the collector aperture C. A tube counter T registers the number of electrons passing through the aperture C as a function of the coil current of the magnetic lens. If the spherical aberration of the lens is negligible, relatively wide cones of rays from the source can be collected.

The fraction of the total emission from an isotropic source that reaches the collector aperture defines the 'collecting power' Ω of the spectrometer.* In the special case of a point source being used in combination with a lens of negligible spherical aberration, the

* In the literature about electron spectrometers, the terms 'transmission' or 'gathering power' or 'light intensity' are sometimes used instead of the term 'collecting power'.

collecting power is equal to $\Omega_0/4\pi$, where Ω_0 is the solid angle subtended by the rays at the source, i.e.

$$\Omega_0 = 2\pi \int_{\theta_1}^{\theta_2} \sin\Theta \, d\Theta = 4\pi(\cos\Theta_2 - \cos\Theta_1) \approx 2\pi(\Theta_1^2 - \Theta_2^2), \quad (7{\cdot}7)$$

if the emission selected by the baffles is enclosed between the cones of semi-vertical angles Θ_1 and Θ_2.

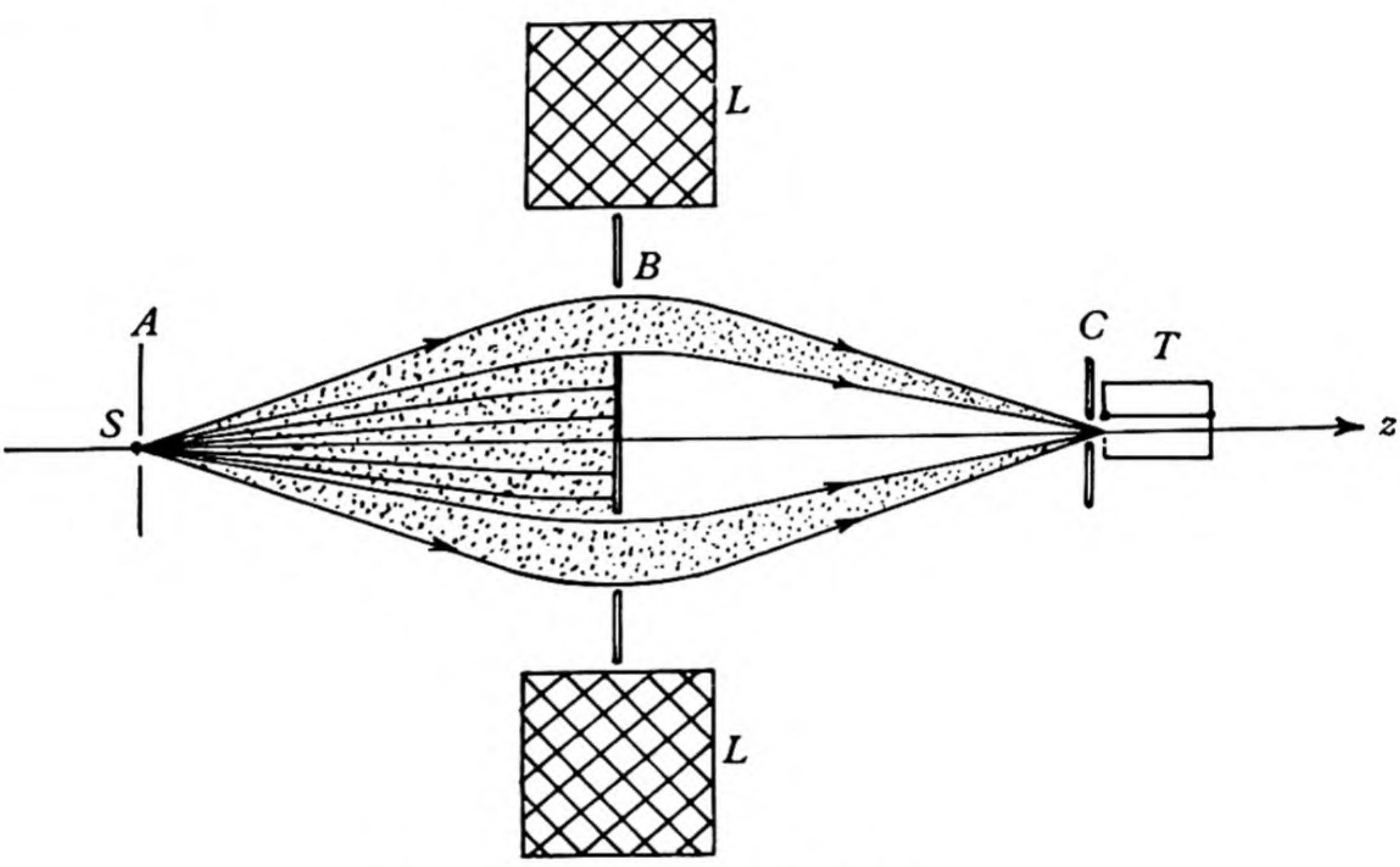

Fig. 7.1. Lens spectrometer.

If the collecting power Ω for an extended source is expressed as the percentage of the total emission of rays that reaches the collector, it can be used for defining an 'effective solid angle' or 'solid angle of acceptance' $\Omega_0 = 4\pi\Omega$, which may be measured in steradians. For instance, a collecting power of 1 % corresponds to an effective solid angle $\Omega_0 = 4\pi \times 1/100 = 0{\cdot}126$ steradian.

A great collecting power is always desirable, expecially if spectra from weak sources have to be investigated. If a point source is used with an aberration-free lens, the maximum semi-vertical angle Θ is limited by the aperture and by the power of the available electron lens only. Now, with an extended source of given emission density, the collected current can be increased by increasing the source area. On the other hand, the selected angular interval $d\Theta$ and hence the collecting power increases with increasing

window area. The momentum spread of the collected rays, however, increases both with source and with window area. This may be shown now for the example of a symmetrical spectrometer with a very narrow ring aperture in the mid-plane. The simple geometrical discussion is due to Cosslett (1940).

In fig. 7.2 rays from an extended source S at O are focused by an aberration-free lens and collected by an extended window in the diaphragm W. The slowest electrons to pass through the window, cross over at O_2 and A_2, the fastest electrons cross over at O_1 and A_1.

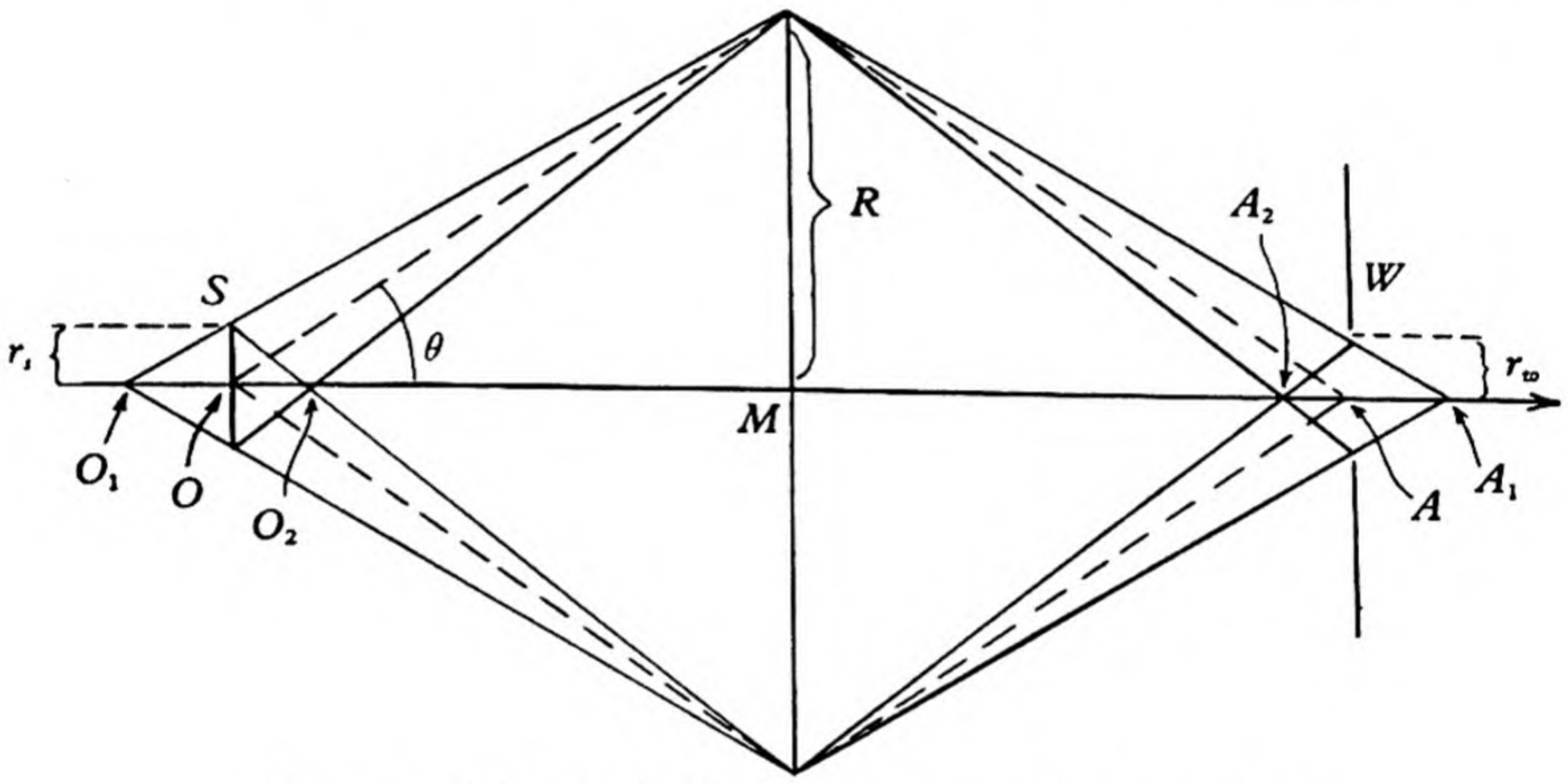

Fig. 7.2. Geometric limit to the resolving power of a lens spectrometer.

Let the radii r_s and r_w of the circular source and window respectively be small compared with the radius R of a ring aperture in the mid-plane M of the thin lens by which the mean semi-vertical angle Θ of the transmitted rays is defined. From similar triangles

$$\frac{O_1O}{MO} \approx \frac{O_2O}{MO} = \frac{r_s}{R}, \tag{7.8}$$

and

$$\frac{A_1A}{MA} \approx \frac{A_2A}{MA} = \frac{r_w}{R}. \tag{7.9}$$

Now, the focal length f of the thin lens, and hence the object-to-image distance OA are, according to § 5.2, proportional to the square of the momentum p of the rays, i.e.

$$OA = 4f \sim p^2. \tag{7.10}$$

Hence, on differentiating,

$$\frac{\Delta OA}{OA} = \frac{2\Delta p}{p}. \tag{7.11}$$

Adding (7.8) and (7.9) and comparing with (7.11) gives

$$\pm\frac{\Delta p}{p} = \pm\frac{r_s + r_w}{4R}. \tag{7.12}$$

It can be shown that if a solenoid is used instead of the short lens, $\Delta p/p$ will be twice as large as the value given by (7.12), since for the solenoid a proportional relationship, (5.5), holds between OA and p instead of (7.10). For thick lenses $\Delta p/p$ will be of an intermediate value between the limits assigned to the thin lens and to the solenoid.

$\pm\Delta p$, the total momentum spread of electrons admitted to the collector at a given, constant coil current, could also be obtained as the total base width of a 'transmission curve'. Such a curve gives the intensity distribution obtained with a monochromatic emission by varying the coil current, i.e. this curve shows the collector currents against the coil currents measuring apparent momenta. A relative momentum range $\Delta p/p$ which indicates the least difference of momenta which can still be resolved is called the 'resolution', and its reciprocal $p/\Delta p$ is called the 'resolving power'.*

In practical spectrometry, the available intensity generally sets a limit to that increase in resolving power which can be obtained by reduction of the aperture of a given apparatus. For instance, for a lens spectrometer with a source of negligible size, the resolving power is, according to (7.12), inversely proportional to the radius of the collecting aperture, namely, $(p/\Delta p) \sim 1/r_w$, but the collecting power is $\Omega \sim r_w^2$, hence

$$\left(\frac{p}{\Delta p}\right)^2 \times \Omega = C, \tag{7.13}$$

where C is a constant for a given spectrometer, characterized by a fixed object-and-image distance and by a fixed baffle arrangement. C can be increased, for example, by using a lens which utilizes a greater solid angle of rays. The greatest obtainable resolving power

* In practice, Δp is obtained as the half-maximum width of the experimental transmission curve. However, a change in momentum of less than $0{\cdot}1\Delta p$, can frequently still be detected.

will always be required simultaneously with greatest possible collecting power. Hence, the value of C can be considered to be a figure of merit for a particular type of lens spectrometer.

A most important limitation to this figure of merit C of (7.13) is given by the spherical aberration of the focusing lens. This may be explained with the help of fig. 7.3, showing a meridional cross-section through some selected bundles of rays emitted from a point source O. Let the rays (1) contain electrons of momentum p_1 travelling along the surface of a cone of semi-vertical angle Θ_1. These

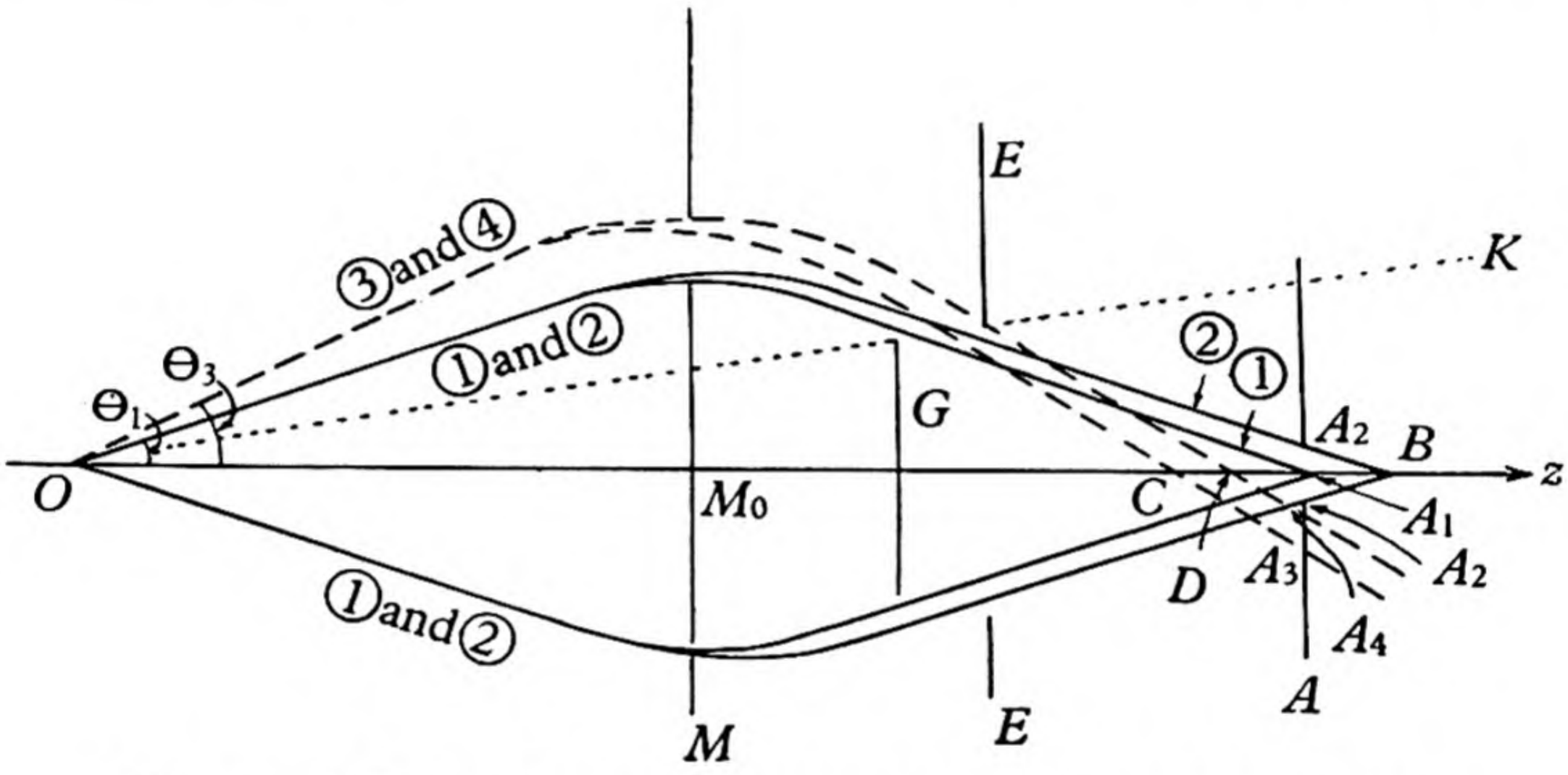

Fig. 7.3. Effects of spherical aberration on a lens spectrometer. Hole collector and ring selector.

rays pass the mid-plane M of the lens and are focused on the lens axis (z) at a point A_1 which is the centre of an aperture in a diaphragm A. Let another bundle of rays (2) be emitted at the same angle Θ_1 as the rays (1) but with slightly greater momentum $p_2 = p_1 + \Delta p$. Hence they will cross the z-axis at a point B slightly farther removed than A_1. These rays (2) will reach the diaphragm A at a circle through A_2 by which the radius ($A_1 A_2$) of the aperture in A is defined. Again, electrons of emission angle Θ_1 but with momentum ($p_1 - \Delta p$) would cross over before reaching A_1, but they too would pass the plane of the diaphragm A at the above circle through A_2.

Now consider the bundles of rays indicated in fig. 7.3 by (3) and (4). Both bundles start along the same conical surface of semi-vertical angle Θ_3, and they may have again the above momenta p_1

and $p_1+\Delta p$ respectively. If spherical aberration is non-existent, the positions of the foci are independent of the emission angle Θ, and all rays within the interval of momenta $p_1 \pm \Delta p$ would again pass through the aperture in the diaphragm A.

In presence of spherical aberration, however, the focal length of the system depends upon the slope angle Θ of the rays. Hence the rays (3) and (4) are now shown to cross the z-axis at the points C and D respectively, and to reach the diaphragm A at the respective distances AA_3 and AA_4 off the axis.

The bundles represented by (3) and (4) are intercepted by the diaphragm and do not pass the collector aperture of radius A_1A_2; hence it can be seen that the collecting power Ω for a fixed interval $(p_1+\Delta p)$ of momenta must be very much smaller than the solid angle Ω_0 defined according to (7.7) by the range of emission angles between Θ_1 and Θ_3. On the other hand, rays emitted at the angle Θ_3 with momenta somewhat greater than $(p_1+\Delta p)$ would cross the axis at somewhat increased focal distance and thus would be able to pass the collecting aperture in the diaphragm A. According to these considerations a natural limitation appears to be set to the design of lens spectrometers by an unavoidable amount of spherical aberration inherent in every electron lens.

A quantitative relationship between the resolving power, the chromatic aberration and the spherical aberration of an electron lens can be obtained by the following argument which is due to Grivet (1950*b*): Let a source be assumed to emit two monochromatic electron energies V and $V+\Delta V$ of equal intensities. Each of these energies will be focused in a separate image point surrounded by a disk of confusion of radius Δr_s due to spherical aberration. Both image points will be surrounded by electrons of the other energy group (differing by ΔV from the focused energy) and spread over a disk of radius $\Delta r_{cr} = x$ due to chromatic aberration. Half-way between the two image points both electron energies produce disks of confusion of radius $\Delta r_{cr} = \frac{1}{2}x$. Assuming superposition of the aberrations, the radius of the total disk of confusion will be proportional to

$$\frac{\Delta r_{cr}+\Delta r_s}{\Delta r_s}, \tag{7.14}$$

and the electron current through a small aperture ($A_2'A_2$ in fig. 7.3)

will be inversely proportional to the square of this expression (7.14). The special case

$$\Delta r_s = \Delta r_{cr} \tag{7.15}$$

leads to the following conclusion: If one of the images is focused on the aperture, the electron current due to the two groups received will be $\frac{1}{2}^2 + 1^2 = 1{\cdot}25$. If the lens is adjusted to focus in such a way that the collector aperture is half-way between the two above images, the current received would be $1/1{\cdot}5^2 + 1/1{\cdot}5^2 = 0{\cdot}89$. Hence the dip in the spectrum between the two monochromatic lines would be $0{\cdot}89/1{\cdot}25 = 0{\cdot}71$. In this case the two spectral lines would be distinctly separated. Hence the resolving power of the lens spectrometer is determined by conditions which are reached when (7.15) is approximately fulfilled.

Great improvements in the design of lens spectrometers have been made after Frankel (1948) showed the advantages of using a 'ring collector' in front of a relatively wide aperture in the diaphragm A shown in fig. 7.3. Already Witcher (1941) recognized that the bundles of rays (1), (2), (3) and (4) form a ring-shaped cross-over before they reach the axis. All these rays which are selected by an annular slot in the baffle at the mid-plane M can be collected by an annular slot enclosed by the two diaphragms E and G as shown in fig. 7.3. By the use of this ring collector, the collecting power appears to be much increased without a corresponding loss in resolving power.

For the practical design of the ring collector, Frankel recommended that its defining edges formed by E and G should lie on a cone (indicated in the figure by the dotted line K) coaxial with the lens and with its vertex at the source, so that no straight rays (e.g. γ-radiation, etc.) can pass the slot. For this purpose, the inner diaphragm G has been placed closer to the source than the outer diaphragm E.

Let the emission from a point source be selected by an aperture subtending a relatively small angular interval which is enclosed between the two cones of semi-vertical angle Θ and $\Theta + \Delta\Theta$. The corresponding solid angle is then given by

$$\Omega_0 = 2\pi \sin\Theta \, \Delta\Theta. \tag{7.16}$$

Hence for fixed $\Delta\Theta$, the collecting power of the lens spectrometer

increases with increasing Θ. On the other hand, position and sharpness of the ring cross-over depend upon Θ. For fixed Ω, an optimum Θ can be determined for which the sharpness of the ring cross-over is best so that the collecting ring aperture can be made of minimum width. In this case, the resolving power reaches a maximum. For any lens spectometer, this optimum ($\Theta_{opt.}$) can be found experimentally, for instance, by observing collector currents while a movable baffle arrangement is varied, or in another way, by tracing cathode rays with a sliding fluorescent target, or by tracing β-rays with photographic plates. Alternatively, $\Theta_{opt.}$ can be determined graphically or numerically by ray tracing through the field of the lens.

For the solenoidal spectrometer with homogeneous magnetic fields, the theory of the ring cross-over is simple enough to be attacked analytically, and Dumond (1949) and Persico (1949) have worked out details of it. The electron paths in the rotating meridional rz-plane (cf. § 5.1) are sinusoids. The intersection of two paths starting at a point source at slightly different slope angles Θ and $\Theta + d\Theta$ respectively, occurs when $(\partial r/\partial\Theta) = 0$. Among such angles, a particular $\Theta_{opt.}$ is selected in such a way that for small deviations on either side thereof the largest possible solid angle at the source results in the smallest possible inhomogeneity of momentum. In this way, the optimum angle of emission from a point source is found to be $\Theta_{opt.} = 45°$. The optimum, however, is not very pronounced, and in practical solenoid spectrometers much smaller angles (10–30°) have been used on account of finite-source dimensions, for reasons of economy in weight of copper wire and to save energizing power.

Detailed theoretical discussions on the ring cross-over in arbitrary magnetic lens fields have been given by Verster (1950) and by Grivet (1950*b*, 1951). There, formulae can be found for the position and for the thickness of the ring cross-over and for resolving and collecting powers as functions of the coefficients of spherical and chromatic aberrations and of the angular apertures of rays.

The gain in collecting power obtained by using a ring-selector aperture can be estimated according to Grivet (1950*b*) in the following manner: The collecting power obtained with an ordinary

small aperture of semi-vertical angle of rays, α, is, according to (7.7), given by

$$\Omega = \frac{\Omega_0}{4\pi} = \frac{1-\cos\alpha}{2} \approx \frac{\alpha^2}{4}. \tag{7.17}$$

The collecting power with a ring selector is, according to (7.16), given by

$$\Omega_r = \frac{\sin\Theta\,\Delta\Theta}{2}. \tag{7.18}$$

Now, if equal magnitudes are chosen for α and $(\Delta\Theta)/2$, a gain of

$$\frac{\Omega_r}{\Omega} = \frac{\sin\Theta}{\alpha} \tag{7.19}$$

can be expected. Take, for instance, a spectrometer of angular semi-aperture $\alpha = 8°$ which, according to (7.17), has a collecting power

$$\Omega = 0{\cdot}14^2/4 = 5 \times 10^{-4}.$$

A spectrometer with ring selector subtending a semi-aperture $\Delta\Theta = \alpha$ at an initial slope angle of rays $\Theta = 45°$ could be expected to show an improvement in collecting power by a factor

$$\frac{\Omega_r}{\Omega} \approx \frac{\sin 45°}{8°} \approx 5.$$

These relatively high gains, however, apply to the use of point sources only. With increasing size of the source, the advantage in having a ring selector is rapidly reduced.

If extended sources have to be used, e.g. in investigations of preparations of low-emission density, an optimum source diameter can be determined, for which the product of source area and collecting power, i.e. the so-called 'luminosity' (cf. § 12.7), reaches a maximum. This optimum source diameter is found to be of the order of four times the width of the ring selector (cf. Grivet, 1950*b*). With this optimum-source diameter the resolving power is about five times smaller than with a point source. Even with large sources, however, the use of the ring selector always definitely improves the resolving power at a given collecting power.

For instance, Keller, Koenigsberg and Paskin (1950) studied the ring cross-over of a thin lens spectrometer with extended sources. They determined a set of trajectories by numerical integration of

the equations of motion. At a given resolution, a comparison between collecting powers of ring selector and of ordinary circular hole collector showed a superiority of the ring-selector instrument by a factor two for the extended source. Again, Graham and Klemperer (1952) investigated experimentally the use of the ring selector aperture for a lens spectrometer with relatively small source and window and with initial beam apertures between 8° and 12°. Under otherwise similar conditions the best gain in resolving power effected by the ring selector was 75 %.

The resolving power of every lens spectrometer (with or without ring selector) is increased at a given collecting power whenever the spherical aberration of the lens is reduced. For this reason, Siegbahn (1946) developed his spectrometer with the iron-shielded dip-field lens which we described in § 6.5. Other authors have shown the merits of spectrometers with dip-fields produced by two separate lenses spaced by about 3–6 times the half-maximum width of their field distributions (cf. §§ 6.5 and 12.7).

The introduction of ring-selector apertures in these dip-field spectrometers has resulted in a further increase in resolving power.

In a spectrometer by Slätis and Siegbahn (1949) a coil with closed iron shield produces a dip-field with two maxima which act like two separate lenses. The source is placed very near to the focus of the first of these lenses, and an angle of emission is chosen of such value (40–50°) that an annular focus is formed in the median plane between the two field maxima. The principal rays of the annular bundle are parallel to the lens axis when they pass the median plane. The annular slot in this plane thus selects a given electron momentum. As far as momentum sorting is concerned, the second lens generally can be disregarded, as it serves only to concentrate the rays towards the small collector aperture. However, according to Grivet (1951), a further increase in resolving power can still be obtained by arranging a supplementary ring diaphragm in front of the collector.

The theory of the dip-field spectrometer consisting of two thin lenses with a ring cross-over between the lenses has been worked out by Bothe (1950 *a*, *b*). The geometry of the rays, which is somewhat similar to that in Slätis and Siegbahn's spectrometer, is shown schematically in fig. 7.4. A point source J is placed in focal

distance from the thin lens L, and the image point J' is projected in focal distance from the thin lens L'. If the lenses L and L' are assumed to be free of spherical aberration, the rays between L and L' would be parallel to the axis of the system as indicated by the broken line. The geometry of rays for lenses with spherical aberration is shown in solid lines. The rays of larger aperture now become convergent, and the rays of smaller aperture become divergent between L and L'. An annular aperture stop B can be introduced at the cross-over of the rays. Apparently very high resolving power and very high collecting power can be obtained with a ring diaphragm and two simple uncorrected electron lenses. It should be mentioned, however, that the advantages of such an arrangement are much reduced when extended sources are em-

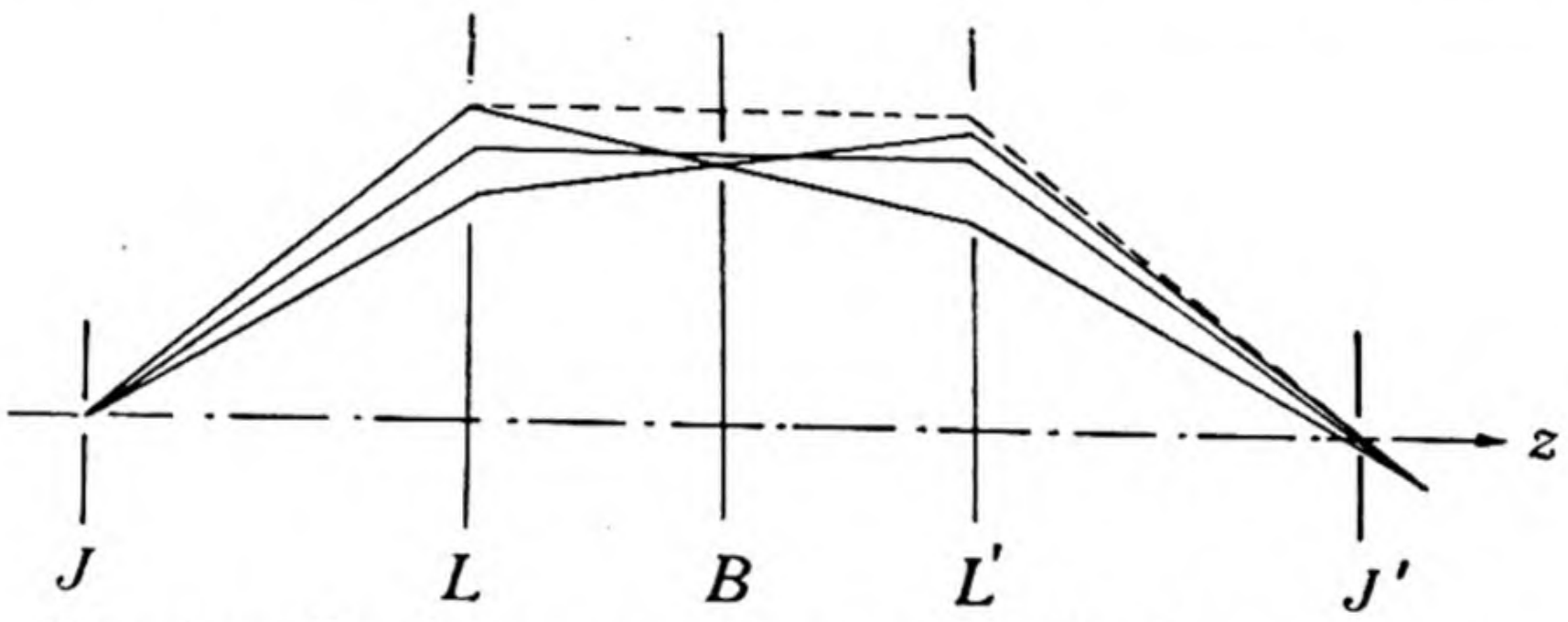

Fig. 7.4. Double lens spectrometer with ring cross-over.

ployed. Also, the whole system is expected to be extremely sensitive to alignment errors and to disturbances by spurious fields.

A highly sensitive velocity analyser which makes use of the chromatic aberration of the initially decelerating saddle-field lens (cf. § 4.5) has been described by Möllenstedt (1949, 1951). The chromatic error in such lenses is relatively large for extreme, marginal rays. For instance, in fig. 7.5 there is shown an einzel lens with two outer electrodes L_o connected to anode potential (say $V_o = +30$ kV.) and an inner electrode L_i at cathode potential ($V_i = 0$). Initially parallel rays 1, 2, 3, ... are seen to enter the lens with increasing semi-aperture y. These rays pass the lens along curved paths as shown in the drawing. The rays with the larger initial aperture cross the axis once or even twice before they reach the target T; they come relatively close to the decelerating inner electrode L_i and hence suffer relatively large decelerations leading to a large chromatic error. As will be shown in § 12.7, velocity analysers with einzel

lens belong to a class of spectrometers with highest resolving power. In practical instruments, einzel lenses with line-focus (cf. Chapter X), i.e. lenses with slots rather than with circular apertures, are used. The aperture of the incident beam is defined by a very fine stop-slot (5 μ wide) parallel to the lens slots but displaced sideways off the lens axis. A similar scheme for velocity analysis of high resolving power with a magnetic microscope objective has been described by Lenz (1951 *b*). The source is arranged off the axis and closer to the lens than one focal length so that a ring focus (as in fig. 7.4) is obtained, a part of which is on the axis and is magnified by a projector lens.

Another scheme of a lens spectrometer based on a chromatic aberration effect still deserves some attention. There, the image of

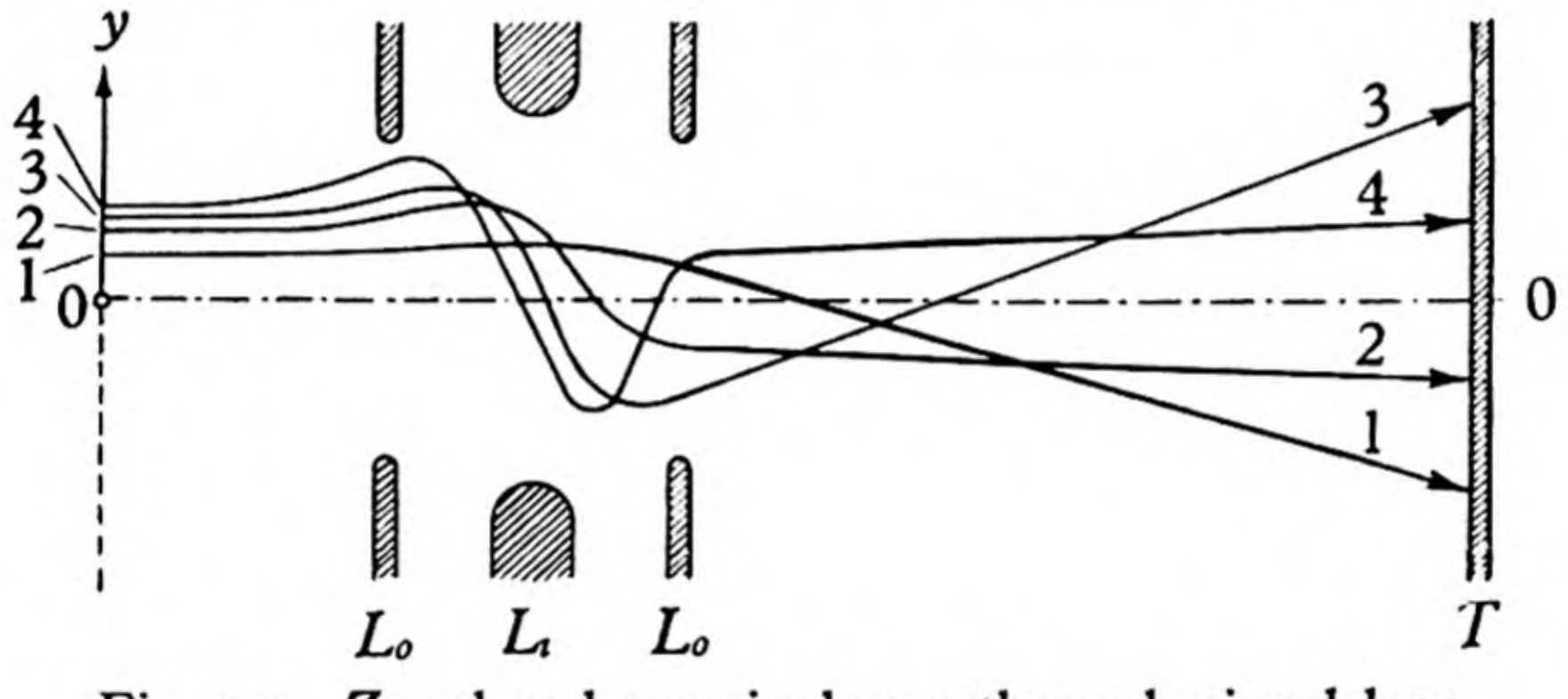

Fig. 7.5. Zonal and marginal rays through einzel lens.

a line source is projected into a slit window by a thick magnetic lens with substantial image rotation (cf. § 5.3). The selection of momenta is given by the angle of twist between line object and image which both extend perpendicularly to the lens axis, the twist angle being proportional to the electron momentum. The method has been tried originally by Siday (1942); more recently Butt (1949) and Georgesco (1949) have pointed out that the scheme should have considerable advantages for spectrometers with long narrow fields of little aberration if line sources of a length-to-width ratio of several hundred could be employed.

7.3. Relativistic aberration

A particular type of chromatic aberration is the relativistic aberration that is due to the variation of the mass of the electron with its velocity. The focal length of a lens for relatively slow electrons, say up to some kilo-electron-volts, depends on the ratio

of voltages applied to the electrodes only, it does not depend on the absolute values of these voltages. However, it has already been pointed out in §§ 4.2 and 4.6 that even for a fixed voltage ratio, the focal length of a lens starts to change when the electron velocities become so great that relativistic increases in electron mass can no longer be neglected. Now, this relativistic influence on the focal length of an electron lens is of great practical interest in connexion with the chromatic aberration of saddle-field lenses. In particular, the univoltage lenses described in § 4.6, in which an intermediate electrode is connected to the potential of the cathode, have negligible ordinary chromatic aberration for electrons up to some kilo-electron-volts travelling near enough to the axis. Since for relatively slow electrons the focal length of a univoltage lens is independent of the voltage of the external lens electrodes it has even been possible to project an image of the cathode by applying a.c. voltage to the external electrodes.

The great advantage of using such univoltage lenses in electron microscopes is based on their being fairly insensitive to voltage fluctuations. Somewhat earlier (§ 7.1) it has been pointed out that the accelerating voltage in magnetic-electron microscopes has to be stabilized within a fraction of 10^{-4} or 10^{-5} in order to avoid a loss in definition due to chromatic aberration. It will be shown in § 12.6 that the voltage in an electrostatic microscope using univoltage lenses need not be stabilized to such a high degree, but nevertheless it needs some stabilization, since the electron velocities are so great that relativistic effects can no longer be disregarded.

The relativistic aberration of einzel lenses (cf. § 4.6) has been studied in detail by Ramberg (1942). He derived the following expression for the relative change in focal length f which applies for large image distances:

$$\Delta f = C_{\text{rel.}} \Delta V, \tag{7.20}$$

where ΔV is the voltage fluctuation and $C_{\text{rel.}}$ is a constant for a given lens. The coefficient $C_{\text{rel.}}$ is of the order of $7 \times 10^{-7} V_o f$ for weak, initially decelerating einzel lenses, in which the potential V_i of the intermediate electrode is not much different from the potential V_o of the two outer electrodes. If the power of the einzel lens is gradually increased by reduction of the potential V_i towards cathode potential, the relativistic aberration constant $C_{\text{rel.}}$ gradually

decreases. Eventually $C_{\text{rel.}}$ reaches a value of about $2{\cdot}5 \times 10^{-7} V_o f$ when V_i reaches cathode potential, i.e. for the univoltage lens.

Equation (7.20) fixes an upper limit for the yoltage fluctuations ΔV that can be tolerated in an electrostatic electron microscope with a univoltage objective. Let the resolution of a certain distance Δr be required, Δr being the radius of the disk of confusion at the object side. For large image distances the permissible fluctuation in focal length is given by $\Delta f = \Delta r/\Theta$, where Θ is the semi-aperture of the focused rays. For example, a semi-aperture $\Theta = 10^{-3}$, a focal length $f = 4$ mm. of the objective and a required resolution of 10 Å. leads with (7.20) to a tolerance of 1 keV. for the voltage fluctuations.

Some technical importance must be attributed to the fact that the relativistic and the ordinary chromatic aberration coefficients are of opposite sign. Le Rutte (1948) pointed out that the two aberrations can be made to cancel one another. For this purpose it is only necessary to apply a slight bias to the inner electrode of the einzel lens so that just the right amount of ordinary chromatic aberration is introduced.

7.4. Space charge error

The optics of a given electron lens is changed sometimes entirely by space-charge effects if it is traversed by an electron beam of great current density. In this way the cardinal points can be displaced and large third-order aberrations can be introduced. In principle it should be possible to distribute space charges in such a way that the properties of the lens are not altered. It should even be possible to correct geometrical lens errors by introducing space charges. Such theoretical possibilities still hold some hopes for future development. Practical electron optics, however, will have to develop still a long way before such beneficial effects of space charge could be realized. As a matter of fact space charge seems at the moment only to upset the correct image formation. The following empirical conclusions may be mentioned in this connexion:

(i) Spherical aberration in a beam of electron rays, focused by an electron lens, appears to increase with increasing beam current as a result of the space charge carried by the beam itself (cf. § 8.3).

(ii) Electron clouds circling about the lens axis have been

injected into magnetic electron lenses in certain experiments which have been started by Marton and Reverdin (1950) with the object of correcting aberration. Such clouds, however, seem to have on electron rays a similar effect to that which frosted glass has on light rays.

(iii) If an electron image from a thermionic cathode surface is to be projected by means of an electron lens, the emission current must be saturated. If, however, the emission density is raised, say by an increased cathode temperature, so that the emission current become space-charge limited, the image disappears, giving way to a diffuse brightness on the target.

Because of such disturbing effects it would be appropriate to deal with space charges here under the heading of electron-optical errors. However, a detailed discussion of 'electron optics and space charge' is given in Chapter VIII, and it seems to be preferable to postpone the discussion of space-charge errors until the general principles and effects of space charge have been expounded.

7.5. Diffraction error

So far a treatment of electrons as charged corpuscles, moving through space according to ballistic laws and being deflected by fields according to electromagnetic laws, has been found to be quite adequate for the determination of electron trajectories. Alternatively the trajectories could be obtained by the geometric-optical approach, studying the refraction of rays at surfaces of given refractive indices. It may be pointed out now that the wave nature of the electron has to be taken into account as soon as electron rays are confined to apertures which are small enough to be comparable with the wave-length of the ray.

From light optics it is well known that two points of the object space will be projected as separate points into the image space only if their mutual distance exceeds a certain minimum which is a function mainly of the wave-length of the rays producing the image.

The wave-length λ of an electron ray is given by

$$\lambda = \frac{h}{p} = \frac{h}{eB_e r_e} = \left(\frac{h^2}{2em_0 V} \frac{1}{1 + \frac{e}{2m_0 c^2} V} \right)^{\frac{1}{2}} \tag{7.21}$$

$$\text{or} \qquad \lambda = \frac{0{\cdot}4135 \times 10^{-14}}{B_e r_e} = \frac{12{\cdot}26}{V^{\frac{1}{2}}} \frac{10^{-10}}{(1 + 0{\cdot}977 \times 10^{-6} V)^{\frac{1}{2}}},$$

where h is Planck's constant, $p = mu$ is the momentum of the electron, $B_e r_e$ the electron momentum and V the electron energy (electron-volts) (cf. Appendix, Tables A. 3 and A. 4).

If a train of waves passes through an array of narrow apertures, it will be diffracted into a sequence of intensity maxima and minima. According to elementary wave theory the first diffraction maximum is found at a deflexion angle α determined by the wave-length λ of the rays, by the refractive index N at the entrance relative to that at the exit side of the apertures, and by the mutual distance D of these apertures, namely, by

$$N \sin \alpha = \frac{\lambda}{D}. \tag{7.22}$$

The diffracted rays emerging from the apertures can be used for the formation of an image if, by a lens, they are projected into the image points. Now practical electron lenses suffer from spherical aberration which grows with the lens aperture (cf. §6.3). To keep this aberration within practicable limits, the lens aperture has to be restricted by a stop. Abbe showed in 1874 that no image could be obtained so long as all the diffraction maxima were excluded from the image-forming beam by the use of too small an aperture stop. The first maximum at least must be admitted in order to give a recognizable image, and all the maxima are theoretically necessary for the formation of a perfect image. Therefore, if the aperture stop admits from the object to the lens a bundle of rays of semi-aperture α, the minimum distance of two object points which will be resolvable in the image should be of the order of D in (7.22), λ being the wave-length of the image-forming rays. The expression at the left-hand side of (7.22) which is characteristic of the resolving power is known as the 'numerical aperture'.

In electron-optical practice, the diffraction error is important only for electron microscopes of high magnification. There, the object is nearly in the focal plane of the lens, the refractive index is the same in the object space and in the image space ($N = 1$) and the angular aperture α_c of the rays is so small that

$$\sin \alpha_c \approx \alpha_c \approx \frac{y_c}{f},$$

where y_c is the aperture radius of the beam at the lens and f is the focal length of the lens. Hence (7.22) may be written

$$D \approx \frac{\lambda}{\alpha_c} = \frac{\lambda f}{y_c}. \tag{7.23}$$

The resolved distance D is reduced to half the value of (7.23) for oblique illumination, as it is usually found in electron-microscopic objectives (see below, fig. 7.6). For any kind of illumination the resolved distance should, furthermore, be reduced as the ratio of condenser aperture to objective aperture decreases (cf. Hopkins and Barham, 1950). In practical electron microscopy the objective aperture ($\alpha_c+\alpha_D$ in fig. 7.6) is of the order of five times greater than the condenser aperture, due to the diffraction in the object. This would lead to a reduction of D in (7.23) by a factor 0·8. Again, D may be smaller than in (7.23) if the object can be treated after Scherzer (1939) as self-luminous. This would be the case if the electron wave becomes incoherent (as Scherzer argues) after its passage through a few atomic layers. The existence of well-defined Fresnel fringes (cf. the end of this section), however, speaks against this argument, since these fringes should only occur with a coherently illuminated object. Hence, for all practical purposes (7.23) can be regarded as giving a sufficiently close estimate for the radius of a disk of confusion due to diffraction.

A scheme of rays as it occurs, for instance, in the first stages of a highly magnifying electron microscope is shown in fig. 7.6. In this figure the positions of the electron source, condenser lens, object, objective lens and intermediate image are indicated. Bundles of rays leaving the source with the small semi-divergence α_s are focused by the condenser on to the object, the angle of convergence α_c being determined by α_s and by the mutual distances of source and object from the condenser lens. The rays passing through the object form a diffraction pattern which is focused by the objective, thus producing the image. As shown in fig. 7.6, the numerical aperture of the electron microscope depends upon α_c, the angle of convergence of rays from the condenser. To α_c has to be added α_D, the angle of diffraction of the electron waves at the object, but $(\alpha_c+\alpha_D)$ is still very much smaller than the angle α_L which is subtended by the free aperture of the objective lens. Since the angle α_c is very small, the electrons transmitted through the object are nearly parallel.

The wave-length of the rays in a highly magnifying electron-microscope objective (60 kV. electrons with 5×10^{-12} m. wave-length) is by a factor 10^5 smaller than the wave-length of the visible

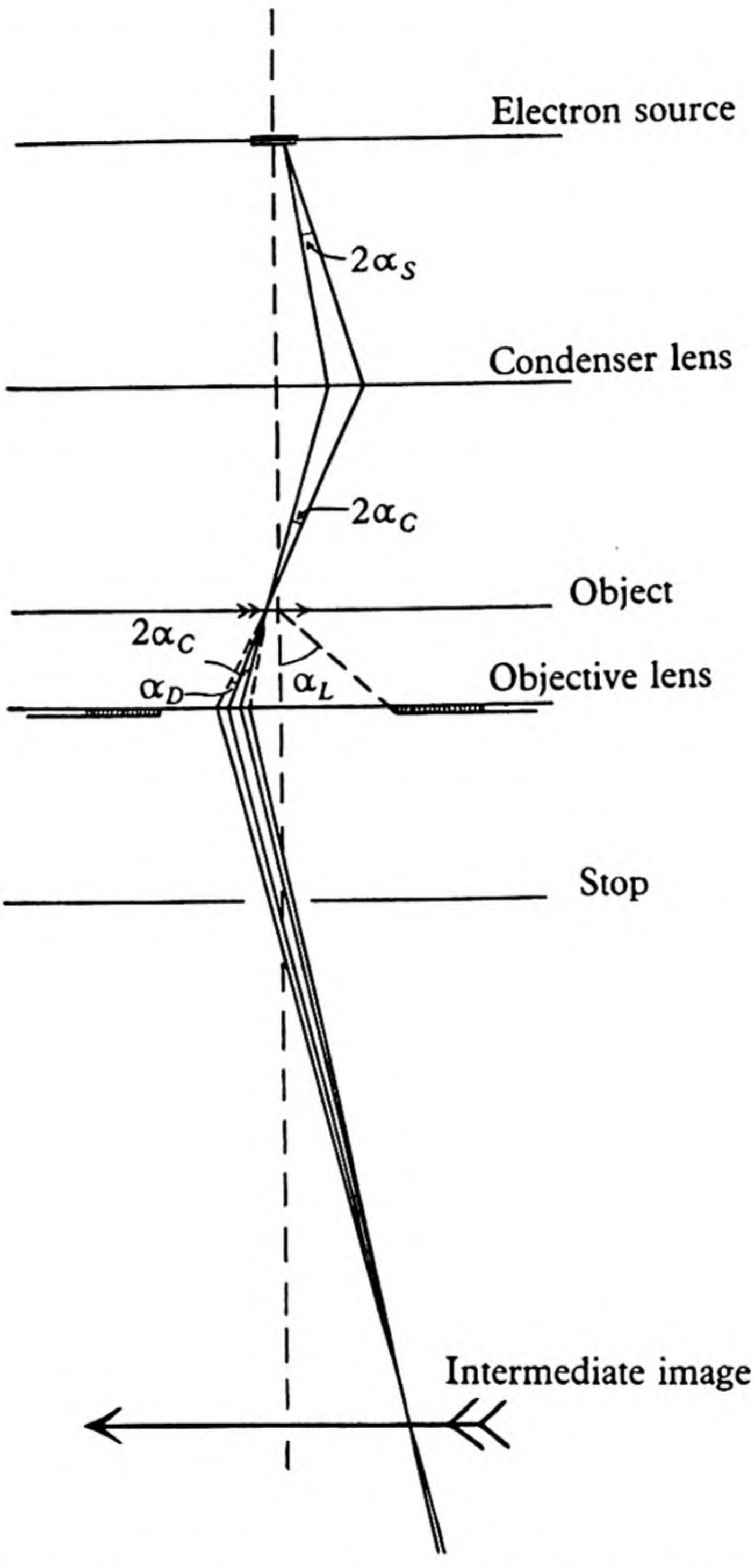

Fig. 7.6. Formations of the image in an electron microscope.

light used in glass microscopy. However, the least resolved distance in the best electron microscopes is only by a factor 10^2 smaller than that resolved in a good oil-immersion light-microscope. The

gain in resolving power obtained with the electron microscope is relatively small because (cf. (7.23)) the numerical apertures used are of the order of $\alpha_c \approx \frac{1}{1000}$ only. They are minute as compared with the numerical apertures to which we are accustomed in light microscopy, since these are of the order of one unit (1·4 for oil-immersion objectives). Another diffraction error may be mentioned in this section. Since the beginning of electron microscopy wide contour lines following the outlines of images have often been observed, especially when the picture was slightly out of focus. Boersch (1940, 1943) and Hillier (1940) interpreted these lines as Fresnel diffraction fringes due to the edges of the object. By their dependence on the focusing of the image these fringes can easily be distinguished from any real surface structures of the object.

7.6. Combination of aberrations

The resolving power of an objective lens is determined by all the limiting aberrations which have been discussed in this and in the previous chapter. However, most of the aberrations can be kept small enough to be neglected in comparison with the three most important errors. These errors are:

(i) the diffraction error D given by (7.23),

(ii) spherical aberration Δr_s given by (6.5), and

(iii) chromatic aberration Δr_{cr} given by (7.1).

These three quantities are radii of disks of confusion in the Gaussian image plane; and the question arises how they are to be added up to yield the least resolvable separation. According to Born (1933) the resulting error S can be calculated to a first approximation by superimposition of the separately calculated intensities, combination terms being neglected. Hence

$$S = D + \Delta r_s + \Delta r_{cr}. \tag{7.24}$$

According to Ardenne (1938) the intensities in the three disks can be assumed to have bell-shaped distributions which should be added as error functions, so that

$$S = \sqrt{\{D^2 + (\Delta r_s)^2 + (\Delta r_{cr})^2\}}. \tag{7.25}$$

Now, the diffraction error D and the spherical error Δr_s vary in opposite senses with the aperture. Thus there will be an optimum

angular semi-aperture $\Theta_{\text{opt.}}$ for which the combined effect reaches the minimum confusion $S_{\text{min.}}$. This minimum can be obtained by substituting $D = \lambda/\Theta$ (see (7.23) and $\Delta r_s = C_s\Theta^3$ (see (6.5*a*)) into (7.24) or (7.25), differentiating with respect to Θ and taking $\mathrm{d}S/\mathrm{d}\Theta = 0$. Experimental results on the resolving power seem to indicate that the actual optimum aperture is slightly greater than that one calculated either from (7.24) or from (7.25).

For practical purposes, the estimation of the minimum combined confusion may be simplified. It seems quite adequate to neglect Δr_{cr} and to assume that $S_{\text{min.}}$ is obtained when D and Δr_s are of the same order of magnitude. Hence

$$D \approx \Delta r_s \approx S_{\text{min.}}/\sqrt{2}.$$

Substituting again from (7.23) and (6.5*a*) and introducing the approximate equation for the wave-length $\lambda = 12{\cdot}2 \times 10^{-10}/\sqrt{V}$ (cf. (7.21)), one obtains for the optimum angular semi-aperture

$$\Theta_{\text{opt.}} \approx \left(\frac{\lambda}{C_s}\right)^{\frac{1}{4}} = \frac{6 \times 10^{-3}}{C_s^{\frac{1}{4}} V^{\frac{1}{8}}}, \tag{7.26}$$

where C_s is the spherical aberration coefficient (cf. §6.3). The minimum radius of the disk of combined confusions is

$$S_{\text{min.}} = 1{\cdot}4 C_s^{\frac{1}{4}} \lambda^{\frac{3}{4}} = 3 \times 10^{-7} C_s^{\frac{1}{4}} V^{-\frac{3}{8}}. \tag{7.27}$$

For example, an objective may be given with an aberration coefficient $C_s = 2$ mm. For electron rays of $V = 60$ kV., (7.26) and (7.27) yield $\Theta_{\text{opt.}} = 7 \times 10^{-3}$ radian and $S_{\text{min.}} = 10$ Å. Using this particular example, it may now be shown that the result of calculating the combined confusion is not much modified by consideration of the effect of chromatic aberration. A voltage fluctuation of 3 in 60,000 and a focal length of the objective $f = 2$ mm. may be given. Using the known value $C_{cr}/f = 0{\cdot}7$ given in §7.1 for the coefficient of chromatic aberration and with the above value $\Theta_{\text{opt.}} = 7 \times 10^{-3}$, one obtains, according to (7.1) and (7.2), a radius $\Delta r_{cr} = 5$ Å. for the chromatic confusion. If this value of Δr_{cr} is, according to (7.25), added quadratically to D and to Δr_s, one calculates $S_{\text{min.}} = 11{\cdot}2$ Å. instead of 10 Å. for D and Δr_s alone.

According to (7.27) it might appear that the most effective method for improving the resolution is to raise the voltage V for

accelerating the electron rays. However, Cosslett (1946*a*) has pointed out that there should exist an optimum voltage since the aberration coefficient C_s is not independent of V. C_s is inversely proportional to the focal length (cf. § 6.4). Since in the available magnetic objectives the magnetic field cannot be raised beyond a certain value, the focal length is bound to increase with voltage once this saturation value for the magnetic field is approached. Already at voltages of about 60 kV., this increase in focal length is rapid enough to offset the parallel reduction in diffraction error, and with present-day best objectives hardly anything is gained by going to the higher voltages.

CHAPTER VIII

ELECTRON OPTICS AND SPACE CHARGE

8.1. Spreading of a homogeneous, homocentric beam

In a homogeneous, homocentric beam, all electrons have strictly the same velocity and they all aim at, or emerge from, a common geometrical centre. Homogeneous, homocentric bundles of electron rays can practically be realized only to some approximation. They are, however, of great interest because their space-charge

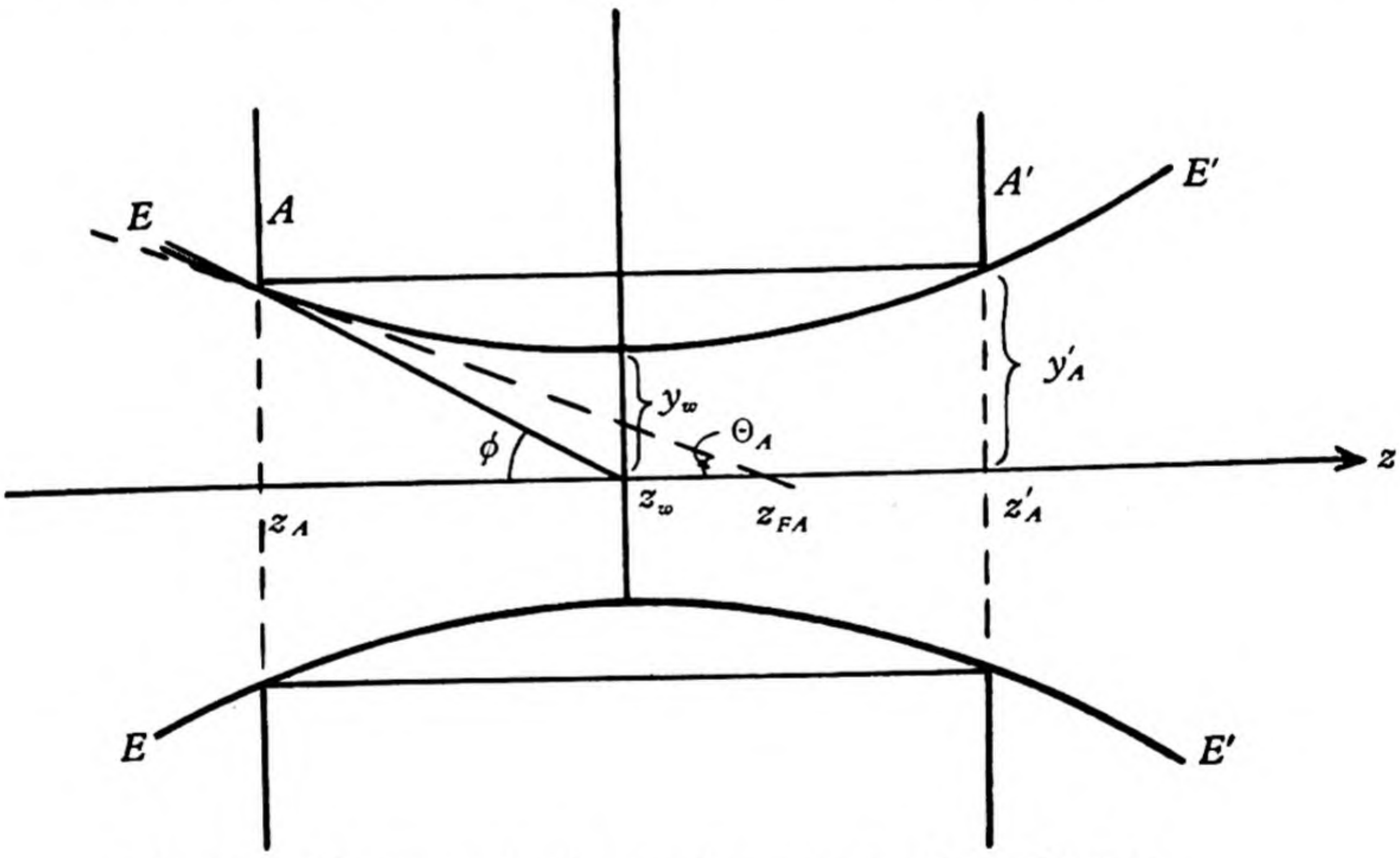

Fig. 8.1. Homocentric electron beam under the influence of its own space charge.

effects are easily accessible to electrodynamical calculation. It can be shown that mutual repulsion in homocentric beams deflects the rays as would an aberration-free optical lens. In fig. 8.1 is shown the cross-section of a homocentric beam of circular symmetry about the axis z, passing through a field-free space. The boundary surface of the beam is represented by the two curves EE'. At z_A the beam passes through a circular aperture A of radius y_A. There, the boundary curve EE' makes the slope angle θ_A with a z-axis. Under the influence of mutual repulsion, the slope angle θ of the progressing rays decreases all the time until it becomes zero at z_w. There

the beam aperture y reaches a minimum y_w, and the beam forms a waist. For further increase of z, the aperture y and the slope angle (now θ') start to increase. They reach the values $y'_A = y_A$ and $\theta'_A = \theta_A$ in a position z'_A which is symmetrical to z_A with respect to z_w.

The spread of an initially parallel beam due to its own space charge was calculated first by McGregor-Morris and Mines (1925) by integration over the Coulomb forces between the electrons. Watson (1927) gave a more complete treatment by considering also the forces of magnetic attraction between the electrons. These magnetic forces, however, become noticeable for very fast rays only for which current density and space-charge effects are generally rather small. We shall follow here a straightforward approach given by Fowler and Gibson (1934) starting with a calculation of the field E at the surface of the beam which is assumed to be a cylinder filled uniformly with electric charge. From Gauss's law follows

$$-\int \rho \, \mathrm{d}v = \int \epsilon E_y \, \mathrm{d}a, \tag{8.1}$$

where $-\rho$ is the electron space-charge density,* $\mathrm{d}v$ the volume element, ϵE_y the normal flux in radial (y-) direction and $\mathrm{d}a$ the surface element. Taking ρ as constant and integrating the volume over a cylinder of length Δz near the waist of radius y_w, we obtain

$$-\rho \pi y_w^2 \Delta z = \epsilon E_y 2\pi y \Delta z. \tag{8.2}$$

For reasons of symmetry, no flux passes through the two flat end-faces of the cylinder, but the flux goes through all cylindrical surfaces of any radius y. The normal field component as given by (8.2) is

$$E_y = \frac{-\rho y_w^2}{2\epsilon y}. \tag{8.3}$$

Now the current* I through the cross-section πy_w^2 is given by the linear velocity u_z of the electrons

$$\frac{I}{\pi y_w^2} = \rho u_z. \tag{8.4}$$

* As in Chapter I (cf. footnote, p. 4) we have taken here $-e$ for the electronic charge and, analogously, we have used $-\rho$ for the electron space-charge density and $-I$ for the current carried by the electrons in the direction of the beam.

Moreover, from Newton's law follows

$$-eE_y = m\frac{\mathrm{d}^2y}{\mathrm{d}t^2}. \tag{8.5}$$

Substituting (8.3) and (8.4) in (8.5), we obtain

$$\frac{\mathrm{d}^2y}{\mathrm{d}t^2} = \frac{e}{m}\frac{\rho y_w^2}{2\epsilon y} = \frac{e}{2m}\frac{I}{u_z\epsilon y\pi}, \tag{8.6}$$

or with the abbreviation $$b^2 = \frac{eI}{mu_z\epsilon\pi}, \tag{8.7}$$

we obtain $$\frac{\mathrm{d}^2y}{\mathrm{d}t^2} = \frac{b^2}{2y}, \tag{8.8}$$

where b is a constant for a beam of given electron velocity u_z and of given current I. According to (8.8) the acceleration of an electron at the surface will be inversely proportional to the radius y if the beam is assumed to have constant total current I. For constant current density $i = I/\pi y^2$, however, the acceleration of an electron in the beam is found to be directly proportional to its axial distance.

Multiplication of (8.8) by $\frac{2\,\mathrm{d}y}{\mathrm{d}t}\,\mathrm{d}t$ and integration yields

$$\int\frac{\mathrm{d}\left(\frac{\mathrm{d}y}{\mathrm{d}t}\right)}{\mathrm{d}t}\,\mathrm{d}t\,2\frac{\mathrm{d}y}{\mathrm{d}t} = \int\frac{b^2}{y}\,\mathrm{d}y,$$

or $$\left(\frac{\mathrm{d}y}{\mathrm{d}t}\right)^2 = b^2\log y + C. \tag{8.9}$$

Now take as the initial radius $y = y_w$, i.e. the coordinate origin may be chosen in the waist. There the rays travel parallel to the axis; thus $\mathrm{d}y_w/\mathrm{d}t = 0$ and the integration constant is

$$C = -b^2\log y_w.$$

Hence (8.9) becomes $$\frac{\mathrm{d}y}{\mathrm{d}t} = b\sqrt{\log\frac{y}{y_w}}. \tag{8.10}$$

With the abbreviation $$\zeta = \sqrt{\log\frac{y}{y_w}},$$

or $$y = y_w\exp\zeta^2, \tag{8.11}$$

(8.10) may be written

$$\frac{dy}{d\zeta}\left(\frac{d\zeta}{dt}\right) = b\zeta,$$

or with (8.11)

$$= y_w 2\zeta \exp(\zeta^2)\left(\frac{d\zeta}{dt}\right).$$

Therefore

$$\int_{t_w}^{t} \frac{b}{2y_w}\,dt = \int_0^{\zeta} \exp(\zeta^2)\,d\zeta. \tag{8.12}$$

The integral at the left-hand side is taken from the time t_w when the electron passes the waist, and the integral at the right-hand side is taken from $\zeta = 0$, since at the waist $y = y_w$, for which $\zeta = \sqrt{\log 1}$.

Integration of the left-hand side of (8.12) and replacement of $(t - t_w)$ by $\frac{z - z_w}{u_z}$ gives

$$\frac{b}{2y_w}\frac{z - z_w}{u_z}.$$

Introducing b from (8.7) this left-hand side becomes

$$\frac{z - z_w}{2y_w}\left(\frac{eI}{\pi\epsilon m}\right)^{\frac{1}{2}}\frac{1}{u_z}.$$

Moreover, expressing the electron velocity

$$u_z = \sqrt{\left(\frac{2e}{m}V\right)}$$

by the energy in electron volts V, we get

$$\frac{z - z_w}{2y_w}\left(\frac{I}{\pi\epsilon}\right)^{\frac{1}{2}}\frac{(e/m)^{-\frac{1}{4}}}{(2V)^{\frac{3}{4}}} = \int_0^{\sqrt{\log(y/y_w)}} \exp(\zeta^2)\,d\zeta,$$

or

$$\frac{z - z_w}{y_w} = \frac{4(\pi\epsilon)^{\frac{1}{2}}\left(\frac{e}{2m}\right)^{\frac{1}{4}}}{\sqrt{(I/V^{\frac{3}{2}})}} D(\zeta) = \frac{1{\cdot}15 \times 10^{-2} D[\sqrt{\log(y/y_w)}]}{\sqrt{(I/V^{\frac{3}{2}})}}, \tag{8.13}$$

where

$$D(\zeta) = \int_0^{\zeta} \exp\zeta^2\,d\zeta = \zeta + \frac{\zeta^3}{3} + \frac{\zeta^5}{5\times 2!} + \frac{\zeta^7}{7\times 3!} + \ldots \tag{8.14}$$

is the 'Dawson function' which first has been tabulated by Dawson (1898) and which has recently been calculated in great detail by Terrill and Sweeny (1944*a*, *b*). Since ζ measures, according to (8.11), the beam spread y/y_w, (8.13) gives the relation for the

radius y of the beam as a function of its distance $(z-z_w)$ from the waist, both quantities being measured in units of the waist radius y_w.

The beam-spread equation (8.13) is of a universal nature. It applies to all homocentric beams in a field-free space. The spread of a particular beam is seen to be completely controlled by the function $I/V^{\frac{3}{2}}$ of beam current I (ampere) and beam energy V (electron-volts); this function is called the space-charge factor of the beam. Again, (8.13) represents not only the paths of electrons along the boundary of the beam, it also represents the path of every electron inside the beam if we substitute for I the current I_1 that

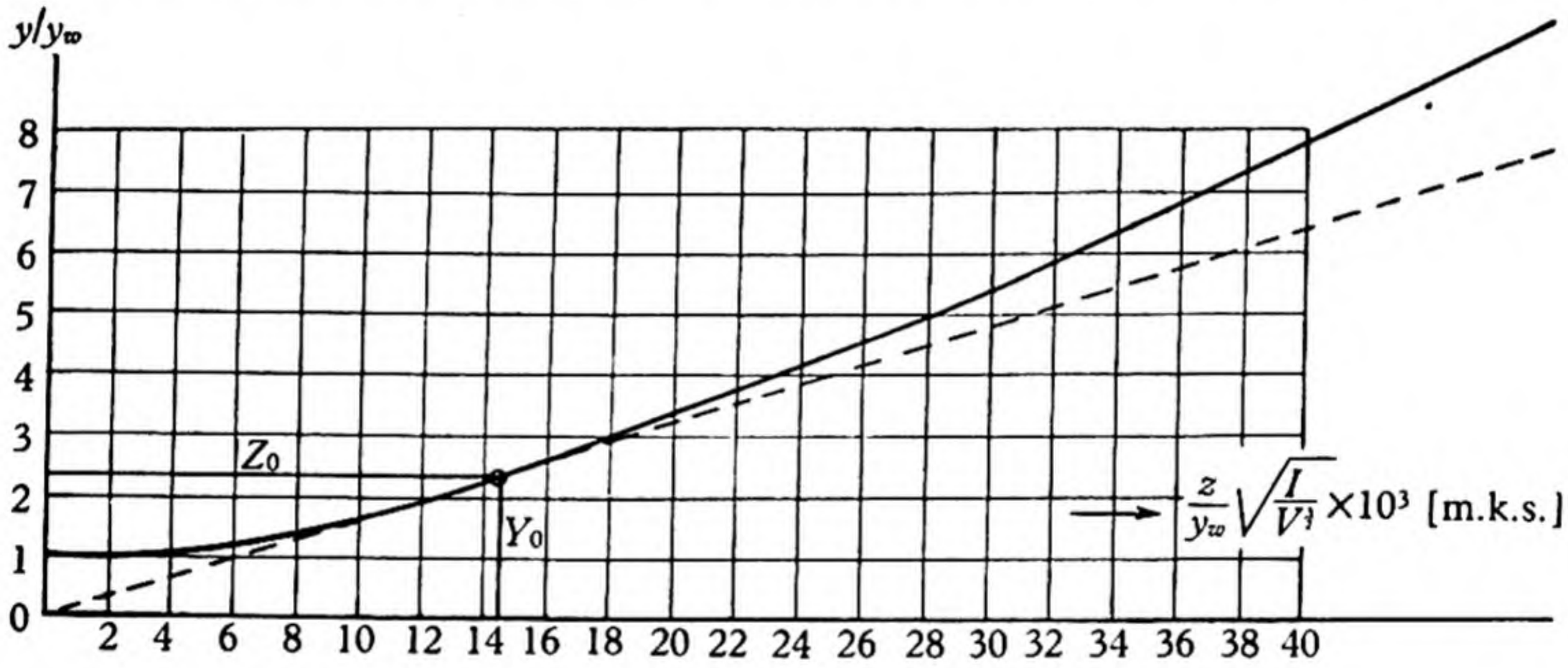

Fig. 8.2. Beam spread curve.

passes through a cross-section of axial symmetry containing the considered electron in its circular cylindrical boundary. This must be so since we can imagine the beam to be divided into an inner part containing the current I_1 passing through the cross-section of radius y_1 and an outer part with the current $I_2 = (I - I_1)$ passing through an annular ring aperture between the radius y and y_1. If we cut the outer part away, it will not affect the inner part, since according to Gauss's law the resultant of the forces exerted by the outer part in the region of the inner part must be zero.

Fig. 8.2 is due to Field, Spangenberg and Helm (1947). There the function

$$Z = \frac{z - z_w}{y_w} \sqrt{\left(\frac{I}{V^{\frac{3}{2}}}\right)} \times 10^3 = 11{\cdot}5D\sqrt{\log(y/y_w)} \qquad (8.15)$$

is plotted as abscissa against the ordinate

$$Y = \frac{y}{y_w}.$$

Thus fig. 8.2 represents the beam-spread equation (8.13). The centre of the beam waist is chosen as the coordinate origin, i.e. $z_w = 0$. The beam radius y measured in terms of waist radii y_w can be read directly as the ordinate Y of the graph. The axial beam coordinate z measured in waist radii y_w may be obtained by dividing the readings Z of the graph by 1000 times the value of the square root of the space-charge factor of the beam. For example, for $\sqrt{(I/V^{\frac{3}{2}})} = 10^{-3}$ (say, 100 V. 10^{-3} amp. or say 10^4 V. 1 amp.) and for a waist radius $y_w = 1$ mm., the figures of the graph could be read directly as millimetres. An initially parallel beam of this kind appears to spread out to $y = 5$ mm. radius within a distance of $z = 28$ mm.

The spread curve of fig. 8.2 applies universally to any beam, since the abscissa can just be scaled up or down in inverse proportion with $\sqrt{(I/V^{\frac{3}{2}})}$. The curve is symmetrical about the value $z = 0$ and applies for electrons moving either to the right or to the left. All electrons, at a given instant, aim towards a virtual focus $z_{F\infty}$; however, when the bundle converges the current density grows, and each electron in the bundle follows a beam-spread curve as in fig. 8.2. The rays are gradually deflected as the current density increases, and they no longer aim towards $z_{F\infty}$, but towards a virtual focus z_F. As the electrons move forward, the focus z_F moves along the axis in the same direction. z_F will reach the coordinate origin which is placed at the beam waist when the slope of the beam envelope reaches the value

$$\left(\frac{\mathrm{d}y}{\mathrm{d}z}\right)_0 = \frac{y_0}{z_0} = \tan\theta_0.$$

Substituting for z_0 from (8.13) yields the coordinates of the critical point

$$\left.\begin{aligned} y_0 &= 2{\cdot}35 y_w, \\ z_0 &= 14{\cdot}6 y_w/[10^3\sqrt{(I/V^{\frac{3}{2}})}]. \end{aligned}\right\} \tag{8.16}$$

The corresponding point (Y_0, Z_0) is plotted in fig. 8.2, where the critical tangent to the curve is shown as a broken line. Bedford (1936), who first calculated the coordinates of the critical point, showed that the electron beam touches there an inscribed cone, the semi-vertical angle θ_0 of which, according to (8.16), only depends

upon the space-charge factor

$$I/V^{\frac{3}{2}} = 3{\cdot}9 \times 10^{-5} \tan^2 \theta_0. \tag{8.17}$$

With further advance of the converging electrons, the rate of change in slope of the rays becomes more rapid. The virtual focus moves farther along the axis and reaches infinity when the electrons reach the waist where the rays are parallel. Then as the beam gradually becomes divergent, the virtual focus moves from infinity in the direction from which the beam has come, it passes through the central position $z_F = 0$ and eventually approaches the extreme position $(-z_{F\infty})$.

For practical purposes it is often convenient to approximate the beam-spread curve by a simple parabola. For a small quantity $x \ll 1$, the approximation $\log(1+x) \approx x$ holds, and, according to (8.14), $D(x) \approx x$. Hence, the beam spread (8.13) may be written in the approximate form

$$\frac{y-y_w}{y_w} = \frac{I/V^{\frac{3}{2}}}{16\pi\epsilon(e/2m)^{\frac{1}{2}}} \left(\frac{z-z_w}{y_w}\right)^2, \tag{8.18}$$

where $1/(16\pi\epsilon(e/2m)^{\frac{1}{2}}) = 0{\cdot}76 \times 10^4$ m.k.s. The ordinates of the parabola approximation deviate by less than 1 % from those of the real beam-spread curve, as long as the incremental spread $(y-y_w)$ is less than 15 % of the waist radius y_w.

Equation (8.18) may also be used to estimate the spreading of an initially very slightly converging or diverging beam. Taking Θ as the initial angle of convergence or divergence, the geometrical change in beam radius,

$$y - y_w = (z - z_w)\,\Theta,$$

may be a very small quantity. This geometrical change may, by independent superimposition, simply be added to the very small increase by space charge given in (8.18).

Though (8.13) gives a complete representation of the beam spread it is generally inconvenient for practical purposes to relate the beam dimensions to the radius y_w of the beam waist, since y_w is rarely accessible to direct measurement. Hence the beam spread may be measured in units of an initial beam radius y_A which could be defined by a circular aperture A (see fig. 8.1) at an axial coordinate

z_A. If this initial radius is introduced into (8.9), the value of the integration constant becomes

$$C = \left(\frac{\mathrm{d}y}{\mathrm{d}t}\right)_A^2 - b^2 \log y_A, \tag{8.19}$$

where $(\mathrm{d}y/\mathrm{d}t)_A = (u_y)_A$ is the radial component of the electron velocity at the aperture A. With (8.19), (8.9) becomes

$$\frac{\mathrm{d}y}{\mathrm{d}t} = \sqrt{\left(b^2 \log \frac{y}{y_A} + (u_y)_A^2\right)}. \tag{8.20}$$

Introducing $\mathrm{d}t = \mathrm{d}z/u_z$ and integrating yields

$$z - z_A = u_z \int_{y_A}^{y} \frac{\mathrm{d}y}{\sqrt{\{(u_y)_A^2 + b^2 \log (y/y_A)\}}}. \tag{8.21}$$

Now the slope of the ray (see fig. 8.1) as it enters the aperture may be expressed either as the ratio of the radial to the axial velocity component

$$\tan \Theta_A = \left(\frac{u_y}{u_z}\right)_A, \tag{8.22}$$

or as the ratio of the beam radius to its subtangent

$$\tan \Theta_A = \frac{y_A}{z_{FA} - z_A}, \tag{8.23}$$

where z_{FA} is the axial coordinate of the virtual focus at which the homocentric bundle is aiming while passing the aperture A.

Expressing again u_z by $\sqrt{\left(\frac{2e}{m} V\right)}$ and substituting the value of b from (8.7), (8.21) with (8.22) and (8.23) becomes

$$z - z_A = (z_F - z_A) \int_1^{y/y_A} \frac{\mathrm{d}\left(\frac{y}{y_A}\right)}{\sqrt{\left\{1 + \frac{1}{\sigma} \log \left(\frac{y}{y_A}\right)\right\}}}, \tag{8.24}$$

where
$$\sigma = 2\epsilon\pi \left(\frac{2e}{m}\right)^{\frac{1}{2}} \frac{\tan^2 \Theta_A}{I/V^{\frac{3}{2}}} = 32{\cdot}95 \times 10^{-6} \frac{\tan^2 \Theta_A}{I/V^{\frac{3}{2}}} \tag{8.25}$$

is called the 'beam-spread coefficient'.

A beam-spread equation equivalent to (8.24) has first been presented by Borries and Dosse (1938). The coordinates (y, z) of

any beam electron may now be calculated everywhere from initial conditions which are accessible to direct measurement. Again, for convenience, the Dawson function, (8.14), could be introduced for the integral in (8.24). For this purpose take

$$\zeta^2 = \sigma + \log\left(\frac{y}{y_A}\right). \tag{8.26}$$

The integration in (8.24) has then to be taken from $\zeta = \sqrt{\sigma}$ (cf. (8.26) with $y/y_A = 1$) up to ζ. Moreover $\mathrm{d}(y/y_A)$ is found by differentiation of (8.26)

$$2\zeta\,\mathrm{d}\zeta = \mathrm{d}\left(\frac{y}{y_A}\right)\Big/\left(\frac{y}{y_A}\right).$$

Hence (8.24) can be written

$$z - z_A = 2(z_F - z_A)\,\sigma^{\frac{1}{2}} \exp(-\sigma) \int_{\zeta=\sqrt{\sigma}}^{\zeta=\sqrt{\{\sigma+\log(y/y_A)\}}} \exp(\zeta^2)\,\mathrm{d}\zeta, \tag{8.27}$$

where σ, the spread coefficient, is given by (8.25). The value of the integral in (8.27) is calculated as the difference of two Dawson functions (cf. (8.14)). Equation (8.27) has been fully discussed by Thompson and Headrick (1940) and by Schwartz (1943).

8.2. Focus spread and focus shift. Space charge equivalent lens

From the electron-optical point of view, we are interested in the sharpest possible focus. Even if the space-charge factor $I/V^{\frac{3}{2}}$ is very small, the homocentric bundle of electrons will not come to a point focus such as is formed by a homocentric bundle of light rays. The radius of the disk of least confusion is the waist radius, which is easily calculated from (8.20). For the waist we have

$$\frac{\mathrm{d}y}{\mathrm{d}t} = 0.$$

Substituting for $u_y^2 = u_z^2 \tan^2\Theta = \frac{2e}{m} V \tan^2\Theta$,

replacing b by (8.7) and using the relation

$$u_z = \sqrt{\left(\frac{2e}{m} V\right)},$$

one obtains

$$\frac{y_w}{y_A} = \exp(-\sigma), \tag{8.28}$$

where σ is given by (8.25). Expression (8.28) has been first derived by Zworykin (1933*a*). It can be seen that the disk of least confusion decreases exponentially with decreasing space-charge factor $I/V^{\frac{3}{2}}$, and it can be made the smaller, the larger the semi-vertical angle Θ of the convergent beam.

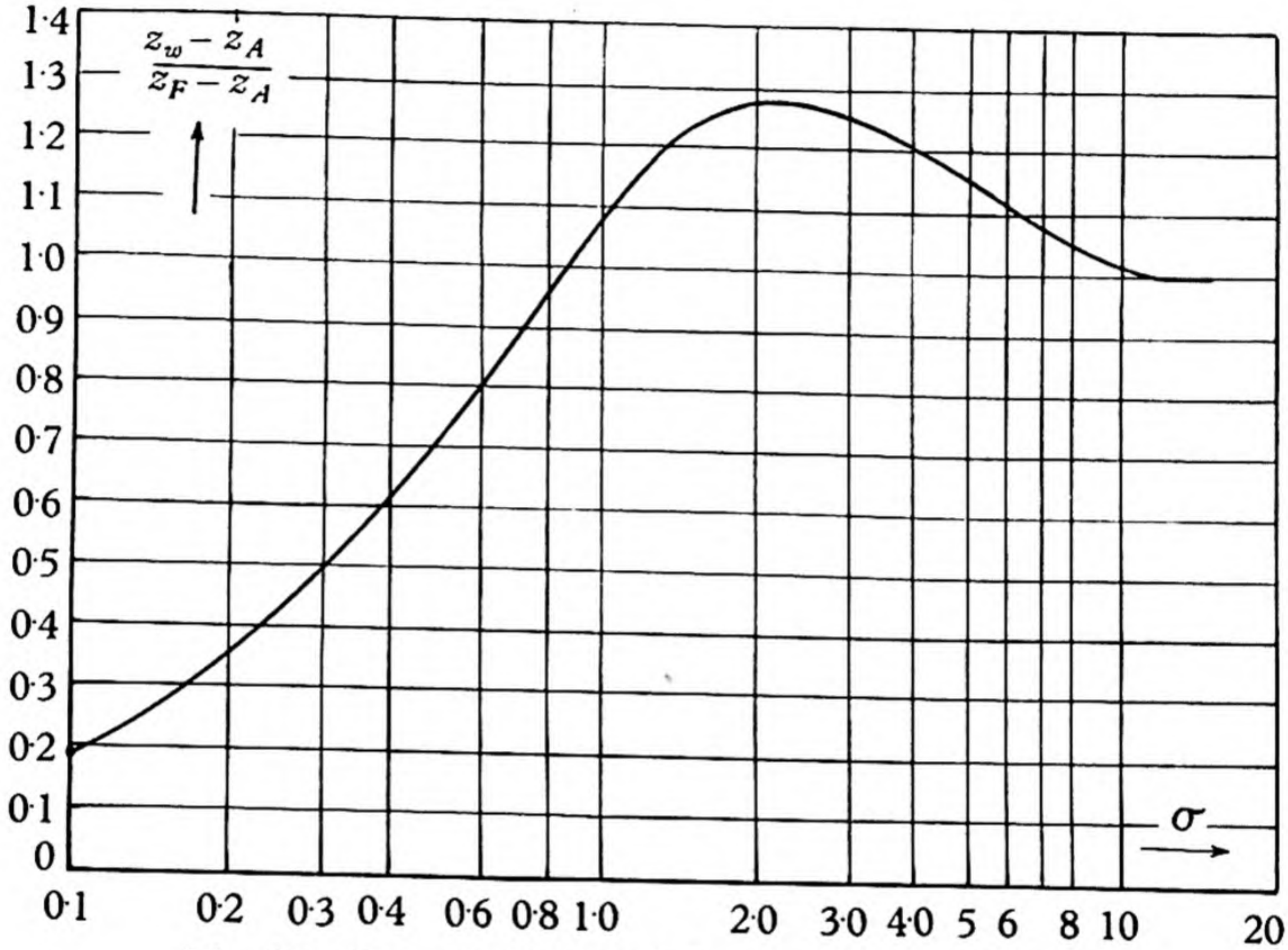

Fig. 8.3. Beam spread coefficient and focus shift.

Of further interest for electron-optical problems is the shift of focus due to space-charge effects. Assume the current of a beam of small space-charge density to be gradually increased. Initially the beam may be directed towards the virtual focus z_F while passing through the aperture A. The shift of the focus at z_w due to an increase in current can be calculated from (8.27). There, substitution of y_w of (8.28) for y yields

$$\frac{z_w - z_A}{z_F - z_A} = -\frac{2\sqrt{(\sigma)}\, D(\sqrt{\sigma})}{\exp \sigma}. \tag{8.29}$$

This equation is represented by fig. 8.3, where $\frac{z_w - z_A}{(z_F - z_A)}$ is plotted against σ. Assume the practical case of a constant Θ_A, with $z_F - z_A = \text{const}$. Now fig. 8.3 shows immediately that with decreasing σ, i.e. with increasing space-charge factor $(I/V^{\frac{3}{2}})$, the distance

of the waist from the aperture will first increase up to a maximum and then decrease again.

Since for every cross-section of a homogeneous, homocentric beam I is proportional to y^2 and hence to $\tan^2\Theta$, the beam-spread coefficient σ follows from (8.25) to be constant for all electrons in a given cross-section. Hence, whatever the value of σ, according to (8.29) a bundle of homocentric rays remains homocentric. Thus space charge effectively acts like an optical lens placed at the aperture A. Taking the actual focus as the waist of the beam, the focal length f of this 'space-charge equivalent lens' is given by

$$\frac{1}{z_w - z_A} - \frac{1}{z_F - z_A} = \frac{1}{f}. \tag{8.30}$$

If (8.30) be multiplied by $(z_F - z_A)$, its first term can be obtained with the help of a graph (fig. 8.3). It appears that the space-charge equivalent lens is generally a diverging lens, which reaches its maximum power $-\frac{1}{f} = \frac{0{\cdot}22}{z_F - z_A}$ at $\sigma = 2{\cdot}28$. Its power vanishes for $\sigma \to \infty$ and for $\sigma = 0{\cdot}86$. On the other hand, for $\sigma < 0{\cdot}86$ the space-charge equivalent lens may be compared with a converging lens in so far as it shortens the image distance. It is of particular interest that space-charge equivalent lenses are free from spherical aberration within the range of application of (8.29). Introducing the current density $i = I/\pi y_A^2$ into (8.25) and eliminating y_A by (8.23), the beam-spread coefficient may be expressed by

$$\sigma = \left(\frac{2e}{m}\right)^{\frac{1}{2}} \frac{2\epsilon}{(z_F - z_A)^2} \frac{1}{i/V^{\frac{3}{2}}}. \tag{8.31}$$

This equation again implies that for a homocentric, homogeneous bundle of rays, the focal length of the space-charge equivalent lens is independent of the aperture.

As an example, the focal length of a space-charge equivalent lens may be calculated for a beam of space-charge factor

$$I/V^{\frac{3}{2}} = 10^{-6}\,[\text{amp./volt}^{\frac{3}{2}}]$$

passing through an aperture stop of $y_A = 5$ mm. radius and aiming towards a virtual focus $(z_F - z_A) = 20$ mm. distant from the stop.

There, $\sigma = 2{\cdot}05$, $\dfrac{z_w - x_A}{z_F - z_A} = 1{\cdot}28$ and the focal length $f = -72$ mm. The focus z_F is shifted by $(z_F - z_w) = 5{\cdot}6$ mm. in the direction of the electron motion.

8.3. Aberrations of the space-charge equivalent lens. Beam spreading under extreme conditions

The theory of the beam spread developed so far is correct to a first approximation only. Homogeneity of electron velocities and homocentricity of the rays can be maintained only for beams of relatively small current density. Already Borries and Dosse (1938) pointed out that the potential V_0 at the axis should always be more negative than the potential V_A at the envelope with the radial co-ordinate y_A. The potential difference is

$$V_0 - V_A = \int_0^{y_A} E_y \, \mathrm{d}y = \frac{\rho}{2\epsilon} y_A^2, \tag{8.32}$$

where E_y is the normal component of the field as given by (8.3) which has to be integrated from $y = 0$ up to the full beam aperture y_A. Eliminating the space-charge density ρ by (8.4), etc., gives

$$V_0 - V_A = \frac{I/V_A^{\frac{1}{2}}}{(2e/m)^{\frac{1}{2}}} = 1{\cdot}52 \times 10^4 I/\sqrt{V_A}. \tag{8.33}$$

Due to this voltage difference, the paraxial electrons should be expected to have smaller velocities than those at the margin. Now, by the slowing down of the paraxial rays, the paraxial space-charge density is increased. This should slow down still more the paraxial part of the beam. As a consequence, the negative voltage in the paraxial region is raised further and so on. On the other hand, increased space charge will lead to increased beam spread and consequently to reduced charge density. Eventually the competing processes set up an equilibrium. A theoretical investigation on the equilibrium potential distribution in an electron beam due to its space charge has been published by Smith and Hartman (1940), and approximate expressions have been derived for the beam spread. According to the calculations of these authors the beam diverges a given amount in about one-half of the distance computed from the first-order theory equation, (8.24).

Klemperer (1947*a*) pointed out that the loss of homogeneity must lead to a loss of homocentricity and to a production of spherical aberration. The potential hump about the axis and the consequent reduction of electron velocities in the paraxial region will be seen to lead (cf. § 8.8) to a variation of current density i along the radial coordinate y. Now, according to (8.31), the beam-spread coefficient σ and hence according to (8.29) the position z_w of the focus must be a function of the ray aperture y. In other words, the focal length of the space-charge equivalent lens (cf. (8.30)) will be a function of the aperture, i.e. the lens suffers from spherical aberration. The coefficient σ always decreases with increasing y, thus

$$\sigma_{Pa} > \sigma_{Ma},$$

where the suffix *Pa* stands for the paraxial region and *Ma* stands for the marginal region of the electron beam. Now, from the fact that the focus shift as shown in fig. 8.3 as a function of σ has a maximum at $\sigma_0 = 2{\cdot}35$, the following conclusion can be drawn: If $\sigma_{Ma} > \sigma_0$, then $(z_w - z_A)_{Pa} < (z_w - z_A)_{Ma}$ and the spherical aberration of the space-charge equivalent lens is negative. On the other hand, if $\sigma_0 > \sigma_{Pa}$, then $(z_w - z_A)_{Pa} > (z_w - z_A)_{Ma}$ and the spherical aberration of the space-charge equivalent lens is positive. To a certain extent, correction of the space-charge equivalent lens should be expected when $\sigma_{Pa} > \sigma_0 > \sigma_{Ma}$.

The case of small σ corresponding to relatively high current densities in which the aberration is positive is the more common one, and this is most troublesome in practice. However, the following examples show that in technical cathode-ray tubes σ is found on either side of the critical value σ_0. For the focused beam of a television receiver tube with 3 kV., 0·5 mA. and $\Theta = 10^{-2}$, σ is found to be ≈ 1. For the focused beam in a projection tube with 50 kV., 3 mA. and $\Theta = 0{\cdot}03$ it is found that $\sigma \approx 100$. It will be shown later on (Chapter IX) that minimum cross-over size in an emission system is likely to occur when σ is of the order of σ_0.

Beams of highest charge density. The optics of electron beams with small spread coefficients σ is often completely modified by space-charge effects. For instance, in the design of some Klystron tubes (cf. § 12·6) beams are used with $\sigma \approx 0{\cdot}3$. Equation (8.28) shows that the formation of a sharp focus of such a beam is quite

out of question. Its waist radius y_w is as large as three-quarters of the aperture radius y_A.

A common problem in the design of high-power tubes is met when it is desirable to pass the maximum current at the minimum voltage through a cylinder of given dimensions. In fig. 8.1 a beam EE' is seen to enter a cylinder through an aperture A. It may be necessary that the whole beam shall leave through the aperture A' which may have the same diameter as A. Obviously, at the entrance aperture A the beam should be convergent, so that it will come to a minimum diameter somewhere in the cylinder and then spread again until it just fills the exit aperture A'. From reasons of symmetry it follows that the waist should be formed exactly in the middle of the cylinder. In addition to these requirements, Spangenberg (1948) showed from the beam-spread curve (fig. 8.2) that the beam should enter the cylinder while aiming towards a point on the axis halfway between A and A'. The two circular edges defining the envelope of the beam as it passes the entrance A and exit aperture A' respectively should correspond to one point ($Y_0 Z_0$) of the beam-spread curve given by (8.16), where the tangent to this curve passes through the origin.

The slope angle of the tangent at $(X_0 Y_0)$ is identical with the semi-vertical angle Θ_0 of the cone tangent to the beam apertures A and A'. If radius and length of a given cylinder are R and $2L$ respectively, then $\tan \Theta_0 = R/L$. Moreover, the maximum current density at a given voltage that can be transmitted according to the first-order theory is determined by the following space-charge factor:

$$I/V^{\frac{3}{2}} = 3{\cdot}9 \times 10^{-5}(R/L) \quad [\text{amp./V.}^{\frac{3}{2}}]. \tag{8.34}$$

According to the theory, the value of Θ_0 for the maximum $I/V^{\frac{3}{2}}$ is not very critical. For example, the waist radius y_w may be varied from 0·25 to 0·6 of the cylinder radius R with an expected loss of only 10% of the maximum current.

According to experimental results by Klemperer (1947*a*), however, the maximum beam currents calculated from the first-order theory are never reached in practice. Under most favourable conditions, not more than 50% of the theoretical current value as calculated from (8.17) can be transmitted through a given cylindrical tube. This again leads to the conclusion that beams of

great current density would only approximately comply with the first-order theory. A large amount of spherical aberration can be shown to exist in beams of great space-charge density. This has been done with a pepperpot diaphragm inserted, for example, in the exit aperture of the above cylinder traversed by the beam (Klemperer, unpublished). The beam was broken up into pencils and its virtual cross-over was traced with the sliding fluorescent target as shown in § 2.1.

Cross-over of low-intensity beams. Deviations from the beam-spread curve (8.13) should be expected for a beam containing so few electrons that its space charge can no longer be considered as a continuum. In particular, there will not be formed a waist of a radius given by (8.28), but some of the electrons will cross the axis. Not much information is available about low-intensity beams, but the following considerations will illustrate the problem. If two isolated electrons travel initially with equal axial coordinates, opposite and in equal distances from the axis they will, owing to their Coulomb repulsion, move along hyperbolic orbits which are somewhat similar to the beam-spread curve. If in another particular case initially homocentric rays again converge towards the axis but the relative positions of electrons travelling along these rays are not diametrically opposite, but interlaced, their mutual repulsion will increase less rapidly than with the inverse square of their distance from the axis. The orbits will form a waist only if the axial distances between single electrons are so small that the kinetic energy of the radial velocity component is outweighed by the potential on the axis. If this is not the case, the electrons will cross the axis. The electron orbits may still be curved near the axis, but with decreasing beam current they will straighten up until rectilinear motion of the electrons is reached. Only the cross-over of a very low-intensity beam completely corresponds to a light-optical focus as far as location and sharpness are concerned.

Now the question arises: When can the continuum theory of § 8.1 be applied and when will the rays of a beam start to cross over? According to Barford and Klemperer (unpublished) a criterion can be developed from the assumption that the continuum theory is expected to fail when the waist radius y_w decreases below a certain critical value y_c which should be of the order of the mutual distance

s of the electrons in the beam, i.e. when

$$y_w \lesssim y_c \approx s. \tag{8.35}$$

The mutual distance of the electrons in a homogeneous beam is given, according to (8.4), by

$$s = \left[\frac{\pi y^2 e}{I}\sqrt{\left(\frac{2e}{m}V\right)}\right]^{\frac{1}{3}}. \tag{8.36}$$

With the assumption of (8.35) we have $y = y_c = s$, hence (8.36) yields

$$y_c = \frac{\pi e}{I}\sqrt{\left(\frac{2e}{m}V\right)} = 3 \times 10^{-12}\frac{\sqrt{V}}{I}. \tag{8.37}$$

By substitution in (8.35) for y_c from (8.37) and for y_w from (8.28) with (8.25) one obtains the required criterion

$$\left(0{\cdot}3 \times 10^{12}\, y_A \frac{I}{V^{\frac{1}{2}}}\right)\exp\left(-33 \times 10^{-6}\frac{\Theta^2 V^{\frac{3}{2}}}{I}\right) \leqq 1. \tag{8.38}$$

If the condition (8.38) is fulfilled, the continuum theory of space charge will fail. It is interesting to notice that according to (8.38) a transition region should exist in which the outer-beam electrons still form a waist while the inner-beam electrons already cross over. This is easily seen. Since in beams of axial symmetry the inner parts (due to Gauss's law) are not influenced by the outer parts, a particular aperture y_{A1} can be derived from expression (8.38) inside which the continuum theory does no longer hold. Hence, for rays of aperture y between y_A and y_{A1}, waist formation should be observed, while for all rays of an aperture $y < y_{A1}$ a true cross-over should be formed. In actual electron beams, conditions are, of course, greatly complicated by the fact that the rays are never strictly homocentric. The waist radius will always be increased by radial velocity components due to the tangential emission velocities at the cathode and due to the spherical aberration originated in the emission system, and in the focusing lenses or caused by the discussed space charge effects in the beam.

Spreading of very fast beams. In addition to the electrostatic repulsion of the electrons there exists a magnetic attraction between the rays. This corresponds to the attraction between the electric currents in two parallel conductors. The magnetic force is by a

factor $(u/c)^2$ smaller than the electrostatic force, where u is the electron velocity and c is the velocity of light. Thus the complete radial acceleration is obtained by multiplying (8.8) by the factor $(1-(u/c)^2)$. The same expression for the radial acceleration is obtained if the field E_y and the space-charge density ρ in (8.3) are taken in a coordinate system which is fixed to a moving electron. If then the expression in (8.8) for the acceleration is transformed to a coordinate system fixed to the observer at rest, relativistic expressions must be introduced for the mass of the electron

$$m = m_0 \Big/ \left(1 - \frac{u^2}{c^2}\right),$$

and for the charge density

$$\rho = \rho_0 \sqrt{\left\{1 - \left(\frac{u}{c}\right)^2\right\}},$$

where ρ is modified by the Lorentz contraction. The relativistically correct expression for the beam-spread curve (8.13) has been derived by Watson (1927), and we may write it here in the form

$$\frac{z - z_w}{y_w} = \frac{2e}{m}(\pi\epsilon)^{\frac{1}{2}} \frac{(B_e r_e)^{\frac{3}{2}}}{I^{\frac{1}{2}}} D \sqrt{\left\{\log\left(\frac{y}{y_w}\right)\right\}}, \tag{8.39}$$

where $(B_e r_e)$ is the electron momentum (cf. § 1.2 and Appendix, Table A. 4) and the constant factor is

$$\frac{2e}{m}(\pi\epsilon)^{\frac{1}{2}} = 1{\cdot}85 \times 10^6 \text{ m.k.s.}$$

The validity of equations (8.13) ff. is extended into the region of great electron velocities simply by multiplying the beam voltage V everywhere by the relativistic correction factor (cf. (1·13)),

$$k_{\text{rel.}} = V_r/V = (1 + 0{\cdot}97 \times 10^{-6} V). \tag{8.40}$$

Thus the relativistically corrected beam-spread coefficient in (8.24) for instance becomes

$$\sigma_{\text{rel.}} = \sigma k_{\text{rel.}}^{-\frac{3}{2}}. \tag{8.41}$$

Thus for a 100 kV. beam, say in a television projection tube (cf. § 12·3), the relativistic reduction of σ by nearly 5 % is quite noticeable. For great electron velocities, however, the practicable beam currents are nearly always so small that space-charge effects become negligible altogether.

8.4. Space charge in interaction with electrodes and electron lenses

The discussions in this section on beam spread were so far concerned with electrons moving through a completely field-free space. No other fields than those set up by the space charge have been considered. In practice, however, the electrons may be accelerated by axial fields or focused by electron lenses and they are emitted and collected by electrodes. The mutual influence between space charge and the fields set up by these electrodes cannot be neglected.

Borgnis (1943), for instance, investigated theoretically the influence of space charge on initially parallel rays in a beam of circular cross-section travelling in a space between two large, plane, parallel electrodes set up at right angles to the axis of the beam. Both electrodes are at a common potential corresponding to the kinetic energy of the electrons. The beam may, for instance, pass these electrodes through apertures covered with wire gauze. Now, in addition to the mutual repulsion of the electrons, the forces between the electrons and their electric images in both electrodes have to be considered. The equipotentials about the beam are no longer coaxial cylinders, but now they are closed, concentric shells cutting the beam axis and the mid-plane (i.e. the plane parallel to and halfway between the conducting planes) at right angles. Along the axis is set up a purely longitudinal field which retards the electrons on their way to the mid-plane but accelerates them after passing this plane. The strength of these fields depends on the ratio y_A/L (= beam radius/conducting plane distance), the maximum possible field value for $y_A \gg L$ being $E = L\rho/8\pi\epsilon$, where ρ is the space-charge density and ϵ is the dielectric constant.

The beam periphery is cut by the equipotentials at angles which decrease from 90° near the conducting planes to 0° at the mid-plane. This accounts for a beam spread, which, however, is much smaller between the planes than it would be in free space. Again, the beam spread is found to depend very much on the relative distance (L/y) of the conducting planes. Details have been calculated by Goudet and Gratzmuller (1944). For instance, if the distance L is of the order of the radius of the entrance aperture $y_A = y_w$, the incremental

spread is only a quarter of that calculated from (8.18). On the other hand, the values obtained from (8.18) would apply to the asymptotic case $L/y_w \to \infty$. For intermediate plate distances the following values may be quoted:

L/y_w	1	2	4	10	20
g	0·25	0·45	0·66	0·85	0·92

where g is a factor by which the right-hand side of (8.18) has to be multiplied in order to allow for the presence of the plane electrodes.

As a particular case of some practical interest, Goudet and Gratzmuller (1945) treated the spread of an initially parallel bundle of circular cross-section emitted from a plane, space-charge-limited cathode and intercepted by a plane anode. The beam spread again differs much from the result derived from (8.18). If the cathode is emitting under space-charge conditions, the spread is found to depend only on the ratio of the cathode-anode distance L to the initial beam radius y_c at the cathode. It is independent of the anode voltage (cf. Chapter IX). The following numerical values may be sufficient to give an impression about the magnitude of the spread $(y_A - y_c)/y_c$, (y_A = beam radius at the anode):

$\frac{L}{y_c}$	1	2	3
$\frac{y_A - y_c}{y_A}$	0·074	0·133	0·182

Moss (1945 *a*) has investigated theoretically the beam spread of an initially convergent beam in an accelerating homogeneous electrostatic field. He found that the beam-spread curve becomes asymmetric, and that with a given initial beam-spread coefficient σ the waist distance $(z_w - z_A)$ increases while the waist radius, y_w, decreases with increasing field.

The beam spread in the accelerating field is of some interest in connexion with the application of post-acceleration (cf. § 12·2) in cathode-ray tubes. In practice, generally the beam current I and the ultimate target voltage V_T are given, and the conditions leading to the least spot-size at the target have to be studied. The two parallel, plane electrodes correspond to the anode and to the target (screen) respectively, of the cathode-ray tube, and the question arises which

fraction of the available potential V_T should be applied to the anode in order to set up the post-acceleration field. As the result of some calculation, however, it follows that the least beam spread is obtained if full voltage is applied to the anode so that the beam between anode and target travels in the field-free space. An example may illustrate the magnitude of the effect. The target may be at 3 kV. and only 1 kV. is applied to the anode which may be spaced within 40 cm. from the target. This implies a post-accelerating gradient of 50 V./cm. Under the given conditions a minimum spot size is calculated as a waist radius of 0·25 mm. However, only by raising the anode voltage up to the target voltage can the waist radius be reduced to 0·1 mm.!

A frequently occurring problem is raised by space-charge influence of a beam upon the position of the cardinal points of an electron lens by which this beam is focused. Unfortunately, no quantitative information is available on this subject. With few exceptions, the focal lengths of electron lenses are increased with an increase in space-charge factor $(I/V^{\frac{3}{2}})$ at the focus. For a beam of constant current I, the space-charge factor changes with $V^{-\frac{3}{2}}$ while the beam passes through the lens. Thus, it is easily understood why the foci of decelerating lenses are found to be more sensitive to space charge than the foci of accelerating lenses.

Initially accelerating saddle-field lenses are little affected by space charge. Initially decelerating saddle-field lenses, however, which are practically more important, sometimes suffer so much from space-charge aberrations that they can be employed for focusing currents of the order of microamperes only. For instance, the three-tube einzel lens with long intermediate tube is greatly affected. Klemperer (1941 *b*) investigated the mid-image distance of such a lens (cf. § 6.4) as a function of the angular aperture of the rays. In fig. 8.4 there are plotted two aberration curves which refer to a three-tube lens in which the outer electrodes are maintained at 3 kV. and the intermediate electrode is at 1 kV. $(\Theta')^2$ is plotted as the ordinate. The continuous line refers to the case in which the beam carries very small currents of the order of only a microampere. This line is approximately straight, and the slope indicates positive aberration throughout. If, however, the beam current is gradually increased, the aberration curve gradually

changes its shape and position. When the current reaches the order of a milliampere, the aberration curve is given by the broken line in fig. 8.4. In this case the aberration is seen to be highly negative for rays near the axis, but it gradually changes with increasing ray aperture into positive values for marginal rays.

Three-diaphragm saddle-field lenses consisting of large, plane, widely spaced electrodes with fairly small apertures are relatively free from space-charge trouble even for initially decelerated electrons. This has been shown by Klemperer (1942*a*), who, in

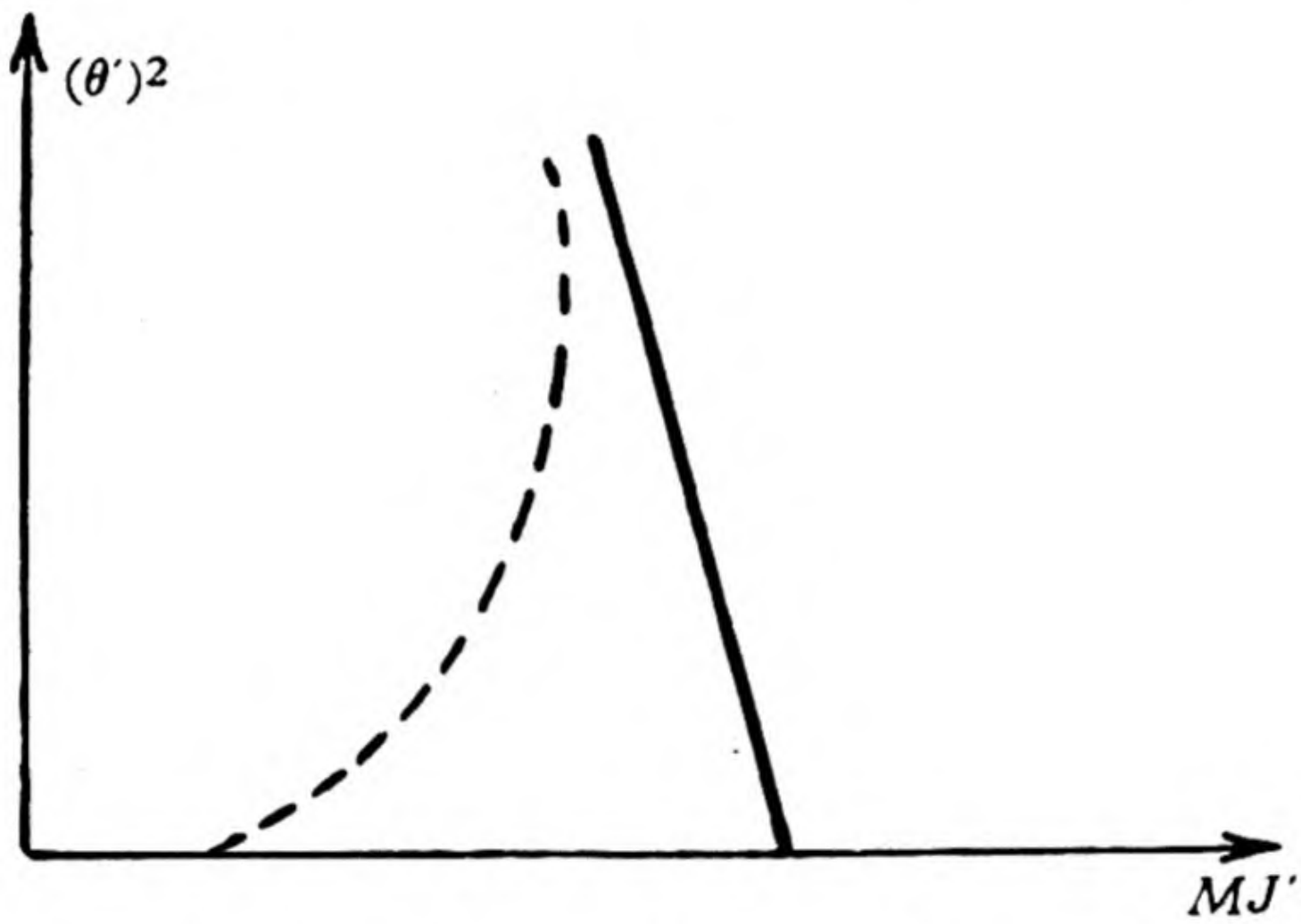

Fig. 8.4. Spherical aberration curves for an initially decelerating three-tube einzel lens with 1 microamp. (——) and 1 milliamp. (– – – –) beam current.

addition, described three-tube saddle-field lenses which are relatively free from space-charge effects. Such tube lenses, however, have to contain some small diaphragm arrangements with the help of which the potential distribution in the tubes is modified to approach closely the potential distribution of the high-quality large-diaphragm lenses. Such tubular lenses are preferable to the plain diaphragm lenses if the space available for the electrode structure is restricted.

8.5. Space charge and positive ions

According to experimental evidence, the beam spread is often appreciably reduced by the presence of positive ions. It is quite unavoidable that electron beams above a critical velocity corresponding to the ionization potential (about 12 V.) should ionize

the residual gas. The highest electron densities now obtainable are of the order of 10^{16} electron/m.^{3}, but even in the best obtainable vacuum, say of 10^{-8} mm. Hg pressure, the number of molecules of residual gas is still of the order of 10^{14} molecules/m.^{3}. In the usual electron-ray tubes the density of residual gas molecules far exceeds the density of electrons.

Owing to their far greater mass, the positive ions generally travel much more slowly than the light electrons, consequently they are very effective in setting up a field to counteract the negative space charge. Field, Spangenberg and Helm (1947) found, even at pressures of 10^{-7} mm. Hg, that the beam spread was reduced—due to the presence of positive ions—to nearly half the value predicted by the simple beam-spread theory.

The positive ions produced by the beam form an ion gas which spreads out by diffusion under the influence of electric forces. If the electron beam travels in accelerating fields, the positive ions will drift along the beam from the positive to the negative electrodes. For instance, the ions may be captured eventually by the cathode. If, however, the electron beam travels through a field-free space, a potential depression will be set up due to the electronic space charge (cf. (8.32)). The depression extends along the axis but decreases when a grid or an apertured diaphragm is approached. For instance, the beam may enter and leave a field-free space through such diaphragms, these being on the potential of the conducting tube which surrounds the beam or—for increasing the above depression—they may be positively biased with respect to the tube. Thus there is formed a potential valley surrounded by higher potential regions on all sides. Such a potential valley acts as a trap by which the positive ions are attracted and retained. On the other hand, low-velocity electrons, formed by the ionization process, are forced away from the centre of the beam.

The resulting accumulation of ions in the beam causes a progressive neutralization of the electron charge and consequently the depression decreases. Eventually the ion trapping becomes ineffective enough to be counterbalanced by the diffusion of the ion gas, and a state of equilibrium is attained. Linder and Hernquist (1950), who discussed this process in detail, derived a quantitative relation between residual gas pressure P and the equilibrium depth

of the potential depression ΔV, namely,

$$P = \frac{R\,{}^{+}\rho_0}{\pi^{\frac{1}{2}} r^2\,{}^{-}\rho S}\left(\frac{m}{M}\frac{{}^{+}V_w}{V_{el}}\right)^{\frac{1}{2}} \exp\left(\frac{\Delta V}{{}^{+}V_w}\right), \tag{8.42}$$

where R and r are the radii of the tube and of the electron beam respectively. ${}^{+}\rho_0$ and $-{}^{-}\rho$ are the charge densities of ions at the axis and of electrons in the beam respectively. m/M is the mass ratio of electron to ion. ${}^{+}V_w$ is the kinetic energy of the ion near the wall as calculated from the kinetic theory, while V_{el} is the energy of the beam electrons. Moreover, S is the number of ions formed per unit length of one beam electron per unit pressure. S is known to be a function of the electron velocity; it rises to a maximum near 100 eV. (e.g. 10^3 ions per meter in air of 1 mm. Hg pressure) and then drops slowly as V_{el} increases. For instance, taking $R = 5$ mm., $r = 1$ mm., $M/m = 52{,}000$, $V_{el} = 300$ V. and ${}^{+}V_w = 0{\cdot}026$ V., and with ${}^{+}\rho_0 \approx {}^{-}\rho$, one obtains from (8.42) the following table for the voltage depression as a function of the gas pressure:

P (mm. Hg)	10^{-4}	10^{-5}	10^{-6}	10^{-7}	10^{-8}
ΔV (V.)	$-0{\cdot}01$	$-0{\cdot}07$	$-0{\cdot}13$	$-0{\cdot}19$	$-0{\cdot}25$

The time to build up the state of equilibrium resulting in the above voltage depression has been calculated by Linder and Hernquist (1950) to be

$$t = \sqrt{(m/2e)}/SPV_{el}. \tag{8.43}$$

For instance, for a 300 eV. beam, build-up times t of the order of 1 μsec. are required at $P = 10^{-5}$ mm. Hg pressure. As t is seen to increase inversely proportional with P, build-up times of the order of milliseconds are needed in the best obtainable vacua.

Linder and Hernquist confirmed their theory by experiments with convergent electron beams emitted from a large spherical concave cathode and accelerated by a concentric grid into a field-free space. The relatively small aperture of a collector cage was arranged at the centre towards which the beam converged. The fraction of the beam current which passed the aperture was found to increase as the beam spread was counteracted by space-charge neutralization due to positive ions formed in the residual gas. Maximum increases in current density from 2 to 60 [mA./mm.^{2}] could be observed due to space-charge neutralization in 300 eV.

beams. The built-up time of the positive-ion gas could be determined from oscillographic studies. Unfortunately, another practical drawback is linked with the relatively long build-up time. When the initial potential depression in the beam is being neutralized by the ion gas which is rapidly increasing in density, an inertia-like overshooting of the equilibrium point and a swing back towards it seems to occur. In this way oscillations are set up. These are observed as noise which appears abruptly at a time when the space-charge neutralization process just appears to be completed.

8.6. Balancing of space charge pressure by external fields

The flow of electrons, even in beams of very great space-charge density, can be kept rectilinear by arranging for a suitable potential distribution around the beam. Potential distributions which fulfil the condition of compensating the mutual repulsion can be found from the laws of electron flow between certain infinitely extended electrodes, the cathode being space-charge limited.

The flow between parallel plane electrodes, between coaxial cylinders and between concentric spheres is well known from the investigations of Langmuir (1913), cf. Langmuir and Compton (1931). In all three cases the flow of the electrons is rectilinear and the potential along any ray changes in proportion with the 4/3 power of the distance from the cathode. Take, for instance, the flow between two infinite parallel planes and imagine a beam of circular cross-section with its axis at right angles to the planes cut out of the flow. There the potential within the beam and at its boundary must change according to the 4/3 power of the axial coordinate. Therefore, an isolated beam of initially parallel electrons could be kept parallel and prevented from spreading by establishing an external potential distribution according to the 4/3 power law. The same reasoning, applied to the flow between concentric spheres, would provide the correct external potential distribution for rectilinear, homocentric, convergent or divergent bundles of rays.

The method of finding the correct potential distribution has been worked out by Pierce (1940*a*). Within the beam, Poisson's equation must hold, namely,

$$\frac{\partial^2 V}{\partial z^2} = \frac{\rho}{\epsilon} = \frac{i}{\epsilon}\left(\frac{m}{2eV}\right)^{\frac{1}{2}}, \tag{8.44}$$

where $V = V(z)$ is the potential, $^{-}\rho$ the electron space-charge density and $-i$ the electron-current density in the beam. If no spreading by mutual repulsion occurs, the radial potential gradient vanishes, i.e.

$$\frac{\partial V}{\partial r} = 0. \tag{8.45}$$

Moreover, if the beam is space-charge limited, the gradient $(\partial V/\partial z)_{z=0}$ at the cathode must vanish. With this condition (8.44) twice integrated yields at the edge of the beam the potential

$$V = Az^{\frac{4}{3}}, \tag{8.46}$$

with $$A = \left(\frac{9i}{2\epsilon}\right)^{\frac{2}{3}} \frac{1}{2}\left(\frac{e}{m}\right)^{-\frac{1}{3}} = 5{\cdot}7 \times 10^3 . i^{\frac{2}{3}} \quad [\text{V./m.}^{\frac{4}{3}}],$$

being independent of z. (8.45) and (8.46) must hold inside the beam as well as in the space-charge-free region surrounding it.

Magnetically balanced space charge pressure in constant diameter beams. Electron motion under the influence of space charges in longitudinal homogeneous magnetic fields has been discussed by Haeff (1939), by Smith and Hartman (1940) and by others. The theoretical study of beams of constant diameter in magnetic fields is due to Brillouin (1945), to Samuel (1949) and to Pierce (1949). Electrons moving in z-direction along a field $B = B_z$ but having a small transverse velocity component will spiral about the z-axis with an angular frequency (cf. (5.6))

$$\omega = \frac{e}{2m} B. \tag{8.47}$$

If the radial distance of the electron from the z-axis of the beam is not to change ($\mathrm{d}r/\mathrm{d}t = 0$), the centrifugal force and the electrostatic force must be balanced by the magnetic force, i.e.

$$mr\omega^2 + e\frac{\partial V}{\partial r} = eBr\omega. \tag{8.48}$$

Substituting for ω the value of (8.47), one obtains

$$\frac{\partial V}{\partial r} = \frac{e}{4m} B^2 r, \tag{8.49}$$

and by integration $$V_1 - V_0 = \frac{e}{8m}(Br)^2. \tag{8.50}$$

Now, according to Poisson's equation, the space-charge density is given by

$$\frac{\rho}{\epsilon} = \frac{\partial^2 V}{\partial r^2} + \frac{1}{r}\frac{\partial V}{\partial r}. \tag{8.51}$$

Substitution of (8.49) for $\partial V/\partial r$ yields

$$\frac{\rho}{\epsilon} = \frac{e}{2m} B^2. \tag{8.52}$$

In order to introduce the current I (cf. (8.4)) for the space charge ρ, u_z has to be known. This is obtained from the energy equation

$$\frac{m}{2} u_z^2 + \frac{m}{2}(r\omega)^2 = eV, \tag{8.53}$$

which, with (8.47) and (8.50), yields

$$u_z = \sqrt{\left(\frac{2e}{m} V_0\right)}. \tag{8.54}$$

Hence it follows that all electrons have the same z-component of velocity depending upon the potential V_0 on the axis only. The current within a cylinder of radius r_1 is then

$$\begin{aligned} I &= \pi r_1^2 \rho u_z \\ &= \frac{\pi\epsilon}{\sqrt{2}} \left(\frac{e}{m}\right)^{\frac{3}{2}} r_1^2 B^2 \sqrt{V_0} \\ &= 1{\cdot}45 \times 10^6 r_1^2 B^2 \sqrt{V_0}. \end{aligned} \tag{8.55}$$

This relation allows us to calculate the flux density B which constrains the space charge of a beam of current I, and of axial electron voltage V_0 within a cylinder of radius r_1. The outer electrons whirl about the axis with an energy $V_1 > V_0$ given by (8.50).

Conditions for starting such beams of constant diameter in the magnetic field have been discussed by Pierce (1949). If a parallel beam of the proper radius given by (8.55) is injected from a field-free region into a magnetic field which suddenly rises to constant flux-density B, the radial component of the field in the transition region will start the marginal, faster electrons whirling about the axis, thus diminishing their forward velocity so that it equals that of the paraxial electrons and at the same time providing by the new motion an inward magnetic force equal and opposite to the

outward force due to space charge and centrifugal force. If the beam is not parallel on injection or if beam radius, voltage and current do not fulfil (8.53), the beam will not stay parallel but will be periodically broad and narrow along its length.

It is of course possible to increase the flux density of the magnetic field to such an extent that the electrons are forced to move about the flux lines in extremely narrow spirals. In this way, for instance, a beam drawn from a cathode of radius r_c by an accelerating voltage V can be constrained within a certain radius r_1. The beam expansion is given according to Pierce (1949) by

$$\frac{r_1}{r_c} = [(k^2+1)^{\frac{1}{2}}+k]^{\frac{1}{2}}, \tag{8.56}$$

where

$$k = 3{\cdot}5 \times 10^{-7} \frac{I}{V^{\frac{1}{2}}(r_c B)^2}. \tag{8.57}$$

Owing to the fluctuations in beam width the effective equilibrium radius of the beam may be expected to be slightly greater than r_1 of (8.56).

8.7. Use of the electrolytic trough for field plotting in presence of space charges

A particular potential distribution which simultaneously satisfies both (8.45) and (8.46) can be found with the help of an electrolytic field-plotting trough. In the wedge-shaped trough as described in Chapter III, all electrodes are represented by metal strips in the usual way, while the edge of the beam has to be represented by an insulating strip. This guarantees the fulfilment of (8.46), since the normal field component must vanish at the beam edge and no current can flow across the insulator. Then the electrode strips representing cathode, anode and other field-shaping electrodes are altered in shape, position and potential until probe measurements show that the potential along the insulating strip varies with the 4/3 power of the distance from the cathode in order to fulfil (8.46). Fig. 8.5 shows such a field plotting trough seen from above; its four corners are marked T_1, T_2, T_3, T_4. Its bottom is slightly tilted against the plane of the drawing. The liquid in the trough forms a wedge with the thin end indicated by the edge W_1W_2. A spherical cathode surface is represented by C. The rectilinear convergent

electron beam is represented by the bakelite strip B standing on the bottom of the trough in the liquid. Five very fine probes P_1, P_2, P_3, P_4, P_5 are permanently fixed to the bakelite, these being spaced to give equal increment of voltage rather than of distance. In this case the distances of the probes from the cathode are given, according to (8.46), by the ratios 1:2·52:4·33:6·35:8·5, etc. Now the electrode strips S_1 and S_2 (or in an alternative case S_1 and S_3)

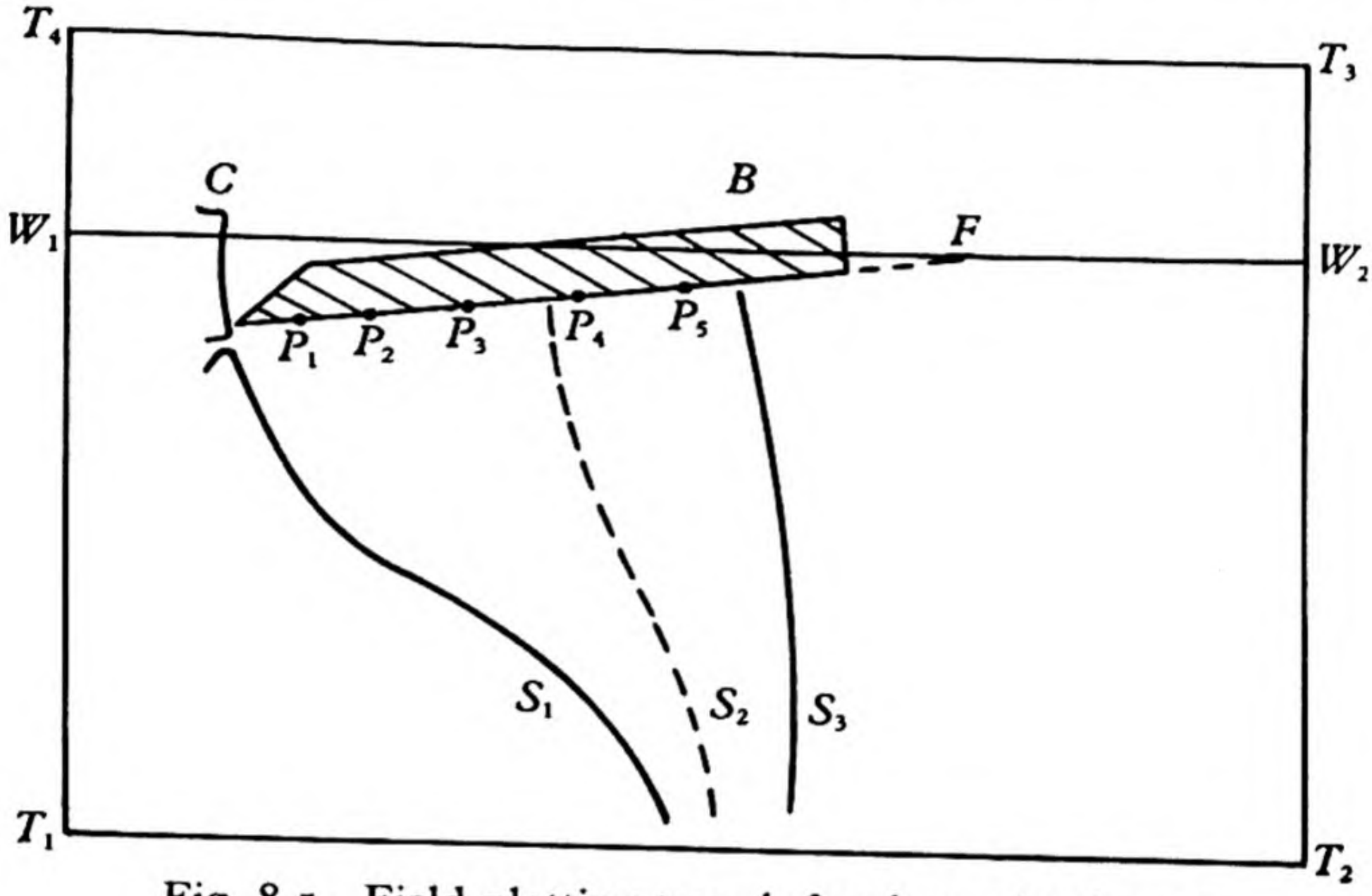

Fig. 8.5. Field plotting trough for determination of electrode shapes in presence of a beam.

connected to cathode and anode potential respectively are shifted and shaped empirically until the voltages at the probes are found to increase in the ratios 1:2:3:4:.... Calculation shows that the electrode S_1 should make an angle of 67·5° with the beam edge simulated by the bakelite. The shapes of electrodes to produce the right field are unique. However, there is a great variety of dissimilar electrode shapes which form the required field to a good approximation. In this way one is at liberty to choose electrode shapes to meet the exigencies of construction.

The electron beam in fig. 8.5 passes through an aperture in the anode S_3 into the field-free space, and in the drawing it simply is extended to reach a focus at F. In the practical gun design, however, difficulties always arise with respect to the location of the actual beam focus. The field between S_1 and S_3 penetrates through the aperture in S_3 as discussed in § 4.4, and a diverging electron lens is

set up; moreover, the beam will diverge outside S_3 by mutual repulsion. Both effects can be estimated to some extent from the formulae and data given in Chapter IV and in this section. To compensate for the later divergence, the beam may be initially overfocused. But in practice it is found that homocentricity and homogeneity of the beam is to some extent lost before it reaches the focus.

An extension of the ordinary method of the electrolytic trough to fields containing space charges has been worked out by Goudet and Musson-Genon (1945) and by Musson-Genon (1947). They found that the bottom of the field-plotting trough could be shaped in such a way as to account for the modification of Laplace's equation by the space charge. Laplace's equation which holds for the distribution of the potential V in an ordinary field plotting trough, can be expressed in cylindrical coordinates (z, r, Θ) as follows:

$$\nabla^2 V = \frac{\partial^2 V}{\partial r^2} + \frac{1}{r}\frac{\partial V}{\partial r} + \frac{\partial^2 V}{\partial z^2} + \frac{1}{r^2}\frac{\partial^2 V}{\partial \Theta^2} = 0. \tag{8.58}$$

The last term usually vanishes for reasons of circular symmetry. Here, however, such a value may be attributed to this term that the artificially introduced asymmetry represents the influence of space charge. Poisson's equation, in the case of circular symmetry may be written as

$$\frac{\partial^2 V_0}{\partial r^2} + \frac{1}{r}\frac{\partial V_0}{\partial r} + \frac{\partial^2 V_0}{\partial z^2} - \frac{i}{\epsilon\sqrt{\left(\frac{2e}{m}V_0\right)}} = 0. \tag{8.59}$$

Comparing (8.58) and (8.59) it follows that for given electrodes a relief surface for the bottom of the trough could be determined in order to produce a distribution $V_0(r, z)$ as in (8.59), which allows for the presence of space charge, at the top surface of the liquid. An equation representing the relief of the bottom surface of the trough can be derived by relating these last terms of (8.58) and (8.59). If the bottom of the trough is an insulator, its equation becomes

$$\frac{\mathrm{d}}{\mathrm{d}s}(\log\Theta) = \frac{-i}{\epsilon E_0\sqrt{\left(\frac{2e}{m}V_0\right)}}, \tag{8.60}$$

where Θ is the angular coordinate of the bottom surface (Θ is counted from the top level of the liquid, its vertex being the thin

end of the liquid wedge) and s is the line element of the field vector E_0, in the distribution of potentials V_0 at the top surface. If, however, the bottom of the trough is a conductor, its shape is represented by

$$V_0 - \frac{i}{2\epsilon\sqrt{\left(\frac{2e}{m}V_0\right)}} r^2\Theta^2 = \text{const.} \tag{8.61}$$

Equations (8.60) and (8.61) apply to the whole field excepting at the cathode surface where the electron velocity is zero, and thus the space-charge density and the Laplacian become infinite. From Langmuir's 4/3 power law equation, (8.46), however, it can be shown that a space-charge-limited plane of zero potential may be represented in the field plotting trough by a conducting plane tilted at an angle $\frac{3}{8}\pi$ to the top surface of the liquid.

For the practical problem of plotting the distribution of potentials and currents in a given system of electrodes the following procedure of successive approximation has to be used:

(i) First all non-emitting electrodes are arranged in the trough in the usual way, i.e. at right angles to the liquid surface. The electrodes representing emitting parts of the cathode, however, should be inclined to the top surface at an angle $\frac{3}{8}\pi = 67{\cdot}5°$ so that they meet the bottom of the trough somewhere in front of their lines of intersection with the top surface.

(ii) Equipotentials are plotted in the usual way with a probe at the top surface. Then current densities are calculated along the lines of force, the absolute values of these densities being derived from the field at the cathode and from the laws of space-charge-limited emission. The obtained values of V_0', E_0' and i_0' represent the first approximation and they are first used for calculating a relief surface according to either (8.60) or (8.61).

(iii) This relief is made from a plastic insulator (e.g. tetrachloronaphthalene) using (8.60), or from metal using (8.61), and put on the bottom of the field plotting trough. A new distribution V_0'', E_0'' and i_0'' is obtained with it as a second approximation, and a new relief is made according to these double-dashed values.

(iv) A new field plot is obtained with this second-approximation relief on the bottom of the trough. The method can be continued step by step until consecutive approximations agree sufficiently

closely. The method presents an interesting new tool for the investigation of space charges. However, a good deal of calculation is involved, and some craftsmanship is required for making the accurate bottom relief.

Another method of attacking the space-charge problem by experimentally solving Poisson's equation for any boundary condition has been proposed by Hogan (1943). A network of conducting small studs covers the insulating bottom of the field plotting trough. The studs are in contact with the electrolyte, and passing through the bottom they are connected to a network of electrical resistances at the outside of the trough in order to keep every stud at a given potential. Through the studs currents I_n are flowing into and out of the electrolyte. The currents representing the electronic space charges must be proportional to a function $f(y, z)$ of the coordinates which is given by Poisson's equation

$$\nabla^2 V = f(y, z).$$

As in the network analogue described in § 3.2 the network here has to be sufficiently fine in order to reach the required accuracy. The corresponding requirement of a very great number of studs greatly reduces the practical value of the method.

A relatively simple, though only approximate, method for the tracing of space-charge loaded beams through electrostatic fields is due to Walcher (1951). The given field is divided into a finite number of steps as shown in § 3.3. At the boundary of each step, a ray is refracted according to Snell's law. In distinction to the procedure of § 3.3, however, the ray is not drawn as a straight line in the field-free space between two boundaries, but, owing to its space charge, it has to follow a beam-spread curve. The method is simple for beams of small incremental spread when the beam spread curve can be approximated by the parabolic law (8.18). For every step, however, the parameter of the parabolic arc representing the ray has to be changed according to the change in potential.

8.8. Minimum in the potential distribution along the beam. The virtual cathode

The influence of space charge on the potential distribution along the axis of a beam has been considered here so far for one case only.

This particular case was concerned with a beam entering the space with zero velocity from a space-charge-limited cathode, and the potential along the beam was found to change according to the 4/3 power law of (8.46). We now want to investigate this longitudinal potential distribution for a beam entering with a given velocity into a field-free space or into a homogeneous retarding field. To avoid edge effects and a lateral potential distribution a flow of infinite

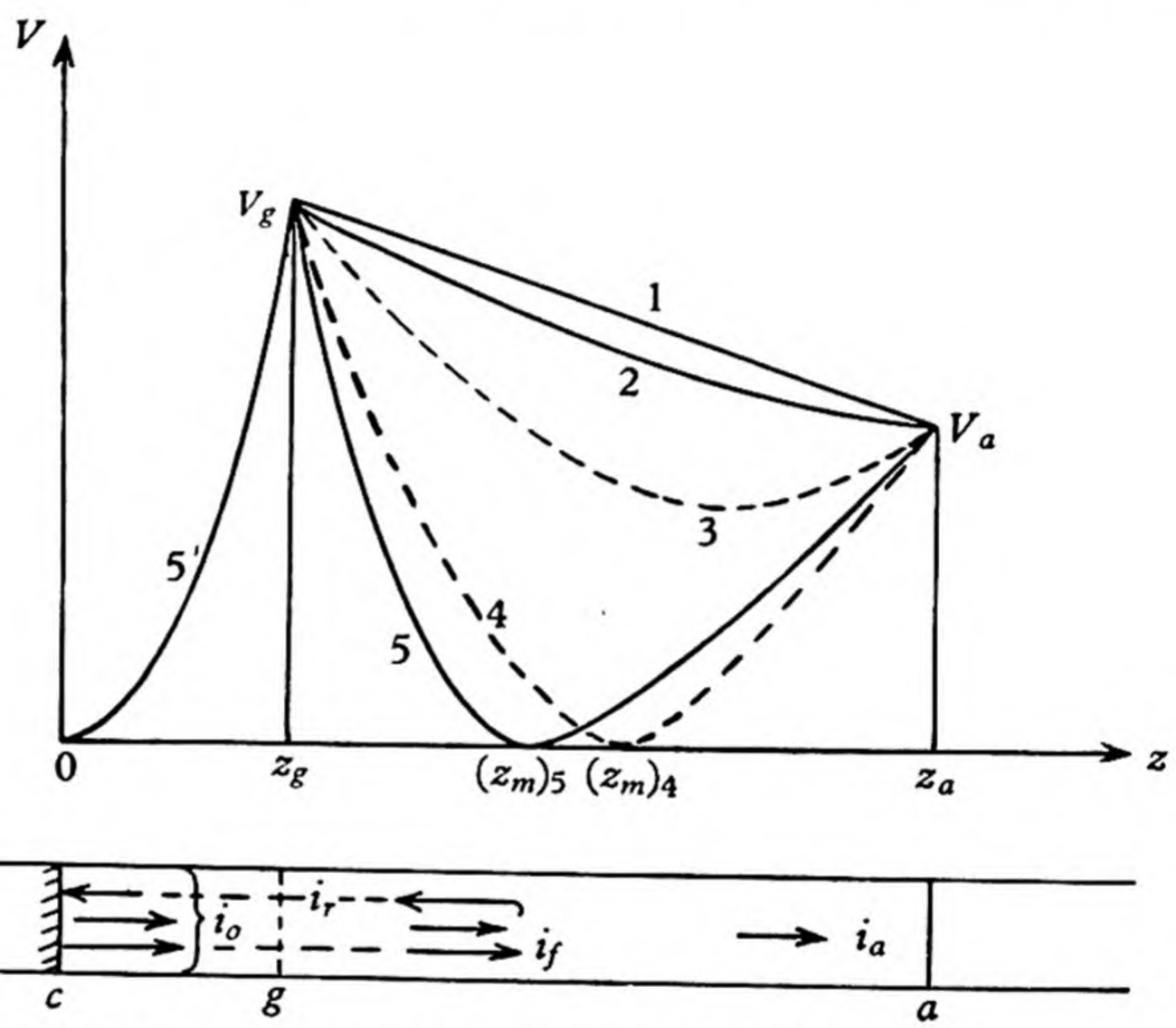

Fig. 8.6. Potential distributions along the beam.

lateral extent may be considered first. This ideal case is of some importance for the study of triodes, of tetrode valves and of beam tubes (cf. § 12.9); and it has been investigated theoretically by Gill (1925), by Plato, Kleen and Rothe (1936), by Salzberg and Haeff (1938), by Bull (1948) and by others. The results are essentially derived by integration of Poisson's law.

In the simple triode arrangement shown in the lower part of fig. 8.6, electrons may be emitted from a plane cathode *c* and may be accelerated by a plane grid *g* into a space which is limited by a plane anode *a*. A z-axis may be assumed at right angles to the three parallel electrodes, the origin ($z = 0$) being in the cathode plane. The potential distribution $V(z)$ between *c* and *g* is known from (8.46), while the current density in this space is given by the

following well-known equation which was first derived by Child (1911), i.e.

$$i = G_0 V_g^{\frac{3}{2}}, \tag{8.62}$$

with $$G_0 = \frac{4\epsilon}{9}\sqrt{\left(\frac{2e}{m}\right)}\frac{1}{s^2} = \frac{2{\cdot}33 \times 10^{-6}}{s^2} \quad \text{[m.k.s.]}, \tag{8.63}$$

where s (here $= z_g$) is the distance between the electrodes.

We now assume the ideal case of a grid electrode which passes all electrons with the full energy of V_g e-volts exactly in the z-direction into the anode space. Some possible potential distributions in the anode space are plotted in the upper part of fig. 8.6. They are essentially determined by the value of a certain constant which appears after a second integration of Poisson's equation. This constant is given by the potentials V_g and V_a and by a current density i_0 which passes through the grid electrode g. Assuming both potentials V_g and V_a to be positive with respect to the cathode and $V_g \geqq V_a$, the electrons are either entering a field-free space or they may run into a retarding field.

There are two ways of altering the current density i_0:

(i) A negatively biased control grid can be inserted between the cathode and the positive grid g. Then i_0 can be controlled by changing the bias just as it is done in a screen-grid tetrode valve.

(ii) The distance between the space-charge-limited cathode c and the grid g is varied. Then i_0 is changed in proportion with $1/z_g^2$ according to (8.62) and (8.63).

For $i_0 = 0$, the potential distribution between the two planes g and a is represented by the straight line (1) in fig. 8.6. If the current i_0 begins to flow, the potential between g and a is depressed as shown by curve (2). Further increase in i_0 leads to a potential distribution as curve (3) in fig. 8.6. There a minimum of potential $V = V_m > 0$ is formed at a plane $z = z_m$, where the field $(\mathrm{d}V/\mathrm{d}z)_m$ vanishes. This potential minimum is initially formed at the anode, but with increasing current it gradually recedes towards the grid. Only for the special case $V_a = V_g$, the minimum always stays halfway between the electrodes.

With increasing i_0, the potential minimum gradually descends until it reaches a critical value. A further increase in injected current starts the following cycle of action: Increase in space charge leads to reduction of potential which by slowing down the electron

current leads to further increase in space charge which leads to further reduction of potential, and so on. The potential curve can drop only to zero, at which point a virtual cathode is formed. When the potential minimum reaches its critical value, a theoretical maximum current density

$$(i_{\text{max.}})_{\text{crit.}} = G_0(V_g^{\frac{1}{2}} + V_a^{\frac{1}{2}})^3 \tag{8.64}$$

can be calculated to pass to the anode. The constant G_0 of (8.64) is given again by (8.63) with $s = (z_a - z_g)$ being the distance between anode and grid. A comparison of (8.64) with (8.62) shows the remarkable result that the maximum current density $(i_{\text{max.}})_{\text{crit.}}$ which can be transmitted through an originally field-free space ($V_g = V_a$) is eight times greater than the current density that is transmitted from a space-charge-limited cathode, provided that anode potentials V_a and electrode distances s are the same in both cases.

In order to force the maximum possible current $(i_{\text{max.}})_{\text{crit.}}$ through the anode space of the simple triode arrangement of fig. 8.6, a cathode-to-grid distance

$$z_g = \frac{z_a - z_g}{\sqrt{8}} \tag{8.65}$$

has to be adjusted according to (8.62). If now the cathode-to-grid distance z_g is still further reduced and additional electrons are injected into the anode space, the potential minimum is found to drop abruptly down to zero. This is the formation of the virtual cathode mentioned above. The unstable distribution (4) is obtained. It implies the reflexion of some fraction i_r of the current density i_f which moves forwards in the $(+z)$-direction. The total current density i_0 in the space between cathode and grid and the current density i_a which proceeds to the anode are thus given by

$$i_0 = |i_f| + |i_r|, \tag{8.66}$$

and

$$i_a = |i_f| - |i_r| = |i_0| - |2i_r|. \tag{8.67}$$

The current density i_r which is reflected by the virtual cathode passes back through the grid g and eventually reaches again the cathode c. The resultant redistribution of space charge changes the potential distribution of fig. 8.6, curve (4), into the distribution

curve (5) with a corresponding shift of the virtual cathode from $(z_m)_4$ to $(z_m)_5$ towards the grid. The potential distribution (5) is stable again.

The left branch of curve (5) between z_m and z_g must be symmetrical about the plane $z = z_g$ to the potential distribution curve (5′) between o and z_g, since the total current density i_0 is the same at both sides. Hence $(z_m - z_g) = z_g$, and the position z_m of the virtual cathode can no longer depend upon V_a but only upon V_g and z_g.

With still further increase in current i_0, say by further reduction of the cathode-to-grid distance z_g, the virtual cathode moves nearer and nearer towards the grid g, and the total current density i_0 between grid and virtual cathode increases correspondingly. Simultaneously, the fraction i_a that reaches the anode, gradually decreases. This can be seen, for instance by applying Child's law equation (8.62) to the right branch of the potential distribution between z_m and z_a, where with decreasing $(z_m - z_g)$ the complementary $(z_a - z_m)$ must increase. Hence, the largest current densities which can be transmitted from the grid to the anode in presence of a virtual cathode are much smaller than the maximum current densities that are transmitted in presence of the potential minimum of positive voltage.

If starting from large current densities the space current i_0 is gradually decreased, the anode current i_a will be found to increase. The operation now, however, cannot be performed in just the reversed way as has been described for gradually increasing current. This is due to the fact that originally the operation began with a potential minimum of finite voltage, now it begins with a virtual cathode. Now with decreasing i_0, the virtual cathode will move back towards the anode. This behaviour will continue until the space-current density reaches a critical value which is calculated to be

$$(i_{\text{min.}})_{\text{crit.}} = G_0(V_g^{\frac{3}{4}} + V_a^{\frac{3}{4}})^2, \tag{8.68}$$

where G_0 is again given by (8.63), with s being the grid to anode distance. The slightest further reduction of space current causes the virtual cathode to disappear. Now, however, the jump in distribution into stage (3) produces no change in current, though it will be observed that the highest current reached on the retrace of

the cycle is less than that obtained when the injected current i_0 was increased. From stage (3) onwards the operation with decreasing current is again the inverse operation to that with increasing current.

The whole cycle for the transmitted current i_a as a function of the injected current i_f is shown in fig. 8.7. Along the points (1), (2), (3) and (4) which mark the corresponding stages shown in fig. 8.7, the curve is a straight line through the origin, since in these stages $i_a = i_0$. At (4) the change from the positive potential minimum to the virtual cathode occurs, and the distribution changes abruptly into that of stage (5). With further increase of the injected current, the transmitted current only decreases. If by decreasing the injected current the cycle is reversed, the transmitted current will gradually increase along the lower branch of the loop shown in fig. 8.7; then, after reaching stage (3), i_a will decrease again with decreasing i_0.

Between stage (3) and stage (5) shown in figs. 8.6 and 8.7, two different values of i_a are seen to be theoretically possible for every given value i_f of injected current. This duality of values for i_a is due to the alternative of a formation either of a virtual cathode or of a positive potential minimum. Both cases correspond to possible solutions of Poisson's equation. Bull (1948), however, has shown that Maupertuis's principle (cf. (1.1)) can be applied to the study of space-charge distribution, since least action can be postulated for the transition of electrons from the grid to the anode. In this way it can be concluded that in the critical range only those solutions with virtual cathode formation lead to physically stable conditions. Hence, the dotted curve of fig. 8.7 belongs to unstable states which should not be observable.

Various attempts have been made to investigate experimentally the distribution along a flow of space charge, but so far only qualitative results have been obtained. The minimum in the potential distribution along an electron beam of high density has been probed experimentally by Klemperer (1947*a*) with the help of a low-intensity probe beam, which on crossing the heavy current beam was deflected in opposite directions at either side of the potential minimum.

Schade (1938) claims to have detected in beam power tubes (cf. § 10·6, fig. 10.17) such characteristic hysteresis loops as

shown in fig. 8.7. Schade varied the grid voltage of such tubes sinusoidally and registered total emission and plate current by the two mutually perpendicular deflexions of a cathode-ray oscillograph. The demonstration of hysteresis loops would seem to indicate the shifting of the virtual cathode changing abruptly into a potential minimum and vice versa, but the results have still to be taken with some reserve.

An inherent difficulty in checking the theory of the unbounded space-charge flow by experiments is given by the unavoidable

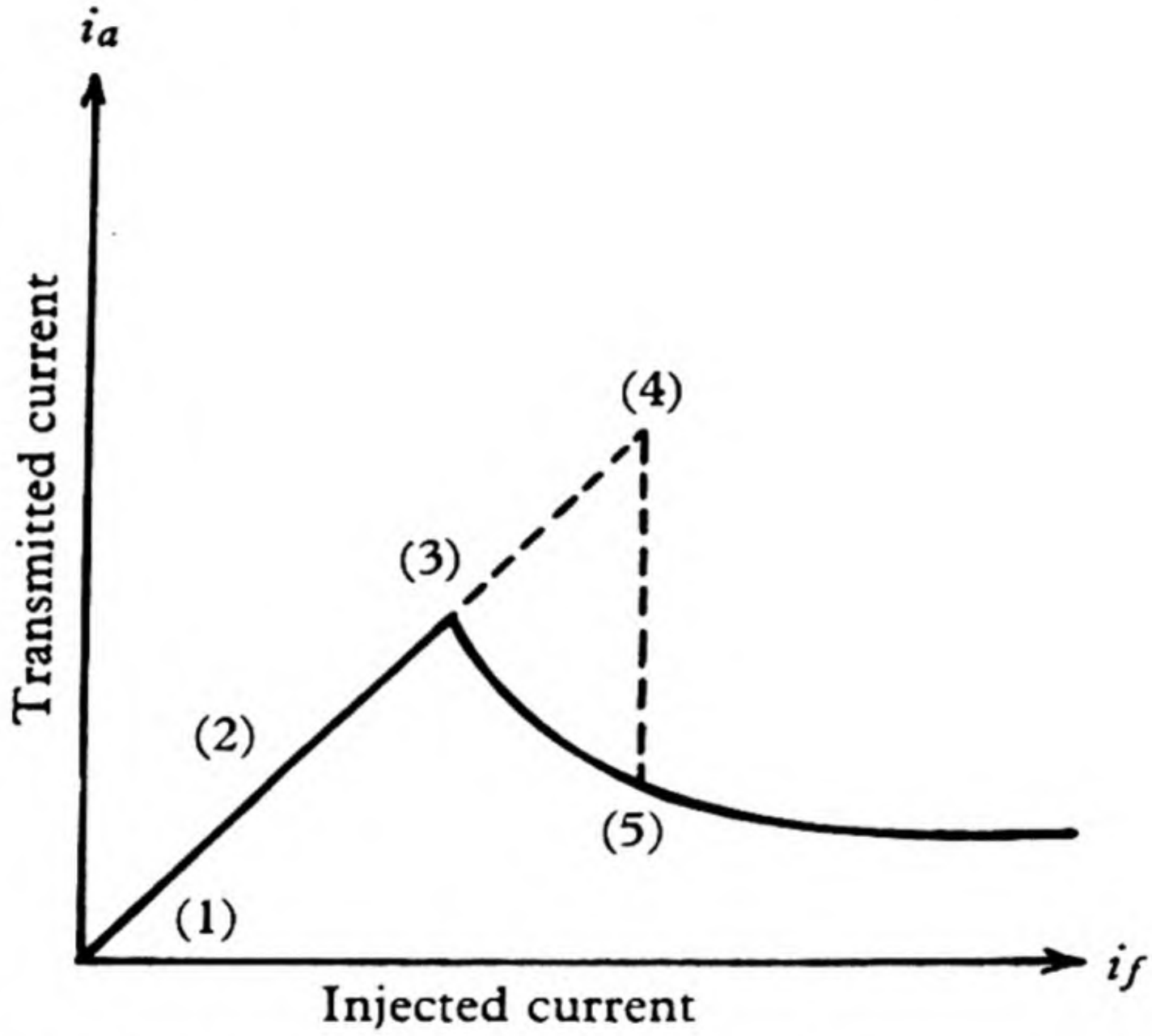

Fig. 8.7. Transmission of current through a space charge.

presence of lateral velocity components in the actual electron flow. These components already appear in the angular distribution of emission at the cathode, and they are produced in a more serious degree if accelerating grid electrodes are used. Their existence and disturbing nature in space-charge experiments has been proved by Rodda (1945).

Some elimination of the disturbing influence of the lateral velocity components has been accomplished by Haug (1943), who claims to have detected hysteresis loops in the voltage-current characteristics of relatively short beams of great diameter. He employed a strong longitudinal magnetic field, thus preventing to some extent sideways movements of the electrons.

Potential distributions in quasi-parallel, magnetically confined

beams which are long in comparison with their radius have been discussed by Haeff (1939), Smith and Hartman (1940) and by Guenard (1945). Let such a beam pass coaxially through a conducting tube at anode potential V_A, and let space-charge spreading be constrained by a very strong longitudinal magnetic field. As the beam current I is increased, the potential V_0 at the beam axis falls progressively with respect to the potential V_1 at the edge until the ratio $V_0/V_1 = 0{\cdot}17$. At this potential distribution the maximum possible current $I_{\text{max.}}$ passes along the beam. If further current is injected into the beam, some electrons are turned back, and by a sudden transition through an unstable region, a virtual cathode is formed in the beam. Now only a reduced current I_0 will be able to pass the beam. Critical space-charge factors $I_{\text{max.}}/V_A^{\frac{3}{2}}$ and $I_0/V_A^{\frac{3}{2}}$ can be found for every ratio of radii of beam and surrounding electrode. Both these factors are the greater, the nearer the beam radius approaches the tube radius, i.e. the nearer the potential V_1 at the edge of the beam comes to the potential V_A of the tube. If the beam completely fills the tube, $V_1 = V_A$, and for this particular case one obtains

$$I_{\text{max.}}/V_A^{\frac{3}{2}} = 32{\cdot}4 \times 10^{-6},$$

and for the flow with virtual cathode

$$I_0/V_A^{\frac{3}{2}} = 29{\cdot}3 \times 10^{-6},$$

while the Brillouin type of flow (cf. (8.50)) in the properly adjusted magnetic flux density yields a maximum

$$I/V_A^{\frac{3}{2}} = 25{\cdot}4 \times 10^{-6}.$$

The potential distribution in a beam need not depend upon the electrode potentials and upon the proper beam current only, but it may be controlled by external electron injection. A control beam, for instance, may intersect a working beam at right angles. The potential depression in the working beam is increased as the injected current is increased and this, in turn, reduces the current of the working beam. Control arrangements of this kind apparently offer much scope for future technical application. For instance, Jonker and Overbeek (1949) claim to have reached by space-charge control a slope of 23 mA./V. extrapolated to a current of 1 mA. This is nearly twice the theoretical maximum slope of grid-control valves.

CHAPTER IX

EMISSION SYSTEMS

9.1. The acceleration of the emitted electrons

The light sources in light optics correspond to the cathodes in electron optics. While, however, a light-emitting body, for instance an incandescent filament, can be used as a source of light-rays immediately, a simple electron emitter such as a thermionic cathode is not sufficient for the production of electron rays in a practical electron-optical gear. When passing through the refracting elements of the glass optics, the speed (phase velocity) of light emitted from the filament is changed by a relatively small fraction only. On the other hand, electrons leaving a filament have to be accelerated first; their kinetic energy must be increased many times, in some cases even many thousand times, before they can enter a particular electron optical device.

The electrons from the cathode have to be injected into a relatively field-free region, i.e. they have to enter a space which is surrounded by an electrode of positive potential with respect to the cathode. This electrode is the anode of the emission system, hence electric lines of force starting at the cathode will end on the anode. The emission will first follow approximately the direction of the lines of force, since within some distance from the cathode, the kinetic energy of all electrons is still small in comparison with the potential drop along the path. On their way to the anode, the electrons are more and more accelerated. Eventually their accumulated kinetic energy will be much greater than the potential drop along a given element of the path. Hence along this path element the electron can deviate considerably from the direction of the field. For this reason it is possible to accelerate the emission of a relatively large cathode surface through a small aperture of the anode into a field-free space which is surrounded by the anode.

In good emission systems, the whole emission from the cathode passes the aperture in the anode, no electrons being intercepted. In this case, the electric field at the cathode is directed initially towards the anode aperture, the deviation of the field from the

initial direction occurring rather close to the anode only. For the production of such a field an auxiliary electrode between cathode and anode is essential. This electrode has always to be substantially negative with respect to the anode. Generally, it is kept at cathode potential or slightly negative with respect to the cathode. As early as in 1903, Wehnelt recommended such auxiliary electrodes for focusing the electron emission towards the anode. The auxiliary

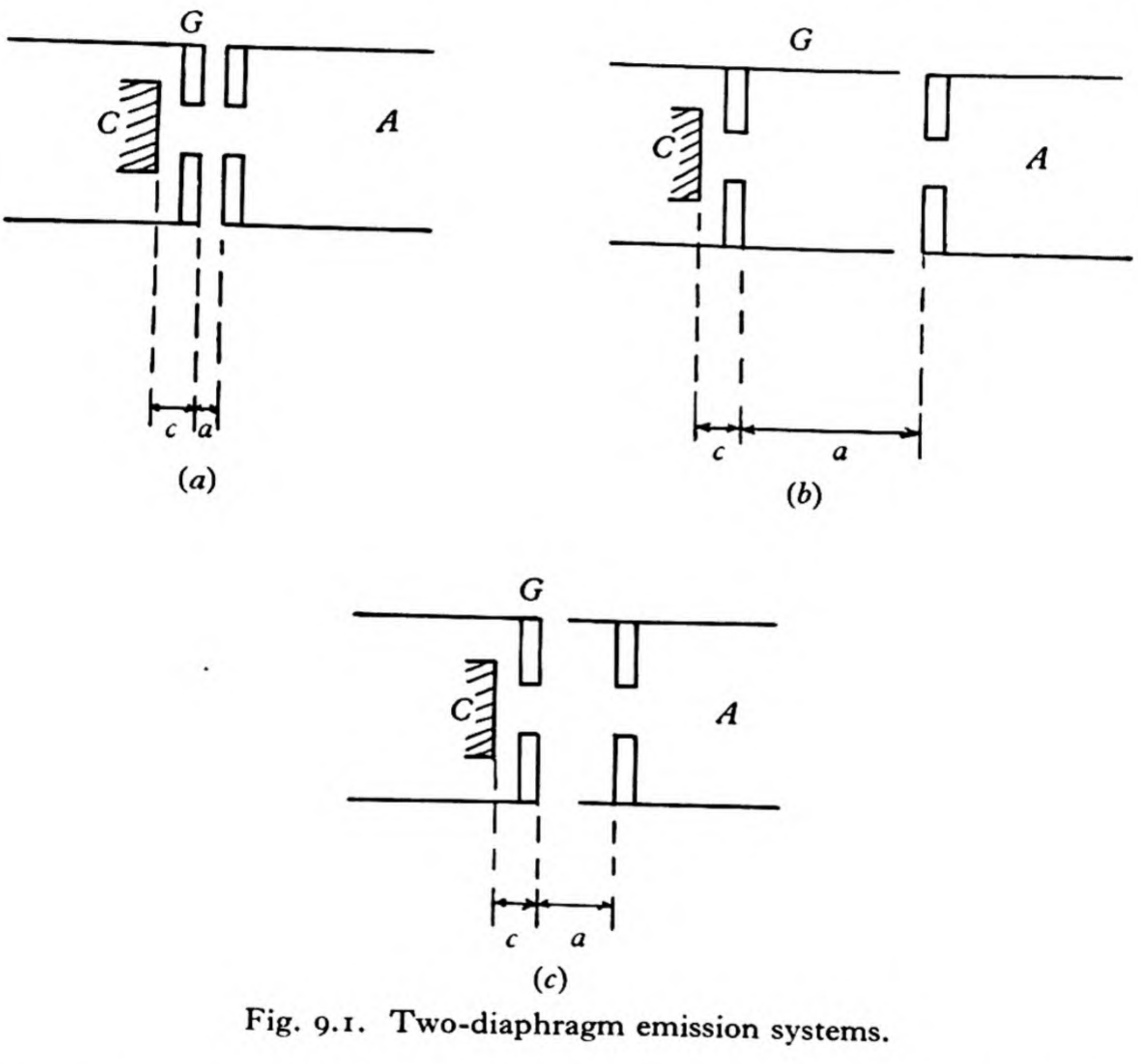

Fig. 9.1. Two-diaphragm emission systems.

focusing electrodes often serve the additional purpose of controlling the intensity of the emission. In this case, 'intensity modulation' is effected by changing the potential of the auxiliary electrode. Hence, in analogy to the terminology in valve technique, this electrode is called the 'grid', the 'screen' or the 'modulator' of the emission system. A complicated emission system might contain many electrodes. However, in order to understand the general properties of emission systems, a study of some simple, empirically

developed triodes with very simple shapes of electrodes is sufficient. A description of such systems will be given here first.

Electrode arrangement in simple triodes. Of some technical importance are the 'two-diaphragm emission system' shown in

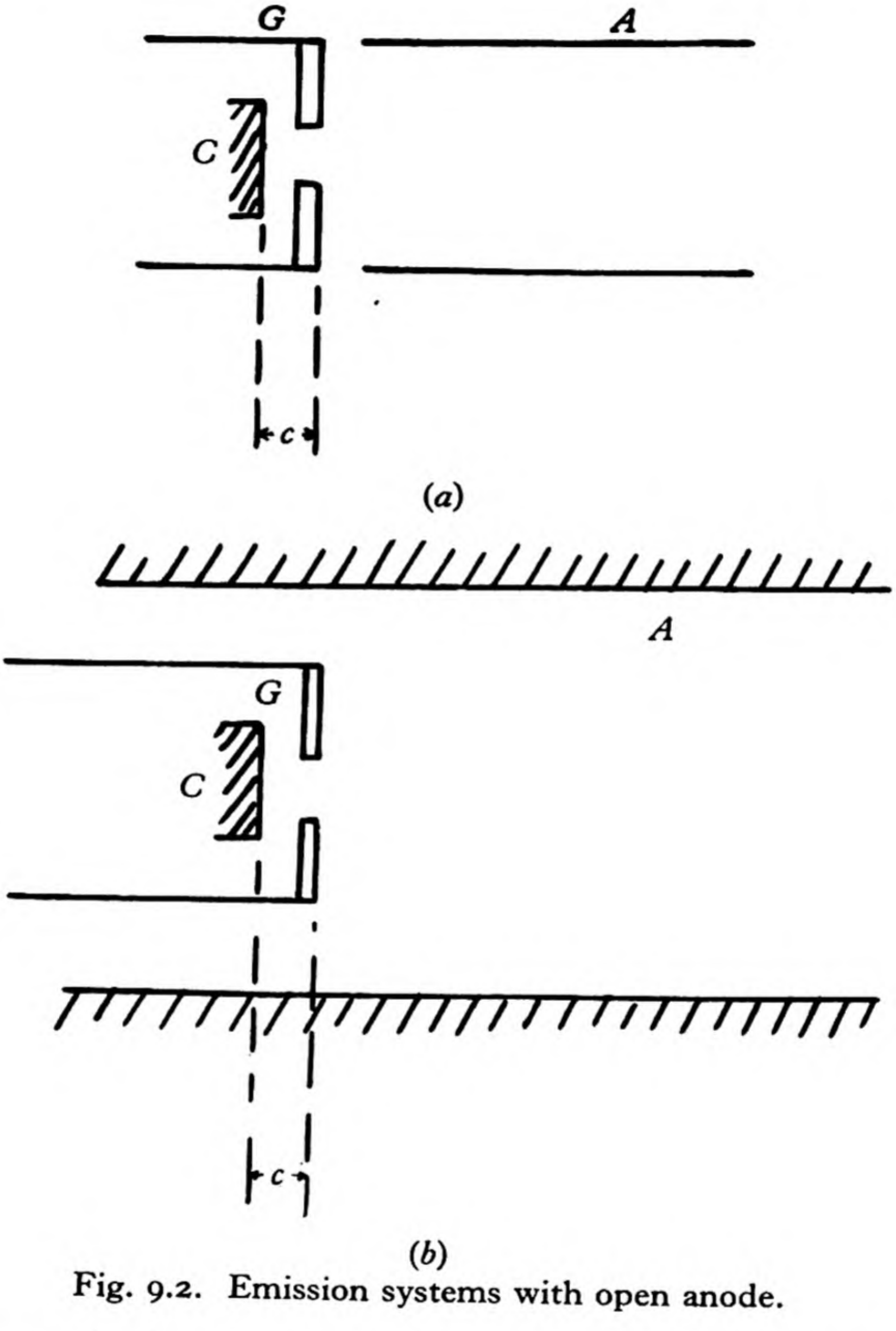

Fig. 9.2. Emission systems with open anode.

fig. 9.1, the emission systems with open anode in fig. 9.2 and the emission systems with conical anode shown in fig. 9.3. In all the drawings, the cathode is marked *C*, the grid electrode *G* and the anode *A*.

The emission systems in figs. 9.1 and 9.2 have flat equipotential cathodes. These are heated either by thermal conduction or radiation from a hot filament directly behind the cathode, or by electron bombardment from a filament behind the cathode and at a few

hundred volts negative with respect to it. The grid electrodes are flat diaphragms with a circular aperture. They are fixed in tubular sleeves which also serve for shielding the electron rays from external electrostatic disturbances.

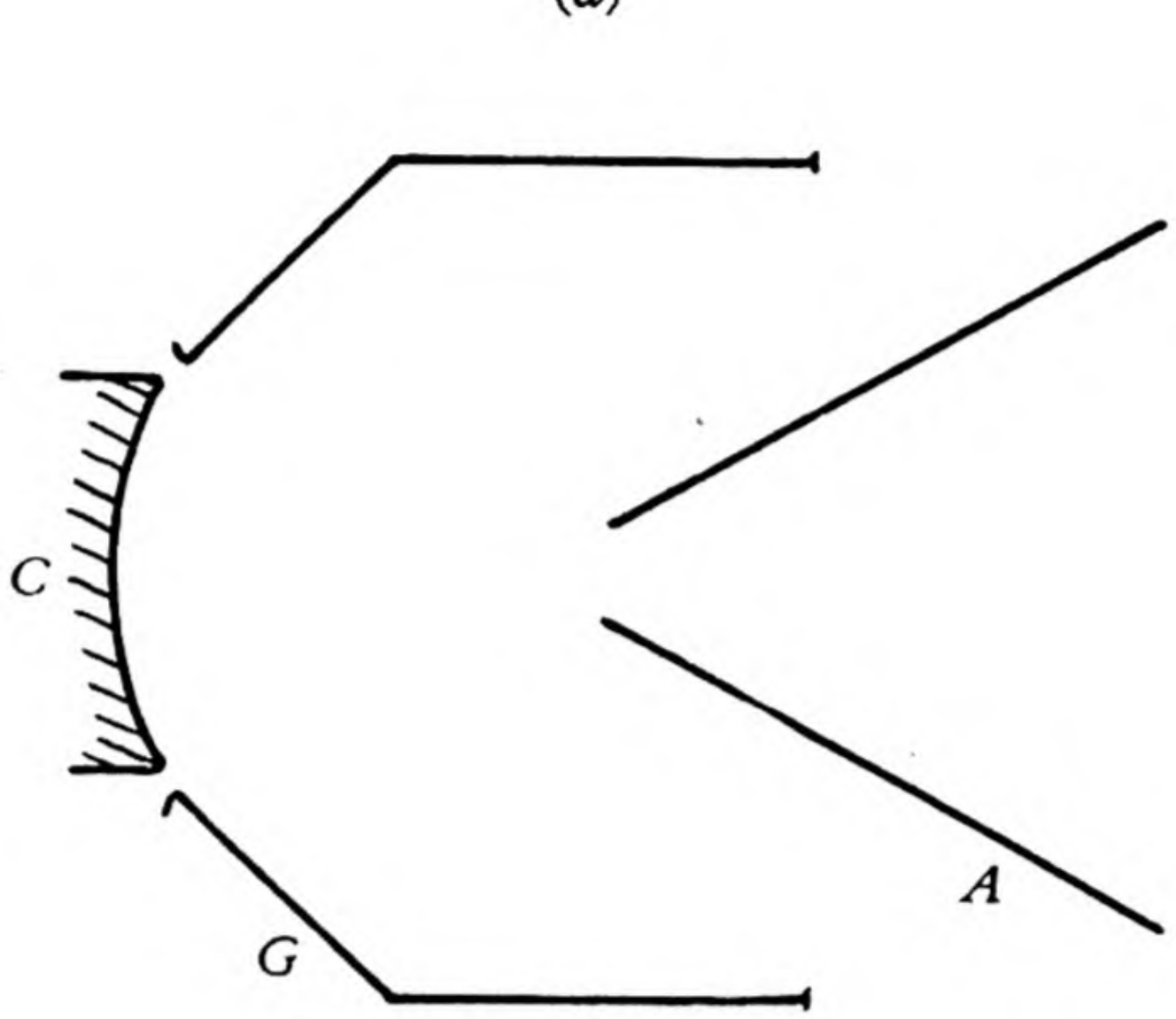

Fig. 9.3. Emission systems with conical anode.

The anodes in the system of fig. 9.1 are also apertured flat diaphragms. In the system of fig. 9.1 (*a*) electrostatic shielding of the space between grid electrode and anode is provided automatically, since the radius of the diaphragms is large in comparison with their spacing. Otherwise, the shielding may be effected by surrounding the grid-anode space with a cylinder that is either

connected to the grid electrode (fig. 9.1 (*b*)) or to the anode (fig. 9.1 (*c*)). The two-diaphragm systems of fig. 9.1 have found wide application. Their use in electron microscopy was first studied by Brüche and Johannson (1932) and by Johannson (1933). In electron guns, the two-diaphragm systems were first described by Zworykin (1933*b*).

Open anode systems as shown in fig. 9.2 are useful when relatively high anode voltages are available and beams of relatively small divergence are required. These systems are employed frequently in magnetically focused television tubes. The anode of the system shown in fig. 9.2 (*b*), for instance, may be the metallized neck of a glass tube.

An ideal arrangement for converging the total emission of a large cathode surface into a small point focus would be provided by a field with strictly spherical equipotentials. Such a scheme could be realized by a spherical, concave cathode with an extremely small anode in the centre of the sphere. Fig. 9.3 (*a*) and (*b*), showing concave cathodes with funnel-shaped anodes, represent to some extent practical examples based on this idea: The anode, which should be very small in comparison with the cathode, is represented by the tip of a funnel electrode *A* protruding towards the centre of the sphere. The electrons are accelerated through the aperture of the funnel. A system with concave cathode and funnel-shaped accelerator was described as early as 1899 by Wiechert; it has been further investigated by Rogowski and Grösser (1925). The system shown in fig. 9.3 (*b*) has been used by Farnsworth (1934), that of fig. 9.3 (*a*) by Klemperer and Wright (1939).

9.2. Fields and electron orbits in emission systems. Cross-over formation

In all practical emission systems, electrostatic fields converge the electron rays into a disk of least confusion which is called the 'cross-over'. The cross-over formation is explained by fig. 9.4. The electrons leave the cathode surface under different angles and with different speeds which are due to the thermal velocity distribution. Let electrons of a homogeneous velocity be considered first. Rays marked in the figure as (1), (2) and (3) leave the

cathode surface C at right angles; they intersect at a common point on the axis (z) forming the centre of the cross-over X. These rays are the chief trajectories of electron bundles, each bundle emerging from a common point of the cathode surface. The peripheral rays of these bundles leave the cathode surface under grazing angles; they are marked in fig. 9.4 by numbers (4)–(9). The widths of the bundles at their mutual intersection is reponsible for the finite extension of the cross-over X. Since the field tends to converge each ray of the bundle towards its chief trajectory, all bundles eventually come to focus at the surface $B_1B_2B_3$ where an optical image of the cathode is formed.

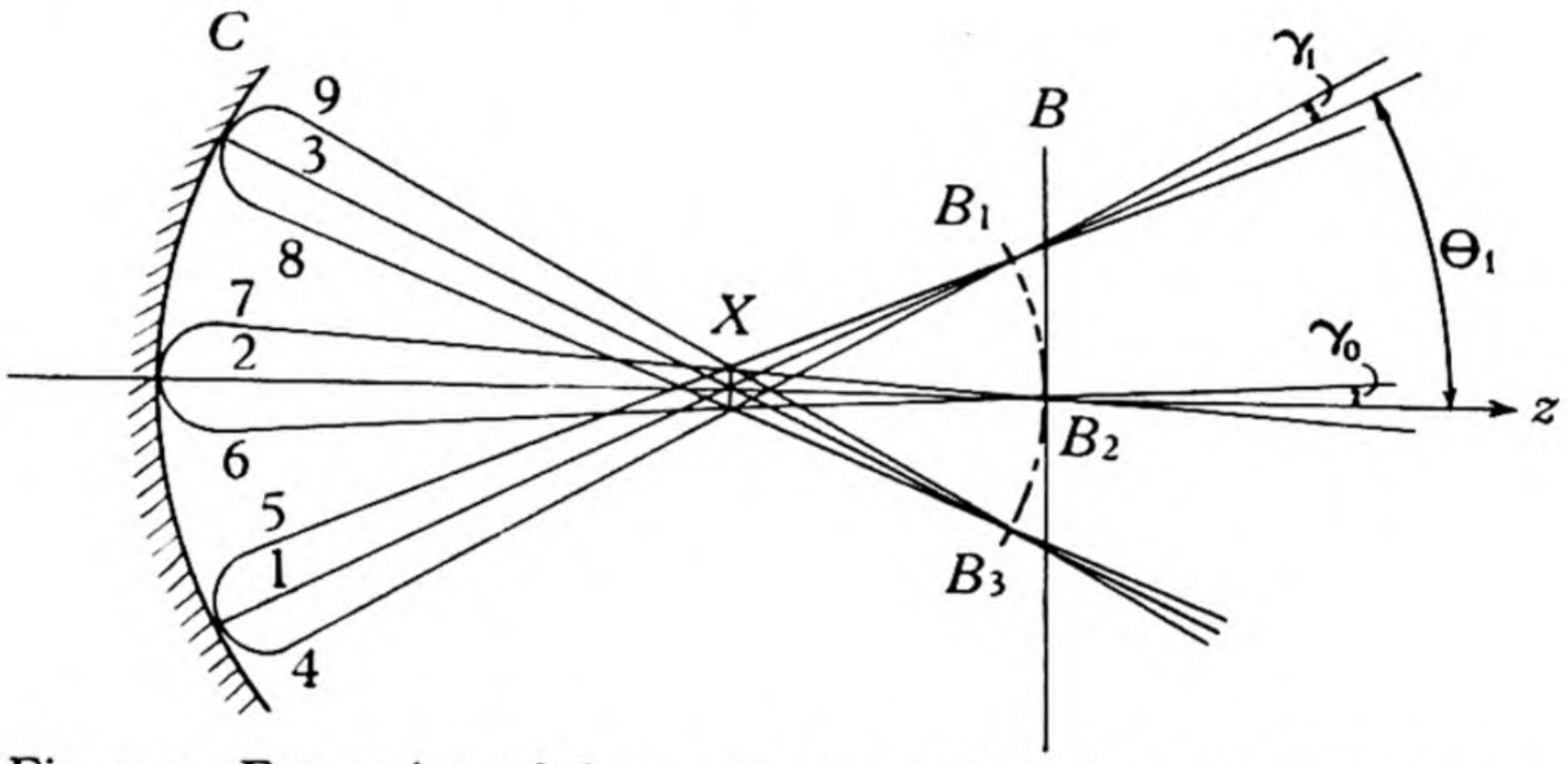

Fig. 9.4. Formation of the cross-over and of the cathode image.

The size of the cross-over has been estimated by Ruska (1933), who assumed the field between cathode and centre of the cross-over to be a central field with strictly spherical equipotentials. He started from the equation of motion for the electrons under these idealized conditions, and derived a radius of cross-over

$$y_x = \frac{y_c}{\sin\Theta}\sqrt{\frac{V_{em}}{V_x+V_{em}}}, \tag{9.1}$$

where y_c is the semi-aperture of the cathode surface, V_{em} is the thermal emission energy (electron-volts) of the electron, V_x the potential at the cross-over and Θ the angular semi-aperture between chief ray and axis. (A derivation of (9.1) from optical principles will be given in the next section.) Law (1937) generalized (9.1) for any non-uniform field of rotational symmetry by introducing a 'field-form factor' L which is a function of the potential

distribution in the system. He expressed the cross-over radius as

$$y_x = \frac{z_x}{L}\sqrt{\frac{V_{em}}{V_x + V_{em}}}, \tag{9.2}$$

where z_x is the distance between cathode and cross-over. Law's factor $L \approx z_x \Theta / y_c$ would be unity for the field with strictly spherical equipotentials. For the fields of practical systems L is found to be of the order of a few tenths. Disregarding aberrations, Dosse (1940) took the field-form factor as the ratio of the cross-over distance from the cathode to the focal length of the emission system, i.e.

$$L = z_x / f'. \tag{9.3}$$

Cross-over size and location depend very much on the field distribution in the system. According to Artsimovitch (1944), general predictions for simple triode systems can be made from the character of the axial potential distribution $V(z)$. There, the field gradient $(\partial E/\partial z) = -(\partial^2 V(z)/\partial z^2)$ may either increase or decrease monotonically with z, or it may be constant. In the first case, the field E_x at the cross-over is at least 5·2 times larger than the field E_c at the cathode, the maximum cross-section of the elementary bundle of rays (cf. fig. 9.4) occurs between cathode and cross-over and a demagnified cathode image is formed. In the third case, $E_x = 5{\cdot}2E_c$, while in the second case where $E_x < 5{\cdot}2E_c$, the cross-over is formed before the elementary bundles reach their maximum cross-section and a magnified image of the cathode is formed.

The calculation of potential distributions in emission systems offers great difficulties and has been successful for very much idealized electrode structures only, replacing the diaphragms, for example, by infinite planes or by short annular rings. In this special way, solutions have been obtained by Wendt (1933) by Waldmann (1937) and by Paehr (1939), which, however, are of little practical value. Plocke (1951) developed the potential near the centre of the cathode by a Taylor series and obtained the following simple potential function

$$V(y, z) = E_0 z[1 - (y/y_c)^2 + (2/3)(z/y_c)^2], \tag{9.4}$$

where E_0 is the field at the centre of the cathode and y_c the radius of the emitting cathode area. For both, E_0 and y_c approximate

expressions can be given in terms of electrode potentials and geometry.

On the other hand, Einstein and Jacob (1948) found that the empirical potential distributions along the axis of triode systems could be expressed by

$$V(z) = A[\exp(kz) - \exp(-kz)], \tag{9.5}$$

where A and k are characteristic constants for a given system. A is a 'voltage scale factor' measuring a certain fraction of the cross-over voltage V_x, while k is a 'geometrical scale factor' which is inversely proportional to the cross-over distance (z_x) from the cathode. The values of the parameters A and k depend mainly upon the grid to cathode distance c; however, k is always of the order of a reciprocal grid-aperture diameter and, for zero grid bias, A is of the order of a small fraction ($\approx 3\%$) of the 'black-out voltage' (cf. § 9.5). Series development of (9.5) allows us to visualize the change of potential at various distances from the cathode. Close to the cathode the field will be approximately constant, since for $z \ll k$,

$$V(z) = 2Akz. \tag{9.6}$$

Farther away from the cathode, there follows a simple exponential region which includes the cross-over. By substituting (9.5) into the paraxial ray equation (3.29), Jacob (1950*b*) obtained an analytical expression for the electron trajectories, from which simple formulae, for instance, for cross-over size and cross-over position can be derived.

Another simplifying treatment of the emission system has been presented by Ellis (1947). There, complicated empirical potential distributions are approximated by two regions of constant field. The proper refraction of the rays is obtained by the additional assumption of two thin equivalent lenses, in the planes of grid and anode aperture respectively. Hence, the potential distribution along the axis as measured with the electrolytic trough (§ 3·2) is replaced by two linear functions, one for the cathode to grid space, and the other for the grid to anode space. The electrons leave the cathode with some transverse velocities. They describe parabolic paths until they reach the grid aperture, where they receive a centripetal impulse in proportion to their distance from the

axis. Following another parabola path to the anode aperture, they receive a centrifugal impulse there, travelling thereafter along straight lines.

Accurate electron orbits can be obtained by ray tracing (§ 3·3 ff.) through the actual field plots. These traced orbits, however, are of little practical value, since in emission systems they generally are only a rough approximation to the actual paths. It will be shown in § 9.4 that all properties of the emission system are mainly controlled by the concentration of space charge.

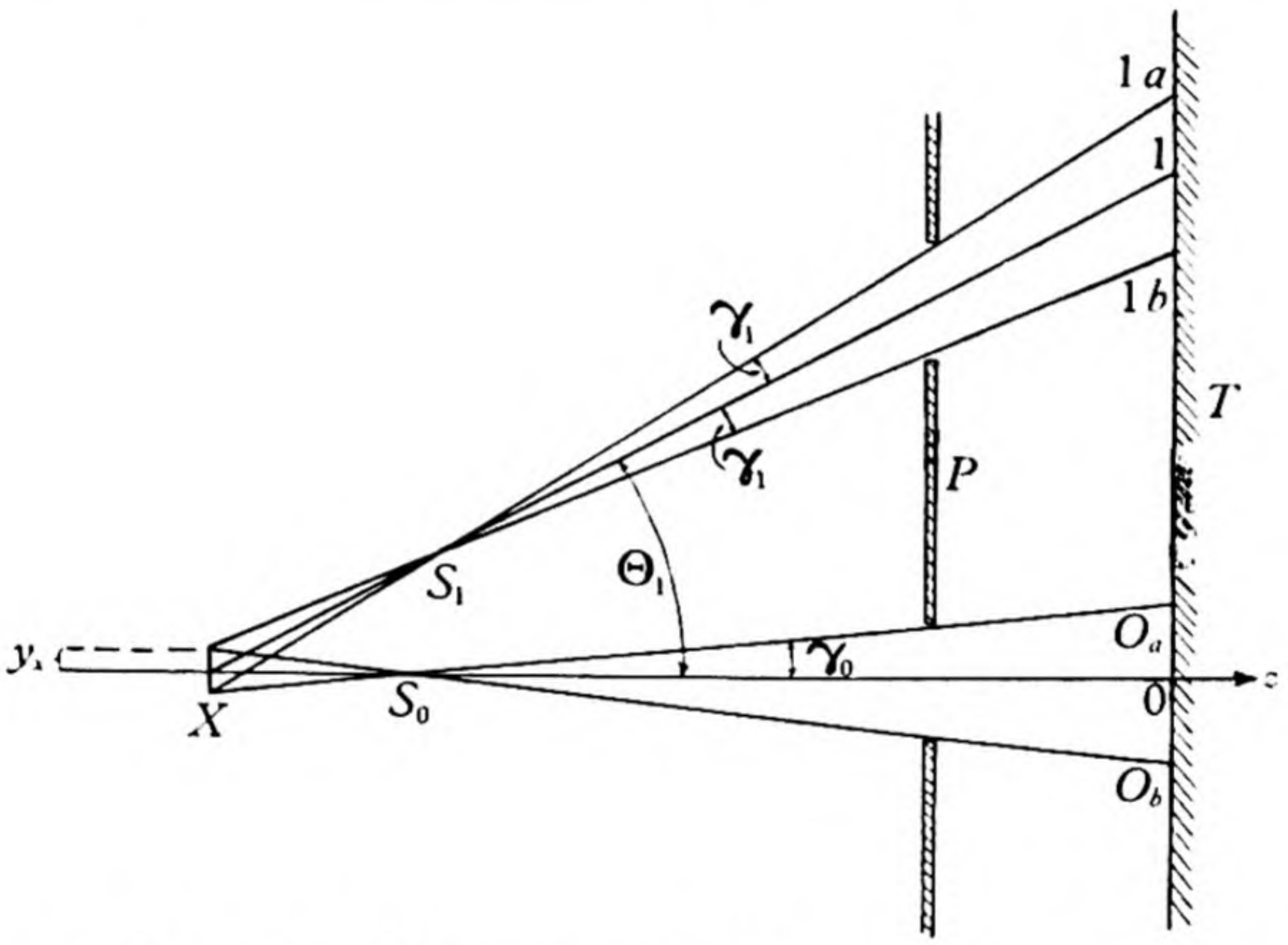

Fig. 9.5. Selection of electron pencils by a pepperpot diaphragm.

Experimental investigation of the cross-over. This has been attempted in two different ways. Usually a magnified electron-optical image of the cross-over is projected by an electron lens on to a fluorescent target (e.g. Jacob, 1939; Klemperer and Mayo, 1948). The use of high-quality electric or magnetic lenses of relatively large diameter is essential so that unavoidable lens errors are sufficiently small and do not modify the projected image.

In an alternative method (Klemperer and Mayo, 1948; Klemperer and Klinger, 1951) pencils emerging from the cross-over are selected by a pepperpot diaphragm and traced by a sliding fluorescent target. In fig. 9.5, X represents the cross-over, P a part of the pepperpot diaphragm and T the target. The diaphragm P contains a large number of circular holes; only two of them are shown in the

figure. Through one of these holes, which is the axial hole, there passes the chief ray o which coincides with the axis z of the system. The two outermost peripheral rays passing through the same hole are marked O_a and O_b. All three rays intersect at the vertex S_0; they represent the axis and, respectively, the axial section through the envelope of a small conical pencil with the semi-vertical angle γ_0. Analogously, the rays through a hole off the axis are the chief ray 1 and the peripheral rays 1a and 1b, forming a cone with the vertex S, and semi-vertical angle γ_1. In each case, the chief rays are traced by following up the centres of the fluorescent spots on a target T which is arranged perpendicularly to z and can be moved along this axis. The extrapolated intersection of the chief rays with the axis allows a location of the cross-over position z_x. If the chief rays of different divergences Θ have no common point of intersection, their tracing will provide information on the spherical aberration of the cross-over.

The divergences γ of the pencils are obtained by tracing the diameters of the fluorescent spots.* The cross-over diameter as traced by the pencil o can be derived from the figure to be

$$(y_x)_0 = (z_p - z_x)\,\gamma_0 - r_p, \tag{9.7}$$

where z_p is the distance of the pepperpot diaphragm from the cathode and r_p is the radius of the pepperpot hole which can be measured directly under a microscope. A pencil intersecting the axis at an angle Θ_1 leads to a cross-over radius $(y_x)_1$, which, in principle, can be different from $(y_x)_0$, since it is formed by a pencil emitted from another zone of the cathode and hence has travelled through a different field. Moreover, the radii $(y_x)_0$, $(y_x)_1$, $(y_x)_2$ belong to a virtual cross-over which is extrapolated from straight rays. Actually after crossing over, the rays are often subject to some deflexion by a field which, still belonging to the emission system, can extend some distance behind the cross-over. Hence the real cross-over does not need to coincide with the virtual.

* A traced spot diameter does not necessarily correspond to the diameter of a disk with sharp boundaries. It is shown below (§ 9.4) that the current density in the cross-over fades away as an exponential function of the radius, and that a cross-over radius can be fixed only by special definitions. The visually determined radius, however, seems roughly to coincide with definitions given below by (9.25).

9.3. Optical approach to emission systems

It has been pointed out that an accelerating electron lens is necessary for the projection of the electron emission from the cathode into a field-free space. This lens should be of positive focal length and located approximately at its focal distance from the cathode. A single aperture in front of the cathode would be insufficient. This follows from the optical properties of apertured

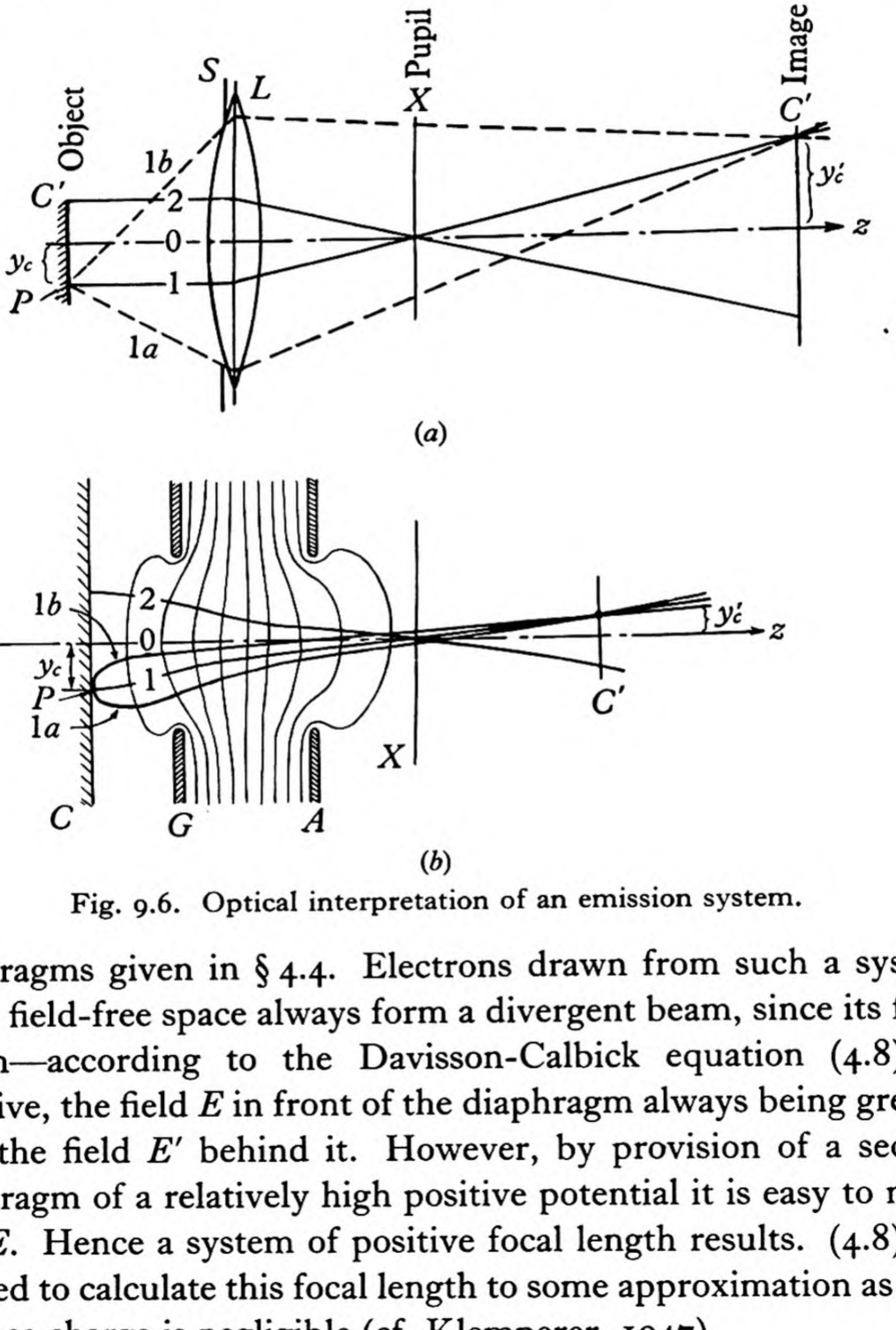

Fig. 9.6. Optical interpretation of an emission system.

diaphragms given in § 4.4. Electrons drawn from such a system into a field-free space always form a divergent beam, since its focal length—according to the Davisson-Calbick equation (4.8)—is negative, the field E in front of the diaphragm always being greater than the field E' behind it. However, by provision of a second diaphragm of a relatively high positive potential it is easy to make $E' > E$. Hence a system of positive focal length results. (4.8) can be used to calculate this focal length to some approximation as long as space charge is negligible (cf. Klemperer, 1947).

The application of some general optical principles to emission systems may be explained after Dosse (1940) by comparing the electron emission system of fig. 9.6 (*b*) with its light-optical analogue in fig. 9.6 (*a*). In both drawings, there are shown three chief rays 0, 1 and 2 which all leave the emitting surface C at right angles. The rays 1*a* and 1*b* form the envelope of the elementary bundle 1 which emerges from the point P.

In the light-optical case, in which the refractive index in object and image space is of the same order of magnitude, the limiting rays 1*a* and 1*b* are given by the aperture stop S of the lens L. In the electron-optical case, however, the refractive index along the electron path increases very rapidly. Hence the radius of an elementary bundle of electrons is decreasing so rapidly that it is not limited by an aperture in a focusing electrode, but 1*a* and 1*b* are rays which are emitted at a grazing angle. At the cathode the elementary bundle then fills an entire hemisphere.

The cross-section of the beam in the plane X forms the cross-over. This corresponds to the exit pupil of the optical system which is defined as the cross-section of the beam in a plane perpendicular to the axis at the point of intersection of the chief rays with the axis (cf. Drude, 1925, p. 73). Again, it can be seen that the size of the pupil of the light-optical system is determined by the limiting physical aperture stop S, while in the electron emitting system the exit pupil is given by the emission velocity of the peripheral electrons which left the cathode at grazing angle.

The chief rays from a plane cathode surface as shown in fig. 9.6 are initially parallel. Hence, in this case, the cross-over X coincides with the focus of the emission system. On the other hand, the image C' of the cathode surface C is formed by the foci of the elementary bundles. The magnification y'_c/y_c is, according to (2.2), given by the ratio of the distance XC' to the focal length f' of the emission system. This relation and (2·8) provide a practical means of determining the focal lengths which are given by

$$f' = XC'\, y_c/y'_c \tag{9.8}$$

and

$$f = f' \left(\frac{V_{em}}{V_{em} + V} \right)^{\frac{1}{2}}, \tag{9.9}$$

where V_{em} is the energy with which the electron is emitted (e.g.

0·1 eV. for an oxide cathode) and V is the electron energy in the image space. Magnifications y_c'/y_c have been measured by Johannson (1933) with the help of a pattern of lines scratched in the cathode surface. The distances of the lines can be measured with a microscope, first on the cathode and later on a fluorescent target, to which the image is projected. Magnifications of the cathode surface of the order of 100 × can be obtained easily with two-diaphragm emission systems. In this way, the system has been used by various investigators (cf. § 12·6), as an electron microscope for studying emission phenomena at thermionic cathodes. The system is called an immersion system, and it can be compared with the immersion objective of a light-microscope, since the object (cathode) is immersed in the field of the two-diaphragm lens. Focal lengths and magnifications of the objective are controlled by the distance c of the cathode from the grid electrode and by the grid bias V_g. Smallest focal lengths ($f/r_g \approx 1$, r_g = radius of grid aperture), and hence largest magnifications, are observed for negative grid bias or for relatively large cathode distances c. On the other hand, for smallest c the focal length can grow to infinity or even become negative.

'Intensity' and 'Brightness' of an electron source. If an emission system is used in an electron gun, the emitted electrons have to be projected on to a fluorescent screen by an electron lens of a given aperture. When attempting to concentrate the maximum current into the smallest spot, it is usually necessary to project the largest possible current density i_x at the cross-over into the smallest possible solid angle Ω (see, for instance, § 12.3). Hence the expression (cf. Dosse, 1940)

$$i_x/\Omega \approx I_x/(\pi y_x^2 \pi \Theta^2) \tag{9.10}$$

should be as large as possible, where I_x is the total current passing through a cross-over of radius y_x into a cone of semi-vertical angle Θ. The expression (9.10) corresponds exactly to the optical definition of the 'intensity' of a light source.

Of further interest is the angular distribution of emission densities. Following an argument by Langmuir (1937*b*) it can be shown that an emission distribution according to Lambert's law—which is known to occur at the cathode surface—is also to be expected at any electron-optical image of the cathode as well as at the cross-over. According to Lambert's law, as stated in Chapter I, eq. (1.29), the

amount of radiation emitted from the cathode between the angles Θ_c and $(\Theta_c + \mathrm{d}\Theta_c)$ with the normal to the surface can be written (cf. (1.30)) as

$$\mathrm{d}I(\Theta_c) = 2\pi B \pi y_c^2 \sin\Theta_c \cos\Theta_c \mathrm{d}\Theta_c, \tag{9.11}$$

where the quantity

$$B = i_{em}/\pi \tag{9.12}$$

is analogous to the brightness (luminance) of an optical source, where i_{em} is the total emission density into the hemisphere and y_c is the radius of the emitting area. At the image (and analogous considerations apply to the cross-over) the radiation $\mathrm{d}I(\Theta')$ will intersect the axis at angles Θ' which are connected to the corresponding quantities at the cathode by Abbe's sine law (1.33), namely,

$$\sin\Theta' = \frac{Ny_c}{N'y'}\sin\Theta_c. \tag{9.13}$$

On differentiation Abbe's law gives

$$\cos\Theta'\,\mathrm{d}\Theta' = \frac{Ny_c}{N'y'}\cos\Theta_c \mathrm{d}\Theta_c. \tag{9.14}$$

Substituting the last two equations into (9.11) yields

$$\mathrm{d}I = 2\pi B\left(\frac{N}{N'}\right)^2 \pi(y')^2 \sin\Theta' \cos\Theta' \mathrm{d}\Theta'$$

or taking

$$B' = B(N/N')^2, \tag{9.15}$$

we obtain

$$\mathrm{d}I = 2B'(\pi y')^2 \sin\Theta' \cos\Theta' \mathrm{d}\Theta'. \tag{9.16}$$

The angular distribution of the radiation is thus the same in (9.11) and in (9.16). That is, if Lambert's law is obeyed by the cathode it will be also obeyed by the cross-over and by the image, provided the emission system is free from aberrations.

There are, however, the two significant differences between the cathode and the other cross-sections under consideration. First, at the cathode, electrons are emitted in all directions, i.e. $\Theta_c \leqq \frac{1}{2}\pi$. Hence, from Abbe's law, follows

$$\sin\Theta' \leqq Ny_c/N'y', \tag{9.17}$$

i.e. the rays pass through the cross-over or through the image at a limited angle of divergence. Secondly, the brightness of the cross-over or of the image is different from that of the emitting

surface and, due to (9.15) with $N \sim \sqrt{V}$ (cf. Chapter I), the ratio of brightness

$$\frac{B'}{B} = \frac{V + V_{em}}{V_{em}} \tag{9.18}$$

is given by the ratio of electron energies at the cathode (V_{em}) and at the cross-over or image respectively ($V_{em} + V$). If $N = N'$, (9.15) becomes the familiar law for ordinary optical instruments that the apparent brightness of a source of light cannot be changed by any focusing process.

9.4. Aberrations in emission systems

Gaussian optics cannot present anything but a very rough qualitative description of emission systems. However, it applies at least to paraxial rays of systems which are operated near to current saturation conditions.

Field curvature. Emission microscopes and image converters (cf. Chapter XII) are essentially emission systems in which the paraxial regions of the cathode are projected into an image of fair definition. The marginal regions of these images, however, are always quite out of focus. The curvature of the image plane is as bad as could be expected from the experience with lenses reported in § 6.7. For a given system with given voltages at the electrodes, the centre of the image will be in focus at a given target distance. Any other zone of the image, however, can be focused by varying the grid voltage.

The curvature of the field has been found to depend upon the spacings and on the shape of the electrodes. For example, for a nearly symmetrical two-diaphragm system Johannson (1933) measured the diameter of the sharply projected paraxial area of the cathode as a function of the grid to cathode spacing c and of the ratio of grid voltage V_g to anode voltage V_a. He found that the radius of this sharp area reaches a maximum of about one-third of the grid aperture radius r_g, when

$$c/r_g \approx 1 \quad \text{and} \quad V_g/V_a \approx +0{\cdot}1.$$

Under these conditions magnifications of about 50× have been reached within an image distance of about $330 r_g$. Such an image can

be seen, for example, in fig. 9.7, which shows the surface of an oxide cathode scratched with a pattern of straight lines. The sharply projected area is marked in the picture by a circle. Johannson (1933) also found that the diameter of this sharply projected area could be increased by about 70 % when the grid electrode was provided with a funnel-shaped aperture with its narrow end extending towards the cathode.

Spherical and chromatic aberration. Current distribution in the cross-over. From the good optical definition of the central part of the image (fig. 9.7), the conclusion can be drawn that spherical aberration in the emission microscope is practically negligible. This is because the aperture of rays reaching the image is very small. Chromatic aberration appears to be negligible too, for the electron energy in the image space is of the order of several hundred volts, which is very large in comparison with the thermionic energy distribution which covers not more than some tenths of a volt.

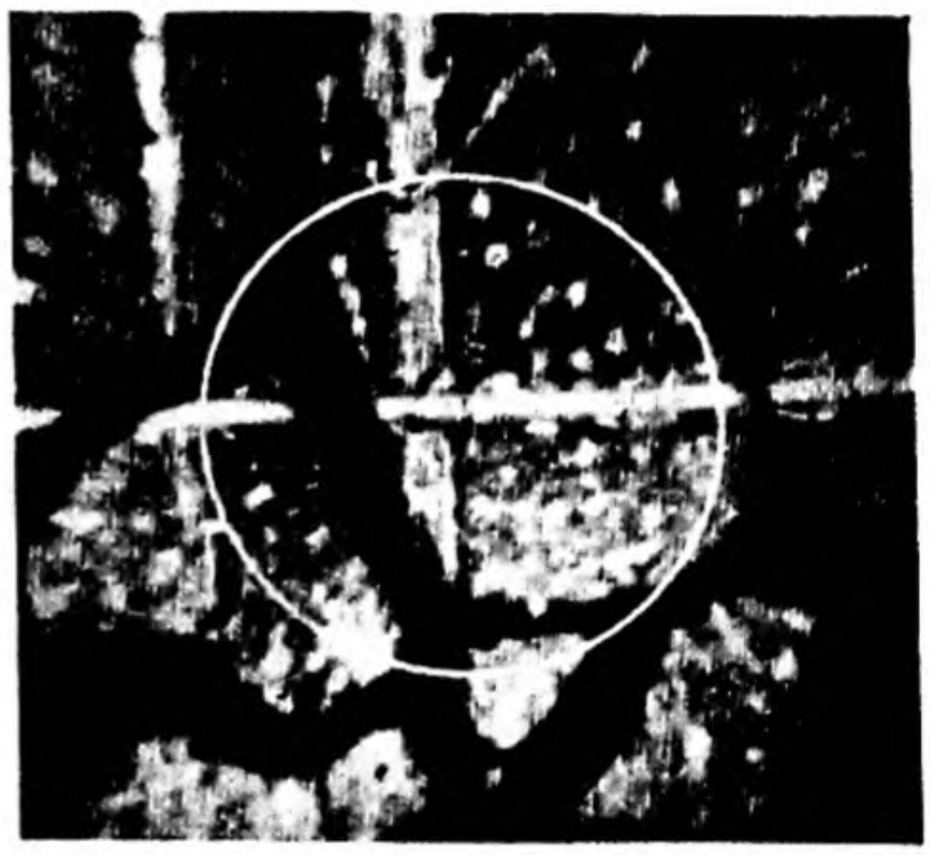

Fig. 9.7. Electron optical image of the cathode of a two-diaphragm emission system. (Photograph.)

Both spherical and chromatic aberration of the emission system form a serious limitation for the sharpness of focus of the electron gun. It has been shown in § 7.1 that in the absence of spherical aberration, the highest obtainable current density in a focused spot (cf. (7.6)) is limited only by the chromatic aberration which is due to the given band width of emission velocities. Law (1937), Langmuir (1937*b*) and Dosse (1940) have discussed the influence of the thermionic energy distribution of the emission on the current density distribution in the cross-over. Each emission velocity group forms a pupil whose radius is given by Abbe's sine law as

$$y_x = \left(\frac{V_{em}}{V_x + V_{em}}\right)^{\frac{1}{2}} \frac{y_c \sin \Theta_c}{\sin \Theta_x}, \tag{9.19}$$

where V_{em} is the kinetic energy of emission of the electron and Θ_c is the initial slope angle, while V_x and Θ_x are the voltage and slope angle respectively at the cross-over. By differentiating (9.19)

one obtains

$$\Delta y_x = \left(\frac{V_{em}}{V_x + V_{em}}\right)^{\frac{1}{2}} \frac{y_c}{\sin \Theta_x} \cos \Theta_c \Delta \Theta_c, \tag{9.20}$$

which means that a small variation $\Delta\Theta_c$ of emission angle at the cathode gives rise to a variation Δy_x in cross-over radius y_x. Therefore, since the number of electrons in the energy range

$$(V_{em}, V_{em} + \Delta V_{em})$$

emitted between the angles Θ_c and $\Theta_c + \Delta\Theta_c$ due to (9.11) is of the form

$$f(V_{em}) \sin \Theta_c \cos \Theta_c \Delta \Theta_c \Delta V_{em},$$

the number of electrons of initial energy $(V_{em}, V_{em} + \Delta V_{em})$ passing through an annulus $(y_x, y_x + \Delta y_x)$ will be of the form

$$I_x = f(V_{em}) \sin \Theta_c \cos \Theta_c g(y_x) \Delta y_x \Delta V_{em}. \tag{9.21}$$

To find the total current passing through a circle of radius y_x of the cross-over expression (9.21) has then to be integrated over V_{em} and over y_x. Hence, there follows a distribution of current density as a function of the radial coordinate y_x of the cross-over which originally is due to Law (1937), namely,

$$i(y_x) = \frac{I_{em}}{\alpha \pi} \exp\left[-\left(\frac{y_x}{\alpha}\right)^2\right], \tag{9.22}$$

where I_{em} is the total emission current from the cathode, where

$$\alpha = \frac{kT}{eV_x}\left(\frac{z_x}{L}\right)^2, \tag{9.23}$$

and where the symbols in (9.23) are e/k = electron charge/Boltzmann constant = 11,600 (degree/volt), T = absolute temperature of the cathode, V_x = voltage at the cross-over, and L = field form factor introduced by (9.2).

The Maxwellian distribution of emission energies spreads to very large values which, however, are very rare. Hence the current density distribution (9.22) must spread up to very large radii y_x. There, however, it contains very few electrons indeed.

The maximum current density is found in the centre of the cross-over ($y_x = 0$) and is, according to (9.22) and (9.3), given by

$$i_{\max.} = \frac{I_{em}}{\alpha \pi} \approx i_{em} \frac{eV_x}{kT}\left(\frac{y_c}{f'}\right)^2. \tag{9.24}$$

With increasing distance from the axis, the current density i decreases according to (9.22) at a rate given by a Gaussian error function. For instance, i decays to $1/n$th of its maximum value at a radius

$$y_x = (\alpha \log n)^{\frac{1}{2}}, \tag{9.25}$$

and, in particular, the half-maximum-width of the distribution is given by

$$2y_x = 1{\cdot}66\sqrt{\alpha}.$$

By definition and with (9.25), Jacob (1939) introduced an 'effective cross-over radius' given by $1/n = 0{\cdot}2$, while Dosse (1940) preferred a conventional cross-over size with a limiting $1/n = 0{\cdot}05$. The current passing outside Dosse's cross-over just amounts to 5 % of the total current, and the emission energies passing through this cross-over do not exceed $3V_\alpha$, where $V_\alpha = (k/e)\,T$ is the most frequent emission energy.

The intensity i/Ω, i.e. the current density per solid angle presented by (9.10), depends upon $i(y_x)$ as given in (9.22). This is of great practical importance, since i can be increased by reducing y_x. Hence the intensity emitted by a given system can be increased by cutting off marginal zones either from the cross-over area or from the cone of emitted rays. The reduction of the cone of rays by aperture stops in the anode is quite usual in the practice of cathode ray tubes. On the other hand, the beam reduction by a stop in the cross-over plane has been successfully performed in the gun design by Law (1937).

Experimental investigations of the current distribution in the cross-over have essentially confirmed the Gaussian distribution of (9.22) though, owing to the presence of various aberrations, the experimental values for the current density are generally by a factor two or more, below the theoretical optimum given by Langmuir's equation (7.6). Various experimental methods have been used for measuring the current distribution in the cross-over. Law (1937), for instance, inserted aperture stops of different sizes into the plane of the cross-over, measuring for each size the ratio of the intercepted to the transmitted current. Reusse (1939) investigated the current distribution in a magnified electron-optical image of the cross-over, sliding across it a very fine wire which acted as a current probe. Jacob (1939) and later Dosse (1940) again in-

vestigated the electron-optical image of the cross-over. They developed the 'slit scanning method' in which the image was moved periodically across the slit of a Faraday cage by means of an alternating deflecting field. The current distribution received in the cage was amplified and registered by an oscillograph.

Experimental investigations on the current-density distribution across the unfocused beam emerging from the cross-over, i.e. the current-density distribution as a function of the angular aperture, have also been made by Jacob (1939), Dosse (1940) and Reusse (1939). They again applied the methods just described, using the Faraday cage with slot and the wire probe respectively. On the other hand, Klemperer (unpublished) used for the measurement of this angular current distribution a Faraday cage with an iris diaphragm such as is commonly employed in photographic cameras. The iris could be opened gradually by a ground joint. In this way, the current in the cage could be measured as a function of the aperture. By differentiation of the measured curves, zonal current distributions were obtained. These zonal distributions divided by the areas of the zones ($a \approx 2\pi\Theta\,\mathrm{d}\Theta$) yield the required angular current density distributions. Examples of such distributions will be shown later on in §9·6 (cf. fig. 9.12).

The measured angular semi-aperture, say β, generally results from superimposition of all elementary bundles with angular semi-aperture γ, the axis of each elementary bundle having the slope angle Θ (cf. figs. 9.4 and 9.5). Since also the distributions in the elementary bundles are error functions, one obtains by superimposition

$$\beta^2 = \Theta^2 + \gamma^2. \tag{9.26}$$

But in most cases $\Theta \gg \gamma$, so that $\beta \approx \Theta$.

Influence of space charge on the cross-over. The cross-over size determined by one of the direct experimental methods generally appears to be far greater than one could expect from the results of ray tracing through the field plot. The 'swollen' cross-over size is quite clearly caused by space-charge repulsion.

The conclusion, that space charge should be the determining factor for the cross-over size, has been reached by Klemperer and Mayo (1948), who investigated the properties of a symmetrical two-diaphragm system as a function of the diaphragm spacings. For

large grid-cathode spacings, the curvature of equipotentials near the cathode is large, hence the electrons reach the cross-over at a steep angle Θ. Simultaneously the space-charge factor $I_{em}/V_x^{\frac{3}{2}}$ is relatively small because the large spacing leads to small fields at the cathode and to small emission currents I_{em}. Under these conditions the beam-spread coefficient $\sigma \sim \Theta^2/(I/V^{\frac{3}{2}})$ (cf. (8.25)) is large. On the other hand, decreasing of the grid-cathode distance flattens the equipotentials near the cathode, decreases Θ and increases $I_{em}/V_x^{\frac{3}{2}}$. Now with decreasing σ the distance of the waist of a convergent beam under space-charge conditions has been shown (cf. fig. 8.3) to increase first and then to decrease again. Precisely this effect has been observed by Klemperer and Mayo to happen with the cross-over diameter of a space-charge-limited emission system.

The maximum displacement of the cross-over from the cathode has been found to occur simultaneously with minimum beam divergence and with least spherical aberration. Again, least aberration is—according to §8.3—expected for a 'space-charge equivalent lens' in the region in which the beam spread coefficient σ reaches its maximum. Hence it appears that the spherical aberration of emission systems must be to a great extent an effect of space charge. Since for practical purposes systems with least errors are required, the grid-cathode spacings at which maximum σ and minimum aberration occurs are of technical importance. These spacings have been called 'preference spacings', and two curves showing the preference grid-cathode spacings c_p measured in grid-aperture radii r are shown in fig. 9.8, as a function of the grid to anode spacing a. The curves have been measured at two different total emission currents $I_{em} = 1$ mA. and $I_{em} = 5$ mA. respectively.

It has so far not been possible to reduce the spherical aberration of a triode system by geometrical modification of the electrodes. Hence it seems very likely that the spherical aberration observed in the cross-over is caused by hardly anything else but by space charge, and that the amount of spherical aberration added by the Laplacian field is negligible. Due to the small quantities involved, it is difficult to measure exact values of the aberrations. For symmetrical two-diaphragm systems with small grid-cathode distances Klem-

perer and Mayo (1948) found the following values of longitudinal aberration Δz in terms of grid radii r_g as a function of the slope angle Θ of the ray, expressed in radians:

Δz	$2r_g$	$9r_g$	$20r_g$
Θ	0·02	0·05	0·07

Here, Δz increases roughly in proportion to Θ^2. The magnitude of the aberrations in a similar system with larger cathode-grid

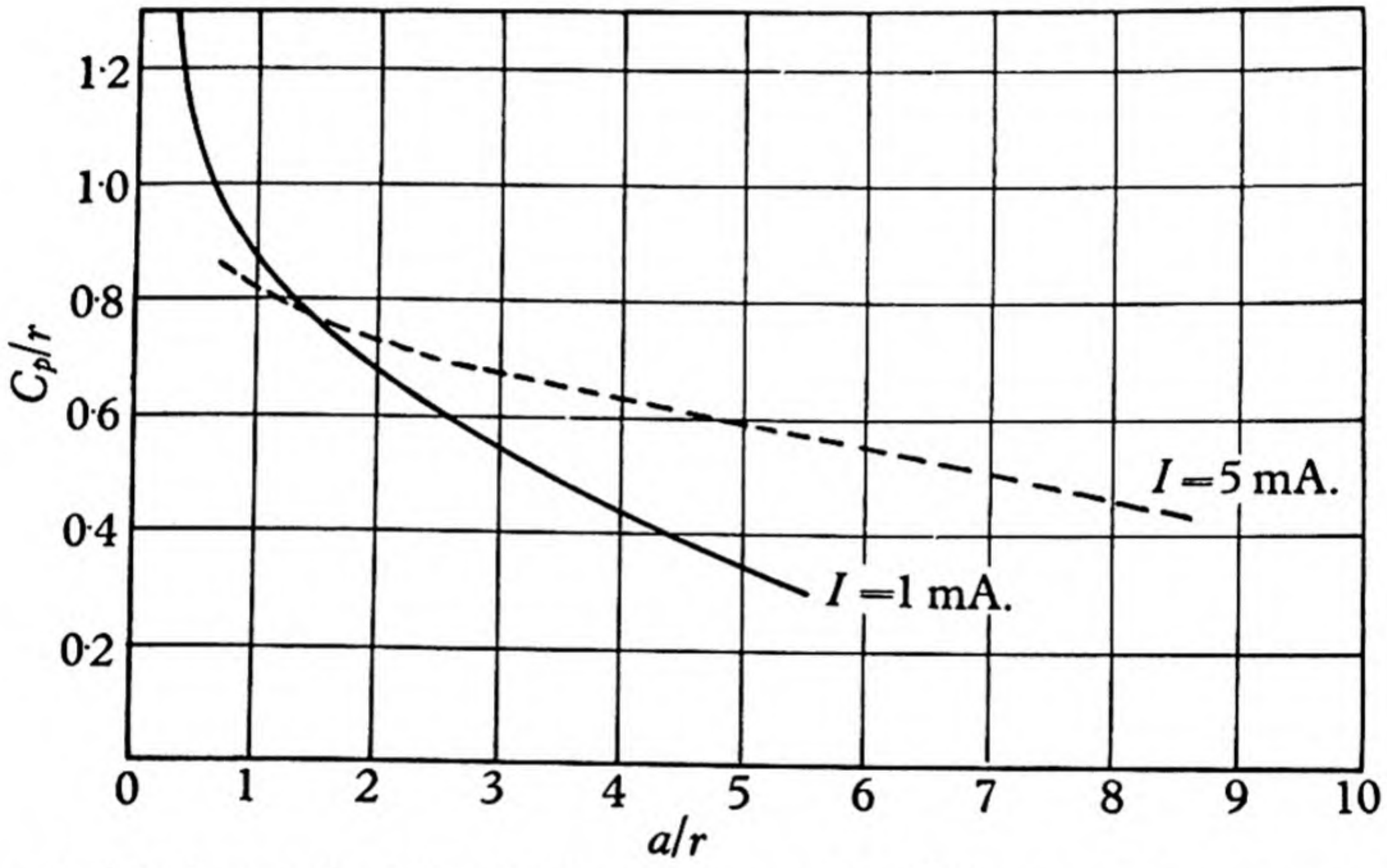

Fig. 9.8. 'Preference' grid-cathode spacings c_p for different grid-anode spacings a_p at emission currents of 1 milliamp. and of 5 milliamp.

distance, producing a bundle of rays of greater divergence, is indicated by the following values measured by Klemperer (unpublished):

Δz	$1r_g$	$3r_g$	$6r_g$
Θ	0·03	0·1	0·3

Here, Δz increases obviously less than in proportion with Θ^2, i.e. the higher aberration coefficients (cf. (6.1)) are negative.

Modification of the potential distribution in an emission system by space charge. This modification is very substantial and has been determined by Maloff and Epstein (1934, 1938) in the following way:

(1) Equipotentials $V(y, z)$ are obtained by measurements in the electrolytic trough as shown in Chapter III.

(2) The electron beam is traced through this potential plot $V(y, z)$.

(3) The charge density is calculated throughout the beam from the values of current and of electron velocities.

(4) From the charge density and the shape of the beam a potential distribution $V_1(y, z)$ due only to the beam is calculated.

(5) The charges induced on the electrodes are calculated and a corresponding potential distribution $V_2(y, z)$ is obtained.

(6) The true potential distribution results by superimposition of the potentials $V + V_1 + V_2 = V'$ at every point (y, z).

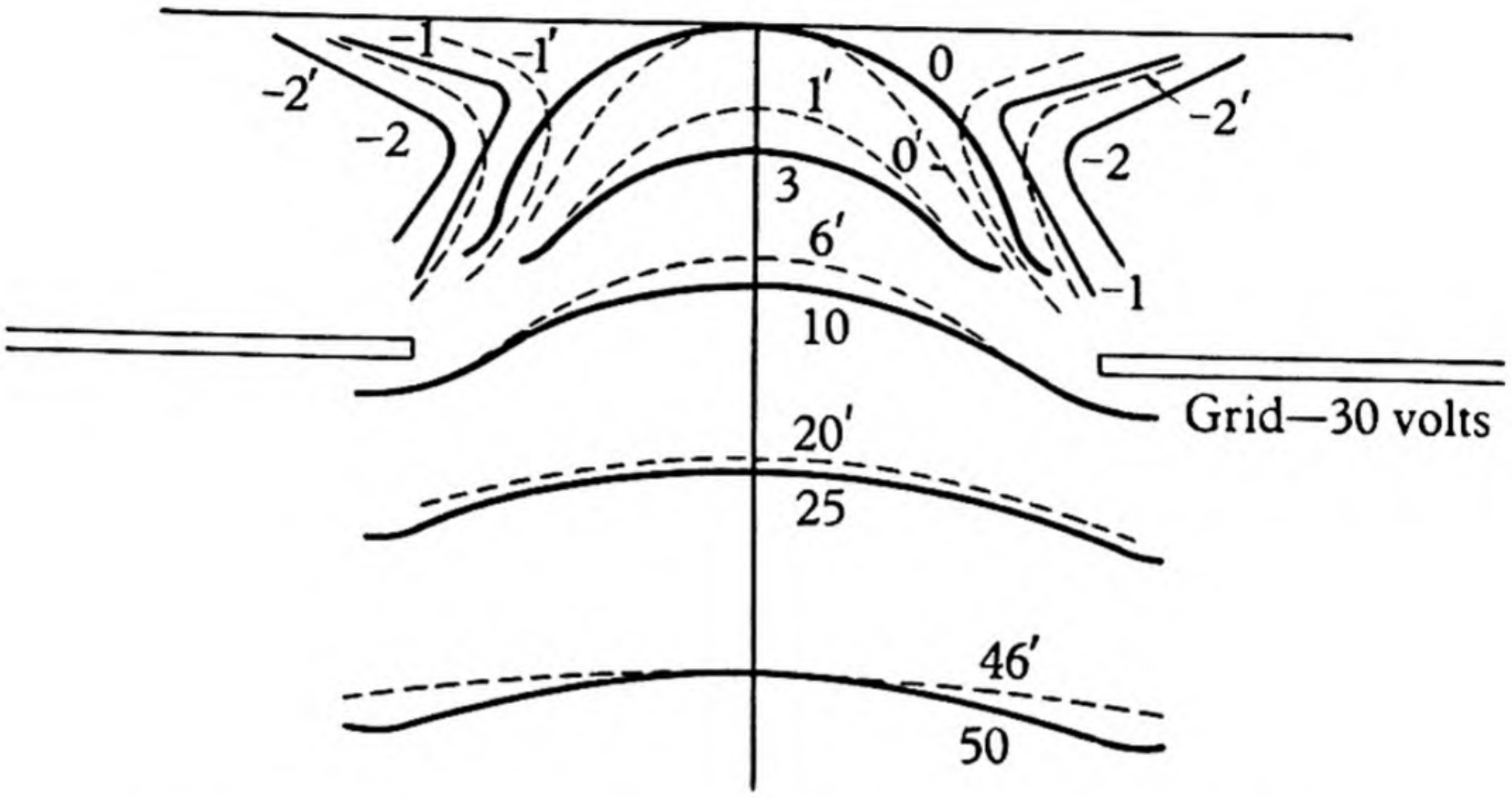

Fig. 9.9. Effect of space charge on potential distribution in an emission system.

(7) A better approximation is then obtained by repeating the above procedure starting with the modified distribution V' instead of the original V.

A field plot obtained in this way is shown in fig. 9.9. The modified equipotentials (V') are indicated as broken lines; the original Laplacian distribution (V) is drawn in solid lines. Near the cathode, the V'-lines are of greater curvature and they are more widely spaced than the V-lines, though the greatest differences $(V' - V)$ are found in the cross-over region. A maximum space-charge density occurs at the potential minimum close to the cathode. In the example of fig. 9.9 this amounts to 10^{17} electrons/m.^{3}. The space-charge density in the cross-over may be of the same order of magnitude or smaller on account of the greater velocity of the electrons. The greatest space-charge densities obtained in modern electron guns are estimated to reach 10^{19} electrons/m.^{3}. The results

by Maloff and Epstein (1938) have been confirmed and extended by Plocke (1952), and the following important effects of space charge in emission systems may be enumerated.

(1) Decrease of the emitting area of the cathode.

(2) Decrease in potential gradient along the axis in the region between cathode and grid.

(3) Increases and decreases in curvature of equipotentials in the grid-cathode and grid-anode region respectively.

(4) Large increases in both focal lengths (f and f') of the emission system, e.g. in the example of fig. 9.9 by a factor 4.

(5) Increase in cross-over size and decrease in beam divergence as discussed earlier in this section.

9.5. Beam intensity modulation

The current drawn from an emission system by the field of the anode can be modulated by changing the potential of the grid electrode. If the grid bias $V_g = 0$, no current is drawn by the grid. By an increase of the negative grid bias (i) the emitting area of the cathode and (ii) the emission density is decreased. The photograph (fig. 9.10) is due to Moss (1946). Fig. 9.10 (a) shows a light optical image of the cathode as seen through the grid aperture. A wire gauze is arranged in contact with the cathode surface so that the different parts of it can be located in the image. Fig. 9.10 (b)–(d) shows electron optical images (cf. fig. 9.4) taken with various values of bias V_g. It can be seen that the magnification y_c'/y_c remains constant, but that the radius y_c of the emitting cathode area decreases. According to a semi-empirical approximate formula given by Moss (1946) this radius is

$$(y_c)_0 = r_g \frac{V_d}{{}^{bl}V_g}, \tag{9.27}$$

where r_g is the radius of the grid aperture and ${}^{bl}V_g$ is the 'black-out' voltage or 'cut-off' voltage, i.e. the grid bias which is just sufficient to black out the image completely or to cut off substantially the whole emission current. V_d is the 'grid-drive' given by $|{}^{bl}V_g - V_g|$, i.e. the absolute value of the difference between black-out voltage and applied grid voltage.

The potential at the cathode surface may be obtained by superimposition of the potentials due to the anode and due to the grid.

It can be checked by field plotting that this combined potential becomes zero along a circle of radius $(y_c)_0$ given by (9.27). With increasing grid bias ($-V_g$), the circle contracts like an 'iris' reaching the axis when V_g reaches the value

$$^{bl}V_g = DV_a, \tag{9.28}$$

where V_a is the anode voltage and D is the penetration factor giving the fraction of the field which from the anode penetrates along the axis through the grid aperture to the cathode. The penetration factor is the reciprocal of the 'voltage-amplification factor' in valve technique. The penetration factor of an emission system changes substantially along the modulation characteristics due to the above 'iris effect'; however, D of (9.28) is its largest value and this is reached at cut-off; it corresponds to the field penetration at the axis.

Cathode loading. Due to the different field penetration at different distances from the axis, the field at the cathode surface is inhomogeneous, it grows from 0 at $y_c = (y_c)_0$ to a maximum value at $y_c = 0$ on the axis. For this reason the emission density is inhomogeneous. A semi-empirical formula given by Moss (1946) allows one to estimate the peak loading at the centre of the cathode:

$$i_0 = 14{\cdot}5\, V_d^{\frac{3}{2}}/r_g^2. \tag{9.29}$$

According to experimental results (9.29) has no discontinuity at zero grid bias. This implies, for instance, that a system with $^{bl}V_g = -20$ V. operating at $V_g = +10$ has the same peak loading as a system with $^{bl}V_g = -50$ operating at $V_g = -20$, provided the aperature radius r_g is the same in both cases. The maximum peak loading that can be afforded depends on the quality of the emissive surface and on the duration of the emission (see next section).

A useful empirical formula for the total current emerging from the grid hole is, according to Moss (1946), given by

$$I_{em} = 3 \times 10^{-6} V_d^{\frac{7}{2}}\, {}^{bl}V_g^{-2}. \tag{9.30}$$

This equation has been discussed by Jacob (1952) and it was found to apply with good approximation for relatively large anode voltages ($V_a \gg V_{em}$) and small grid-cathode spacings ($c \lessapprox r_g$). Alternatively, the current obtained from an emission system under

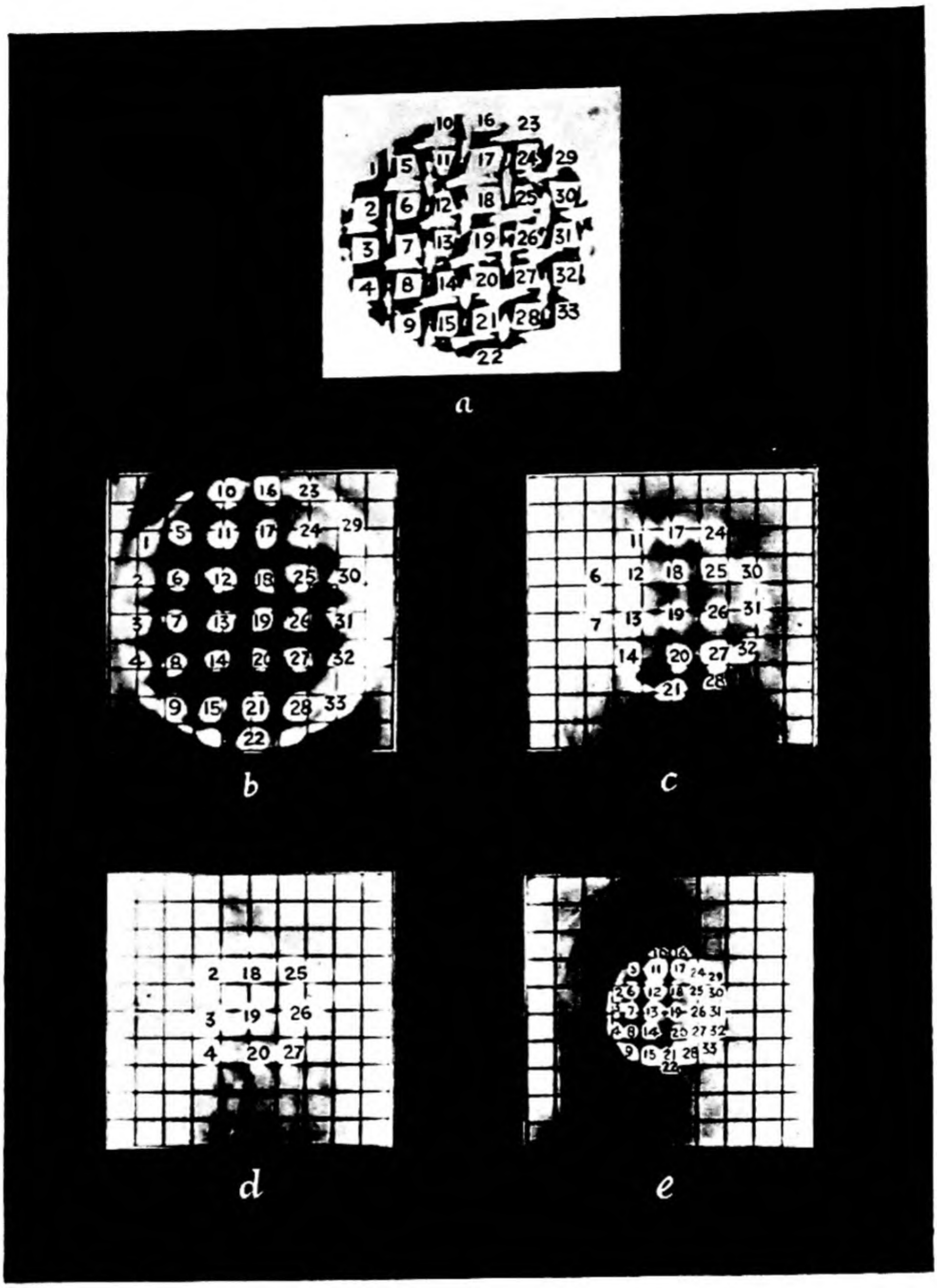

Fig. 9.10. Emitting cathode area, and modulator voltage. (Photograph.)

(*a*) Light-optical image as seen through grid aperture. (*b*)–(*e*) electron-optical images at $V_a = 4$ kV. anode voltage, taken with the following ratios of grid-anode spacing (a) to grid aperture radius (r_g), and with the following grid bias (V_g):

(*b*) $\frac{a}{r_g} = 1{\cdot}6$, $V_g = 0$;

(*c*) $\frac{a}{r_g} = 1{\cdot}6$, $V_g = -30$;

(*d*) $\frac{a}{r_g} = 1{\cdot}6$, $V_g = -50$;

(*e*) $\frac{a}{r_g} = 3{\cdot}3$, $V_g = 0$.

space-charge conditions can be estimated from Child's law (8.62), the emission system being treated as a diode. In this 'equivalent diode', the flow is somewhat different from that specified in (8.62); hence the proportionality constant between I_{em} and $V^{\frac{3}{2}}$ cannot be expected to have exactly the value G_0 of the plane parallel diode. The potential difference at the equivalent diode which results from a superimposition of the potentials of the electrodes of the emission system is, according to Schottky (1919), given by

$$V = \frac{V_g + DV_a}{1 + D}. \tag{9.31}$$

This equation essentially applies to the paraxial region where the field penetration is represented exactly by D. However, (9.31) substituted into Childs equation, (8.62), allows us, for technical purposes, to obtain a fair estimate of the total emission current over the whole cathode surface as a function of V_g and V_a. For the particular case of emission with zero grid bias ($V_g = 0$) and with small penetration factor ($D \ll 1$) one obtains by substituting (9.28) into (9.31) the familiar approximation

$$I_{em} = G\,{}^{bl}V_g^{\frac{3}{2}}, \tag{9.32}$$

which also follows from (9.30). (9.32) is of much practical use for the design of cathode-ray tubes.

Emission velocities and grid modulation. In the discussions of this section no account has been taken so far of the Maxwellian distribution of emission velocities. Though the fluorescent spot of a cathode-ray tube appears to be blacked out at a fairly well-defined grid voltage ${}^{bl}V_g$, it appears to be impossible completely to cut-off the emission current of a thermionic cathode if sufficiently sensitive current meters are used for its measurement. The emission current I_{em} can be shown to decrease with grid bias according to the following exponential law:

$$\log_{10}(I_{em}/I_s) = 0{\cdot}4\frac{eV}{kT}, \tag{9.33}$$

where V is the equivalent diode voltage (see (9.31)), and I_s is the ideal saturation current that can be drawn from the cathode which is, for example, of the order of 10 A. for an oxide cathode of 1 mm.^{2} surface. Again, $e/k = 11{,}600°/\text{V}$. and T is the absolute temperature

of the cathode. If, for instance, by visual measurements black-out is found to occur when the emission is suppressed to 10^{-7} A., a retarding voltage V of about -2 V. would be calculated from (9·33). Now, if ${}^{bl}V_g$ is plotted as a function of V_a, the straight-line relation through the origin implied by (9.28) should be expected to hold only if the above retarding voltage $|V| = 2$ were subtracted as a correcting term from every measured value of black-out voltage.

In practice the correcting term is found by measuring a few ${}^{bl}V_g/V_a$ ratios for different V_a and by subtracting an empirical term from ${}^{bl}V_g$ such as to make D approximately independent of the anode voltage. The empirical term is found to be of the order of a volt. Besides the correction for the emission velocities it actually includes a correction for contact potential difference between cathode and grid and another term which is due to the curvature of the modulating equipotential (cf. Langmuir and Compton, 1931, p. 231), but this cannot be discussed here. The correction term cannot be neglected for emission systems with large grid-cathode spacings or with very small cathodes (e.g. hair-pin cathode, § 9.6), but in technical cathode-ray tubes which have black-out voltages of the order of 50 V. it is quite unimportant.

Beam divergence. Of practical interest is the relatively large change of angular divergence of the emitted cone of rays observed for any change of grid bias. Such a change is demonstrated by the pictures shown in fig. 9.10. According to Jacob (1948) a linear relation holds, namely,

$$\Theta = \frac{\Theta_0}{{}^{bl}V_g} V_d, \tag{9.34}$$

where ${}^{bl}V_g$ is the black-out voltage of the emission system and Θ is the semi-divergence of the bundle of rays when a grid drive V_d is applied, while Θ_0 is the corresponding semi-vertical angle for zero grid drive. Θ may refer to a cone comprising all rays about the axis from the maximum value of the Gaussian intensity distribution curve down to any conventional value of it as defined, for example, by (9·25). Jacob (1944) found (9.34) to hold accurately enough to utilize the variation of beam angle for the design of an electron-optical voltmeter. According to measurements of Moss (1946), however, the relation is fulfilled with good approximation only if the angles are not too large.

Cross-over changes. Important effects of grid modulation concern a change of cross-over size and a cross-over shift. Both are mainly space-charge effects and can be understood qualitatively by applying the conclusions drawn in § 8.2. These modulation effects can be very disturbing in high-definition television tubes for instance. The high lights in the picture tend to be blurred, and a simultaneous sharp focusing of the high lights and shadows of the scanned picture is impossible. Both the change of cross-over size and the cross-over shift are generally the larger, the greater the space-charge factors $I/V^{\frac{3}{2}}$ involved. However, both effects are reduced to a relative minimum when the beam spread factor (cf. (8.28) and (8.29)) reaches its maximum shown in fig. 8.3. This apparently happens for the preference spacings discussed in the preceding § 9.4.

9.6. Design of triode systems

For the practical application of emission systems in electron-optical gear certain qualities of performance are required. Homogeneous cathode loading, high-emission density, great homocentricity but small divergence of the emitted cone of rays, great slope of the modulation characteristics and various other properties may be desirable. From the study of the previous sections, however, it appears that not all requirements can be fulfilled simultaneously. A gain in one of the desirable properties might necessarily mean a loss in others. Practical compromises have to be effected in operational performance, and for this purpose some knowledge of the dependence of the various properties on the geometry of the electrodes is desirable.

Control of properties of simple triodes by the choice of cathode-to-grid and grid-to-anode spacings. Let the well-established empirical systems of figs. 9.1 and 9.2 be discussed in the first instance. Their electrodes consist of plane diaphragms and of cylindrical tubes only. For a given aperture radius r_g all essential geometrical information is contained in the two spacings c and a indicated in figs. 9.1 and 9.2. It should be emphasized that both c and a are defined as the distances of cathode and anode respectively from the top surface of the grid electrode which is facing the anode. If these 'grid-top' spacings are given, the thickness of the grid diaphragm

can be disregarded, since its effect is unimportant for the electron optics of the system. Both spacings c and a may be measured in terms of grid-aperture radii r_g so that the given information can be applied to any size of emission system. Generally, the scale of the system does not affect its performance excepting for a limitation of the peak loading of emission density at the cathode (cf. 9.29).

Most important for the electrical performance of the systems are two parameters, namely, the penetration factor D defined by (9.28) and the geometric factor G of Child's equation (9.32). Now, nearly all experimental values for G of systems of the pattern of figs. 9.1 and 9.2 under full space-charge conditions are found to lie between the extreme values 3×10^{-6} and 5×10^{-6} [Amp/Volt$^{\frac{3}{2}}$]. The higher values of G are reached only at extremely small values of c/a. For technical purposes G is near enough to $3{\cdot}5 \times 10^{-6}$ and independent of the particular geometry of the system. The reason for the approximate constancy of G may be recognized by considering the equivalent diode system (cf. §9.5). Any change in geometry of the emission system results in a change in effective diameter of the emitting cathode area. Simultaneously, however, it leads to changes in the opposite sense in spacing and/or voltage of the equivalent diode (cf. (8.63)).

The penetration factor D, on the other hand, changes greatly even for small changes in the spacings of the emission system. Experimental values of D for the systems of figs. 9.1 and 9.2 are plotted in fig. 9.11 as a function of the spacing c from the cathode to the top of the grid. In case of the two-diaphragm systems, various spacings a from the top of the grid to the anode are taken as constant parameters of the curves. Both c and a are measured in grid-aperture radii r_g. The six solid curves belong to the symmetrical two-diaphragm system (fig. 9.1). The broken curves belong to the diaphragm-tube system (fig. 9.2). The penetration factors of these systems hardly depend upon a spacing between grid electrode and anode as long as the tube radius is many times greater than the grid aperture.

A knowledge of the G and D values is most useful when the design of a system of given emission current I_{em} is required for a given anode voltage V_a. For instance, let a system be required which emits about 550 μA. at 1 kV. The necessary black-out

voltage is calculated from (9.32) to be

$$^{bl}V_g = \left(\frac{I_{em}}{G}\right)^{\frac{2}{3}} = \left(\frac{550 \times 10^{-6}}{3{\cdot}5 \times 10^{-6}}\right)^{\frac{2}{3}} \approx 30 \text{ volts.}$$

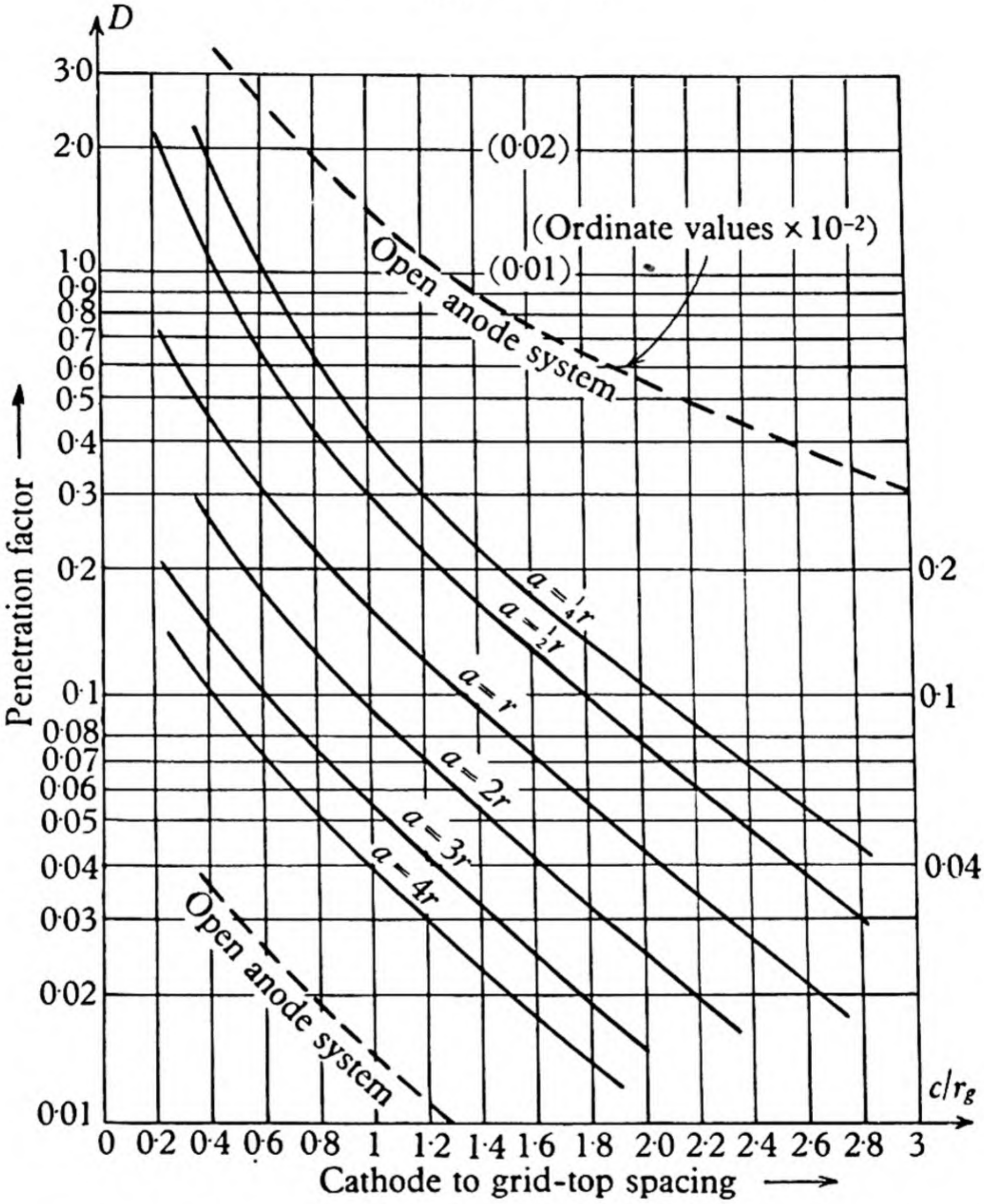

Fig. 9.11. Penetration factors D of symmetrical two-diaphragm systems (fig. 9.1) and of diaphragm tube systems (fig. 9.2).

The necessary penetration factor is calculated from (9.28) to be

$$D = \frac{^{bl}V_g}{V_a} = \frac{30}{1000} = 3\%.$$

A glance at the curve of fig. 9.11 shows that the necessary D can be realized either by an open anode system with $c = 0{\cdot}5r_g$ or by a series of symmetrical two-diaphragm systems, e.g. with $a = 4r_g$

and $c = 1{\cdot}2r_g$, or with $a = r_g$ and $c = 2{\cdot}3r_g$, or with any other combination of c and a which may be taken from the given curves or interpolated for intermediate values.

For the electron-optical performance of emission systems in electron guns, a knowledge of the intensity of the emission would be very desirable. However, little information is available about the cross-over size and about the angular distribution of the emission.

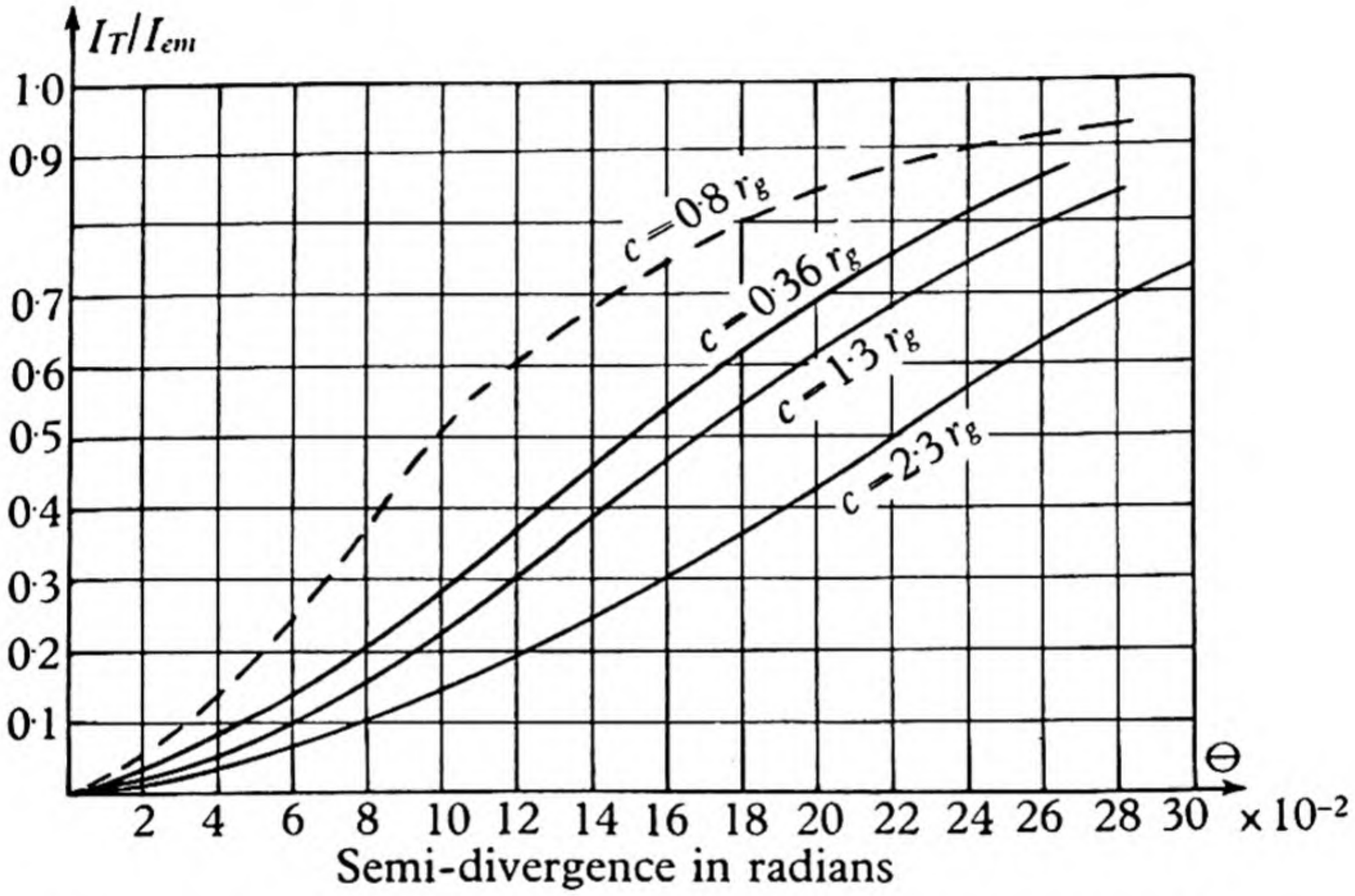

Fig. 9.12. Angular current distributions of some symmetrical two-diaphragm emission systems.

The curves shown in fig. 9.12 give some examples for angular current distributions which have been taken by Klemperer (unpublished) with the iris method described in § 9.4. Abscissae are the semi-vertical angles Θ of coaxial cones into which the current I_T is emitted. Ordinates are the fractions (I_T/I_{em}) of the emission into the cone divided by the total emission into the hemisphere. All curves apply to two-diaphragm systems with equal grid and anode aperture $(r_g = r_a)$ in which the grid to anode spacing is equal to the grid-aperture radius $(a = r_g)$. The three solid curves have been taken with grid-cathode spacings $c = 0{\cdot}36r_g$, $1{\cdot}3r_g$ and $2{\cdot}3r_g$ respectively. They seem to suggest that the beam spread increases monotonically with c. Actually, however, a pronounced minimum for the beam spread is found at about $c = 0{\cdot}8$, which corresponds

to the preference spacing c_p introduced in §9.4. The relevant distribution is shown in fig. 9.12 as a dotted curve.

It has already been pointed out that the angular distributions are controlled mainly by space-charge effects. Hence it is not surprising that—even under full space-charge conditions—these distributions depend on the magnitude of the emission current I_{em} and on the vacuum pressure P (cf. §8.5). In particular, the angular distribu-

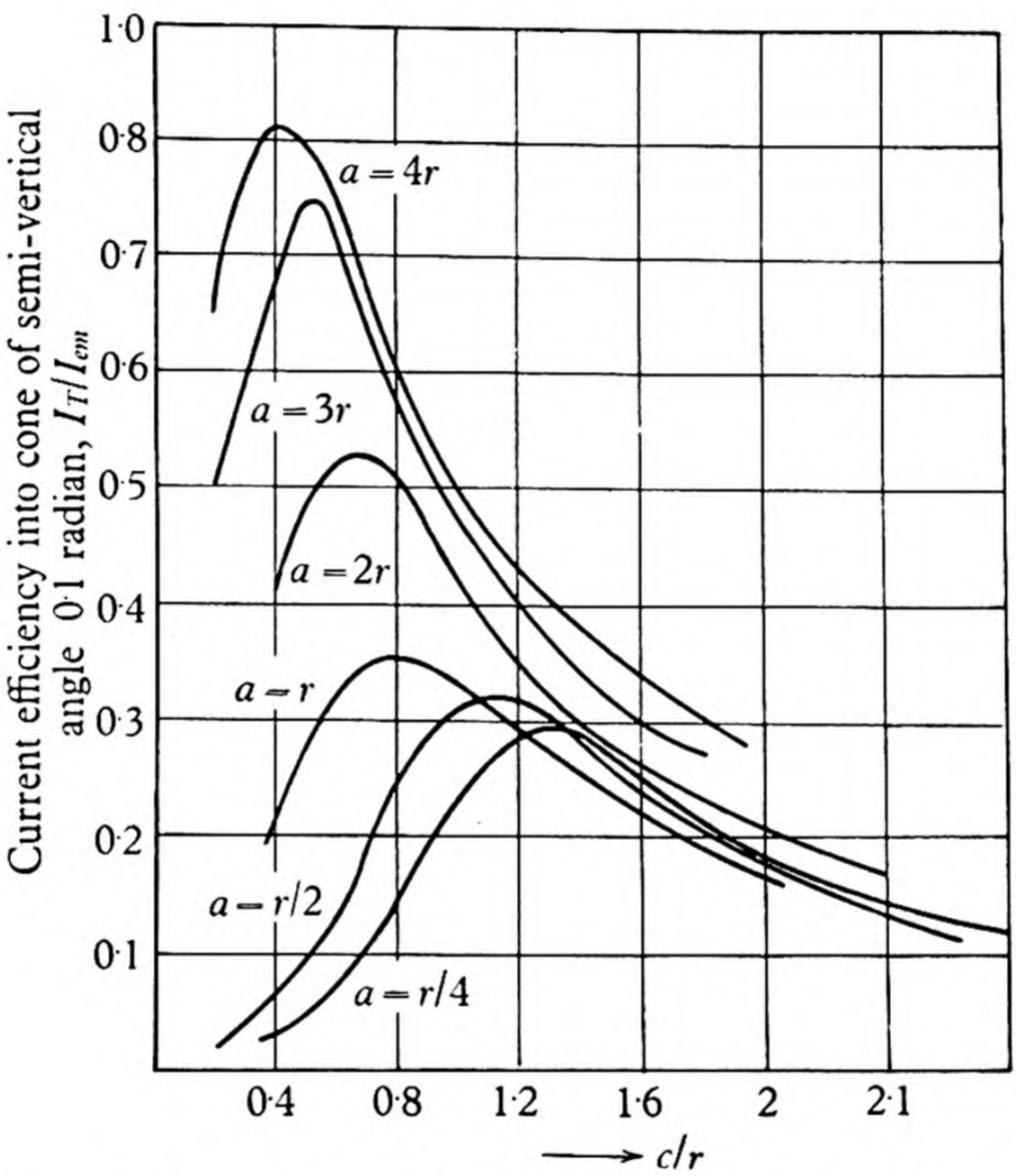

Fig. 9.13. Current efficiencies of two-diaphragm systems for various grid-anode spacings a and grid-cathode spacings c.

tions of systems with spacings in the region of the preference spacings (cf. fig. 9.8) are rather sensitive to changes in I_{em} and P. The curves in fig. 9.12 have been taken at $I_{em} = 1$ mA. and at $P \approx 10^{-5}$ mm. Hg pressure.

The ratio I_T/I_{em} for the fixed semi-vertical angle $\Theta = 0{\cdot}1$ radian as a function of c/r has been measured by Klemperer and Mayo (1948), and six curves are shown in fig. 9.13. These curves apply to different grid-anode spacings a as parameter. They all show pro-

nounced maxima at the preference spacings. Similar curves are obtained for open anode systems. There, however, the angular divergences are much smaller. For example, the ratios I_T/I_{em} obtained for $\Theta = 0{\cdot}1$ radian are as high as $0{\cdot}12$ and $0{\cdot}27$ for systems with grid to cathode spacings $c = 1{\cdot}6r_g$ and $c = 0{\cdot}6r_g$ respectively. The preference spacing c_p of the open anode system is so small that it can hardly be realized experimentally with grid electrodes of practicable thicknesses.

The Pierce system. It has been pointed out (cf. §§ 7.1 and 9.3–9.5) that the available current, as well as, for instance, brightness, intensity and current density focused in a spot, can be increased by increasing the emission density at the cathode. The available emission density, however, is strictly limited and it is a property of the emitting surface. In order to preserve the cathode for a reasonable lifetime, say of a few thousand hours, its temperature must not be raised too much. Up to 10^3 A./m.^{2}, for instance, may be drawn from a bright emitter like tantalum or tungsten. Continuous currents of 5×10^3 A./m.^{2} or even about 100 times greater currents in very short pulses may be obtained from good oxide cathodes (cf. Wright, 1949).

In order to reach optimum performance of an emission system, the maximum available emission density should be drawn everywhere from the emitting cathode surface. Now, in the systems with plane diaphragms shown in figs. 9.1 and 9.2, the field at the cathode surface and hence the emission density vary considerably (cf. § 9.5). In the resulting emission-density distribution, however, the maximum or peak value is limited as a given property of the emitting substance, and the average emission density is substantially below the peak. On the other hand, in a system with a constant field over the whole cathode, the resulting homogeneous density of emission can be taken right up to the maximum possible value. In the system of fig. 9.3 (*a*), for instance, the approximately radial field between the spherical cathode and the tip of the conical anode provides some degree of homogeneity of emission density.

A general procedure for the design of emission systems with a homogeneous field at the cathode surface has been put forward by Pierce (1940*a*). He argued that the emission density is homo-

geneous if the beam from the cathode can be considered to be cut from an unbounded rectilinear flow of space charge. In this way he reduced the problem to finding electrode arrangements which produce such fields and potentials at the boundaries of the actual beam as the 'removed' charge would have produced there. Now, the rectilinear flow of space charge has already been treated in § 8.6. It also has been shown that in a space-charge limited flow the voltage decreases with the 4/3 power of the distance from the cathode. Moreover, detailed explanations have been given in § 8.7 for the use of the field-plotting trough for finding experimentally

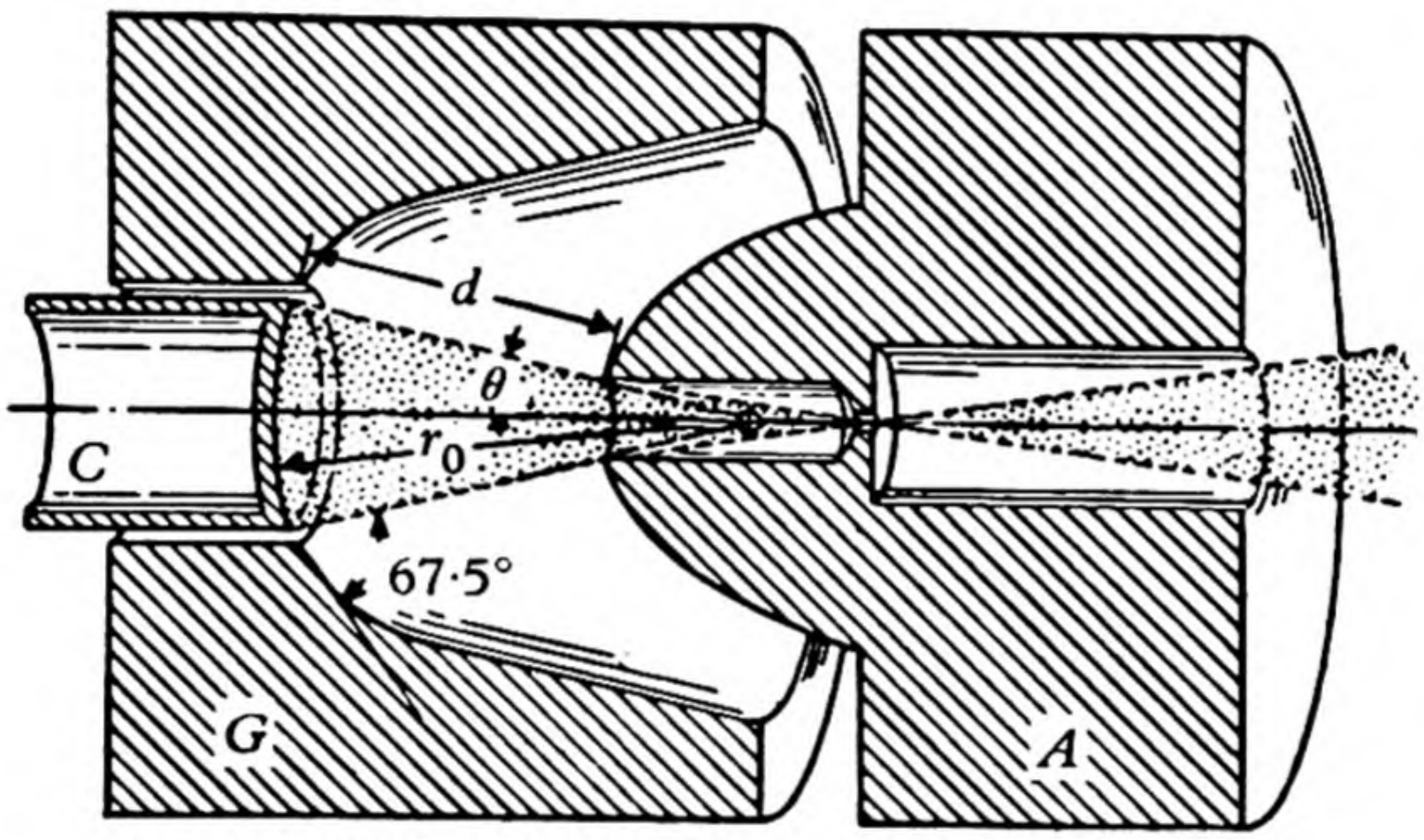

Fig. 9.14. Pierce system.

the right electrode arrangement which produces a potential decrease at the edge of a limited beam according to the 4/3 power law.

An emission system according to Pierce is shown in fig. 9.14. The surface of the grid electrode G meets the beam envelope under the universal angle 67·5° as postulated in § 8·7. Samuel (1945) has published some detailed material about the relationship between perveance ($I/V_A^{\frac{3}{2}}$), semi-vertical angle (Θ) of the conical beam and anode-to-cathode spacing (d) measured in terms of the radius of curvature (r_c) of the cathode. For any required $I/V_A^{\frac{3}{2}}$, Θ can be presented as a unique function of d/r_c.

An interesting conclusion may be drawn regarding the design of a Pierce system for transmitting a beam of maximum current through a given fairly long cylindrical electrode. Such arrangement is of practical interest, for example, for Klystron tubes (cf. §12·9), in which intense beams have to be transmitted through a drift space. By combination of the laws of space-charge-limited

emission (cf. (8.62)) with the laws connecting space charge and beam spread (cf. (8.17)), an optimum cathode to anode spacing can be derived for the emission system. This spacing is about three-eighths of the length of the drift-space cylinder.

Unfortunately, the method of Pierce cannot exactly be applied to the design of systems of high perveance for which it was devised originally. For high perveance $I/V_A^{\frac{3}{2}}$, the anode aperture must be made comparable in size with the anode to cathode spacing. This results in some non-uniformity and in a decrease of the fields at the cathode surface. As a consequence, the experimental perveances obtainable so far from systems like that in fig. 9.14 hardly reach about one-third of the calculated value, even if some compensating shaping of all electrodes is applied in order to render the field at the cathode surface more homogeneous (cf. Samuel, 1945; Klemperer, 1947*a*). It should, however, be mentioned that Samuel (1945) obtained perveances as high as 66×10^{-6} A./V.$^{\frac{3}{2}}$ from a specially shaped gun with toroidal cathode which he designed in accordance with Pierce's principles.

Point cathodes in emission systems. Relatively small perveance but extremely high emission densities at the cathode are obtained in emission systems with pointed cathodes. The relatively high anode voltages which can be applied to the system due to its low perveance produce strong fields at the cathode. In case of a thermionic emitter these fields tend to depress the work function of the cathode and thus ensure that ample emission is being drawn at relatively low temperature.

Sharply bent metal filaments, the so-called hair-pin cathodes, have found wide application in various emission systems. For instance, they are now commonly used in the highly magnifying electron microscopes (cf. § 12·6). The use of the hair-pin cathode in a two-diaphragm system has been studied by Hillier and Baker (1945, 1946), and by Ellis (1947). A schematic drawing of the system is shown in fig. 9.15. There, *c* represents the hair-pin cathode, which is a V-shaped tungsten filament of about 0·1 mm. diameter. It may be heated by symmetrical supply of a.c. of the order of 1 A. The vertex of the hair-pin is of roughly spherical shape; it is the hottest part and forms an electron source of small dimensions which under favourable conditions may emit current densities

of the order of 10^5 (A./m.^{2}). To avoid disturbances from the filament wires, these have to be bent to go directly back, nearly parallel to the axis.

The divergence of the emitted cone of rays depends (as above in flat cathode-type systems) on the grid to cathode spacing *c* and on the grid to anode spacing *a*. The very small tip of the hair-pin cathode,

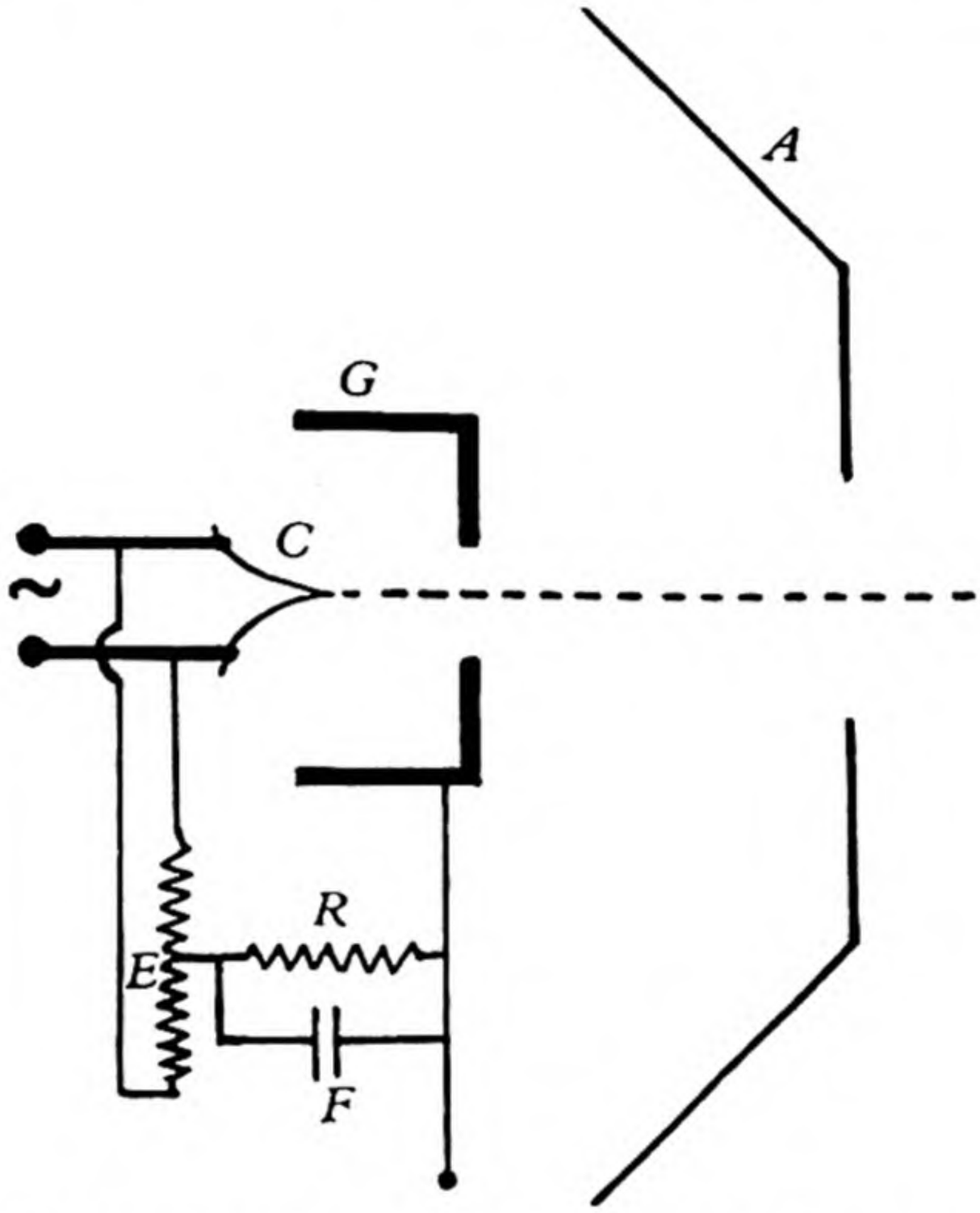

Fig. 9.15. Emission system with hair-pin cathode automatically biased.

however, can be moved into the grid aperture, and the grid-top to cathode spacing can be reduced to zero. In all cases, a divergent bundle appears to be emitted from a virtual cross-over at the centre of the grid aperture. By increasing *c* the divergence of rays is reduced and the current decreased. The great influence of the distance *c* on the performance of the system makes a fine adjustment under working conditions desirable. Hence, in commercial microscopes the hair-pin filament mounting often is connected to sylphon bellows, so that its position can be adjusted in the evacuated instrument by a micrometer screw on the outside.

A frequently experienced difficulty in the operation of emission systems with hair-pin cathodes consists in the occurrence of 'side-spots' when the electrons appear to be emitted from a multiple source. This is a space-charge phenomenon which is not fully

understood. However, the side spots can generally be suppressed by increasing the cathode spacing c, by using larger grid apertures (beyond a certain minimum value) or by application of a sufficiently negative grid bias.

To safeguard the system from sudden discharges Hillier and Baker (1946) have recommended an automatic biasing as shown in fig. 9.15. The centre tap of a resistance E across the filament C is connected to the grid electrode G via a small condenser $F \approx 0{\cdot}5\,\mu$F., and via a large resistance R, the optimum value of which is very sensitive to the cathode spacing c but which is usually of the order of a few Megohms. G is directly connected to the negative high-voltage supply, while the anode A is connected to earth. Every increase in emission will increase the potential drop at R, thus producing a positive bias at the cathode which will counteract further increase in emission. Under working conditions, the filament temperature is set slightly above the value at which the beam current reaches saturation and the grid electrode is near black-out voltage. Combined action of space charge and dependence of the cathode voltage on the beam current serve to stabilize the emission and to centre automatically the effective source to the focusing aperture. The electron current may be of the order of 100–300 μA. It is emitted from the tip of the hair-pin only, and apparently a very small space-charge cloud is formed before it reaches a potential saddle which must exist between cathode and grid. This cloud acts as a definitely single, intense source which remains on the axis, even if the tip of the hair-pin filament is slightly misaligned.

Klemperer and Klinger (1951) have shown by ray-tracing experiments (cf. §§ 9.2 and 9.4) that the bundle of rays emitted from a hair-pin system is extremely homocentric. The aberration coefficient C_s and the radius y_c of the emitting disk (virtual cathode) were found to be smaller than in any other known emission system, namely, $C_s < 100 r_g$ and $y_c < 0{\cdot}1 r_g$, where r_g is the radius of the grid aperture.

Because of this homocentricity the emission of the hair-pin system can be focused into a very fine spot of extreme brightness. Hillier and Ellis (1949) for instance, who investigated zero-biased and self-biased systems as used in magnetic electron microscopes, found an optimum grid-to-cathode spacing $c \approx 2-3 r_g$ for a grid aperture radius $r_g \approx 2$ mm. where a spot of 5–10 μ radius and of

10^{-3} A./mm. current density could be focused by a magnetic condenser lens on to a microscopic object at 50 kV. Haine and Einstein (1952) measured for similar hair-pin systems source radii of a few hundredths of a mm. and maximum intensities $(i/\Omega) \approx 10^9$ [Amp./m.^{2}/unit solid angle].

Steigerwald (1949) obtained a very slightly convergent beam of great intensity with a hair-pin system which he designed for an electrostatic electron microscope. This system is shown in fig. 9.16. Focusing is achieved here by the particular shape of the grid electrode which is at a slightly negative bias. The equipotentials shown in the figure have first a diverging and later on a converging effect on the electron orbits. Without the help of a condenser lens, a focus of 0·5 mm. diameter is obtained at 90 cm. distance from the cathode.

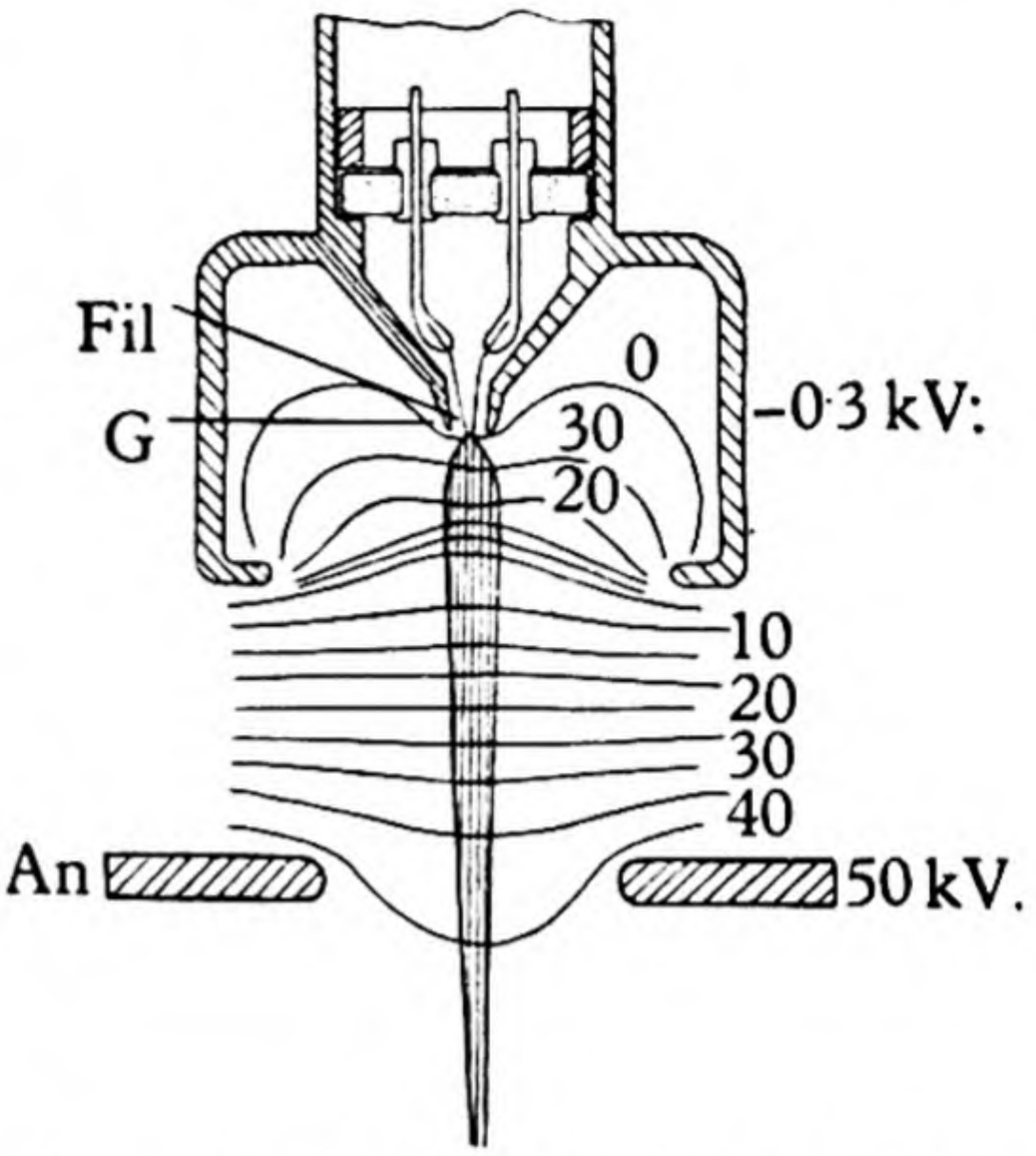

Fig. 9.16. Telefocus emission system.

Ehrenberg and Spear (1951) have investigated the use of the hair-pin system for an X-ray tube. They obtained electron concentrations of 30 μ half-width with beam currents of 0·5 mA. on a plane anode at 50 kV. A bias of -50 V. was applied to the grid, and the tube which surrounded all electrodes was at grid potential.

Emission densities up to 10^8 A./m.^{2} have been obtained from cold-cathode points of about 10^{-3} mm. radius by application of fields of the order of 10^8 V./m. The emission from point cathodes has been investigated in the point projector electron microscope (e.g. Benjamin and Jenkins, 1940, 1942). The emission densities just mentioned are so extreme that cold-point cathodes should be expected to have great prospects for future use in emission systems of extremely small spherical aberration. So far, however, the cathode surface has been found to be rather variable and the emission has not been brought under control.

Cavity cathodes. These are of some technical interest for use in emission systems; they have been employed in cathode-ray tubes

by Dobke (1932) and in electron microscopes by Liebmann (1948*b*). The filament may have the form of a circular loop or of a short coil, and it should be coaxial with the grid aperture, its internal diameter being slightly larger than this aperture. The accelerating field of the anode draws electrons sideways from the filament towards the axis and then through the grid aperture, while the magnetic field due to the filament current tends to focus the slow electrons towards the axis. The aperture of a cavity cathode can emit relatively large currents owing to the relatively large electron-emitting surface of the filament. A particular merit of this cathode is its long life even in poor vacuum, since the filament is little exposed to ion bombardment.

9.7. Multielectrode systems

A great variety of emission systems with more than three electrodes has been described, especially in the patent literature. If some of these systems have a particular merit this is usually not because they provide greater intensity of emission or less aberrations than could be obtained with triode systems. However, some technical advantage can frequently be gained by the addition of a new electrode, since this implies a new degree of freedom for the adjustment of a desirable potential distribution. In this way, for instance, uncomfortably small spacings could be avoided, and the whole design can be made less critical with respect to the adjustment, to the alignment or to a desired shape of the electrodes.

Screen-grid tetrode systems. These were proposed as early as 1930 by Zworykin, and they have since found some important application in television tubes. Descriptions of such systems have been given by Swedlund (1945) and by Morton (1946). Between the control grid and anode there is inserted an additional electrode called the 'screen grid', 'shield' or 'accelerator'. If, for instance, an apertured, flat diaphragm is inserted as screen grid into the simple triodes shown in figs. 9.1 or 9.2, optimum current densities may be obtained without an adjustment of the critical preference spacings as given by the graph of fig. 9.8. Moreover, owing to the early acceleration of the beam by the accelerator, the cross-over can be kept at a relatively high potential and thus a reduction of space-charge errors appears to be possible. On the other hand, the

increased spacing between accelerator and anode allows the formation of a narrower beam. The electrostatic fields tend to pull this beam through the centres of the electrode apertures so that the mechanical alignment becomes less critical.

Apart from these constructional advantages, special merits become evident when the screen-grid tetrode is used in electron-optical gear. For instance, if this system is used in an electron gun, the interaction between focus and brightness control which is sometimes disturbing in triode emission systems can be largely overcome. The screen-grid tetrode is very suitable for high-

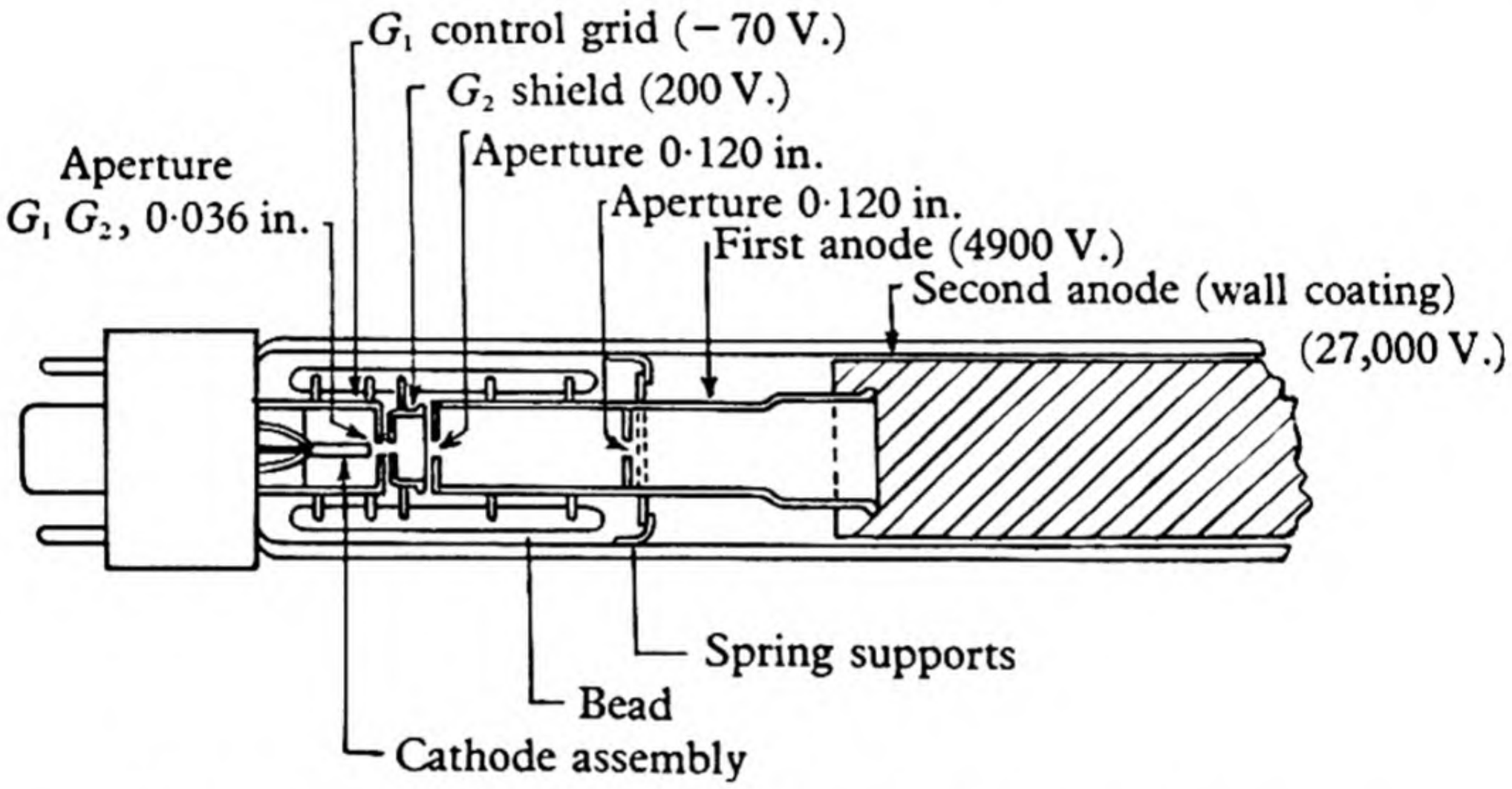

Fig. 9.17. Screen-grid emission system in high voltage gun.
(R.C.A. gun 5TP4.)

voltage guns in television projection tubes. There, excessive fields between grid and anode are avoided by the insertion of the screen-grid electrode. A typical high-voltage gun which is used in R.C.A. projection tubes is shown, for example, in fig. 9.17.

The use of the screen-grid system as an immersion objective in emission microscopy has been investigated by Johannson (1934*b*). The objective has the merit that its principal planes can be shifted by a change of the electrode potentials only. Hence the magnification of the microscope can be controlled without moving the grid electrode which is required for such a control in a triode system.

Emission systems with einzel lens. These contain a decelerating electrode *D* which is arranged between an accelerator *Ac* and an anode *An* as shown in the schematic drawing of fig. 9.18. The

electron emission from a cathode *C* is controlled by the usual grid electrode *G* and focused by the saddle field which is formed between *Ac* and *An*. As in fig. 9.18, the decelerator is usually connected to the control grid, while the accelerator is connected to the anode *A*. If the system is used in a gun, the usual second anode is still necessary for producing an electrostatic focusing lens; otherwise, a magnetic lens is employed for projecting the image of the cross-over on to the target. A system similar to that shown in fig. 9.18 was first described by Dobke (1932), but many other systems based upon the same principles have been used since in guns for television tubes; e.g. by Standard Telephones and Cables, by Philips, by G.E.C., and others. We only mention here an einzel-lens system described by the Mullard Co. (1938). The electrodes corresponding to *G*, *Ac*, *D* and *An* of fig. 9.18 are represented in this system by four flat diaphragms in front of a flat cathode. The apertures in these diaphragms are of the order of 1–2 mm. in diameter and their mutual spacings are slightly smaller. Guns equipped with einzel-lens systems have been found to combine good brightness of the spot with a steep modulation characteristic.

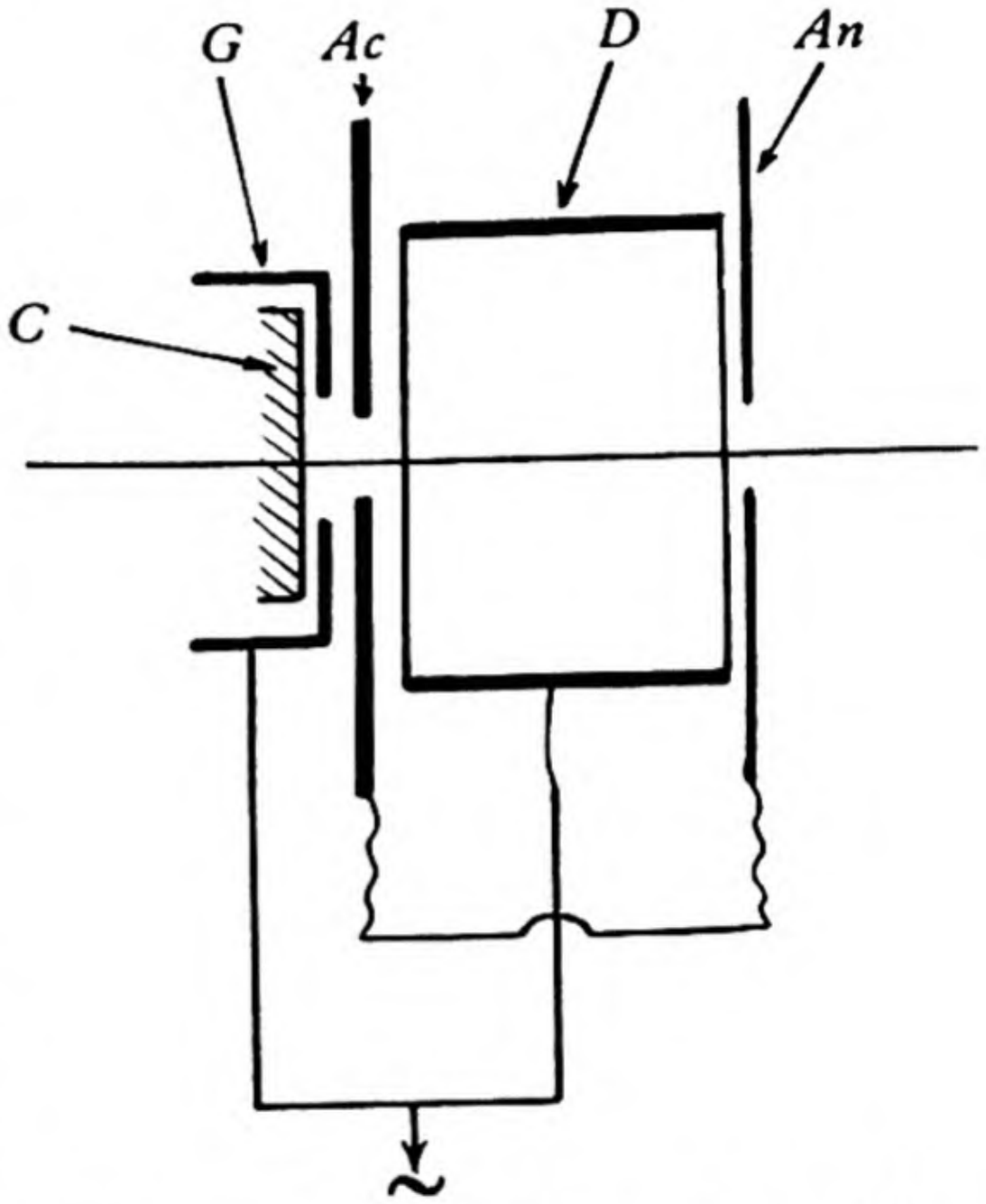

Fig. 9.18. Emission system with einzel lens.

Emission systems with virtual cathode modulation. These are theoretically interesting, since the intensity modulation is not effected by the usual grid electrode *G* in front of the cathode *C* but by an extra electrode, the 'modulator' *Mo*, which is inserted between the accelerator *Ac* and the anode *An*. Such a system is shown in fig. 9.19, which is taken from a patent specification by Condliffe, Shoenberg and Tedham (1933). The grid electrode *G* is permanently at cathode potential, accelerator *Ac* and anode *An* are at the fixed potentials of 250 and 800 V. respectively. A second anode at 4 kV. (not shown in the figure) may be employed to focus the

beam on the target if the system is used in a gun. Normally, the modulator is at cathode potential or at slightly negative bias. A signal of negative voltage is applied to it for an intensity modulation of the electron beam. The beam forms a waist in the aperture of the accelerator, enters the modulator with much divergence but is constricted again to a minimum diameter in the modulator aperture.

A strong field-saddle is set up by the low modulator potential, and the resulting lens will vary in focal length if a signal is applied to the modulator. However, this variable lens will have the least effect in changing the beam geometry when the beam crosses over

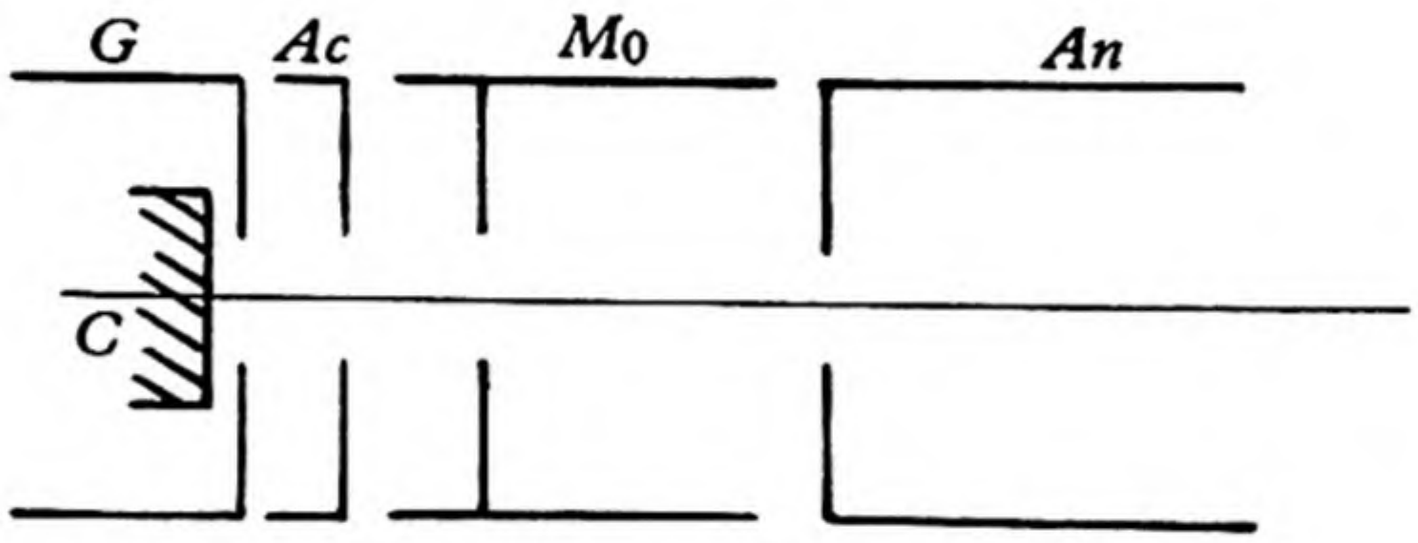

Fig. 9.19. Emission system with virtual cathode modulation.

in the lens centre so that the actions of both halves of the lens balance each other. For this purpose, fields of equal intensity should be established in the two sleeves of the modulator, i.e. the lengths of these sleeves should be proportional to the voltages of accelerator and anode respectively. In this ideal case, the modulation of the beam is effected by lifting up the negative potential of the field-saddle. Now, first the marginal electrons can no longer reach it, and as the saddle is lifted higher the rays nearer and nearer to the axis are returned. When the centre of the saddle reaches cathode potential or rather reaches the negative potential corresponding to the thermionic emission velocity, then even the paraxial electrons are reflected. In this case, the modulator electrode has reached 'black-out potential' which is of the order of -25 V.

Though the described system provides a sharp spot of great brightness, combined with an excellent slope of the modulation characteristic, its utility is restricted, since the spot which is produced in a gun is surrounded by a fine halo ring. So far it has

not been possible to remove this halo. According to Klemperer (1951) the formation of this halo has to be explained as an effect of spherical aberration of the saddle-field lens in the modulator. The aperture in the anode cuts out some intermediate rays in the electron bundle in the way explained by fig. 6.10 of §6.4, thus leaving a small spot separated from a wider halo ring. Emission systems with virtual cathode modulation have found a good deal of practical application in the early development of television; however, they have now been superseded by other systems which do not suffer from halo formation.

Emission systems with magnetic fields. Superimposition of a strong magnetic field over an emission system perpendicularly to its cathode has been shown in §8.6 to restrict the cross-section of the emitted beam. The electrons emitted at all angles from a cathode are known to move in spiral orbits about the magnetic lines of force of a strong axial magnetic field. The diameter of the spiral orbit is a function of the tangential velocity of emission, of the local electric potentials and of the intensity of the magnetic field.

Quantitative data have, so far, been obtained theoretically only for simplified models. Pierce (1945) treated the flow of electrons from a circular, plane cathode disk immersed in a strong magnetic field at right angles to the cathode surface. The distance from the axis of an electron which leaves the cathode at a radial distance y is in the course of its spiralling trajectory increased by a maximum amount

$$\Delta y = \frac{m}{e}\frac{E_y(t)}{B^2}, \tag{9·35}$$

where B is the flux density of the intense magnetic field and E_y is the radial field due to the combined effect of space charge and of accelerating voltages at the electrodes which as a function of the time t tends to displace the electrons. The effect of making the magnetic field very intense is to make the electron paths approach straight lines normal to the cathode. Emission can be started in a magnetic field so that the electrons have only axial velocities. According to Pierce (1951), the electrons emerging from a two-diaphragm emission system, immersed in a homogeneous, axial magnetic field, will have no radial velocity components if the ratio of anode potential V_A to grid potential V_g is chosen to have the

following relationship with the ratio of cathode spacing c to anode spacing a:

$$\frac{c}{a} = \left(\left(\frac{V_g}{V_A}\right)^{\frac{1}{2}} + 1\right)\left(\frac{V_A}{V_g} - 1\right). \tag{9.36}$$

c/a has to be multiplied by $\frac{3}{4}$ if space charge is taken into account.

The use of an intense convergent magnetic field tending to guide the emission to a focus has been described in a patent specification

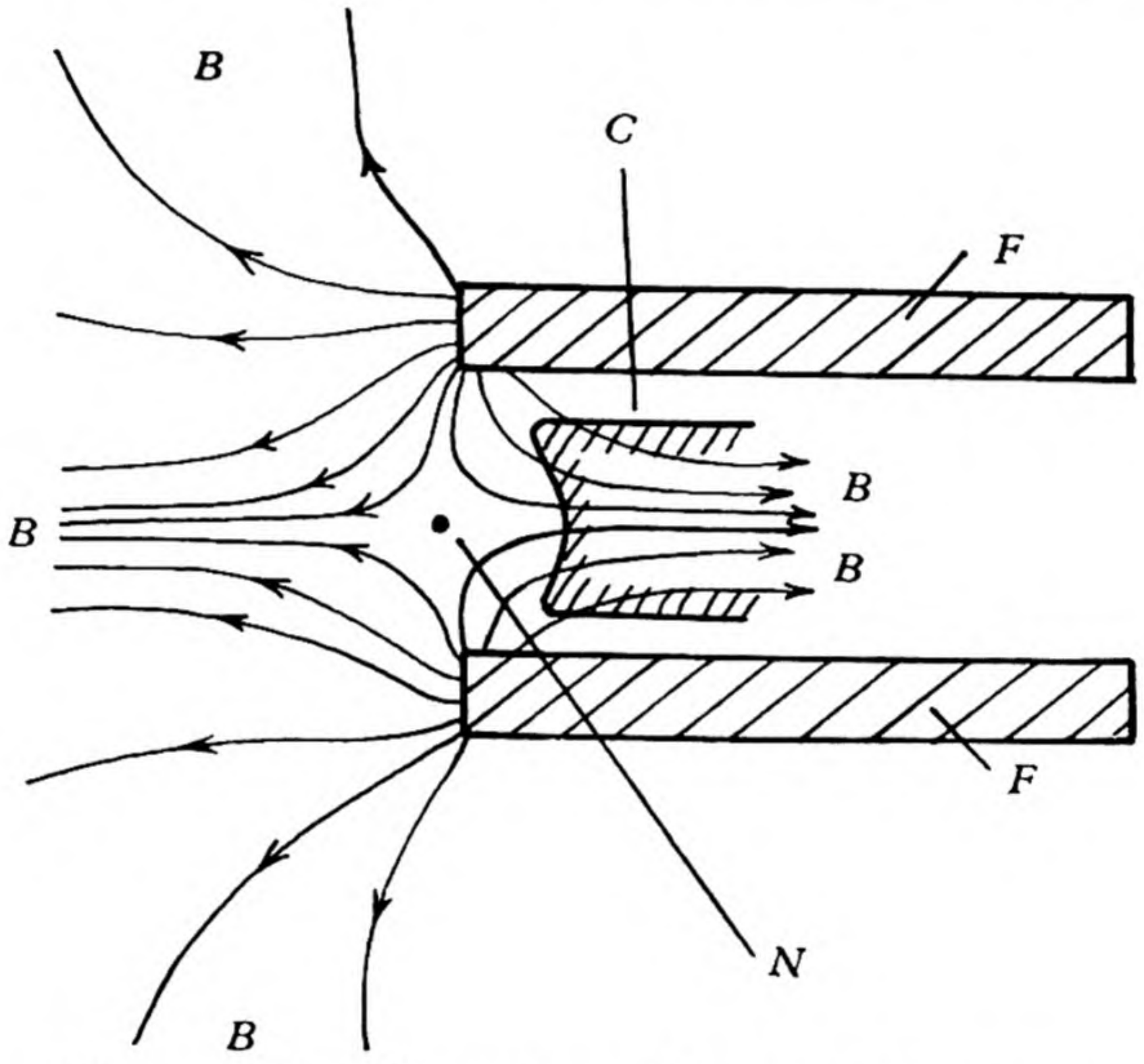

Fig. 9.20. Emission system with magnetic focusing.

by the Philips Co. (1941). There (see fig. 9.20) a concave cathode C is surrounded by a ferromagnetic body F which is polarized magnetically in the direction of the axis. Magnetic lines B pass from the circular edge of F into the vacuum and through the cathode surface as indicated in the figure, and a magnetically neutral point N is formed near the emissive surface. Though emission systems with magnetic focusing might have important application in the future, so far little practical knowledge is available about them.

Only in one particular case has magnetic constriction of the electron emission found important practical application, namely, in the electron gun of the Orthicon television tube (cf. § 12.3). This gun (cf. Morton, 1946) produces a narrow electron beam

of about 200 eV. A magnetic field of about 70 gauss extends nearly uniformly from cathode to target. The emission system that is immersed in the magnetic field is essentially a two-diaphragm system (cf. fig. 9.1) with strongly biased grid electrode close to the cathode. In one instance the grid aperture radius is $r_g = 0{\cdot}5$ mm. At a relatively large distance a from the grid ($a \approx 4r_g$) follows an anode diaphragm with an extremely small aperture ($r_a \approx r_g/20$) so that a very narrow beam is formed, the current being of the order of 1 μA. only. The action of the magnetic field in such a gun, however, is more essential for the constriction of the emerging beam than for its actual formation in the emission system.

CHAPTER X

ELECTRON LENSES AND EMISSION SYSTEMS WITH LINE FOCUS

10.1. Focusing by two-dimensional fields. Terminology

All the previous chapters have dealt with electron lenses of circular symmetry only. The focus of such lenses—in the ideal case—is a point. They correspond to glass-optical lenses with spherical refracting surfaces. Another lens type quite common in glass optics has cylindrical refracting surfaces. Such lenses have line foci parallel to the axes of the refracting cylinders. At right angles to a line focus can be found a plane of 'translational' symmetry for all refracting surfaces.

In electron optics use has been made of systems of equipotential surfaces with a common plane of 'translational' symmetry which are able to form line foci of electron rays. Such 'line-focus lenses' and 'line-focus emission systems' are found to a large extent in valves, electron multipliers, X-ray tubes and in some particular cathode-ray tube constructions (cf. Chapter XII).

Line-focus lenses may be represented by drawing a cross-section of the electrodes in the plane of symmetry at right angles to the line focus. For instance, fig. 4.4 of § 4.3 can now be taken as a representation of the cross-section through some simple electrostatic line-focus lenses. The plane of the paper now corresponds to a plane of a 'translational' (but no more of circular) symmetry. The main constructional elements of the line-focus lenses of fig. 4.4 are the slotted diaphragm and the double plate, corresponding respectively to the circular diaphragm and to the tube of circular-symmetrical electron optics.

A fundamental practical difficulty is now presented by the problem of terminating such slots and plate electrodes. These should ideally all extend to infinity. In glass optics, rectangular aperture stops are normally used to confine the bundles of rays to a given maximum distance from the plane of symmetry so that the neighbourhood of the ends of the lenses is avoided by the rays. A similar procedure, however, cannot always be applied in electron optics. In

order to avoid penetration of spurious fields through the open ends of the lens electrodes, these electrodes would often have to be of a prohibitive length. Some practical solutions of this problem will be offered below in § 10.4. However, to study the general aspect, let electrodes and line foci first be regarded as infinitely long, so that their optics can be treated as a purely two-dimensional problem. In the following we shall refer all line-focus lenses to a coordinate system with y- and z-axis in a plane of translational symmetry and with the line focus parallel to the x-axis. If the line focus is of finite length, it is assumed to extend symmetrically to the z-axis.

10.2. Field plotting and ray tracing. Computational mapping

It has been explained in Chapter III, that potential distributions in space can be completely calculated from Laplace's equation (3.2), but the analytical procedure is generally difficult. However, numerical methods become very useful whenever experimental facilities (described below) are not available. For the two-dimensional case, Laplace's equation reduces to

$$\frac{\partial^2 V}{\partial y^2}+\frac{\partial^2 V}{\partial z^2}=0. \tag{10.1}$$

For a numerical method of extrapolating the potentials off the electrodes, let the yz-plane of translational symmetry be covered by a net of equidistant lines parallel to the two axes, as shown in fig. 10.1. The potential V_0 at any lattice point should be completely determined by the potentials V_1, V_2, V_3, V_4 of its neighbouring four lattice points. Calling g the distance between the lattice lines, it is obvious that

$$\frac{V_2-V_0}{g}-\frac{V_0-V_4}{g}\approx\left(\frac{\partial V}{\partial y}\right)_{2,0}-\left(\frac{\partial V}{\partial y}\right)_{0,4}\approx g\left(\frac{\partial^2 V}{\partial y^2}\right)_0 \tag{10.2}$$

and

$$\frac{V_1-V_0}{g}-\frac{V_0-V_3}{g}\approx\left(\frac{\partial V}{\partial z}\right)_{1,0}-\left(\frac{\partial V}{\partial z}\right)_{0,3}\approx g\left(\frac{\partial^2 V}{\partial z^2}\right)_0. \tag{10.3}$$

According to Laplace's equation, (10.1), the expressions (10.2) and (10.3) are equal, hence

$$V_0\approx\tfrac{1}{4}(V_1+V_2+V_3+V_4). \tag{10.4}$$

With the help of (10.4) the potential distribution between electrodes of known potential can be extrapolated. This is done in practice by starting from an arbitrary distribution.

To give an example, let the two heavy lines A and B in fig. 10.1 represent two plate electrodes at a common potential $V = 10$ V., and let the y-axis be the section through an electrode at zero potential. The electrode arrangement corresponds practically to a four-plate lens, A and B being the cross-section of one pair of plates while the y-axis represents the section through the mid-plane.

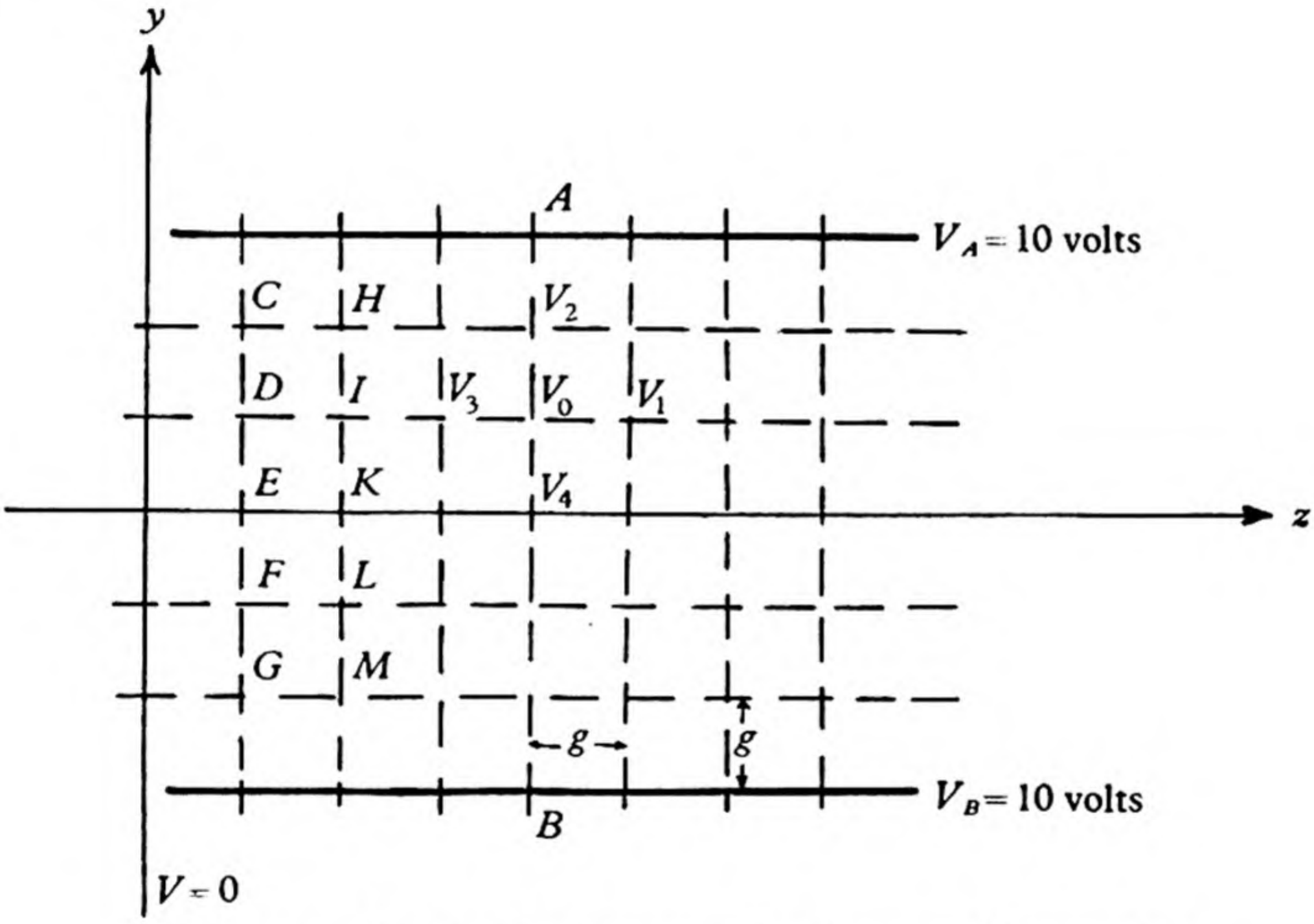

Fig. 10.1. Lattice for computational potential mapping.

If, for a start, all lattice points are assumed to be at $V = 10$, the potential distribution is not in disagreement with (10.4) excepting for those points which adjoin the y-axis. There, one has to begin with reducing the assigned V values. First, new values may be obtained for the points C and G, since these points are surrounded each by two neighbouring lattice points of the fixed potentials 0 and 10 respectively. From (10.4) follow the values $V_c = V_g \approx \frac{30}{4}$. Hence we may try to assign the values 7 to these two points noting the 'residuals' (+2) for each. We then calculate with (10.4) new values for the neighbouring points D and F and we see that both will be changed to $V = 6$. The values of further neighbouring points can

then be adjusted in the same way noting that V_E is doubly affected, i.e. both by the changes in D and in the symmetrical point F; this applies to all points on the z-axis. The procedure explained is further applied in turn to all other points recording always the effect of a change at any point upon its immediate neighbours. Then

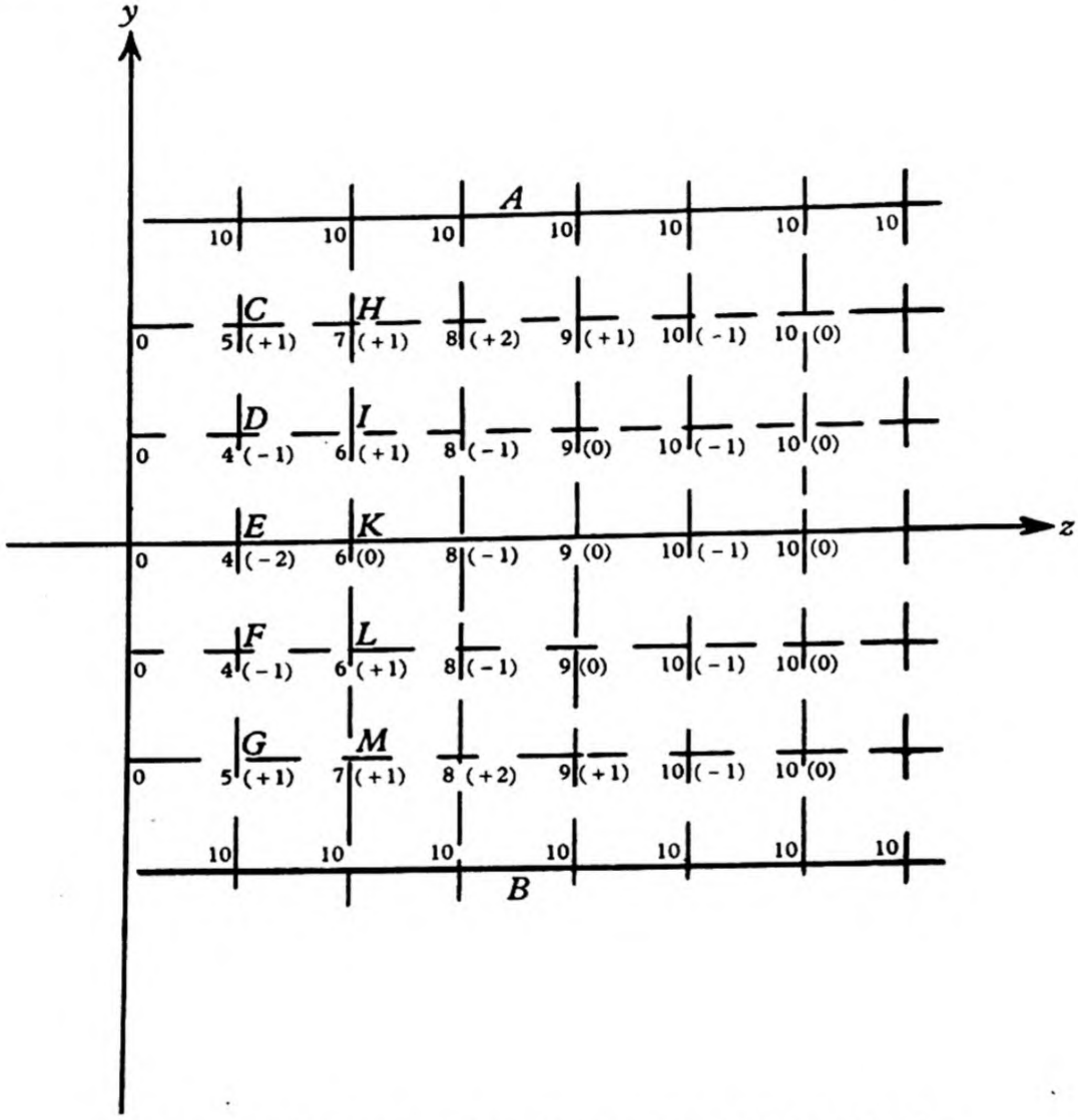

Fig. 10.2. First approximation to potential distribution.

the whole process is repeated until the residual for each potential is below a given value which may be ± 2 at a first trial. In this way an approximate potential distribution is obtained as shown in fig. 10.2, where the final residuals are given in brackets.

To obtain higher accuracy the potential at every point (and all the residuals) of the first solution (fig. 10.2) may be multiplied, for instance, by a factor 10 and the process of approximation continued, until the residuals are again reduced to (± 2). A comparison

of such a refined numerical plot with the corresponding analytical solution (also compare the paraxial values of the rough plot of fig. 10.2 with the curve shown later in fig. 10.3) indicates that an error of a few percent only can be reached by a few repetitions of the process. For greater accuracy, a lattice with smaller intervals may be chosen. Details of the method will be found in the literature quoted in § 3.1. Some of the references given there deal with specialized methods for speeding up the procedure of the computational potential mapping. It appears, however, that a great deal of labour is involved to reach the accuracy that is required for many practical problems, and generally experimental methods for field plotting are preferable.

Electrolytic field plotting. The electrolytic method described in § 3.2 is very suitable for the investigation of a potential distribution that changes in two dimensions (y and z) only. It has been pointed out that a surface of the electrolyte terminated by an insulator acts as a mirror producing a mirror-image of the potential distribution adjoining the insulator. Hence for the representation of a two-dimensional potential distribution a very shallow trough can be used with a strictly horizontal, plane, insulating bottom, filled with electrolyte to a height of the order of a centimetre only.

The electrodes are made from strips of metal which rest on the bottom of the trough; they are connected in the usual way to the appropriate potentials of a potentiometer across an a.c. source. Now either of the planes represented by top and bottom of the plane-parallel slab of liquid can be considered as a plane of translational symmetry for the line-focus optics, since, like mirrors, both these planes extend the picture of the electrode structure and of the potential distribution in the vertical direction to infinity (Barkhausen and Bruck, 1933).

The equipotentials measured in the plane-parallel slab of electrolyte may be labelled in the way explained in § 3.2. Again, the tracing of the electron rays through the equipotential plot of a two-dimensional distribution can be performed by exactly the same methods as have been applied to the fields of circular symmetry. The rays may be traced, for instance, by direct application of Snell's law, or with the circle method or by any of the methods mentioned in Chapter III. Even the automatic tracing machines described in

§3.6 can be employed directly in connexion with the plane-parallel trough.

Elastic-membrane model. A stretched rubber sheet provides a most convenient device for tracing the electron path through a two-dimensional potential distribution. This was recognized first by Oliphant and Moon (1929), and details of the method have been developed by Kleynen (1937), by Pierce (1938), by Zworykin and Morton (1940), by Fremlin and Walker (1947) and others. The method is based on the principle that the distribution of height h of deformation of a slightly distorted membrane follows the same law as a two-dimensional potential distribution.

A two-dimensional potential distribution $V(y, z)$ is described by Laplace's equation, (10.1). The deformation of a stretched membrane is then represented by a similar equation, namely,

$$\frac{\partial^2 h}{\partial y^2} + \frac{\partial^2 h}{\partial z^2} = 0. \tag{10.5}$$

This equation applies because a stretched membrane tends to contract everywhere so as to make the surface area a minimum. This implies that the membrane will assume such a shape as to minimize the surface energy. It has been shown, for example, by Zworkyin and Rajchman (1939) that (10.5) can be derived by minimizing an integral expression for this energy if the slopes $\partial h/\partial y$ and $\partial h/\partial z$ of the membrane are small.

In the practical model, a round or rectangular elastic membrane is stretched uniformly over a horizontal frame. A stretch leading to an increase of 20–50 % of the linear element can be applied to a rubber sheet of about $\frac{1}{2}$ mm. thickness, its edge being pulled by clips spaced equally along the whole circumference. The membrane is then deformed vertically by pressing it down over a model of the electrode system. The height of each electrode has to be proportional to the negative voltage it represents. On the other hand, electrodes representing positive potentials must be pressed down on the membrane from above. Such electrodes may be fixed, for instance, on a gantry arranged within a few centimetres above the membrane. Care has to be taken that the rubber is in full contact with all electrodes, so that it is stretched over the full length of their top or bottom edges respectively. In this way, a series of mountains and valleys is formed with the contours of the membrane corre-

sponding to the equipotentials of the electrostatic field between electrodes of 'infinite length'.

To trace an electron orbit, a small steel ball-bearing is released at a point corresponding to the cathode. It will roll along the rubber surface in such a way that its horizontal projection describes the electron path in the electrode system under investigation. Since the emission at the cathode occurs with negligible initial velocity, care has to be taken that the steel ball is set free without the slightest initial acceleration. For this purpose it may be released from a small electromagnet or from the nozzle of a tubing to which it is held initially by suction of a vacuum which, at the given moment, is gradually decreased. A photographic technique may be employed for recording the track of the ball. For obtaining a good contrast, the use of black rubber and of highly reflecting balls is recommended. If a pulsating light source (about 50 cyc./sec.) is employed, the path appears as a dotted line and the spacings between the dots are a measure for the velocity of the electron.

Walker (1949) made a detailed investigation about the sources of errors and the accuracy of the elastic-membrane method of ray tracing. The most serious cause of error is the frictional retardation of the ball. Larger balls have less friction, but a certain amount of sag in the membrane is caused by too heavy balls. Also, since the position of the ball is recorded by observing the image of a light source, the apparent position of that image relative to the ball centre will vary as the ball moves and may give rise to an appreciable error for balls of large diameter. A practical diameter of $\frac{3}{16}-\frac{1}{4}$ in. is recommended. Friction of the ball may be reduced by making the model smaller without reducing the slope at corresponding points. However, in every particular case a lower limit is set to the reduction in scale by the mechanical difficulties in setting up boundaries and by the difficulty of locating and recording the ball at any point. An error of minor importance is sometimes introduced by a spin of the ball, generated about an axis through the point of contact, and normal to the membrane. All other errors can be reduced without limit by decreasing the slope of the membrane. The ball will still be accelerated on an incline of less than 1°, but slopes as large as 30° have been found to give sufficiently accurate results for all practical purposes.

10.3. 'Two-dimensional' electrostatic line-focus lenses

The electric fields set up between the electrodes of a line-focus lens extend much farther along the z-axis than the fields set up

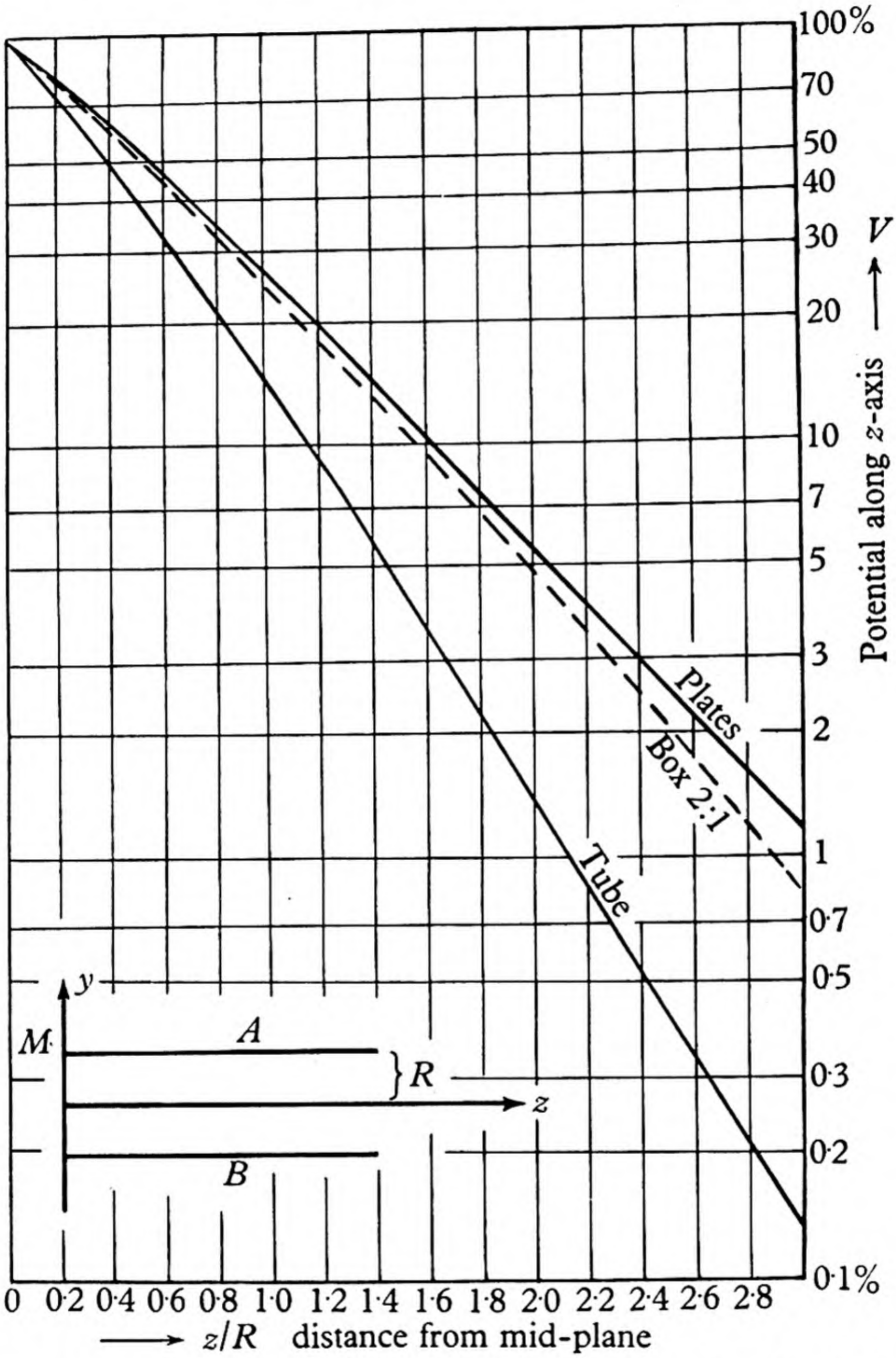

Fig. 10.3. Potential decay in tube lens and in corresponding line focus lenses.

between corresponding electrodes of circular structure. This is shown, for instance, by the curves of fig. 10.3. The lens electrodes are drawn in cross-section at the bottom of the figure. For a circular

structure, A and B together represent a tube of radius R with the axis z. For a two-dimensional structure, however, each, A and B, represent conducting plates extending to infinity in the x-direction, i.e. at right angles to the plane of the drawing. The mutual distance of the plates is $2R$, where R may be called the 'semi-aperture' of the 'plate lens'.

At the right-hand side ($+z$-direction), tube and plate electrodes respectively may be imagined as extended to infinity. At the left-hand side let the electrodes be terminated, with a plane electrode M spaced closely to A and B and arranged at right angles to the z-axis. M corresponds to the midplane of a two-tube lens as shown in fig. 3.3. M also represents a plane of symmetry in the two-dimensional case of a 'four-plate lens'. The gaps between M and A, B are assumed to be negligibly small as compared with the semi-aperture R. Let A and B be earthed ($V = 0$) and a given potential ($V = 100\,\%$) be applied to M.

The three-dimensional and the two-dimensional potential distributions along the z-axis can be measured in the electrolytic wedge trough and in the plane-parallel field-plotting trough respectively; or they can be calculated (cf. Bertram, 1942). The corresponding curves representing the potentials along the z-axis of tube lenses and of plate lenses are drawn in fig. 10.3.

The potential can be seen to decrease very much faster in the tube lens than in the plate lens. Going, for instance, one semi-aperture R along the z-axis, the potential decays in the tube lens by a factor of about 10, in the plate lens by a factor of about 4 only.

The broken curve in fig. 10.3 corresponds to the case of a line-focus lens in which the plates do not extend to infinity but are chopped off at the distances $\pm x = \pm 2R$ from the yz-plane of the drawing and connected by another plate parallel to this yz-plane so that a box-like electrode structure is obtained, the cross-section being a rectangle of side ratio 1:2 in the xy-plane. The potential decay along the z-axis of this 'two-box lens' is seen to be slightly more rapid but still rather similar to that of the four-plate lens.

The relatively slow potential decay in line-focus lenses is evident also, when slot lenses are compared with diaphragm lenses with circular apertures (see again fig. 4.4). Corresponding potential distributions for slots and round holes have been calculated by Fry

(1932) and by Strashkevitch (1940) and measured by Glaser and Henneberg (1935).

Owing to the strong field penetration through the electrodes, the focal lengths of line-focus lenses are relatively short. If, for instance, calculations for the slotted diaphragm are carried out by methods similar to those given in § 4.4 for the circular diaphragm, the following formula is obtained for the focal length of the slot:

$$f = 2V_A/(E' - E), \tag{10.6}$$

where V_A is the voltage of the slotted diaphragm with respect to

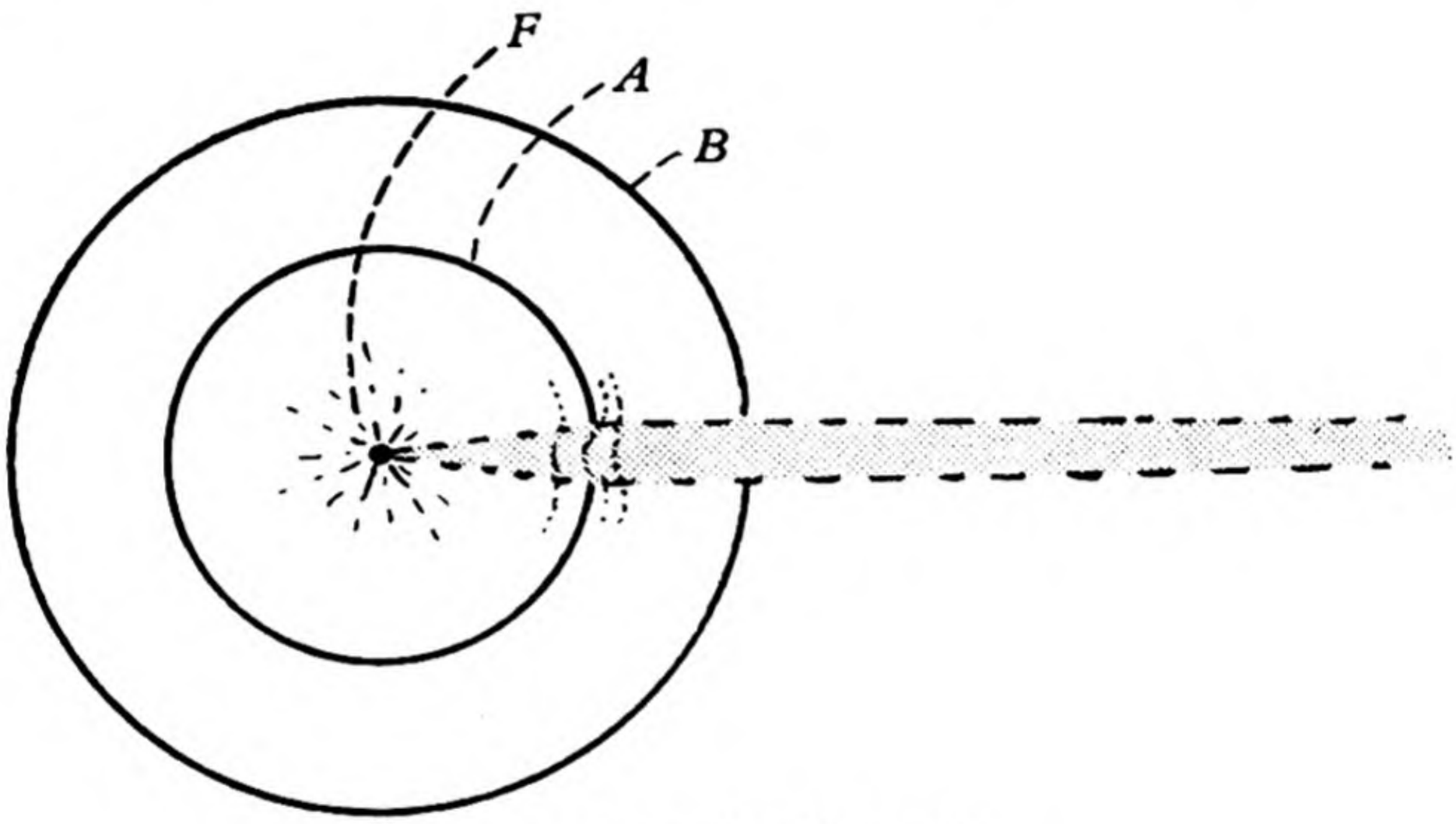

Fig. 10.4. Focusing by a slot.

the cathode, and E and E' are the field intensities in front of and behind the diaphragm. The focal lengths given by (10.6) are exactly half as long as the corresponding focal lengths of the circular aperture as given by (4.8).

The historical arrangement by which Davisson and Calbick (1931) verified (10.6) and measured for the first time a focal length of an electrostatic lens is shown in fig. 10.4. There, a thin filament F is surrounded by two coaxial, slotted cylinders A and B. Because of the logarithmic decay of the potential near the thin filament, the field E on the inside of and close to the first cylinder A can be assumed to be approximately zero ($E = 0$). The field E' at the outside and close to this cylinder A is found from the potential difference and the distance between the two cylinders A and B. If the potentials are chosen in such a manner that the rays leaving

the cylinders are parallel, then the filament F must be at the focus of the cylinder A.

Two-dimensional saddle-field lenses can be produced in analogy to the lens types described in § 4.6. For example, electrodes may be arranged corresponding to fig. 4.4 (h) with three pairs of parallel plates, with a potential of the middle pair not being intermediate but either higher or lower than the potential of either of the two external pairs of plates. The saddle-shaped potential distributions between such pairs of plates, however, are different from those found in the corresponding tube lenses. In both cases the equipotentials in the yz-plane of symmetry are families of symmetrical hyperbolae separated by two singular, straight lines which cross over on the z-axis. However, for the two-dimensional lens these lines represent cross-sections of planes and they cross the z-axis at a much smaller angle than in the three-dimensional case. This can be shown in the following way:

The potential $V(y, z)$ near a saddle at the potential V_0 with the coordinates $y_0 = 0$ and $z_0 = 0$ can be expanded in a Taylor series:

$$V(yz) = V_0 + y\frac{\partial V_0}{\partial y} + z\frac{\partial V_0}{\partial z} + \frac{y^2}{2}\frac{\partial^2 V_0}{\partial y^2} + \frac{z^2}{2}\frac{\partial^2 V_0}{\partial z^2} + \ldots. \qquad (10.7)$$

Close to the saddle point, one has $V(y, z) \to V_0$ and the first differentials of V_0 vanish. Moreover, with Laplace's equation, (10.1), the Taylor series (10.7) reduces to

$$y^2 - z^2 = 0, \qquad (10.8)$$

which is the equation of two straight lines cutting the axes at angles $\gamma = \pm 45°$. This slope angle of the asymptotic equipotentials is much smaller than the corresponding angle γ marked in the equipotential plot of circular symmetry in fig. 4.8.

10.4. Some practical lenses with line focus

An obvious practical difficulty in two-dimensional electron optics has already been mentioned at the beginning of this chapter. The electrodes which produce strictly two-dimensional fields near the plane of translational symmetry have to extend far in x-direction, i.e. perpendicularly to this plane. On the other hand, the electrodes should fit into evacuated tubes of smallest possible dimensions,

hence they should extend as little as possible beyond the physical boundaries of given electron beams.

Box and slot lenses. An obvious method for terminating two plates at a common potential with a simultaneous electrostatic shielding of the space between them consists in connecting these two plates by two plane conductors. These conductors may be 'shield plates' parallel to the plane of translational symmetry and equally spaced

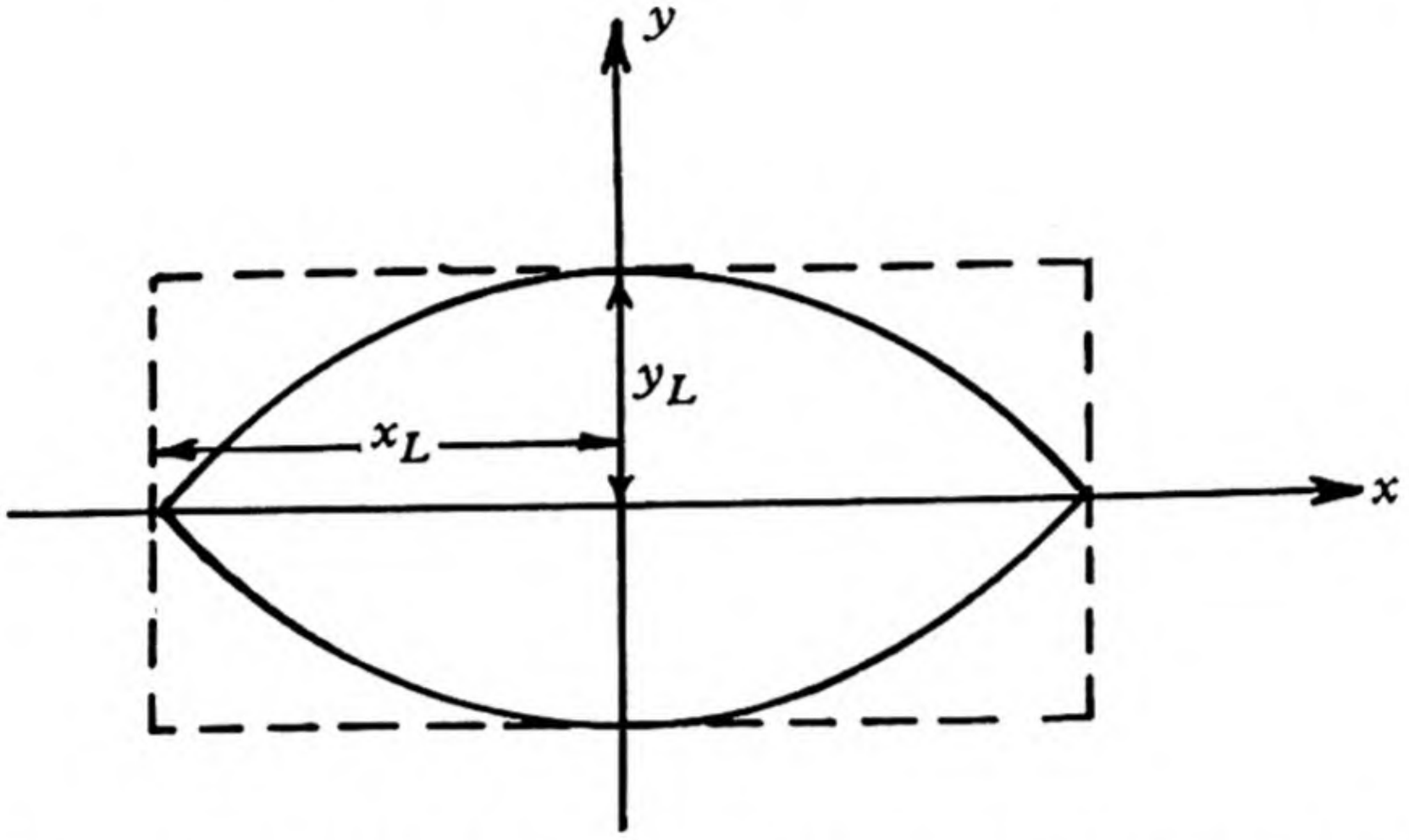

Fig. 10.5. Cross-section through an uncorrected ---- and through a corrected —— box-lens electrode.

from it at a distance x_L. In this way closed electrodes of a box-like structure are produced. Of course, the shield plates of such a 'box lens' will tend to attenuate the field penetrating into the box electrode. In addition, they will tend to focus the beam into a line parallel to the y-axis just as the proper focusing plates tend to produce the desired x-line focus.

As a consequence, the ends of the line focus produced by a two-box lens are found to be curved. The curvature is convex towards the direction of the beam and increases with the approach of the beam to the shielding plates. In other words, the focal length f increases with the distance x from the plane of symmetry.

Klemperer (1942*b*) has shown that this curvature of line focus can be corrected by changing the cross-section in the way indicated by fig. 10.5. Since the focal length of a four-plate lens is proportional to its aperture (y_L), this aperture y_L of the box electrodes has to be decreased as a function of x at the rate at which the focal length f is found to be too long.

The broken line in fig. 10.5 gives the cross-section of an ordinary box electrode of side ratio $x_L/y_L = 2:1$ for which the potential decay along the z-axis has been given in fig. 10.3. The solid line gives in proper scale the cross-section through the corrected box electrode. The y-coordinate decreases with x to a surprising extent. The two curved plates of common potential meet eventually.

In the use of this lens, a strip beam proceeds in z-direction, i.e. at right angles to the plane of the drawing. The beam is of rectangular cross-section and may extend up to three-quarters of the electrode aperture x_L. The line focus of the corrected lens is now found to be

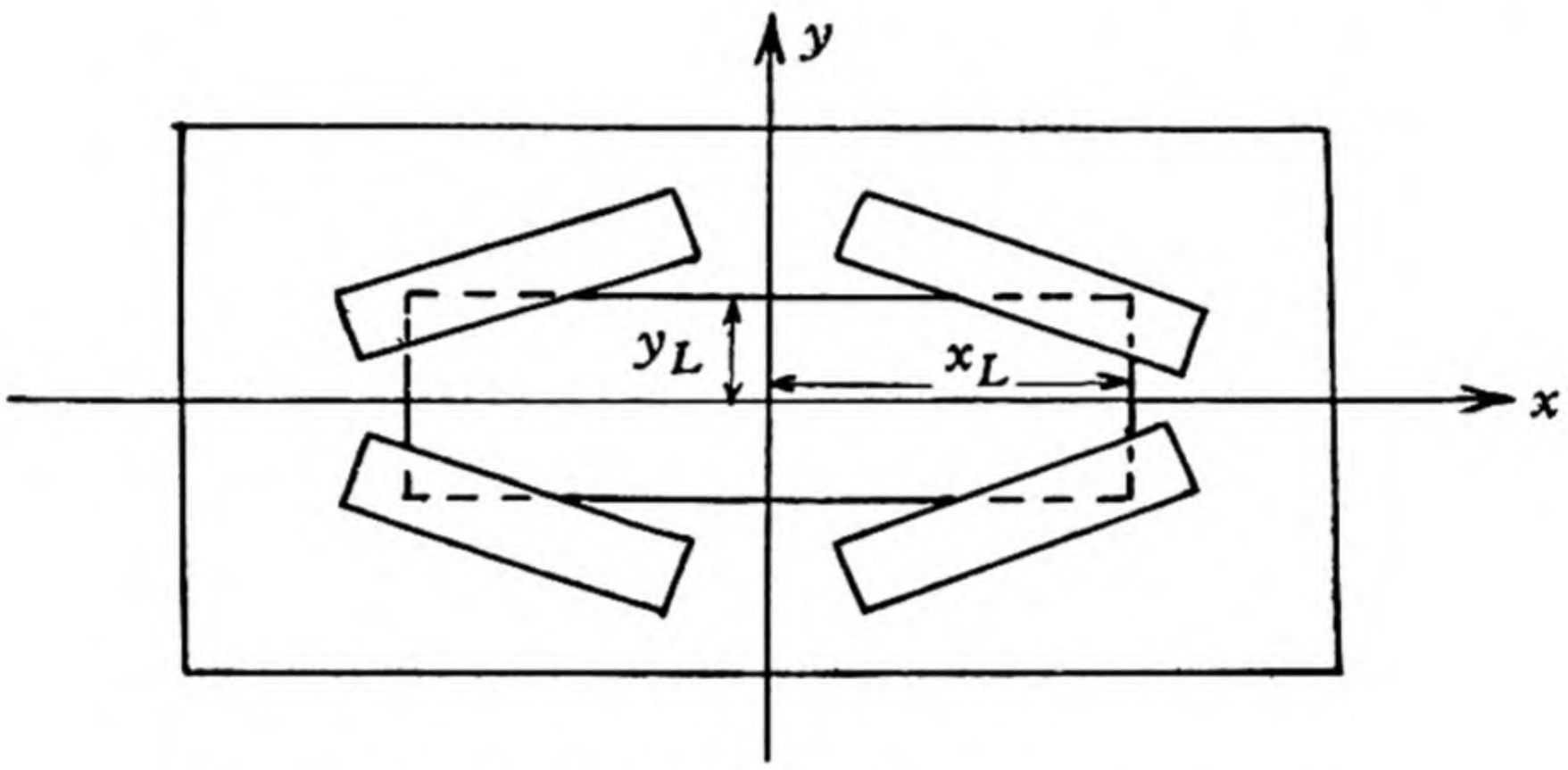

Fig. 10.6. Correction of slotted diaphragm lens.

perfectly straight. In the case of an uncorrected box lens, the mid-focal length near the z-axis is found to be about 2·5 times shorter than the mid-focal length in a distance $x = (\frac{3}{4})\,x_L$ from this axis.

The spherical aberration of the line-focus lens is given by the change of focal length as a function of the y-aperture of the ray. No accurate information is available but the spherical aberration of plate lenses appears to be of the order of magnitude of the aberration of the corresponding tube lenses.

Diaphragm lenses with rectangular slots generally suffer from a similar curvature of line focus to that of the box lenses with rectangular cross-section, however, the focal curvature of the slot lenses is not quite as strong. Consequently, the defect can again be corrected by narrowing the slot near its ends, but relatively simple means can be applied for this purpose. For example, it has been found quite convenient to attach metal patches to the ends of the slot in the way shown in fig. 10.6. There, the corners of a slot are simply covered

by four straight strips of metal which are welded on the diaphragm. The slope of the strips with respect to the sides of the slot is not very critical.

Lipped lenses. Different ways of terminating the electrodes of plate lenses and slot lenses without introducing a curvature of the line focus have been described by Klemperer (1942*c*) and are explained by figs. 10.7–10.9. In fig. 10.7 the two pairs of shield plates S and S' which are parallel to the yz-plane and at right angles to the lens plates P and P' are terminated by arcs. Thus the lens electrodes again consist of boxes of rectangular cross-section, but these electrodes are no longer symmetrical with respect to a mid-plane (cf. for instance, the mid-plane M in fig. 4.4). The two-lens electrodes which are at different voltages are now equally spaced from

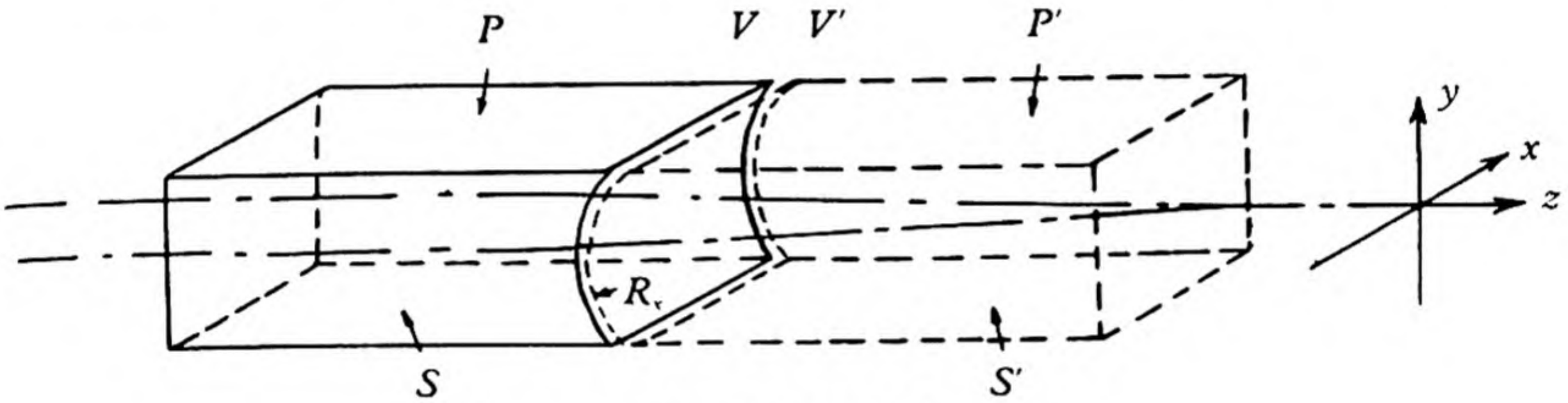

Fig. 10.7. Single-lipped box-lens.

an imaginary curved 'mid-surface' which, in case of the lens of fig. 10.7, is a circular cylinder, the axis of which is parallel to the x-axis. The shield plates S' of the box on the right-hand side thus are terminated by 'lips' which are separated by a short gap from the concave edges of the left-hand box. Near the mid-surface the fields are strongest. There the equipotentials are curved roughly to the shape of this surface. Hence the properties of the lens are controlled mainly by the radius of curvature R_x of the mid-surface. If the potential V of the left-hand box electrode is less positive than the potential V' of the right-hand box, rays in $+z$-direction are converged to a line-focus in x-direction. If, however, $V' < V$, a decelerating lens is produced which diverges the rays and the x-line focus is virtual. Again, the electrode arrangement of fig. 10.7 acts as a diverging accelerating lens for rays transmitted in $(-z)$-direction passing from the right-hand box at lower potential to the left-hand box at higher potential ($V' < V$). In this way the rays are

accelerated while passing through a mid-surface which is concave towards their direction.

Diverging lenses have been realized in electron optics, for the first time, with the help of lipped electrodes (Klemperer, 1942*c*). The use of lips at lens electrodes has introduced a new degree of freedom. A great new range of focal lengths has been produced and aberrations have been corrected by proper variation of the lip curvature. The focusing action of sufficiently curved lips completely over-balances the focusing action of the lens plates. Hence, the lipped shield plates (*yz*-planes) can be made even wider than the original focusing plates (*xz*-planes), and still an undisturbed *x*-line focus is obtained.

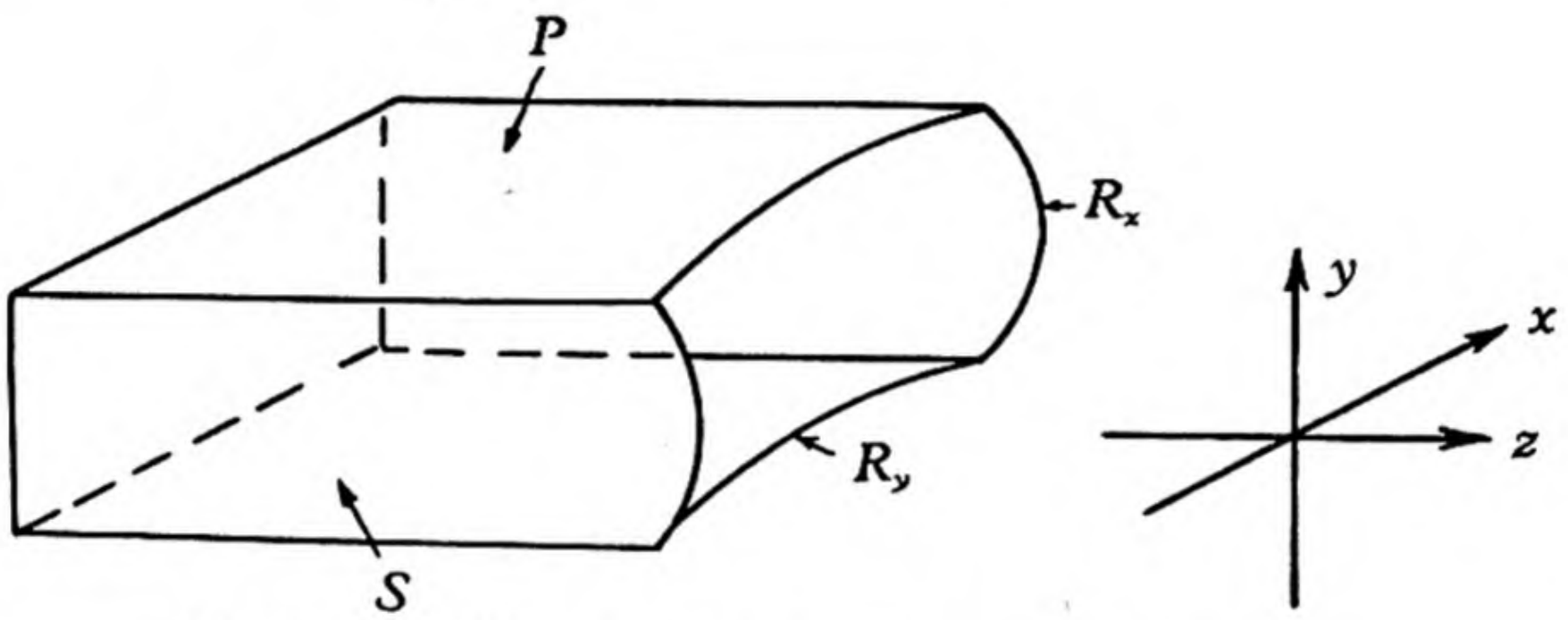

Fig. 10.8. Electrode of double-lipped box-lens.

All residual focusing towards a *y*-line can be eliminated from a box lens which produces an *x*-line focus. The method of doing this is illustrated by fig. 10.8. There, a double-lipped lens electrode is drawn in perspective. The mid-surface has now a double curvature with the radii $-R_x$ and $+R_y$ having opposite signs. A lens made up of two complementary box electrodes of this kind focuses into an *x*-line. Residual focusing into a *y*-line is now eliminated by a relatively slight curvature of the mid-surface about a *y*-axis. If this latter curvature, however, is not very small, the resulting lens will produce an *x*-line focus of extended length.

The scheme of the curved mid-surface can also be applied to slot lenses. For example, an electrode of such a lens is shown in fig. 10.9. A complete lens may consist of two slotted diaphragms of complementary curvature separated by a small gap and charged to a different potential. The diaphragms terminate lens boxes as shown in the figure. Alternatively, either of the lens boxes could be left

open without a diaphragm, so that a lens with one slot only would result.

The scheme of the curved mid-surface can also be applied to tube

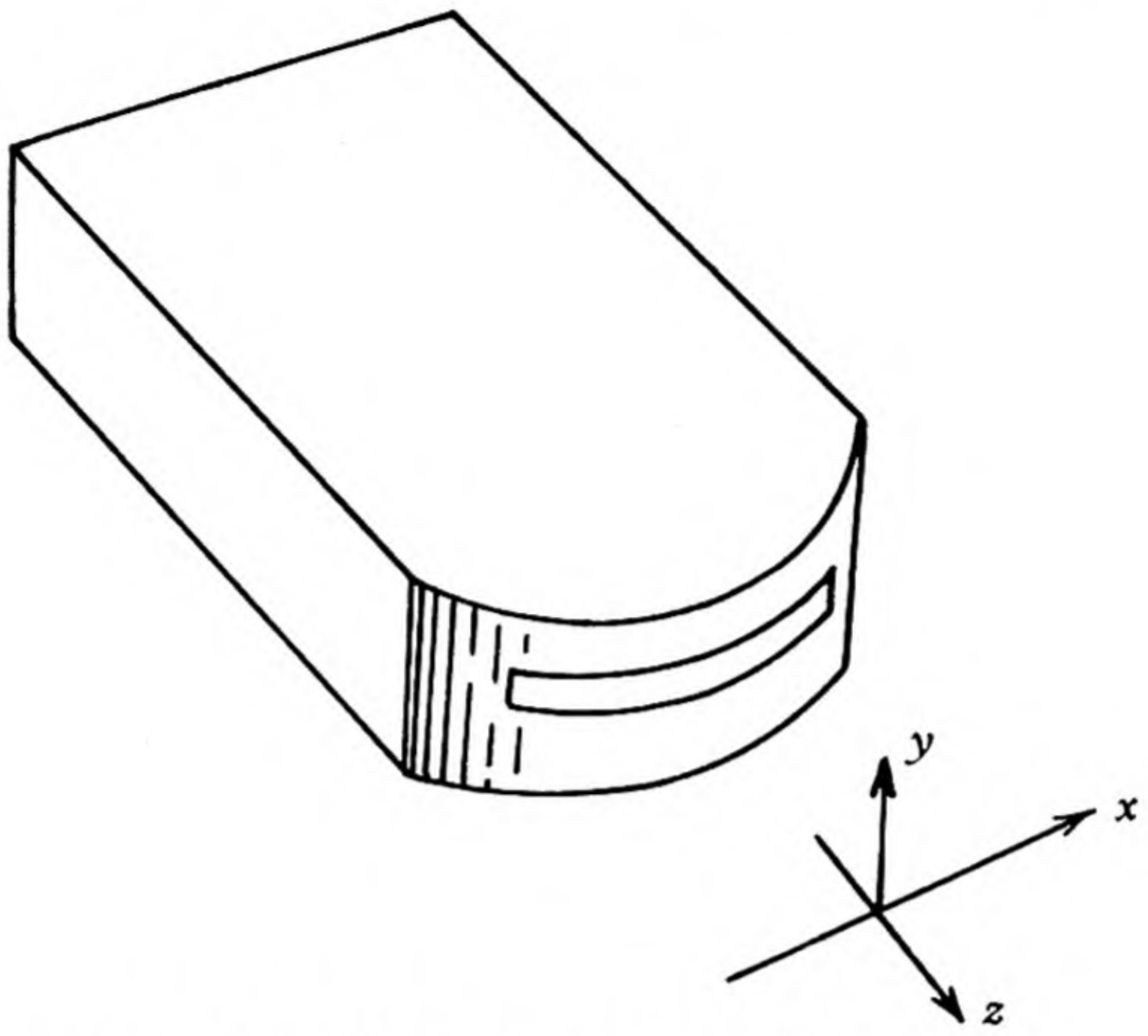

Fig. 10.9. Slot lens with curved diaphragm.

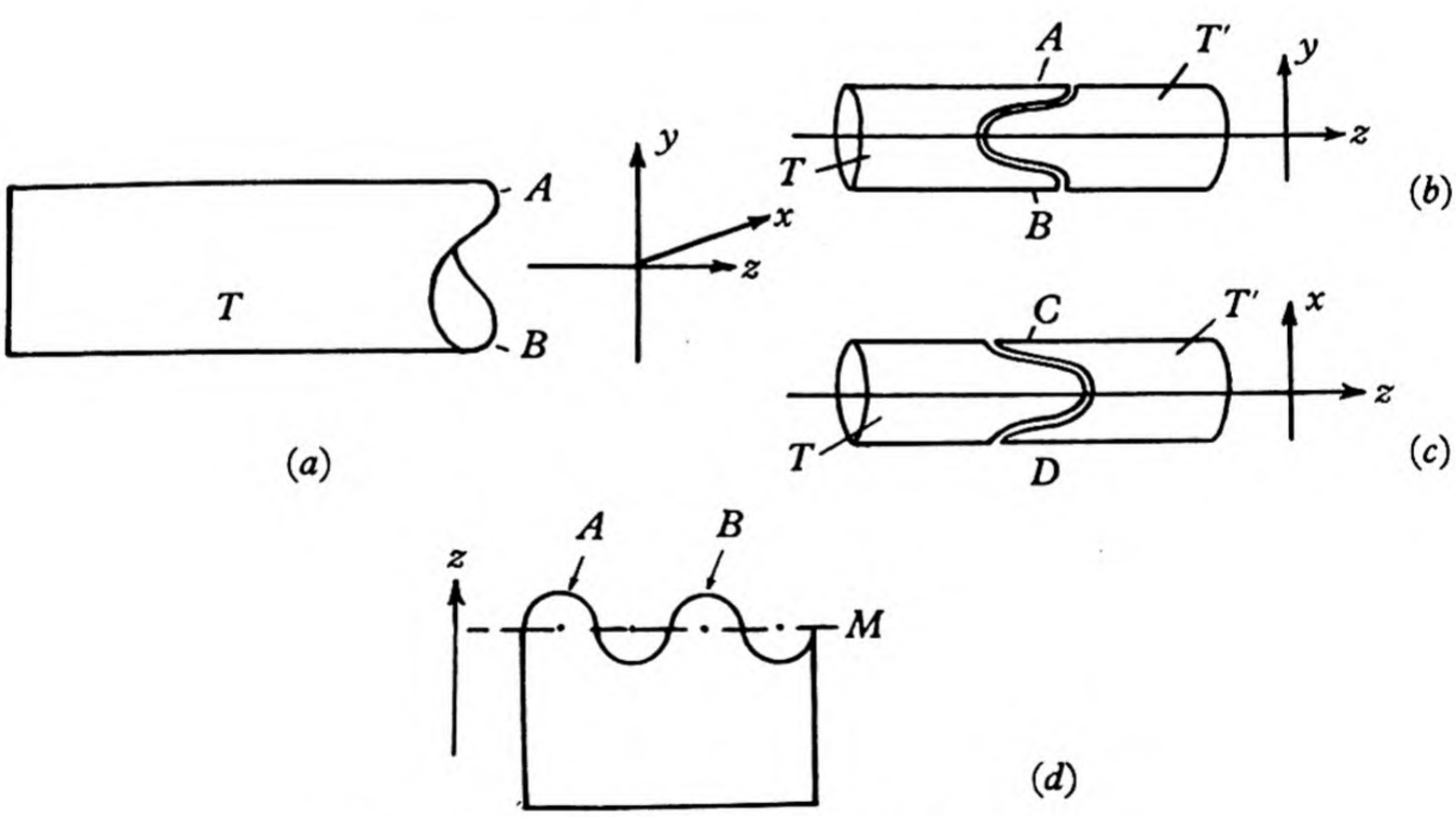

Fig. 10.10. Double-lipped two-tube lens.

lenses. Fig. 10.10(*a*), for instance, shows a perspective drawing of a double-lipped tubular electrode. The shape of such lens electrodes is further illustrated by figs. 10.10(*b*) and (*c*) showing the side elevations of a double-lipped two-tube lens in the *yz*-plane

and in the xz-plane respectively. Fig. 10.10(d) shows the cylinder surface of one of the tubes developed into a plane; the lips A and B can clearly be recognized in all drawings.

The simplest double-lipped tube lenses have equal pairs of lips of constant radius of curvature $R_x = R_y = R_L$. The lip radii R_L of such a lens can be stated as a certain fraction n of half the tube periphery

$$R_L = n\pi R_T, \tag{10.9}$$

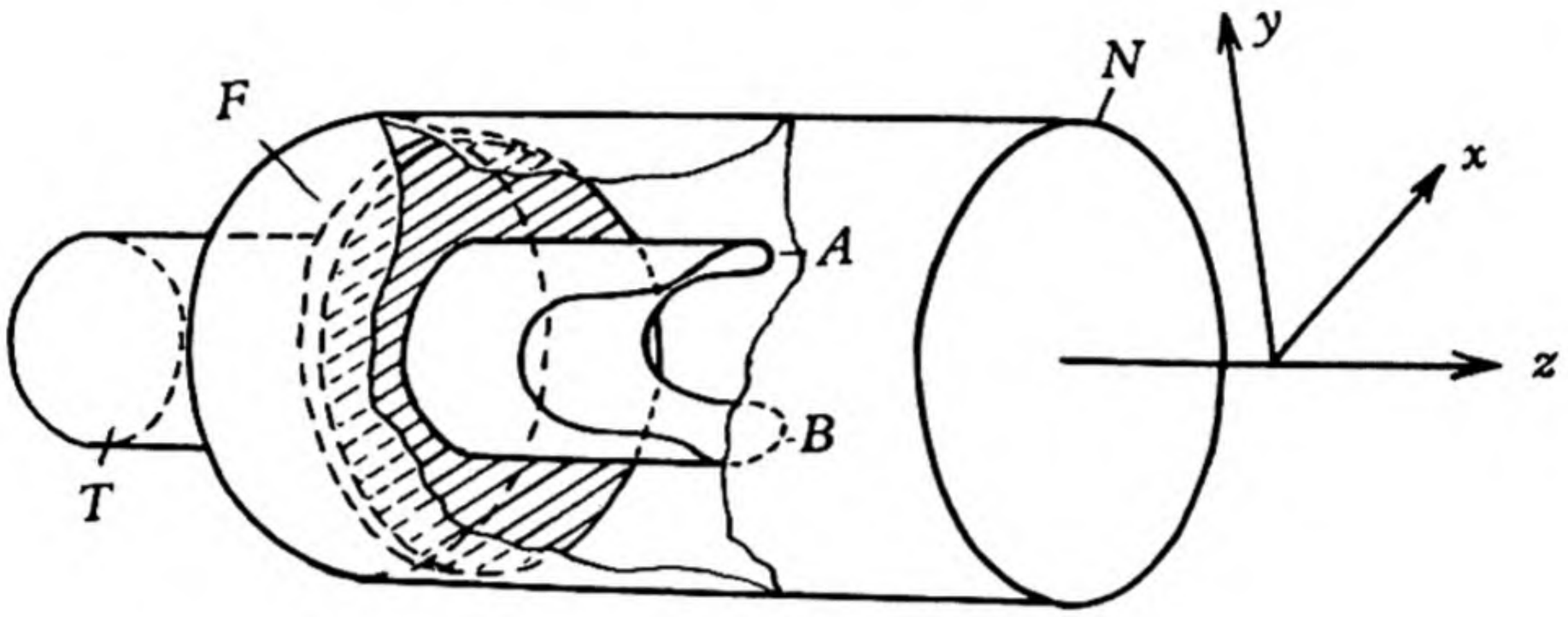

Fig. 10.11. Double-lipped electrodes in tube neck.

where R_T is the tube radius. For example, in fig. 10.10(d), $n = \frac{1}{4}$ and the arcs are semicircular. The lens tube in fig. 10.10(a) has shorter lips with $n = \frac{1}{2}$, the circular arcs terminating the lips being joined by tangential straight lines.

The value of n controls the optical properties of the lens. For example, as n increases from $\frac{1}{4}$ to 2 the diverging action in longitudinal direction to the line focus is gradually eliminated, the focal length of the lens is gradually increased and its spherical aberration is increased too. If n is infinitely increased, a system producing a point focus is eventually obtained, identical with the symmetrical two-tube lens of § 4.2. For the lip radii greater

than $2\pi R_T$, an initially parallel bundle of rays will be converged by the lens in such a way that two real focal lines are produced at different distances from the principal plane, these focal lines being at right angles to each other.

Instead of employing two complementary lipped lens electrodes it has been found very convenient in practice to use only one lipped electrode which protrudes into a wide tube such as the conductive neck of a cathode-ray tube. Examples of such constructions are shown in figs. 10.11 (*a*) and (*b*), where a lipped tube T and a lipped box S of square cross-section are shown to protrude into a neck N of a cathode-ray tube which is drawn cut away to show the inside more clearly. Such lenses may be shielded by a flat circular flange F. The construction is relatively insensitive to bad alignment. If the curvature of the lips is sufficiently large ($n \approx \frac{1}{4}$) the resulting spherical aberration is generally very small, in some cases even slightly negative, and the lenses belong to the best corrected systems in electron optics.

TABLE X. *Double-lipped two-tube lenses*

R_L/R_T	Voltage ratio for MF/R_T				X_F/X_0
	5	10	15		
$\pm\frac{1}{4}\pi$	1·37	1·15	1·08	A.P.	2·1
	1·38	1·6	1·10	D.P.	
$\pm\frac{1}{2}\pi$	2·05	1·5	1·32	A.P.	1·4
	2·3	1·57	1·42	D.P.	
$\pm\pi$	2·5	1·6	1·4	A.P.	1·2
	2·9	1·9	1·6	D.P.	
$\pm 4\pi$	3·5	2·0	1·7	A.P.	0·6
	3·9	2·4	2·1	D.P.	
∞	4·6	3·1	2·5	A.P.	0
	5·1	3·3	2·6	D.P.	

Table X gives some examples for mid-focal lengths MF of double-lipped lenses of the type shown in fig. 10.10. The values obtained for other double-lipped lens types are of the same order of magnitude. The given values have been measured with the pepperpot method described in § 2.1. The reference plane M is assumed to be at right angles to the z-axis, halving the lip structure in the way indicated in fig. 10.10 (*d*). The first column of Table X gives the radii of curvature R_L of the lips measured in tube radii R_T. The following three columns give the voltage ratios which have to be

applied to the lens electrodes in order to produce mid-focal lengths of 5, 10 and 15 tube radii respectively. The next column indicates whether these voltage ratios apply to the acceleration (A.P.) or to the deceleration (D.P.) of initially parallel rays. The last column gives the ratio of the length X_F of the line focus to the initial width X_0 of the ribbon-shaped beam. In other words, the X_F/X_0 values indicate how much initially parallel beams are spread or contracted in x-direction while they are focused in y-direction. These X_F/X_0 values are largely independent of the original beam width X_0.

The principal planes of the lipped tube lenses are located as usual in the tube of higher potential. The distances between mid-plane and principal planes decrease with decreasing radius of curvature of the lips. From the known values of the symmetrical tube lens (fig. 4.2) which are of the order of several tube radii, they gradually decrease to a small fraction of a tube radius when R_L is decreased from ∞ to $\frac{1}{4}\pi R_T$. Also, the spherical aberration of double-lipped lenses has been found to decrease with decreasing R_L. However, the double-lipped two-tube lenses of fig. 10.10 never reach the extremely low aberration values which are obtained with the double-lipped tube lenses of fig. 10.11.

Double-lipped lenses have hardly been applied so far in practical constructions. However, they are likely to be important in future development. In this connexion a theoretical paper should be mentioned again (cf. §6.5) in which Scherzer (1947) recommends the design of aberration-free systems producing perfect point foci by a combination of proper line-focus lenses.

10.5. Space-charge effects in ribbon-shaped beams

Two-dimensional electron optics is superior to the optics of circular symmetry, not only so far as it implies a better chance for the correction of geometrical errors. Also space-charge errors are much less pronounced in flat beams than in beams of circular cross-section.

The simple theory of the spread of ribbon-shaped beams has been developed by Bouwers (1935) and by Thompson and Headrick (1940). This theory can be applied to all parts of the beam in which the velocity of the electrons is constant and in which the direction of the electrons is homocentric. If calculations similar

to those of § 8.1 are made for two-dimensional beams, the spread curve can be shown to be a parabola. The parabolic path of each electron in the strip beam is then given by

$$y = y_A - \Theta z + (I/V^{\frac{3}{2}})\frac{z^2}{4k}, \qquad (10.10)$$

where y_A is the initial semi-aperture of the beam at $z = 0$ and Θ is the initial slope angle of its envelope with the z-axis. Moreover, V is the electron energy (e-volts), I is the beam current per unit

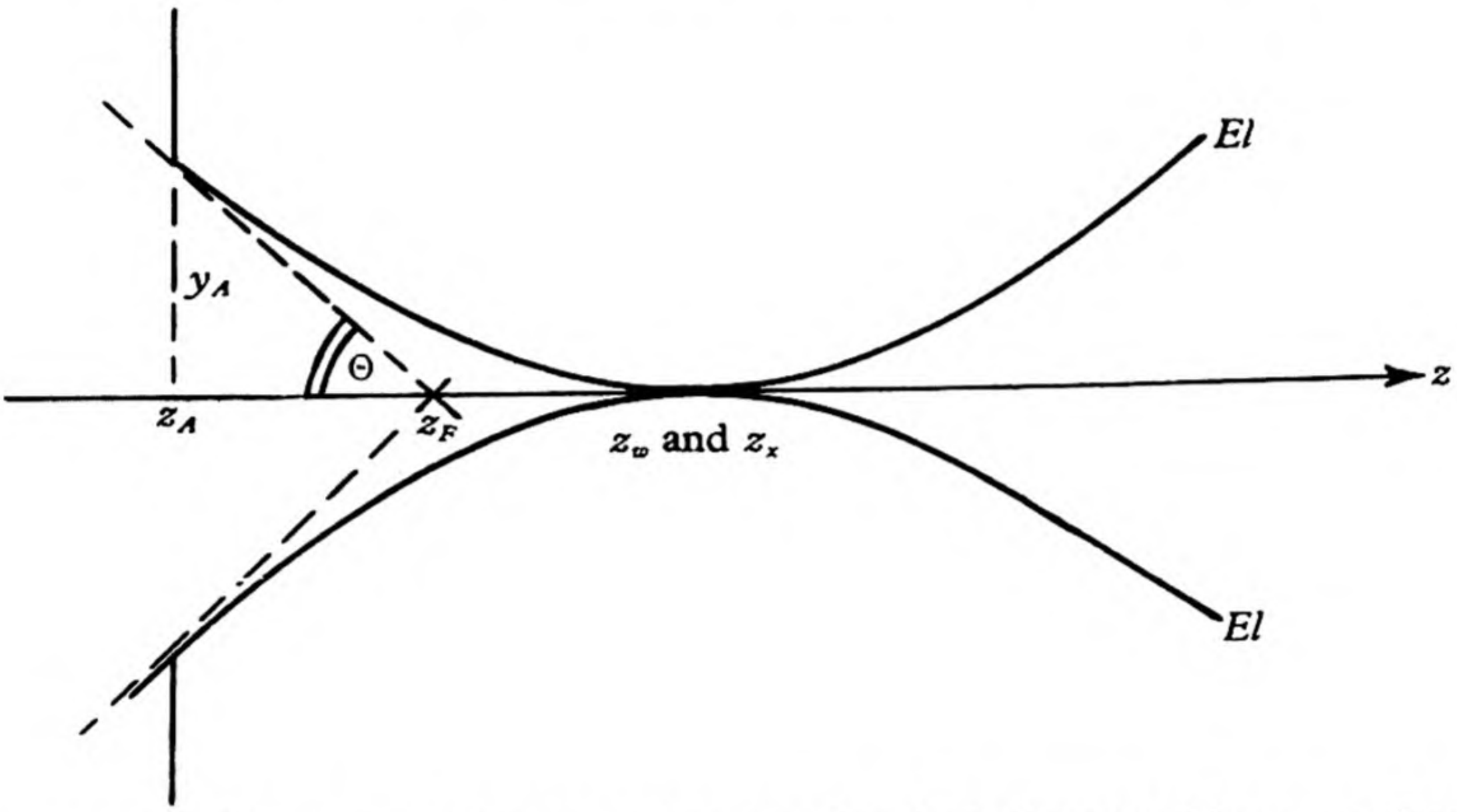

Fig. 10.12. Ribbon-shaped electron beam under the influence of its space charge.

beam width in x-direction (amperes/m.) (i.e. for a width of the strip beam $2x_A = 1$ m.) and k is a constant of the value

$$k = 10{\cdot}4 \times 10^{-6} \quad [\text{A./V.}^{\frac{3}{2}}].$$

Differentiating (10.10) and taking $dy/dz = 0$ gives us the co-ordinates of the beam waist formed by convergent rays: location and aperture of the waist are seen to depend upon the initial angle Θ and upon the space-charge factor $I/V^{\frac{3}{2}}$ only.

With a decreasing ratio of $(I/V^{\frac{3}{2}})/\Theta^2$ the waist aperture gradually decreases. Very much in distinction with beams of circular cross-section, however, the beam waist of an intense strip beam can become of vanishingly small aperture ($y_W = 0$). For this critical case, the waist distance (z_W) from the initial aperture is found to be just twice as large as the distance (z_F) of the virtual focus. This critical case is presented in fig. 10.12, drawn to scale in the y-coordinate but

scaled down by a factor 10 in the z-coordinate in order to make the essential features more visible. There, the initial convergence of the boundary of the beam (El) corresponds to $\Theta = 0{\cdot}1$ radian, the critical space-charge factor being $0{\cdot}1 \times 10^6$ (A./V.$^{\frac{3}{2}}$). For further decrease of $(I/V^{\frac{3}{2}})/\Theta^2$, i.e. beyond the critical value, the strip beam forms a real cross-over. This again cannot possibly occur with a quasi-continuous beam of circular cross-section.

The critical case represented by fig. 10.12 is of some practical interest; it defines theoretically the optimum-beam geometry if the maximum current has to be transmitted through a tunnel terminated by two equal slots. There, the waist has to be located in the middle of the tunnel.

With increasing space charge, the beam geometry deviates from the predictions of the simple theory. A hump of negative potential is built up near the axial xz-plane. This hump slows down preferentially the paraxial part of the beam, which eventually causes spherical aberration (cf. Klemperer, 1947). Space-charge errors are very similar to those discussed in §§ 8.1–8.3; however, the disturbances of strip beams appear to be much smaller than those experienced with circular beams.

The influence of the termination of strip beams (i.e. of the final width in x-direction) upon the beam-spread has been discussed by Houtermans and Riewe (1941). The boundary of the finite beam in the yz-plane is given again by a parabola, the beam edges having little influence upon the spread in the yz-plane as long as the cross-section of the beam in the xy-plane is a long rectangle with $x \gg y$. If, however, this cross-section approaches the shape of a square the expansion becomes rather similar to that of a round beam and the corners of the square beam do not play a great part.

10.6. Emission systems with line focus

Strip-cathode systems corresponding to the simple circular triodes discussed in §§ 9.1 and 9.6 may be represented by figs. 9.1–9.3, to show the relevant cross-sections in the yz-plane of translational symmetry. The apertures in the diaphragms are now rectangular slots.

Voltage-current relations. The comparison of a strip system with the corresponding circular system of the same cross-section and of

the same electrode voltages shows that the strip systems always yield appreciably larger currents than the circular emission systems described in Chapter IX, even if the strip cathode is much restricted in length. The reason for this is found not only in the relatively larger area of the strip cathode but also in the relatively larger penetration of fields from the anode to the cathode surface. Two quantities are again of practical interest for the design of strip-cathode systems of a desired electrical performance: (i) the penetration factor D defined by (9.28) and (ii) the geometry factor G of Child's equation, (8.62), applying to an equivalent-diode voltage as defined by (9.32). These significant parameters (D and G) are tabulated below for some strip-cathode systems characterized as in Chapter IX by their spacings:

c/y_{gr} = grid top to cathode spacing measured in terms of slot semi-apertures, and

a/y_{gr} = grid top to anode spacing also measured in terms of slot semi-apertures.

The rectangular slots all have the ratio of semi-apertures $(x_{gr}/y_{gr}) = 20/1$, i.e. their length is 20 times greater than their width. The penetration factors D are found to vary over a large range and, for strip systems, they are quite generally larger than for the corresponding circular systems (cf. fig. 9.11). D increases with the slot length x_{gr} up to about $x_{gr}/y_{gr} \approx 5$, but for longer slots, D is very nearly independent of x_{gr}.

TABLE XI. *Penetration factors D for strip-cathode systems*

Grid top to cathode spacing (c/y_{gr})		1	2	3	5	8
($D \times 100$) for symmetrical two-slot systems (cf. fig. 9.1)	$a = y_{gr}$	38	15	8·6	4·3	2·3
	$a = 2y_{gr}$	21	9·3	5·2	2·8	1·5
	$a = 6y_{gr}$	7	3·3	1·9	0·8	—
($D \times 100$) for open-anode system (cf. fig. 9.2)		2·2	0·88	0·55	0·30	0·16

TABLE XII. *Factors G for symmetrical two-slot systems*

Grid top to cathode spacing (c/y_{gr})	1	2	3	5
G	52	38	27	17

On the other hand, G is to some extent proportional to x_{gr}. For a given (c/y_{gr}) spacing, G does not depend very much upon the geometry of the anode. Table XII contains only G values for the symmetrical two-slot system with equal grid-cathode and grid-anode spacings ($a = c$). All systems of Table XI, however, have within 15 % the same G values as those given in Table XII.

Since for any strip-cathode system G is much larger than for the corresponding circular system, the anode voltage V_A required for drawing a given emission current is relatively small. For the same reason the black-out voltage ${}^{bl}V_g$ of a strip system of a given D value is relatively small but the correction term (cf. § 9.5) for the measured black-out voltages is quite substantial.

Of practical interest is the wide range of obtainable perveances $(I_{em}/V_A^{\frac{3}{2}} \approx GD^{\frac{3}{2}})$ for different strip-cathode systems of a given G. For example, for the fixed grid spacing $c = y_{gr}$ one obtains the very different perveances of 10 [μA./V.$^{\frac{3}{2}}$ per m. slot length] for a system with wide, open anode and of 500 [μA./V.$^{\frac{3}{2}}$ per m. slot length] for an unsymmetrical two-slot system with $y_a = 0{\cdot}5y_{gr}$ and $a = y_{gr}$. These data should be compared with those of the corresponding circular symmetrical structures namely the open-anode system and the symmetrical two-diaphragm system: these circular systems reach only the relatively small perveances of 0·006 and 0·2 [μA. per V.$^{\frac{3}{2}}$] respectively.

Angular current distribution from line-focus emission systems. Electrons emitted from the strip cathode form a beam waist or a cross-over line in x-direction and then fan out in shape of a wedge. Now, let a stop slot with adjustable y-aperture cut off a given external part of the emitted beam. The fraction of the transmitted beam current to the total emission is the current efficiency of the system for a given wedge angle 2Θ.

Experimental values for this current efficiency referring to the fixed angle $\Theta = \pm 0{\cdot}1$ radian and to full space-charge conditions are plotted in fig. 10.13 as a function of electrode spacings for a few characteristic representative systems (Klemperer, 1947*a*). The efficiency is high (0·8) for an open, wide anode and low (0·24) for a symmetrical two-slot system with anode spacing equal to one semi-aperture of the slot. Within the range of the figure, the efficiency of both these systems is not markedly dependent on the cathode-grid spacing c which is plotted as abscissa.

On the other hand, the efficiency of an unsymmetrical two-slot system with an anode slot half as wide as the grid slot ($y_a = \frac{1}{2}y_{gr}$)

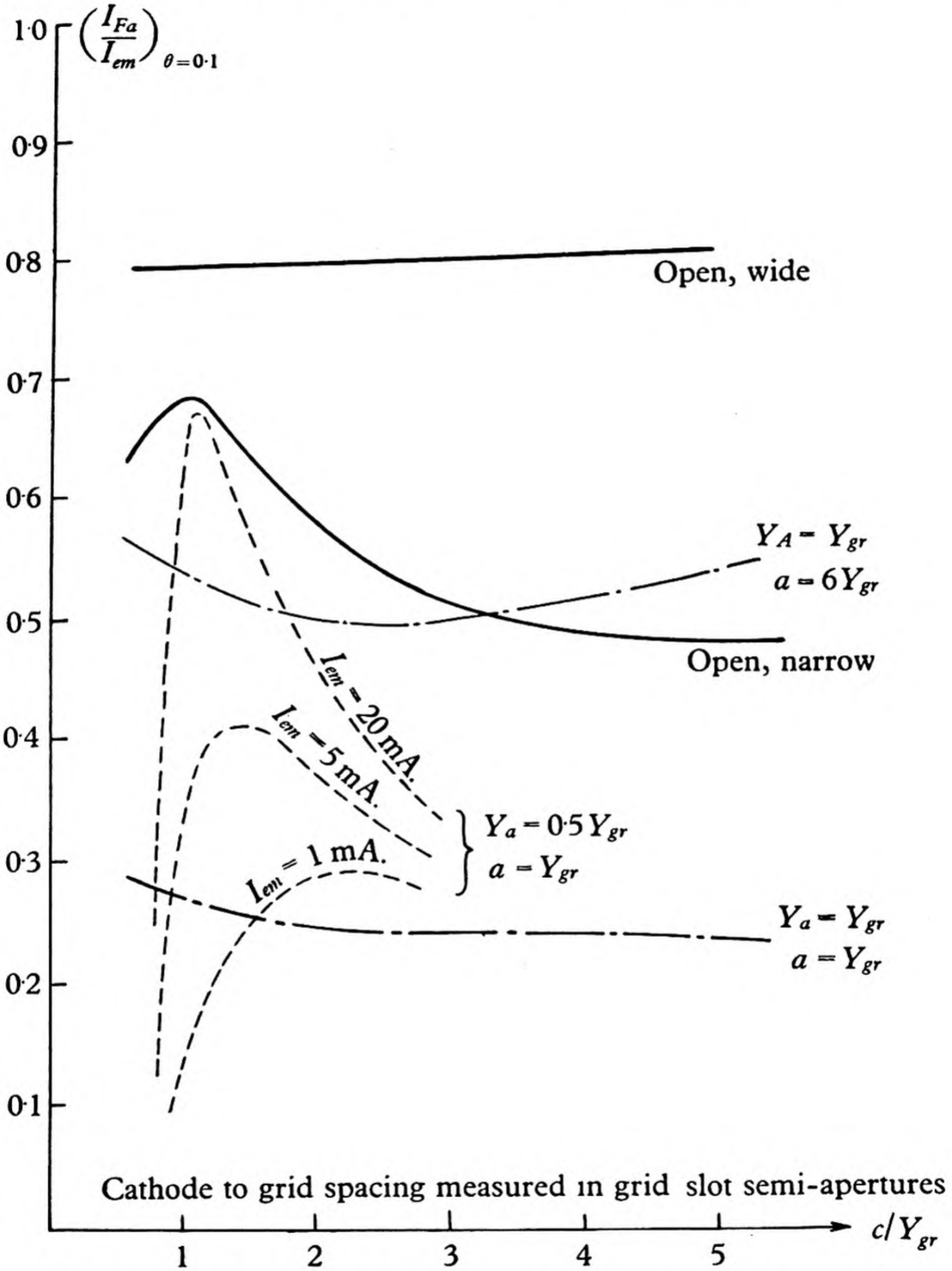

Fig. 10.13. Efficiency of line focus emission systems; fraction of total emission projected into an angle $\Theta = \pm 0{\cdot}1$ radians.

shows a very pronounced maximum for a critical grid-to-cathode spacing. The broken curves in fig. 10.13 belong to this unsymmetrical slot system and correspond to three different total emission currents

of 1, 5 and 20 mA. Apparently, the maxima of these curves correspond to the critical conditions represented by fig. 10.12, where the beam waist is smallest and reaches its greatest elongation. Interpreted in this way, the spacings at which the efficiency maxima occur are 'preference spacings' of the kind explained in detail in our discussion of the influence of space charge on the circular systems as given in §9.4. Again, the angular current distribution from strip-cathode systems depends a great deal upon space charge and often changes entirely when the emission is reduced from full space-charge conditions to temperature-limited saturation.

Space-charge pressure in line-focus systems can be balanced by external fields in the way we described for circular structures in §8.6. Electrodes have to be found which produce a potential distribution proportional to the 4/3 power of the distance from the cathode. According to Pierce (1940*a*) fields of this kind are determined as above (§8.7) in the electrolytic trough with the electron beam being replaced by a piece of insulator, for the two-dimensional case the electrolyte having parallel bottom and top faces. Though the practical performance of two-dimensional 'Pierce guns' is much below the theoretical expectations, the discrepancies are not as great as those found for the corresponding circular systems (cf. Klemperer, 1947*a*).

10.7. Some practical line-focus emission systems

Slot systems with equipotential cathode as described in § 10.6 are useful for line-focus electron guns, say in cathode-ray tubes for sound recording or as emission systems for special Klystron designs. The use of a tungsten hairpin cathode (§ 9.6) for the production of fine line-foci of relatively small currents was described by Vauthier (1952).

Somewhat different systems are used for line-focus X-ray tubes. Such systems employ straight tungsten filaments or tungsten helices as cathodes, the emission being concentrated towards a solid anode face with the help of focusing cap or hood electrodes which are at the average cathode potential or slightly negative with respect to it.

Beese (1937) made the first investigations on the quality of the focus by means of pin-hole radiographs with the X-rays emitted from the electron focus on the anode. Beese's experiments, how-

ever, refer to relatively ill-defined helical cathodes in wide 'mouth and throat' caps or in parallel-sided caps of large aperture. Gaedke (1938) investigated beam spread and focus from a straight filament cathode arranged parallel to the axis of a circular cylindrical auxiliary electrode by which it was partially surrounded in a reflector-like manner.

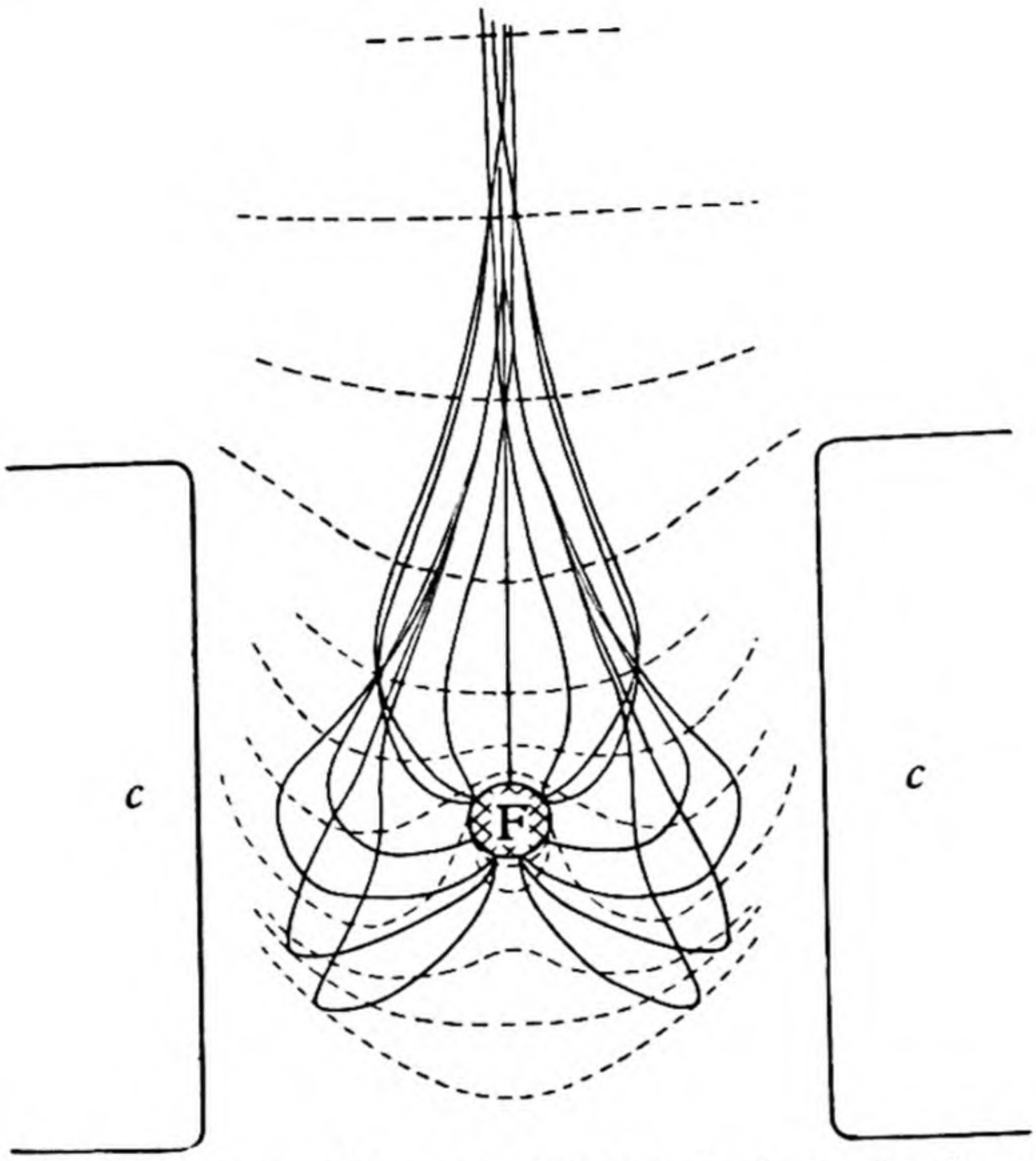

Fig. 10.14. Equipotentials and electron trajectories in an X-ray tube line-focus emission system.

Thorp (1949, 1950) again investigated the focus obtained from a straight filament in parallel-sided focusing electrodes. Fig. 10.14 represents in proper scale a perpendicular section through the filament *F* and through the side-plates *C*. Electron trajectories as obtained by electrolytic field plotting and ray tracing are shown in the figure. The electrons emitted from the front, from the sides, or from the back of the filament are focused in very different distances. This aberration explains to some extent a 'banded' focal structure which is observed in the pin-hole camera photographs (cf. §6.4, halo test). Ray-tracing results for different filament positions confirm the observed decrease of focal width as a function of an increasing depth to which the filament can be drawn back into the gap.

However, tracings and photographs differ largely. This should be expected, since the tracings do not take space charge and end-effects (§ 10.4) into account. By choosing proper spacings and bias of the focusing electrodes it is possible to reduce the band width to a minimum. Constructional details of an adjustable cathode assembly for a demountable crystallographic X-ray tube have been published by Arndt (1948). He obtained at 50 kV. and 15 mA. a focus of 1 cm. length and $\frac{1}{3}$ mm. width without a surrounding halo.

In a further development of systems for focusing highest intensities into line foci of smallest area, long cathodes with long grid electrodes have been used, both being curved about an axis which is transverse to the direction of the beam and to the line focus. A complete emission system consisting of a curved strip cathode *C*, a grid electrode *G*, a box-shaped first anode *E* and a lipped tubular second anode *A* is shown in the perspective drawing in fig. 10.15.

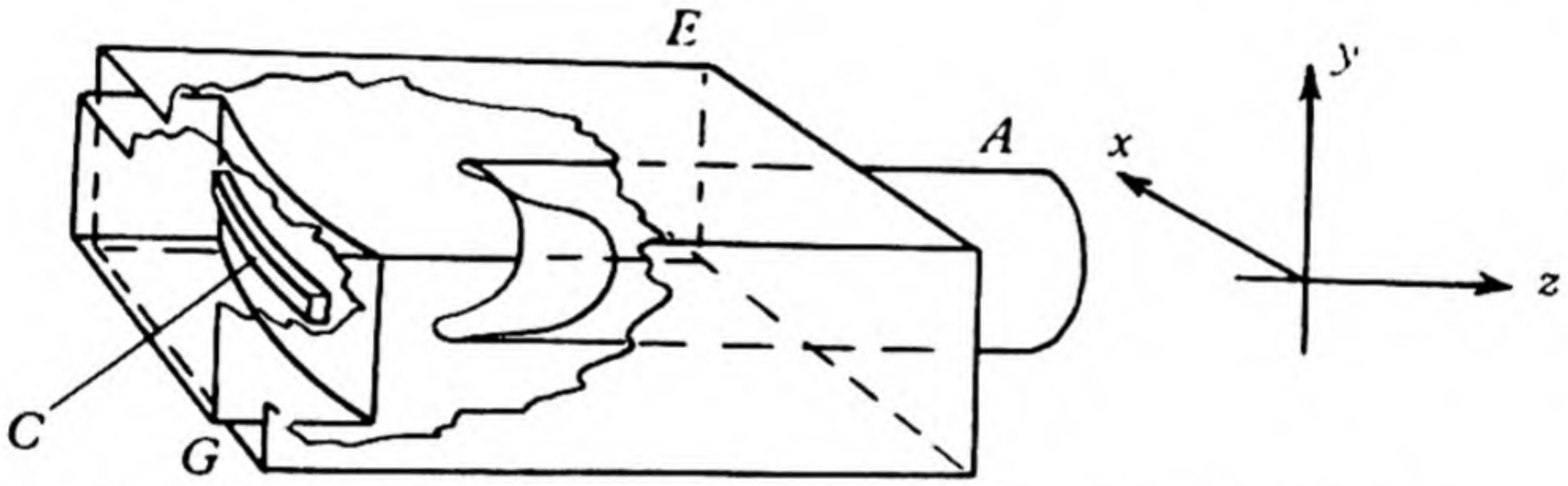

Fig. 10.15. Line-focus system with curved strip cathode.

This system has been used by Klemperer (1944*c*). Poittevin (1947) has applied the same principle of longitudinal cathode curvature to the design of an X-ray tube. He used a tungsten helix of curved generatrix as cathode, built into a grid electrode of similar curvature and placed opposite to a slanting flat anode. With this arrangement he claims to have concentrated 1200 watts/mm.^{2} into a line focus of 2·5 mm. length and less than 0·1 mm. width.

The most promising field for the application of line-focus electron optics is found in the problems of valve technique. Knoll (1934) has given a detailed discussion of the bunching action of the control grid in valves. Fig. 10.16 shows the field plot of a plane electrode arrangement with some electron paths which were estimated by rough ray tracing through the equipotentials measured in the electrolytic trough. Seven different diagrams are shown in this

figure corresponding to conditions of different grid bias. If the voltage ratio V_g/V_A between grid and anode is about equal to the ratio of distances from grid to anode and from cathode to anode, hardly any lens action will occur. If (going from the right to the left in the figure) this voltage ratio decreases, the focal length of the elementary lens decreases and the electrons are focused near the anode. For still smaller voltage ratio, the electron paths cross over and a widely distributed spray is produced at the anode. Proceeding

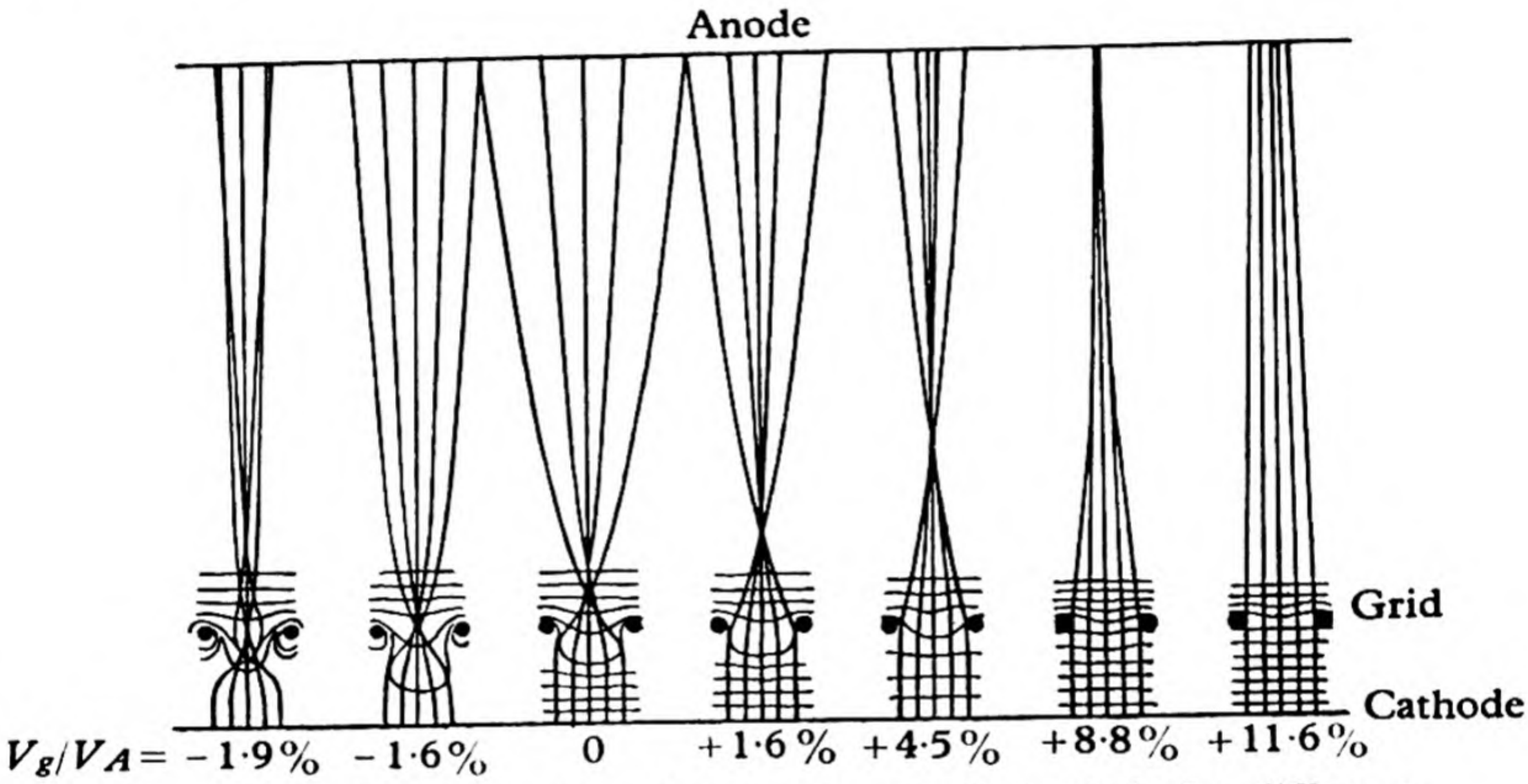

Fig. 10.16. Paths of electrons in a grid-controlled triode for different voltage ratios V_g/V_A between grid and anode.

to negative voltage ratios, the power of the elementary lens becomes still larger and the beams are once more concentrated. Finally, for still more negative grid bias a second cross-over of the electron beams will be produced.

For triode valves these electron-optical considerations might seem to be superfluous, since the valve characteristics can be calculated with a high degree of accuracy without any knowledge of the paths of the electrons. On the other hand, the study and the control of electron paths in multi-electrode valves has produced valuable results. Shoenberg, Bull and Rodda (1933) first recommended proper alignment of the grids. Later, Knoll (1934) has shown that the characteristic of a screen-grid tetrode is improved if the screen is properly aligned with respect to the grid. In this case, the screen current could be reduced by a factor 10 and the slope of

the grid characteristic improved by a factor 2. More details about grid alignment in valves can be found in the papers by Bull (1945) and by Jonker (1949).

Shoenberg, Bull and Rodda (1933) realized that a pentode power valve can be replaced by a 'beam tetrode' with similar characteristics if the electrodes are properly shaped in order to produce a confined electron beam, building up a space-charge region near the anode. A detailed study of the performance of this 'beam power tube' has been made by Schade (1938). As shown in

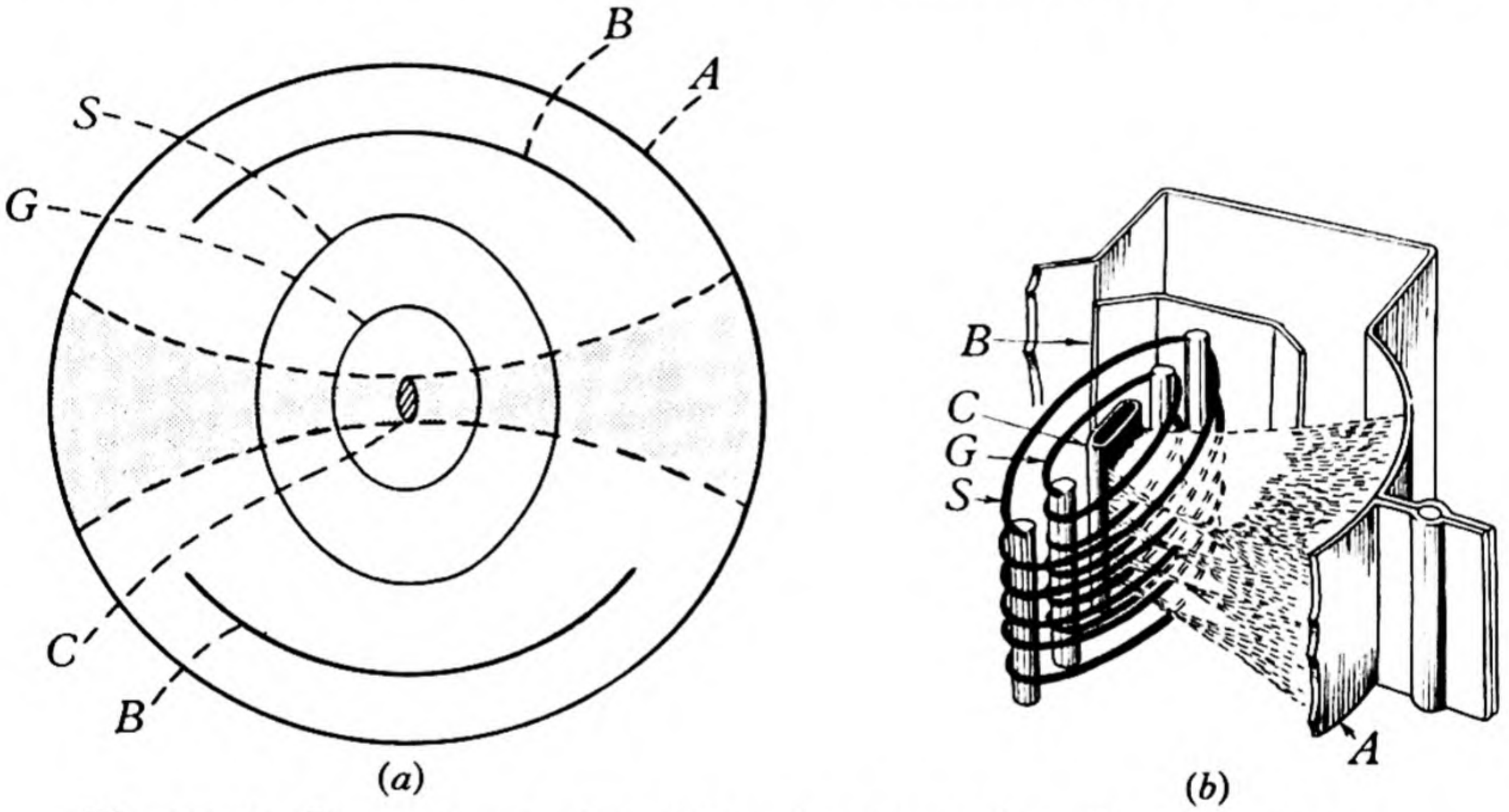

Fig. 10.17. Beam power valve: (*a*) horizontal section; (*b*) electrode form.

fig. 10.17, the valve consists of an indirectly heated strip cathode C, a control grid G of oval cross-section, a screen grid S also of oval cross-section at about $+250$ V. with respect to the cathode, an anode or plate electrode A at about $+50$ V. with respect to the cathode and two beam-forming plates B which are at cathode potential. The electron current is formed into a beam as indicated by the dotted lines in the figure. This beam is confined to a sector by the two beam-forming plates at cathode potential. Moreover, by these beam-forming plates, the electrons of the beam are slowed down and a space charge is formed which stops the secondary electrons coming from the anode.

The current within the two above-mentioned sectors is also subdivided by the individual grid wires into directed beams of disk sector shape; the disks lying parallel to the plane of drawing of

fig. 10.17(*a*) are clearly seen in the perspective drawing of fig. 10.17(*b*). The voltage of the control grid governs the divergence of these disk-shaped beams. If the screen grid is properly aligned, it is scarcely struck by the electron beams, so that the screen current can be reduced in this way to less than 2 % of the anode current. The practical advantages resulting from the focusing of beams in valves will be pointed out in § 12.9.

The development of line-focus electron optics has been greatly stimulated by its use for the design of electron multipliers; these will be described in § 12.4. The electron-optical problem in the design of multipliers which is discussed in this section consists in the focusing of the electron emission from an emitting electrode to a receiving electrode of similar size and shape. This receiving electrode, however, has to act at the same time as a secondary emitter, the electrons of which have to be directed again to another receiving electrode, and so on.

The electron optics of all practical multipliers is essentially of the two-dimensional type. Errors introduced by the final length of the electrodes have so far been disregarded. No particular need has arisen yet for any degree of homocentricity of the beams in the planes of translational symmetry. It is required only that the current issued from the whole surface of an emitter electrode should be spread homogeneously over the whole surface of the appropriate receiving electrode.

The electron-optical problems involved may be illustrated by the three following figures, showing electron paths between very different types of electrodes of multipliers which are considered to represent the technically most important types. Fig. 10.18 shows equipotentials and electron paths between two target electrodes of an R.C.A. photo-multiplier (cf. fig. 12.4) as described by Zworykin and Rajchman (1939). Four target electrodes drawn by bold lines are at -100, 0, $+100$ and $+200$ volts. Paths of secondary electrons emitted from the 0-electrode are drawn as dotted lines. These electrons travel across the equipotential lines shown in the figure and eventually strike the $+100$ V. electrode, the secondary emission of which travels on similar paths to the 200 V. electrode and so on.

Fig. 10.19 shows electron paths in an E.M.I. photo-multiplier (cf. Lubszynski, 1947). The targets T_1 and T_2 are of the 'louvre

type', i.e. they are narrow slats arranged like a Venetian blind so that they incercept most of the primary electrons but are pervious to the secondaries withdrawn by the field from the following target. The complete tube is shown in fig. 12.5.

Fig. 10.20 shows a cross-section of a thermionic electron multiplier designed by Bull (1944). *C* represents a thermionic equipotential cathode of cylindrical surface of about 1 mm. diameter. *G*, *B* and *A* are wire-wound grids fixed to support rods *R*. In particular, *G* is a control electrode at about (−2) V., *B* an accelerator

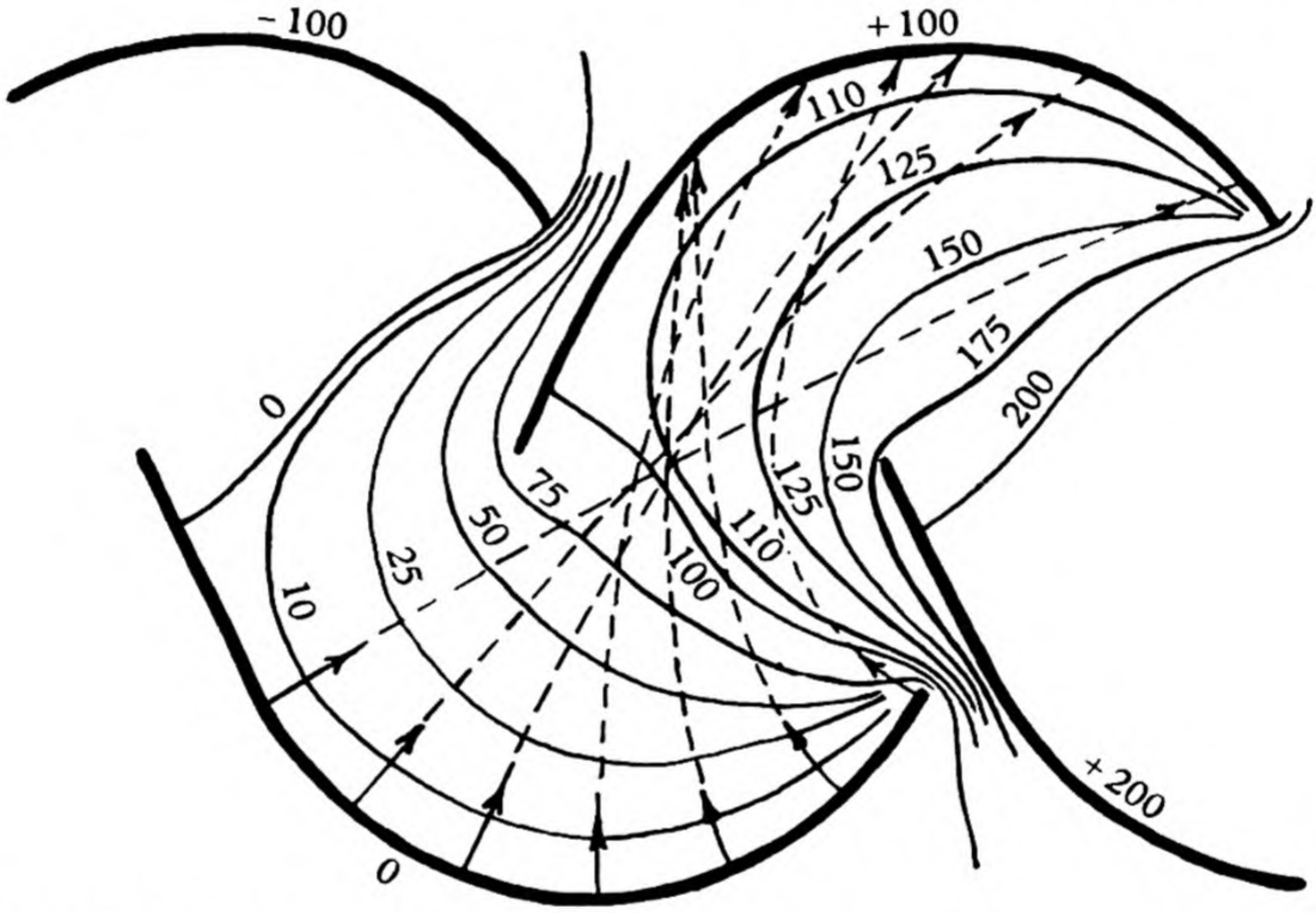

Fig. 10.18. Equipotentials and electron paths between target electrodes of R.C.A. photo-multiplier.

at +100 V. The anode *A* of +350 V. surrounds the secondary emitter *S* of +250 V. The whole electrode system is arranged inside a large cylindrical shield *E* of elliptical cross-section. *E* is at cathode (zero) potential and sharply focuses the electron paths as shown by the dotted lines in the figure. Secondary emission from the line focus on *S* is collected by the anode *A*. *S* has to be shielded from molecules evaporated from the hot cathode surface. Hence, it is arranged 'out of sight' of the cathode, in the shadow area of the support rods *R*.

The electron optics of multipliers differs from that of the other line-focus lenses discussed so far in this chapter. Fields and orbits

in the multipliers are not symmetrical with respect to the yz-plane which contains their line focus. A deflexion of the principal rays is here connected with the focusing of the beam. For this reason

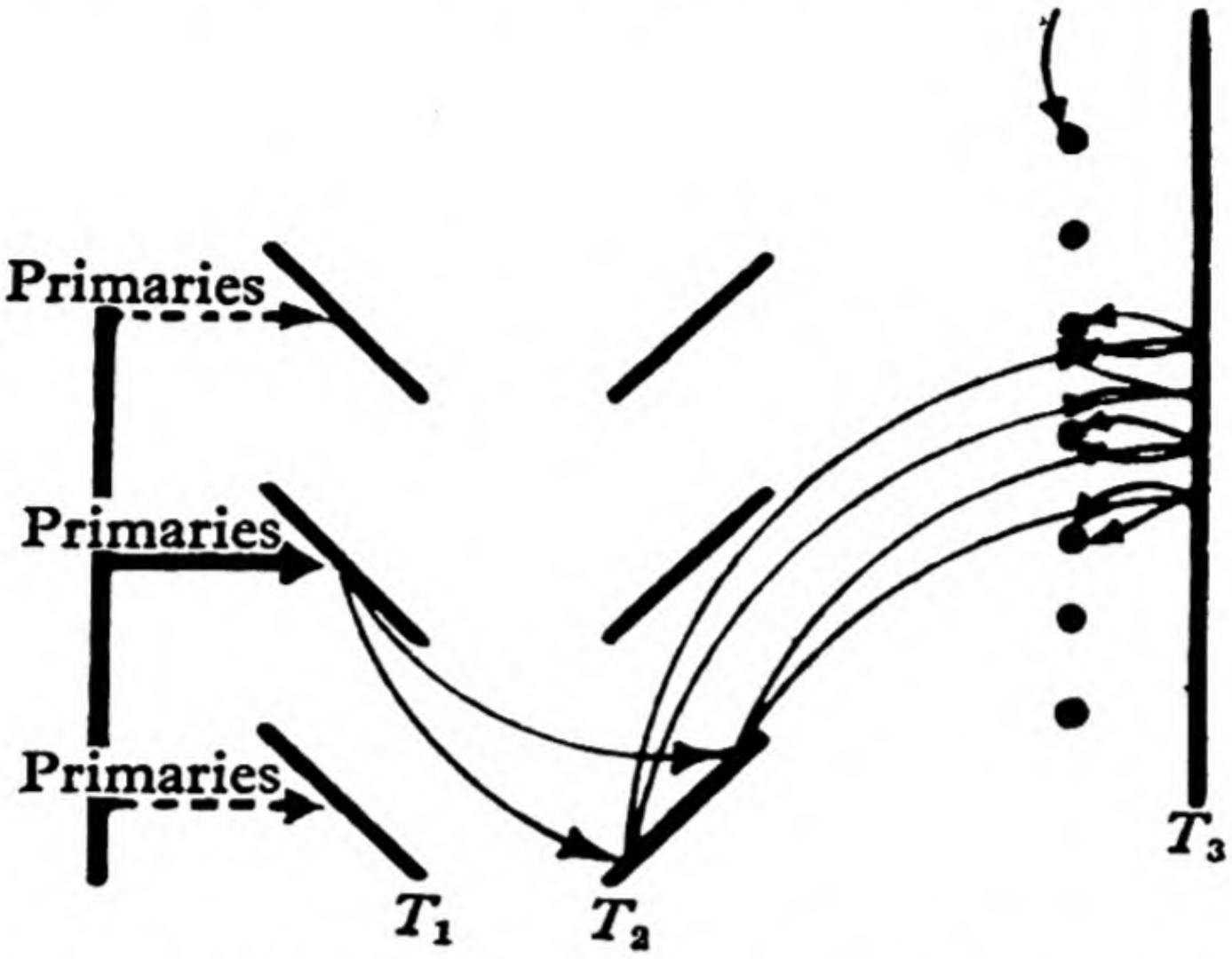

Fig. 10.19. Electron paths in E.M.I. photo-multiplier with pervious targets.

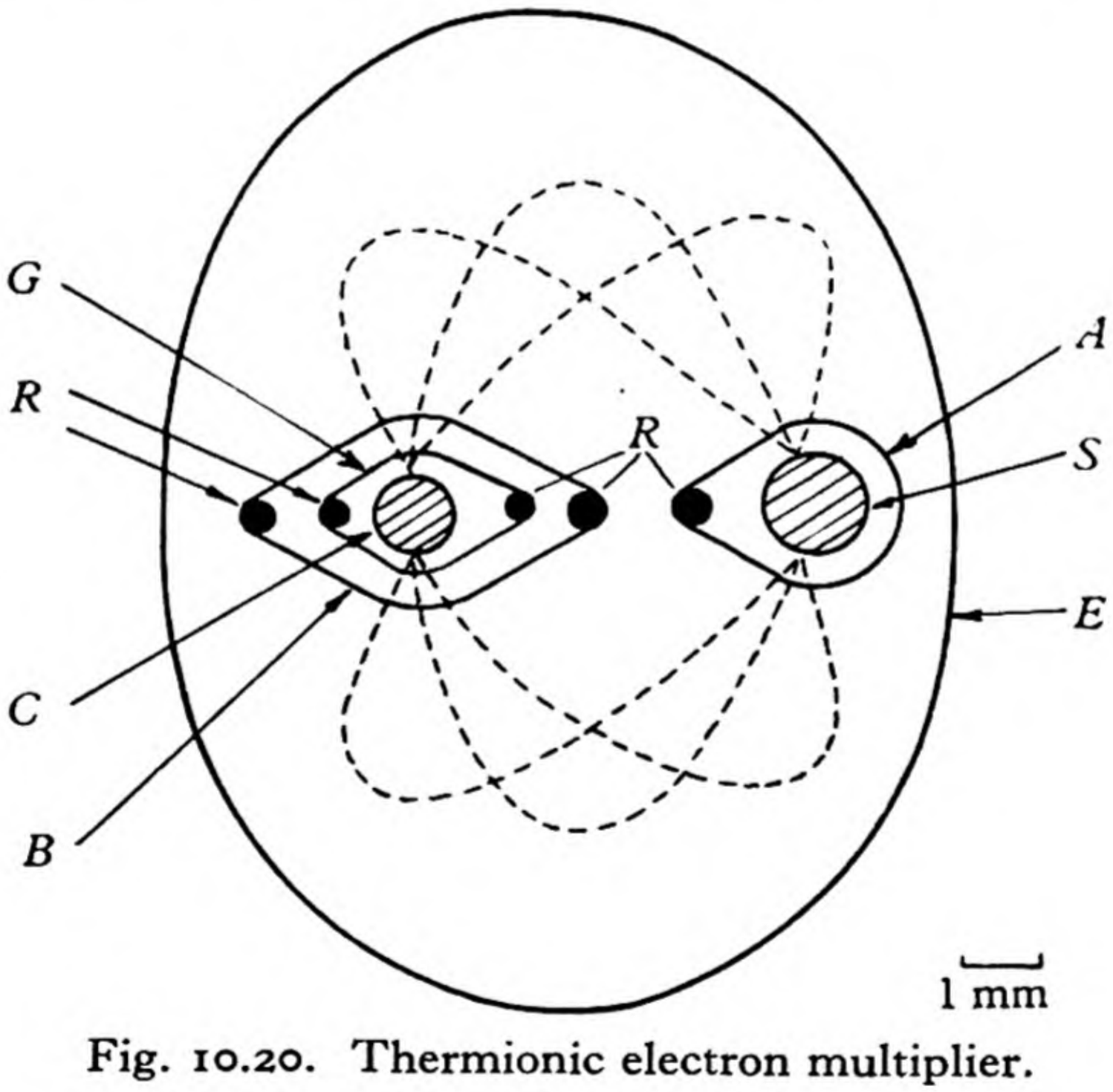

Fig. 10.20. Thermionic electron multiplier.

the discussion of the fields in these multipliers could have been postponed to the next chapter (cf. § 11.5, focusing deflexion). This however, has not been done, because only focusing properties of the fields are discussed here while the particular angle of deflexion is unimportant. On the other hand, for the focusing fields in Chapter XI the angles of deflexion are of primary importance.

10.8. Magnetic lenses with line focus

The theoretically simplest type of two-dimensional magnetic lens is formed by the magnetic stray fields around a pair of slot gaps between plane, parallel plates of magnetic material. Fig. 10.21 shows a cross-section through such a lens in the yz-plane of translational symmetry. The four plates P_1, P_2, P_3 and P_4 extend to 'infinity' in the x-direction at right angles to the plane of the drawing. These plates are magnetized in order to form two pairs of linear poles which, adjoining the mid-plane M, extend in x-direction at right angles to the plane of the drawing. Their polarity is indicated in the

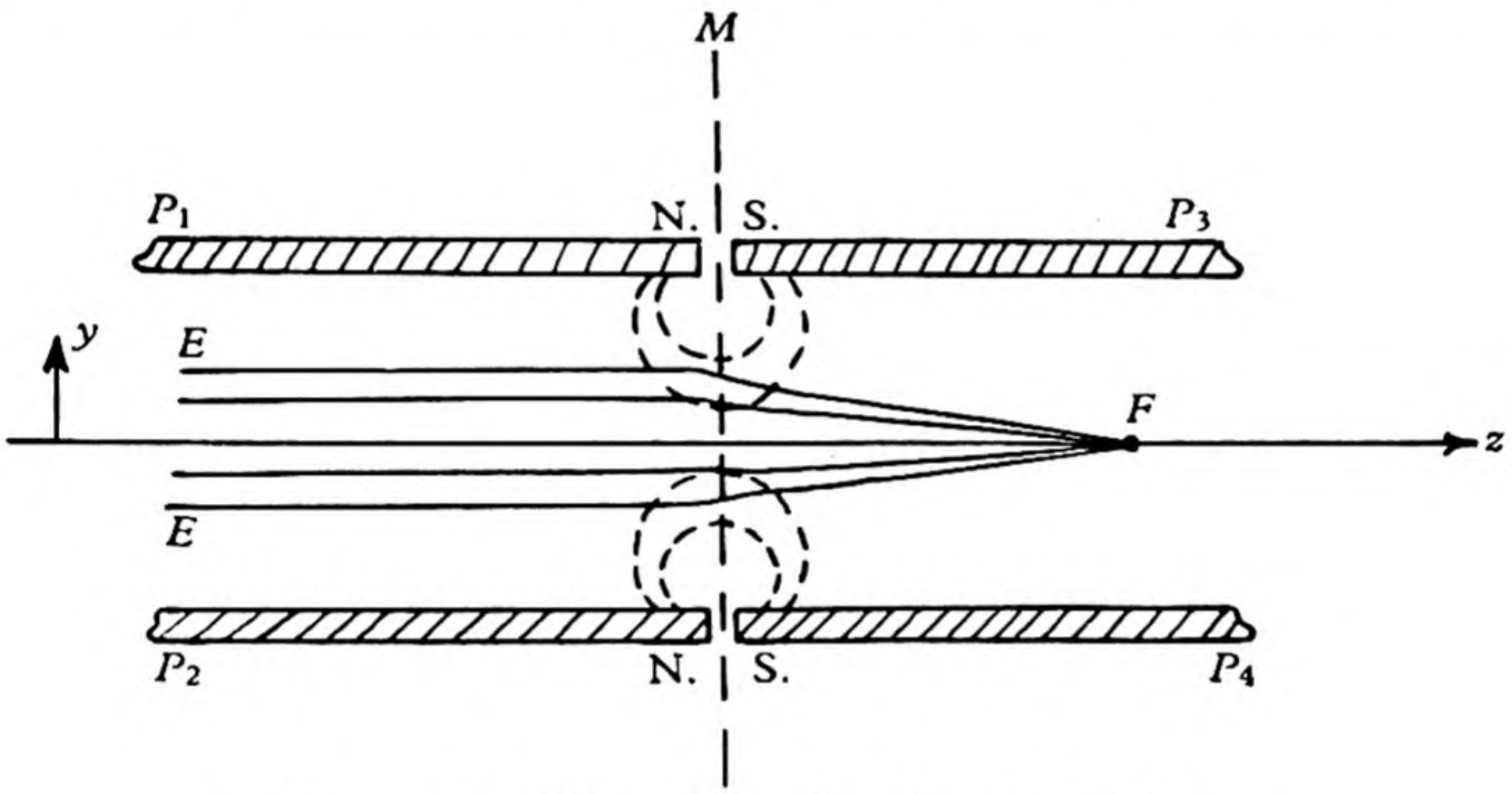

Fig. 10.21. Two-dimensional magnetic lens.

figure by the inscriptions N. and S. The stray field spreads from the poles as shown by the broken lines. A flat bundle of initially parallel rays E—E originally travelling in the yz-plane—is twisted by the lens field around the z-axis; it eventually passes through a line focus F in the xz-plane.

The cross-section of the two-dimensional lens in fig. 10.21 is identical with the axial cross-section of a magnetic lens of circular symmetry such as is represented, for instance, by fig. 5.2 of Chapter V, where a circular gap is arranged in a cylindrical mild-iron shield in circular symmetry about the z-axis. The focal length of the two-dimensional lens, however, is found to be much shorter than the focal length of the corresponding lens of circular symmetry.

Assuming a lens field that is short in comparison with the distance of the focus F from the mid-plane M, it has been shown by Zworykin

et al. (1945) that the focal length of the two-dimensional lens is given by

$$MF \approx f \approx \tfrac{1}{4} f_{\text{Busch}}, \qquad (10.11)$$

where f_{Busch} is the focal length of the short magnetic lens of circular symmetry calculated from Busch's formula ((5.23), § 5.2). Hence, the focal length of a short magnetic line-focus lens can be calculated from the flux-density distribution on the z-axis.

The relatively great power of the line-focus lens is again (cf. § 10.3) due to the relatively small rate of decay of the fields of translational symmetry. Moreover, (10.11) and the comparison of (10.6) with (4.8) show that the factor by which the powers of thin lenses of circular and of translational symmetry are distinguished is the same (4) for the magnetic as for the electrostatic lenses.

The practical realization of magnetic line-focus lenses is of some technical interest. The problem of producing fields corresponding to an infinite extension of the magnetic gaps in x-direction has not been attacked yet. Practical magnets with relatively short gaps, however, produce lenses which correspond to the combinations of spherical and cylindrical lenses in glass optics. In this way it has been shown experimentally that not only line foci, but even electron-optical image formation, is feasible with the help of a lens produced by two small horse-shoe magnets with their poles arranged in alternating sequence as shown in fig. 10.22 (*a*). Moreover, Brüche and Scherzer (1934) quote some early German patents on cathode-ray tubes used for sound-recording purposes proposing arrangements of magnetic poles as shown in perspective drawings of fig. 10.22 (*b*) and (*c*) respectively. These two-pole and four-pole lenses converge the electron rays in a direction which bisects the right angle between the x-axis and the y-axis of the drawing and they produce surprisingly sharp line foci with hardly any aberrations. Hehlgans (1935) has described a four-pole magnet consisting of four mutually perpendicular, straight iron cylinders energized in alternating sense by solenoids and mounted like the spokes of a wheel inside an octagonal iron ring which serves as a magnetic yoke. An electron beam travelling along the axis of the wheel-like structure was focused into a line on a fluorescent screen. The arrangement has been employed for producing sound tracks on sound films. Panofsky and Baker (1950) have used a four-pole

magnet for focusing a 350 MeV. proton beam which emerged from a cyclotron. The line-focus lens in this case was produced by two anti-parallel bar-magnets arranged as the sides of a rectangle through the centre of which the electron beam passed normally.

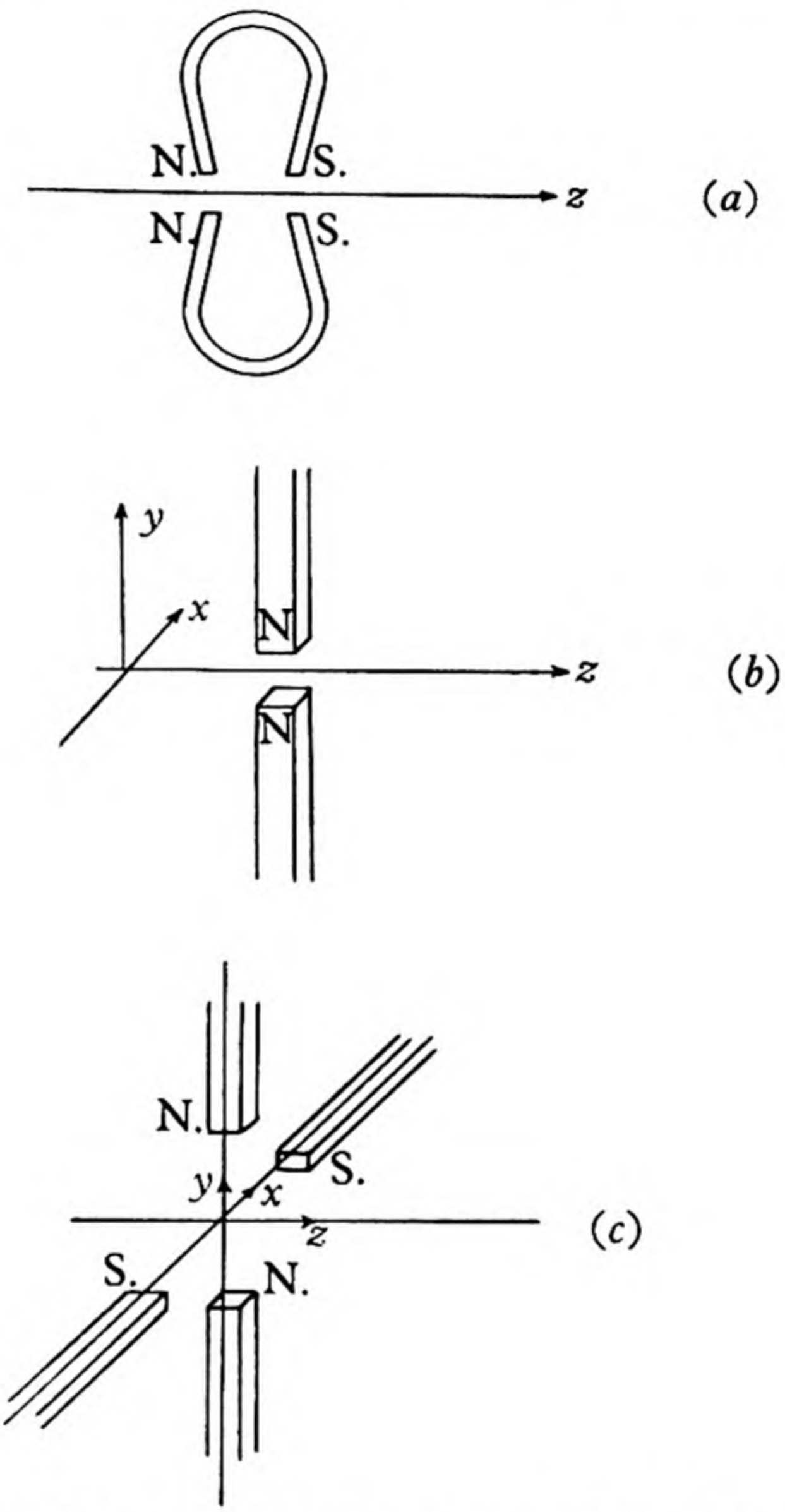

Fig. 10.22. Magnetic line focus lenses (*a*), (*b*), (*c*).

Possibly some other useful combinations of magnetic poles might lead in the future to an unexpected extension of the subject of magnetic electron optics. In this connexion we can only mention an arrangement of four long pole-pieces described by Kelman, Korsunsky and Lange (1939). The resulting magnetic field is said to reflect and to focus electron beams like the combination of a mirror with two cylinder lenses in glass optics.

Field plotting for two-dimensional magnetic lenses. Magnetic fields of line-focus lenses can be investigated by any of the methods described in § 5.5., e.g. by search-coil measurement, or by electrolytic plotting, etc. For electrolytic field plotting of two-dimensional magnetic fields the plane parallel trough (cf. § 10.2) has again to be used. The pole faces may again (cf. § 5.5) be regarded as being at uniform magnetic potentials, and they are represented by the metal electrodes in the trough.

As an alternative to this standard electrolytic method, Peierls (1946) recommended the convenient procedure of using the conjugate problem in which the roles of lines of force and equipotentials are interchanged. The magnetic lines of force of the real problem are represented by equipotentials in the electrolytic trough. This equivalence of conjugate fields, however, applies for two-dimensional problems only. By the new procedure, the source-free field of the magnet is turned into a vortex-free field in the electrolyte. The conductors in the electrolyte now represent the current-carrying conductors of the real problem (wires and coils) which extend at right angles to the plane of translational symmetry, i.e. to the surface of the electrolyte. Materials of high permeability like the magnetic pole-pieces are met by the magnetic field lines at right angles. Hence in the conjugate problem of the trough, iron has to be represented by insulating material which provides for a termination of the electrolyte with equipotentials at right angles to the insulator surface.

Peierls and Skyrme (1949) have shown that the conjugate electrolytic field plotting method can be extended to problems of axial symmetry for solving some practical magnetostatic problems in a region of linear dimensions small compared to the distance from the axis of symmetry. The exact solution of the conjugate problem with circular symmetry could be obtained by tilting the bottom of the trough so that the bottom plane would intersect the liquid surface at the axis of symmetry. This, however, would not provide directly a solution of the magnetic problem in the same way as field plotting in the wedge-shaped trough (cf. § 3.2) is used for investigating electrostatic fields of circular symmetry. The curvature effect in the magnetic problem can be shown to be of opposite sign to the curvature effect in the trough. However, if that effect is

small, its value can be calculated as the reverse of the difference between the conjugate solutions obtained in the level trough and in the tilted trough.

The practical importance of the conjugate field plotting arises in cases in which the curvature effect is small enough to be neglected within the limits of the required accuracy, so that the three-dimensional problem can be treated as purely two-dimensional. In this

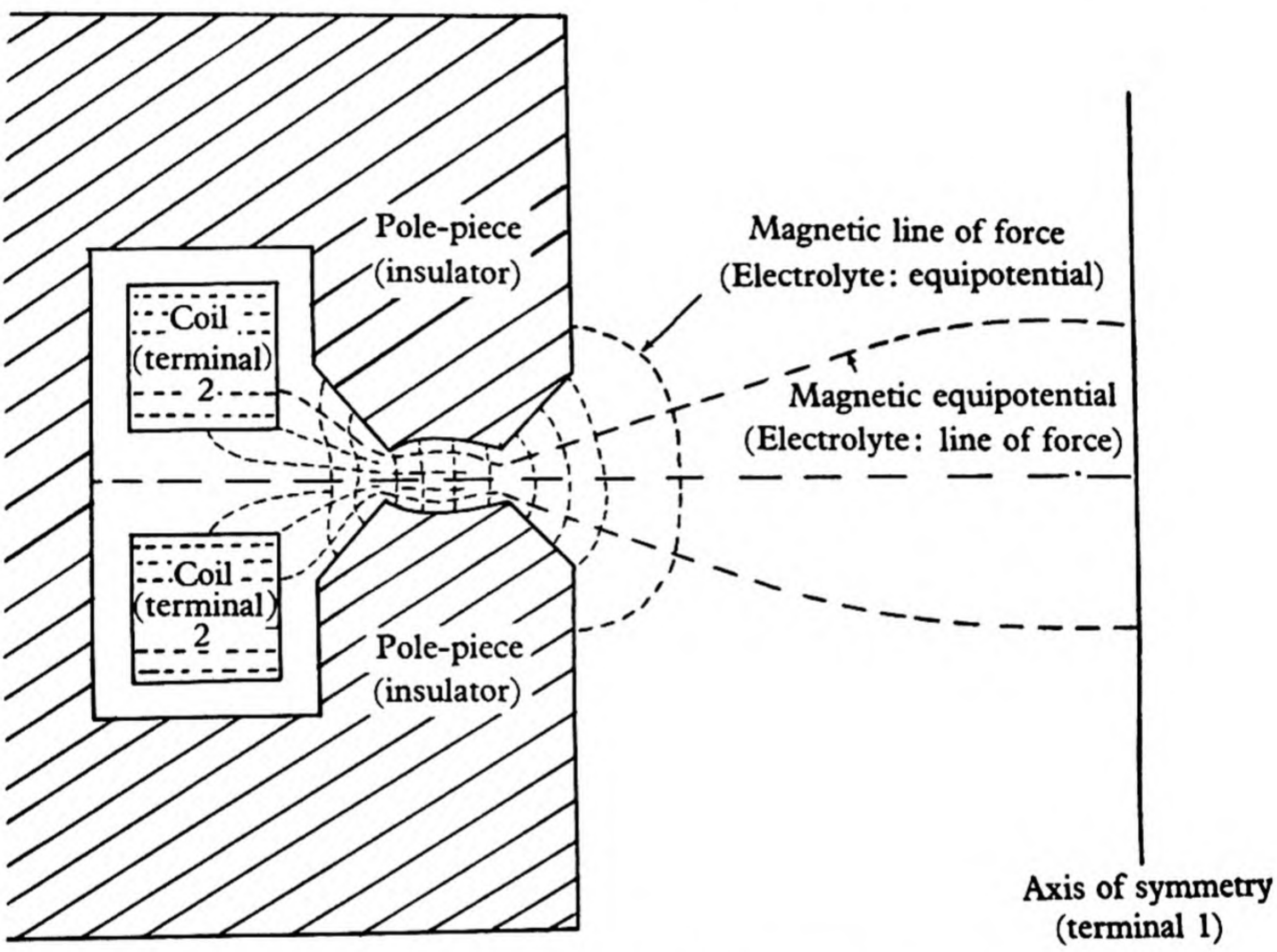

Fig. 10.23. Conjugate field plotting for synchrotron magnet.

way, conjugate field plotting has been applied for the investigation of the shape of pole-pieces for synchrotron magnets (cf. § 12.8). The poles are of the shape of rings of such large diameter that two-dimensional approximations are well applicable (cf. Goward and Wilkins, 1948).

The procedure of the conjugate field plotting is explained in fig. 10.23, which represents an axial cross-section through a magnet of a synchrotron. In the plane-parallel electrolytic trough, the axis of the synchrotron is an equipotential and is represented by a metal sheet connected with terminal (1) of the a.c. source. The two coils

which energize the magnet are represented by two strips of metal both bent to rectangular shape and both connected to terminal (2) of the a.c. source. The wires of the coil in the real problem are at right angles to the plane of the drawing, and their combined magnetic field is sufficiently uniform to be represented summarily for each coil by one electrode in the electrolytic trough. The pole-pieces (cross-hatched in the figure), which are made of mild steel, are represented in the trough by pieces of bakelite or some other insulating material. Equipotentials in the electrolyte correspond to magnetic lines of force, and lines of force in the electrolyte correspond to magnetic equipotentials as indicated in the drawing.

According to results obtained by Wilkins (1950) electrolytic conjugate field plotting combines rapidity of tests and of adjustment with adequate accuracy for the design of magnets. The fields in large and small synchrotron magnets (orbital radii 125 and 10 cm. respectively) have been investigated in this way.

On the other hand, Robinson (1949) has computed the fields of similar magnets by a relaxation process taking full account of the cylindrical symmetry. The procedure is laborious, but the results hardly differ from those of similar computations on a two-dimensional basis or from the results of electrolytic conjugate field plotting.

CHAPTER XI

DEFLECTING FIELDS

11.1. Optical approach

The deflecting and dispersing fields of electron optics have often been compared with the prisms of glass optics. The analogy, however, is superficial. First, a light beam is refracted at the well-defined boundaries of the prism only, while an electron beam is gradually bent through the whole deflecting field, the orbit being smoothly curved all the way. In this respect, however, prisms and deflecting fields do not differ to a greater extent than glass lenses and electron lenses. A more serious distinction arises from the fringing fields in the electron-optical case. These are always so different from the main deflecting fields in their action on the electron beam that they nearly always need a quite separate treatment. Of greatest importance, however, is the focusing action on the electron beam which is inherent in all deflecting fields and which becomes very evident as soon as large-angle deflexions are produced. In this respect, the glass optical analogy to the deflecting field would be given by a glass prism with strongly curved boundaries or by a prism-lens combination. This applies in particular to the focusing deflexion which plays such a great part in modern electron spectroscopy.

Essentially optical methods can be applied as an alternative to well known ballistic calculations for deriving the deflexion angle in simple electric or magnetic fields. It will be seen, however, that such methods are interesting in principle only, but they are practically not useful. On the other hand, the optical theory of lens errors has played a useful part in the classification and discussion of the deflexion errors which are important, e.g. for the scanning of the beam in a television tube.

Most promising of all has been the optical approach to focusing deflexion. There, the various fields are treated quite analogously to either line-focus lenses or to lenses with circular symmetry. It will be shown that even optical image formation can be effected by suitable deflecting fields, and that foci and principal points can be

determined on the 'curvilinear axis' of the deflected beam. Again, errors in deflexion focusing are analogous to the corresponding lens errors. The study of these errors is of practical interest, since they set a limit to the resolving power of modern electron spectrometers.

11.2. Homogeneous weak deflecting fields

Consider the deflexion in a homogeneous electric field of length $2z_p$ with lines of force E_y in the $(-y)$-direction as shown in fig. 11.1.

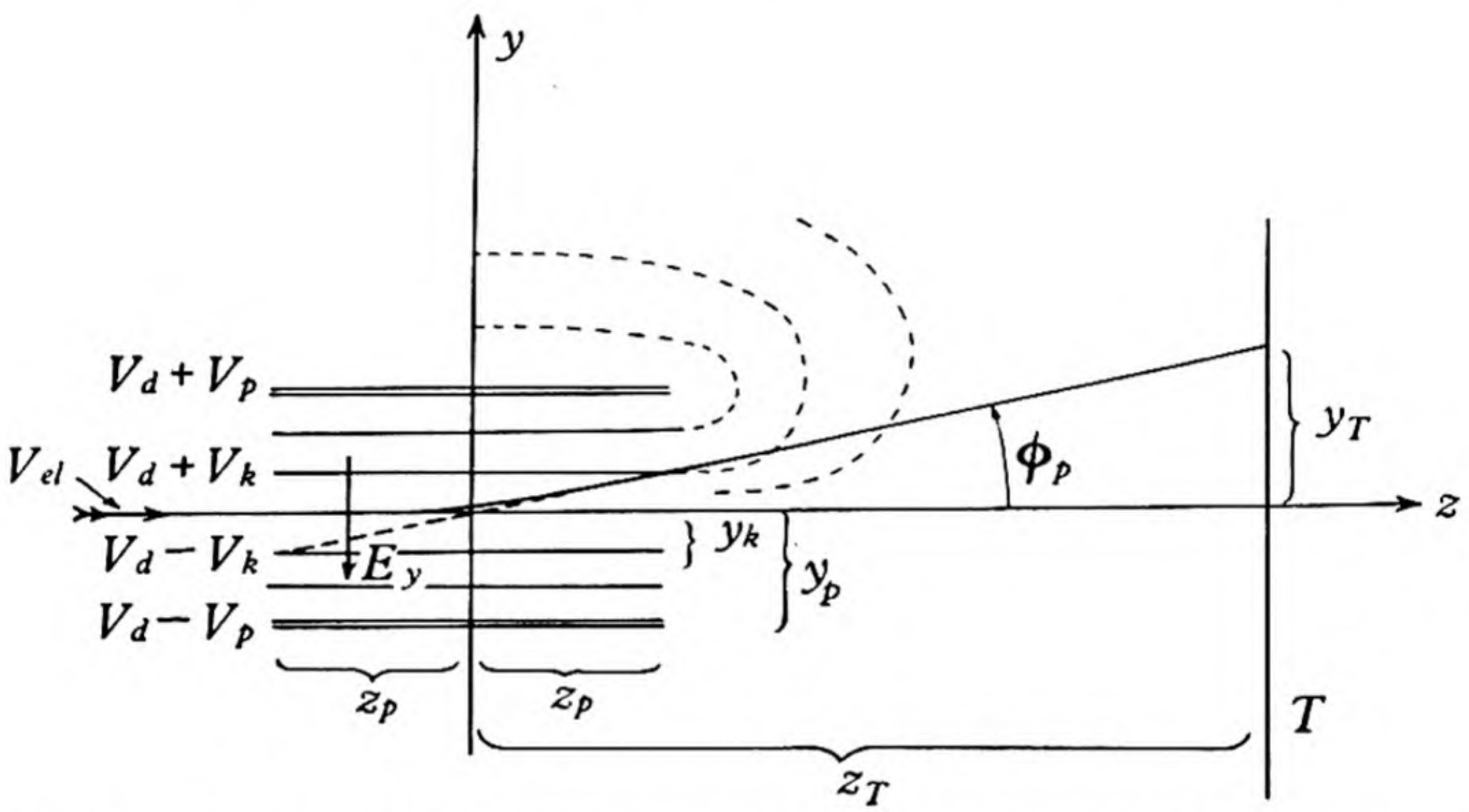

Fig. 11.1. Electron deflexion in a short, homogeneous electrostatic field.

Let the electrons enter the field along the z-axis with an initial velocity

$$u_z = \left(\frac{2e}{m} V_{el}\right)^{\frac{1}{2}}, \tag{11.1}$$

where V_{el} is the initial electron energy in electron-volts. The angle of deflexion ϕ is assumed to be so small that the change of electron energy in the field when passing through different equipotentials is negligible in comparison with V_{el}. Now the equations of motion are

$$\left.\begin{aligned} m\frac{\mathrm{d}^2 y}{\mathrm{d}t^2} &= eE_y, \\ m\frac{\mathrm{d}^2 z}{\mathrm{d}t^2} &= 0, \end{aligned}\right\} \tag{11.2}$$

where the field strength is $-(-E_y)$. Integrating twice and using the initial conditions gives

$$\left.\begin{aligned} z &= u_z t, \\ y &= \frac{e}{2m} E_y t^2, \end{aligned}\right\} \tag{11.3}$$

and elimination of t leads to the equation of the electron orbit

$$y = \frac{e}{2m} E_y \left(\frac{z}{u_z}\right)^2, \tag{11.4}$$

which is a parabola. After passing through a field of length $2z_p$ the beam reaches a distance y_k from the z-axis. Now equation (11.1) can be substituted in (11.4) for u_z and V_p/y_p can be substituted for E_y, where $2V_p$ is the potential difference of the plane-parallel plates producing the field E_y when spaced a distance $2y_p$ apart. Thus

$$y_k = 2\frac{e}{m} E_y \left(\frac{z_p}{u_z}\right)^2 = \frac{E_y}{V_{el}} z_p^2 = \frac{V_p}{V_{el} y_p} z_p^2. \tag{11.5}$$

The angle of deflexion after passing the field of the length z follows, for sufficiently small deflexions, by differentiating (11.4)

$$\tan\phi_p = \frac{\mathrm{d}y}{\mathrm{d}z} = \frac{e}{m} E_y \frac{z}{u_z^2} = \frac{E_y}{2V_{el}} z = \frac{V_p z_p}{V_{el} y_p}. \tag{11.6}$$

At a target in a field-free space at the distance z_T from the centre of the deflecting field, i.e. at a distance $(z_T - z_p)$ from the end of this field, the deflexion y_T is obtained from (11.5) and (11.6):

$$\begin{aligned} y_T &= y_k + (z_T - z_p)\tan\phi_p = \frac{V_p}{V_{el} y_p}\left[z_p^2 + (z_T - z_p) z_p\right] \\ &= \frac{V_p}{V_{el}} \frac{z_T z_p}{y_p} = z_T \tan\phi_p, \end{aligned} \tag{11.7}$$

Therefore

$$\tan\phi_p = \frac{y_T}{z_T}.$$

Thus the deflected beam can be produced back to the origin of the coordinate system, i.e. it seems to come from the centre of the deflecting condenser, intersecting there the initial beam direction.

The deflexion of an electron beam in a homogeneous transverse magnetic field of flux density B_x acting in the $(-x)$-direction can

be derived from the equation of motion with the Lorentz force $-e[u \times B]$ acting on the electron

$$\left.\begin{aligned} m\frac{\mathrm{d}^2z}{\mathrm{d}t^2} &= eB_x\frac{\mathrm{d}y}{\mathrm{d}t}, \\ m\frac{\mathrm{d}^2y}{\mathrm{d}t^2} &= -eB_x\frac{\mathrm{d}z}{\mathrm{d}t}. \end{aligned}\right\} \tag{11.8}$$

Integrating and introducing the initial condition $y = z = 0$ and $u_y = 0$, $u_z = u_0$,

$$\left.\begin{aligned} \frac{\mathrm{d}z}{\mathrm{d}t} &= \frac{e}{m}B_x y + u_0, \\ \frac{\mathrm{d}y}{\mathrm{d}t} &= -\frac{e}{m}B_x z. \end{aligned}\right\} \tag{11.9}$$

The electron speed in a purely magnetic field, namely,

$$(u_y^2 + u_z^2)^{\frac{1}{2}} = u_0,$$

is constant. Thus squaring and adding (11.9) gives

$$y^2 + \frac{2mu_0}{eB_x}y + z^2 = 0. \tag{11.10}$$

This is the equation of a circle of radius $r_e = mu_0/(eB_x)$ with the z-axis as tangent. If a relatively weak field extends only over a relatively short, limited distance $2z_p$ along the z-axis, the deflexion y_k at the end of the field will be small so that y^2 in (11.10) can be neglected and

$$y_k \approx \frac{eB_x}{2mu_0}z^2 = \left(\frac{e}{8m}\right)^{\frac{1}{2}}\frac{B_x}{\sqrt{V_{el}}}z^2 = \frac{z^2}{2r_e} = \frac{2z_p^2}{r_e}, \tag{11.11}$$

where again r_e is the radius of curvature of the electron path in the homogeneous field.

The angle of deflexion ϕ_p is given by

$$\tan\phi_p = \frac{\mathrm{d}y}{\mathrm{d}z} = \left(\frac{e}{2m}\right)^{\frac{1}{2}}\frac{B_x}{\sqrt{V_{el}}}2z_p = \frac{z}{r_e} = \frac{2z_p}{r_e}. \tag{11.12}$$

At a target placed in the field-free space at a distance z_T from the centre of the field, the deflexion of the beam is analogous to (11.7):

$$y_T = z_T z_p\left(2\frac{e}{m}\right)^{\frac{1}{2}}\frac{B_x}{\sqrt{V_{el}}}. \tag{11.13}$$

In the magnetic as in the electrostatic case, the produced directions of initial and deflected beam intersect at the centre of the field. While, however, the electrostatic deflexion is inversely proportional to the electron energy V_{el}, the magnetic deflexion is inversely proportional to the square root, $\sqrt{V_{el}}$.

In an optical analogy to the electric or to the magnetic deflexion the homogeneous short deflecting field is replaced by a slab of thickness y_k and of refracting index N' extending as shown in fig. 11.2 down to the plane $y = 0$. The refractive index at the other side of

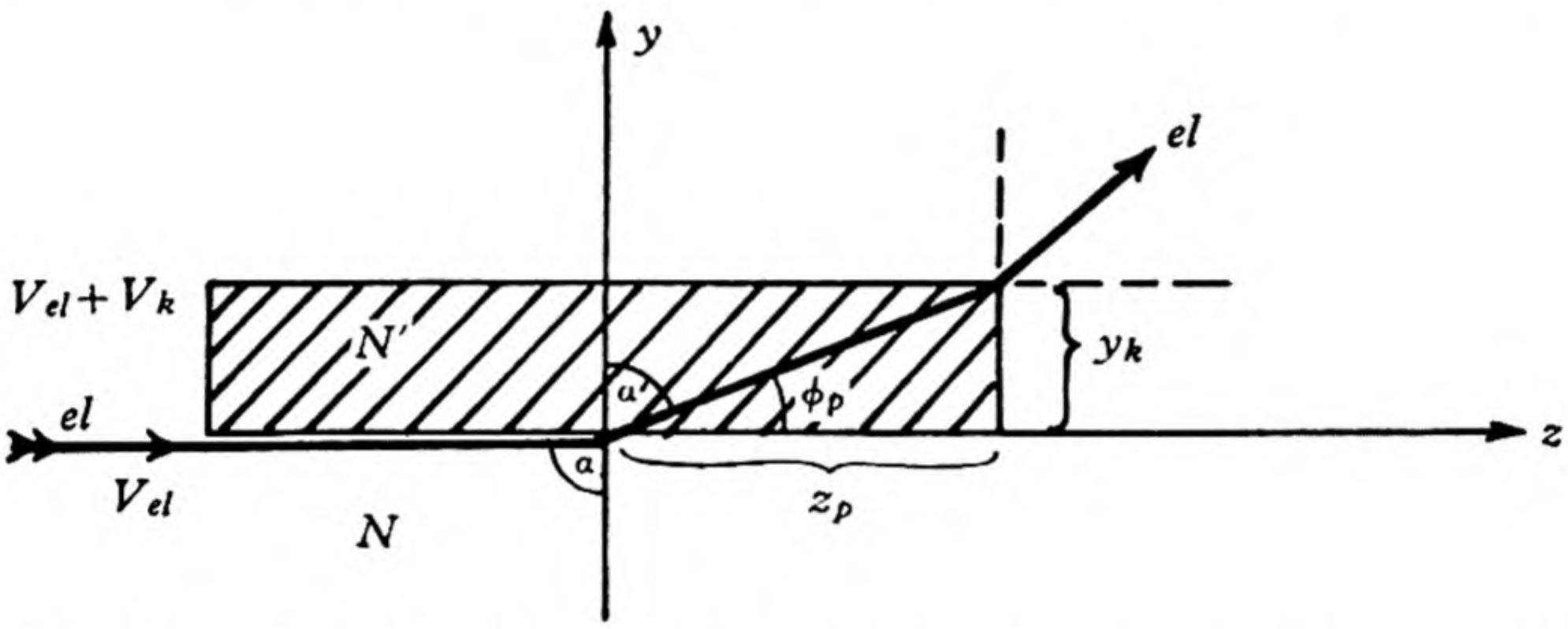

Fig. 11.2. Optical analogy to the weak, homogeneous deflecting field.

this plane is N. The electron ray *el* enters the slab under a grazing angle at the coordinate origin, and leaves it at a distance y_k from the z-axis.

We first consider the electrostatic field. At y_k the potential is V_k, and the refractive index N' of the slab is given by this potential. It follows from Snell's law, (1.10),

$$\frac{\sin\alpha}{\sin\alpha'} = \frac{\sin(\frac{1}{2}\pi)}{\cos\phi_p} = \frac{N'}{N} = \sqrt{\frac{V_{el}+V_k}{V_{el}}} = \sqrt{\left(1+\frac{V_k}{V_{el}}\right)},$$

therefore
$$\tan^2\phi_p = \frac{V_k}{V_{el}};$$

introducing $\frac{V_k}{V_p} = \frac{y_k}{y_p}$ and $y_k = z_p \tan\phi_p$, (11.6) is obtained at once.

We now consider the optical analogy for the deflexion of electrons in a homogeneous magnetic field of flux density B_x. The refractive index is given, according to (1.20), by $N' = \sqrt{V_{el}} - \sqrt{\left(\frac{e}{2m}\right)} A\cos\gamma$. We have again to imagine a slab of this refractive index, the plane

boundaries of the slab being parallel to the xz-plane should be planes of equal N', i.e. of equal A. A solution of the equation $B_x = (\text{curl}\, A)_x = \dfrac{\partial A_z}{\partial y} - \dfrac{\partial A_y}{\partial z}$ which fulfils this condition is $A = A_z = -yB_x$. The beam enters the slab again under grazing incidence along the z-axis; thus $\sin\alpha = \cos\gamma = 1$. With a refractive index outside the slab being $N = \sqrt{V_{el}}$, Snell's law may be written

$$\frac{N'}{N} = \frac{1}{\sin\alpha'} = 1 + \sqrt{\left(\frac{e}{2m}\right)}\frac{B_x}{\sqrt{V_{el}}}y_k.$$

Now, since $y_k = z_p \tan\phi_p$ and

$$\frac{1}{\sin\alpha'} = \frac{1}{\cos\phi_p} = \sqrt{(1+\tan\phi_p^2)} \approx 1 + \tfrac{1}{2}\tan^2\phi_p$$

(for small ϕ_p), a relation for $\tan\phi_p$ is obtained which is identical with (11.12).

11.3. Practical electrostatic deflexion systems

The glass-optical analogy of the beam deflexion in homogeneous fields given at the end of § 11.2 shows most clearly that the electrons could not possibly leave the field and pass into the field-free space without being subject to further deflexion. For instance, in fig. 11.2 the beam entering the slab of refractive index N' from the medium with smaller index $N = \sqrt{V_{el}}$ is refracted towards the normal of the boundary between the media. Leaving the slab, i.e. entering back into the medium of refractive index N, it would be refracted away from the normal, and the final angle of deflexion ϕ given by $\sin\phi/\sin\phi_p = N'/N$ would be larger than the angle of deflexion ϕ_p before leaving the slab, where ϕ_p is given by (11.6) and by (11.12) respectively. The replacement of the homogeneous deflecting field by a rectangular slab with plane boundaries is of course a crude approximation, and the value of ϕ/ϕ_p calculated from the refraction at a simple plane boundary at right angles to the initial beam direction (z) would be much too small. The actual boundary of the homogeneous deflecting field is complicated. A gradually decaying 'fringing field' extends far into the field-free region, as is indicated by a few equipotential lines drawn in fig. 11.1. In the electrostatic case, the fringing field has been the object of

extensive calculations and experiments in connexion with early precision measurements of the specific charge (e/m) of the electron by Bucherer (1909) and by Neumann (1914) respectively. According to their results the fringing field acts as though the deflecting condenser of length $2z_p$ were extended at the exit side by a relatively small amount Δz_p. Formulae have been derived giving Δz_p as a function of the separation $2y_p$ of the plates and of their shape. For the plane-parallel plate condenser with straight edge, Recknagel (1938) has derived

$$\Delta z_p = \frac{2y_p}{\pi}\left(1 - \log_e \frac{y_p}{2\pi z_p}\right). \qquad (11.14)$$

For small plate distances, for example, $y_p = 0{\cdot}1\ z_p$ to $0{\cdot}2z_p$, Δz_p is found to be of the order of $3y_p$.

The most important practical application of the weak electrostatic deflecting field is found in cathode-ray tubes for television or for measuring purposes. There it is desirable to obtain a maximum deflexion y_T at the target for any given deflecting voltage difference $2V_p$ applied to the plates. In other words, the field should be shaped in such a way that its 'deflecting power' becomes as large as possible. The deflecting power is usually defined (cf. Knoll, 1939) by

$$G = \tan\phi_p \frac{V_{el}}{V_p} = \frac{z_{\text{eff.}}}{y_{\text{eff.}}}, \qquad (11.15)$$

where by comparison with (11.6) $2z_{\text{eff.}}$ and $2y_{\text{eff.}}$ are seen to be an 'effective' length and an 'effective' separation respectively of an ideal condenser producing a strictly homogeneous field of limited length, $2V_p$ being the potential difference between the plates.

Obviously, the deflecting power increases with decreasing plate separation. If, however, for a required deflexion the separation is reduced too much, the deflected beam will foul one of the deflecting plates. Hence, the minimum separation $2(y_p)_{\text{min.}}$ and maximum deflexion $(y_T)_{\text{max.}}$ are connected by the relation

$$\tan\phi = \frac{(y_T)_{\text{max.}}}{z_T} = \frac{(y_p)_{\text{min.}} - y_{el}}{z_p}, \qquad (11.16)$$

where y_{el} is the radius of the circular cross-section of the electron beam at the point of leaving the deflecting condenser. $2z_p$ and z_T

are, as in fig. 11.1, the length of the plates and the distance of the target from the centre of the condenser respectively.

In practical tube design, a desired deflexion should be produced by the smallest possible voltage $2V_p$ applied to the plates. For this purpose an optimum plate length $2(z_p)_{\text{opt.}}$ has to be determined for a given total beam length $(z_p + z_T) = c$. A relationship between the variables V_p and z_p with the constants y_{el}, y_p and c can be obtained by combining (11.6) with (11.16). Moreover, by minimizing V_p with respect to z_p, the optimum plate length can be calculated. According to Maloff and Epstein (1938) this is found to be

$$(z_p)_{\text{opt.}} = \tfrac{3}{4}c\,\frac{y_{el}}{y_T - y_{el}}\left(\sqrt{\left[1+\frac{8}{9}\frac{y_r - y_{el}}{y_{el}}\right]}-1\right). \qquad (11.17)$$

The corresponding optimum separation $2(y_p)_{\text{opt.}}$ may then be calculated from (11.16) by substitution for z_p from (11.17).

The use of (11.17) may be illustrated by the following example: In a television tube with screen distance $c = 30$ cm., the size of the picture requires a maximum deflexion at the target $y_T = 10$ cm. The beam radius at the end of the deflecting condenser is $y_{el} = 2{\cdot}5$ mm. According to (11.17), the least deflecting voltage will be required if the length of the deflecting plates is $2z_p = 5{\cdot}8$ cm. and if their separation is $2y_p = 2{\cdot}7$ cm.

The plane-parallel plate condenser of dimensions as given by (11.17) does not yet represent the best electrode arrangement for maximum deflecting power. The separation of plane plates can be further reduced without danger of fouling if the plates are tilted towards the axis of the undeflected beam. At the entrance of the beam, the necessary plate distance has to be only slightly larger than the diameter of the beam. At the exit side, however, the plate distance has to be large enough to account for the deflexion of the beam after its passage through the field of the condenser.

We refrain from discussing the theory of the tilted plate condenser, but we present in the nomogram (fig. 11.3) some results about it after Knoll (1939). Though these results have been obtained under neglect of the fringing fields they were found to be satisfactory for the purpose of practical design. The nomogram of fig. 11.3 contains the necessary information on the optimum geometry of the tilted plane plates for any given maximum angle of

deflexion. The abscissae in fig. 11.3 represent the ratios of the condenser length ($2z_p$) to the separation of the plates ($2y_1$) at the entrance of the beam. The ordinates represent the deflecting power

$$G = \tan\phi_{\text{max.}} V_{el}/(V_p)_{\text{max.}},$$

where $\phi_{\text{max.}}$ is the maximum angle through which the beam can be deflected without fouling the plates, and $2(V_p)_{\text{max.}}$ is the corresponding maximum possible deflecting voltage difference between the plates.

For instance, for parallel plates ($y_1/y_2 = 1$) and for a required $\tan\phi_{\text{max.}} = 0{\cdot}2$, there can be found with the help of fig. 11.3:

(i) the ratio of plate length to separation $z_p/y_1 = 4{\cdot}8$.

(ii) the deflecting power $G = 4{\cdot}8$.

Thus for an electron energy of 5 keV. the plate voltages are $\pm V_p = \dfrac{0{\cdot}2 \times 5000}{4{\cdot}8} = 208\,\text{V}$. If the plates are tilted in the ratio $y_2/y_1 = 2$, the ratio $z_p/y_1 = 9$ is obtained for the above $\phi_{\text{max.}}$. The corresponding deflecting power is now 6·4, and the maximum deflecting voltage is reduced to $V_p = \pm 156\,\text{V}$. The increase in z_p/y_1 implies that either the length $2z_p$ of the plates has to be increased or that their initial separation $2y_1$ has to be reduced. Since it is always desirable to reduce the overall dimensions of the condenser, the latter alternative will be chosen as far as possible, i.e. the initial separation $2y_1$ of tilted plates will be reduced until it reaches its natural limit, namely, the width of the beam diameter.

Further increase in deflecting power has been obtained by the introduction of 'kinked' deflecting plates, each consisting of two plane parts joined at an obtuse angle. In this way the beam passes in succession through two adjoining condensers, the plane plates of the second condenser having a greater tilt angle than the plane plates of the first one. The relative lengths of the two part-condensers are chosen to produce approximately equal beam deflexions (i.e. half the total deflexion each), and under these conditions their lengths and tilt angles can be determined from the nomogram in fig. 11.3.

The maximum theoretically possible deflecting power, however, is obtained when the condenser plates are shaped flush with the outer boundary of the deflected beam throughout the path. Maloff and Epstein (1938) have calculated the shape of deflexion plates under the assumption that the field everywhere along the z-axis is

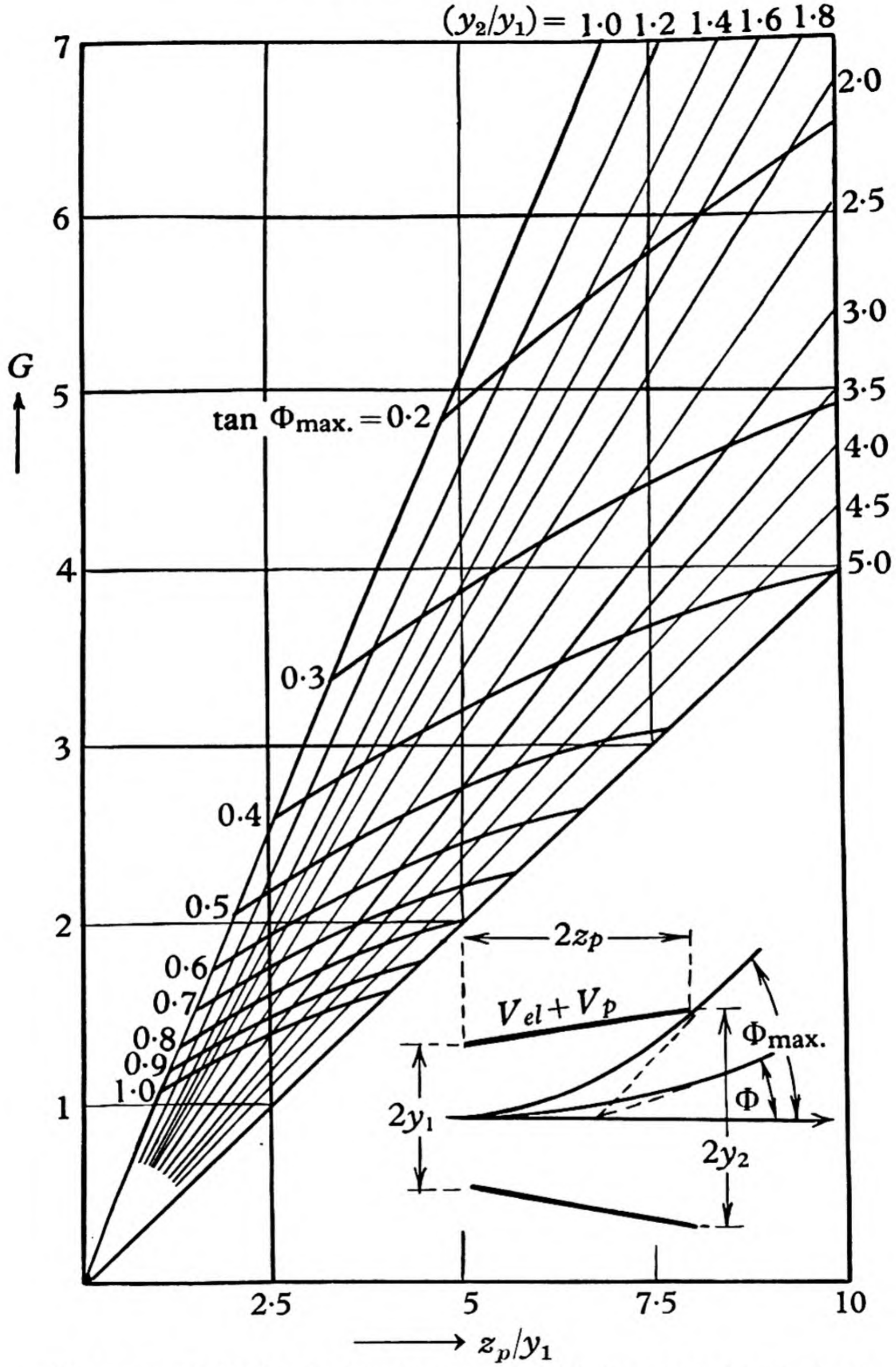

Fig. 11.3. Deflexion in the electrostatic field between tilted, plane condenser plates.

given by $E_y(z) = V_p/y_p(z)$, where y_p, the ordinate of the plate, is a function of z. They derived an optimum curve for the cross-sectional

shape of the optimum deflecting plates which is similar to the general space-charge curve given in fig. 8.2. Though such curved deflecting plates would attain the maximum possible deflecting power, they are not frequently met in practice because the effort of shaping the plates is not sufficiently repaid by the relatively small increase in deflecting power that can be gained in comparison with the above kinked plates or even with plane deflecting plates tilted about the correct angle.

The relatively small advantage gained by curving the plates may be seen in the following example quoted from a paper by Borries (1941). A condenser with the plate length $2z_p = 60\,\text{mm.}$ and with the distance $z_T = 300\,\text{mm.}$ between plates and target is used for

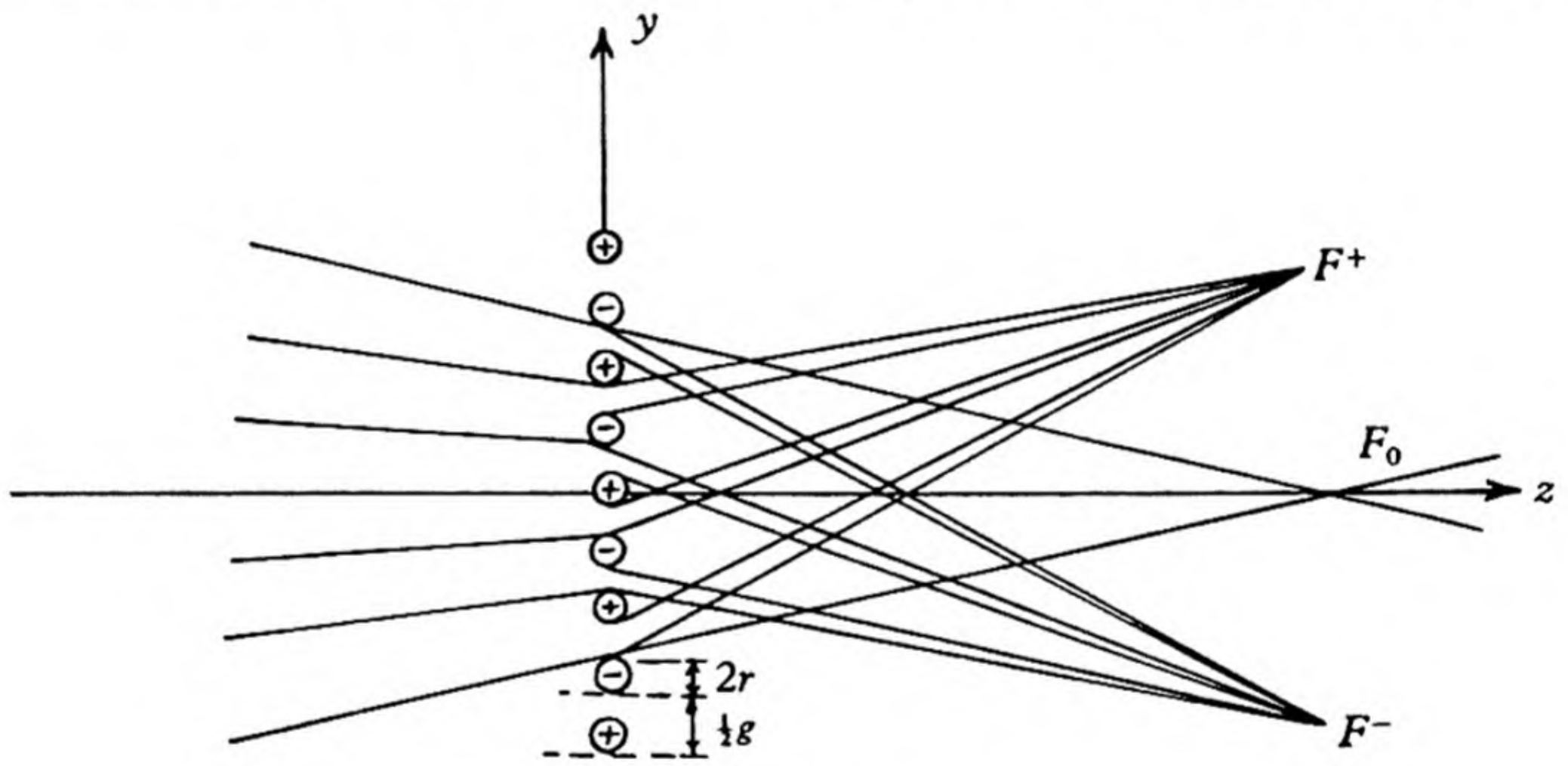

Fig. 11.4. Deflexion grid.

deflecting a 1000 eV. beam of width $2y_{el} = 4\,\text{mm.}$ through an angle given by $\tan\phi = 0{\cdot}3$. The deflecting power (cf. (11.15)) of the condenser in terms of the theoretical optimum (= 100 %) may be stated as:

100 % for curved plates,
93 % for kinked plates,
75 % for tilted, plane plates,
41 % for plane, parallel plates.

The shorter the condenser (smaller z_p), the smaller becomes the difference in deflecting power for the different types of plates.

Apart from plate condensers, various other electrostatic deflexion devices have been described in the literature. These devices have so far not found much practical application. However, being of some interest in principle, they may be mentioned here.

Deflecting grids as shown in fig. 11.4 have been investigated experimentally by Hilsch and Pohl (1928), and by Klemperer (1940); their theory has been given by Bethe (1929). In fig. 11.4 a plane grid of alternately connected wires, all parallel to the x-axis, is placed at right angles to an electron beam which initially converges towards a focus F_0. If the grid wires are charged alternately positive and negative as indicated by the (+) and (−) symbols in the figure, the beam will be split up in halves and it will be deflected through the angles $\pm\phi$, to converge into the two foci F^+ and F^-. The deflecting power of the grids can be shown to increase as a function of $\log(r/g)$, where r is the radius of the circular wires and $\frac{1}{2}g$ is the pitch of the grid. The deflecting power is, for instance, 0·56 for $r/g = 0{\cdot}02$ and 3·4 for $r/g = 0{\cdot}2$. An upper limit to the value of r/g, however, is set by the fraction of electrons intercepted by the grid wires that can be tolerated in practice.

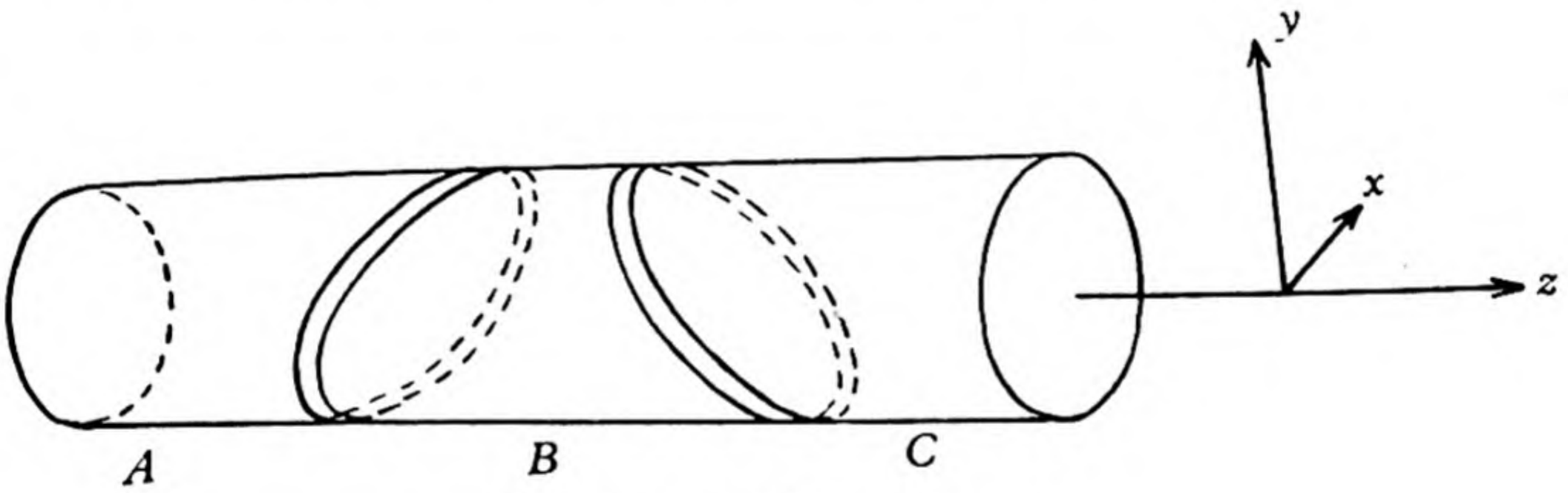

Fig. 11.5. Prism deflector.

Deflecting grids are advantageously used when relatively wide beams have to be deflected within a relatively short interval of the electron path, since the effective length of the deflecting field extends only over a distance of about three times the grid pitch. Hence the transit times of the electrons through the deflecting fields are always very short, and the deflecting grids can be operated by voltages of relatively high frequencies.

An unusual type of deflexion device shown in fig. 11.5 has a great similarity to the glass optical prism. It consists of a tube cut by two planes obliquely, say at an angle of 45° to the axis, into three separate parts A, B and C. An electron beam passing along the axis (z) of the tubes is deflected if a potential difference is applied between tube B and the two external tubes A and C which are at a common potential. For wide-angle deflexion trumpet-shaped

deflectors of circular or of square cross-section have been used analogously to the curved deflexion plates described earlier in this section. As compared with the deflecting condenser of equal length, the deflecting power of the 'prism deflector' is inferior. Its merit is given by the perfect shielding of the deflected beam which is enclosed completely by the deflecting electrodes (cf. Klemperer, 1943).

Great deflecting powers of the order of $G = 20$ have been observed with deflecting electron mirrors by Klemperer (1937). In these deflectors the electron beam is slowed down until it meets a reflecting equipotential surface under a sufficiently small angle of incidence, say $\alpha < 45°$, so that the remaining transverse velocity component of the electron is small. An auxiliary electrode is provided which changes the direction of the reflecting equipotential by an angle β, say, if a potential $2V_p$ is applied to it. The angle of deflexion ϕ is equal to the change in angle of reflexion which, however, is always twice as large as the angle by which the reflecting mirror is turned. Various types of deflexion mirrors have been proposed; however, no design with a satisfactory range of proportionality between ϕ and V_p has been obtained so far.

The great deflecting power of the deflexion mirror is mainly due to the fact that the electrons are exposed to the deflecting field when their velocity is very small, the deflexion being (cf. (11.4)) inversely proportional to the square of the velocity. In this way the deflexion mirror utilizes a principle which can be applied to every deflexion condenser or a deflecting magnetic field, namely, electrons may be deflected while they are of very small velocity, and they may be 'post-accelerated' later on to whatever speed is required, say, for producing sufficient light intensity on a fluorescent target. At a superficial examination post-acceleration seems to recommend itself wherever great deflexion sensitivity is required. A critical discussion in § 12.2, however, will show that only in a few particular cases real advantages are gained by it.

11.4. Practical magnetic deflexion systems

The design of these systems varies considerably according to their particular use. For instance, the scanning coils of a television tube should consume a minimum of power for building up the field,

and their overall frequency response should be sufficiently high; moreover, the deflexion of the beam should be proportional to the coil current and it should not depend upon the initial coordinates of the beam. On the other hand, very different problems turn up in the design of deflexion magnets for electron spectrometers. For example, great flux density, or great field homogeneity, or a certain law of decrease of field strength with one of the coordinates, etc., may be required.

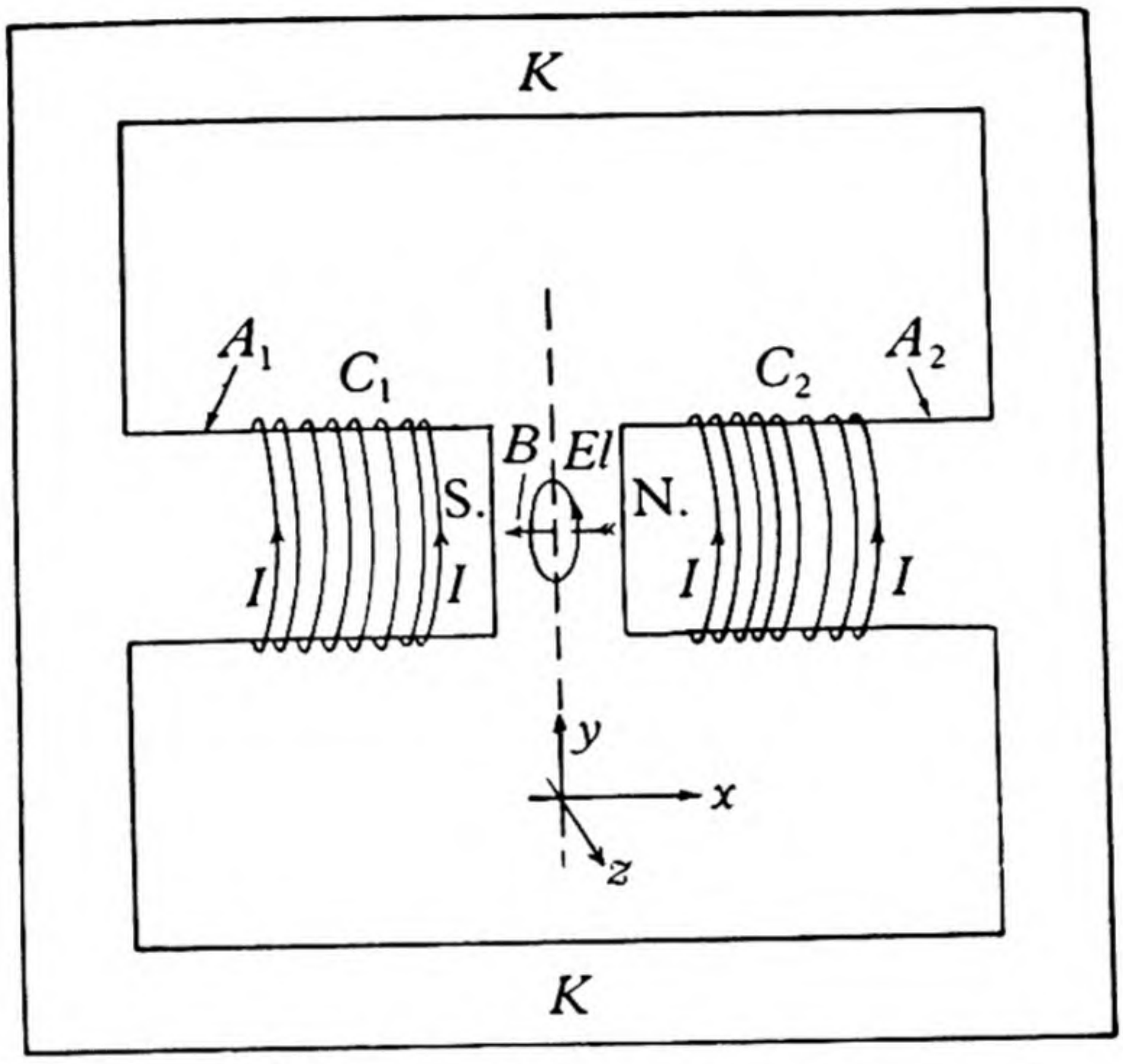

Fig. 11.6. Deflexion magnet.

The general scheme of a simple deflexion magnet is shown in fig. 11.6. This magnet is able to produce strong homogeneous fields over a relatively large region inside the gap between its pole-pieces A_1 and A_2. These pole-pieces are of cylindrical shape with flat end-faces, and they are made from soft, perfectly homogeneous iron, energized by the two current coils C_1 and C_2. An 'iron-yoke' K is used to reduce the volume of the useless flux outside the magnetic gap, thus saving a substantial amount in energizing ampere-turns. The cylindrical pole-pieces and the yoke have approximately the same cross-sectional area. The cross-section of the cylindrical pole-pieces can be made to any shape required for the particular purpose. The distance between the flat ends should be as small as the aperture of the deflected electron beam allows, so that the stray

field at the edges is as small as possible in comparison with the proper field inside the gap.

If a deflexion magnet of the type of fig. 11.6 has to be designed for producing a certain density of flux B in the gap, the number of ampere-turns, nI, necessary to produce B can be estimated from the relation

$$V_H = nI = \oint H\,\mathrm{d}s = \frac{Bg}{\mu_0} + \int \frac{B}{\mu}\,\mathrm{d}s, \qquad (11.18)$$

where V_H, the magnetomotive force is given by the line integral of the magnetic field H about a closed path s. V_H also equals the current (nI) threading a surface which is bounded by this path. The closed line integral in (11.18) may be replaced by two terms, the magnetic potential difference across the air gap of width g and a line integral along the path of the field lines inside the iron. Since the permeability μ in the iron is many thousand times larger than the permeability μ_0 in air, the second term can be neglected and (11.18) gives

$$Bg = \mu_0 In, \qquad (11.18a)$$

where B is measured in Wb./m.^{2}, g in metres and I in amperes.

Various designs for electromagnets, based on the scheme of fig. 11.6, have been described in the literature. For instance, constructional details for a large model are found in a paper by Hudson (1949). His magnet dissipated 100 kW. in two water-cooled, layer-wound coils, and it produced up to 2 Wb./m.^{2} in a gap of 3–5 cm. between circular pole-pieces of 10 cm. diameter. Overall dimensions of the whole magnet were 60 × 30 × 30 cm. Details of a very powerful permanent magnet for the deflexion of electron momenta up to 20×10^{-3} Wb./m. (= 20 k.Gauss × cm.) have been published by Cockcroft, Ellis and Kershaw (1932). The magnet had plane-parallel pole-faces 17 × 29 cm., spaced by a gap of 5·5 cm. Its permanent part consisted of two rectangular prisms made up from straight steel laminations weighing 500 lb. It was closed magnetically by a mild steel yoke of 1500 lb. weight. The field could easily be set to any desired value by passing suitable current through field coils which surrounded the permanent part of the magnet. This design has proved very useful for the photographic exposure of a β-spectrum in a deflexion spectrometer where great constancy of field was required over long times. A permanent

magnet of similar dimensions (0·6 Wb./m.^{2} over 150 cm.^{2} in a 5 cm. gap) has been described by Shutt and Whittemore (1951). This magnet is composed of straight, relatively short bars made from Alnico, and from mild steel respectively, and it has found useful application for deflexion of fast electrons in a cloud chamber.

Relatively small deflexion magnets are required for cathode-ray scanning in television tubes. In the early stages of development, magnets of the type shown in fig. 11.6 were in use. However, since relatively large gaps were required, the effects of the inhomogeneous stray fields could not be avoided, and the deflexion errors, which will be discussed in § 11.8, became troublesome.

More satisfactory results have been obtained by the application of 'saddle-coils' with parallel conductors (Knoll, 1939), as shown

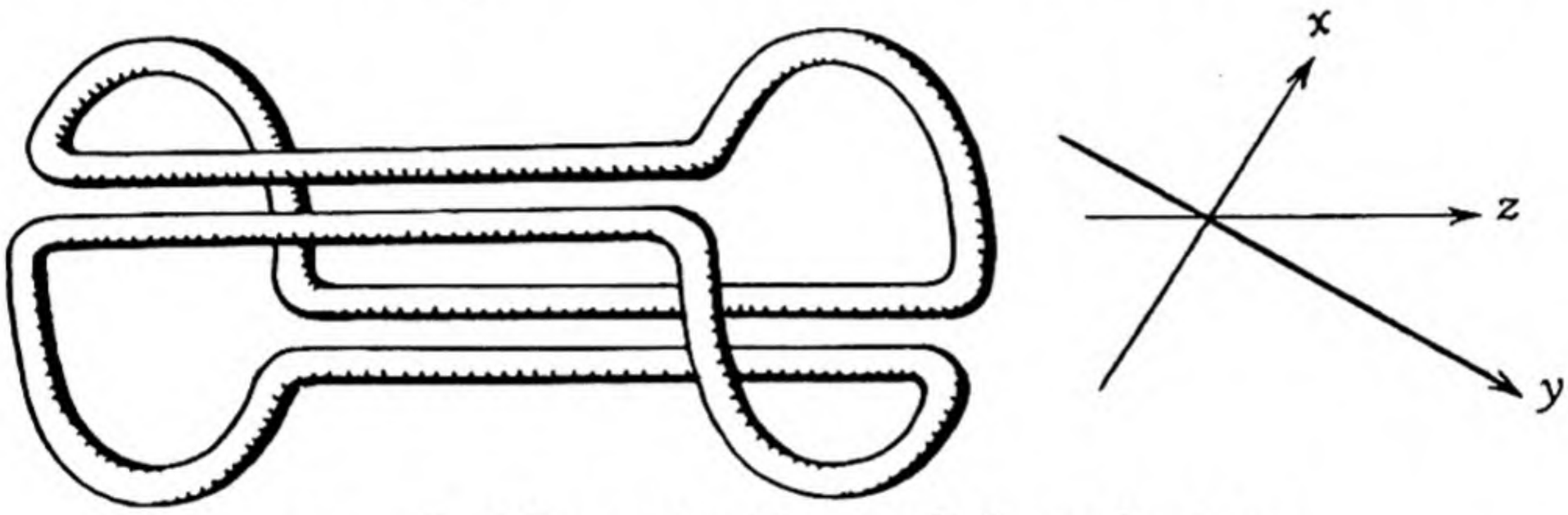

Fig. 11.7. Saddle-coil with parallel conductors.

in fig. 11.7. These coils can be placed over the glass neck of the cathode-ray tube. In order to reduce the volume of the useless flux, mild iron wire can be wound round the saddle coils, the windings of the iron wire being coaxial with the undeflected electron beam. Further improvements have been obtained by the introduction of elliptical saddle coils (Marschall and Schröder, 1942) shown in fig. 11.8.

The great merits of the saddle coils in comparison with ordinary circular coils are due to a particular distribution of flux density which is by no means homogeneous. Fig. 11.9, for instance, shows the distribution of the x-component of the flux density $B_x(z)$ along the z-axis which is taken as the axis of the undeflected beam. In the same figure there is shown also a distribution of the x-component of flux density $B_{x1}(z)$ taken along a line parallel to the z-axis at a distance $x = 1$ cm. from it. These two curves are in principle sufficient for a calculation of the deflexion of any ray that passes anywhere through the given field.

Of some technical interest is the power consumption of cathode-ray scanning fields in television; it is relatively much larger for a magnetic field than for the corresponding electrostatic field. A comparison of the forces exerted on the electron in magnetic and in electrostatic fields of equal energy density $\left(\frac{B^2}{2\mu} = \frac{\epsilon E^2}{2}\right)$ yields

$$\frac{F_B}{F_E} = \frac{euB}{eE} = \frac{u}{c}, \tag{11.19}$$

where the ratio (u/c) of electron velocity to light velocity in television tubes is of the order of 1/8. Hence a more powerful scanning

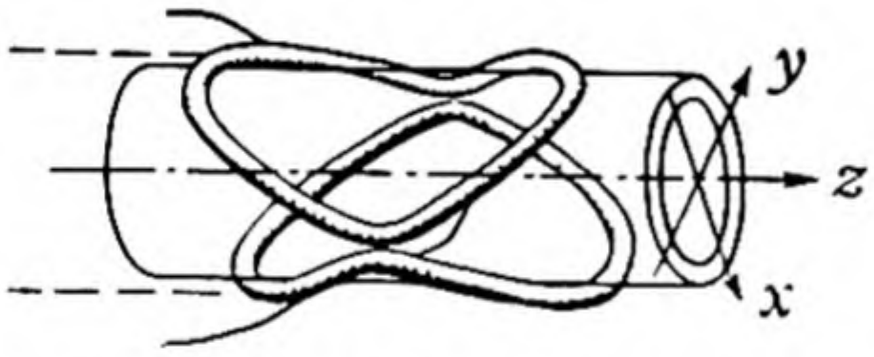

Fig. 11.8. Elliptical saddle-coils.

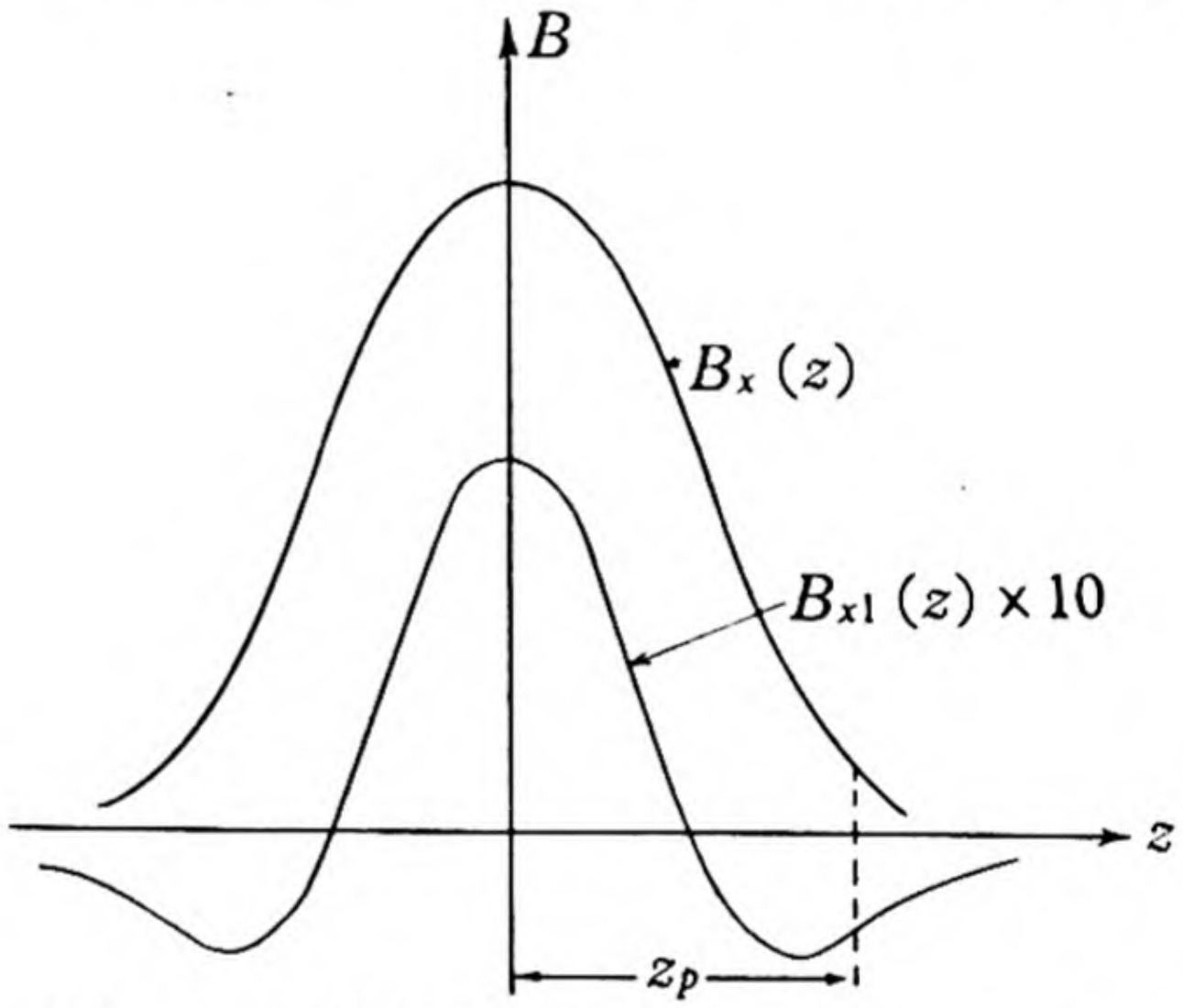

Fig. 11.9. Distribution of flux density for elliptical coils.

oscillator will be needed to produce a given deflexion by magnetic fields than by electrostatic fields. This difference is increased by the fact that deflecting plates are put inside the vacuum envelope, while magnetic deflecting coils have to be arranged outside it and hence tend to produce stray fields and stored energy over a much greater volume than that occupied by the beam.

11.5. Focusing deflexion in electrostatic fields

It can be shown that every deflecting field acts as a combination of a prism with a line-focus lens. For the following obvious reason every electrostatic field should have focusing properties: different rays of an electron beam, travelling at some angle to the field lines, will be at a given time at different potentials. Hence these rays will

have different velocities and, according to (11.5), they will be subject to different deflexion. Thus rays of a homogeneous electron beam of finite aperture which enter a field E_y parallel to the z-axis will ultimately form a line-focus parallel to the x-axis. According to Recknagel (1938), the focusing power of a short field is given by

$$\frac{1}{f} = \left(\frac{1}{2V_{el}^2}\right) \int_{-\infty}^{+\infty} E_y^2 \, \mathrm{d}z, \tag{11.20}$$

where V_{el} is the initial energy of the electrons. For the 'chopped-off' homogeneous deflecting field of § 11.2, (11.20) yields

$$\frac{1}{f} = \left(\frac{V_p}{V_{el}}\right)^2 \frac{z_p}{y_p^2} = \frac{\tan^2 \phi_p}{z_p}, \tag{11.21}$$

where all designations are those introduced in § 11.2.

According to Recknagel (1938) the focusing effect of the stray fields at the end of the parallel plate condenser may be taken into account by substituting the 'equivalent length' $(2z_p + \Delta_1 z_p)$ for the length $2z_p$ of the homogeneous deflecting field, where $\Delta_1 z_p = 2y_p/\pi$. This correction $(\Delta_1 z_p)$ for focusing is usually smaller than the corresponding stray field correction (Δz_p) for deflexion introduced in § 11.3 (cf. (11.14)).

Focal lengths of weak electrostatic deflecting fields, as used in cathode-ray tubes, are always large in comparison with the dimensions of the deflecting plates. For example, for plate length $2z_p = 2$ cm. and for a deflexion angle $\phi = 0{\cdot}2$ radian the focal length is found to be as large as $f = 25$ cm.

On the other hand, strong fields resulting in large deflexions have very much shorter focal lengths. Yarnold and Bolton (1949), for instance, have used the homogeneous electrostatic field as a focusing velocity separator, deflecting the rays through a right angle. This separator is essentially a plane-parallel plate condenser, having two parallel slots representing entrance and exit aperture respectively, both cut in the positive plate at some given mutual distance z_f. The electron beam crosses this plate through the entrance slot at a slope angle α, it is then retarded by the deflecting field and bent back to the plate describing a parabolic trajectory according to (11.3). The distance at which the beam is returned to the plate is given by

$$z_f = 2V_{el} \frac{y_p}{V_p} \sin 2\alpha, \tag{11.22}$$

where, as above, $2y_p$ and V_p are separation and potential difference respectively of the condenser plates, and V_{el} is the initial electron energy. It will be shown later on (cf. § 11.9) that slight changes $\pm\Theta$ in slope angle α have a relatively small influence upon the range z_f, if the deflexion angle $\phi = \frac{1}{2}\pi$. In this case, the slope angle is $\alpha = \frac{1}{4}\pi$, and a bundle of rays leaving the entrance slot with a given small divergence $\mp\Theta$ will be focused through an exit slot of sufficient width. The homogeneous field can be used for sorting electron velocities when certain electron energies V_{el} are selected for transmission by proper adjustment of the plate voltage V_p. The method, however, suffers from two disadvantages. First, the defining slots have to be arranged at the boundary of a strong field; thus unwanted electron lenses are set up with relatively large aberrations (cf. § 10.4). Secondly, the electrons are slowed down appreciably while they are approaching the vertex of their parabolic path. This would involve the danger of space-charge disturbances for all beams of high intensity (cf. Chapter VIII).

Both these disadvantages can be avoided to a large extent if the electrons are deflected and focused while they are moving approximately along equipotential lines. In this way, a frequently applied deflexion method uses the radial field of a cylinder condenser confined within a quadrant and deflecting the rays by an angle $\phi = \frac{1}{2}\pi$. For example, Löhner (1930) has given constructional details of a small energy selector for slow electrons. Aperture slots were arranged at the entrance and at the exit between the condenser plates, and any desired voltage of electrons was selected with an accuracy of $\pm 10\%$ from an initially continuous energy distribution.

Another model for a cylindrical electrostatic 90° deflector, described by Allison, Frankel *et al.* (1949), has been used for the sorting of very fast electrons. A voltage difference of 50 kV. was applied to cylinder plates of 15 cm. mean radius spaced by a mutual distance of only 0·5 cm. The width of the selected energy range depends on the ratio of the selecting slot width to the mean curvature of the cylinder condenser. In the described model, electrons of 0·75 MeV. have been selected within a range of a fraction of 1 %.

The full advantages of the cylinder condenser, however, are realized only if the electrons are deflected through an arc of

$\pi/\sqrt{2} = 127{\cdot}28°$, since only after such a deflexion is a line object projected into a line image. This has been shown analytically by Hughes and Rojanski (1929). The discussion of the focusing properties of the cylinder condenser which is presented here is due to Brüche and Scherzer (1934).

Let the electric field half-way between the condenser plates be adjusted to a value E_0 to keep the principal ray on a circle of radius r_0. By balancing in this way the centrifugal force of the electrons on their circular orbit one obtains

$$mr_0\omega_0^2 = eE_0, \tag{11.23}$$

where ω is the angular velocity of the electron, and the indices o refer to the circular orbit. The equation of motion for the radial component of an electron which does not move exactly on the circular orbit is

$$m\frac{\mathrm{d}^2r}{\mathrm{d}t^2} = mr\omega^2 - eE. \tag{11.24}$$

For this orbit which deviates but little from the circular shape, the local field is given by

$$E = E_0\frac{r_0}{r} = E_0\frac{r_0}{r_0+\Delta r} = E_0\left(1-\frac{\Delta r}{r_0}\right). \tag{11.25}$$

This value of E may be substituted into (11.24). Moreover, the law of conservation of angular momentum, $mr^2\omega = \text{const.} \approx mr_0^2\omega_0$ may be used to eliminate ω. Hence (11.24) yields

$$\frac{\mathrm{d}^2r}{\mathrm{d}t^2} = \omega_0^2\frac{r_0^4}{r^3} - \frac{e}{m}E_0\left(1-\frac{\Delta r}{r_0}\right). \tag{11.26}$$

Substituting $r = r_0+\Delta r$ and neglecting higher terms, (11.26) becomes

$$\frac{\mathrm{d}^2(\Delta r)}{\mathrm{d}t^2} = r_0\omega_0^2 - 3\omega_0^2\Delta r - \frac{e}{m}E_0 + \frac{e}{m}E_0\frac{\Delta r}{r_0},$$

which reduces by substitution of (11.23) to

$$\frac{\mathrm{d}^2}{\mathrm{d}t^2}(\Delta r) + 2\omega_0^2\Delta r = 0. \tag{11.27}$$

This is the differential equation of a simple harmonic motion with the solution

$$\Delta r = C\sin\left[\omega_0\sqrt{2}\,(t-t_0)\right]. \tag{11.28}$$

The angular frequency of the simple harmonic motion is $\omega_0\sqrt{2}$. In a time interval of 2π sec., in which a principal electron ray

completes ω_0 circles, the 'marginal' electrons oscillate about the circular orbit $\omega_0\sqrt{2}$ times, intersecting the circle twice in each period of oscillation. Thus the points of intersection are spaced by

$$\phi = \pi/\sqrt{2} = 127^\circ\,17'. \tag{11.29}$$

Focusing deflexion between coaxial cylinder electrodes has been used in many experimental investigations. For example, fig. 11.10 shows an application of this electrostatic focusing method in a velocity separator which has been used by Hughes and MacMillan

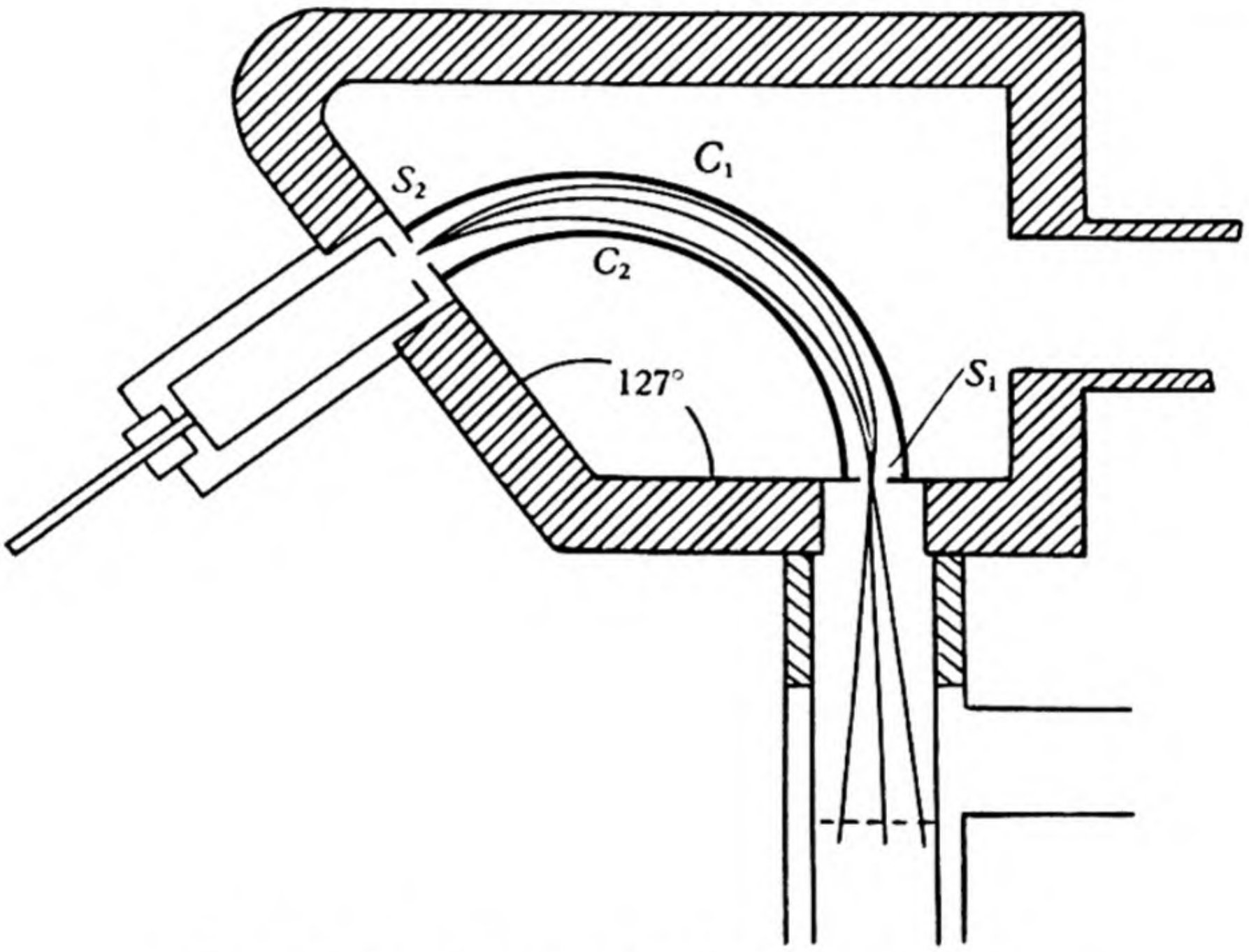

Fig. 11.10. Electrostatic focusing deflexion.

(1929) for verifying experimentally the theoretical value of (11.29) for the focusing deflexion angle. Electron rays diverging up to 12° enter the velocity analyser through a narrow slot S_1 and are focused through a narrow exit slot S_2. The voltage difference $2V_p$ which was applied to the plates C_1 and C_2 of the cylinder condenser in order to pass electrons of the velocity V_{el} through the device is given by

$$V_p = V_{el}\log_e\frac{r_1}{r_2}, \tag{11.30}$$

where r_1 and r_2 are the radii of curvature of the outer and of the inner cylinder plates C_1 and C_2 respectively. For instance, radii $r_1 = 60$ mm., $r_2 = 50$ mm., slot widths $S_1 = 0{\cdot}3$ mm., $S_2 = 1$ mm., and slot lengths of 10 mm. were used by the above authors. The

deflexion voltage was $2V_p = 0{\cdot}3650V_{el}$, and rays of 99·1 and 100·7 eV. could still be separated.

Of further interest is the possibility of a focusing deflexion in the spherical condenser. Purcell (1938) investigated theoretically the focusing properties of Kepler orbits in the Coulomb field, and he derived, in distinction to the result with the cylinder condenser, that focusing takes place after a deflexion of $\phi = \pi$. Purcell verified his theoretical results by experiments in a spherical condenser. The focusing voltage which he applied to the condenser plates was of the order of a third of the electron-volt energy of the electrons. Purcell's arrangement has the merit of collecting relatively large intensities, since focusing is effected in two directions: the Coulomb field projects the rays from a point source into an image point. However, a theoretical discussion by Rogers (1951) has shown that the high optical qualities of the spherical condenser field are greatly reduced for fast electrons by relativistic modifications of the trajectories. Also, the construction of accurate spherical condensers involves some technical difficulties, so the method is not likely to find a wide application.

To obtain focusing deflexion, there is no need for the electrons to travel entirely in the deflecting field. Source and focus may lie outside given field boundaries. For instance, a focusing field sector (cylindrical or spherical condenser) may be bounded by two radial planes enclosing a given central angle ϕ. Electrons coming from an outside source travel along straight lines until they meet the sector boundary at right angles to the principal ray. Then they travel along curved orbits through the field. After leaving the field they again travel along straight lines until eventually they reach the focus. Herzog (1934) was the first to point out that lens properties can be ascribed to a field sector, and he derived relatively simple expressions for the focal length of the sector field between coaxial cylinder plates.

Very suitable for the treatment of focusing deflexion problems is the introduction of curvilinear coordinates. The principal ray of the deflected bundle is chosen as the curvilinear axis (ζ). η- and ξ-ordinates are plotted along the normal and the binormal respectively of the principal ray. For example, in the simple case of focusing deflexion in the cylinder condenser, the ζ-axis is a circle

half-way between the plates, the ξ-coordinates are parallel to the cylinder axis and the η-coordinates extend in radial direction. By transforming the curvilinear (ξ, η, ζ)-coordinates into a Cartesian system $(\bar{\xi}, \bar{\eta}, \bar{\zeta})$, the principal orbit of the deflected electron bundle appears to be stretched out into a straight ray serving as the $\bar{\zeta}$-axis, and the marginal orbits appear to be focused towards the $\bar{\zeta}$-axis just like the rays in an ordinary electron lens. For example, after transformation into the Cartesian system, the one-directionally focusing cylinder condenser would appear like an ordinary line-focus lens of the type described in Chapter X. On the other hand, the two-directionally focusing spherical condenser would appear like an ordinary lens of circular symmetry converging a homocentric beam into a point focus. In every case, the $\bar{\zeta}$-axis connects the centre of an object space with the centre of an image space. In the 'stretched-out' $(\bar{\xi}, \bar{\eta}, \bar{\zeta})$ system the laws of Gaussian dioptrics can be applied to determine the image point for any given paraxial object point. Hence in the 'stretched-out' system focal points and principal points $(\bar{F}, \bar{F}', \bar{P}, \bar{P}')$ can be located in the customary way (cf. Chapter II). If the transformation is reversed back into the curvilinear (ξ, η, ζ) system, the location of the cardinal points (F, P, etc.) is considered to determine the characteristic optical properties of the original deflecting field.

Wendt (1943) found that the electron orbits in a focusing deflecting field can be expressed in the above curvilinear coordinate system by relatively simple equations if the principal ray representing the curvilinear axis coincides with an equipotential line. In this case, the potential field about the ζ-axis which can be derived from Laplace's equation can be developed as a power series, and the equations of motions are obtained from Fermat's principle. Marschall (1944) and Hachenberg (1948) presented these equations in terms of the two radii of curvature r and ρ of the equipotential surface half-way between the condenser plates. They obtained the following pair of equations for an electron orbit:

$$\left.\begin{aligned} \frac{\mathrm{d}^2\xi}{\mathrm{d}\zeta^2} + \frac{1}{r\rho}\,\xi &= 0, \\ \frac{\mathrm{d}^2\eta}{\mathrm{d}\zeta^2} + \left(\frac{2}{r^2} - \frac{1}{r\rho}\right)\eta &= 0. \end{aligned}\right\} \tag{11.31}$$

For example, for the cylinder condenser one radius is infinite ($\rho = \infty$), hence (11.31) are reduced to the following simple form

$$\left.\begin{aligned} \frac{\mathrm{d}^2\xi}{\mathrm{d}\zeta^2} &= 0 \\ \text{and} \qquad \frac{\mathrm{d}^2\eta}{\mathrm{d}\zeta^2} + \frac{2\eta}{r^2} &= 0, \end{aligned}\right\} \tag{11.32}$$

which by integration yield

$$\begin{aligned} \xi &= A\zeta + B, \\ \eta &= C\sin\left(\frac{\sqrt{2}}{r}\zeta\right) + D\cos\left(\frac{\sqrt{2}}{r}\zeta\right). \end{aligned} \tag{11.33}$$

This result confirms that an electron beam in the cylinder condenser is not influenced in the ξ-direction but only in the η-direction, i.e. in the direction of its deflexion (one-directional focusing). The solution for η is periodical, and the rays starting from a point on the ζ-axis return to the ζ-axis after the argument $\left(\frac{\sqrt{2}}{r}\zeta\right) = \pi$ of the sine or the cosine function respectively. Hence, the points of intersection are spaced by a distance ζ given by $\phi_0 = \zeta/r = \pi/\sqrt{2}$ in agreement with (11.29), where ϕ_0 is the angle of deflexion. Moreover, if (11.33) are applied to a cylinder condenser of finite length subtending the arbitrary centre angle ϕ, the following expression can be derived for the focal length of this sector:

$$f = \frac{r}{\sqrt{2}} \frac{1}{\sin(\phi\sqrt{2})}. \tag{11.34}$$

Hence f is found to be a function of the geometry of the condenser.

The electron-optical properties of the spherical condenser can be derived from (11.31) by introducing $\rho = r$. There periodical solutions result both for ξ and η, i.e. two-directional focusing is obtained.

Quite generally, the focusing properties of all double-curved condensers can be derived from (11.31). Positive coefficients of both ξ and η in (11.31) which are obtained, either with $r > 0$ and $(\frac{1}{2}r) < \rho < \infty$, or with $r < 0$ and $(\frac{1}{2}r) > \rho > -\infty$, lead to periodical solutions composed of the sum of two trigonometric functions.

Hence, the corresponding field not only deflects but also converges the bundle of rays. On the other hand, negative coefficients of ξ or of η in (11.31) lead to solutions with hyperbolic functions; consequently the distance of a ray from the ζ-axis should increase all the time. Hence the corresponding field diverges the deflected rays in one direction. In particular, systems with a relatively small positive ρ within the boundaries $0 < \rho < \frac{1}{2}r$ still converge the rays in the ξ-direction, but they diverge them in the η-direction. Examples of this class are given by some toroidal ring condensers; there ρ is small in comparison with the radius r of the electron orbit. On the other hand, all systems with negative ρ have diverging action in the ξ-direction but converging action in the η-direction.

Amongst all deflecting condensers, the spherical one only appears to produce a faithful optical image. If, however, no geometrical similarity is required, point-by-point projection can still be obtained by any two-directional focusing deflexion. Such a point projection is achieved sometimes after a relatively long orbit subtending a large centre angle since the rays generally first pass through an intermediate line-shaped cross-over before they are focused eventually into a point.

A great variety of deflecting fields (amongst them some with diverging action) can be employed in combination with electron lenses of circular symmetry. Again, some of these combinations lead to a final point-by-point projection via an astigmatic intermediate image. For example, rays diverging from an object point may be collected by an electron lens in order to enter the deflecting field as a convergent bundle. An astigmatic intermediate image is formed in the deflecting field, while a second lens arranged in the field-free space after the deflexion is used for projecting the image point on to a distant target. An application of this scheme to electron spectrometry will be discussed in § 12.7.

11.6. Focusing deflexion in magnetic fields

So far, the most important method for electron spectrometry has been the well-known method of semicircular focusing deflexion in the homogeneous magnetic field. Magnetic deflexion in a semicircle has been utilized for a long time. We only mention the experimental investigations by Meyer and Schweidler (1899), by Classen

(1908) and by Danysz (1911). However, Rutherford, Robinson and Rawlinson (1914) first fully realized the focusing effects of the semicircular deflexion. In fig. 11.11, J represents a linear source of electrons which extends at right angles to the plane of the drawing. S is the intensity stop. The foci J'_1, J'_2, ... of electron beams of various velocities all lie on a straight line along which may be placed a photographic plate or a fluorescent screen PP. Let the distances of the images J' from the centre of the slot S be $SJ' = s$. If the plate PP is arranged at right angles to $JS = c$, the hypotenuses JJ'_1, JJ'_2, etc., are the diameters of the semicircular orbits given by

$$(2r_e)^2 = s^2 + c^2, \tag{11.35}$$

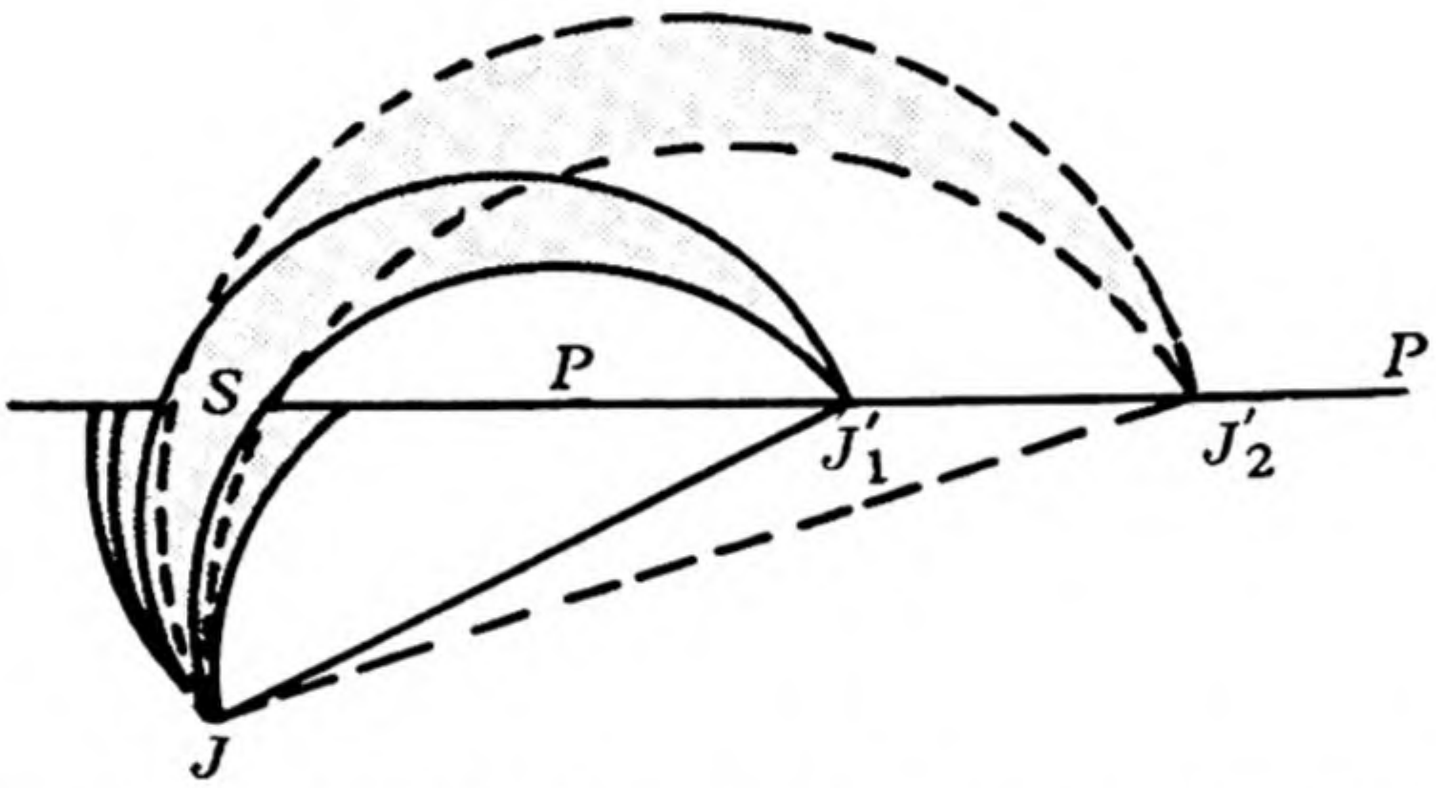

Fig. 11.11. Focusing deflexion in a homogeneous magnetic field.

from which the electron momentum $B_e r_e$ of the rays focused into a line at J' can be determined if the flux density B_e of the homogeneous magnetic deflecting field is known.

The need for focusing deflexion of particles with relatively large momenta by magnetic fields of limited flux density which originally arose in atomic mass spectroscopy, led to the investigation of the properties of bounded fields. Barber (1933) and Stephens (1934) recognized the focusing properties of a homogeneous magnetic field confined within a triangular cross-section in a plane at right angles to the field lines. Such a field, which may be called a 'magnetic prism', is produced—to some approximation—between closely spaced pole-pieces of triangular cross-section. The focusing deflexion by such a prism is shown in fig. 11.12 (*a*). The prism is enclosed between the two planes S and S' intersecting at the angle ϕ and extending perpendicularly to the plane of the drawing. A narrow wedge-shaped electron beam is emitted from a line-shaped source

or from a slot J which extends parallel to the field lines but is situated in the field-free space. The chief ray of this beam enters and leaves the field at right angles to the boundary planes. All rays travel through the field along relatively short circular arcs. The focusing effect of the prism is apparent from the drawing which shows that the outer rays stay longer in the field than the inner rays. Barber calculated that rays of equal velocity are focused into a line image at J', so that J, J' and the apex M_0 of the prism lie on a straight line (the z-axis in fig. 11.12 (a)). The angle ϕ enclosed between the

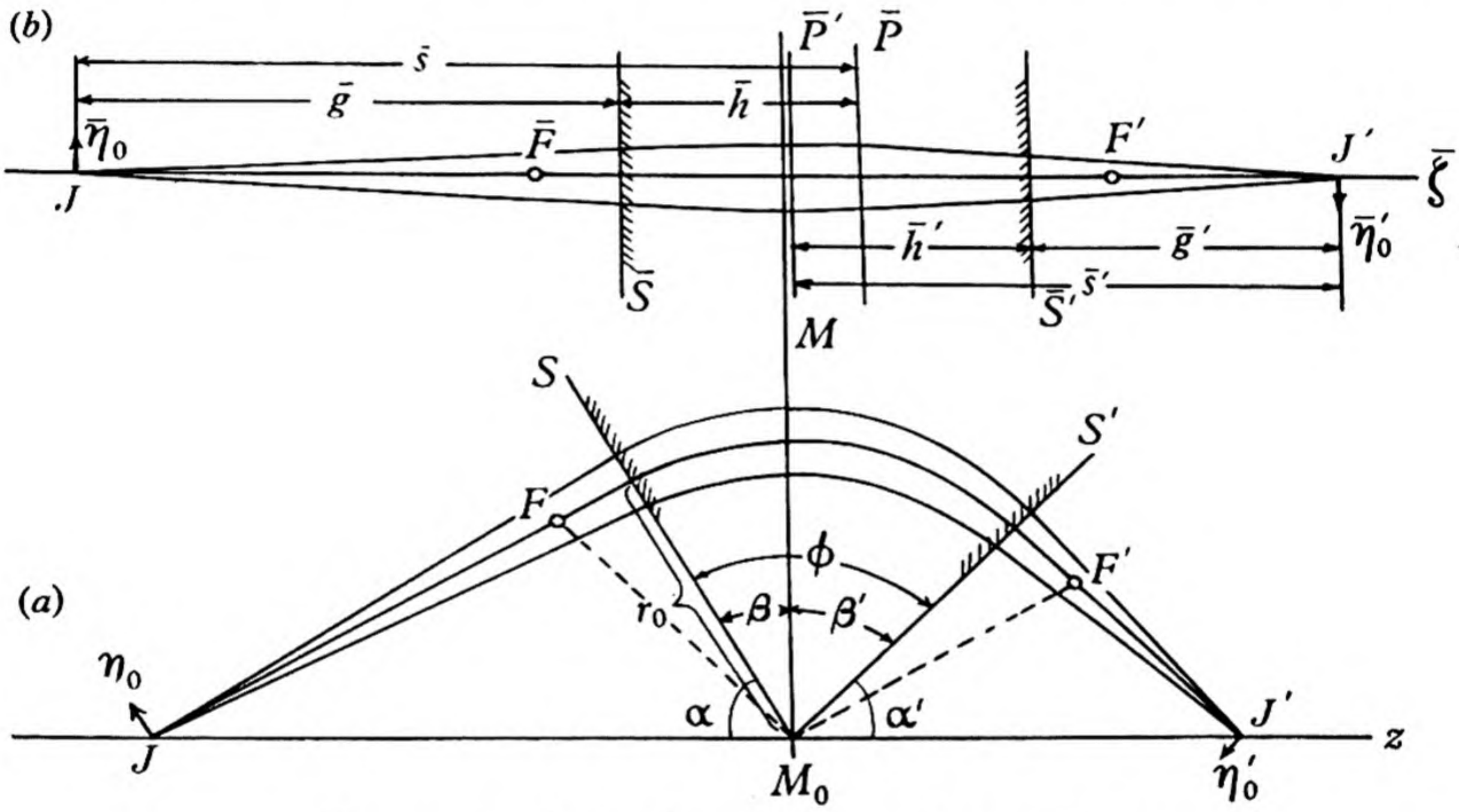

Fig. 11.12. Image formation by a homogeneous magnetic sector field.

field boundaries is also the angle of deflexion of the beam, and this angle ϕ may have any value up to 180°. For $\phi = \pi$ the focusing deflexion is again semicircular. Another interesting case arises if $\phi = \frac{1}{2}\pi$. There, electrons starting from an x-line focus situated at one of the field boundaries will leave the other boundary as a parallel bundle.

There are obvious advantages in deriving electron optical properties of the focusing deflexion in homogeneous magnetic fields with the aid of curvilinear coordinates. An elementary treatment due to Walcher (1949) may be followed up here. As shown in fig. 11.13, a bundle of electrons with homogeneous velocity may be characterized by three circular orbits. The principal orbit crosses

the z-axis at right angles at the object point J_0 and again at the image point J_0'. The two 'zonal' orbits (1) and (2) each make a small angle Θ with the principal orbit while passing through J_0. All orbits are strictly perpendicular to the magnetic flux which crosses the plane of the drawing at right angles.

The loci for the centres of the various circular orbits are on a circle of radius r_e about J_0. Now, draw a radius $r_e = J_0 C_2$ of this circle

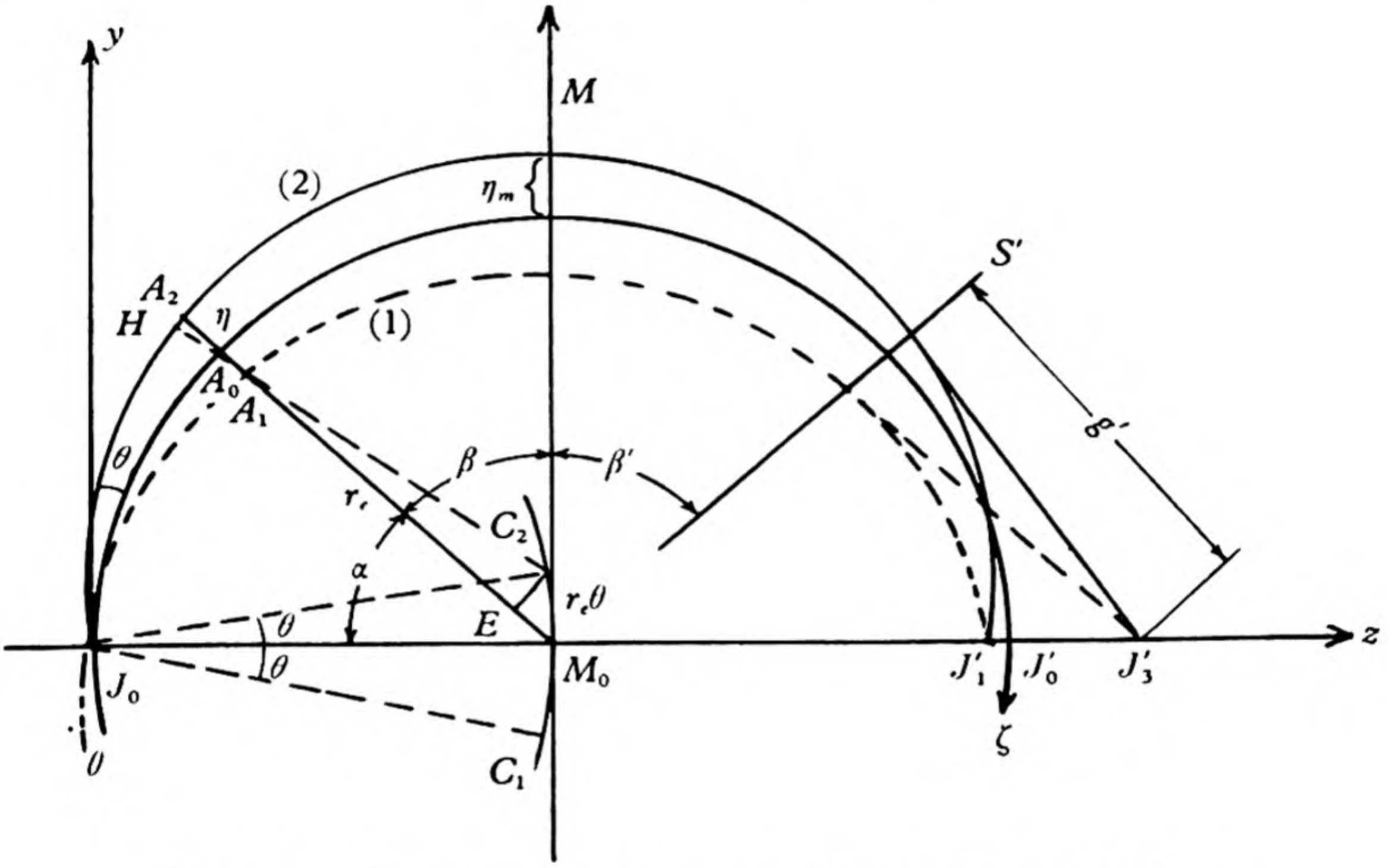

Fig. 11.13. Homogeneous magnetic field as a line-focus lens in a curvilinear coordinate system.

to make the angle Θ with the z-axis. The arc $C_2 M_0$ of this circle (M_0 is the centre of the principal orbit) has the length $r_e\Theta$. If the perpendicular $C_2 E$ is dropped from C_2 on a radius vector $M_0 A_0$ of the principal orbit, it will cut a length $M_0 E \approx r_e \Theta \sin\alpha$ from the radius vector, where α is the angle between the radius vector $M_0 A_0$ and the z-axis. On the other hand, the distance $\eta = A_0 A_2$ between the principal orbit and the zonal orbit (2) (measured along the radius vector $M_0 A_0$) equals very approximately $M_0 E$, since the radius $C_2 H$ of orbit (2) equals the radius $M_0 A_0$ of the normal orbit. Hence, the distance between the two orbits is

$$\eta = r_e \Theta \sin\alpha = r_e \Theta \sin\frac{\zeta}{r_e}, \tag{11.36}$$

where ζ is the length of the arc of the principal orbit between J_0 and A_0. If the values of the curvilinear coordinates (η, ζ) of (11.36) are plotted in a Cartesian system $(\bar{\eta}, \bar{\zeta})$, the zonal rays would appear as simple sine curves, and the principal orbit would coincide with a straight optical axis $(\bar{\zeta})$ of the refracting system.

Returning to the curvilinear system it is clear that the distance η of the zonal orbit from the ζ-axis reaches a maximum η_m at a 'mid-plane' M_0M which intersects the z-axis at M_0. Since all orbits are parallel at the mid-plane, the arc length ζ between J_0 and M represents the focal length f of an optical system. This system is the homogeneous magnetic field enclosed within a rectangular sector between the mid-plane M_0M and the xz-plane.

It may be shown now that any sector field enclosed between two planes intersecting at the vertex M_0 and being perpendicular to the plane of the drawing of fig. 11.13 can act as a line-focus lens. In particular, it can be shown that a field sector is able to project an electron-optical image near the z-axis for any object near the z-axis. Let the homogeneous field in fig. 11.13 be terminated by any sector plane S'. After passing this boundary the rays will travel along straight lines through the field-free space, and they will cross over at J_3' in the zx-plane. Now, the semi-aperture η' of a zonal ray at the sector plane S' may be represented as a function of the angle β' between mid-plane M and sector plane S'. For this purpose, $\alpha = (\beta' + \frac{1}{2}\pi)$ may be substituted into (11.36). Using η_m for the maximum η-value at $\alpha = \frac{1}{2}\pi$ (11.36) yields

$$\eta' = \eta_m \sin \frac{\zeta}{r_e} = \eta_m \cos \beta'. \tag{11.37}$$

The slope of the zonal ray with respect to the principal ray when leaving the S'-plane is obtained by differentiating (11.37), namely,

$$-\tan \Theta' = \left(\frac{\mathrm{d}\eta'}{\mathrm{d}\zeta}\right)_{r_e, \beta'} = \left(\frac{\eta_m}{r_e}\right) \cos\left(\frac{\zeta}{r_e}\right) = \left(\frac{\eta_m}{r_e}\right)(-\sin \beta'). \tag{11.38}$$

On the other hand, it is evident from fig. 11.13 that the angular semi-aperture Θ' is also given by the relation

$$\tan \Theta' = \eta'/g', \tag{11.38a}$$

where g' is the distance of the image J_3' from the S'-plane. Substituting for η' from (11.37) and for $\tan\Theta'$ from (11.38), the following relation results from (11.38a)

$$g' = r_e \cot\beta', \tag{11.39}$$

i.e. the distance of the focus J_3 from the sector plane S' is independent of the beam aperture (η' or Θ'), and it depends only on the sector angle β' and the electron momentum given by r_e.

In Gaussian optics the focal length f' is defined (cf. Chapter II) by

$$f' = {}^{\circ}\eta_m/\tan\Theta', \tag{11.40}$$

and by substituting for $\tan\Theta'$ from (11.38) one obtains

$$f' = r_e/\sin\beta'. \tag{11.41}$$

The position of the principal plane P' is defined by this value of f'. Hence the distance of P' from the sector boundary S' is obtained by subtraction of (11.39) from (11.41), namely,

$$h' = f' - g' = r_e \tan\tfrac{1}{2}\beta'. \tag{11.42}$$

In a similar way focus and principal plane can be determined for parallel rays moving through the mid-plane in the opposite direction in a sector field terminated by a plane S making an angle β with the mid-plane M.

Now, formulae (11.39)–(11.42) which apply to a field sector with the vertical angle β' between the mid-plane M and the boundary S' will also apply to a sector with the vertical angle ϕ between the boundaries S and S'. In this sector the angular position of the mid-plane where all orbits are parallel and where $\eta = \eta_m$ is defined by the position of the object J, the straight line joining object and sector vertex being the z-axis which has to be normal to the mid-plane. If $s = JP$ and $s' = J'P'$ are the distances of object J and image J' from their respective principal planes P and P', all measured along the principal ray representing the ζ-axis of the curvilinear system, then the well-known lens equation (cf. (2.5)) $(f/s)+(f'/s') = 1$ can be applied for finding the position of the image J'.

The analogy to the ordinary lens optics, however, goes still further. If the object extends perpendicularly to the ζ-axis along

the η-coordinate to a height η_0, the height of the image η_0 is determined by the usual relation for the magnification, viz. $\eta_0'/\eta_0 = s/s'$. All these relationships are well illustrated if the curvilinear system (ζ, η) is transformed into the Cartesian system $(\bar{\zeta}, \bar{\eta})$ as shown in fig. 11.12(*b*).

Besides the magnetic field sectors which have been discussed so far, a great variety of bounded homogeneous fields is suitable for an electron-optical line-focus projection. For instance, homogeneous magnetic fields bounded by a circular cylindrical surface, the flux being parallel to the cylinder axis, have been used, for example, in Aston's mass spectrograph and in an electron spectrometer by Klemperer (1935). Such fields can be produced to some approximation, for instance, between closely spaced co-axial cylindrical pole-pieces of circular cross-section (cf. for instance the magnet shown in fig. 11.6). The focusing properties of these fields have been discussed by Siday (1947), by Jennings (1950, 1952) and by Ehrenberg and Jennings (1952). These authors found that a relatively sharp line focus parallel to the cylinder axis is formed by 'paraxial rays', i.e. by rays of an initial small (perpendicular) distance from the cylinder axis. The angle of deflexion ϕ and the focal length f in the yz-plane (perpendicular to the cylinder axis) are given by

$$\tan \tfrac{1}{2}\phi = R/r_e \qquad (11.43)$$

and

$$f = \frac{R^2 + r_e^2}{2R}, \qquad (11.44)$$

where R is the radius of the circular cross-section of the field boundary and r_e is the radius of curvature of the electron orbit in the field as obtained from the electron momentum $(B_e r_e)$ of the deflected electron ray. The principal points may be taken to coincide with the centre of the circular field boundary. The ordinary lens formulae of Chapter II are found to apply to object and image distance and to magnification.

The focal length of the homogeneous field with circular boundaries decreases, according to (11.43) and (11.44), inversely with the angle of deflexion. This is shown by the following table:

f/R	13·0	1·95	1·22	1·00	0·82	0·54
ϕ	23°	60°	80°	90°	102°	146°

It can be seen that initially parallel rays are focused outside the field boundary if $\phi < 90°$, but inside it if $\phi > 90°$. Of particular interest is the deflexion through 90°. There, initially parallel rays are focused on the periphery of the field of circular cross-section. This latter case has been studied by Korsunsky (1945), who made use of it in the design of his 'four-pole spectrometer'. This consists of two magnets each having two closely spaced pole-pieces of circular cross-section. There are two deflexions through 90°. In the first deflexion, rays of given velocity emitted from a point-source are made parallel; in the second deflexion, the parallel rays are reunited in a point image.

If the chief ray of an incident bundle is initially not directed towards the centre of the circular homogeneous field, focal length and deflexion will differ from the values given by (11.43) and (11.44). For instance, a bundle travelling at the convex side of, and near to the central bundle will suffer greater deflexion and it will be subject to shorter focal length than the bundle travelling at the concave side of it, since the focusing and deflecting power of a homogeneous field increases with increasing path length of the beam in the field. Also, the principal planes of the field for the eccentric bundles no longer coincide with the field centre; they are now located at the feet of the perpendiculars from the field centre to the straight continuation of the rectilinear part of the incident and of the emergent chief ray respectively.

The ideal case of the homogeneous field with circular boundaries can of course only be approximated experimentally. If the gap between the pole-pieces is not kept very small in comparison with their radius, the field in the gap becomes inhomogeneous and the effect of fringing fields can no longer be neglected. Details about the orbits in the mid-plane between two plane-faced, circular pole-pieces spaced by one radius have been given by Siday (1947). Electron orbits between the end-faces of two long coaxial solenoids at various mutual distances have been studied by Jennings (1950, 1952). We shall come back to these particular cases at the discussion of focusing errors in § 11.9.

Electron deflexion in inhomogeneous fields of a simple symmetry can sometimes conveniently be treated by analytical methods. In this manner, Coggeshall and Muscat (1944), for instance,

obtained the electron orbits by integration of the equations of motion. They investigated two-dimensional fields varying linearly or exponentially with one Cartesian (or radial) coordinate.

Of much practical importance are circular-symmetrical fields which, in their equatorial plane, are characterized by the relation

$$\frac{B}{B_0} = \left(\frac{r_0}{r}\right)^n, \tag{11.45}$$

where B_0 is the flux density at a distance $r = r_0$ from the axis and where n is the 'magnetic field index' which indicates how rapidly the field decays with increasing distance from the axis. With $n = 3$, for instance, (11.45) describes the rapidly decaying field of a magnetic dipole (Henneberg, 1934*c*), and the study of electron orbits in this dipole field has played an important part in the investigation of the aurora borealis (Störmer, 1933; Brüche, 1930) and in cosmic-ray research (Johnson, 1938).

Slowly decaying fields of an index $n \approx \frac{1}{2}$ show important focusing properties which have been utilized for the stabilization of electron orbits in electron accelerators (cf. § 12.8). In particular, the 'two-directional' focusing by such fields has found application in a most promising type of beta-ray spectrometer, introduced by Siegbahn and Swartholm (1946*a*, *b*).

Two-directional deflexion-focusing may be explained here by considering the free oscillations of electron orbits about a line of constant field intensity. Such oscillations are well known from the study of orbital stability conditions established by Kerst and Serber (1941) for their betatron accelerator (cf. § 12.8). Equilibrium between the centrifugal force and the constraint by the magnetic field (cf. § 5.1) will lead to a stable electron orbit provided the flux B_1 along this orbit and its radius r_1 are connected by the relation

$$e\omega_L B_1 = m r_1 \omega_L^2, \tag{11.46}$$

where ω_L is the orbital frequency (cf. (5.2)). If an electron, moving in an inhomogeneous field $B(r)$ of circular symmetry, is to be restored to an equilibrium orbit, when displaced radially, the magnetic force $e\omega_L B$ should become larger than the centrifugal force for larger radii, and for smaller radii the converse should hold. Hence it is required that

$$\frac{\mathrm{d}B}{\mathrm{d}r} = -\left(\frac{B}{r}\right) n, \tag{11.47}$$

where n is again the magnetic field index. (11.47) is the differential equivalent to (11.45). According to (11.47) the field index should be smaller than unity ($n < 1$) if the field is expected to decrease more slowly than with $1/r$.

For all positive values of n the magnetic field deflects the electron trajectories towards the equatorial mid-plane. This can be shown in the following way: For homogeneous fields ($n = 0$) the boundaries of flux tubes are given by straight lines in the meridional planes. If the field, with increasing distance from the axis, decreases in the mid-plane, the cross-section of the flux tubes will increase correspondingly due to the principle of conservation of flux (cf. § 3.1). Hence, the flux lines in the meridional planes will become increasingly concave towards the axis as their distance from the axis increases. By this curvature of flux lines, however, all electrons with velocity components in equatorial planes are accelerated towards the mid-plane, since the Lorentz force always acts at right angles to the momentum of the electron and to the tangent of the flux line.

It follows that the restoring forces will set up oscillations about a principal orbit if

$$0 < n < 1. \tag{11.48}$$

Kerst and Serber (1941) calculated the angular frequencies of these radial and axial oscillations of the orbits to be

$$\left.\begin{aligned} \omega_r &= \omega_L (1-n)^{\frac{1}{2}} \\ \text{and} \qquad \omega_a &= \omega_L n^{\frac{1}{2}}, \end{aligned}\right\} \tag{11.49}$$

respectively, where ω_L is again, as in (11.46), the orbital (Larmor) frequency. It is clear that if $n = \frac{1}{2}$, the radial and axial frequencies are equal. Thus, electrons diverging from a point source in such a magnetic field will take up their oscillations and will pass through a second point on the equilibrium orbit after half an oscillation period. Since both the axial and the radial frequencies are by a factor $1/\sqrt{2}$ smaller than the orbital frequency ($= 2\pi$), it is clear that this second or 'image' point will be at an angular distance of $\pi\sqrt{2} = 254{\cdot}56°$ from the first object point.

Equation (11.45) can be expanded to the following form:

$$\frac{B}{B_0} = 1 - C_1\left(\frac{r-r_0}{r_0}\right) + C_2\left(\frac{r-r_0}{r}\right)^2. \tag{11.50}$$

For instance, when $n = \frac{1}{2}$, then $C_1 = \frac{1}{2}$, $C_2 = \frac{3}{8}$. Shull and Dennison (1947) pointed out that if for purposes of practical design C_1 and C_2 are considered as adjustable constants, for high-quality focusing C_1 is found to be necessarily $= \frac{1}{2}$, but C_2 is free to take a certain range of values. $C_2 = \frac{1}{4}$, for instance, gives an image of minimum size; however, with the view to keeping the gap between the pole-pieces short so that the deleterious effects of fringing fields are avoided as far as possible, a practical value of $C_2 \approx 8$ might be more convenient.

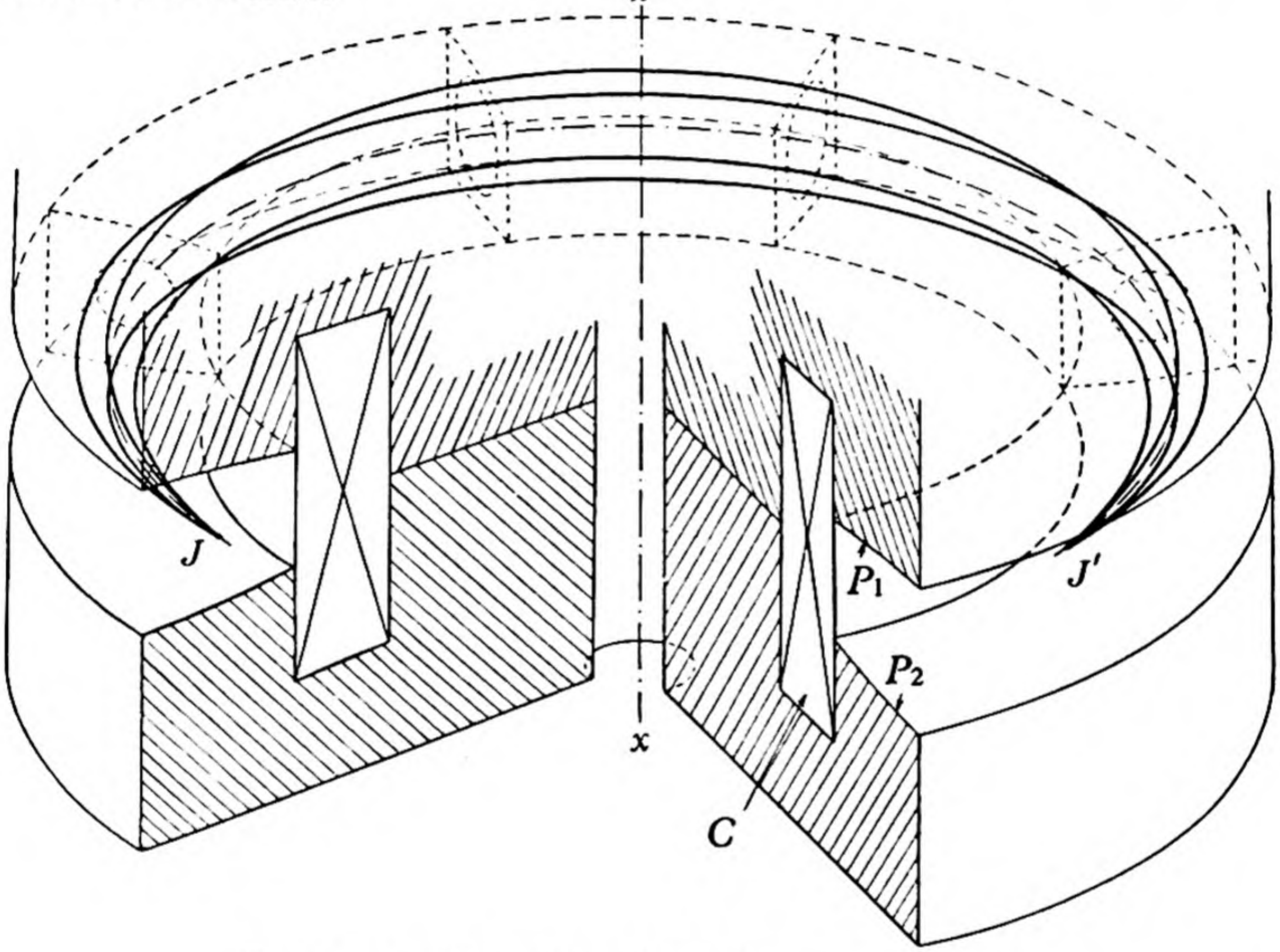

Fig. 11.14. Two-directional focusing deflexion.

Two-directional focusing fields as described by (11.50) can be produced between specially shaped pole-pieces. For example, the deflexion magnet of Siegbahn and Swartholm (1946*b*) is shown in fig. 11.14. The annular magnet M, which for sake of clarity is drawn cut open, shows circular symmetry about the x-axis. It is energized by the current coil C. The deflexion field is produced in the ring-shaped outer gap between the pole-pieces P_1 and P_2. The profiles of these pole-pieces were ground step by step to an approximately parabolic shape until the optimum focusing was obtained. In fig. 11.14 a small bundle of rays emitted from the point source J is shown to be focused in the image point J'.

Sharp line images with a fair degree of two-directional focusing can, according to an analysis by Richardson (1947), still be obtained in fields decaying inversely with the distance from the axis, i.e. fields represented by (11.45) with $n = 1$. Such fields can be approximately generated in a relatively simple way, e.g. between a pair of inclined, plane pole faces. In practice, the inclined pole-pieces are bevelled so as to become parallel at their closest approach. The electrons move in trochoidal orbits, with the principal ray being in the median plane between the pole-pieces.

A high degree of two-directional focusing over relatively large solid angles is obtained when the surfaces of the pole-pieces of the magnet are hyperboloids of revolution (Richardson, 1949). The magnetic lines of force are confocal ellipses. The electron source has to be arranged near one of the pole-pieces on the axis of revolution (e.g. a wire along the axis), and the image is formed on the axis near the other pole-piece. According to results by Braid and Richardson (1951) a conical sheaf of rays emitted at about 80° to the field axis within a solid angle of 1·4 % of 4π is focused practically into a point image.

It has been shown in the discussion of the focusing deflexion by a homogeneous magnetic field that a sector of the field is sufficient for the projection of a deflected electron image. The same can be shown to apply for axially symmetric fields of any field index $n \geqslant 0$. In every case, object point, vertex of the field sector and image point lie on a straight line as in fig. 11.12(*a*). Moreover, (11.39), (11.41) and (11.42), which define the location of the cardinal points for a homogeneous field ($n = 0$), can be generalized to apply for all field indices $n \geqslant 0$. Generally the location of foci F principal points P and images J will be different for the focusing in radial η-direction and axial ξ-direction. General formulae derived by Judd (1950) giving the location of these points with respect to the field boundary (S) of a field sector with vertical angle ϕ (cf. fig. 11.12(*a*)) may be quoted as follows:

$$PF = f_\xi = \frac{r_e}{\sqrt{n}} \frac{1}{\sin(\phi\sqrt{n})}, \tag{11.51}$$

$$SP = h_\xi = \frac{r_e}{\sqrt{n}} \tan\left(\frac{\phi}{2}\sqrt{n}\right), \tag{11.52}$$

$$SJ = g_\xi = \frac{r_e}{\sqrt{n}} \tan\alpha. \tag{11.53}$$

These formulae apply for the focusing in the axial ($\xi-$)-direction. For the focusing in the radial ($\eta-$)-direction, the corresponding quantities f_η, h_η, g_η are obtained by replacing $\sqrt{n}$ by $\sqrt{(1-n)}$. Radial and axial focus again coincide for $n=\frac{1}{2}$. As another special case, one-directional focusing occurs for $n=0$, where the expressions for g_η, h_η and f_η coincide with (11.39), (11.41) and (11.42) respectively.

The technical problem of shaping the pole-pieces of a magnet to produce an axially symmetrical field sector of a given field index is not easy. However, if only approximate focusing is required, the proper shape of pole-pieces may be approximated by conical surfaces or even by plane end-faces, spaced at a given distance and tilted towards the mid-plane at a given angle. According to Swartholm (1950) a flux distribution

$$B = B_0 \frac{2r_0}{r+r_0} \tag{11.54}$$

can be produced by high-permeability pole-pieces with conical surfaces given in cylindrical coordinates by the equation

$$2x = \frac{x_0}{r_0}(r+r_0), \tag{11.55}$$

where $2x$ is the pole-piece distance as a function of the radial distance r from the vertex. Such pole-pieces have found satisfactory application, for instance, in velocity analysers. Focusing errors due to the deviation of the actual shape of the pole faces from their theoretically exact form seem to be comparable in magnitude with the focusing errors produced by fringing fields (cf. § 11.9).

11.7. Superposition of electrostatic and magnetic fields

The path of an electron subjected to the combined action of both electrostatic and magnetic fields is generally quite complex. However, some relatively simple cases which have obtained practical importance may be discussed in this section.

If an electron of given velocity u_0 is injected into combined homogeneous electrostatic and magnetic fields which are crossed at right angles and which are also perpendicular to the initial motion of the electron, a certain ratio of the two field strengths can be found for which the electron is not deflected in its path. In this case the

electrostatic and magnetic forces acting upon the electron must be equal and opposite, the total force $F = 0$ and (1.21) yields

$$\frac{E_y}{B_z} = (u_0)_x. \tag{11.56}$$

This straight motion of the electron is utilized for sorting electron velocities in the well-known 'velocity filter' of Wien (1898).

If an electron starts from rest in the homogeneous fields $E = -E_y$, $B = -B_z$ which are crossed at right angles, it is first accelerated by the electrostatic field but it is unaffected by the magnetic field since it has no velocity. As it gathers speed, it is deflected by the magnetic field, being gradually turned round until it moves against the electrostatic acceleration and eventually comes to rest at some distance x_L from its initial position. The net motion of the electron is a drift in the x-direction. The electron orbit can be obtained from the equations of motion:

$$m\frac{\mathrm{d}^2y}{\mathrm{d}t^2} = -eE - eBu_x, \tag{11.57}$$

$$m\frac{\mathrm{d}^2x}{\mathrm{d}t^2} = eBu_y, \tag{11.58}$$

with the initial conditions that the coordinates x, y, z of the electron and their derivatives u_x, u_y, u_z are zero for $t = 0$. Integrating (11.58) yields

$$\frac{\mathrm{d}x}{\mathrm{d}t} = \omega y, \tag{11.59}$$

where $\omega = \omega_L = (e/m)\,B$ is the Larmor frequency (cf. Chapter V) of the electron in the homogeneous field. Substituting from (11.59) into (11.57) leads to

$$\frac{\mathrm{d}^2y}{\mathrm{d}t^2} = -\left(\frac{e}{m}E + \omega^2 y\right). \tag{11.60}$$

A solution of this linear differential equation by standard methods yields

$$y = -\frac{e}{m}\frac{E}{\omega^2}(1 - \cos\omega t). \tag{11.61}$$

By integration of (11.59) and combination with (11.61) we obtain

$$x = -\frac{e}{m}\frac{E}{\omega^2}(\omega t - \sin\omega t). \tag{11.62}$$

(11.61) together with (11.62) represent a cycloid orbit in parametric form. The electron motion is seen to consist of a uniform

translation in x-direction with a superimposed circular motion. The radius of this circular motion is half the maximum displacement in the y-direction which, according to (11.61) is,

$$\tfrac{1}{2}y_{\max.} = r_0 = \frac{e}{m}\frac{E}{\omega^2} = 7{\cdot}0 \times 10^{-10}\frac{E}{B^2}. \qquad (11.63)$$

The displacement in the x-direction corresponding to one cycle of the motion is

$$x_L = 2\pi r_0. \qquad (11.64)$$

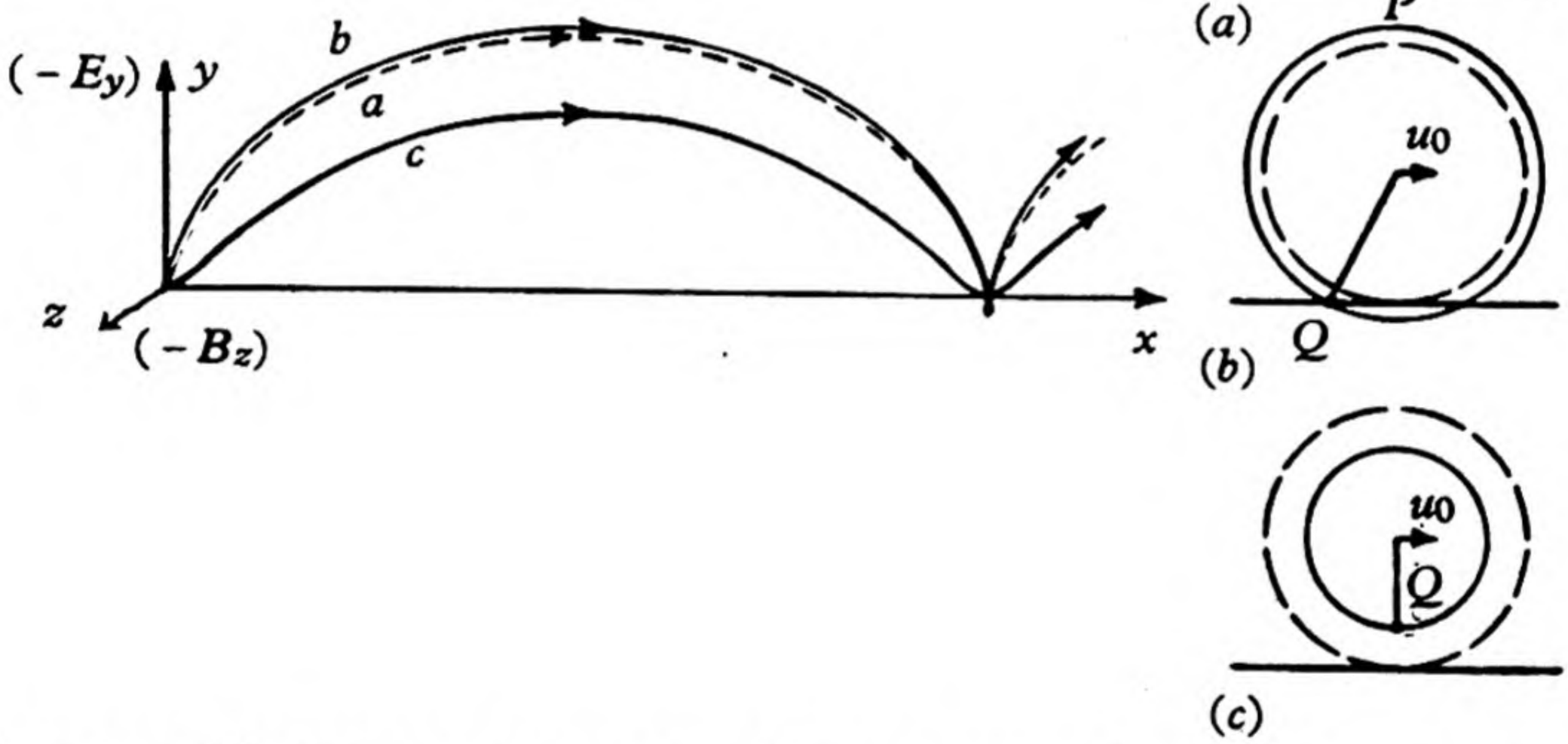

Fig. 11.15. Electron orbits in crosssed homogeneous electrostatic and magnetic fields: (*a*) for zero initial velocity; (*b*) for initial velocity in the y-direction; (*c*) for initial velocity in the x-direction.

The cycloidal path of the electron is shown in fig. 11.15(*a*). It is described by a point P on the rim of a wheel rolling on the x-axis with the forward velocity

$$u_0 = r_0\omega = \frac{E}{B}. \qquad (11.65)$$

We now consider the case in which the electron does not start with zero velocity but is injected into the crossed fields $(-E_y, -B_z)$ with some initial velocity in the xy-plane. An integration of (11.57) and of (11.58) with the initial coordinates are $x = 0$, $y = 0$, $z = 0$ and with the initial velocity component $u_z = 0$ but with u_x and u_y having given, finite values, leads to the parametric representation of trochoid orbits such as are shown by the curves (*b*) and (*c*) in

fig. 11.15. Such curves can be generated if the rim of a wheel of radius r_0 given by (11.63) is rolling on the x-axis with a uniform forward velocity u_0 given by (11.65). The electron orbit is such as described by a point Q (see fig. 11.15) on a spoke of the wheel a distance r_Q from the centre. r_Q can be either larger or smaller than r_0 of (11.63), giving rise to the two types of trochoid shown in the figure. The ratio of r_0/r_Q essentially depends upon the relative magnitudes of the initial components u_x and u_y and of the forward velocity u_0 of the rolling wheel, and it can be calculated to be

$$\frac{r_Q}{r_0} = \frac{1}{u_0}[(u_x - u_0)^2 + u_y^2]^{\frac{1}{2}}. \tag{11.66}$$

The deflexion of electrons in crossed homogeneous magnetic and electric fields has found various applications in the past. It had been used very early by J. J. Thomson (1897) to measure the velocity of cathode rays preliminary to the determination of the specific charge of the electron. As another historically interesting application of the crossed fields, we mention the electron deflexion in the early electron multipliers by Zworykin, Morton and Malter (1936). There, electrons leaving a plane photocathode are accelerated by an electric field perpendicular to it but are turned back by a superimposed homogeneous magnetic field until they reach a target electrode in the plane of the cathode. Secondary electrons are released from this target, are deflected to a next target in the plane of the cathode and so on.

Of some technical importance is the deflexion of electrons entering crossed homogeneous electrostatic and magnetic fields (E_y, B_z) with a velocity u_z in the direction of the magnetic flux only. It can be shown that an electron will travel through the flux in a slanting direction while performing a certain number n of loops, given by

$$2\pi n = \frac{\omega_L L}{u_z}, \tag{11.67}$$

where ω_L is again the Larmor frequency in the flux density B_z, and L is the length of the electrostatic field as given, for instance, by the length of the deflexion condenser plates. Rose and Iams (1939) have shown that the deflexion will eventually not lead to a change in direction u_z but just to a shifting of the electron beam in the x-direc-

tion if the values of u_z and of ω_L are such that an integral number n of loops is performed during the traversal of the crossed fields. The displacement in the x-direction is proportional to the electrostatic field E_y, and it amounts to nx_L where x_L has the value given by (11.64). By a reversal of the direction of the electrostatic field, the direction of the displacement will also be reversed.

The displacement of electron beams by crossed fields has found practical application for the scanning of the cathode ray in a slow-electron television pick-up tube called the 'Orthicon', described later in § 12.5. A practical difficulty in effecting pure displacement is given by the fringing fields of the scanning condenser. Rose (1940*a*, *b*), however, solved the problem by properly curving the edges of the condenser plates (cf. fig. 12.3*a*).

Of great practical interest is a field combination called the 'magnetron field'. It consists of an electrostatic field between two coaxial cylinders, the smaller cylinder being the cathode, the larger, the anode; parallel to the cylinder axis extends a homogeneous magnetic flux. Electrons move from the cathode in cardioid-like orbits returning again to the cathode with zero velocity, provided that the orbits are not intercepted by the anode cylinder. The analysis of the orbits has been given by Hull (1921). For small cathode radii, the orbits are represented by

$$r = r_{\max.}\left(\sin\frac{2\Theta}{3}\right), \tag{11.68}$$

where r and Θ are cylindrical coordinates, $r_{\max.}$, the maximum elongation from the axis, being given by

$$r_{\max.} = \frac{1}{B}\sqrt{\left(\frac{8e}{m}V\right)}, \tag{11.69}$$

where V is the electric potential at the distance $r_{\max.}$ from the axis. The curve representing (11.69) is called the 'cut-off parabola', since in a given flux density B the total electric current to an anode of radius $r_{\max.}$ would be cut off as soon as the anode voltage dropped below the value of V.

We have to refrain here from giving more details about the electron motion in the combined fields. We can only quote the treatment of electron motion in superimposed cylindrical electrostatic

and magnetic fields by Rose (1940*a*). Further reference should be made to a paper by Coggeshall (1946) who has integrated the equations of motion for electrons in homogeneous magnetic fields which were superimposed, for example, to the following types of simple inhomogeneous electrostatic fields:

$$E = \text{const. } z,$$
$$E = \text{const. } z^2,$$
$$E = \text{const. } r,$$
$$E = \text{const.}/r,$$

where z and r are a Cartesian and a cylindrical coordinate respectively.

The possibility of a focusing deflexion in superimposed electrostatic and magnetic fields was first observed experimentally by Bartky and Dempster (1929). They used the electrostatic field between coaxial cylinders in combination with a homogeneous magnetic field parallel to the axis of the cylinders. According to Henneberg (1934*b*) the focusing properties of this field combination can be easily derived from the equation of motion of the radial component in the purely electrostatic field (cf. (11.24)) while accounting for the magnetic field by adding the magnetic contribution of the total force upon the electron. Hence

$$\frac{m\,\mathrm{d}^2r}{\mathrm{d}t^2} = mr\omega^2 - eE - eBr\omega^2. \tag{11.70}$$

The law of conservation of angular momentum now leads to

$$mr^2\omega - \frac{eBr^2}{2} = \text{const.} \tag{11.71}$$

Combination of (11.70) and (11.71) and application of the new equation to the circular orbit, where $\mathrm{d}^2r/\mathrm{d}t^2 = 0$, gives

$$mr_0\omega_0^2 = eE_0 + er_0\omega_0 B, \tag{11.72}$$

which for $E_0 = 0$ or for $B = 0$ corresponds to (5.2) or to (11.23) respectively, the index (0) referring again to the circular orbit.

Now take

$$eE_0 = Kmr_0\omega_0^2, \tag{11.73}$$

where K is the fraction of the centrifugal force which is compensated by the electrostatic field. Then, a calculation quite analogous

to that given by (11.24)–(11.28) leads to the angle of deflexion (= angle between the radius vectors through two foci)

$$\phi = \frac{\pi}{\sqrt{(1+K^2)}}. \tag{11.74}$$

For positive K, the electrostatic force, $-eE$, is directed towards the centre of the circular orbit, i.e. $-eE$ is acting against the centrifugal force. For negative K, $-eE$ is directed outwards, i.e. acting in direction of the centrifugal force. For $K = 0$, E vanishes and semi-circular focusing in the purely magnetic field is obtained. For $K = +1$ purely electrostatic focusing with $\phi = \pi/\sqrt{2}$ follows in agreement with the earlier result (11.29).

Another particular case given by $K = \pm\infty$ occurs according to (11.73) if the centrifugal force $mr_0\omega_0^2 = mu_0^2/r_0 = 0$, i.e. either if $u_0 \to 0$ or if $r \to \infty$. In the second alternative the orbit is straight, i.e. electrostatic and magnetic forces on the electron are compensated and the field intensities are given again by (11.56), the condition applying to Wien's velocity filter.

The focusing deflexion of very fast electrons in the cylinder condenser with superimposed magnetic field has been studied by Millet (1948), who extended Henneberg's calculations into the relativistic region. Equations (11.70)–(11.74) are found to apply as before if for m the relativistic mass $m_0/[1-(u/c)^2]$ is substituted.

Two-directional focusing can also be effected in superimposed electrostatic and magnetic fields (cf. Swartholm, 1948). For this purpose the magnetic field should be given the form determined by (11.50) but with the parameters $C_1 = \frac{1}{2}$ and $C_2 = \frac{3}{8}$. The electrostatic field should be of a form determined by an analogous equation for $E(r)/E_0$. The corresponding parameters C_1' and C_2' depend on the ratio of electrostatic and magnetic intensities, and their values can be expressed as simple functions of the value of K of (11.73). The homogeneous magnetic field superimposed over the cylinder condenser is contained as a special solution in Swartholm's results with the characteristic parameters assuming the values $C_1 = C_2 = 0$ and $C_1' = C_2' = -1$.

11.8. Deflexion errors

For small deflexions (cf. § 11.2) the angle of deflexion is expected to be proportional to the deflecting field. This proportionality, however, gradually ceases to hold when the deflexion becomes large. Moreover, for a given field, the deflexion is only to a first approximation independent of the x- and y-coordinate at which the ray enters (parallel to z) into the deflecting field. Thus different rays of an electron beam of finite aperture are equally deflected only when the deflexion is small. However, peripheral rays of beams of finite aperture are subject to different deflexion as soon as the angle of deflexion is sufficiently increased. It has already been shown in §§ 11.5–11.7 that focusing effects are connected with large-angle deflexions. The focusing effect is generally not symmetrical with respect to the axis of the electron beam. If a beam is focused on a fluorescent screen it may produce (when undeflected) a small circular spot. This spot will be distorted as the deflexion of the beam is increased. All these deflexion errors can be demonstrated, for instance, in a television tube, when a picture is produced by the scanning of an intensity-modulated electron beam over a fluorescent target.

In a first-order 'Gaussian' theory (cf. § 1.3) collinear projection is considered to apply independently of the image aperture. Hence, deformations of the spot due to large deflexion and the lack of proportionality between deflecting field and deflexion angle can be treated as aberrations (cf. Chapter VI), i.e. as deviations from the first-order theory. Theoretically and experimentally, there have been found deflexion errors corresponding to distortion, coma, astigmatism and field-curvature. There are no deflexion errors corresponding to spherical aberration or to anisotropic coma. The general theory of deflexion errors belongs to the most complicated problems in electron optics. We have to refrain from giving details, but we refer to the papers by Picht and Himpan (1941) and by Glaser (1949*c*) which contain a very comprehensive treatment.

Some special cases of practical interest, however, may now be discussed. Deserno (1938) and Wallraff (1935) investigated the errors of weak, substantially homogeneous deflecting fields. In the electrostatic condenser the deflexion must depend on the path of

the ray, since the potential in the condenser is a function of the coordinates. Hence the velocity of the electrons is altered according to the position of the beam and according to the position of the electron within the beam. The alteration in electron velocities causes both a change in deflecting power and a defocusing of the spot off the Gaussian plane which increases as the deflected beam approaches one of the deflecting electrodes. In practice, however, it is found that the defocusing effect of the field inside the deflecting condenser is cancelled to some extent by the action of the stray field at the edge of it.

According to Recknagel (1938) the change in deflexion sensitivity can be represented by an additive correction term which increases with the third power of the deflecting voltage. On the other hand, the 'spurious' focusing depends according to (11.21) upon the square of the deflecting voltage.

Some more detailed theoretical papers on the electric deflexion condenser, given by Herzog (1934–40), can only be quoted. We mention here that least deflexion errors are experienced if for geometrically symmetrical condenser electrodes the deflecting voltages can be kept symmetrical about V_{el}, i.e. if the plate voltages are $(V_{el}+V_p)$ and $(V_{el}-V_p)$ respectively, where V_{el}, the energy of the electrons as they enter the deflecting field, is given by the anode voltage V_A of the electron gun ($V_{el}=V_A$). If, however, unsymmetrical voltage distribution has to be applied, the shape of the deflecting electrodes too has to be chosen to be unsymmetrical for compensation. For instance, if one deflexion plate has to be connected with the anode of the gun so that its voltage is permanently $=V_{el}$, while the other plate is connected to the full deflecting voltage $(V_{el}+2V_p)$, very serious errors will be observed unless diaphragms are placed at the entrance and at the exit of the deflexion condenser, these diaphragms being connected to the voltages V_{el} and $(V_{el}+2V_p)$ respectively.

All attempts at correcting the deflexion condenser had only rather limited success. However, according to a proposal by Hutter and Harrison (1950), the difficulty of field correction can be avoided by the introduction of a complementary 'predistortion' of the beam before it enters the condenser. In practical cathode ray tubes line-focus lenses (cf. Chapter X) have been introduced into the electron

gun. For proper correction of both size and shape of the focused spot on the fluorescent screen, these line-focus lenses are operated by a certain fraction of the voltage applied to the deflexion plates.

Magnetic deflexion errors can generally be made much smaller than the errors obtained by electric deflexion. In a short homogeneous field, the angle of deflexion ϕ equals the angle between the two radius vectors r_e of the circular electron orbit at the beginning and at the end of the field. If (as in § 11.2) the first radius vector is perpendicular to the z-axis, the deflexion is geometrically given by

$$\sin\phi = \frac{2z_p}{r_e}, \tag{11.75}$$

where $2z_p$ is the length of the deflecting field. The ratio $2z_p/r_e$ which, according to § 11.2, is proportional to the deflexion y_T of the spot on the target, approaches the value $\tan\phi$ of (11.12) for small angles

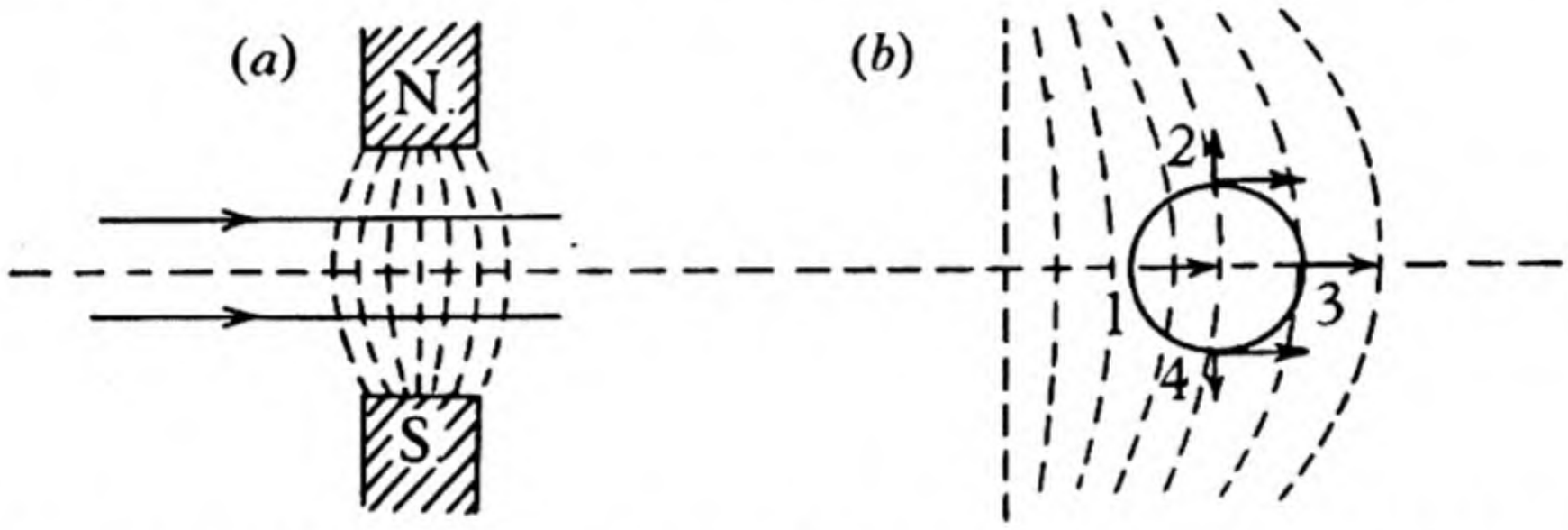

Fig. 11.16. Distortion in a magnetic deflecting field: (*a*) longitudinal section; (*b*) enlarged transverse section of initially circular beam.

ϕ only, i.e. when $r_e \gg z_p$, otherwise it is distinguished from it by a factor $\cos\phi$. In practice, however, this cosine error which is characteristic for the homogeneous field is always small in comparison with the error produced by the inhomogeneous fringing fields.

The influence of the inhomogeneity of the magnetic field is schematically shown in fig. 11.16(*a*) and (*b*) after Zworkyin and Morton (1940). In fig. 11.16(*a*) a beam of circular cross-section is seen passing through the barrel-shaped pattern of field lines between the pole-pieces N. and S. An enlarged transverse section in fig. 11.16(*b*) shows that the rays 1 and 3 on the horizontal diameter will suffer different displacements as indicated by the force vectors. The vertical field is less spread out and therefore stronger at 1 than at 3. Hence, in being deflected to the right, the beam will also be contracted in horizontal direction. On the other hand, rays

2 and 4 on a vertical diameter through the beam experience the same horizontal force but vertical forces in opposite senses, since the horizontal component of the magnetic field is finite and oppositely directed at the two points. Hence the beam will suffer an elongation in the vertical plane, and the resulting shape of the deflected spot will be elliptical. If the beam is not in the horizontal plane of symmetry, as assumed here, the ellipse will be rotated about the axis also.

Loss of proportionality between deflecting current and deflexion arises from variation of flux density with distance from the axis.

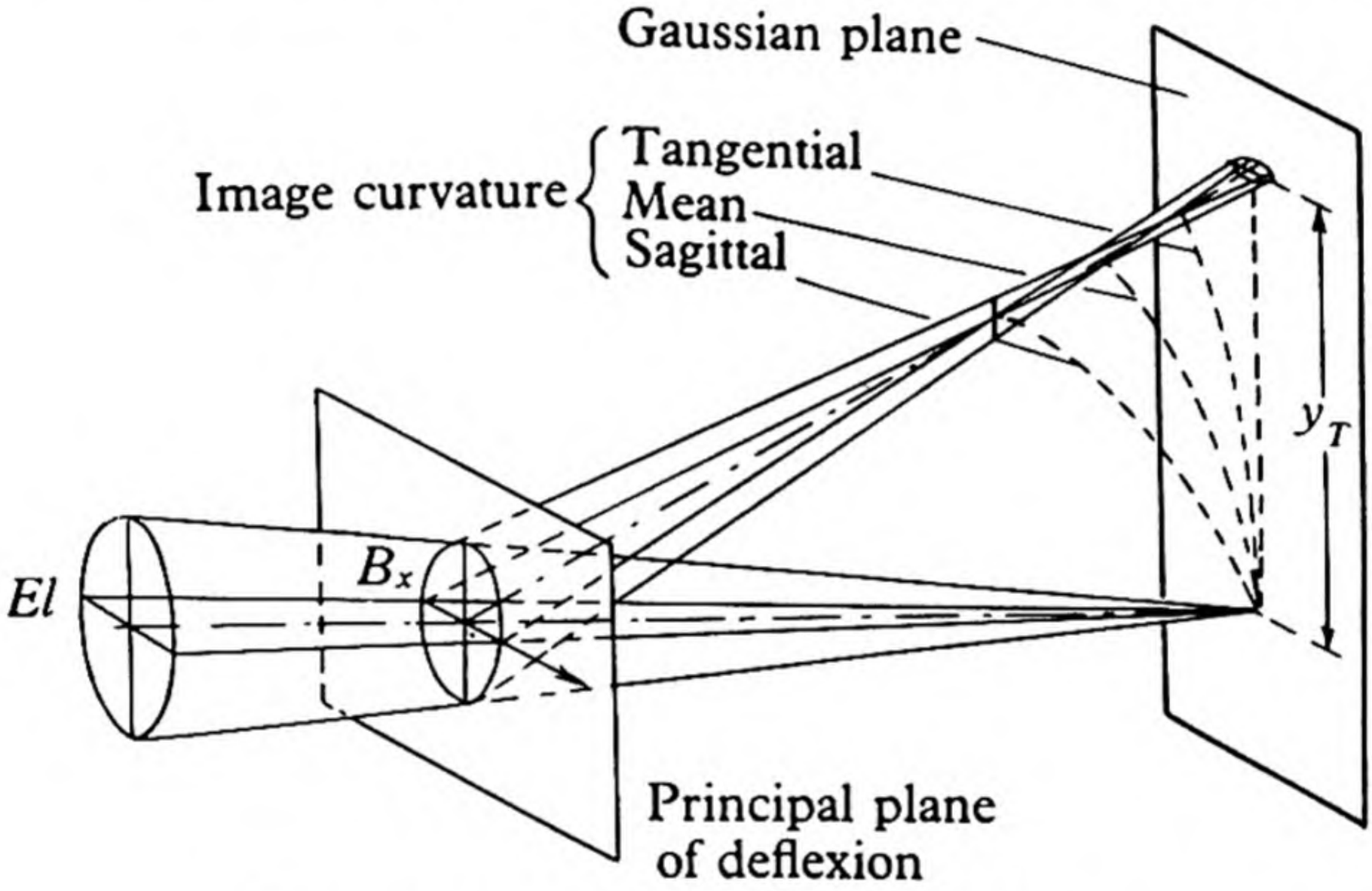

Fig. 11.17. Astigmatic deflexion error.

In a barrel-shaped pattern of field lines as shown in fig. 11.16(*a*) the beam will enter a region of smaller flux density as it moves away from the axis, and thus the deflexion will grow less than proportional to the deflecting current. Increasing deflecting power with increasing current, however, will be experienced if the pattern of field lines is pin-cushion-shaped.

The magnetic deflexion error has been treated quite generally by Glaser (1938*b*) and by Wendt (1938, 1942), and some experimental tests of the theory have been described by Marschall and Schröder (1942). It appears that for practical purposes, in particular for the scanning in television tubes, field curvature and astigmatism are by far the most serious errors. The effect of the latter error, due to which the undeflected, sharp circular spot on the fluorescent target is changed into a large elliptical spot, is shown in fig. 11.17.

The tangential, sagittal and mean image surfaces differ here from the Gaussian plane in the same manner as was explained by fig. 6.22 for the corresponding lens errors. The principal plane of deflexion which is shown in the figure is obtained as locus of intersection of the undeflected rays with the backwards produced direction of the deflected rays.

Practical suggestions for the design of deflecting coils with some degree of correction have been given by Woroncow (1946). He proposed the use of iron-cored, toroidal coils with the greatest density of windings near the plane of the undeflected beam. According to Schlesinger (1949), deflexion errors and defocusing can be in principle always cured by introducing a controlled amount of inhomogeneity into the deflecting field. In the required field distribution, the field intensity increases with increasing distance from the undeflected beam in the direction of the deflexion. This distribution can be determined by calculation, and Schlesinger claims that it can be produced experimentally by a proper arrangement of one main coil with two auxiliary coils, or alternatively by application of slotted iron yokes of appropriate shape.

Some technically important magnetic deflexion fields, however, have been found by a systematic empirical research, independently from any theoretical approach. These fields have been produced by saddle coils such as are shown above in figs. 11.7 and 11.8. If the length $2z_p$ of the deflecting field is defined as the distance between the points at which the flux density has decreased to one-tenth of its maximum value, the radius of the mean image field curvature is found to be of the order of

$$R \approx \tfrac{4}{3} z_p$$

under the best available conditions.

11.9. Deflexion-focusing errors, monochromatic line-width and field correction

It has been shown in §§ 11.5 and 11.6 that some deflecting fields act like electron lenses having definite foci and principal points for all paraxial rays moving within small apertures from a curvilinear axis. It seems quite obvious that lens errors, such as those treated in Chapters VI and VII for ordinary electron lenses, should also occur for focusing deflexion fields. Spherical aberration, for instance,

should be noticed as a difference in focus for paraxial and for marginal rays. Or, if the focus of a marginal pair of rays is observed at some distance from the principal ray, this could be taken as the coma of the deflecting field, and so on. So far, however, the optical treatment of focusing deflexion is still relatively new, and no proper attempts have been made to classify the errors of the important focusing fields systematically. Moreover, errors of deflexion focusing are practically important so far in spectrometry only. Hence attention has been drawn rather to the general question of confusion of spectral line width in the plane of the photographic plate or of the collector slot. For a discussion of this question, however, a simple investigation by means of ballistic laws is generally sufficient.

Take, for example, the deflexion focusing in the homogeneous electric field which has been discussed in the beginning of § 11.5. The principal orbit may be compared with the ballistic parabola rising from the 'horizontal' xz-plane at a slope angle α. The least change Δz in 'range' z_f for a given small change in α is known to occur for $\alpha = 45°$. Now, the changes $\pm\Theta$ in α are equivalent to a semi-aperture Θ of a bundle of rays and the corresponding shortening Δz in range is equivalent to the departure from perfect focusing. From (11.22) with $\alpha = \frac{1}{4}\pi$, there follows immediately

$$\Delta z \approx 2 z_f \Theta^2, \tag{11.76}$$

e.g. a semi-aperture $\Theta = 0{\cdot}1$ of the beam gives rise to a width of confusion of the line focus of about 2 % of the ideal range z_f.

Next may be considered the important case of semicircular focusing in the homogeneous magnetic field. As shown in fig. 11.13 a diverging bundle of rays of semi-aperture Θ may be emitted from the coordinate origin at J_0. All rays having exactly the same velocity describe circles of radius r_e in the strictly homogeneous field. The principal ray may travel initially along the y-axis, hence the centre M_0 of this circular orbit has the coordinates ($y_0 = 0$, $z_0 = r_e$). The centres C_1 and C_2 of the two limiting rays (1) and (2) of the bundle are given by the coordinates ($y_1 = -r_e \sin\Theta$, $z_1 = r_e \cos\Theta$) and ($y_2 = r_e \sin\Theta$, $z_2 = r_e \cos\Theta$) respectively.

The two marginal rays (1) and (2) cut the z-axis at the common point J_1' having from J_0 the distance $z = 2r_e \cos\Theta$, while the

principal orbit intersects the z-axis at J_0' given by $J_0J_0' = 2r_e$. Hence, the point object J_0 is projected into a confused image of width

$$J_0'J_1' = \Delta r = 2r_e(1-\cos\Theta), \tag{11.77}$$

which for small Θ is approximated by

$$\Delta r = r_e\Theta^2. \tag{11.78}$$

As the confusion Δr extends to the inside of the principal circular orbit only, the image width obtained from an object of finite width b is found to be

$$b' = b+\Delta r = b+2r_e(1-\cos\Theta). \tag{11.79}$$

This result is of interest in electron spectrometry. If the value of the electron momentum $(B_e r_e)$ of a monochromatic spectral line has to be determined from the position of an experimental line image, the radius r_e of the electron orbit which is required for the determination of the $(B_e r_e)$-value is given as half the distance from the outer edge of the line image to the inner edge of the source.

A detailed analysis of the effect of finite apertures of the electron beam in space and of the length and width of the electron source has been given by Wooster (1927) and by Li (1937). As an essential result it may be reported here that a filament object or an emitting straight slot is projected into a slightly curved line image. The inner edge of the object again corresponds to a sharp outer edge of the image, i.e. at the high-velocity side the image is limited sharply. The outer edge of the object, however, is represented by the maximum of an intensity distribution in the image. Towards the low-velocity side this intensity distribution falls off steeply, ending eventually in a long tail of low intensity which for most purposes in spectrometry can be disregarded. In the three-dimensional problem the electron orbits can, in general, not be considered as circles but rather as spirals, the pitch of which is limited by the length of the source and the aperture stops. If, however, the maximum slope angles γ of the spiral orbits with the equatorial plane ($\perp B$) are small as compared with the beam semi-aperture Θ or practically, if

$$\gamma \lesssim 0{\cdot}1\Theta, \tag{11.80}$$

the intensity distribution in the image is found to be little affected by the extension of source and stops in the direction of the magnetic

flux B. Thus, the image width calculated for the two-dimensional case (cf. (11.79)) gives a fair approximation of the actual width of the line image.

Owen (1949) has given a general analytic derivation of intensity distributions across the line image. He presented his results by a set of curves for various conditions of lengths and widths for source and stop slots respectively; all these curves are useful for the spectrometer designer. Detailed descriptions for wide-angle, short-source semicircular spectrometers to which condition (11.80) applies, have been given by Gurney (1925) and by Lawson and Tyler (1940). On the other hand, Geoffrion (1949) has pointed out that by increasing the source length and slightly decreasing its width the intensity of the line image can be greatly increased without affecting its width. We shall come back to this important conclusion later on (cf. § 12.7).

The confusion of the line width can always be reduced by cutting down the marginal rays, i.e. by reducing slot dimensions. On the other hand, (11.77) shows a possibility of bringing the focus of the marginal rays into coincidence with the paraxial focus by the correct increase of the radii of curvature (r_e) of the marginal rays. For rays of given electron momentum ($B_e r_e$) this can be done by reducing the deflecting field B at both sides of the principal ray. The exact calculation of the field distribution $B(r)$ as a function of the distance r from the centre of the principal ray, as required for correct focusing, was first attempted by Bock (1933). His results were later slightly modified and corrected by Beiduck and Konopinski (1948), who arrived at the solution

$$\frac{B(r)}{B_0} = 1 - \frac{3}{4}\left(\frac{r-r_0}{r_0}\right)^2 + \frac{7}{8}\left(\frac{r-r_0}{r_0}\right)^3 - \frac{9}{16}\left(\frac{r-r_0}{r_0}\right)^4 + \ldots, \quad (11.81)$$

where r_0 is the radius of curvature of the principal orbit as determined by the flux density B_0.

The first experimental arrangement for correcting the focusing errors of the homogeneous magnetic field was described by Voges and Ruthemann (1939). These authors modified the field in the gap between two coaxial cylindrical air coils by the superposition of the field of two circular coaxial strip conductors, and in this way they succeeded in developing a slow-electron spectrometer of very high

resolving power (cf. § 12.7). In a different manner, the proper departure from uniformity of the magnetic deflecting field has been obtained by Korsunsky, Kelman and Petrov (1945). These authors gradually changed the profile of the pole faces of their magnet until they reached the desired sharpness of focus. The maximum aperture of rays still reaching this focus was $2\Theta = 40°$.

A correction of focusing by bounded homogeneous fields such as, for instance, Barber's magnetic prism (cf. § 11.6), can be obtained by shaping of the field boundaries. Hintenberger (1948, 1949) and Kerwin (1949) investigated theoretically the great variety of boundary curves that give perfect focusing of an electron beam of wide divergence. In some cases the boundary correction simultaneously enables a reduction of the necessary size of the magnet. The discussion, however, deals with focusing in the equatorial plane ($\perp B$) only. Practically it would apply to short sources and short aperture slots only, and this restriction is not likely to lead to the optimum intensity of a line image. Moreover, the theoretical field boundary is not easily simulated by the shape of the magnetic pole-pieces. Coggeshall (1947) has shown how the fringing flux can be accounted for by using virtual field boundaries displaced outwards from the edges of the pole-pieces. However, even if the method of the virtual field boundaries is helpful for finding the boundary design leading to the desired orbits, it leaves the absolute energy determination in the electron spectrum as an unsolved difficulty.

The homogeneous field prism of circular symmetry (cf. § 11.6) offers the interesting chance of reducing focusing errors to a minimum by a proper choice of the angle of deflexion. Korsunsky (1945) realized that for smallest spacings of the pole-pieces focusing errors disappear completely at 90° deflexion. Siday (1947), who calculated the focusing errors for such vanishingly small spacing of pole-pieces over a large range of deflexion angles, found, in agreement with Korsunsky, minimum errors about the rectangular deflexion.

Electron orbits in the equatorial plane half-way between pole-pieces separated by one radius of their circular cross-section have been studied by Siday (1947) by means of numerical computation. There, the fringing flux was properly taken into account. The

deflexion focusing aberrations were found—in distinction to lens aberrations—to be unsymmetrical, changing sign with the ray aperture. For example, the aberrations are positive or negative (cf. §6.3) for rays travelling outside or inside, respectively, of a principal ray which is initially directed towards the centre of the field. The aberrations depend greatly upon the angle of deflexion. For initially parallel rays the aberrations pass through a minimum at a deflexion angle of 76°.

According to Jennings (1950, 1952) the deflexion angle with minimum aberration gradually decreases with increasing pole spacing. However, by choosing bundles with eccentric incidence, conditions for minimum aberration can be found at any given pole spacing for a wide range of deflexion angles. For this focusing with least aberration, the eccentricity of the principal ray of the bundle is found to increase with increasing angle of deflexion.

The image confusion for two-directional focusing has been discussed by Swartholm (1946) and by Shull and Denison (1947). In a field given by (11.45) with $n = \frac{1}{2}$ the intersection between principal and zonal ray in the equatorial plane ($\perp B$) of symmetry may be traced or calculated as a function of the semi-aperture Θ. The distance ζ between this intersection and the object point as measured along the principal ray is approximately given by

$$\zeta(\Theta) = r_0(\phi_0 - \tfrac{4}{3}\Theta), \tag{11.82}$$

where r_0 is the distance of the object from the field axis and where $\phi_0 = \pi\sqrt{2}$ is the angle of deflexion for paraxial focusing as given in §11.6. According to (11.82) the deflexion focusing suffers from positive spherical aberration, and the image in the 'Gaussian plane' will be confused towards the field axis by an amount (cf. transverse aberration §6.3) given by

$$\Delta r = \tfrac{4}{3} r_0 \Theta^2. \tag{11.83}$$

(11.83) also gives a fair estimate of the monochromatic line width for a negligibly narrow object in the two-directional focusing deflexion fields described by (11.50). Only slight influence is exerted on the focused line width by a finite value of the coefficient C_2 ($< \frac{3}{8}$) of this equation (cf. §11.6). Other slight modifications of (11.83) are due to a finite beam aperture at right angles to the equatorial plane.

The focusing deflexion by a cylindrical condenser on which a homogeneous magnetic field is superimposed (B parallel to the cylinder axis) can be adjusted by proper choice of the electric and magnetic field ratio. If this ratio is again (cf. § 11.7) defined by the parameter K of (11.73) the monochromatic line width for a vanishingly small source is, according to Henneberg (1934*b*), to a first approximation given by

$$\Delta r = -r_0 \Theta^2 (1 + \tfrac{1}{3}K + K^2 + 3K^3)/(1+K^2)^2, \qquad (11.84)$$

where r_0 is the radius of the principal orbit and Θ the semi-aperture of the beam. It can be seen that Δr, as calculated from the above approximation formula, vanishes for $K = -0{\cdot}76$. Actually, the value of the line width becomes very small for this particular field combination.

For the purely electric case ($K = 1$), (11.84) yields

$$\Delta r = -\tfrac{4}{3} r_0 \Theta^2. \qquad (11.85)$$

For the purely magnetic case ($K = 0$) one obtains $\Delta r = r_0 \Theta^2$, which is the line width given by (11.78). Of further interest is the line width in Wien's velocity filter (cf. § 11.7). Taking $K \to \infty$, (11.84) yields

$$\underset{\left[\substack{r\to\infty \\ K\to\infty}\right]}{\Delta r} = -3\Theta^2 \lim \left(\frac{r_0}{K}\right) = -3 \frac{m}{e} \frac{u_0^2}{E_0} \Theta^2, \qquad (11.86)$$

the last transition in this equation having been obtained by introducing (11.73) for K and substituting $r_0 \omega_0^2 = u_0/r_0$, where u_0 is the linear velocity of the rays which travel at right angles to E and B.

11.10. Dispersion, resolving power and collecting power of focusing deflexion fields

The application of deflecting fields for analysing a distribution of electron velocities is based upon the different deflexion of beams of different velocities. Separate images are formed for separate velocities. In distinction to the chromatic aberration of electron lenses (cf. lens spectrometry, § 7.2) the images are not located along the axis, i.e. along the principal rays of the deflected beam but along its radius of curvature.

Two images with the coordinates s and $(s + \mathrm{d}s)$ may correspond to the velocities u and $u + \mathrm{d}u$. The displacement $\mathrm{d}s$ per velocity

change du is the dispersion of velocities by the deflecting field, it is given by ds/du. Analogously, the dispersion of momenta and the dispersion of energies are defined by ds/dp and by ds/dW respectively.

As the dispersion for a given geometry of rays still depends on the velocity or on the momentum of the beam, let a 'specific dispersion' be defined by

$$D = | p(\mathrm{d}s/\mathrm{d}p) |. \tag{11.87}$$

It is well known in spectrometry that dispersion is necessary but not sufficient for the resolution of a spectrum. It is also required that the line width, i.e. the width of the image of the source, be small enough, so that two images of sufficiently small displacement may be separated.

The smallest possible displacement Δr that still can be separated is of the order of the width of the image, the total image width being composed of that of a Gaussian (first order) image and of the confusion by the deflexion focusing errors (cf. § 11.9). For images with a wide intensity distribution the 'half-maximum width' (i.e. the full width of the distribution curve in half the height of the maximum) is generally taken as a practical value of Δr. The expression

$$\frac{D}{\Delta r} = \frac{p}{\Delta p} \tag{11.88}$$

is the resolving power, where Δp is the difference in momenta that corresponds to the smallest resolvable displacement Δr. For a vanishingly small object, Δp is a function of the focusing deflexion errors only.

Equation (11.88) gives a practical prescription for finding the resolving power for a given focusing deflexion field. Take, for instance, a homogeneous magnetic field spectrometer with the source in the plane of the photographic plate (cf. fig. 11.13) and with constant field B_0. The line width $\Delta r = r_0\Theta^2$ is given by (11.78). Moreover, $p = eB_0r$ and $s = 2r$, hence $D = p\dfrac{ds}{dp} = 2r$ and, according to (11.88),

$$p/\Delta p = 2/\Theta^2. \tag{11.89}$$

On the other hand, if the photographic plate is arranged in line with the aperture slot (cf. fig. 11.11) the radius r of an electron orbit

is given by (11.35). Hence the momentum is $p = \frac{1}{2}eB_0(s^2+c^2)^{\frac{1}{2}}$. The dispersion has to be taken along the photographic plate in the direction of s, and one obtains $D = p\Big/\frac{\mathrm{d}p}{\mathrm{d}s} = \frac{s^2+c^2}{s} = \frac{(2r)^2}{s}$. With $\Delta s \approx \Delta r$ of (11.78) the resolving power becomes

$$\frac{p}{\Delta p} = \frac{4r^2}{s}\frac{1}{r\Theta^2}. \tag{11.90}$$

For $s \approx 2r$, i.e. if the perpendicular distance c between source and photographic plate is small, the result given by (11.90) will be nearly enough identical with that of (11.89).

If the registration is carried out with a Faraday cage or Geiger counter, it is convenient to define the resolving power in another manner. The dimensions of source and slit may be negligible, but owing to the finite image-width electrons of homogeneous momentum p_0 will still reach the slit if the flux density is slightly different from the value for exact focusing given by

$$B_0 = \frac{p_0}{er_0}. \tag{11.91}$$

Suppose the flux density is reduced to $B < B_0$. Then the principal ray is displaced outwards to $r > r_0$, and

$$B = \frac{p_0}{er}. \tag{11.92}$$

If p_0/e $(= Br)$ is independent of r one obtains on differentiation

$$\frac{\mathrm{d}B}{\mathrm{d}r} = -\frac{p_0}{e}\frac{1}{r^2} = -\frac{Br}{r^2}, \tag{11.93}$$

or considering magnitudes only

$$\frac{B}{\mathrm{d}B} = \frac{r}{\mathrm{d}r}. \tag{11.94}$$

After decreasing B_0 by $\mathrm{d}B$, the new principal orbit is displaced both outside source and detector slit by a distance $\mathrm{d}r$. However, the orbit which starts from the source and leads to the displaced image would require half this change in radius only, i.e. $\frac{1}{2}\mathrm{d}r$. Hence for constant object position with an image displacement by one line

width Δr, (11.94) may be used to give the following equation for the resolving power of the homogeneous field:

$$\frac{B_0}{\Delta B} = \frac{2r_0}{\Delta r}, \tag{11.95}$$

which on substitution of (11.78) for Δr yields again the result of (11.89). Thus the two results for the resolving power of the homogeneous field, namely, $B_0/\Delta B$ for fixed collector slot and variable field, and of $p/\Delta p$ for fixed flux density and variable image position, are identical.

The resolving power of a circular-symmetrical magnetic field decaying with a field index $0 < n < 1$ as given by (11.45), namely,

$$B = B_0(r_0/r)^n,$$

could be derived analogously to the above calculation as follows. (11.47) would replace (11.93) and instead of (11.95) one would obtain

$$\frac{B_0}{\Delta B} = \frac{2r_0}{(1-n)\,\Delta r}. \tag{11.96}$$

The resolving power is seen to increase with increasing n. This seems to be quite plausible if one considers electrons of the momenta p and $p + \mathrm{d}p$. In a field with $n > 0$, the radius of curvature of the ray of the larger momentum will be increased on two accounts, namely, the greater momentum and the weaker field, whereas in the homogeneous field with $n = 0$ only the first effect would be present. For example, for the two-directional focusing spectrometer by Siegbahn and Swartholm (cf. fig. 11.14) n is nearly enough $\frac{1}{2}$, and $\Delta r = \frac{4}{3}r_0\Theta^2$ is given by (11.83). By substitution of these values in (11.96) we obtain

$$B_0/\Delta B = 3/\Theta^2. \tag{11.97}$$

For values of resolving power of other arrangements, reference has to be made to the literature quoted in §§ 11.5–11.7 and in § 11.9. Since it is of practical interest to compare the merits of the most important focusing-deflexion fields, the approximate values of their resolving powers are collected in Table XIII. There it can be seen that the resolving power quite generally increases to a first approximation inversely with the square of the beam aperture.

For obtaining high resolving power the beam aperture should be kept as small as the requirements for intensity in the image would

allow. This intensity $I(\Theta)$ may be written as the product of the total emission I_{em} from the source and of the collecting power Ω of the field. In agreement with a definition given in § 7.2 the collecting power may be noted as

$$\Omega = I(\Theta)/I_{em}. \tag{11.98}$$

The collecting power is an important feature in practical spectrometer design. Approximate values of Ω for the important focusing deflexion fields are given in Table XIII as a function of the geometry of the arrangement. For a point source, Ω simply equals $1/(4\pi)$ of the solid angle Ω_0 into which the focused electron beam is emitted and which is subtended by the aperture stops. For example, for two-directional focusing arrangements with circular aperture stops the solid angle of acceptance is $\Omega_0 \approx \pi\Theta^2$, where Θ is the semi-vertical angle of the collected bundles at the source.

Small sources with approximately isotropic emission can be treated like point sources. Thus the collecting power is independent of the source area a as long as the source dimensions are small with length of the electron orbit.

The collecting power for one-directional focusing deflexion may be estimated from the product of the two maximum semi-apertures of the rays, namely, Θ in the equatorial plane and γ at right angles to this plane, since the solid angle is given simply by

$$\Omega_0 \approx 4\Theta\gamma. \tag{11.99}$$

In one-directional focusing arrangements the meridional aperture 2γ is approximately defined by

$$2\gamma = \frac{h}{\phi_0 r_e}, \tag{11.100}$$

where h is the length of the aperture slot (or of the collector slot) and $\phi_0 r_e$ is the length of the electron orbit from source to line image, ϕ_0 being the angle of deflexion and r_e being the radius of the electron orbit. Hence follow the values of Ω for one-directional focusing given in Table XIII; e.g. a value $\Omega = \Theta h/2\pi r_e$ is obtained for semi-circular magnetic deflexion (cf. Gurney, 1925).

The values for resolving and collecting power presented in Table XIII are seen to be independent of the absolute size of the spectrometer, in particular, the resolving power of a spectrometer

seems to be quite independent of the radius of the electron orbit. It should be pointed out, however, that all results in Table XIII refer to negligibly small electron sources, and for sources of finite size the optical image size has always to be added to the line width that is due to confusion. From this point of view it is practically always worth while to make a spectrometer as large as economic considerations would allow.

TABLE XIII. *Focusing deflexion angle ϕ_0, resolving power $p/\Delta p$ and collecting power Ω of some practically important focusing deflexion fields*

Field	ϕ_0	$p/\Delta p$	Ω
(1) $B = \text{const.}$	π	$2/\Theta^2$	$\dfrac{\Theta h}{2\pi r_e}$
(2) $E = E_0 \dfrac{r_0}{r}$ (cylindrical condenser)	$\dfrac{\pi}{\sqrt{2}}$	$3/(2\Theta^2)$	$\dfrac{\Theta h}{\pi r_e \sqrt{2}}$
(3) $E \perp B$ $\begin{cases} B = \text{const.} \\ E = E_0 \dfrac{r_0}{r} \end{cases}$	$\dfrac{\pi}{\sqrt{(1+K^2)}}$	$\dfrac{2}{\Theta^2}\left[\dfrac{1+K+K^2+K^3}{1+K/3+K^2+3K^3}\right]$	$\dfrac{\sqrt{(1+K^2)}\,\Theta h}{2\pi r_e}$
(4) $E \perp B$ $\begin{cases} B = \text{const.} \\ E = \text{const.} \end{cases}$ (Wien velocity filter)	0	$2/(3\Theta^2)$	—
(5) $E = E_0(r_0/r)^2$ (spherical condenser)	π	$2/\Theta^2$	$\pi\Theta^2$
(6) $B = B_0(r_0/r)^{\frac{1}{2}}$ two-directional magnetic focusing deflexion	$\pi\sqrt{2}$	$3/\Theta^2$	$\pi\Theta^2$

Θ = angular semi-aperture in equatorial plane.
r_e = radius of principal orbit.
h = length of source and of collector slit.
K = parameter defined by (11.73).

Since in spectrometer design the use of bounded fields implies certain economic advantages, such fields can be recommended for reaching high resolving power. For instance, with Barber's homogeneous magnetic field sector (cf. § 11.6) a maximum possible resolving power $p/\Delta p = 8/3\Theta^2$ is obtained for $\phi = 120°$ deflexion with the object placed directly at the field boundary. As another example the spherical condenser may be mentioned here which

for a portion subtending 90° reaches a maximum resolving power $p/\Delta p = 8/3\Theta^2$ if the image distance is twice the object distance.

Both examples show that compared with the data of Table XIII higher resolving power can be obtained if source and collector are placed outside the deflecting fields. The advantage of using bounded fields should become still greater if correction of focusing errors is achieved by proper shaping of the boundary (cf. § 11.9). So far, however, bounded deflecting fields have found little application in electron spectrometry because of the greatly upsetting influence of the fringing field which in practice is by no means under control.

Another important aspect not touched in this section concerns the increase in resolving power by proper modification of a field distribution, as is done for instance in the exact semicircular focusing as discussed in § 11.9 (cf. (11.81)). However, the resolving power that can be achieved appears to be limited rather by the technical difficulties in the production of the prescribed field and by the economical maximum of the size of the spectrometer than by any theoretical reasons. Some practical data on resolving power and collecting power which have been obtained in actual spectrometers will be given in § 12.7.

CHAPTER XII

APPLICATION OF ELECTRON OPTICS IN INDUSTRY AND RESEARCH

12.1. Introduction

It has been shown in the beginning of this book (§ 1.1) how electron optics as a scientific subject had originated and developed under the pressure of a strong practical need. It should be noted, however, that some 'electron-optical' devices were already in existence a long time before the advent of the science of electron optics. The best known example is the cathode-ray tube which was described as early as 1897. Although such devices have been studied from the electron-optical point of view at a relatively late stage, this study has led eventually to great practical improvement.

Electron optics has been utilized for practical purposes in rather different ways. For instance, entirely new instruments like the electron microscope have been created by reasoning along electron-optical lines. In other cases new lines for development and improvement of existing electronic apparatus have been indicated by the electron-optical approach, e.g. in the case of electron multipliers and of image converters. Again, for example, in some valves or in deflexion spectrometers, electron optics first provided the key for understanding the working of the apparatus, and after a lapse of time has been used again in the improvement of the apparatus. In particular, electron optics has been very often connected with the ultimate limits of performance to which electronic gear can be developed. For example, in electron spectrometry and in electron microscopy such limits are being reached gradually and systematically by application of electron-optical knowledge. On the other hand, electron-optical reasoning has been successful in indicating ultimate limits a long time before they were reached in practice, as, for instance, in the case of Langmuir's law for the limitation of current density in cathode-ray tubes (cf. § 12.3).

The condensation of such a large subject as applied electron optics into one single chapter must necessarily be rather sketchy. However, there are excellent review articles and systematic books

available on nearly every branch of this subject. We shall be satisfied here to form a guide to the most important literature and to give a brief survey on the possibilities of application, enlarging only on those items which provide typical interest for application of electron-optical principles, in particular on those which have not received sufficient attention in the reviewing literature.

12.2. Cathode-ray oscillographs

The cathode-ray tube as an instrument for the study of alternating voltages or currents is historically the first electron-optical device (F. Braun, 1897.) In the early tubes, a beam of cathode rays was produced by gas discharge from a cold cathode and cut down by application of aperture stops into a narrow pencil, the end of the pencil being made visible as a spot on a fluorescent target or on a photographic plate. Electric voltages under investigation were registered by deflecting the pencil magnetically or electrically. Deflecting coils or, alternatively, deflecting condensers were used for this purpose.

With a gradually growing need for an increased writing speed of the cathode ray, means were developed for increasing the intensity of the spot. In 1899 Wiechert demonstrated the concentrating action of the magnetic coil (cf. Chapter V), and in 1906 Wehnelt used a metal cylinder for surrounding his newly discovered oxide cathode, thus performing the first electrostatic concentration of the electron emission (cf. Chapter IX). Various other electron-optical principles have been discovered and studied on the long way of development to the modern cathode-ray oscillograph. We can only mention the early studies of electric field distributions in the emission systems (1925) and the 'preconcentration' of the rays by Rogowski and Flegler (1925), which in modern electron-optical terms could be described as a first formation of an intermediate image of the cathode.

The first example of a modern 'low-speed' electron gun was described by Zworykin (1933*b*). The general scheme of this gun is shown in fig. 12.1. It consists of a two-diaphragm emission system (cf. Chapter IX) with cathode *Ca*, grid electrode *G* and anode *A*. The electron beam is seen to form a cross-over near the anode aperture. An electrostatic focusing lens between *A* and a second

anode Z serves to project an electron-optical image of the cross-over on to the fluorescent target. The progress in Zworykin's design was obtained by systematic applications of electron-optical principles. With this gun, currents of a few hundred microamperes could be projected into a spot of the order of 1 mm.^{2} at electron velocities of a few kilo-electron-volts. Though this gun was originally designed for television purposes, its application opened new prospects for low-voltage ray oscillography. On the other hand, in high-voltage tubes (50–100 kV.) cold cathode gas discharges were still employed for a long time.

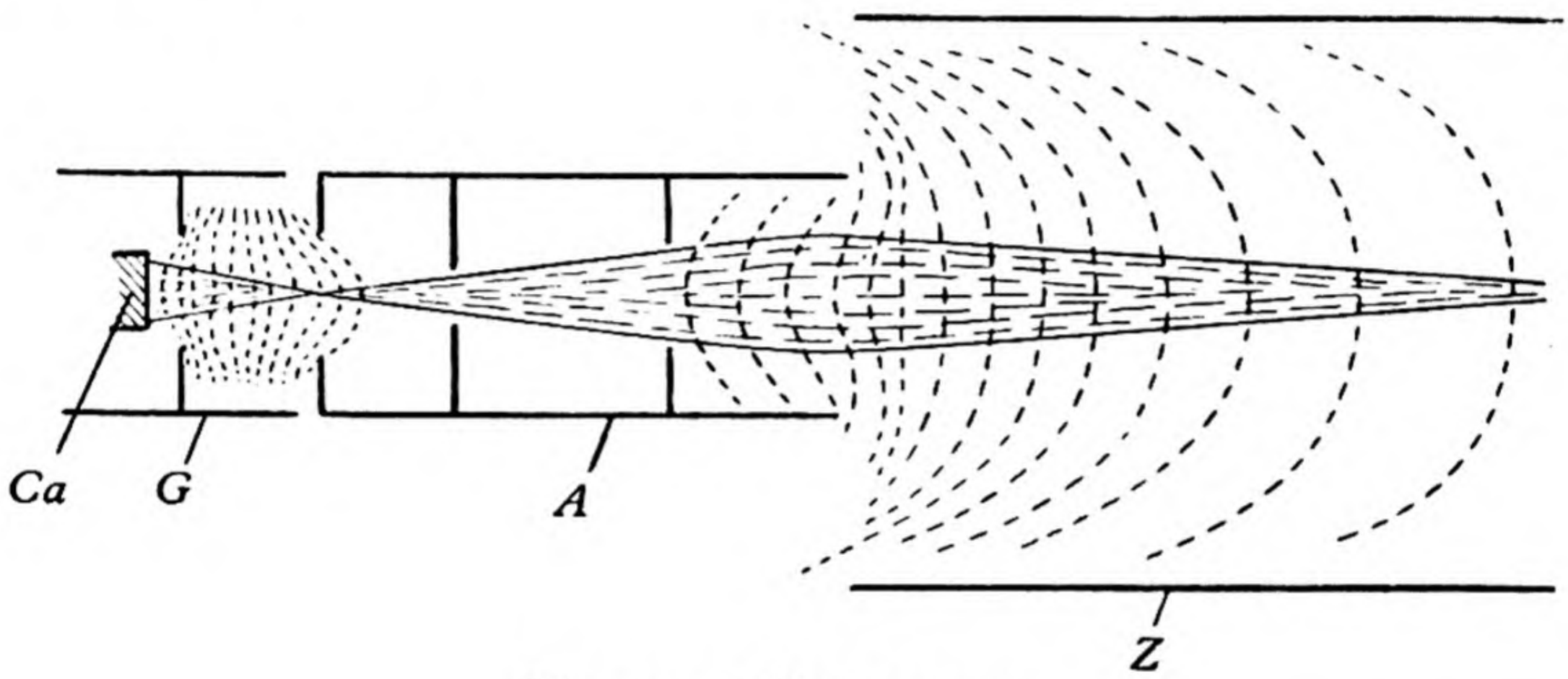

Fig. 12.1. Electron gun.

The cathode-ray oscillograph generally has two sets of deflexion elements for deflecting the ray in the x-direction and in the y-direction. For either of these, condenser plates or deflecting coils can be used. The design of deflexion elements, with a view to obtaining good sensitivity and freedom from deflexion errors, has been discussed in Chapter XI.

An estimation of the obtainable sensitivity is of practical interest for measuring-tubes. The term 'deflexion sensitivity' is often used loosely in the literature for the amplitude of deflexion of the spot on the target divided by the voltage applied to the deflecting condenser (or, respectively, divided by the current applied to the deflecting coil). Accepting this definition for the time being, the sensitivity of a given tube may be measured, for instance, directly in mm./V., namely,

$$S_1 = Y_T/2V_p, \tag{12.1}$$

where Y_T is the deflexion of the spot and $2V_p$ is the potential difference applied to the deflecting plates.

However, a more adequate definition of the deflexion sensitivity is based on a measurement of the deflexion of the spot at the target in units of spot diameters rather than in any absolute unit. If the spot diameter is D_{sp}, the deflexion of the spot as measured in spot diameters is given by Y_T/D_{sp}. Hence the deflexion sensitivity may be defined as

$$S_D = Y_T/(D_{sp} \times 2V_p). \tag{12.2}$$

The minimum observable ratio Y_T/D_{sp} gives the smallest voltage which can be measured by the tube.

On the other hand, the deflexion sensitivity S_D can be estimated in advance from the geometry of the arrangement and from the voltage V_{el} of the electron beam (i.e. the anode voltage which is available for the electron gun). Using the definitions introduced in § 11.3 we can write

$$S_D = Gz_T/(2V_{el}D_{sp}), \tag{12.3}$$

where z_T is the distance of the target from the deflexion plates (or coils respectively) and G is deflecting power which, according to (11.15), is a function of the geometry of the deflecting member only. For instance, the deflecting power of the plane-parallel plate condenser is, according to (11.6) and (11.15), given by the ratio of plate length to plate spacing, and the deflecting power of various other deflecting arrangements is given numerically in § 11.3.

According to (12.3), the sensitivity of a cathode-ray oscillograph cannot be increased simply by increasing the distance of the fluorescent screen from the deflecting field, i.e. by increasing the 'length of the pointer'. The spot is an electron-optical image. Image distance and thus magnification and consequently spot width would be increased in the same proportion as the target distance. The sensitivity of a good commercial monitor tube is of the order of one spot diameter per volt. Electronic amplifiers are employed if small alternating voltages are observed.

For registration of very rapidly changing voltages, cathode-ray oscillographs of high 'time resolution' are required. This latter property can be defined as the ratio of the spot diameter D_{sp} (or of the width of the written line) to the writing speed u_{sp}, namely,

$$t_0 = D_{sp}/u_{sp}.$$

Thus, t_0 is the time which the 'flying spot' needs to pass along a distance equal to its own width while moving with the maximum

velocity that is still registered. For instance, Borries and Ruska (1940) designed a commercial cathode-ray oscillograph with a hot filament cathode, using 25 kV. in a sealed-off tube with fluorescent screen. The line on the screen was photographed by an external camera. Time resolutions of the order $t_0 = 10^{-10}$ sec. could be obtained. Rogowski *et al.* (1930) resolved time intervals down to 10^{-9}–10^{-10} sec. with a cold cathode oscillograph. There, a 70 keV. beam was registered directly on a photographic plate with a spot velocity reaching 6×10^7 m./sec. ($= \frac{1}{5}$ light velocity!).

It has been pointed out that the sensitivity of a measuring-tube may be increased by reducing the beam voltage. However, a limit for this reduction is soon reached. Even for very small velocities of the spot, a given beam energy is necessary to produce a visible trace. *Post-acceleration*, i.e. acceleration of the beam after the deflexion, has been proposed as an expedient and numerous papers have dealt with it since 1920. Tubes have been built in which a metal mesh was placed parallel to and at a small distance in front of the target; thus post-accelerating fields could be maintained between mesh and target. These first attempts were not successful, since appreciable enlargement of the spot, due to the field penetration through the apertures of the mesh, largely upset the gain in sensitivity. Later on, Schwartz (1938*b*) showed theoretically that the scheme of post-acceleration was sound and that an ideal double layer should be efficient in increasing the sensitivity of a tube, but the gain would depend not only upon the voltage difference but also upon the shape and position of this double layer. Rogowski and Thielen (1939) investigated the use of an accelerating electric lens after the deflexion. The change in observed voltage sensitivity was found to depend very much on the position of the lens. The sense of the deflexion at the target may even be reversed by the lens action. Increase in deflexion sensitivity was observed when the lens was sufficiently close to the deflecting field and when the post-accelerating voltage applied to the lens electrodes was sufficiently high.

Lampert and Feld (1946) published details about a tube with post-acceleration voltage ratio 10:1 which was applied to several conducting bands deposited on the inside of the cylindrical glass tube. They found not only greatly increased light output but also somewhat increased deflexion sensitivity, since the decrease of spot

size due to post-acceleration overbalanced the decrease of the deflexion.

For general surveys on the cathode-ray oscillograph we quote the books by Reyner (1947) and by Wilson (1948) and the 'encyclopedia' by Rider and Uslan (1950). The use of cathode-ray tubes in radar for displaying the information gained by the timing of pulses of electromagnetic waves is described in the M.I.T. Lab. Series, vol. 22. Also the survey by Jesty *et al.* (1946) may be recommended for the study of radar display tubes. The development of cathode-ray tubes due to their application in television receivers is reviewed by Moss (1950). Some points of interest in television tubes will be discussed in the following section.

12.3. Television*

The demand for improvement of viewing tubes and of pick-up tubes for television has had, as compared with other applications, by far the greatest effect on the early development of electron optics.

The viewing tube is effectively a cathode-ray oscillograph. For television, however, the cathode ray has to be scanned in a perfectly regular manner over the whole fluorescent screen. In addition, the intensity of the rays has to be modulated in proportion to the light intensity of the televised object. The electron gun as shown already in § 12.2 (fig. 12.1) represents one of the first models which fulfilled to some extent the necessary requirements. The beam could be modulated by application of the signal to the grid electrode, and it could be scanned by saw-tooth waves applied to two mutually perpendicular sets of electrostatic deflexion plates. Small cheap television receivers nowadays still employ tubes of a similar kind (cf. Swedlund and Saunders, 1951). A substantial change in some recent guns is the introduction of an 'ion trap' (cf. Morton, 1946). This trap applies an electrostatic deflexion which, for the electron beam, is later on compensated by a corresponding magnetic deflexion. Negative ions which are frequently emitted from the oxide cathode of the gun suffer in the trap (owing to their relatively large mass-over-charge ratio) sufficiently large overall deflexions

* Books on electron optics in television: Maloff and Epstein (1938); Zworykin and Morton (1940).

so that they are sorted out of the electron beam. In this way, the fluorescent screen of the tube is saved from the damaging influence of these ions.

In more expensive television sets magnetic focusing lenses and magnetic scanning coils are preferred. The magnetic lens is arranged outside the tube and thus can be made of such a large aperture that its spherical aberration (cf. Chapter VI) is of relatively small importance so that the resulting spot is relatively sharp and small. Again, in magnetic deflexion systems deflexion errors (cf. § 11.8) can be ruled out to a greater extent than in electrostatic ones. However, more electrical energy is required for driving deflexion coils than for charging condensers as has been shown in § 11.4.

The question, whether the necessary brightness of the fluorescent screen should be excited either by low-voltage rays with large current or by high-voltage rays of correspondingly small current, may be answered decidedly in favour of the higher voltages. According to an analysis by Langmuir (1937*b*) and by Law (1937) (cf. § 7.1 and § 9.4) an upper limit to the obtainable current density in the focused spot due to the Maxwellian distribution of emission velocities is given by

$$i_{\text{max.}} = i_{\text{cath.}} \left(V' \frac{e}{kT} + 1 \right) \sin^2 \Theta', \qquad (12.4)$$

where $i_{\text{cath.}}$ is the density of emission at the cathode, T is the absolute temperature of the cathode, V' the final voltage and Θ' the semi-angle of the beam subtended at the final spot. e and k are electronic charge and Boltzmann's constant, so that $e/k = 11{,}600$ [degrees/e-volt]. To illustrate this important conclusion, we quote with a few slight alterations a table given by Langmuir.

TABLE XIV. *Theoretical maximum current density in the spot of focused cathode rays*

Final voltage $= V'$. Half-angle subtended by beam $= \Theta'$.
Cathode temperature $= 1160°$ K. Cathode current density $= 10^3$ A./m.^{2}

V' volts	sin Θ'		
	0·01	0·032	0·10
	(Amp./m.^{2})	(Amp./m.^{2})	(Amp./m.^{2})
100	100	10^3	10^4
1,000	1,000	10^4	10^5
10,000	10,000	10^5	10^6

The major requirements for producing intense electron beams are therefore indicated; that is, the final voltage has to be increased as much as possible, cathode surfaces have to be used from which highest current densities can be drawn, and focusing lenses have to be employed which are able to handle beams of widest angle without aberration.

Nothing could raise the current density above the value defined by (12.4). The actual value of the current density in the spot generally lies below this theoretical maximum for two reasons. First, for wide beam apertures it will hardly be possible to correct the whole lens system completely with respect to spherical aberration (cf. Chapter VI). Secondly, mutual repulsion of the electrons can no longer be neglected in beams with high current densities. Well-known results on space charge (cf. §8.2) indicate that the focus spread due to mutual repulsion of the electrons rapidly decreases with increasing voltage of the beam, and this fact provides another reason for using the highest feasible voltage for television viewing tubes. A limit to the increase of voltage is set by difficulties in insulation, by the danger of breakdown by sparking and by the mounting costs for the set providing the power for scanning the fast beams.

A small spot is essential in a television tube in order to obtain high 'geometric resolution' of the picture. This resolution is given by the number of picture points, n_p, that can be distinguished in a scanned area, namely, $n_p = x_T y_T / r^2$, where $2x_T$ and $2y_T$ are length and width of the picture and $2r$ is the diameter of the scanned spot. For example, the resolution of the commercial British television tubes is of the order of 2×10^5 picture points per frame.

The beam currents which are necessary for production of sufficiently bright television pictures may be judged from the following standards: 100 lumens/m.^{2} are required as a recommended minimum for reading of a lighted page, and this brightness should also be desirable for large screen projection television.

On the other hand, an efficient fluorescent screen produces up to several candles per watt for an incident cathode ray of the order of 5 keV. (1 candle emits 4π lumen). The brightness of the screen is roughly proportional to the screen current, and it is approximately a linear function of the square of the screen voltage. Hence direct viewing tubes using about 4–6 keV. beams scanned over picture of

the order of 0·1 m.^{2} need beam currents of at least 10^{-4} A. Projection tubes of $0{\cdot}5 \times 10^{-2}$ m.^{2} fluorescent screen area and operated with 30–80 keV. need 10^{-3}–10^{-2} A. beam current, depending on the final size of the projected picture (cf. Epstein and Maloff, 1945; Epstein and Pensak, 1946; and Swedlund and Thierfelder, 1951).

For all types of television tubes, economy in the scanning power that is supplied to the deflexion field is of technical importance. The question arises whether power could be saved by the use of a post-accelerating field. For a given beam velocity at the fluorescent screen, introduction of acceleration after the deflexion—as discussed in § 12.1—would allow us a decrease of beam velocity in the deflexion field and hence a decrease in field intensity. But for best economy in power the distance of the deflecting condenser plates (or the diameter of the deflecting coils) would have to be as small as feasible with respect to the maximum angle of deflexion and with respect to the given diameter of the beam. Decrease of beam velocity, on the other hand, implies, according to Lagrange's law (cf. (2.7)), a corresponding increase in beam diameter. Thus the separation of the deflecting plates (or the coil separation) would have to be increased correspondingly. The volume of the deflecting field would be increased and so would be the supply of power which is proportional to the volume of the field. Thus the advantage of a decrease in scanning power which may have been expected owing to decrease in deflexion field intensity on account of reduced beam velocity is cancelled out by the increased volume of the field.

A wide field for the application of electron optics is provided in the design of pick-up tubes for television. A considerable development of these tubes has taken place over the last 20 years and is still going on. The principles of the most important types of pick-up tubes will be described here. They are the iconoscope, the projection iconoscope or superemitron and the orthicons. For a more comprehensive discussion, the summary by McGee (1947) is recommended.

In the iconoscope devised by Zworykin (1933*b*) the image to be transmitted is focused on a mosaic screen consisting of a vast number (order of 10^7) of minute photosensitive islands. These islands are densely spread over a thin mica sheet which is backed by a metal electrode, the so-called 'signal plate'. The mosaic screen

is scanned by an electron beam of 1·5 keV. Under the beam impact each island—by secondary electron emission—suddenly charges up to a given small positive voltage. As the beam scans the whole picture, a train of impulses will be passed to the signal plate; these impulses can be amplified for transmission. The magnitude of each impulse depends upon the potential of the mosaic element at the moment of the impact of the scanning beam, the original potential being given by the cumulative photo-effect due to the illumination of the element in the optical image during the frame period. The uncharged ('dark') element must lose more secondaries than the positively charged ('bright') element to bring them both back to the same positive potential.

The electron gun in the iconoscope has to provide a focus of about 0·1 mm. diameter. Great depth of focus is required for the scanned beam to remain sufficiently in focus over the whole mosaic screen which generally is arranged at an angle of 45° to the axis of the gun. Small beam currents of only a fraction of a microampere are required. A symmetrical two-diaphragm emission system (cf. §9.1), with proper spacings to produce a widely divergent beam, is suitable for the purpose. However, a fine aperture-stop of width a fraction of that of the anode diaphragm, arranged about half-way between emission system and focusing lens, is necessary to cut away the bulk of the beam leaving the paraxial rays only, to form a very narrow pencil of hardly any aberration and of great depth of focus.

For reasons which cannot be discussed here (low photo-efficiency of mosaic; stray secondary electrons falling back to the mosaic and interfering with the storage action of the photo-elements), the iconoscope has an efficiency of the order of only 1 %. An increase by a factor 10 in efficiency has been achieved in the superemitron or image-iconoscope by Lubszynski and Rodda (1934), shown in fig. 12.2. There, the light image is projected by a glass objective on to the transparent photocathode *P*. This light image is converted into an image of photo-electrons and projected with the aid of the magnetic lens *L* on to the mosaic screen *M*. Each photo-electron impinging on the mosaic liberates about five secondaries, thus charging the mosaic at the rate of the brightness of the picture points. An electron beam from the gun *G* is scanned over the mosaic screen, and in the signal plate *S* which backs the screen electric

impulses are generated in the same manner as just discussed in the description of the iconoscope. Of special electron-optical interest in the superemitron is the projection of the photo-electric image on to the signal plate. This will be discussed in connexion with image converter tubes in § 12.5.

The pick-up tubes described so far suffer from the difficulty that the secondary electron emission from the mosaic screen cannot be fully withdrawn to the anode represented by the conductive coating of the tube. Secondaries returning to the mosaic prevent full efficiency of charge storage; in addition, they cause variation in background and spurious signals.

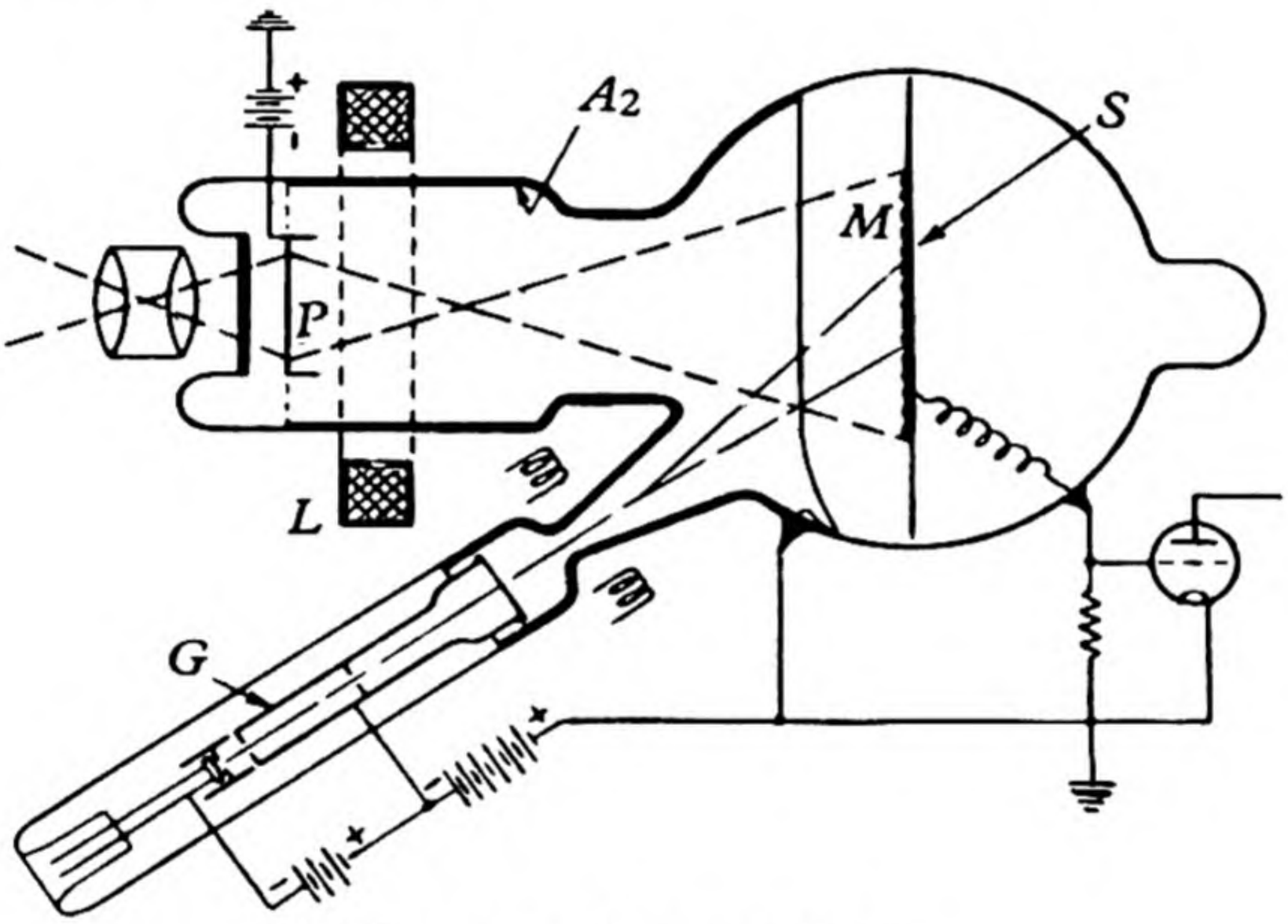

Fig. 12.2. Superemitron.

On the other hand, if in front of the mosaic an electric field is set up which decelerates the approaching scanning beam to almost zero velocity, the photo- or secondary-electrons emitted from the mosaic are accelerated away from it. At the low energy of impact of the scanning beam on the mosaic very much less than one secondary per primary electron is emitted. Hence at each scan, the mosaic elements are returned to an equilibrium at cathode potential.

The idea of a cathode-potential-stabilized pick-up tube ('C.P.S. tube') has been applied in the orthicon by Rose and Iams (1939). These authors first realized that particular electron-optical field arrangements were needed to keep the scanning beam at the moment of its impact perpendicular to the mosaic plane, otherwise a tangential velocity component of the electrons as they graze the

surface could soon become large enough for the secondary emission coefficient to exceed unity and the cathode potential stabilization would be upset.

The scheme of an orthicon is shown in fig. 12.3. There, the tube is seen to be surrounded by a solenoid C superimposing a homogeneous magnetic flux of the order of 10^{-2} Wb./m.^{2} over the whole arrangement. A scanning beam of about 100 eV. is emitted from the slow-electron gun G which consists of a two-diaphragm emission

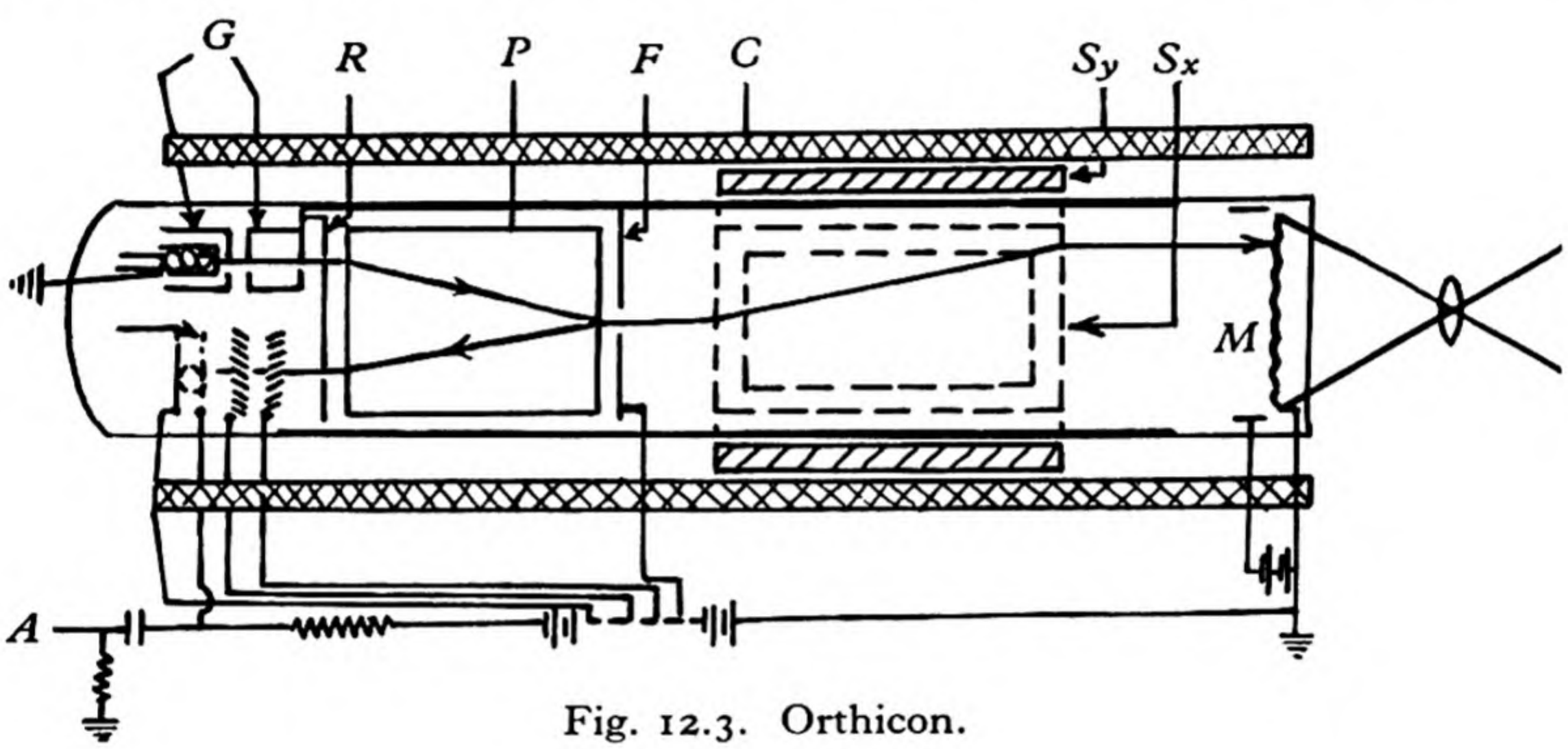

Fig. 12.3. Orthicon.

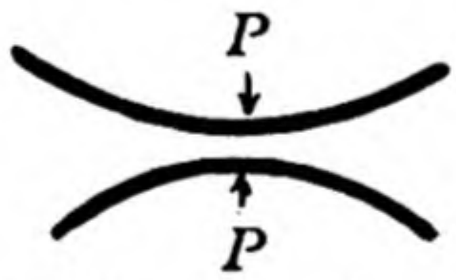

Fig. 12.3*a*. Deflecting plates in fig. 12.3.

system (cf. §9.1) having an anode with very fine aperture stops (0·1 mm.). The beam then passes through a transverse electric field between the deflecting plates P; this field is shielded by two apertured diaphragms, namely, the rear screen R and the front screen F. The plates P are curved approximately as shown in fig. 12.3 (a) representing a cross-section in a plane at right angles to the main figure. The curvature of the plates allows the beam to pass into, and out of, the deflecting field gradually, and it minimizes the loss of focus and the distortion due to edge effects by the termination of the field by the two screens R and F.

Both screens, the wall of the tube and the mean potential of the deflexion plates are all maintained at the anode potential of the gun. Hence, after leaving the gun, the electrons travel with constant

velocity until they approach the target. All the time they move in narrow helical orbits around a magnetic line of force (cf. § 5.1) except when they are between the plates. There, the path is substantially the cycloidal one that also occurs in superimposed homogeneous electric and magnetic fields when the electron has an initial velocity in the direction of the magnetic field (cf. § 11.7).

The net result of this type of deflexion is a shifting of the beam without a change from the original direction. Another shifting of the beam is effected by the magnetic fields of two pairs of saddle coils S_x and S_y (cf. § 11.4), these scan the beam over the whole mosaic screen M.

The mosaic elements pick up a fraction of the electron beam at the rate of their positive charge storage which was acquired by photoemission while the light optical image was projected on to them. The rest of the electron beam returns on the way it came until it reaches the electric deflecting field between the plates P. There the shift is now effected in the opposite direction as is indicated in the figure. This makes it possible to shift the electrons away from the electron gun from which they were emitted. They now leave the rear screen R through a different aperture and they enter an electron multiplier (cf. § 12.4) in which the current is multiplied about 100 times before it is conducted to the amplifier.

The axis of the very narrow pencil leaving the electron gun must be accurately lined up with the magnetic lines of force. This can be done with the help of small auxiliary coils (not shown in the figure). The lining up is necessary to keep the diameter of the helical orbit very small and to avoid transverse velocity components as far as possible. By the helical movement the beam passes through a series of nodes which become more and more closely spaced as the beam is retarded in front of the mosaic. If an element of the mosaic has acquired a small positive potential, the beam will not be slowed down completely to zero velocity. By adjusting beam voltage or magnetic field it is possible to bring the beam to a node, i.e. to an optimum focus on the mosaic.

Apart from the orthicon type just described, two other variants have been applied with practical success. First, the signal need not be picked up from the return beam but it may be taken from a transparent signal plate backing the mosaic screen. One can dispense

with the multiplier and with the electric deflecting plates in this version of the orthicon. Secondly, the single-sided mosaic screen can be replaced by a double-sided one. The one side is discharged periodically by the scanning cathode ray as in the version of fig. 12.3. On the other side, however, there is projected an electron-optical image originating from a continuous transparent photocathode which has greater sensitivity than a mosaic. 'Image-orthicons' of this kind have been described by Rose, Weimar and Law (1946). Images from objects illuminated by only 0·2 lumen/m.^{2} (illumination by bright full moon light) have been picked up clearly by such tubes.

12.4. Photo-multipliers*

In these multipliers the emission from a photocathode is directed on to a target which at the impact of every primary photo-electron releases a relatively large number of secondary electrons. The liberated secondaries are accelerated away from the target surface and directed to a next target, and so on. The yield of secondary electrons, i.e. the average number of secondary electrons released by each primary electron, depends not only on the material and structure of the target surface but also on the energy of the primary electrons and on their angle of incidence. Yields of 5–20 have been obtained under optimum conditions.

It is the task of electron-optical design to provide electric or magnetic fields which accelerate the primary electrons to the proper energy and direct them to the sensitive target surface. At the same time, the secondary emission has to be withdrawn and accelerated towards the next target without interfering with the acceleration of the primary electrons.

The idea of using secondary emission for the purpose of amplification dates back to 1919, but the design of the practically useful multipliers became possible only after the development of highly sensitive secondary emitting surfaces and after the electron-optical methods of design became available.

Excellent reviews are available (see footnote in the beginning of this section) on every aspect of multiplier design, and it will be

* Survey articles: Lubszynski (1947), Zworykin and Ramberg (1949).

sufficient just to draw attention here to the two most important photo-multiplier types.

Fig. 12.4 shows the cross-section through the R.C.A. multiplier which has been developed originally by Rajchman (cf. Engstrom, 1947; Morton, 1949). It contains the photocathode 0, the nine secondary emission targets 1, ..., 9 and the collector 10. It reaches an over-all sensitivity of 5 A./lumen with a gain per stage of 5–6 and requires an over-all working voltage of 1·5 kV.

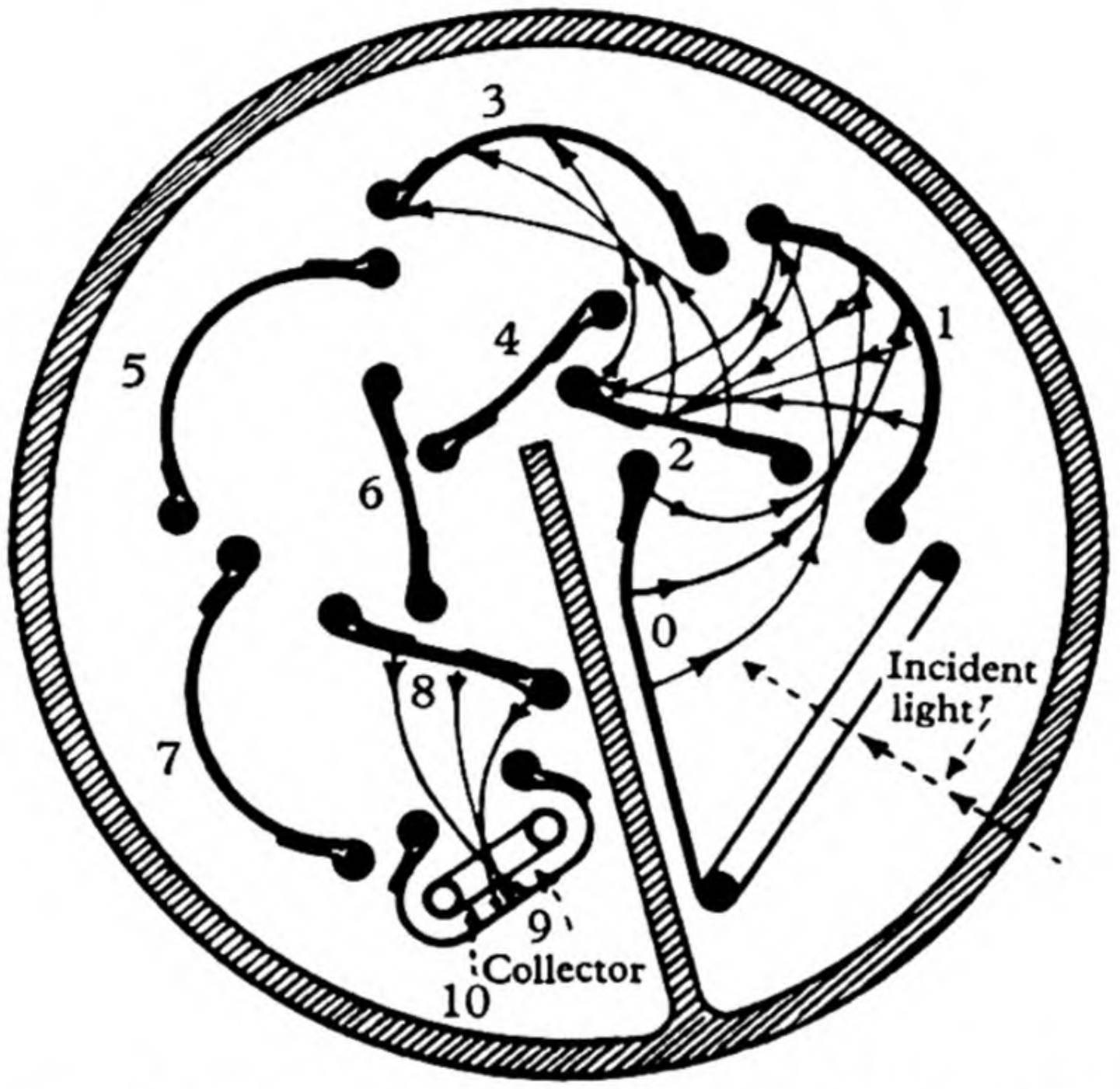

Fig. 12.4. Cross-section through R.C.A. photo-multiplier tube.

Fig. 12.5 shows a section through an E.M.I. multiplier (Sommer and Turk, 1950) which is particularly suitable for picking up the weak scintillations of fluorescent materials utilized for the registration of nuclear radiations. The tube contains 11 multiplying stages D_1 to D_{11} connected to the base B. The collecting electrode E is brought out through the side wall of the tube (O). T is a transparent photocathode of 30 μA./lumen sensitivity, the incident light being marked by arrows L. The multiplication is 10^7 when 160 V. are applied per stage.

The electron optics of the photo-multipliers of figs. 12.4 and 12.5 has been explained in § 10.6. Both these multipliers have been designed for the registration of low light intensities, and the majority of a great number of other multiplier types serve for the

same purpose. In few instances only, multipliers have been used for direct amplification of electron currents (cf. multiplier valves, § 12.9) or for direct registration of single fast electrons or atomic particles. We refer in this connexion to the review article by Allen (1950).

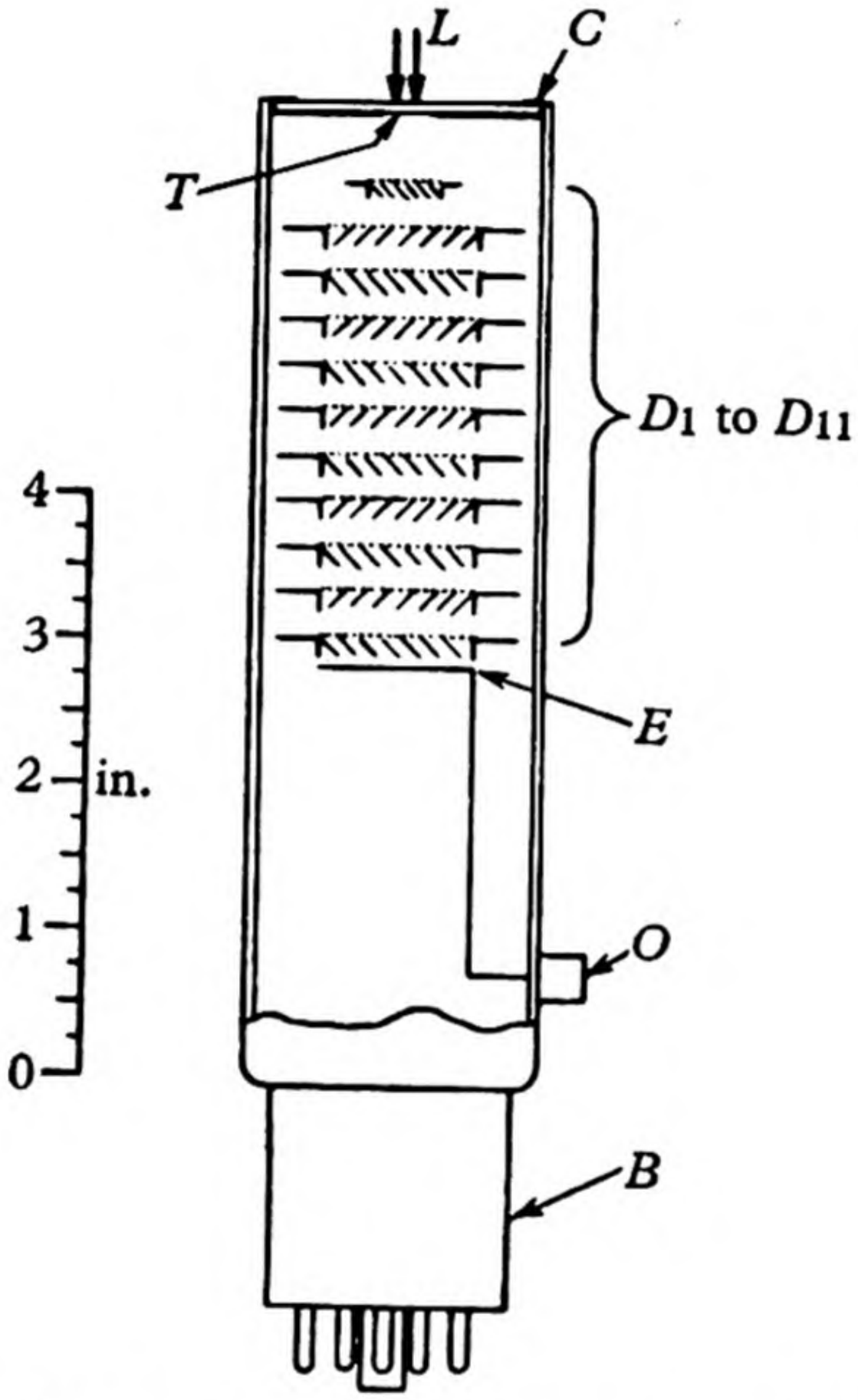

Fig. 12.5. E.M.I. photo-multiplier for scintillation counting.

The sensitivity of a multiplier tube is ultimately limited by random fluctuations (noise) of an electron current which is superimposed over the signal and will make weak signals unintelligible. This noise current is due to thermionic emission from the cathode and to unavoidable leaks in the insulation. For example, the dark current in the particularly efficient multiplier of fig. 12.5 is of the order of 10^{-8} A. at the collector, corresponding to a cathode emission of 10^{-15} A. or 10^4 electrons per sec. With a quantum yield of 0·1 at the photocathode, pulses of 1000 incident light quanta could still easily be detected.

12.5. Image tubes

In these tubes, a light optical image is projected on to a photo-electric surface. There it is converted into photo-electrons forming the electron-optical object. The photo-electrons are projected by an electron-optical lens system on to a fluorescent target where the electron image is reconverted into a light image. Intermediate processes may be employed to increase the intensity of the electron-optical image.

The image tube can serve for two different purposes. It may be used as an 'image converter' for picking up invisible images of infra-red or of ultra-violet rays and for converting them into images of visible light. As an 'image amplifier', the tube may reproduce visible pictures, thereby greatly increasing their brightness.

The earliest image tubes, as first described in 1934 by Holst *et al.*, were still used extensively during the second world war, and consisted of a plane, transparent infra-red sensitive Ag-O-Cs photocathode arranged parallel and in close spacing to a plane, transparent fluorescent screen. Several kilovolts applied between these plane, parallel electrodes provided an accelerating field for the photo-electrons to be drawn directly to the screen and to produce there an image of sufficient brightness. No electron lenses were used for focusing. However, if the spacing between the two plane electrodes was of the order of a few millimetres only, the circle of confusion about every picture point, caused by the initial tangential velocities of the photo-emission, could be kept down to a fraction of a millimetre. Cold emission from the cathode sets the limit to a reduction of the spacing and to an increase of the accelerating voltage.

The simplest image tubes employing electron focusing have been obtained by superposing a homogeneous magnetic field on a homogeneous electrostatic accelerating field. Such arrangements are still incorporated in some types of television pick-up tubes, e.g. in the so-called 'image-dissector' by Farnsworth (1934) in which the electron-optical image is scanned over the small aperture of an electron multiplier. A similar arrangement is also used in the image orthicon described in § 12.3. The target on to which a full-size electron image is projected may have a distance of many centimetres

from the photocathode, a sharp focus being obtained by adjusting the magnetic field intensity.

An image converter, using a combination of an inhomogeneous electrostatic field with a short magnetic lens, has already been shown in fig. 5.19 of § 5.7. This converter is employed, for example, in the superemitron shown in fig. 12.2. There, the flat photocathode P and the surrounding short cylinder ring for concentrating the photo-electron beam are on a common negative potential (-400 V.). The second anode of the scanning gun is extended into the projection neck; it is earthed and serves to accelerate the photo-electrons. The beam of photo-electrons is focused on the target M by the iron-clad magnetic lens L; the rays, however, do not cross over as the schematic figure seems to suggest, but they continuously spread away from the axis. The electron-optical image is magnified about five times. The optical error of spiral distortion (cf. § 6.9) cannot be eliminated completely.

Much effort has been spent in the past on the development of a purely electrostatic image converter. It has been found quite impossible so far to overcome the enormous curvature of the image field if the electron optical object is emitted from a flat photocathode. It has been explained (§ 6.7) how Morton and Ramberg (1936) succeeded in obtaining perfectly flat images by using photocathodes which were concave towards the target. It has also been explained (cf. § 6.8) why the same curvature of the cathode simultaneously served for correcting image distortion. Since, however, high-class glass objectives are designed to produce flat images, a flat cathode on to which the light optical image is projected should be greatly preferable.

Grid controlled image tubes have been used for high speed photography (Jenkins and Chippendale, 1951). There, a tube about halfway between cathode and anode potential was employed as a grid electrode. The exposure was shut electrically by raising the cathode potential to a slightly positive value with respect to the grid. Exposures of a fraction of a microsecond have been obtained.

Some progress in the design of electrostatic image converters had been made during the war, where these tubes served for the observation of infra-red emitters or for objects which were illuminated by infra-red searchlights (cf. Morton and Flory, 1946). Fig. 12.6 shows

the scheme of a German tube (cf. Schaffernicht, 1948) with three electrodes, namely, the curved photocathode terminating the cathode space *C*, the cylindrical accelerator *B* and the conical anode *A* which is on the potential of the fluorescent target (+ 20 kV. with respect to the cathode).

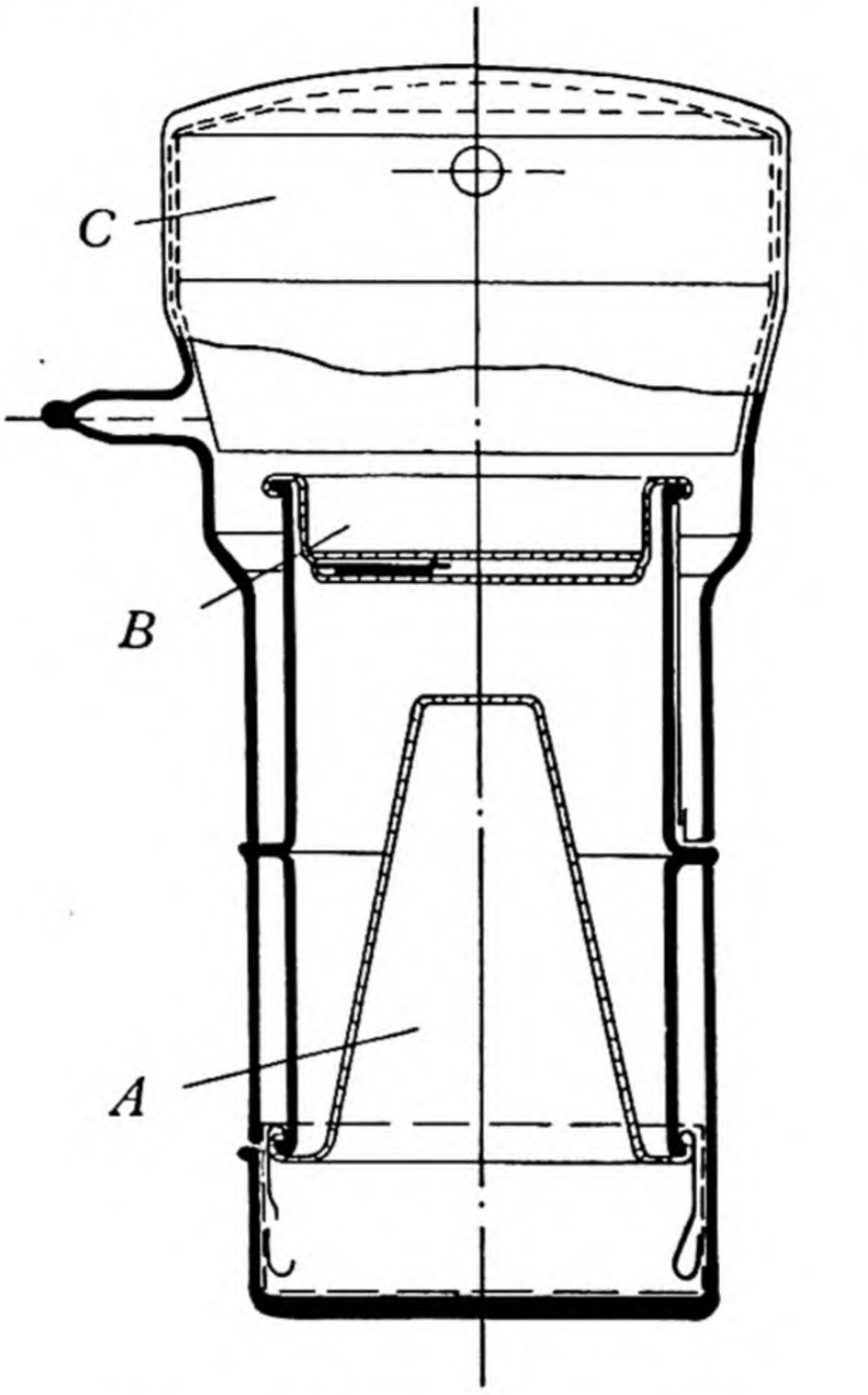

Fig. 12.6. Image converter.

The curvature of the cathode is—as compared with other image tubes—relatively low. The concave equipotentials between cathode and accelerator are kept as concentric as possible by proper arrangement of the latter electrode. Hence the electron rays are initially directed towards a focus near the axis of the system. Thereafter, the rays are made nearly parallel by passing them through convex equipotentials which are produced by field penetration through the accelerator aperture. In this way a slightly reduced image of great depth of focus is projected on to the fluorescent target. The image may be focused sharply by adjustment of the accelerator potential which, however, is kept near to cathode potential in order to avoid field emission from the cathode. Image tubes with six electrodes

allowed in this way an application of 50 kV. to the anode with corresponding increase in light sensitivity and resolving power.

The least resolved distance has been shown to be inversely proportional to the anode voltage (cf. § 7.1). At the moment, however, the limit for resolution is not given by electron optics but rather by the fluorescent screen. With screens of finest grain (1–2 μ) and of suitable thickness (10 μ) distances down to 10 μ could still be resolved.

Various schemes have been tried for increasing the light sensitivity of the image tube. One particular type working with electron multiplication by secondary emission is shown in fig. 12.7 (cf. Schaffernicht, 1948). There two coaxial image-projecting systems

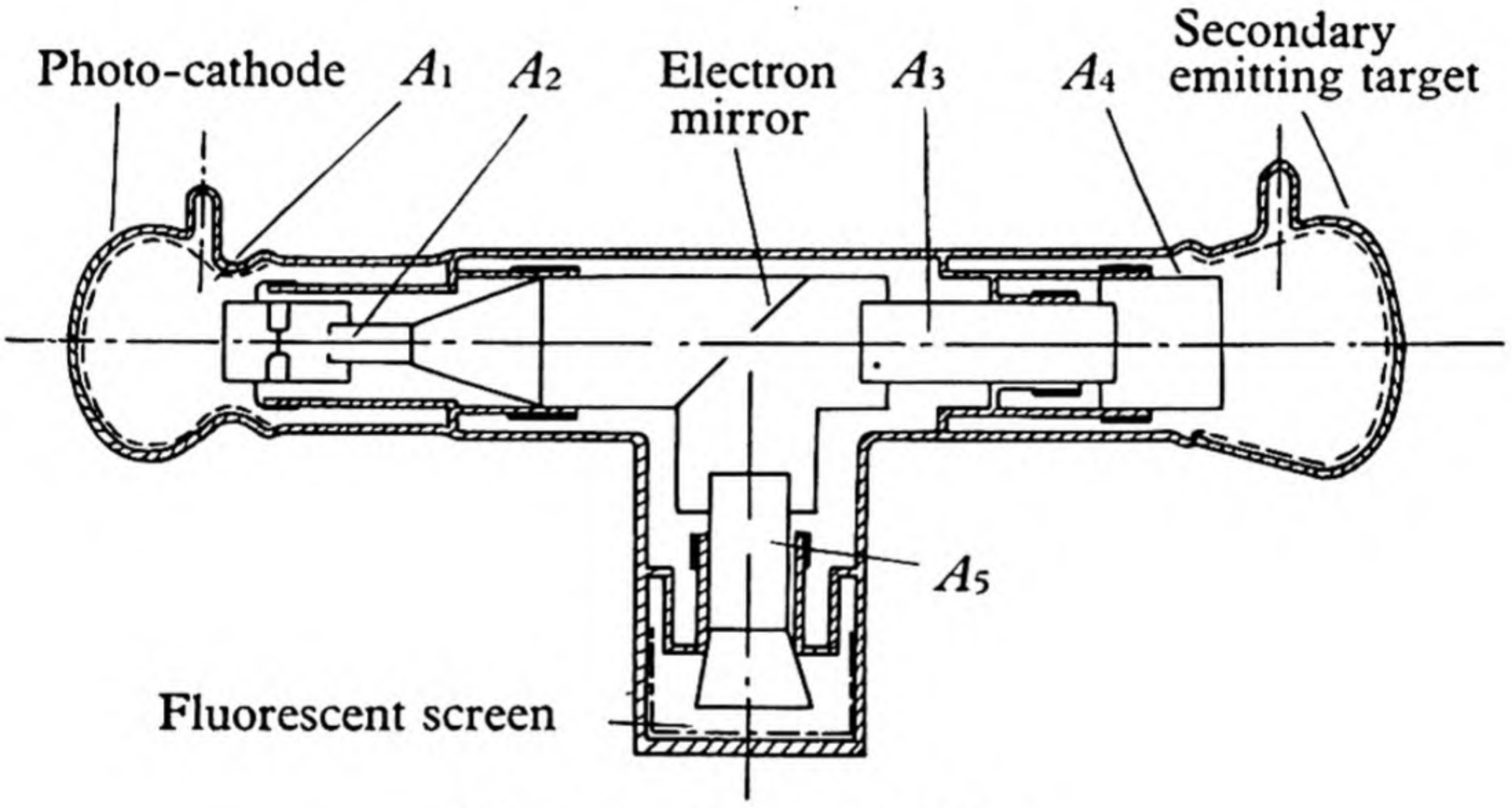

Fig. 12.7. Image amplifier.

are facing one another; they contain a photocathode and a secondary emitting cathode respectively. These systems are separated by an apertured diaphragm which is inclined at an angle of 45° towards the axis. The field about this diaphragm allows the photo-electrons to pass straight on, but it reflects the secondary electrons at right angles into an image tube where they are accelerated and observed on a fluorescent screen. There are five different anodes: By A_1 the photo-electrons are accelerated up to 10 keV. and by A_2 they are again decelerated down to 100 eV. With this energy they pass the aperture of the 45° diaphragm. By A_3 and A_4 the electrons are accelerated again to 10 keV. and respectively decelerated to 100 eV. With this energy they impinge on the secondary emitter. The

secondary electrons passing through A_4 and A_3 are accelerated to 9·9 keV. only, and they are slowed down to zero voltage in front of

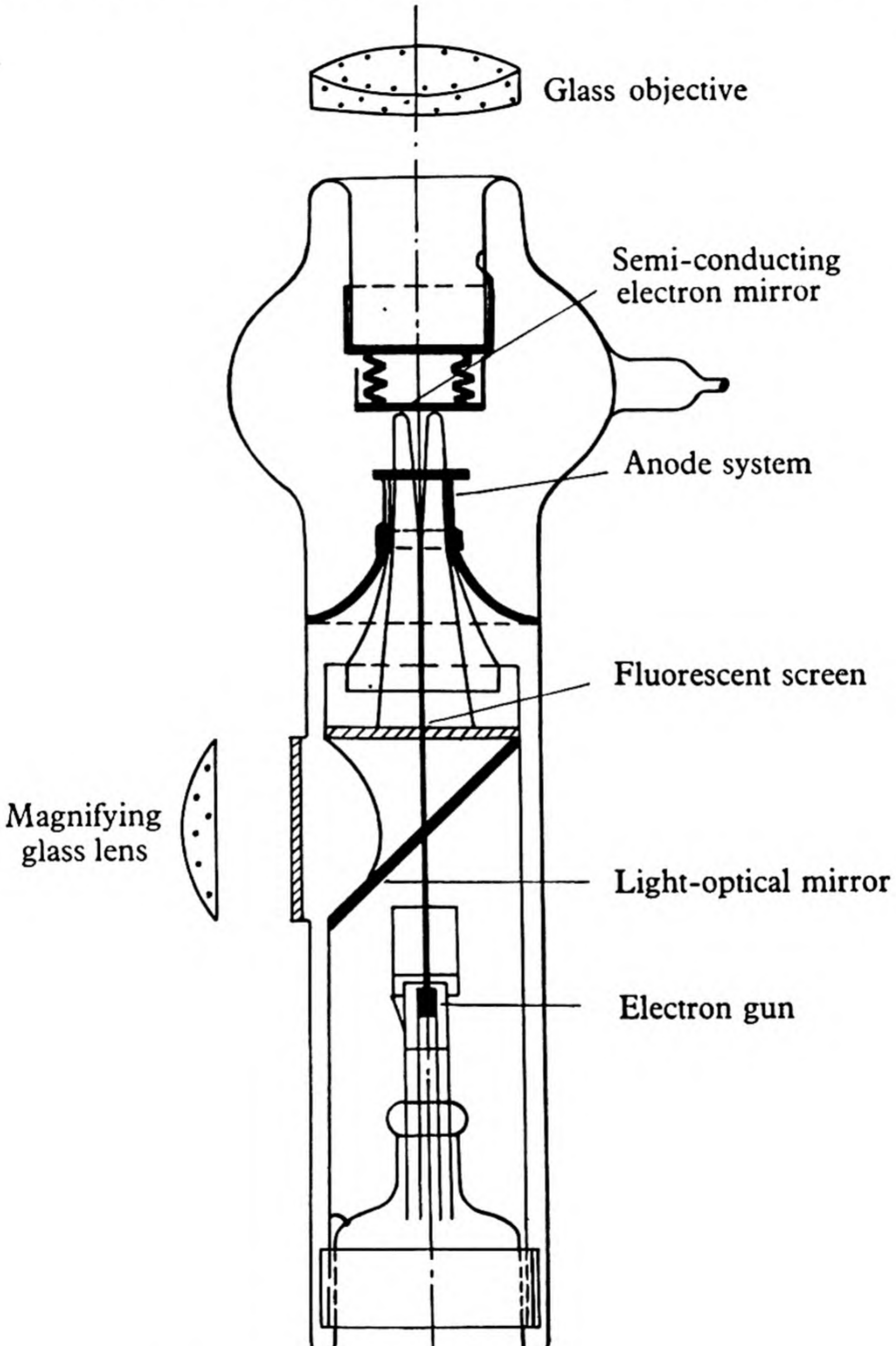

Fig. 12.8. Image tube with semiconducting electron mirror.

the 45° diaphragm so that they are reflected into the image tube. By A_5 the electrons are eventually accelerated to 20 keV. and they reach the screen with this energy. Inertia-less amplifications by a

factor up to 20 have apparently been obtained. However, the resolution of the image appeared to be much reduced by the relatively great chromatic error due to the broad energy distribution of the secondary emission.

A further example for image intensity multiplication is shown in fig. 12.8, which represents ani mage tube employing a semi-conducting electron mirror (cf. Schaffernicht, 1948). In this tube, a 5 keV. beam is projected from an electron gun. On its way along the axis of the tube the beam passes first through a small aperture in a light-optical mirror which is inclined at 45° towards it, then through an aperture in the fluorescent screen. Eventually, the beam reaches the semi-conducting electron mirror by which it is reflected on to the fluorescent screen. The image on this screen is observed through the magnifying glass via the light-optical 45° mirror.

The semi-conducting electron mirror consists of an infra-red sensitive photoconductive layer of high specific resistance (e.g. bismuth selenide, $10^{11}\,\Omega\,\text{cm.}$, $3\,\mu$ thick) on to which the light-optical image is projected by the glass objective shown in the figure. According to the light distribution in the image, a 'potential relief' is formed on the surface of the semi-conductor by which the reflexion of the electrons is modulated. The incident electron beam should be of low density ($\approx 10^{-2}\,\text{A./m.}^2$) so that scattered secondary electrons, produced by the impinging fraction of the primary electrons, do not become large enough to disturb the original potential relief. Though the development of this novel kind of image tube is still in its infancy, high sensitivity in the 2μ infra-red and a resolution of $\frac{1}{100}$ mm. are claimed already by the author.

12.6. Electron microscopes*

Almost immediately after the discovery of the lens properties of magnetic and of electrostatic fields, investigations were started on the possibility of utilizing these fields for image projection with high magnification. In 1931, Knoll and Ruska gave the first account on the use of magnetic lenses for obtaining high magnifications, while

* Books on the electron microscope see Bibliography B, under: Ardenne (1940*b*), Burton and Kohl (1945), Borries (1949), Cosslett (1947, 1950, 1951), Drummond (1950*a*), Gabor (1945), London Institute of Physics (1950), Mahl and Gölz (1951), Wycoff (1949), Zworykin *et al.* (1945).

Brüche and Johannson (1932) succeeded about the same time in developing electrostatic microscopes for inspection of emitting surfaces.

The 'immersion objective' of the electrostatic 'emission microscope' consists of two closely spaced, charged diaphragms with circular apertures. By using the right geometrical dimensions, the focal length of these objectives can be made as short as 1 mm. Hence magnifications of several hundred are produced easily by the direct projection of the image of a self-emitting surface on to a fluorescent screen.

For high magnification of transparent objects, powerful iron-shielded coils with special magnetic pole-pieces (cf. § 5.4) or alternatively electrostatic saddle-field lenses (cf. § 4.6) are used. Both types of lenses reach down to focal lengths of the order of 1 mm.

The scheme of a highly magnifying magnetic electron microscope is shown in fig. 12.9 (cf. Zworykin *et al.* 1945). The electron source consists of a hair-pin emission system (cf. § 9.6); the emitted beam is first accelerated to about 60 keV. and then concentrated on to the object by means of an iron-shielded condenser coil. A special object chamber makes a controlled lateral displacement of the object possible during the observation, and it allows insertion or withdrawal of specimens with a minimum time loss. Moreover, the chamber is operated with an air lock for preventing major disturbances of the vacuum in the microscope during the latter operation. An objective coil of the kind described in § 5.4 forms from the object an electron-optical 'intermediate image' of a few hundred times magnification. By a projection coil (cf. § 5.4) the intermediate image is again magnified a few hundred times, while it is projected as a final image on to a fluorescent screen or photographic plate as shown in the figure. A diffusion pump seen in the stand of the microscope provides for continued maintenance of a good vacuum during the operation.

A high degree of stability of voltages and currents is necessary for reaching highest resolutions. The objective lens current and the accelerating anode voltage both have to be constant within 1/10,000, while any fluctuations in condenser current or in projection coil current should be less than 1/1000.

Simpler in operation and cheaper in construction are the electrostatic electron microscopes of high magnification (Mahl, 1939), though they have not reached the high performance of the magnetic type. A schematic diagram in fig. 12.10 shows the filament of a hair-

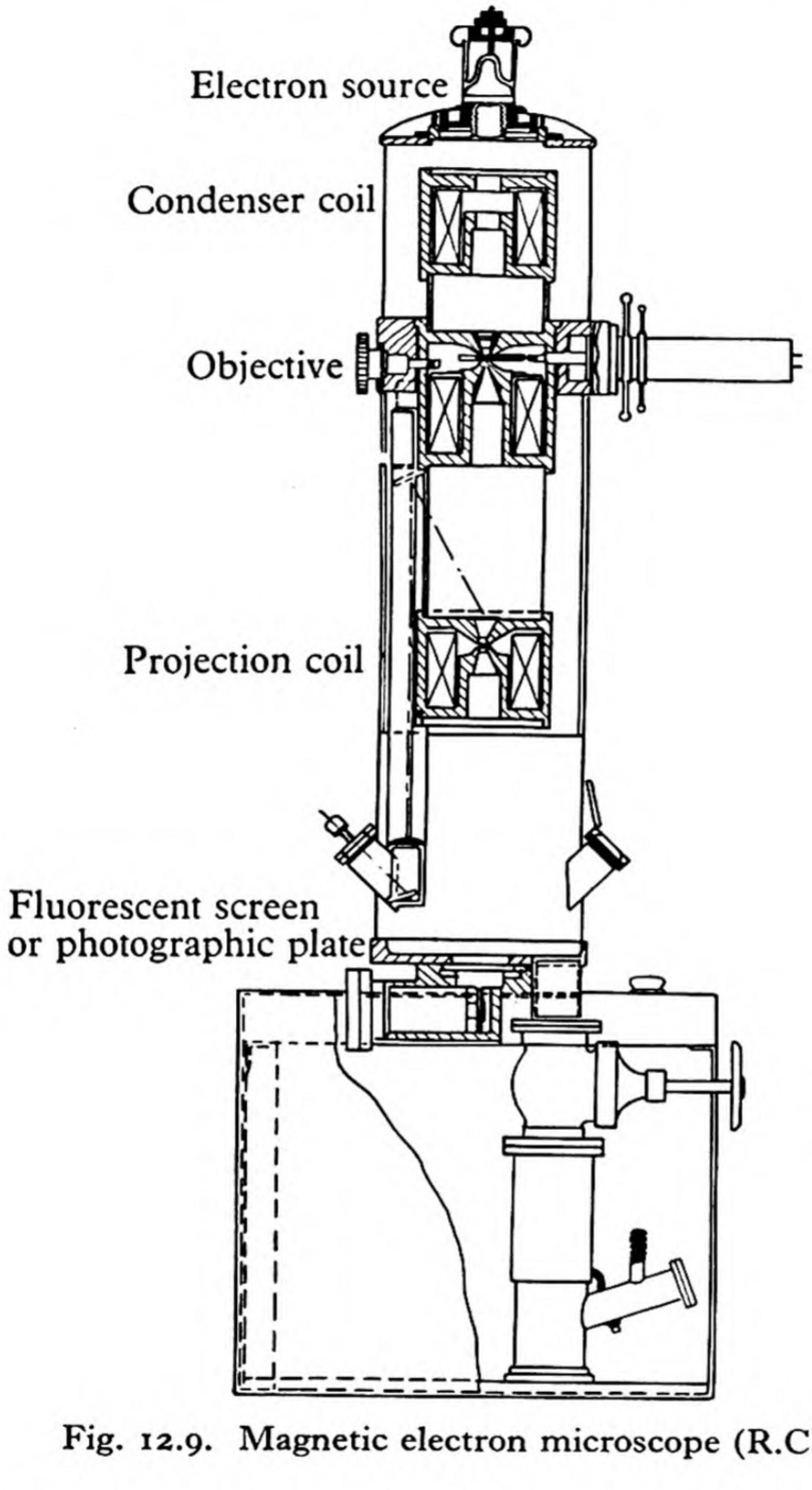

Fig. 12.9. Magnetic electron microscope (R.C.A. type).

pin emission system (cf. § 9.6) and the two high-voltage saddle-field lenses marked as objective and projector. The inner diaphragms of both these lenses are connected together with the hair-pin filament to the negative terminal of a source of, say, 40 kV., while the anode of the emission system and the two external electrodes

of both saddle-field lenses are connected to earth. Hence both lenses are operated as univoltage lenses (cf. §4.6), and the errors arising from small voltage fluctuations are largely eliminated (cf. §7.1).

A few other types of highly magnifying electron microscopes are interesting in principle but have not been much used in practice. We only mention:

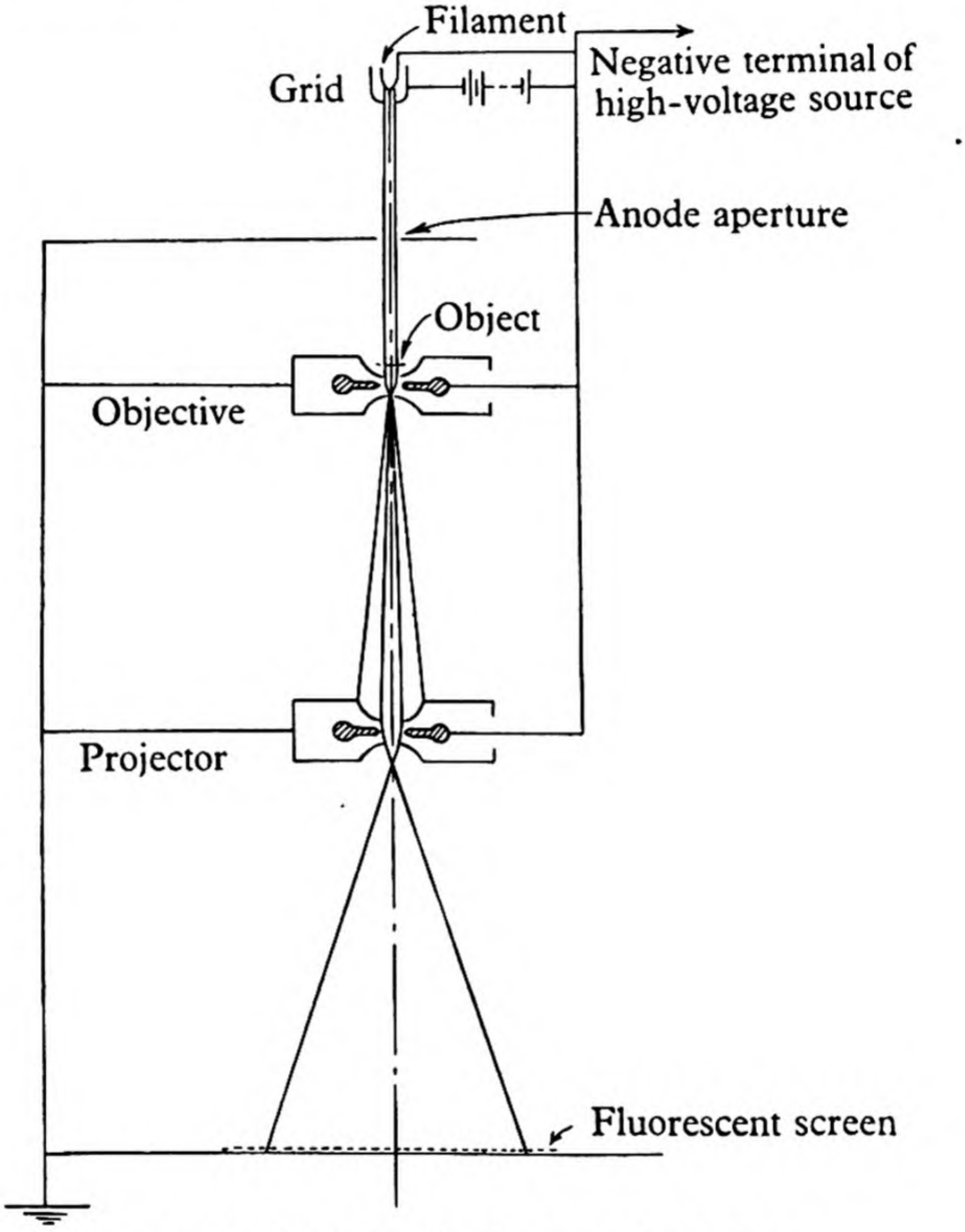

Fig. 12.10. Electrostatic electron microscope.

(1) The point-projector, or shadow microscope (Boersch, 1939), in which a minute electron source, the 'probe', is brought very close to the object casting an electron shadow on to a relatively distant fluorescent screen.

(2) The mirror microscope (Mahl and Pendzich, 1943) which has been developed from the electrostatic microscope shown in

fig. 12.10. By connecting the middle electrode of the projector lens to a voltage about 10 % more negative than cathode voltage, the projection lens is converted into a mirror of about 2 mm. focal length. It projects a highly magnified electron image on to a photographic film arranged directly at the back of the objective. The film has to have a hole for the passage of the electrons on their way to the mirror.

Progress in the technique of overcoming alignment and adjustment difficulties (§ 6.2) has led to the development of three-stage

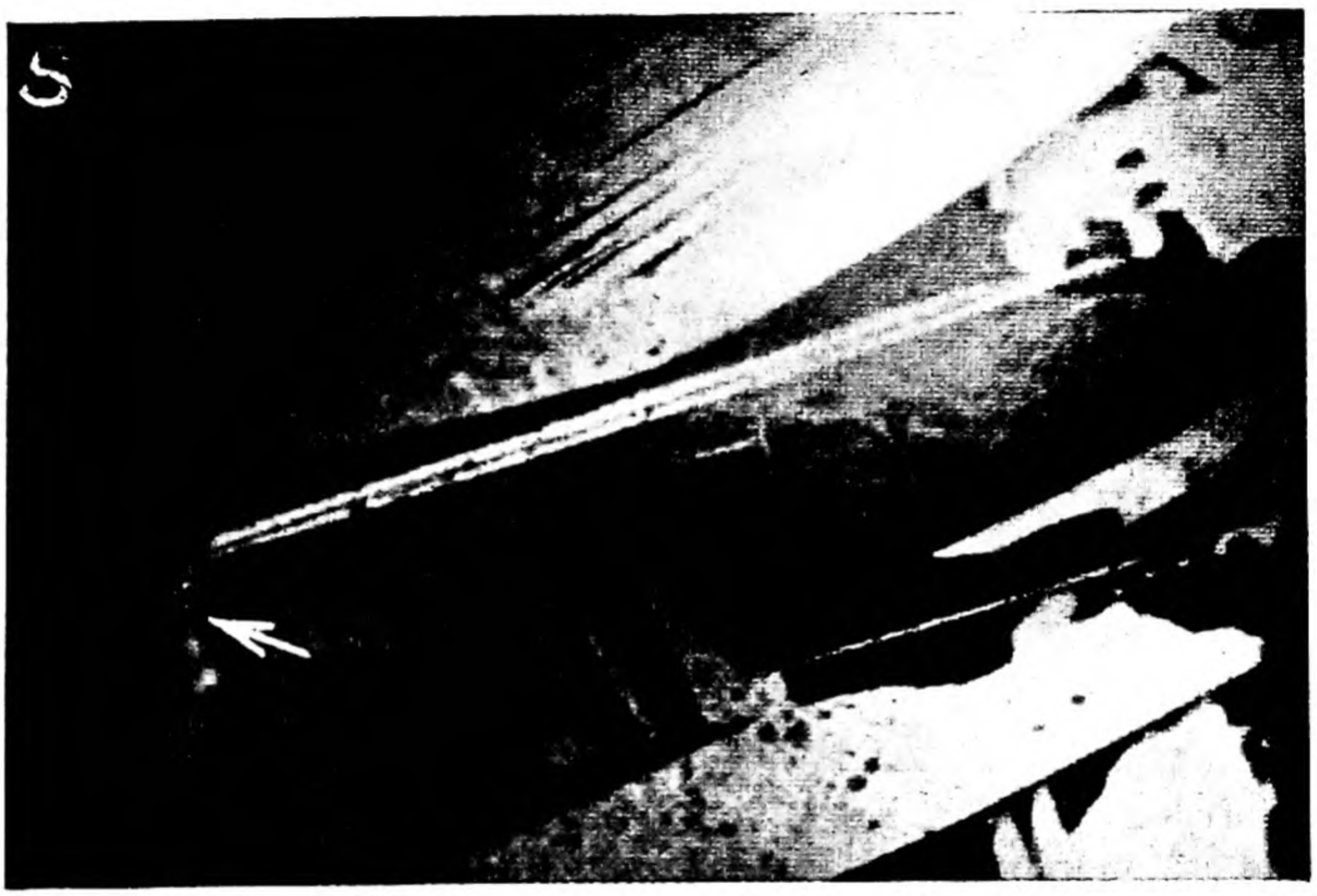

Fig. 12.11. Emission microphotograph: transition of α- to γ-iron.

magnetic lens microscopes (Haine *et al.* (1950), Challice (1950)). In addition to the objective and to the final projector, these instruments have an intermediate projection lens of relatively long focal length. Usually, magnifications of about 50×, 10× and 60× are employed in the three stages, instead of about 150× and 200× magnifications which are common in the two-stage instruments. The three-stage microscopes offer an advantage in compactness, range of magnification, depth of focus and freedom from distortion in comparison with the earlier two-stage microscopes. We have, however, to refrain from going into further detail.

To characterize the very different fields of application of electron microscopy, only four microphotographs are presented here. The picture shown in fig. 12.11 has been taken by Burgers and Amstel

(1938) with an electron-optical immersion objective. It shows the crystal texture of the surface of a thermionic cathode which was made from a tapered iron strip, activated with strontium and barium. As the tapered cathode varied in its electrical resistance from place to place, a temperature gradient occurred along the strip. At the wider side of the strip the temperature was below the transition temperature of the iron (about 900° C.), and the cubic body-centred α-modification is seen. At the narrower side of the strip the temperature was above the transition point, and the cubic face-centred γ-modification is apparent. The boundary line

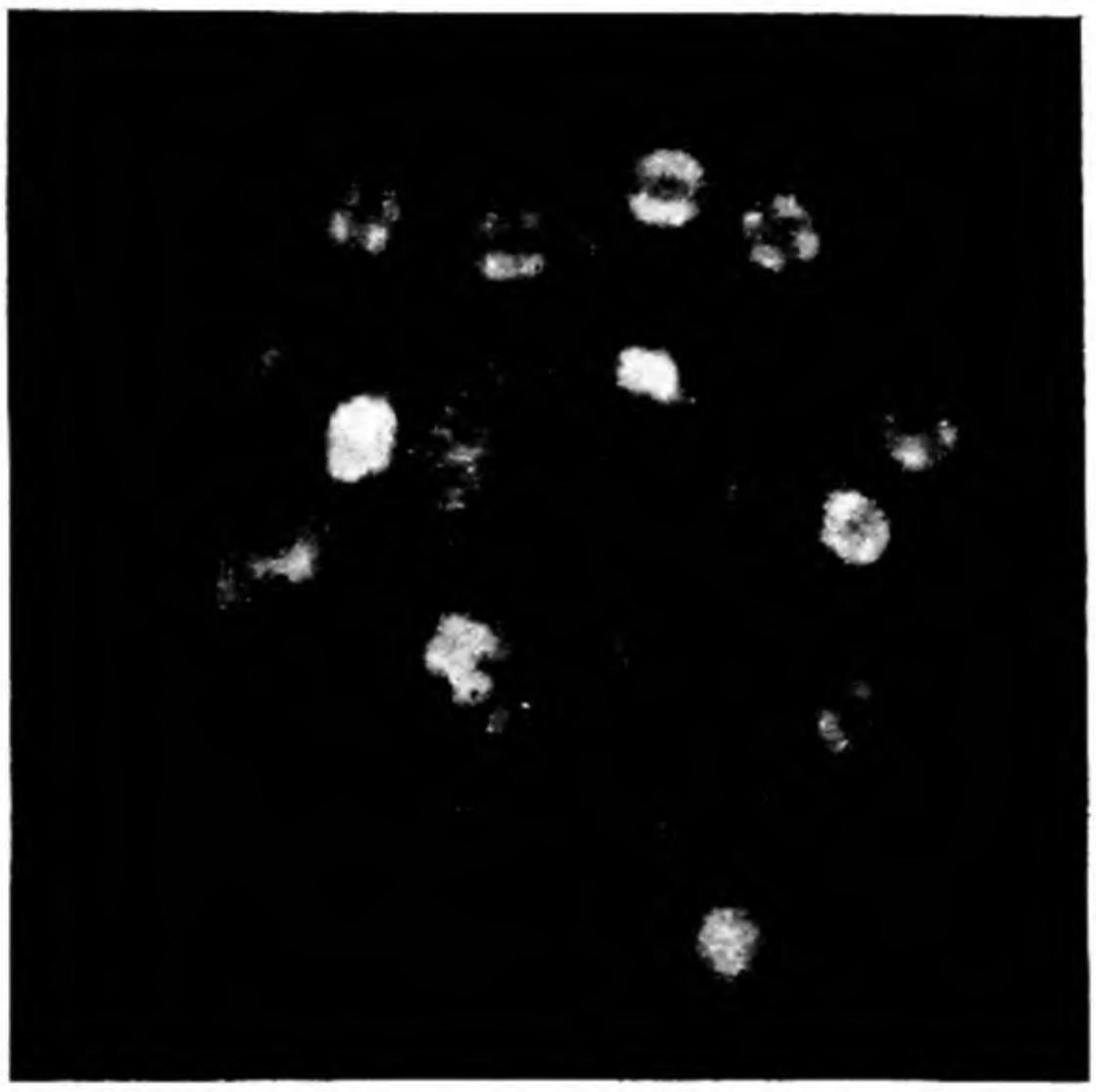

Fig. 12.12. Field emission micrograph of single copper-phthalo-cyanin molecules.

between the two modifications which is clearly visible in the photograph is marked by an arrow. The photograph may serve as an example for surface investigations which have brought new information about the mechanism of thermionic emission, and which have opened new lines for metallographic research.

Fig. 12.12 shows a picture which has been obtained by Müller (1950*a*, *b*) from a small tungsten point by field emission. The emitted electrons were drawn directly by a strong radial field on to the inner fluorescent surface of a spherical anode bulb which surrounded the point cathode concentrically. The arrangement contained no lens system. The magnification obtained is given simply by the ratio of the radii, e.g. magnifications of 10^5–10^6 have been obtained from points of 10^{-3}–10^{-4} mm. radius in a bulb of 10 cm. radius. Such field-emission microscopes have reached higher resolution than any

other type of microscope. The image seen in fig. 12.12 shows details of single copper-phthalo-cyanin molecules which were evaporated on to the point. The clover-leaf structure of the four benzene rings surrounding the copper atom is distinctly visible. Seven Angstrom units, corresponding to the mutual distance of these benzene rings, are still resolved. Single molecules which slightly protrude from the spherical surface of the tungsten point cause an initial divergence of the field lines. This will lead to an initial divergence of the orbits of electrons emitted from the edges of the molecules, the current density at the fluorescent screen is modified and the picture of the molecule becomes visible. However, owing to the above divergence of lines, the image of the molecule is projected with a somewhat greater magnification ($2{\cdot}8 \times 10^6 \times$) than the background ($3{\cdot}5 \times 10^5 \times$). The range of application of the field-emission microscope is still rather limited. Apart from the investigation of structures of a few selected molecules, it has been applied to the study of cold electron emission, in particular to the change of this emission by absorption of atoms with relatively low work function (Jenkins (1943)).

A third micrograph shown in fig. 12.13 (Nixon, Rothamsted Exp. Station) represents a highly magnified image of the tobacco mosaic virus, taken with the magnetic microscope of fig. 12.9. This picture is given here as only one characteristic example of the very wide field of biological application where the electron microscope has been found to be of greatest importance. Objects beyond the resolving power of the best light microscopes (1000 Å.) belong to the proper domain of the electron microscope. For instance, viruses, genes, internal structures of bacteria and proteins have been recognized clearly. The picture in fig. 12.13 is not the result of straightforward exposure of the object. The contrast has been improved by 'metal-vapour shadowing', i.e. before the exposure an atomic beam of heavy metal vapour has been projected at a slight angle (5–10°) to the surface, casting an outline of the elevations of the specimen upon the surface. This example for preparing the object serves to show that new specimen techniques have been developed for electron microscopy.

As another example may be mentioned the replica technique for investigation of surface structures of solids. For instance, in

fig. 12.14 (cf. Drummond, 1950*b*) is shown a micrograph obtained by exposure of a thin aluminium oxide film which has been stripped off from an etched aluminium surface. The contrasts in the picture are due to the varying thickness of the replica film produced by the varying height of the investigated surface relief. Frequently the replica film is made from a plastic substance, e.g. from Formvar, which is dissolved in a volatile solvent and deposited on the surface. After evaporation of the solvent, the film is stripped off and investigated with the electron microscope.

For more information on the numerous methods of practical electron microscopy, the reader should consult the specialized books quoted in the footnote at the beginning of this section. The large range of novel applications of electron microscopes is due to their superior resolving power. It has been explained in § 7.5 why the resolving power of an objective is essentially limited by its spherical aberration and by the diffraction error. The ultimate limit of resolution has found a great deal of theoretical discussion in the literature. We can draw attention only to a recent thorough wave-mechanical treatment by Glaser (1949*b*) who derived explicit expressions from which it appears that for the best available magnetic objectives a resolution of 4 Å. should still be possible at 60 kV. If the measured values (20 A.U.) are considerably greater, this is probably due to secondary disturbances, e.g. to the field asymmetries discussed in § 6.2, to movements of the object, to the grain of the photographic plate, etc.

12.7. Electron spectrometers*

These instruments have been of great importance for the development of modern physics. Their design has undergone a gradual evolution during the last 50 years, but systematic application of electron-optical principles has come into play only recently. Some primitive spectrometer arrangements were used for the first measurements of the specific charge e/m at the end of last century. Electron-spectroscopic precision methods came in use in 1908–11 for three purposes, namely, for e/m measurements, for measuring velocity spectra of cathode rays after their transmission through thin

* Survey articles: Cavanagh (1950), Persico and Geoffrion (1950).

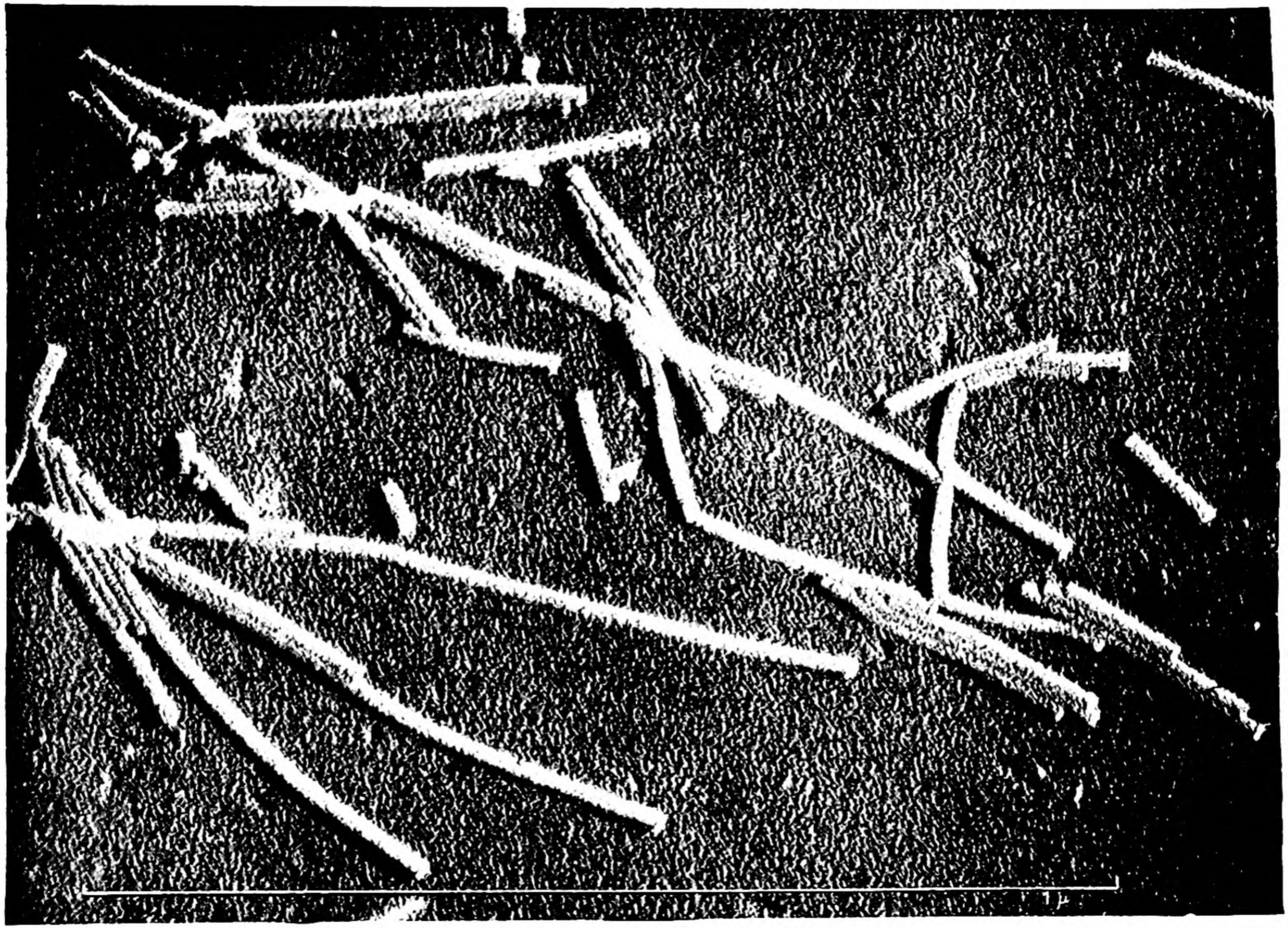

Fig. 12.13. Tobacco mosaic virus, shadowed with palladium.

Fig. 12.14. Aluminium oxide replica of aluminium surface, etched with hydrochloric acid and deformed.

foils and for the investigation of β-spectra. Further progress in electron spectrometry was derived from experience evolved in the mass spectroscopy of atomic rays. This branch, however, developed along different lines, mainly because small apertures are sufficient for mass spectroscopy while wide-angle focusing is desired for electron spectrometers.

The recent development of electron spectrometry is derived (i) from the use of electron lenses as lens spectrometers described

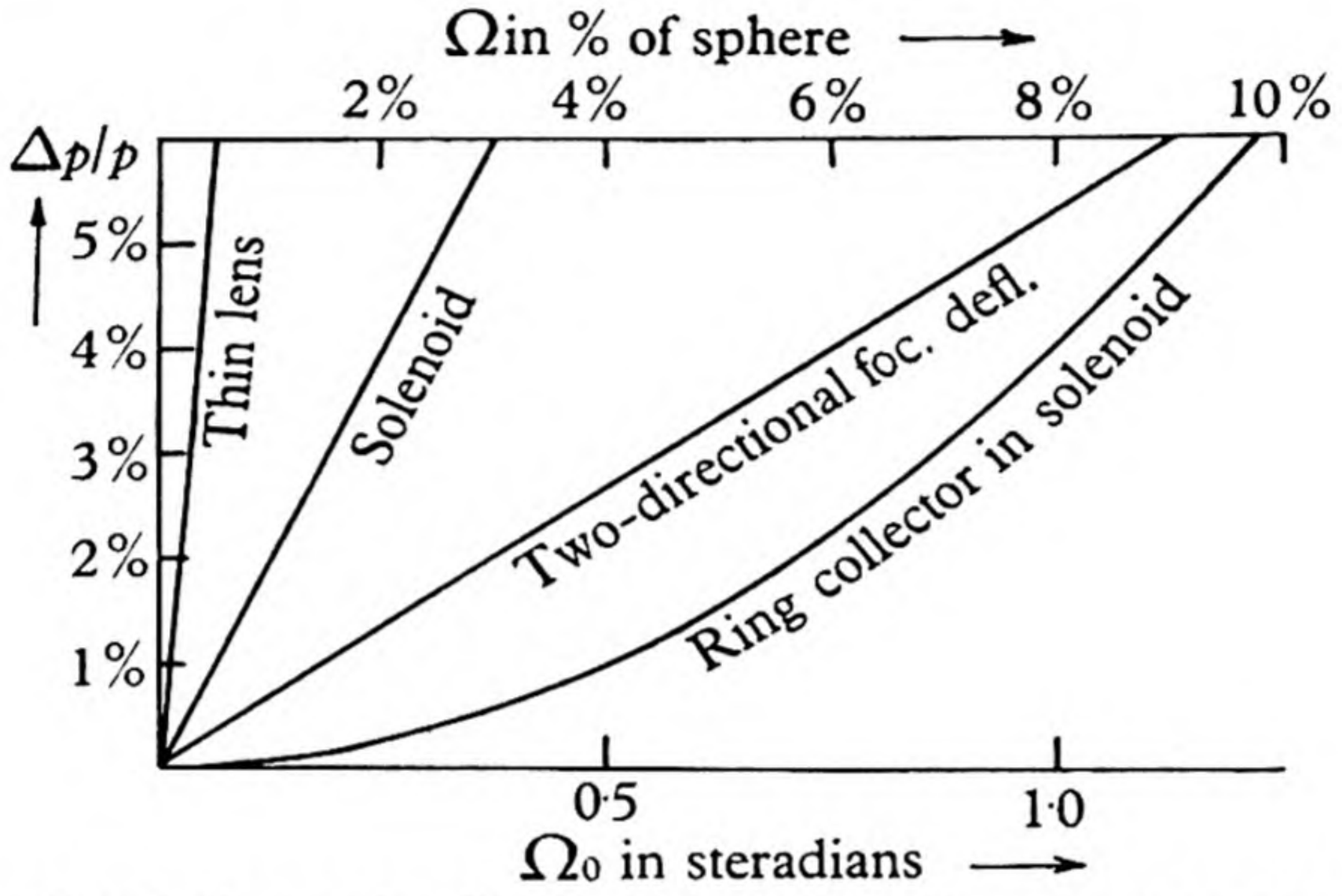

Fig. 12.15. Resolution and collecting power in various electron spectrometers.

in detail in §7.2. (ii) from the electron-optical study and improvement of focusing deflexion, an account of which has been given in §§ 11.5–11.7 and 11.9–11.10.

The most important criteria for the merit of a spectrometer are given by its resolving power $p/\Delta p$ and its collecting power Ω (cf. Chapters VII and XI). These two characteristics are compared, according to Frankel (1948), by fig. 12.15 for a few representative spectrometers. If point sources are used, both $p/\Delta p$ and Ω are simple functions of the beam aperture. For example, as seen in fig. 12.15, a simple proportional relationship holds between resolution $\Delta p/p$ and collecting power Ω for the thin magnetic lens, for the solenoid, and for the two-directional magnetic focusing deflexion. For every value of Ω, the resolving power of the two-directional focusing deflexion is seen to be superior to that of the solenoid; again the latter is superior to the resolving power of the thin lens.

The widespread application which the lens spectrometer has found in the past is not due to a superior collecting and resolving power but rather to the technical simplicity of the lens coil and to the easy accessibility of the components (counter, source, etc.). On the other hand, the excellent two-directional deflexion focusing spectrometer requires a large expensive magnet with precision-ground pole-faces by which all the components are enclosed. The solenoidal spectrometer takes an intermediate position in the rank of merits. In comparison with the lens, its collecting and resolving powers are higher but source and collector are less accessible. The number of ampere-turns needed for the solenoidal focusing of a given electron momentum is much higher than the number of ampere-turns required by a focusing lens.

Now the introduction, due to Frankel (1948), of the annular slit in front of the collector has rather changed the whole position. A curve given in fig. 12.15 for the solenoid with ring collector shows how this type of spectrometer (and the same applies to the lens type) can be improved greatly by the judicious use of a simple ring-baffle (cf. § 7.2). On the other hand, when using a ring-collector slit, the relationship between collecting power and resolution is no longer linear. As the curves in fig. 12.15 show, the superiority of the ring-collector spectrometer is most pronounced for instruments with relatively small collecting power.

All curves of fig. 12.15 refer to point sources. On the other hand, it is rather difficult to assess resolving power and collecting power for an extended source. Hence the following Tables XV and XVI, containing a collection of empirical data about various kinds of spectrometers described in the literature, will be of interest to those who have to choose the appropriate instrument for any electron-spectrometric investigation. The figures presented in columns (2) and (3) of Table XV refer to the principal electron orbit, giving its radius of curvature, r_e, and its length, ζ, between source and collector. On the other hand, column (2) of Table XVI refers to the maximum semi-aperture of the beam (i.e. the maximum elongation of the orbit from the axis), while column (3) of this table gives the distance along the axis between source and collector. The next column (4) of both tables refers to the dimensions of the source, e.g. (height × width) of the emitter slot (or strip, or wire),

or, in case of a circular source, to the diameter. The next two columns refer to the collecting power Ω and to the resolving power $p/\Delta p$, respectively, of the spectrometers. The figures for $p/\Delta p$ have either been taken directly from the references or they have been estimated here from other information (geometry of apparatus, spectral distribution curves, etc.) contained in the papers.

The product $\Omega \times p/\Delta p$ may be considered as a figure of merit for any given spectrometer design. By changing the aperture of a given spectrometer, one of the factors of this product is always increased at the cost of the other factor. By scaling up the dimensions of a given spectrometer type the product $(\Omega \times p/\Delta p)$ can generally be improved until the object (which for intensity reasons has to be of a given size) can be considered to be small in comparison with the dimensions of the electron orbit.

For the investigation of a substance of low emission density, however, sources of relatively large size have to be employed in order to obtain sufficient intensity at a given collecting power. There the influence of the size of the source on the resolving power cannot be neglected, and the value of the collecting power is no longer adequate for describing the merits of a spectrometer. Geoffrion (1949) introduced, for this reason, the product of source area and collecting power as the 'luminosity' of the spectrometer. It is seen, for example, in Table XV that the luminosity of the semicircular magnetic spectrometer can be increased about six times by increasing the source length in the direction of the field by a factor three.

All spectrometers listed in Tables XV and XVI have been designed originally for electrons, excepting Cockcroft's apparatus, which has been used by Rutherford and his collaborators for their celebrated measurements on the fine-structure of α-ray spectra.

The promising type of 'compound spectrometers' has been omitted from Tables XV and XVI, since suitable information is not available. These spectrometers consist of a combination of a deflexion field with electron lenses. An early attempt to investigate the potentials of such a compound type is due to Klemperer (1935), who started building up the exactly analogous case to the glass spectrometer. The compound spectrometer is supposed to combine the great collecting power of lenses with the great dispersion of the

TABLE XV. *Comparison of deflexion spectrometers*

Spectrometer	Electron orbit		Source (mm.)	$\Omega \times 10^{-3}$	$p/\Delta p$	Reference
	r_e (cm.)	Length ζ (cm.)				
Semicircular magnetic	9	28	$6 \times 0{\cdot}2$	$\approx 0{\cdot}1$	≈ 200	Ellis (1920–30)
	3	10	10×3	1	10	Gurney (1925)
	12	38	20×3	$1{\cdot}0$	60	Lawson and Tyler (1940)
	12	38	10×1	$0{\cdot}1$	220	Siegbahn (1944)
	30	95	$20 \times 1{\cdot}4$	$0{\cdot}22$	300	Geoffrion (1949)
Semicircular magnetic (long source)	30	95	$60 \times 1{\cdot}2$	$0{\cdot}45$	300	Geoffrion (1949)
Semicircular magnetic (α-ray)	40	126	$10 \times 0{\cdot}1$	$0{\cdot}03$	3200	Cockcroft (1933)
Corrected semicircular (air coils)	17	55	$1{\cdot}5 \times 0{\cdot}1$	$0{\cdot}1$	4000	Ruthemann (1948)
Corrected semicircular (ground pole pieces)	40	126	25×4	$1{\cdot}0$	200	Langer and Cook (1948)
Two-directional magnetic	$12{\cdot}5$	54	$8 \times 0{\cdot}2$	$1{\cdot}4$	150	Siegbahn and Swartholm (1946 *b*)
	50	222	20×3	10	100	Hedgran, Siegbahn and Swartholm (1950)
			20×1	2	600	
	$24{\cdot}3$	110	2	2	300	Kurie, Osoba and Slack (1948)
Spherical condenser 90°-portion	46	150	1	$0{\cdot}4$	1000	Browne *et al.* (1951)
Circular cylindrical magnetic prism, 76° deflexion	25	50	$20 \times 0{\cdot}1$	$0{\cdot}1$	1300	Siday and Silverston (1952)

TABLE XVI. *Comparison of electron lens spectrometers*

Spectrometer	Max. semi-aperture (cm.)	Source-collector distance (cm.)	Source (mm.)	$\Omega \times 10^{-3}$	$p/\Delta p$	Reference
Thin lens (air coil or iron shielded)	3·5	120	3	0·8	14	Klemperer (1935)
Thin lens (iron)	4	60	4 × 0·2	0·8	100	Siegbahn (1942)
Thick lens (iron)	4·5	60	4 × 0·2	0·3	150	Siegbahn (1944)
Thick lens, spherically corrected	7	50	4 × 0·2	20	20	Siegbahn (1946)
Thick lens, spherically corrected	7	50	4 × 0·2	6	35	Siegbahn (1946)
Thick lens, spherically corrected with ring diaphragm	7	50	4 × 0·2	80	25	Slätis and Siegbahn (1949)
Thin lens (air coil)	7·5	100	4	1	59	Deutsch, Elliott and Evans (1944)
	7·5	100	5	8	17	
Solenoid (air coil)	12·5	90	20	10	18	Witcher (1941)
Solenoid with ring collector	40	100	0	10	≈80	Frankel, theor. (1948)
Spaced coils (iron)	50	96	4	14	91	Agnew and Anderson (1949)
Spaced coils (iron)	50	96	25	110	11	Agnew and Anderson (1949)
Thick air coil for 16 MeV. rays	7	100	1	6	70	Graham and Klemperer (1952)
Thick air coil for 16 MeV. rays with ring collector	7	100	1	6	125	Graham and Klemperer (1952)
Einzel lens	10^{-3}	70	$(5 \times 10^{-3}) \times 4$	10^{-3}	7×10^{4}	Möllenstedt (1949)

prism. However, in its present state of development focusing errors are still large and the expected high resolving power has not yet been realized.

The result of any spectrometric measurement may be represented as a velocity distribution or a momentum distribution or an energy distribution. The plotting of these distributions is quite elementary, however, as Kollath (1936) pointed out; mistakes about it are met so frequently in the literature that a short discussion of it seems worth while.

The momentum distribution curve of a given total number of electrons indicates the number of electrons with momenta between the values p and $p + \mathrm{d}p$ and may be represented by

$$N(p)\,\mathrm{d}p = \mathrm{d}N. \tag{12.5}$$

The distribution of energies W in the same assembly of electrons may be written as

$$n(W)\,\mathrm{d}W = \mathrm{d}n. \tag{12.6}$$

Now since

$$W = \frac{p^2}{2m}, \tag{12.7}$$

the band widths $\mathrm{d}p$ and $\mathrm{d}W$ in (12.5) and (12.6) are connected by

$$\mathrm{d}W = \frac{p}{m}\,\mathrm{d}p, \tag{12.8}$$

i.e. the abscissa interval of the momentum band $\mathrm{d}p$ is changed into the abscissa interval of the energy band $\mathrm{d}W$ by multiplication with p/m. However, if the band area, i.e. the number of electrons belonging to the band, is supposed to be unchanged by the transformation, $\mathrm{d}N$ in (12.5) should equal $\mathrm{d}n$ in (12.6). Hence the ordinate values of the two bands are connected by

$$n(W) = \frac{m}{p}N(p). \tag{12.9}$$

A general survey of the plotting of momentum and energy distribution curves respectively from the results of the four important experimental methods is given in Table XVII. There, column (2) refers to a magnetic deflexion spectrometer with constant field. The current indicator may be a photographic plate of known sensitivity or any movable electron collector of given aperture.

Thus, B = const., dr = const. and r = variable. Since $p = (eB)\,r_e$ and d$p = (eB)\,$dr, the collector current $I = f(r)\,$dr is, according to (12.5), proportional to the ordinate of the momentum distribution curve, i.e. $N(p) \propto I$, its abscissa being proportional to the radius of the electron orbit, i.e.

$$p \propto r_e.$$

On the other hand, for plotting the energy distribution curve from measurements with B = const., dr = const. and r = variable, (12.7) and (12.8) show that

$$W \propto r_e^2, \tag{12.10}$$

hence, d$W \propto r_e\,$dr, and since dn = dN is postulated, it follows that

$$n(W) \propto \frac{\mathrm{I}}{r_e} N(p) \propto \frac{\mathrm{I}}{r_e} I, \tag{12.11}$$

i.e. the abscissae W of the energy distribution curve are proportional to the square of the measured radii r_e of the orbits, while the ordinates $n(W)$ are proportional to the collector currents divided by these radii.

TABLE XVII. *The plotting of spectral distribution curves*

	Magnetic spectrometry		Electric spectrometry	
	B = const.	B = variable	Variable deflecting field	Variable retarding field
Values measured directly: Abscissa	Orbital radius r_e	Flux density B	Condenser voltage V_p	Retarding voltage V_z
Ordinate	Collector current I	Collector current I	Collector current I	Collector current I
Plotted as momentum distribution curve: Abscissa	r_e	B	$\sqrt{V_p}$	$\sqrt{V_z}$
Ordinate	I	I/B	$I/\sqrt{V_p}$	$\dfrac{\mathrm{d}I}{\mathrm{d}\sqrt{V_z}}$
Plotted as energy distribution curve: Abscissa	r_e^2	B^2	V_p	V_z
Ordinate	I/r_e	I/B^2	I/V_p	$\dfrac{\mathrm{d}I}{\mathrm{d}V_z}$

Column (3) of Table XVII refers to any magnetic spectrometer (deflexion field, lens, solenoidal field, etc.) with fixed collector position and constant collector aperture. There the electron

momentum is proportional to the variable flux density B. The current which, as a function of B, enters the collector aperture is $I \propto f(p)\,\mathrm{d}p$. However, since here $\mathrm{d}p \propto \mathrm{d}B \propto B$, the ordinate of the momentum distribution curve $f(p)$ should be proportional to the collector current I divided by the flux density B, as given in the table. Again, in the present case of variable B, abscissae ($\propto B^2$) and ordinates ($\propto I/B^2$) have to be plotted for the energy distribution curve, as can be shown by considerations quite analogous to those given above.

The functions to be plotted as coordinates of spectral distribution curves derived from electric deflecting field measurements are given in column (4) of Table XVII. In practice, one generally uses variable electric deflexion fields, hence the current I, picked up by a collector of given aperture $\mathrm{d}s$, is measured as a function $f(V_p)$ of a condenser plate voltage V_p.

In any case, the coordinate s of the collector slot (s may stand, for example, for the range z_f of the parabolic path in (11.22) or it may stand for the radius r_0 of the circular path in (11.23)) is proportional to the kinetic energy W of the electron and inversely proportional to the condenser voltage V_p, namely,

$$s \propto W/V_p. \tag{12.12}$$

Hence

$$\mathrm{d}s \propto (W/V_p^2)\,\mathrm{d}V_p. \tag{12.13}$$

In particular for fixed collector position $s = \text{const.}$ there follows from (12.12)

$$W \propto V_p. \tag{12.14}$$

(12.13) and (12.14) yield

$$\mathrm{d}s \propto \mathrm{d}V_p/V_p,$$

which shows that for fixed collector aperture $\mathrm{d}s$ one obtains $\mathrm{d}V_p \propto V_p$. The ordinate of the energy distribution (12.6) is consequently given by

$$n(W) = \mathrm{d}n/\mathrm{d}W \propto I/\mathrm{d}V_p \propto I/V_p. \tag{12.15}$$

(12.14) and (12.15) show that the measured function $I = f(V_p)$ leads to an energy distribution the abscissa of which is proportional to the potential difference at the condenser plates and the ordinate of which is proportional to the collector current divided by the corresponding condenser plate voltage.

Again, calculation of the momentum distribution (cf. (12.5)–(12.9)) from (12.14) and (12.15) leads to an abscissa $p \propto \sqrt{V_p}$ and to an ordinate $N(p) \propto I/\sqrt{V_p}$ as shown in the table.

The last column of Table XVII deals with the determination of the coordinates of momentum and energy distribution curves from measurements with the electric retarding field method. The electron-optical problem connected with this important method is given by the requirement of keeping the retarded electrons exactly parallel with the electric field lines. In practice, the electron beam often passes through two grid electrodes between which is maintained a decelerating electric field, though such a field cannot be directed everywhere exactly parallel and opposite to the electron motion. An electron can overcome the field only if its kinetic energy W surpasses the voltage difference V_z between the two grid electrodes. All electrons which are able to pass the field enter the collector and contribute to the current,

$$I = \int_{W_1 = eV_z}^{W_2 = \infty} n(W)\,\mathrm{d}W. \qquad (12.16)$$

Hence, to find the ordinate $n(W)$ of the energy distribution curve the measured currents have to be differentiated, i.e.

$$n(W) = \mathrm{d}I/\mathrm{d}V_z,$$

the abscissae $W \propto V_z$ being proportional to the retarding voltage. The calculation (cf. (12.5)–(12.9)) of the corresponding momentum distribution leads to values $p \propto V_z$ for the abscissa and

$$N(p) \propto \mathrm{d}I/\mathrm{d}\sqrt{V_z}$$

for the ordinate as shown in Table XVII.

Table XVII applies to moderate electron velocities for which the relativistic change in mass can be neglected. The relatively fast electrons of β-spectra are generally investigated with magnetic spectrometers which immediately yield momentum distribution curves with coordinates as specified in Table XVII. Spectrometric investigations, however, frequently aim at the determination of atomic or nuclear energy levels. Hence energy distributions have to be calculated from the well-known relativistic formulae.

On the other hand, the electric deflexion or the retarding field method immediately yield energy distribution curves with co-

ordinates as specified in Table XVII. However, electric methods are in practice not frequently applied to the spectrometry of fast electrons.

Another problem arising in the transition from momenta to energies and vice versa is concerned with the resolving power. From

$$p^2 = (mu)^2 = 2\,\mathrm{mW} = 2\,\mathrm{meV},$$

there follows

$$p/\mathrm{d}p = G(W/\mathrm{d}W). \tag{12.17}$$

The value of the factor G for moderate electron energies, i.e. for $m = m_0$, is $G = 2$. There, the momentum resolving power has twice the value of the energy-resolving power. In the relativistic region, however, the total energy of the electron is given by

$$U = eV + m_0c^2. \tag{12.18}$$

It is connected with the momentum by

$$U^2/c^2 = p^2 + m_0^2c^2, \tag{12.19}$$

where c and m_0 are the velocity of light and the rest mass of the electron respectively. Differentiating (12.19) and combining with (12.17) and (12.18) yields

$$G = \left(1 + \frac{2m_0c^2}{eV}\right) \Big/ \left(1 + \frac{m_0c^2}{eV}\right). \tag{12.20}$$

Hence one finds, for instance,

Energy in 10^6 eV.	V	0·1	0·5	1	10
Factor G in (12.17)	G	1·81	1·51	1·34	1·05

12.8. Electron accelerators*

The motion of particles with highest energies has recently become important in nuclear physics and has presented many interesting problems to the electron-optical approach. In particular, the recently evolved technique of particle acceleration has utilized much information from the established stock of electron-optical knowledge; in addition, it has stimulated a new development of electron optics in the relativistic region.

* Survey articles: Goward, Rotblat and Shire (1950); Livingston (1948).

The earliest particle accelerator was the so-called 'linear accelerator'. In this device, charged particles are accelerated by an oscillating electric field, applied to a linear array of electrodes. The frequency of the field must be in resonance with the particle motion, i.e. the length of the electrodes must be equal to the distance traversed by the particle in a half-cycle of the field. The first accelerator (Wideroe, 1928) consisted of a set of metal-tube electrodes arranged within short mutual distances along a straight axis. These electrodes were alternately connected to the terminals of a high-frequency power supply. The lengths of the electrodes were chosen in proportion with the increasing velocity of the particle

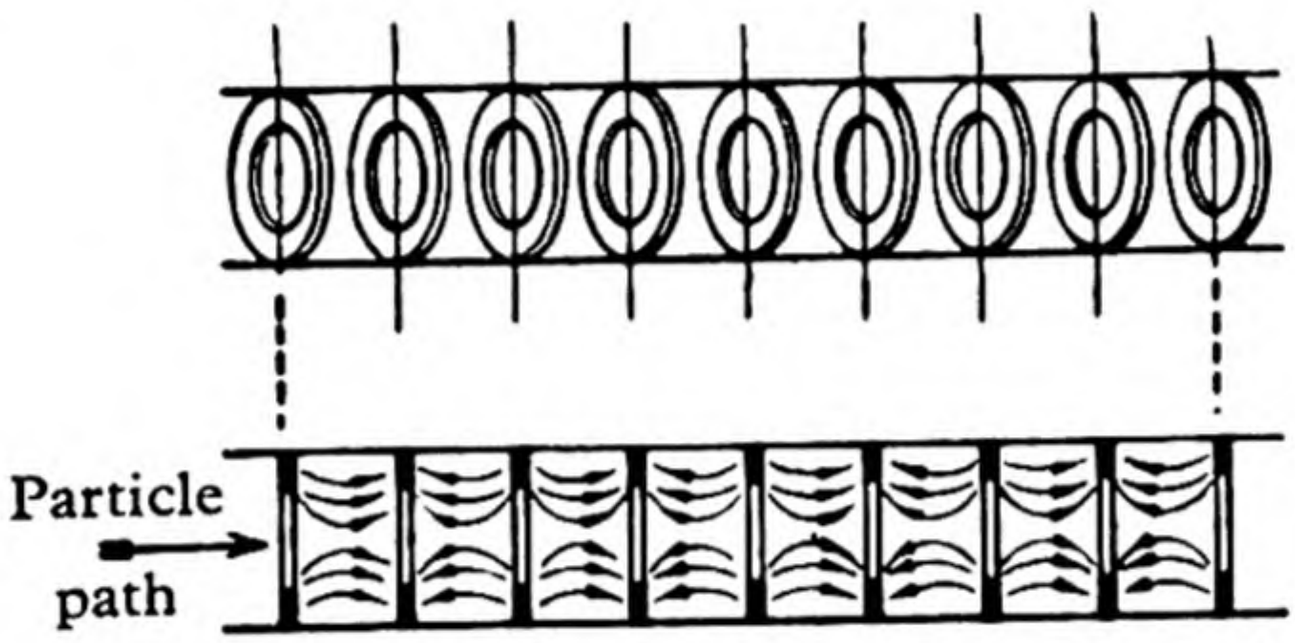

Fig. 12.16. Iris loaded wave guide for electron acceleration, and shape of electric field lines.

so that particles travelling along the axis would meet an accelerating phase of the field at every gap between the alternately charged electrodes.

The periodic electrode structure of the above linear accelerator is electrically equivalent to a wave guide, loaded so that the phase velocity of the travelling wave is the same as the velocity of the particles. The application of wave-guide technique, however, opened new possibilities for linear acceleration, in particular for the acceleration of electrons to extreme energies.

A type of loaded wave guide frequently used for electron acceleration is shown in fig. 12.16. Diaphragms are seen to subdivide a straight tube into an array of cavities which, according to their geometrical dimensions (length, depth, etc.) can be made to resonate with a wave of a few kM. cycles/sec. fed into the guide. Tapered loading of the guide is needed at the start where the electron velocity is changing greatly. At high velocities, however, when nearly the whole increase in kinetic energy is stored by increase in

relativistic mass, the sections can be uniformly spaced for the velocity of light. If the phase velocity of the travelling wave is all the way the same as the electron beam velocity, each electron will pick up energy continuously.

The main electron-optical problem connected with the linear acceleration is due to the distribution of the accelerating field which, as shown in the lower part of fig. 12.16, is by no means purely axial. Generally, the conditions required for phase stability lead to a lateral spread of the electron beam. Additional focusing by strong magnetic coils has to be provided to keep the electrons close to the axis, particularly in the early stage of the acceleration. The maximum

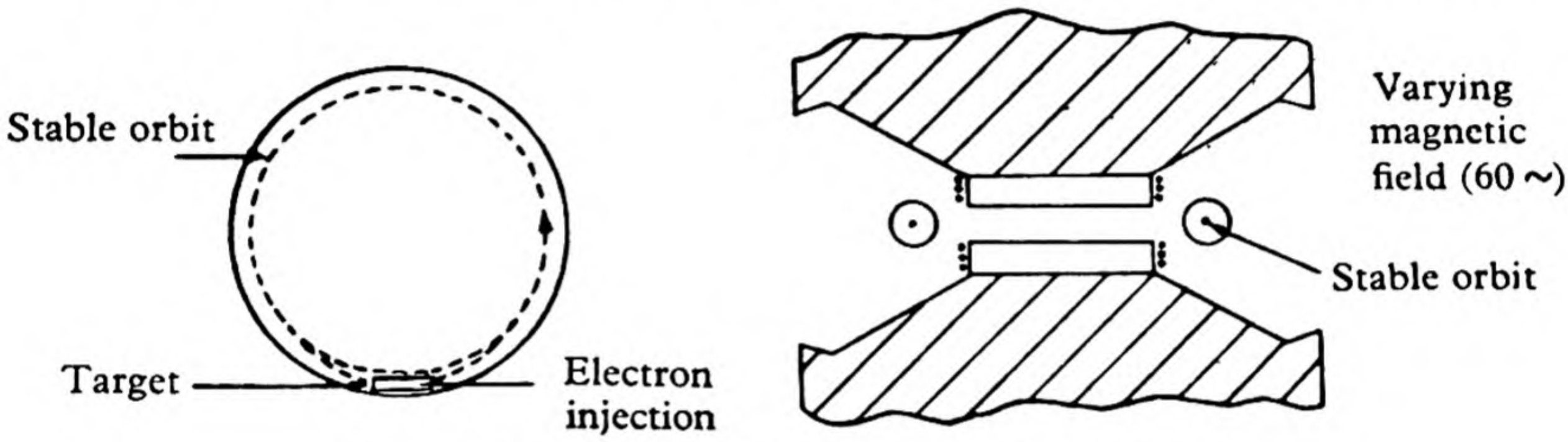

Fig. 12.17. Diagrammatic representation of Betatron.

obtainable acceleration is limited by the available cm.-wave power. The design of accelerators is discussed in a report by Fry and Walkinshaw (1949).

The 'Induction Accelerator' or 'Betatron' was the first successful device by which high-energy acceleration of electrons was achieved practically. In principle the betatron is a transformer in which the electron beam takes the place of the secondary winding. The beam moves in a circular orbit of constant radius r_e within a toroidal vacuum tube as shown in fig. 12.17. The alternating-current magnet produces a variable flux ϕ linking the orbit and accelerating the electrons. As for the transformer, the induced voltage per turn is $\mathrm{d}\phi/\mathrm{d}t$, and the electric field (voltage per unit length) is given by

$$E = \frac{\mathrm{d}\phi}{\mathrm{d}t}\frac{1}{2\pi r_e}. \tag{12.21}$$

The force on the electron is $-eE$ and the equation of motion can be written as

$$\frac{\mathrm{d}p}{\mathrm{d}t} = \frac{e}{2\pi r_e}\frac{\mathrm{d}\phi}{\mathrm{d}t}. \tag{12.22}$$

On the other hand, by differentiation of $p/e = r_e B_e$ (cf. (5.1) it follows that

$$\frac{\mathrm{d}p}{\mathrm{d}t} = e r_e \frac{\mathrm{d}B}{\mathrm{d}t}. \tag{12.23}$$

The last two equations yield

$$2(\mathrm{d}B_e/\mathrm{d}t)\,\pi r_e^2 = \mathrm{d}\phi/\mathrm{d}t. \tag{12.24}$$

(12.24) is often called the 'betatron 2:1 rule'; it shows that for accelerating the electron on an orbit of constant radius r_e the linking flux ϕ must change at a rate twice that which would occur if the flux density inside the orbit were homogeneous and given by the value B_e at the orbit.

The important condition (12.24) was recognized already by Wideroe (1928) and independently and nearly simultaneously by Cockcroft and Walton, who were first to propose and to try the betatron accelerator. All the early workers, however, were unsuccessful in their attempts to obtain electron acceleration, since they did not master the electron-optical problems of the electron injection and of the orbital stabilization. These problems were solved many years later by Kerst (1940–50).

If the beam from an electron gun is injected into the desired circular path nearly tangentially, with small divergence and with sufficiently low velocity, the restoring forces of a properly designed magnetic field distribution will be able to keep the electrons within a small distance about this 'equilibrium orbit'. In the right kind of field for effecting such focusing, the flux density near the orbit should decrease inversely with a certain power n of the radial coordinate. There, the problem of focusing the electrons is the same as in the case of the two-directional focusing deflexion spectrometer (cf. § 11.6). In both cases, the electrons set up oscillations about the equilibrium orbit. The frequencies of these oscillations in radial and in axial direction are given by (11.49), and they depend on the field index n only. In Kerst's first machine, for instance, n was $\frac{2}{3}$.

Owing to the orbital oscillations, the rays form nodes and antinodes along the equilibrium orbit. Now the frequency, and hence the field index n, has to be chosen in such a way that after each full revolution the beam would not strike the back of the electron gun

but would avoid it by being in a suitable phase of the orbital oscillation.

The electron gun in a betatron generally consists of a short line-focus system with deflexion plates to adjust the critical injection direction and with grid electrode in order to time the injection correctly to occur near the start of the accelerating phase of the sinusoidally changing field.

An injection of the order of 1 A. peak current must be completed within a few microseconds. During the first quarter-cycle, i.e. as the magnetic field builds up, the electrons are accelerated from, say, 50 keV. injection energy up to their full energy of many MeV. In this short interval, they complete many hundred thousands of revolutions, gaining only of the order of 10^2 eV. per turn by induction. While they gather energy they are oscillating about the equilibrium orbit, but the orbital oscillations are damped in amplitude owing to the increase in the restoring magnetic force. Here, however, the field raised by the circulating electron beam seems to play a critical part, since the output beam is obtained for a critical range of input beam currents only.

Eventually the electrons have to be ejected out of the stable orbit before the magnetic field enters the decelerating phase. This can be done by, for example, an auxiliary coil which distorts the field so that the orbit is shifted radially or axially to strike a target.

If the kinetic energy W of the electrons has been increased up to the relativistic region, where the total electron mass is large compared with its rest mass, the momentum becomes $p \approx W/c$, where c is the velocity of light (cf. Appendix A. 4(19)). Hence, the maximum energy reached in the betatron is simply given by the orbital radius and the maximum flux density, namely,

$$W_{\text{max.}}/e = V_{\text{max.}} \approx c r_e (B_e)_{\text{max.}}. \qquad (12.25)$$

For instance, with $(B_e)_{\text{max.}} = 0{\cdot}3$ Wb./m.^{2} ($= 3$ kilogauss) and $r_e = 0{\cdot}25$ m. the maximum energy is seen to be 22·5 MeV. Kerst's first model (1941) yielded 2·3 MeV. The largest models now reach up to 300 MeV. (cf. Westendorp, 1945; Dietze and Dickinson, 1949).

The most successful accelerator is the 'cyclotron' invented by Lawrence and Livingston (1931, 1932). The cyclotron has

originally been used for acceleration of ions only, but in its modified forms, as 'microtron' and as 'synchrotron', it is well adapted for the production of very fast electrons. In the original cyclotron shown in fig. 12.18, ions are produced between two hollow, D-shaped electrodes placed between the poles of a large electromagnet. The ions are accelerated in the diametral gap between the D-electrodes to which radio-frequency alternating voltage is applied. In the field-free space inside these electrodes the electrons are deflected by the homogeneous magnetic field so that they return to the gap. The magnetic field and the radio-frequency are adjusted in order

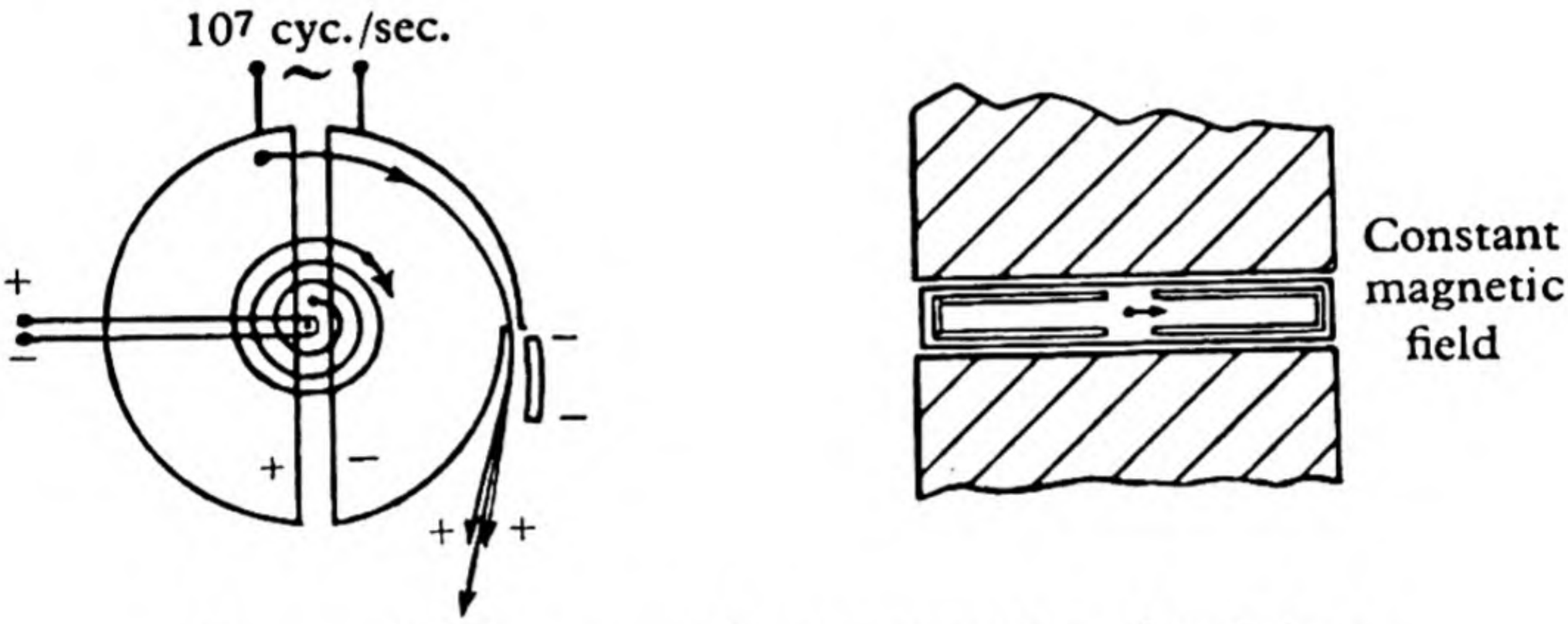

Fig. 12.18. Diagrammatic representation of cyclotron.

to bring the latter into resonance with the Larmor frequency (cf. (5.2)) of the circulating ions. Under these conditions the ions find an accelerating field and obtain additional energy each time they cross the gap between the D-electrodes. They travel in wider and wider semicircular paths until they reach the periphery of the electrodes, where they are deflected outwards against the target. As the ions gather momentum, however, their mass increases in a relativistic manner and their Larmor frequency ω_L falls out of step with the accelerating radio-frequency ω_0. This untuning effect $\omega_L \neq \omega_0$ becomes serious when the kinetic energy becomes large enough to be significant in relation to the rest energy (cf. § 5.3). For instance, the rest energy of a proton corresponds to 938 MeV., and kinetic energies in excess of about 10 MeV. will cause an appreciable change in resonant frequency. Heavier ions can be accelerated to higher energies in proportion with their greater masses. The rest mass of the electron, however, corresponds to 511 keV.; hence,

increases in kinetic energies would already start to become troublesome at about 5 keV.

Now, three modifications of the cyclotron have been developed with the view of keeping the Larmor frequency in tune with the frequency of the accelerating field.

First may be mentioned the 'synchro-cyclotron' suggested in 1945 by McMillan, in which the radio-frequency applied to the accelerating electrodes is modulated so as to keep it in step with the gradually decreasing Larmor frequency of the particle revolving with increasing orbital radius in the constant magnetic field. In practice, these machines have been used for acceleration of heavy particles only, their ranges extending to 100–350 MeV. proton energies.

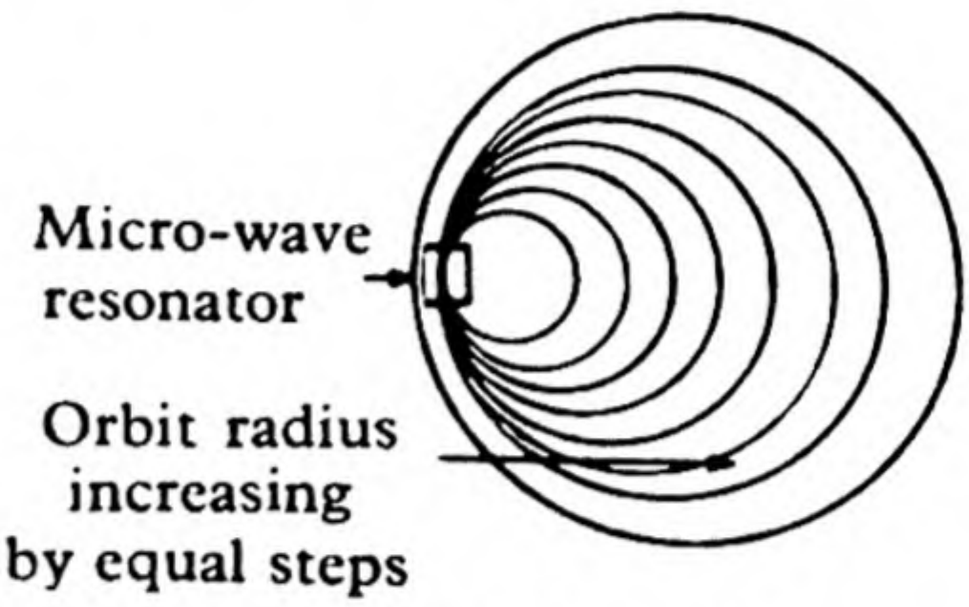

Fig. 12.19. Diagrammatic representation of microtron.

As a second modification may be mentioned the 'microtron', suggested in 1945 by Veksler and by Schwinger. A diagrammatic representation is shown in fig. 12.19. A centimetre-wave hollow resonator is placed at the fringe of a constant homogeneous magnetic deflexion field. The electric field in the resonator is directed parallel to its axis, and it is so intense that electrons are accelerated by just one mass-equivalent, $m_0c^2/e = 511$ keV., in every single transit. Hence the Larmor frequency of revolution after N transits is

$$\omega_L = \frac{eB}{m_0(1+N)} = \frac{\omega_0}{1+N}. \tag{12.26}$$

If the resonator frequency ω_0 is chosen to be an integral multiple of the frequency of revolution, then the electrons which return through the magnetic field in ever-increasing circles to the resonator will pass it always during the accelerating phase of its field. Henderson and Redhead (1949) used a microtron at 0·1 Wb./m.^{2} with 2·8 kMc./sec., yielding about 100 μA. at 5 MeV.

The most important development from the cyclotron, as proposed in 1945 by Veksler and by McMillan, has led to the 'synchrotron' (cf. Bohm and Foldy, 1946). In this machine, electrons are accelerated along a substantially unchanging path, the magnetic

guiding field being modulated in order to fix the orbital radius of the steadily accelerated electrons. This radius is given by

$$r_e = \frac{mu}{eB_e}.$$

During the early part of the accelerating cycle, both the velocity u and the mass m of the electron increase. Hence B_e has to be increased correspondingly to keep r_e constant. Also the frequency of the accelerating electric field has to be modulated to match the changing Larmor frequency of revolution, given by $\omega_L = \frac{eB_e}{m} = \frac{u}{r_e}$. However, the electrons reach practically light velocity c at about 2 MeV., hence from these energies on, the frequency is substantially constant, namely,

$$\omega_0 = c/r_e. \tag{12.27}$$

For instance, for an orbital radius of 1 m., one finds

$$\omega_0/2\pi = c/2\pi = 48\,\text{Mc./sec.}$$

Most electron synchrotrons use a 'betatron start' to accelerate electrons by induction from about 50 keV. injection energy to about 2 MeV. This may be done, for example, by a number of 'flux bars' of high permeability metal threading the electron orbit. The bars 'short' the magnetic field at low inductions but become saturated at high inductions. In the betatron region the electrons are uniformly distributed around the orbit; at the transition to synchrotron action the electrons 'lock in' and become bunched. The whole acceleration takes place within the first quarter-period of the alternating magnetic field, this period being of the order of $\frac{1}{50}$ sec. The betatron start is always short compared with the time of the synchrotron action. The electric accelerations of the beam are provided, for instance, by a C-shaped electrode as shown in fig. 12.20. This electrode, which is inserted into the toroidal vacuum tube, is connected to a radio-frequency power supply and provides two accelerations per revolution. For the acceleration of fast electrons, a synchrotron is more economical than a betatron, since it does not need the massive magnet for producing an accelerating magnetic flux.

Only a narrow annular magnetic field is required; however, the flux distribution in this field is of great importance, and many new

problems have been presented to electron-optical research with the view of finding the optimum shape of the pole-faces. The use of the field plotting trough for the design of synchrotron pole-pieces has been discussed in § 10.8, and the cross-section through a synchrotron magnet has been shown in fig. 10.23. In order to obtain the proper focusing of the electrons into an equilibrium orbit, the index n of the magnetic field has again to be chosen within a given range (as for the betatron, cf. beginning of this section). At high energies where radiation losses become significant a value $n = \frac{3}{4}$ has been found to lead to anti-damping of orbital oscillations; hence this n value represents an upper limit.

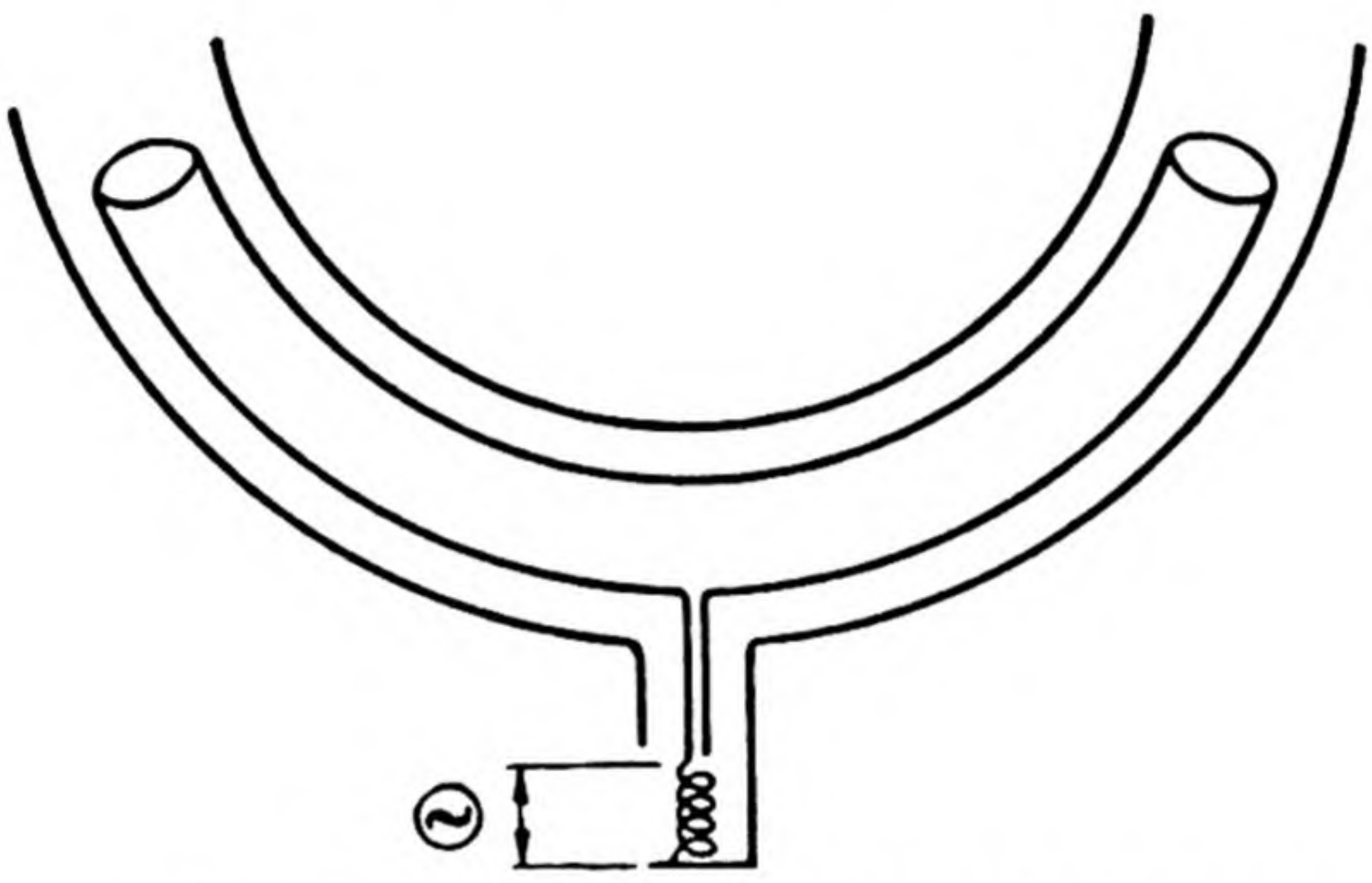

Fig. 12.20. Cee-electrode for synchrotron.

Another problem arises through the need of having relatively large regions of uniform n value, especially in the beginning of the cycle when the amplitude of the orbital oscillations is still large. It has been suggested, for instance, that 'lips' of high permeability ferromagnetic material should be added at the edges of the gap to widen the aperture at low fields. These lips would saturate at high inductions and so allow the fields to concentrate about the equilibrium orbit. Synchrotron acceleration is likely to reach up to very high electron energies (1000 MeV. region). An ultimate limit, however, will be set by radiation losses which have been shown to increase with the fourth power of the electron energy.

12.9. Electron optics in thermionic valves

The technical study of thermionic tubes had much stimulating influence on the development of electron optics in the presence of space charge. The focusing action of valve grids has been discussed in § 10.6. The beam tube shown there in fig. 10.17 has found technical application as a power-output valve. The application of suitable beam valves at the input side of an amplifier is also likely to be of technical interest. It seems that valve noise really limits the least signal strength which can be received. This valve noise can be largely reduced in multi-electrode valves if by proper focusing the electron current is prevented from striking the screen and other auxiliary electrodes.

Electron-optical design has been of great assistance for the construction of deflexion valves, which, however, are so far of hardly any technical importance. In these tubes the electrons are focused on a collector slot and modulated by beam deflexion (e.g. Harries, 1944). The 'slope' of such a valve is proportional to the ratio of beam current to voltage sensitivity, the latter quantity being defined in the manner known for cathode-ray oscillographs (cf. § 12.2). New electron optical methods for increasing the slope have utilized space charge deflexion of the electron beam (Jonker and Overbeek, 1949 (cf. § 8.8), Wallmark, 1952). A high-quality focus in combination with a large deflexion condenser yields very high slope values, but the quality of the valve for amplifying purposes depends on the slope-to-capacity ratio, and the large capacity of the deflecting condenser upsets any advantage which deflexion modulation may have over ordinary grid modulation.

Special electron-optical design has been applied to thermionic electron multipliers with the view of using these tubes as amplifier valves in the ultra-high-frequency region. To keep the inter-electrode capacities small, all electrodes have to be arranged at relatively large distances. Moreover, the time of travel between cathode and anode should be very nearly equal for all electrons. A schematic drawing of a thermionic electron multiplier has been shown in fig. 10.20 as an example for the electron optics of a line-focus emission system.

Another interesting type of thermionic multiplier for ultra-high-frequency amplification is the 'orbital beam multiplier' by Wagner

and Ferris (1941). There, two relatively narrow beams are emitted from the cathode; they pass through a control grid and through a screen grid and are then bent into semicircular orbits in the electrostatic field between two relatively large cylinder electrodes. Eventually they strike a secondary emitter which is arranged opposite to an anode.

Of very great technical importance are the velocity modulation valves,* and electron optics has made some helpful contributions

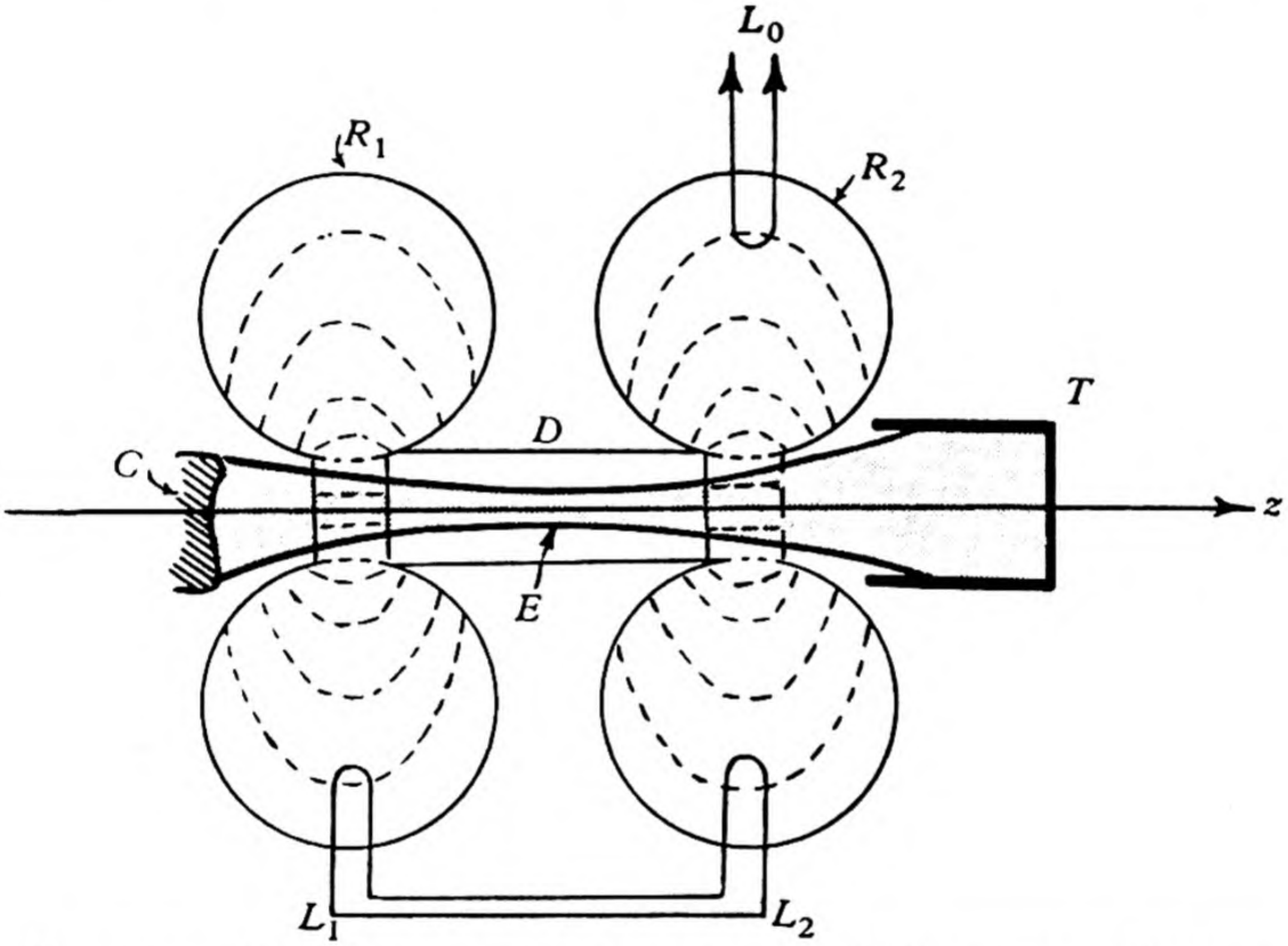

Fig. 12.21. Diagrammatic representation of multiple-resonator klystron.

to their development. The electron-optical problems may be elucidated by the following drawings.

Fig. 12.21 represents the cross-section through a multiple-resonator klystron invented by Varian (1939). It may be thought of in space as a figure of revolution about the z-axis, except for the coupling loops L_0, L_1 and L_2. E represents an electron beam which is emitted by the cathode C, passes through the two resonators R_1 and R_2 and is collected in the cage T. The two resonators are able to store high-frequency electrical energy, the electric field being directed, as shown, along the broken lines. If the beam is passed through the

* Cf. surveys by Beck (1948), Hamilton (1948) and Thompson (1947).

gap between the two apertures or grids of the 'buncher-resonator' R_1, a periodic change of velocity is applied to it by means of the varying longitudinal electric field. The result will be a bunching of the electrons in the longitudinal direction since magnitude and sense of the increment in velocity is determined by the phase at which each electron enters the field.

After leaving the modulating gap, the beam travels through a field-free space inside the conducting 'drift-tube' D. There the charge density along the axis will become more and more concentrated in the bunches in consequence of the fact that the faster moving electrons overtake the slower ones. At the point where bunching has reached a maximum, the beam enters the gap of the 'catcher-resonator' R_2. If the phase of the oscillations in R_2 is such that the electrons are retarded during the period of maximum beam intensity and accelerated during the minimum intervals, there will be a net gain of power by R_2. A fraction of this power is returned via the coupling loops L_2 and L_1 to the buncher-resonator R_1; another part, taken out by the loop L_0, is available as power output. Now, the electron-optical problem consists in passing at a given voltage a beam of maximum current through the resonators. Spreading of the beam by mutual repulsion of the electrons limits the current, and power is lost if marginal electrons are intercepted. In practice, concave cathodes or plane cathodes in connexion with a focusing cylinder are used to direct the beam towards the centre of the drift space, where a waist is formed as explained in § 8.2. Thereafter the beam diverges until it reaches the collector. The maximum possible current is given by (8.34). By another effect of mutual repulsion some longitudinal energy transfers take place and upset the density distribution needed for good bunching.

The most common form of klystron is the 'reflex' type in which a single resonator serves both as buncher and catcher. Such a tube is shown in fig. 12.22. Electrons emitted from the cathode pass through the gap of the resonator where they are bunched. The beam then drifts into a retarding field which reflects it back through the resonator gap again. The resonant condition between the two transits of the beam through the gap which is necessary to supply oscillation energy to the resonator is achieved by varying the potential of the

reflecting electrode. The reflex klystron has no collector electrode; during and after the first cycle, most electrons are scattered and collected by the walls of the tube. Only a small fraction approaches the cathode to be re-accelerated and to perform a second cycle. In the design of the klystron, care is taken to minimize the number of these re-accelerated electrons, since they do not behave as primary electrons.

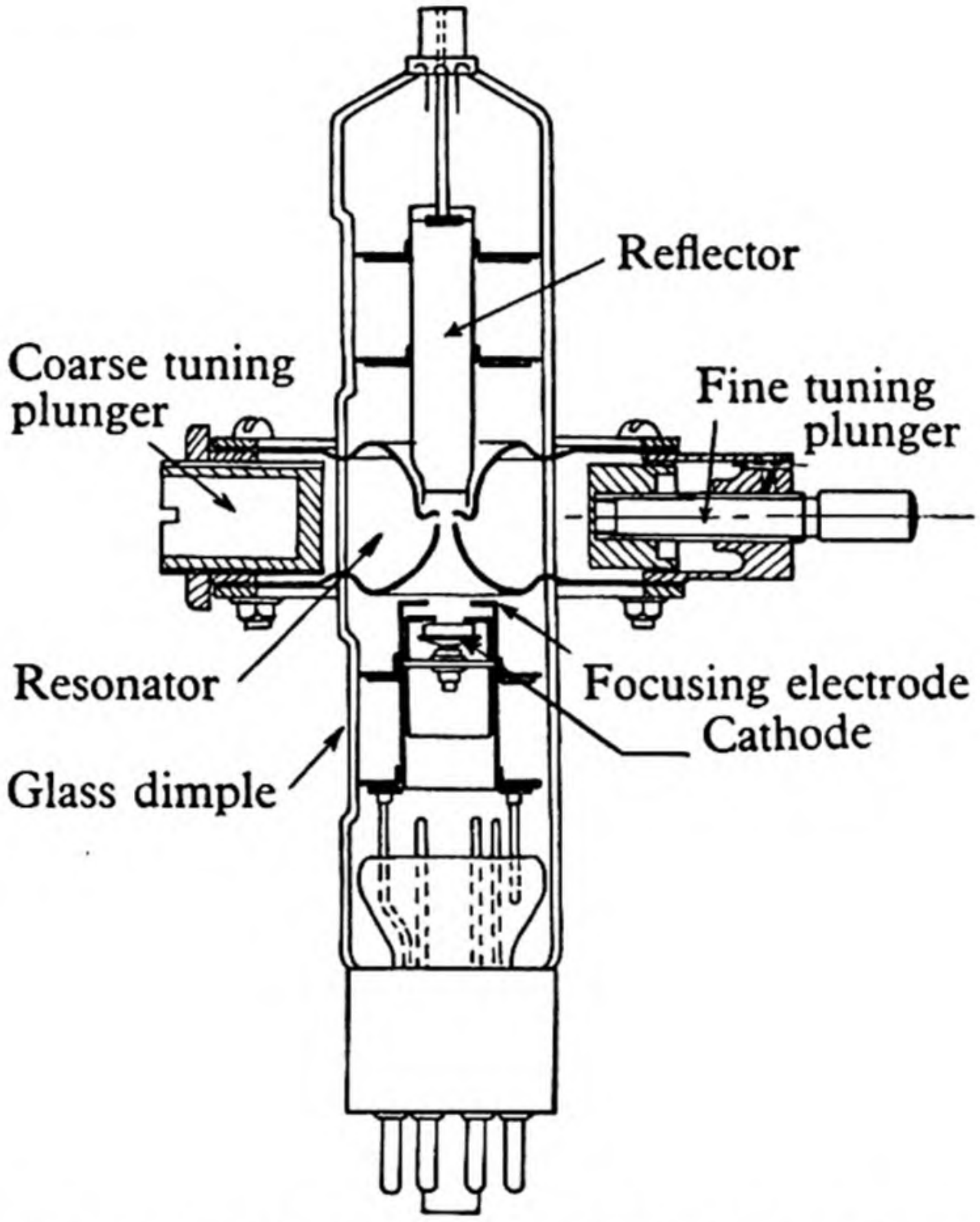

Fig. 12.22. Sectional view of reflexion oscillator.

The application of the field-plotting and ray-tracing method to klystron design is shown after Pearce and Mayo (1946) by fig. 12.23. The method has been helpful in devising the appropriate shape of the outer resonator surface acting as an anode and also for finding shape and distance of the reflector electrode which, at relatively high negative potential with respect to both anode and cathode, acts as a focusing electron mirror. It has to be admitted, however, that the technical design has been developed largely by trial and error in making a large number of practical models, since the electron-optical problem is substantially complicated by space-charge effects and by the defocusing action of the resonator fields.

The electron gun in a klystron is generally kept as short and compact as possible; it is just a wide cathode with a short focusing electrode, closely spaced to the resonator which gives the most satisfactory performance.

The reflex klystron serves for low power production (e.g. 100 mW. of a continuous wave of about 10 cm.). On the other

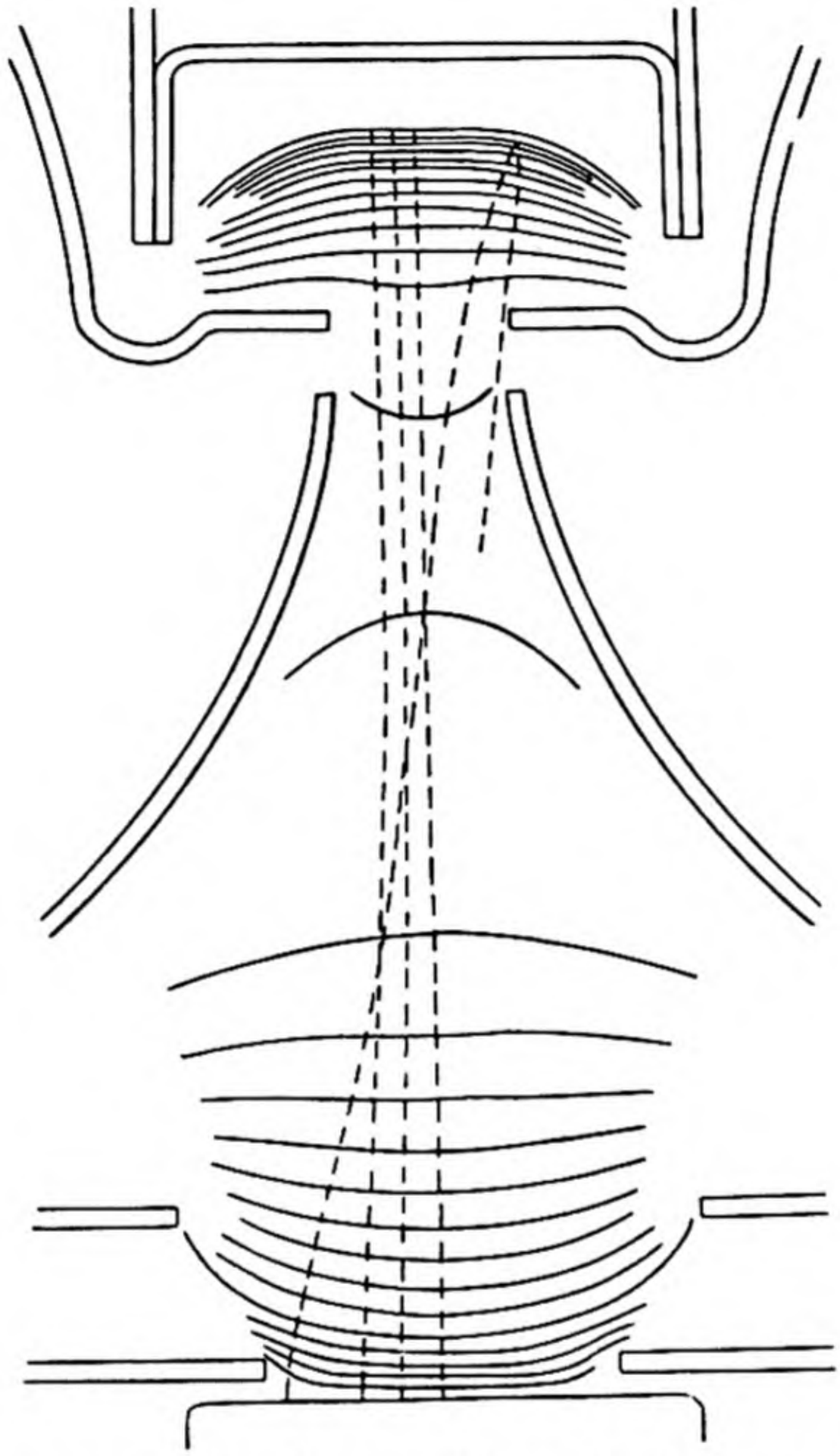

Fig. 12.23. Equipotentials and electron paths in the klystron of fig. 12.22.

hand, high power output (20 kW., 10 cm. wave, in microsecond pulses) has been obtained with two-resonator klystrons. In such tubes, electron beams of half a square centimetre cross-section carry 12 A. at 12 kV., and it can well be imagined that space-charge effects completely modify all ordinary electron-optical laws in this region.

'Cavity magnetrons'* are now in use when highest power output (e.g. Megawatt-microsecond pulses, 10 cm. wave band) is required.

* Cf. surveys by Collins (1948), Fisk *et al.* (1946).

The first low-power magnetrons consisted of a cylindrical anode with a filament cathode along the axis, the tube being placed in a magnetic field extending approximately parallel to the axis (Hull, 1921). The cycloidal electron orbits in this arrangement have been discussed in § 11.7. On the other hand, the cavity magnetron (Randall and Boot, 1946) consists essentially of a coaxial cathode-anode system with a number of resonant cavities coupled to the anode. A strong magnetic field extends parallel to the axis. The electron emission rotates about the highly emitting cathode as a circular cloud. The size of the cloud depends upon the anode voltage and the applied magnetic field. In the cloud the electron velocities will have small oscillations due to noise. If the impedance of the cloud exhibits a negative resistive component, oscillations will build up to stable space-charge configurations depending upon the wave-length excited in the cavities. The electron trajectories are not simply calculable, but the magnitudes of the fields are such that the rotation of the electronic space charge is in synchronism with the oscillatory mode excited in the anode cavities. The energy of oscillation is supplied by the electron motion against the local tangential electric fields at the inner anode surface. The operation of the magnetron can be pictured as a rotary generator. There, the space charge would act as the armature with as many poles as the actual cloud has serrations, and the resonant anode segments would correspond to the field windings.

Electron-optical considerations have so far played hardly any part in the development of the magnetron or in the study of its space-charge motion.

Two more high-frequency valves may be mentioned in this section: the travelling wave tube invented by Kompfner (1947, 1952, cf. also Pierce, 1950), and the two-stream tube invented by Haeff (1948). Both tubes are still at the beginning of their development and may turn out eventually to be useful high-frequency amplifiers. The electron-optical problem is similar in both cases and consists in keeping electron beams of great space-charge density with the help of magnetic fields within a given small beam aperture on a long straight path. In the Kompfner tube the electron beam passes through a long metal spiral and is in interaction with a high-frequency wave travelling along the spiral. In

the Haeff tube, two electron streams of different velocities (either within the same beam or as two separate, parallel beams) are in interaction to give a space-charge wave of increasing amplitude (cf. Pierce and Hebenstreit, 1949).

12.10. More applications of electron optics

Attention should be drawn to a few electronic devices which cannot be classified under the headings of the earlier sections of this chapter.

Most important amongst these is the X-ray tube. In it, a short, intense electron beam, generally of relatively high voltage, is focused upon an anode target, the electron focus forming the source of X-rays. Two different methods for obtaining high-intensity X-ray beams have been worked out in practice (cf., for instance, Barr and McArthur, 1950; or Glocker, 1949). The first method uses a comparatively large rectangular focus in conjunction with a rapidly rotating anode, and in this way high power loadings can be achieved without damaging the anode target. The other method is to concentrate the electron beam into an exceedingly small region of the anode (cf. §9.6). In this way high specific loading can be achieved with a small power input, and the brilliance of the point focus is considerable. As the heat flow from a point occurs radially in all directions into the target volume, the dissipation of heat is much more rapid than in the case of a large focus where the heat flow is effectively linear as it proceeds substantially normal to the surface.

In practical micro-focus tubes, currents of the order of a milliampere can be concentrated at 40–60 kV. within dimensions of about $\frac{1}{10}-\frac{1}{100}$ mm., and specific loadings of the order of 10 kW./mm.^{2} are used without injuring the target.

On the other hand, in practical line-focus tubes, the X-radiation is taken off at a glancing angle to the anode surface. The focal line then appears to be perspectively foreshortened into a very short patch. Such an arrangement can serve essentially as a point source not only for shadowgraphs but also for taking diffraction patterns in structural X-ray analysis. The electron optics of suitable line-focus systems has been discussed in § 10.6.

Of some technical importance is the electron diffraction camera.

In it, a very fine beam (e.g. of 50 kV., 0·5 mA.) is produced by a gas discharge, for example, or in the more modern cameras by a hot filament emission system (cf. Chapter IX) in high vacuum. A magnetic lens serves for focusing the beam on to the specimen. The diffracted electrons leaving the specimen make a small angle (of the order of 1°) with the initial beam direction and are intercepted by a photographic plate where they produce the diffraction pattern. A full account of the method and of experimental details is found in the book by Thomson and Cochrane (1939).

The design of the diffraction camera has developed much along the lines of the modern high-speed cathode-ray oscillograph (cf. § 12.2). On the other hand, it shows much similarity with the high magnification electron microscope (cf. § 12.6). Since both microscope and diffraction camera are used for the investigation of material structures, it is not surprising that diffraction adapters have been developed for the electron microscope.

Another adaptation of the electron microscope which has become of some technical interest for material investigation is the 'micro-analyser'. In it, a fine electron probe is focused on to a thin film of the specimen, and the transmitted electrons are refocused on to the slit of a velocity spectrometer (cf. § 12.7). Different materials are characterized by different losses of quantum energy of the transmitted electrons. With the degree of stabilization and fine-focusing now achieved, resolving powers of 10^4 can be obtained, and traces of a substance down to 10^{-12} mg. can still be identified (cf. Hillier and Baker, 1944; Möllenstedt, 1949).

The 'memory tube' is becoming of increasing practical importance for the development of calculating machines, computers, predictors, etc. This tube is closely related to the television pick-up tubes (cf. § 12.3). Its essential part is a storage plate consisting of an insulator sheet (e.g. a 0·1 mm. mica foil) which is covered by a mosaic of mutually insulated metallic islands (e.g. oxidized beryllium, 0·04 sq.mm.) and backed by a signal plate (e.g. a silver film). Close in front of the storage plate there is arranged a collector grid (e.g. wire mesh of 0·2 mm. pitch) which is always kept on earth potential. The mosaic is scanned by a 'high-voltage writing beam' (e.g. 2 kV., 20 μA.), and each picture element bombarded will emit secondary electrons which at those voltages exceed in number the

primaries. As secondary emission is picked up by the earthed collector grid, the picture element will charge up to the collector (= anode) potential. This process is termed 'positive writing'.

When a negative spot is to be written, a positive 'gate', i.e. a positive potential of about 100 V. with respect to the collector, is applied to the signal plate. This raises capacitatively the level of the whole storage surface to a positive potential with respect to the collector, so that the secondary emission of a scanned picture element cannot leave the element but is retained by it. The gate to the signal plate then is again connected to earth, which makes the potential of this picture element negative with respect to the collector.

Thus the sign of the writing (+ or −) can be controlled by the signal plate potential, and the writing action is not dependent on the potential of the picture element before the writing operation. Therefore no erasure is required to store new information.

For 'reading' the stored information both positive and negative picture elements have to be detected by a high-voltage beam. This requires 'gating' the signal plate to a level intermediate between the two above charge levels. The picture element being 'read' then is charged up or discharged upon scanning towards this intermediate level, and the change in charge produces a positive or negative signal accordingly.

To prevent changes in the stored charge by leakage or other disturbances, a 'holding' beam of relatively slow electrons (e.g. 100 eV.) is constantly flooded or scanned over the mosaic surface. By a differential secondary emission effect the positive and negative picture elements will be stabilized at anode or cathode potential respectively of the flooding gun. We have, however, to refrain from going into details.

The memory tube is still very much in the course of development. The tube given here as an example is due to Dodd, Klemperer and Youtz (1950). Other models have been developed by Haeff (1947), by Rajchman (1951) and by Williams and Kilburn (1949); the latter paper discusses a storage system of great technical interest.

The impressive list of electron-optical applications can be ended here with the enumeration of a few tubes of minor interest. There is the beam tube by Skellett (1944) which serves as an electronic

commutator; it contains a flat radial beam made to rotate about the axis of a cylindrical electrode structure. Another type of line-focus tube worth mentioning has been used for producing sound tracks on films (cf. Brüche and Scherzer, 1934). Moreover, electron optics has found application in some photoelectric cells with special electron-focusing electrode arrangement (cf. Zworykin and Ramberg, 1949), in rapid counting tubes like the 'Trochotron' by Alfven *et al.* (1947, 1948), or the decade counter valve by Jonker *et al.* (1952) in various types of electron beam voltmeters (e.g. Ehrenberg and Hirsch, 1943), and in many more experimental tubes which are hardly important enough to deserve enumeration here.

Two subjects are very closely related to the geometrical electron optics treated in this volume: first, the study of motion of charged particles other than electrons, e.g. atomic ions, by means of optical laws. The same laws apply of course to electron and ion focusing after their respective e/m values are taken into account. However, problems of particular interest turn up in 'ion optics' which do not exist in electron optics. Take, for example, the problem of velocity focusing in a mass spectrometer which was solved first by Aston (1919), by using a particular combination of subsequent electrostatic and magnetic deflexion. Mass spectrometry has been developed in the past by a great number of investigations leading to various other ion-optical problems (cf. for instance, Inghram, 1948; Thode and Shields, 1949). To mention another example, ions are distinguished from electrons by their smaller diffraction effect which has been utilized in the design of ion microscopes of high magnification (cf. for instance, Magnan, 1946, 1949). Again, a great deal of work has been done on the development of ion sources which are quite different from the electronic emission systems treated in Chapter IX. All these problems, however, are outside the scope of this book.

A second subject very much less important than ion optics, though also closely related to geometrical electron optics, is the 'electron phase optics' which has grown out of the study of velocity-modulated valves (cf. Brüche and Recknagel, 1938; Harrison, 1944). If a uniform electron beam passes the bunching gap of a resonator (cf. § 12.9) focusing occurs in the longitudinal direction. As the electron bunch passes along the drift tube it becomes more and more

concentrated so that it could be said the 'phase aperture' decreases. Eventually the slower electrons are overtaken by the faster ones. This occurs at the 'phase focus' where the phase aperture reaches a minimum. The phase focusing in an electron beam can be represented graphically by a distance-time diagram with the time as abscissa and with the distance of the electron along the axis of the beam as ordinate. Any beam of uniform velocity (whether geometrically divergent or convergent or parallel) is represented in the distance-time diagram as a parallel beam, the slope of each ray being proportional to its velocity. The bunching resonator changes the slope in proportion to the phase aperture of the ray, and hence it acts as a 'phase-lens' with a certain focal length given by the distance of the phase focus from it. Spherical aberration can be defined for phase focusing when its focal length is not proportional to the phase aperture. Debunching space-charge effects and other errors can be studied by optical methods. Though interesting in principle, phase optics in practice has not been more than a pleasant illustration of the bunching process.

APPENDIX

TABLE A. 1. *M.k.s. and c.g.s. units*

Quantity	Symbol	m.k.s.		c.g.s.
Length	s	m.	*equals*	100 cm.
Mass	m	kg.		10^3 g.
Time	t	sec.		1 sec.
Area	a	m.^{2}		10^4 cm.^{2}
Volume	v	m.^{3}		10^6 cm.^{3}
Velocity	$u = \mathrm{d}s/\mathrm{d}t$	m./sec.		100 cm./sec.
Force	F	newton or kg.-m./sec.^{2}		10^5 dynes
Pressure	P	newton/m.^{2}		10 dynes/cm.^{2} (or 10^5 bar or $7{\cdot}5 \times 10^{-3}$ mm. Hg)
Energy	W, U	Joule or W.-sec. or m.^{2}-kg.^{2}/sec.^{2}		10^7 ergs
Momentum	$p = mu$	kg.-m./sec.		10^5 g./cm./sec.
Angular velocity	$\omega = \mathrm{d}\Theta/\mathrm{d}t = u_\Theta/r$	radians/sec.		radians/sec.
Torque, couple	Γ	newton-m.		10^7 dynes-cm.
Moment of inertia	I	kg.-m.^{2}		10^7 g.-cm.^{2}
Angular momentum	$p_\Theta = I\omega = rmu_\Theta$	kg.-m.^{2}/sec.		10^7 g.cm.^{2}/sec.

TABLE A.2. *Rationalized m.k.s. electrostatic and electromagnetic units*

Quantity	Dimensions				Symbol	m.k.s.		e.s.u.		e.m.u.
	m.	kg.	sec.	coulomb						
Resistance	2	1	−1	−2	Ω	1 ohm	*equals*	$(1/9) \times 10^{-11}$ statohm	*equals*	10^9 abohms
Current	0	0	−1	1	I	1 A.		3×10^9 statamperes		10^{-1} abamperes
Potential	2	1	−2	−1	V	1 V.		1/300 statvolt		10^8 abvolts
Charge	0	0	0	1	q	1 coulomb		3×10^9 statcoulombs		10^{-1} abcoulombs
Capacitance	−2	−1	2	2	C	1 farad		9×10^{12} statfarads		10^{-9} abfarad
Inductance	2	1	0	−2	L	1 H.		$(1/9) \times 10^{-11}$ stathenry		10^9 abhenrys
Magnetic flux	2	1	−1	−1	—	1 Wb. or volt-sec.		1/300 statweber		10^8 c.g.s. lines 10^8 Maxwells
Magnetic flux density = magnetic induction	0	1	−1	−1	B	1 Wb./m.^{2} or volt-sec./m.^{2}		$(1/3) \times 10^{-6}$ statweber/cm.^{2}		10^4 gauss
Magnetic field strength	−1	0	−1	1	H	1 ampere-turn per metre or A./m.		$12\pi \times 10^7$ statoerstedt		$4\pi \times 10^{-3} = 1/79{\cdot}6$ oerstedt
Magnetomotive force or magn. potential difference	0	0	−1	1	V_H	1 ampere-turn		$12\pi \times 10^9$ statgilbert		$4\pi/10$ gilbert or oersted cm.
Electric flux density = dielectric displacement	−2	0	0	1	D	1 coulomb/m.^{2}		$12\pi \times 10^5 \frac{\text{statcoulomb}}{4\pi \text{ cm.}^2}$		$10^{-5} \frac{\text{abcoulomb}}{4\pi \text{ cm.}^2}$
Electric field strength	1	1	−2	−1	E	1 V./m.		$(1/3) \times 10^{-4}$ statvolt/cm.		10^6 abvolts/cm.
Electron momentum or magnetic rigidity	1	1	−1	−1	mu/e or $B_e r_e$	1 Wb./m.		$(1/3) \times 10^{-4} \frac{\text{g.cm./sec.}}{\text{e.s.u.}}$		10^6 gauss-cm. or 'Hρ value'
Electron energy	2	1	−2	0	eV or $mu^2/2(e/q_1)$	1 eV. ($1{\cdot}602 \times 10^{-19}$ Joules)				$1{\cdot}602 \times 10^{-12}$ erg

TABLE A.3. *Constants**

Dielectric const. for free space	$\epsilon_0 = 10^7/4\pi c^2 = 8{\cdot}855 \times 10^{-12}$	farad/m. or sec./(m.-ohm)
Permeability for free space	$\mu_0 = 4\pi/10^7 \quad = 1{\cdot}257 \times 10^{-6}$	henry/m. or ohms-sec./m.
Light velocity for free space	$c_0 = 3 \times 10^8$	m./sec.
Mass of electron	$m_0 = 9{\cdot}107 \times 10^{-31}$	kg.
Charge of electron	$e = 1{\cdot}602 \times 10^{-19}$	coulombs
	$e/m_0 = 1{\cdot}759 \times 10^{11}$	coulombs/kg.
Velocity of a 1 V. electron	$\sqrt{(2e/m_0)} = 5{\cdot}932 \times 10^5$	m./sec.
1 eV.	$1{\cdot}602 \times 10^{-19}$	Joules
Boltzmann const.	$k = 1{\cdot}380 \times 10^{-23}$	Joules/degree
	$e/k = 11{,}600$	degrees/eV.
Planck's const.	$h = 6{\cdot}624 \times 10^{-34}$	Joules-sec.

TABLE A.4

Electron volts $V = W/e$ [Joules/coulomb], *Electron momentum* $ep = B_e r_e$ [Wb./m.], *electron mass* m [kg.], *velocity* u [m./sec.], *and electron wave-length* λ [m.].

(I) Non-relativistic formulae, for very small velocities only, where $m \approx m_0$ (cf. A. 3):

$$V = \frac{m}{2e}u^2 \qquad = 2{\cdot}843 \times 10^{-12}u^2, \tag{1}$$

$$u = \sqrt{\left(\frac{2e}{m}V\right)} \quad = 0{\cdot}5932 \times 10^6\sqrt{V}, \tag{2}$$

$$B_e r_e = \frac{mu}{e} \qquad = 5{\cdot}685 \times 10^{-12}u, \tag{3}$$

$$u = \frac{e}{m}B_e r_e \qquad = 1{\cdot}759 \times 10^{11}B_e r_e, \tag{4}$$

$$V = \frac{e}{2m}(B_e r_e)^2 = 8{\cdot}795 \times 10^{10}(B_e r_e)^2, \tag{5}$$

$$B_e r_e = \sqrt{\left(\frac{2m}{e}V\right)} = 3{\cdot}372 \times 10^{-6}\sqrt{V}. \tag{6}$$

(II) Change of mass with velocity.

$$\frac{m}{m_0} = \frac{1}{\{1-(u/c_0)^2\}^{\frac{1}{2}}} = 1 + \frac{V}{V_0}, \tag{7}$$

where

$$eV_0 = m_0 c_0^2 \tag{8}$$

* Birge, R. T. (1941), *Rev. Mod. Phys.* **13**, 233.

is the relativistic energy-equivalent of the electronic mass:

$$V_0 = 0{\cdot}5115 \times 10^6 \,[\text{eV}]$$

$$(mc_0)^2 - (mu)^2 = (m_0 c_0)^2, \tag{9}$$

$$m = m_0 + \frac{e}{c_0^2} V. \tag{10}$$

(III) General formulae:

$$V = \frac{m_0 c_0^2}{e}\left(\frac{1}{\sqrt{\left\{1-\left(\frac{u}{c_0}\right)^2\right\}}} - 1\right) = 0{\cdot}5115 \times 10^6 \left(\frac{1}{\sqrt{\left(1 - \frac{u^2}{9\times 10^{16}}\right)}} - 1\right), \tag{11}$$

$$u = c_0\left\{1 - \frac{1}{(V/V_0+1)^2}\right\}^{\frac{1}{2}} = 3\times 10^8 \left\{1 - \frac{1}{(1{\cdot}955\times 10^{-6}V+1)^2}\right\}^{\frac{1}{2}}, \tag{12}$$

$$B_e r_e = \frac{m_0}{e}\frac{u}{\sqrt{\left\{1-\left(\frac{u}{c_0}\right)^2\right\}}} = 5{\cdot}685\times 10^{-12} u \Big/ \sqrt{\left(1 - \frac{u^2}{9\times 10^{16}}\right)}, \tag{13}$$

$$u = \frac{c_0}{\sqrt{\left\{1+\left(\frac{m_0 c_0}{eB_e r_e}\right)^2\right\}}} = 3\times 10^8 \Big/ \sqrt{\left(1 + \frac{2{\cdot}908\times 10^{-6}}{(B_e r_e)^2}\right)}, \tag{14}$$

$$V = V_0\left[\sqrt{\left\{1+\left(\frac{eB_e r_e}{m_0 c_0}\right)^2\right\}} - 1\right]$$

$$= 0{\cdot}5115\times 10^6 \left(\sqrt{\{1 + 0{\cdot}3438\times 10^6 (B_e r_e)^2 - 1\}}\right), \tag{15}$$

$$B_e r_e = \sqrt{\left\{\frac{2m_0}{e} V\left(1 + \frac{V}{2V_0}\right)\right\}} = 3{\cdot}372\times 10^{-6}\sqrt{(V + 0{\cdot}977\times 10^{-6} V^2)}, \tag{16}$$

$$B_e r_e = \frac{1}{c_0}\sqrt{(V^2 + 2VV_0)} = \tfrac{1}{3}\times 10^{-8}\sqrt{(V^2 + 1{\cdot}023\times 10^6 V)}, \tag{17}$$

$$\lambda = \frac{h}{eB_e r_e} = \frac{0{\cdot}4135\times 10^{-14}}{B_e r_e}. \tag{18}$$

(IV) Extreme velocities ($u \to c_0$): $m \gg m_0$,

$$W = c_0 p, \tag{19}$$

$$V = c_0 B_e r_e = 3\times 10^8 B_e r_e. \tag{20}$$

The following table gives numerical values obtained from formulae (1)–(20).

V [eV.]	u [m./sec.]	$B_e r_e$ [Wb./m.]	λ [m.]
1	$5{\cdot}932 \times 10^{5}$	$3{\cdot}372 \times 10^{-6}$	$1{\cdot}226 \times 10^{-9}$
10	$1{\cdot}876 \times 10^{6}$	$1{\cdot}066 \times 10^{-5}$	$3{\cdot}878 \times 10^{-10}$
20	$2{\cdot}653 \times 10^{6}$	$1{\cdot}508 \times 10^{-5}$	$2{\cdot}742 \times 10^{-10}$
30	$3{\cdot}250 \times 10^{6}$	$1{\cdot}847 \times 10^{-5}$	$2{\cdot}239 \times 10^{-10}$
40	$3{\cdot}752 \times 10^{6}$	$2{\cdot}133 \times 10^{-5}$	$1{\cdot}938 \times 10^{-10}$
50	$4{\cdot}195 \times 10^{6}$	$2{\cdot}385 \times 10^{-5}$	$1{\cdot}735 \times 10^{-10}$
60	$4{\cdot}595 \times 10^{6}$	$2{\cdot}613 \times 10^{-5}$	$1{\cdot}583 \times 10^{-10}$
70	$4{\cdot}963 \times 10^{6}$	$2{\cdot}822 \times 10^{-5}$	$1{\cdot}465 \times 10^{-10}$
80	$5{\cdot}306 \times 10^{6}$	$3{\cdot}016 \times 10^{-5}$	$1{\cdot}371 \times 10^{-10}$
90	$5{\cdot}628 \times 10^{6}$	$3{\cdot}199 \times 10^{-5}$	$1{\cdot}293 \times 10^{-10}$
1×10^{2}	$5{\cdot}932 \times 10^{6}$	$3{\cdot}373 \times 10^{-5}$	$1{\cdot}226 \times 10^{-10}$
2×10^{2}	$8{\cdot}388 \times 10^{6}$	$4{\cdot}771 \times 10^{-5}$	$8{\cdot}668 \times 10^{-11}$
3×10^{2}	$1{\cdot}028 \times 10^{7}$	$5{\cdot}846 \times 10^{-5}$	$7{\cdot}075 \times 10^{-11}$
4×10^{2}	$1{\cdot}186 \times 10^{7}$	$6{\cdot}748 \times 10^{-5}$	$6{\cdot}127 \times 10^{-11}$
5×10^{2}	$1{\cdot}326 \times 10^{7}$	$7{\cdot}547 \times 10^{-5}$	$5{\cdot}479 \times 10^{-11}$
6×10^{2}	$1{\cdot}453 \times 10^{7}$	$8{\cdot}270 \times 10^{-5}$	$5{\cdot}000 \times 10^{-11}$
7×10^{2}	$1{\cdot}569 \times 10^{7}$	$8{\cdot}935 \times 10^{-5}$	$4{\cdot}629 \times 10^{-11}$
8×10^{2}	$1{\cdot}678 \times 10^{7}$	$9{\cdot}555 \times 10^{-5}$	$4{\cdot}328 \times 10^{-11}$
9×10^{2}	$1{\cdot}779 \times 10^{7}$	$1{\cdot}013 \times 10^{-4}$	$4{\cdot}080 \times 10^{-11}$
1×10^{3}	$1{\cdot}873 \times 10^{7}$	$1{\cdot}067 \times 10^{-4}$	$3{\cdot}877 \times 10^{-11}$
2×10^{3}	$2{\cdot}645 \times 10^{7}$	$1{\cdot}509 \times 10^{-4}$	$2{\cdot}740 \times 10^{-11}$
3×10^{3}	$3{\cdot}234 \times 10^{7}$	$1{\cdot}849 \times 10^{-4}$	$2{\cdot}237 \times 10^{-11}$
4×10^{3}	$3{\cdot}730 \times 10^{7}$	$2{\cdot}137 \times 10^{-4}$	$1{\cdot}935 \times 10^{-11}$
5×10^{3}	$4{\cdot}166 \times 10^{7}$	$2{\cdot}391 \times 10^{-4}$	$1{\cdot}730 \times 10^{-11}$
6×10^{3}	$4{\cdot}555 \times 10^{7}$	$2{\cdot}620 \times 10^{-4}$	$1{\cdot}578 \times 10^{-11}$
7×10^{3}	$4{\cdot}911 \times 10^{7}$	$2{\cdot}830 \times 10^{-4}$	$1{\cdot}461 \times 10^{-11}$
8×10^{3}	$5{\cdot}245 \times 10^{7}$	$3{\cdot}028 \times 10^{-4}$	$1{\cdot}366 \times 10^{-11}$
9×10^{3}	$5{\cdot}554 \times 10^{7}$	$3{\cdot}213 \times 10^{-4}$	$1{\cdot}287 \times 10^{-11}$
1×10^{4}	$5{\cdot}846 \times 10^{7}$	$3{\cdot}389 \times 10^{-4}$	$1{\cdot}220 \times 10^{-11}$
2×10^{4}	$8{\cdot}151 \times 10^{7}$	$4{\cdot}816 \times 10^{-4}$	$8{\cdot}588 \times 10^{-12}$
3×10^{4}	$9{\cdot}846 \times 10^{7}$	$5{\cdot}927 \times 10^{-4}$	$6{\cdot}978 \times 10^{-12}$
4×10^{4}	$1{\cdot}122 \times 10^{8}$	$6{\cdot}875 \times 10^{-4}$	$6{\cdot}014 \times 10^{-12}$
5×10^{4}	$1{\cdot}237 \times 10^{8}$	$7{\cdot}722 \times 10^{-4}$	$5{\cdot}355 \times 10^{-12}$
6×10^{4}	$1{\cdot}338 \times 10^{8}$	$8{\cdot}501 \times 10^{-4}$	$4{\cdot}865 \times 10^{-12}$
7×10^{4}	$1{\cdot}427 \times 10^{8}$	$9{\cdot}220 \times 10^{-4}$	$4{\cdot}485 \times 10^{-12}$
8×10^{4}	$1{\cdot}506 \times 10^{8}$	$9{\cdot}903 \times 10^{-4}$	$4{\cdot}177 \times 10^{-12}$
9×10^{4}	$1{\cdot}578 \times 10^{8}$	$1{\cdot}055 \times 10^{-3}$	$3{\cdot}919 \times 10^{-12}$
1×10^{5}	$1{\cdot}644 \times 10^{8}$	$1{\cdot}117 \times 10^{-3}$	$3{\cdot}702 \times 10^{-12}$
2×10^{5}	$2{\cdot}084 \times 10^{8}$	$1{\cdot}649 \times 10^{-3}$	$2{\cdot}508 \times 10^{-12}$
3×10^{5}	$2{\cdot}329 \times 10^{8}$	$2{\cdot}101 \times 10^{-3}$	$1{\cdot}968 \times 10^{-12}$
4×10^{5}	$2{\cdot}482 \times 10^{8}$	$2{\cdot}515 \times 10^{-3}$	$1{\cdot}644 \times 10^{-12}$
5×10^{5}	$2{\cdot}588 \times 10^{8}$	$2{\cdot}911 \times 10^{-3}$	$1{\cdot}421 \times 10^{-12}$
6×10^{5}	$2{\cdot}663 \times 10^{8}$	$3{\cdot}292 \times 10^{-3}$	$1{\cdot}256 \times 10^{-12}$
7×10^{5}	$2{\cdot}718 \times 10^{8}$	$3{\cdot}662 \times 10^{-3}$	$1{\cdot}129 \times 10^{-12}$
8×10^{5}	$2{\cdot}761 \times 10^{8}$	$4{\cdot}027 \times 10^{-3}$	$1{\cdot}027 \times 10^{-12}$
9×10^{5}	$2{\cdot}795 \times 10^{8}$	$4{\cdot}388 \times 10^{-3}$	$9{\cdot}423 \times 10^{-13}$
1×10^{6}	$2{\cdot}822 \times 10^{8}$	$4{\cdot}742 \times 10^{-3}$	$8{\cdot}720 \times 10^{-13}$
2×10^{6}	$2{\cdot}935 \times 10^{8}$	$8{\cdot}200 \times 10^{-3}$	$5{\cdot}044 \times 10^{-13}$
4×10^{6}	$2{\cdot}979 \times 10^{8}$	$1{\cdot}495 \times 10^{-2}$	$2{\cdot}765 \times 10^{-13}$
6×10^{6}	$2{\cdot}989 \times 10^{8}$	$2{\cdot}166 \times 10^{-2}$	$1{\cdot}909 \times 10^{-13}$
8×10^{6}	$2{\cdot}993 \times 10^{8}$	$2{\cdot}834 \times 10^{-2}$	$1{\cdot}459 \times 10^{-13}$
1×10^{7}	$2{\cdot}995 \times 10^{8}$	$3{\cdot}503 \times 10^{-2}$	$1{\cdot}181 \times 10^{-13}$
1×10^{8}	$2{\cdot}999 \times 10^{8}$	$3{\cdot}352 \times 10^{-1}$	$1{\cdot}231 \times 10^{-14}$

For more detailed tables cf. Klemperer (1933), pp. 14, 15 and 61.

BIBLIOGRAPHY

A. List of General Works

Broglie, L. de (1950). *Optique Electronique et Corpusculaire.* Paris.

Broglie, L. de, Magnan, C., Fauré-Frémiet, E., Chancon, P., Ertaud, A., Grivet, P., Dupony, G. and Leauté, L. (1946). *L'Optique Electronique.* Paris.

Brüche, E. and Recknagel, A. (1941). *Elektronengeräte, Prinzipien und Systematik.* Berlin.

Brüche, E. and Scherzer, O. (1934). *Geometrische Elektronenoptik.* Berlin.

Busch, H. and Brüche, E. (editors) (1937). *Beiträge zur Elektronenoptik.* Leipzig.

Cosslett, V. E. (1946). *Introduction to Electron Optics.* Oxford.

Dupouy, G. (1952). *Eléments d'Optique Electronique.* Paris.

Glaser, W., Ruska, E. and Borries, B. von (1937). *Elektronenoptik.* Berlin.

Hatschek, P. (1948). *Electron Optics* (popular, elementary), 2nd ed. Boston.

Jacob, L. (1950). *An Introduction to Electron Optics.* London.

Myers, L. M. (1939). *Electron Optics.* London.

Picht, J. (1939). *Theorie der Elektronenoptik.* Berlin.

Pierce, J. R. (1949). *Theory and design of electron beams.* New York.

Rusterholz, A. (1950). *Grundlagen der theoretischen Elektronenoptik.* Basel.

Zworykin, V. K., Morton, G. A., Ramberg, E. G., Hillier, J. and Vance, A. W. (1945). *Electron Optics and the Electron Microscope.* New York.

B. Special References

(The chapter or section quoted after each item indicates where in this volume reference is made to that item)

Agnew, H. M. and Anderson, H. L. (1949). *Rev. Sci. Instrum.* **20**, 869. Ch. VI; §12.7.

Aharoni, J. (1944). *Phil. Mag.* **35**, 36. Ch. VIII.

Alfven, H. *et al.* (1947). *Nature, Lond.*, **160**, 614. §12.10.

Alfven, H. *et al.* (1948). *Trans. Roy. Inst. Tech. Stockholm*, no. 22. §12.10.

Allen, J. S. (1950). *Proc. Inst. Radio Engrs, N.Y.*, **38**, 346. §12.4.

Allison, S. K., Frankel, S. P. *et al.* (1949). *Rev. Sci. Instrum.* **20**, 735. Ch. XI.

Ardenne, M. v. (1938). *Z. Phys.* **108**, 338. Ch. VII.

Ardenne, M. v. (1939*a*). *Naturwissenschaften*, **27**, 614. Ch. IV.

Ardenne, M. v. (1939*b*). *Z. Phys.* **112**, 744. Ch. VI.

Ardenne, M. v. (1940*a*). *Naturwissenschaften*, **28**, 113. Ch. VI.

Ardenne, M. v. (1940*b*). *Elektronen Übermikroskopie.* Berlin. §12.6.

ARDENNE, M. v. (1941). *Phys. Z.* **42**, 72. Ch. VII.
ARNDT, U. W. (1948). *J. Sci. Instrum.* **25**, 414. Ch. X.
ARTSIMOVITCH, L. A. (1944). *Izvest. Akad. U.S.S.R.* **8**, 313. Ch. IX.
ASTON, F. W. (1919, 1933). *Mass Spectra and Isotopes.* Cambridge. §12.10.
BACHMAN, C. H. and RAMO, S. (1943*a*). *J. Appl. Phys.* **14**, 8. Ch. IV; VI; VII.
BACHMAN, C. H. and RAMO, S. (1943*b*). *J. Appl. Phys.* **14**, 69 and 155. Ch. VI.
BALACHOWSKY, M. (1946). *Bull. Soc. Franc. Elect.* **6**, 181. Ch. III.
BARBER, N. F. (1933). *Proc. Leeds Phil. Lit. Soc.* **2**, 427. Ch. XI.
BARKHAUSEN, H. and BRUCK, J. (1933). *Elektrotech. Z.* **54**, 175. Ch. X.
BARR, A. E. DE and MCARTHUR, I. (1950). *Brit. J. Appl. Phys.* **1**, 305. §12.10.
BARTKY, W. and DEMPSTER, A. J. (1929). *Phys. Rev.* **33**, 1019. Ch. XI.
BECK, A. H. (1948). *Velocity-modulated Thermionic Tubes.* Cambridge. §12.9.
BECKER, H. and WALLRAFF, A. (1938). *Arch. Elektrotech.* **32**, 664. Ch. V; VI.
BECKER, H. and WALLRAFF, A. (1939). *Arch. Elektrotech.* **33**, 491. Ch. VI.
BECKER, H. and WALLRAFF, A. (1940*a*). *Arch. Elektrotech.* **34**, 43. Ch. VI.
BECKER, H. and WALLRAFF, A. (1940*b*). *Arch. Elektrotech.* **34**, 115. Ch. V; VI.
BECKER, H. and WALLRAFF, A. (1940*c*). *Arch. Elektrotech.* **34**, 230. Ch. VI.
BEDFORD, L. H. (1936). *J. Sci. Instrum.* **13**, 177. Ch. VIII.
BEESE, N. C. (1937). *Rev. Sci. Instrum.* **8**, 258. Ch. X.
BEIDUCK, F. M. and KONOPINSKI, E. (1948). *Rev. Sci. Instrum.* **19**, 594. Ch. XI.
BENJAMIN, M. and JENKINS, R. O. (1940). *Proc. Roy. Soc.* A, **176**, 264. Ch. IX.
BENJAMIN, M. and JENKINS, R. O. (1942). *Proc. Roy. Soc.* A, **180**, 236. Ch. IX.
BERTEIN, F. (1947). *Ann. Radioelect.* **2**, 397. Ch. VI.
BERTEIN, F. (1948*a*). *Ann. Radioelect.* **3**, 49. Ch. VI.
BERTEIN, F. (1948*b*). *J. Phys. Radium*, **9**, 104. Ch. VI.
BERTRAM, S. (1940). *Proc. Inst. Radio Engrs, N.Y.*, **28**, 418. Ch. IV.
BERTRAM, S. (1942). *J. Appl. Phys.* **13**, 496. Ch. IV; X.
BERZ, F. (1950). *Phil. Mag.* **41**, 209. Ch. III.
BETHE, H. (1929). *Z. Phys.* **54**, 703. Ch. XI.
BLEWETT, J. P. (1948). *Proc. Inst. Radio Engrs, N.Y.*, **36**, 69. Ch. III.
BLOCH, J. (1936). *J. Sci. Instrum.* **13**, 302. Ch. III.
BOCK, C. D. (1933). *Rev. Sci. Instrum.* **4**, 575. Ch. XI.
BOERSCH, H. (1939). *Z. Tech. Phys.* **20**, 346. §12.6.
BOERSCH, H. (1940). *Naturwissenschaften*, **28**, 709. Ch. VII.
BOERSCH, H. (1943). *Phys. Z.* **44**, 32. Ch. VII.
BOERSCH, H. (1949). *Z. Tech. Phys.* **20**, 364. Ch. VI.
BOHM, D. and FOLDY, L. (1946). *Phys. Rev.* **70**, 249. §12.8.
BORGNIS, F. (1943). *Ann. Phys., Lpz.*, **43**, 616. Ch. VIII.
BORN, M. (1933). *Optik.* Berlin. Ch. VI; VII.

BORRIES, B. v. (1941). *Tel. Fernsp. Funk.* **30**, 295. Ch. XI.
BORRIES, B. v. (1949). *Die Übermikroskopie.* Berlin, §12.6.
BORRIES, B. v. and DOSSE, J. (1938). *Arch. Elektrotech.* **32**, 221. Ch. VIII.
BORRIES, B. v. and RUSKA, E. (1939). *Z. Tech. Phys.* **20**, 225. Ch. VII.
BORRIES, B. v. and RUSKA, E. (1940). *Arch. Elektrotech.* **36**, 106. §12.2.
BORRIES, B. v., RUSKA, E., KRUMM, J. and MÜLLER, H. O. (1940). *Naturwissenschaften*, **28**, 350. Ch. V.
BOTHE, W. (1950*a*). *Naturwissenschaften*, **37**, 41. Ch. VII; XI.
BOTHE, W. (1950*b*). *Heidelberg. Akad.* p. 191. Ch. VII; XI.
BOUWERS, A. (1935). *Physica*, **2**, 145. Ch. X.
BOUWERS, A. (1937). *Physica*, **4**, 200. Ch. V.
BRAID, T. H. and RICHARDSON, H. O. W. (1951). *Proc. Phys. Soc.* A, **64**, 163. Ch. XI.
BRILLOUIN, L. (1945). *Phys. Rev.* **67**, 260. Ch. VIII.
BROGLIE, L. DE (1946, 1950). *See* Bibliography A.
BROGLIE, M. DE (1922). *C.R. Acad. Sci., Paris*, **174**, 939. Ch. XI.
BROWN, W. F. and SWEER, J. H. (1945). *Rev. Sci. Instrum.* **16**, 276. Ch. V.
BROWNE, C. P., CRAIG, D. S. and WILLIAMSON, R. M. (1951). *Phys. Rev.* **81**, 304 (abstr.); *Rev. Sci. Instrum.* **22**, 952. Ch. XI; § 12.7.
BRÜCHE, E. (1930). *Phys. Z.* **31**, 1011. Ch. XI.
BRÜCHE, E. and JOHANNSON, H. (1932). *Naturwissenschaften*, **20**, 49 and 353. Ch. I; IX; §12.6.
BRÜCHE, E. and RECKNAGEL, A. (1938). *Z. Phys.* **108**, 459. §12.10.
BRÜCHE, E. and SCHERZER, O. (1934). *See* Bibliography A.
BRUCK, H. and GRIVET, P. (1950). *Rev. Opt.* (*théor. instrum.*), **29**, 164. Ch. VI.
BRUCK, H. and ROMANI, L. (1944). *Cahiers de Physique*, no. 24, 15. Ch. IV.
BUCHERER, A. H. (1909). *Ann. Phys., Lpz.*, **28**, 513. Ch. XI.
BULL, C. S. (1944). Brit. Pat. 601,966. Ch. X.
BULL, C. S. (1945). *J. Instn Elect. Engrs*, pt. III, **92**, 86. Ch. X.
BULL, C. S. (1948). *J. Instn Elect. Engrs*, pt. III, **95**, 17. Ch. VIII.
BURFOOT, J. C. (1952). *Brit. J. Appl. Phys.* **3**, 22. Ch. III.
BURGERS, W. G. and AMSTEL, I. P. v. (1937). *Physica*, **4**, 5 and 15. §12.6.
BURGERS, W. G. and AMSTEL, I. P. v. (1938). *Physica*, **5**, 305 and 313. §12.6.
BURTON, E. F. and KOHL, W. H. (1945). *The Electron Microscope*, 2nd ed. New York. §12.6.
BUSCH, H. (1926). *Ann. Phys., Lpz.*, **81**, 974. Ch. I; V.
BUSCH, H. (1927). *Arch. Elektrotech.* **18**, 583. Ch. V.
BUTT, D. K. (1949). *Proc. Phys. Soc.* B, **62**, 551. Ch. VII.
CAVANAGH, P. E. (1950). *Progr. Nucl. Phys.* **1**, 140. §12.7.
CHALLICE, C. E. (1950). *Proc. Phys. Soc.* B, **63**, 59. § 12.6.
CHANCON, P. (1947). *Ann. Phys., Paris*, **2**, 333. Ch. IV; VI.
CHANCON, P., ERTAUD, A. and MAGNAN, C. (1945). *C.R. Acad. Sci., Paris*, **221**, 233. Ch. IV.
CHRISTOPHERSON, D. G. and SOUTHWELL, R. V. (1938). *Proc. Roy. Soc.* A, **168**, 317. Ch. III.
CLASSEN, J. (1908). *Verh. deutsch. phys. Ges.* **10**, 700. Ch. XI.
COCKCROFT, J. D. (1933). *J. Sci. Instrum.* **10**, 71. Ch. XI; §12.7.

COCKCROFT, J. D., ELLIS, C. D. and KERSHAW, H. (1932). *Proc. Roy. Soc.* A, **135**, 228. Ch. XI.
COGGESHALL, N. D. (1946). *Phys. Rev.* **70**, 270. Ch. XI.
COGGESHALL, N. D. (1947). *J. Appl. Phys.* **18**, 855. Ch. XI.
COGGESHALL, N. D. and MUSKAT, M. (1944). *Phys. Rev.* **66**, 187. Ch. XI.
COLE, R. H. (1938). *Rev. Sci. Instrum.* **9**, 215. Ch. V.
COLLINS, G. B. (1948). *M.I.T. Radiation Lab. Series*, vol. **6** (Magnetron). New York. §12.9.
CONDLIFFE, G. E., SHOENBERG, I. and TEDHAM, W. F. (1933). Brit. Pat. 431,327. Ch. IX.
CONRADY, A. E. (1929). *Applied Optics and Optical Design.* Oxford. Ch. III; VI.
COSSLETT, V. E. (1940*a*). *J. Sci. Instrum.* **17**, 259. Ch. V.
COSSLETT, V. E. (1940*b*). *Proc. Phys. Soc.* **52**, 511. Ch. VII; XI.
COSSLETT, V. E. (1946*a*). *Proc. Phys. Soc.* **58**, 443. Ch. VI; VII.
COSSLETT, V. E. (1946*b*). *See* Bibliography A.
COSSLETT, V. E. (1947). *The Electron Microscope.* (An introduction.) London. §12.6.
COSSLETT, V. E. (1950). *Bibliography of Electron Microscopy* (2500 references). London. §12.6.
COSSLETT, V. E. (1951). *Practical Electron Microscopy.* London. §12.6.
CRAIG, H. (1947). *Proc. Phys. Soc.* **59**, 804. Ch. VI.
DANYSZ, J. (1911). *C.R. Acad. Sci., Paris*, **153**, 339. Ch. XI.
DAVISSON, C. J. and CALBICK, C. J. (1931). *Phys. Rev.* **38**, 585. Ch. I; IV; X.
DAVISSON, C. J. and CALBICK, C. J. (1932). *Phys. Rev.* **42**, 580. Ch. I; X.
DAWSON, H. G. (1898). Cf. Jahnke-Emde, *Funktionentafeln.* Ch. VIII.
DESERNO, P. (1935). *Arch. Electrotech.* **29**, 139. Ch. XI.
DEUTSCH, M., ELLIOTT, L. G. and EVANS, R. D. (1944). *Rev. Sci. Instrum.* **15**, 178. Ch. V; VII; §12.7.
DIELS, K. and WENDT, G. (1937). *Z. Tech. Phys.* **18**, 65. Ch. VI.
DIETZE, T. W. and DICKINSON, T. M. (1949). *Proc. Inst. Radio Engrs*, **37**, 1171. §12.8.
DOBKE, G. (1932). *Z. Tech. Phys.* **13**, 433. Ch. IX.
DODD, S. H., KLEMPERER, H. and YOUTZ, P. (1950). *Elect. Engng, N.Y.*, **69**, 990. §12.10.
DOSSE, J. (1936). *Z. Tech. Phys.* **17**, 315. Ch. V.
DOSSE, J. (1940). *Z. Phys.* **115**, 530. Ch. IX.
DOSSE, J. (1941). *Z. Phys.* **117**, 316, 437 and 722. Ch. III; V; VI; VII.
DOSSE, J. (1942). *Z. Phys.* **118**, 375. Ch. VI.
DRUDE, P. (1925). *Theory of Optics* (Translation by R. A. Millikan). New York. Ch. I; II; IX.
DRUMMOND, D. C. (1950*a*). *Practice of Electron Microscopy.* London, Inst. Phys. §12.6.
DRUMMOND, D. C. (1950*b*). *J.R. Micr. Soc.* **70**, pt. 1. §12.6.
DUMOND, J. W. M. (1949). *Rev. Sci. Instrum.* **20**, 160. Ch. VII.
DUNGEY, J. W. and HULL, C. R. (1947). *Proc. Phys. Soc.* **59**, 828. Ch. VI.
EHRENBERG, W. and HIRSCH, H. (1943). *J. Sci. Instrum.* **20**, 161. §12.10.

EHRENBERG, W. and JENNINGS, J. C. E. (1952). *Proc. Phys. Soc.* B, **65**, 265. Ch. XI; § 12.7.
EHRENBERG, W. and SIDAY, R. E. (1949). *Proc. Phys. Soc.* B, **62**, 8. Ch. I.
EHRENBERG, W. and SPEAR, W. E. (1951). *Proc. Phys. Soc.* B, **64**, 67. Ch. IX.
EINSTEIN, P. A. (1951). *Brit. J. Appl. Phys.* **2**, 49. Ch. III.
EINSTEIN, P. A. and JACOB, L. (1948). *Phil. Mag.* **39**, 20. Ch. IX.
ELLIS, C. D. (1930). In Rutherford, E., Chadwick, J. and Ellis, C. D., *Radiations from Radioactive Substances*. Cambridge. Cf. also Li, K. T. (1937). §12.7.
ELLIS, S. G. (1947). *J. Appl. Phys.* **18**, 879. Ch. IX.
ENGSTROM, R. W. (1947). *J. Opt. Soc. Amer.* **37**, 420. §12.4.
EPSTEIN, D. W. (1936). *Proc. Inst. Radio Engrs*, **24**, 1095. Ch. II; IV; VI.
EPSTEIN, D. W. and MALOFF, I. G. (1945). *J. Soc. Mot. Pict. Engrs*, **14**, 443. §12.3.
EPSTEIN, D. W. and PENSAK, L. (1946). *R.C.A. Rev.* **7**, 5. §12.3.
ERTAUD, A. (1946). *See* Broglie, Bibliography A. Ch. III.
FARNSWORTH, P. T. (1934). *J. Franklin Inst.* **218**, 411. Ch. IV; IX; §12.5.
FIELD, L. M. (1946). *Rev. Mod. Phys.* **18**, 353. Ch. IX.
FIELD, L. M., SPANGENBERG, K. R. and HELM, R. (1947). *Elect. Commun.* **24**, 108. Ch. VIII.
FISK, J. B., HAGSTRUM, H. D. and HARTMAN, P. L. (1946). *Bell Syst. Tech. J.* **25**, 167. §12.9.
FOWLER, R. D. and GIBSON, G. E. (1934). *Phys. Rev.* **46**, 1075 (1084). Ch. VIII.
FOX, L. (1947). *Proc. Roy. Soc.* A, **190**, 31. Ch. III.
FOX, L. (1948). *Quart. J. Mech. Appl. Math.* **1**, 253. Ch. III.
FRANKEL, S. (1948). *Phys. Rev.* **73**, 804. Ch. VII; XI; §12.7.
FREMLIN, J. H. and WALKER, J. (1947). *J. Sci. Instrum.* **24**, 50. Ch. X.
FRY, D. W. and WALKINSHAW, W. (1949). *Rep. Progr. Phys.* **12**, 102. §12.8.
FRY, T. C. (1932). *Bell Syst. Monogr.* B, 671. Ch. X.
GABOR, D. (1937). *Nature, Lond.*, **139**, 373. Ch. III.
GABOR, D. (1946). *Nature, Lond.*, **158**, 198. Ch. VI.
GABOR, D. (1947). *Nature, Lond.*, **159**, 303. Ch. IV.
GABOR, D. (1951). *Proc. Phys. Soc.* B, **64**, 244. Ch. VII.
GABOR, D. (1945). *The Electron Microscope*. London. §12.6.
GAEDKE, W. (1938). *Z. Tech. Phys.* **19**, 204.
GANS, R. (1937). *Z. Tech. Phys.* **18**, 41. Ch. III.
GEOFFRION, C. (1949). *Rev. Sci. Instrum.* **20**, 638. Ch. XI; §12.7.
GEORGESCO, M. (1949). *C.R. Acad. Sci., Paris*, **229**, 297. Ch. VII.
GILL, E. W. B. (1925). *Phil. Mag.* **49**, 993. Ch. VIII.
GILL, E. W. B. (1930). *Phil. Mag.* **10**, 134. Ch. VIII.
GLASER, A. and HENNEBERG, W. (1935). *Z. Tech. Phys.* **16**, 229. Ch. IV; X.
GLASER, W. (1933*a*). *Z. Physik*, **80**, 450. Ch. I; VI.
GLASER, W. (1933*b*). *Z. Physik*, **81**, 649. Ch. VI.
GLASER, W. (1933*c*). *Z. Physik*, **83**, 104. Ch. VI.

GLASER, W. (1935). *Z. Physik*, **97**, 177. Ch. VI.
GLASER, W. (1938*a*). *Z. Physik*, **109**, 700. Ch. VI.
GLASER, W. (1938*b*). *Z. Physik*, **111**, 357. Ch. XI.
GLASER, W. (1940*a*). *Z. Physik*, **116**, 19, 737. Ch. VI.
GLASER, W. (1940*b*). *Z. Physik*, **116**, 56. Ch. VII.
GLASER, W. (1941*a*). *Z. Phys.* **117**, 285. Ch. I; VI.
GLASER, W. (1941*b*). *Z. Phys.* **118**, 264. Ch. V.
GLASER, W. (1943). *Z. Phys.* **120**, 1, 121 and 647. Ch. VI.
GLASER, W. (1949*a*). *Z. Phys.* **125**, 541. §12.6.
GLASER, W. (1949*b*). *Acta Phys. Austriaca*, **3**, 38. §12.6.
GLASER, W. (1949*c*). *Ann. Phys., Lpz.*, **4**, 389. Ch. XI.
GLASER, W. (1950). *Ann. Phys., Lpz.*, **7**, 213. Ch. V.
GLASER, W. (1951). *Proc. Phys. Soc.* B, **64**, 114. Ch. I.
GLASER, W. and LAMMEL, E. (1941). *Ann. Phys., Lpz.*, **40**, 367. Ch. V.
GLASER, W. and LAMMEL, E. (1943). *Arch. Elektrotech.* **37**, 347. Ch. VI.
GLOCKER, R. (1949). *Materialprüfung mit Röntgenstrahlen*, 3rd ed. Berlin. §12.10.
GOBRECHT, R. (1941). *Arch. Electrotech.* **35**, 672. Ch. IV; VI.
GOBRECHT, R. (1942). *Arch. Electrotech.* **36**, 484. Ch. VI.
GODDARD, L. S. (1944). *Proc. Phys. Soc.* **56**, 372. Ch. III.
GODDARD, L. S. (1946*a*). *Proc. Camb. Phil. Soc.* **42**, 106. Ch. IV.
GODDARD, L. S. (1946*b*). *Proc. Camb. Phil. Soc.* **42**, 127. Ch. VI.
GODDARD, L. S. and KLEMPERER, O. (1944). *Proc. Phys. Soc.* **56**, 378. Ch. III; V; VI.
GOUDET, G. and GRUTZMULLER, A. M. (1944). *J. Phys. Radium*, **5**, 142. Ch. VIII.
GOUDET, G. and GRUTZMULLER, A. M. (1945). *J. Phys. Radium*, **6**, 153. Ch. VIII.
GOUDET, G. and MUSSON-GENON, R. (1945). *J. Phys. Radium*, **6**, 185. Ch. VIII.
GOWARD, F. K., ROTBLAT, J. and SHIRE, E. S. (1950). *Acceleration of Particles to High Energies*. London, Inst. Phys. §12.8.
GOWARD, F. K. and WILKINS, J. J. (1948). *Proc. Phys. Soc.* **61**, 580. Ch. X.
GRAHAM, R. L. (1949). Thesis, London. Ch. V; §12.7.
GRAHAM, R. L. and KLEMPERER, O. (1952). *Proc. Phys. Soc.* B, **65**, 921. Ch. V; § 12.7.
GRAY, F. (1939). *Bell Syst. Tech. J.* **18**, 1. Ch. IV.
GRIVET, P. (1950*a*). *Advances in Electronics*, **2**, 582. Ch. IV; V.
GRIVET, P. (1950*b*). *J. Phys. Radium*, **11**, 582. Ch. VII.
GRIVET, P. (1951). *J. Phys. Radium*, **12**, 1. Ch. VII.
GRIVET, P. (1952). *J. Phys. Radium*, **13**, 1 A. Ch. V.
GUENARD, P. (1945). *J. Phys. Radium*, **6**, 43. Ch. VIII.
GUNDERT, E. (1939). *Z. Phys.* **112**, 689. Ch. VI.
GUNDERT, E. (1941). *Telefunkenröhre*, no. 20, 61. Ch. VI.
GURNEY, R. W. (1925). *Proc. Roy. Soc.* A, **109**, 540. Ch. XI; §12.7.
HACHENBERG, O. (1948). *Ann. Phys., Lpz.*, **2**, 225. Ch. XI.
HADFIELD, D. (1950). *Electronic Engng*, **22**, 132. Ch. V.
HAEFF, A. V. (1939). *Proc. Inst. Radio Engrs*, **27**, 586. Ch. VIII.

HAEFF, A. V. (1947). *Electronics*, **20** (Sept.), p. 80. §12.10.
HAEFF, A. V. (1948). *Phys. Rev.* **74**, 1532. §12.9.
HAINE, M. E. and EINSTEIN, P. A. (1952). *Brit. J. Appl. Phys.* **3**, 40. Ch. IX.
HAINE, M. E., PAGE, R. S. and GARFITT, R. G. (1950). *J. Appl. Phys.* **21**, 173. §12.6.
HAMILTON, D. R. (1948). *M.I.T. Radiation Lab. Series*, vol. **7** (Klystron). New York. §12.9.
HANSEN, W. W. and WEBSTER, D. L. (1936). *Rev. Sci. Instrum.* **7**, 17. Ch. IV.
HARDY, A. C. and PERRIN, F. H. (1932). *The Principles of Optics*. New York. Ch. III.
HARRIES, S. H. O. (1944). *Wireless Engr*, **21**, 261. §12.9.
HARRIS, F. K. (1934). *Bur. Stand. J. Res.* **13**, 391. Ch. VI.
HARRISON, A. E. (1944). *J. Appl. Phys.* **15**, 709. §12.10.
HAUG, A. (1943). *Z. Tech. Phys.* **24**, 143. Ch. VIII.
HAYNES, S. K. and WEDDING, J. W. (1951). *Rev. Sci. Instrum.* **22**, 97. Ch. VI.
HEATH, H. S. (1887). *Geometrical Optics*. Cambridge. Ch. III.
HEDGRAN, A., SIEGBAHN, K. and SWARTHOLM, N. (1950). *Proc. Phys. Soc.* A, **63**, 960, and private communication. Ch. XI; §12.7.
HEHLGANS, F. (1935). *Z. Tech. Phys.* **16**, 197. Ch. X.
HEISE, F. (1948). *Optik*, **4**, 251. Ch. VI.
HEISE, F. (1949). *Optik*, **5**, 479. Ch. VI.
HEISE, F. and RANG, O. (1949). *Optik*, **5**, 201. Ch. II; IV; VI.
HENDERSON, W. J. and REDHEAD, P. A. (1949). *Nucleonics*, **5** (Oct.), 60. §12.8.
HENNEBERG, W. (1934*a*). *Z. Phys.* **90**, 747. Ch. VII.
HENNEBERG, W. (1934*b*). *Ann. Phys., Lpz.*, **19**, 335. Ch. XI.
HENNEBERG, W. (1934*c*). *Ann. Phys., Lpz.*, **20**, 1. Ch. XI.
HENNEBERG, W. (1934*d*). *Ann. Phys., Lpz.*, **21**, 390. Ch. XI.
HENNEBERG, W. and RECKNAGEL, A. (1935*a*). *Z. Tech. Phys.* **16**, 621. Ch. IV.
HENNEBERG, W. and RECKNAGEL, A. (1935*b*). *Z. Tech. Phys.* **16**, 230. Ch. VII.
HEPP, G. (1939). *Philips Tech. Rev.* **4**, 223. Ch. III.
HERZOG, R. (1934). *Z. Phys.* **89**, 447. Ch. XI.
HERZOG, R. (1935). *Z. Phys.* **97**, 596. Ch. XI.
HERZOG, R. (1939). *Z. Phys.* **113**, 166. Ch. XI.
HERZOG, R. (1940). *Phys. Z.* **41**, 13. Ch. XI.
HESS, E. (1934). *Z. Phys.* **92**, 274. Ch. II.
HESSE, M. B. (1950). *Proc. Phys. Soc.* B, **63**, 386. Ch. V.
HILLIER, J. (1940). *Phys. Rev.* **58**, 842. Ch. VII.
HILLIER, J. (1946). *J. Appl. Phys.* **17**, 411. Ch. VI.
HILLIER, J. (1948). *J. Appl. Phys.* **19**, 226. Ch. VI.
HILLIER, J. and BAKER, R. F. (1944). *J. Appl. Phys.* **15**, 663. §12.10.
HILLIER, J. and BAKER, R. F. (1945). *J. Appl. Phys.* **16**, 469. Ch. IX.
HILLIER, J. and BAKER, R. F. (1946). *J. Appl. Phys.* **17**, 12. Ch. IX.
HILLIER, J., BAKER, R. F. and ZWORYKIN, V. K. (1942). *J. Appl. Phys.* **13**, 571. §12.10.

HILLIER, J. and ELLIS, S. G. (1949). *J. Appl. Phys.* **20**, 700. Ch. IX.
HILLIER, J. and RAMBERG, E. (1947). *J. Appl. Phys.* **18**, 48. Ch. VI.
HILSCH, R. and POHL, R. W. (1928). *Nachr. Ges. Wiss. Göttingen*, **29**, 124. Ch. XI.
HINTENBERGER, H. (1948). *Z. Naturforsch.* **3**A, 125, 669. Ch. XI.
HINTENBERGER, H. (1949). *Rev. Sci. Instrum.* **20**, 748. Ch. XI.
HOGAN, T. K. (1943). *J. Instn Engrs Aust.* **15**, 89. Ch. III; VIII.
HOLST, G., BOER, J. H. DE and VEENEMANS, C. F. (1934). *Physica*, **1**, 297. § 12.5.
HOPKINS, H. H. and BARHAM, P. M. (1950). *Proc. Phys. Soc.* B, **58**, 737. Ch. VII.
HOTTENROTH, G. (1936). *Z. Phys.* **103**, 460. Ch. IV.
HOUTERMANS, F. G. and RIEWE, K. H. (1941). *Arch. Elektrotech.* **35**, 686. Ch. X.
HUBERT, P. (1951). *C.R. Acad. Paris*, **233**, 943. Ch. V; VI.
HUDSON, R. P. (1949). *J. Appl. Phys.* **26**, 401. Ch. XI.
HUGHES, A. L. and MCMILLAN, J. H. (1929). *Phys. Rev.* **34**, 291. Ch. XI.
HUGHES, A. L. and ROJANSKI, V. (1929). *Phys. Rev.* **34**, 284. Ch. XI.
HULL, A. W. (1921). *Phys. Rev.* **18**, 31. Ch. XI.
HUTTER, R. G. E. (1945*a*). *J. Appl. Phys.* **16**, 678. Ch. IV.
HUTTER, R. G. E. (1945*b*). *Phys. Rev.* **67**, 248. Ch. XI.
HUTTER, R. G. E. (1947*a*). *J. Appl. Phys.* **18**, 740. Ch. XI.
HUTTER, R. G. E. (1947*b*). *J. Appl. Phys.* **18**, 797. Ch. III.
HUTTER, R. G. E. and HARRISON, S. W. (1950). *J. Appl. Phys.* **21**, 84. Ch. XI.
IAMS, H. (1939). *Proc. Inst. Radio Engrs*, **27**, 103. Ch. IV.
INGHRAM, M. G. (1948). *Advances in Electronics*, **1**, 219. § 12.10.
JACOB, L. (1938). *Phil. Mag.* **26**, 570. Ch. III.
JACOB, L. (1939). *Phil. Mag.* **28**, 81. Ch. IX.
JACOB, L. (1944). *J. Instn Elect. Engrs*, pt. III, **91**, 512. Ch. IX.
JACOB, L. (1948). *Phil. Mag.* **39**, 20 and 400. Ch. IX.
JACOB, L. (1950*a*). *Proc. Phys. Soc.* B, **63**, 75. Ch. IX.
JACOB, L. (1950*b*). *J. Appl. Phys.* **21**, 966. Ch. IX.
JACOB, L. (1952). *Proc. Phys. Soc.* B, **65**, 421. Ch. IX.
JACOB, L. and MULVEY, T. (1949). *Nature, Lond.*, **163**, 525. Ch. VI.
JENKINS, J. A. and CHIPPENDALE, R. A. (1951). *J. Brit. Instn Radio Engrs*, **11**, 505. § 12.5.
JENKINS, R. O. (1943). *Phys. Prog. Rep.* **9**, 177. § 12.6.
JENNINGS, J. C. E. (1950). Thesis, London. Ch. XI.
JENNINGS, J. C. E. (1952). *Proc. Phys. Soc.* B, **65**, 256. Ch. XI.
JESTY, L. C., MOSS, H. and PULLESTON, R. (1946). *J. Instn Elect. Engrs*, pt. III, **93**, 149. § 12.2.
JOHANNSON, H. (1933). *Ann. Phys., Lpz.*, **18**, 385. Ch. VI; IX.
JOHANNSON, H. (1934*a*). *Ann. Phys., Lpz.*, **21**, 275. Ch. VI; IX.
JOHANNSON, H. (1934*b*). *Z. Phys.* **90**, 748. Ch. IX.
JOHANNSON, H. and SCHERZER, O. (1933). *Z. Phys.* **80**, 183. Ch. IV.
JOHNSON, T. H. (1938). *Rev. Mod. Phys.* **10**, 193. Ch. XI.
JONKER, J. L. H. (1949). *Philips Res. Rep.* **4**, 357. Ch. X.

JONKER, J. L. H. and OVERBEEK, A. J. W. (1949). *Nature, Lond.*, **164**, 276. Ch. VIII.
JONKER, J. L. H., OVERBEEK, A. J. W. and BEURS, P. H. DE (1952). *Philips Res. Rep.* **7**, 81. § 12.10.
JUDD, D. L. (1950). *Rev. Sci. Instrum.* **21**, 213. Ch. XI.
KELLER, J. M., KOENIGSBERG, E. and PASKIN, A. (1950). *Rev. Sci. Instrum.* **21**, 713. Ch. VII.
KELMAN, V., KORSUNSKY, M. and LANGE, F. (1939). *J. Exp. Theor. Phys. U.S.S.R.* **9**, 681. Ch. X.
KERST, D. W. (1940). *Phys. Rev.* **58**, 841. § 12.8.
KERST, D. W. (1941). *Phys. Rev.* **60**, 47. § 12.8.
KERST, D. W. (1942). *Rev. Sci. Instrum.* **13**, 387. § 12.8.
KERST, D. W. (1945). *Phys. Rev.* **68**, 233. § 12.8.
KERST, D. W. *et al.* (1950). *Rev. Sci. Instrum.* **21**, 462. § 12.8.
KERST, D. W. and SERBER, R. (1941). *Phys. Rev.* **60**, 53. Ch. XI.
KERWIN, L. (1949). *Rev. Sci. Instrum.* **20**, 36. Ch. XI.
KIRKPATRICK, P. and BECKERLEY, J. G. (1936). *J. Sci. Instrum.* **7**, 24. Ch. IV.
KLEMPERER, O. (1925). *Z. Phys.* **34**, 532. Ch. XI.
KLEMPERER, O. (1933). *Elektronik.* Berlin. Ch. I.
KLEMPERER, O. (1935). *Phil. Mag.* **20**, 45. Ch. V; VII; § 12.7.
KLEMPERER, O. (1937). Brit. Pat. 498,511. Ch. XI.
KLEMPERER, O. (1940). Brit. Pat. 567,228. Ch. XI.
KLEMPERER, O. (1941*a*). *Phys. Progr. Rep.* **7**, 107. Ch. V; § 12.6.
KLEMPERER, O. (1941*b*). Brit. Pat. 534,215. Ch. VIII.
KLEMPERER, O. (1942*a*). Brit. Pat. 568,572. Ch. VI; VIII.
KLEMPERER, O. (1942*b*). Brit. Pat. 573,901. Ch. X.
KLEMPERER, O. (1942*c*). Brit. Pat. 574,056. Ch. X
KLEMPERER, O. (1943). Brit. Pat. 570,213. Ch. XI.
KLEMPERER, O. (1944*a*). *J. Sci. Instrum.* **21**, 88. Ch. III.
KLEMPERER, O. (1944*b*). Brit. Pat. 580, 762. Ch. X.
KLEMPERER, O. (1944*c*). Brit. Pat. 609,480. Ch. X.
KLEMPERER, O. (1947*a*). *Proc. Phys. Soc.* **59**, 302. Ch. VIII; IX; X.
KLEMPERER, O. (1947*b*). *Proc. Roy. Soc.* A, **190**, 376. Ch. IX.
KLEMPERER, O. (1951). *Proc. Phys. Soc.* B, **64**, 790. Ch. VI; VIII.
KLEMPERER, O. and KLINGER, Y. (1951). *Proc. Phys. Soc.* B, **64**, 231. Ch. IX.
KLEMPERER, O. and MAYO, B. J. (1948). *J. Inst Elect. Engrs*, pt. III, **95**, 135. Ch. IX.
KLEMPERER, O. and MILLER, H. (1939). *J. Sci. Instrum.* **16**, 121. Ch. VI.
KLEMPERER, O. and WRIGHT, W. D. (1939). *Proc. Phys. Soc.* **51**, 296. Ch. II; III; IV; VI; IX.
KLEYNEN, P. A. (1937). *Philips Tech. Rev.* **2**, 338. Ch. X.
KNOLL, M. (1934). *Z. Tech. Phys.* **15**, 584. Ch. X.
KNOLL, M. (1939). *Telefunken Hausmit.* **20**, 72, no. 81. Ch. XI.
KNOLL, M. and RUSKA, E. (1931). *Z. Tech. Phys.* **12**, 394. Ch. I; § 12.6.
KNOLL, M. and RUSKA, E. (1932*a*). *Ann. Phys., Lpz.*, **12**, 607 and 641. Ch. I; IV; VIII.
KNOLL, M. and RUSKA, E. (1932*b*). *Z. Phys.* **78**, 318. Ch. I.
KNOLL, M. and WEICHARDT, H. (1938). *Z. Phys.* **110**, 233. Ch. IV.

KOHAUT, A. (1937). *Z. Tech. Phys.* **18**, 198. Ch. V.
KOLLATH, R. (1936). *Ann. Phys., Lpz.*, **27**, 721. §12.7.
KOMPFNER, R. (1947). *Proc. Inst. Radio Engrs, N.Y.*, **35**, 124. §12.9.
KOMPFNER, R. (1952). *Phys. Prog. Rep.* **15**, 275. § 12.9.
KORSUNSKY, M. (1945). *J. Phys. U.S.S.R.* **9**, 14. Ch. XI.
KORSUNSKY, M., KELMAN, V. and PETROV, B. (1945). *J. Phys. U.S.S.R.* **9**, 7. Ch. XI.
KURIE, F. N. D., OSOBA, J. S. and SLACK, L. (1948). *Rev. Sci. Instrum.* **19**, 771. Ch. XI; §12.7.
LAMPERT, I. E. and FELD, R. (1946). *Proc. Inst. Radio Engrs, N.Y.*, **34**, 432. §12.2.
LANGER, L. M. and COOK, C. S. (1948). *Rev. Sci. Instrum.* **19**, 257. Ch. XI; §12.7.
LANGER, L. M. and SCOTT, F. R. (1950). *Rev. Sci. Instrum.* **21**, 522. Ch. V.
LANGMUIR, D. B. (1937*a*). *Nature, Lond.*, **139**, 1067. Ch. III.
LANGMUIR, D. B. (1937*b*). *Proc. Inst. Radio Engrs, N.Y.*, **25**, 977. Ch. VII; IX; §12.3.
LANGMUIR, D. B. (1950). *R.C.A. Rev.* **11**, 143. Ch. III.
LANGMUIR, I. (1913). Cf. Langmuir, I. and Compton, K. T. (1931), *Rev. Mod. Phys.* **3**, 191. Ch. VIII; IX.
LAPLUME, J. (1947). *Cahiers de Physique*, no. 29 30, 55. Ch. IV.
LAW, R. R. (1937). *Proc. Inst. Radio Engrs, N.Y.*, **25**, 954. Ch. IX; §12.3.
LAWRENCE, E. O. and LIVINGSTON, M. S. (1931). *Phys. Rev.* **37**, 1707.
LAWRENCE, E. O. and LIVINGSTON, M. S. (1932). *Phys. Rev.* **40**, 19. §12.8.
LAWSON, J. L. and TYLER, A. W. (1940). *Rev. Sci. Instrum.* **11**, 14. Ch. XI; §12.7.
LENZ, F. (1950). *Z. angew. Phys.* **2**, 337. Ch. V.
LENZ, F. (1951*a*). *Ann. Phys., Lpz.*, **9**, 245. Ch. V.
LENZ, F. (1951*b*). *Naturwissenschaften*, **38**, 524. Ch. VII.
LENZ, F. (1952). *Optik*, **9**, 3. Ch. V.
LE POOLE, J. B. (1948). *J. Sci. Instrum.* **25**, 24. Ch. VI.
LE RUTTE, W. A. (1948). *Nature, Lond.*, **161**, 392. Ch. VII.
LI, K. T. (1937). *Proc. Camb. Phil. Soc.* **33**, 164. Ch. XI; §12.7.
LIEBMANN, G. (1946). *Phil. Mag.* **37**, 677. Ch. VI.
LIEBMANN, G. (1948*a*). *Phil. Mag.* **39**, 281. Ch. IV.
LIEBMANN, G. (1948*b*). *J. Sci. Instrum.* **25**, 37. Ch. IX.
LIEBMANN, G. (1949*a*). *Proc. Phys. Soc.* B, **62**, 213. Ch. IV; VI.
LIEBMANN, G. (1949*b*). *Proc. Phys. Soc.* B, **62**, 753. Ch. III.
LIEBMANN, G. (1950*a*). *Brit. J. Appl. Phys.* **1**, 92. Ch. III.
LIEBMANN, G. (1950*b*). *Advances in Electronics*, **2**, 101. Ch. III.
LIEBMANN, G. (1950*c*). *Phil. Mag.* **41**, 1143. Ch. V.
LIEBMANN, G. (1951). *Proc. Phys. Soc.* B, **64**, 972. Ch. V; VI.
LIEBMANN, G. (1952*a*). *Proc. Phys. Soc.* B, **65**, 94. Ch. V; VI.
LIEBMANN, G. (1952*b*). *Proc. Phys. Soc.* B, **65**, 188. Ch. V; VI.
LIEBMANN, G. and GRAD, E. M. (1951). *Proc. Phys. Soc.* B, **64**, 956. Ch. V; VI.
LINDER, E. G. and HERNQUIST, K. G. (1950). *J. Appl. Phys.* **21**, 1088. Ch. VIII.

LIVINGSTON, M. S. (1948). *Advances in Electronics*, **1**, 269. §12.8.
LÖHNER, H. (1930). *Ann. Phys., Lpz.*, **6**, 66. Ch. XI.
LONDON INST. OF PHYS. (1950). *Symposium on Metallurgical Applications of the Electron Microscope.* London Inst. Phys. §12.6.
LUBSZYNSKI, G. (1947). Chapter II of *Electronics*, ed. Lovell, London. Ch. X; §12.4.
LUBSZYNSKI, G. and RODDA, S. (1934). *See* McGee and Lubszynski (1939).
LYDDANE, R. H. and RUARK, E. A. (1939). *Rev. Sci. Instrum.* **10**, 253. Ch. VI.
M.I.T. RADIATION LAB. SERIES, vol. 22, *Cathode Ray Tube Displays.* New York, 1948. §12.2. *See also* Collins, Hamilton.
MAGNAN, C. (1946). *See* Broglie, L. de, in Bibliography A. §12.10.
MAGNAN, C. (1949). *Nucleonics*, **4**, no. 4, 52. §12.10.
MAHL, H. (1939). *Z. Tech. Phys.* **20**, 316. §12.6.
MAHL, H. (1940). *Z. Tech. Phys.* **21**, 17. §12.6.
MAHL, H. and GÖLZ, E. (1951). *Elektronenmikroskopie.* Leipzig. §12.6.
MAHL, H. and PENDZICH, A. (1943). *Z. Tech. Phys.* **24**, 38. §12.6.
MAHL, H. and RECKNAGEL, A. (1944). *Z. Phys.* **122**, 60. Ch. VI.
MALOFF, I. G. and EPSTEIN, W. D. (1934). *Proc. Inst. Radio Engrs, N.Y.*, **23**, 1386. Ch. III; IX.
MALOFF, I. G. and EPSTEIN, W. D. (1938). *Electron Optics in Television.* New York. Ch. III; IX; XI; §12.3.
MANIFOLD, M. B. and NICOLL, F. H. (1938). *Nature, Lond.*, **142**, 39. Ch. III.
MARSCHALL, H. (1939). *Telefunkenröhre*, no. 16, 190. Ch. VI.
MARSCHALL, H. (1944). *Phys. Z.* **45**, 1. Ch. XI.
MARSCHALL, H. and SCHRÖDER, W. (1942). *Z. Tech. Phys.* **23**, 297. Ch. XI.
MARTON, L. (1950). *J. Opt. Soc. Amer.* **40**, 269. Ch. VI.
MARTON, L. and BOL, K. (1947). *J. Appl. Phys.* **18**, 522. Ch. VI.
MARTON, L. and HUTTER, R. G. C. (1944). *Proc. Inst. Radio Engrs, N.Y.*, **32**, 3 and 546. Ch. V; §12.6.
MARTON, L. and REVERDIN, D. L. (1950). *J. Appl. Phys.* **21**, 842. Ch. VII.
MCGEE, J. D. (1947). Chapter IV of *Electronics*, ed Lovell, London. §12.3.
MCGEE, J. D. and LUBSZYNSKI, G. (1939). *J. Instn Elect. Engrs*, **84**, 468. §12.3.
MCGREGOR-MORRIS, J. T. and MINES, R. (1925). *J. Instn Elect. Engrs*, **63**, 1065. Ch. VI; VIII.
MCMILLAN, E. M. (1945). *Phys. Rev.* **68**, 143. §12.8.
MENTS, M. v. and LE POOLE, J. B. (1947). *Appl. Sci. Res.* B, **1**, 3. Ch. V.
MEYER, S. and SCHWEIDLER, E. (1899). *Phys. Z.* **1**, 90. Ch. XI.
MIDDLETON, L. R. (1937). *A Textbook on Light*, 2nd ed. London. (Elementary, with good explanations on sign conventions.) Ch. II.
MILLET, W. E. (1948). *Phys. Rev.* **74**, 1058. Ch. XI.
MÖLLENSTEDT, G. (1949). *Optik*, **5**, 499. Ch. VII; XI; §§12.7, 12.10.
MÖLLENSTEDT, G. and RANG, O. (1951). *Z. angew. Phys.* **3**, 187. Ch. VII; §12.10.

MORTON, G. A. (1946). *Rev. Mod. Phys.* **18**, 362. Ch. IX; §12.3.
MORTON, G. A. (1949). *R.C.A. Rev.* **10**, 525. §12.4.
MORTON, G. A. and FLORY, L. E. (1946). *R.C.A. Rev.* **7**, 385. §12.5.
MORTON, G. A. and RAMBERG, E. G. (1936). *Physics*, **7**, 451. Ch. VI.
MOSS, H. (1945*a*). *Wireless Engr*, **22**, 316. Ch. VIII.
MOSS, H. (1945*b*). *J. Brit. Instn Radio Engrs*, **5**, 10. Ch. IX.
MOSS, H. (1946). *J. Brit. Instn Radio Engrs*, **6**, 99. Ch. IX.
MOSS, H. (1950). *Advances in Electronics*, **2**, 1. §12.2.
MOTZ, H. and KLANFER, L. (1946). *Proc. Phys. Soc.* **58**, 30. Ch. III.
MULLARD CO. (1938). Brit. Pat. 525, 601. Ch. IX.
MÜLLER, E. W. (1950*a*). *Naturwissenschaften*, **37**, 329. §12.6.
MÜLLER, E. W. (1950*b*). *Z. Naturforsch.* **5**a, 437. §12.6.
MUSSON-GENON, R. (1947). *Ann. Telecom.* **2**, 254, 298. Ch. III; VIII.
NEUMANN, G. (1914). *Ann. Phys., Lpz.*, **45**, 529. Ch. XI.
NICOLL, F. H. (1938*a*). *Proc. Phys. Soc.* **50**, 888. Ch. IV.
NICOLL, F. H. (1938*b*). *Wireless World*, **43**, 583. Ch. VI.
OLIPHANT, M. L. and MOON, P. B. (1929). *Proc. Camb. Phil. Soc.* **25**, 461. Ch. X.
OPATOWSKI, I. (1944). *Phys. Rev.* **65**, 45. Ch. I.
OWEN, G. E. (1949). *Rev. Sci. Instrum.* **20**, 916. Ch. XI.
PACKH, D. G. DE (1947). *Rev. Sci. Instrum.* **18**, 798. Ch. III.
PAEHR, H. W. (1939). *Z. Fernseh A.G.* **1**, 193. Ch. IX.
PANOFSKY, W. K. H. and BAKER, W. R. (1950). *Rev. Sci. Instrum.* **21**, 445. Ch. X.
PEARCE, A. F. and MAYO, B. J. (1946). *J. Instn Elect. Engrs*, pt. III*a*, **93**, 918. §12.9.
PEIERLS, R. (1946). *Nature, Lond.*, **158**, 831. Ch. X.
PEIERLS, R. and SKYRME, T. H. R. (1949). *Phil. Mag.* **40**, 269. Ch. X.
PERSICO, E. (1949). *Rev. Sci. Instrum.* **20**, 191. Ch. VII.
PERSICO, E. and GEOFFRION, C. (1950). *Rev. Sci. Instrum.* **21**, 945. §12.7.
PETRIE, D. P. R. (1941). *Elect. Commun.* **20**, 100. Ch. VIII.
PHILIPS CO. (1941). Brit. Pat. 554,828. Ch. IX.
PICARD, R. G., SMITH, P. and REISNER, J. H. (1949). *Rev. Sci. Instrum.* **20**, 601. §12.10.
PICHT, J. (1932). *Ann. Phys., Lpz.*, **15**, 926. Ch. III.
PICHT, J. (1933). *Z. Tech. Phys.* **14**, 239. Ch. VI.
PICHT, J. and HIMPAN, J. (1941). *Ann. Phys., Lpz.*, **39**, 401, 436 and 448. Ch. XI.
PIERCE, J. R. (1938). *Bell Lab. Rec.* **16**, 305. Ch. X.
PIERCE, J. R. (1939). *Physics*, **10**, 713. Ch. VIII.
PIERCE, J. R. (1940*a*). *J. Appl. Phys.* **11**, 548. Ch. III; VIII; IX.
PIERCE, J. R. (1940*b*). *Bell Monogr.* B, no. 1248. Ch. III.
PIERCE, J. R. (1945). *Phys. Rev.* **68**, 229. Ch. IX.
PIERCE, J. R. (1949). *See* Bibliography A. Ch. VIII.
PIERCE, J. R. (1950). *Travelling Wave Tubes*. New York. (Collected articles from *Bell Syst. Tech. J.* (1950–1), **29–30**.) §12.9.
PIERCE, J. R. (1951). *Bell Syst. Tech. J.* **30**, 825. Ch. IX.
PIERCE, J. R. and HEBENSTREIT, W. B. (1949). *Bell Syst. Tech. J.* **28**, 33. §12.9.

PLASS, G. N. (1942). *J. Appl. Phys.* **13**, 49, 542. Ch. IV; VI.
PLATO, G., KLEEN, W. and ROTHE, H. (1936). *Z. Phys.* **101**, 509. Ch. VIII.
PLATO, G., KLEEN, W. and ROTHE, H. (1937). *Z. Phys.* **104**, 711. Ch. VIII.
PLOCKE, M. (1951). *Z. angew. Phys.* **3**, 441. Ch. IX.
PLOCKE, M. (1952). *Z. angew. Phys.* **4**, 1. Ch. IX.
POITTEVIN, M. (1947). *J. Phys. Radium*, **8**, 102. Ch. X.
POLOTOVSKI, L. S. (1934). *Isv. Elect. Slabovo Toka*, **5**, 22; **6**, 13. Ch. IV.
PURCELL, E. M. (1938). *Phys. Rev.* **54**, 818. Ch. XI; §12.7.
QUADE, E. A. and HALLIDAY, D. (1948). *Rev. Sci. Instrum.* **19**, 234. Ch. VI.
RAJCHMAN, J. (1938). *Arch. Sci. Phys. Nat. Geneve*, **20**, 9. Ch. III.
RAJCHMAN, J. (1951). *R.C.A. Rev.* **12**, 53. §12.10.
RAKHIMOV, S. M. and SUSHKIN, N. G. (1948). *J. Tech. Phys. U.S.S.R.* **18**, 1166. Ch. V.
RAMBERG, E. G. (1942). *J. Appl. Phys.* **13**, 582. Ch. III; IV; VI; VII.
RAMBERG, E. G. (1949). *J. Appl. Phys.* **20**, 183. Ch. VI; VII.
RANDALL, J. T. and BOOT, H. A. H. (1946). *J. Instn Elect. Engrs*, pt. III, **93**, 182. §12.9.
RANG, O. (1948). *Optik*, **4**, 251. Ch. VI.
RANG, O. (1949). *Optik*, **5**, 518. Ch. VI.
REBSCH, R. (1938). *Ann. Phys., Lpz.*, **31**, 551. Ch. VI; VII.
REBSCH, R. (1940). *Z. Phys.* **116**, 729. Ch. VI.
REBSCH, R. and SCHNEIDER, W. (1937). *Z. Phys.* **107**, 138. Ch. VI.
RECKNAGEL, A. (1936). *Z. Tech. Phys.* **17**, 643. Ch. IV.
RECKNAGEL, A. (1937). *Z. Phys.* **104**, 381. Ch. III.
RECKNAGEL, A. (1938). *Z. Phys.* **111**, 61. Ch. XI.
RECKNAGEL, A. (1940). *Z. Phys.* **117**, 67. Ch. VI.
RECKNAGEL, A. (1943). *Z. Phys.* **120**, 331. Ch. VII.
REGENSTREIF, E. (1951*a*). *Ann. Radioelect.* **6**, 51. Ch. IV; VI.
REGENSTREIF, E. (1951*b*). *Ann. Radioelect.* **6**, 114. Ch. IV; VI.
REISNER, J. H. (1951). *J. Appl. Phys.* **22**, 561. Ch. V.
REISNER, J. H. and DORNFIELD, E. G. (1950). *J. Appl. Phys.* **21**, 1131. Ch. V.
RICHARDSON, H. O. W. (1947). *Proc. Phys. Soc.* **59**, 791. Ch. XI.
RICHARDSON, H. O. W. (1949). *Phil. Mag.* **40**, 233. Ch. XI.
REUSSE, W. (1939). *T.F.T.* **28**, 184. Ch. IX.
REYNER, J. H. (1947). *Cathode Ray Oscillographs*, 3rd ed. London. §12.2.
RIDER, J. F. and USLAN, S. D. (1950). *Encyclopedia on cathode ray oscilloscopes*. New York.
RIEDEL, H. (1937). *Z. Phys.* **107**, 210. Ch. VI.
ROBINSON, C. (1949). *Proc. Phys. Soc.* A, **62**, 592. Ch. X.
RODDA, S. (1945). *Electronic Engng*, **17**, 541, 589, 649 and 652. Ch. VIII.
ROGERS, F. T. (1951). *Rev. Sci. Instrum.* **22**, 723. Ch. XI.
ROGOWSKI, W. (1937). *Arch. Elektrotech.* **31**, 555. Ch. VI.
ROGOWSKI, W. and FLEGLER, E. (1925). Brit. Pat. 295,710. §12.2.
ROGOWSKI, W., FLEGLER, E. and BUSS, K. (1930). *Arch. Elektrotech.* **24**, 563. §12.2.

ROGOWSKI, W. and GRÖSSER, W. (1925). *Arch. Elektrotech.* **15**, 377. Ch. IX.
ROGOWSKI, W. and THIELEN, H. (1939). *Arch. Elektrotech.* **33**, 411. §12.2.
ROSE, A. (1940*a*). *Proc. Inst. Radio Engrs, N.Y.*, **28**, 30. Ch. XI.
ROSE, A. (1940*b*). *J. Appl. Phys.* **11**, 711. Ch. XI.
ROSE, A. and IAMS, H. (1939). *Proc. Inst. Radio Engrs, N.Y.*, **27**, 547. Ch. XI; §12.3.
ROSE, A., WEIMER, P. K. and LAW, H. B. (1946). *Proc. Inst. Radio Engrs, N.Y.*, **34**, 424. §12.3.
RUDENBERG, R. (1948). *J. Franklin Inst.* **246**, 311, 377. Ch. IV.
RUSKA, E. (1933). *Z. Phys.* **83**, 684. Ch. IX.
RUSKA, E. (1934*a*). *Z. Phys.* **87**, 580. Ch. V.
RUSKA, E. (1934*b*). *Z. Phys.* **89**, 90. Ch. V; VI.
RUSKA, E. (1942). *Arch. Elektrotech.* **36**, 431. Ch. VI.
RUSKA, E. (1944). *Arch. Elektrotech.* **38**, 102. Ch. V.
RUTHEMANN, G. (1948). *Ann. Phys., Lpz.*, **2**, 113. Ch. XI; §12.7.
RUTHERFORD, E., ROBINSON, H. and RAWLINSON, W. E. (1914). *Phil. Mag.* **28**, 281. Ch. XI.
SAGUTA, E. (1939). *Electrotech. J. Tokyo*, **3**, 271. Ch. V.
SALINGER, H. (1937). *Electronics*, **10**, no. 10, 50. Ch. III.
SALZBERG, B. and HAEFF, A. V. (1938). *R.C.A. Rev.* **2**, 336. Ch. VIII.
SAMUEL, A. L. (1945). *Proc. Inst. Radio Engrs, N.Y.*, **33**, 233. Ch. III; IX.
SAMUEL, A. L. (1949). *Proc. Inst. Radio Engrs, N.Y.*, **37**, 1252. Ch. VIII.
SANDER, K. F., OATLEY, C. W. and YATES, J. G. (1949). *Nature, Lond.*, **163**, 403. Ch. III.
SANDER, K. F., OATLEY, C. W. and YATES, J. G. (1952). *J. Inst. Elect. Engrs*, Pt III, **99**, 169. Ch. III.
SANDOR, A. (1941). *Arch. Elektrotech.* **35**, 217, 259. Ch. V.
SAVCHENKO, F. (1939). *J. Tech. Phys. U.S.S.R.* **9**, 2211. Ch. IX.
SCHADE, O. H. (1938). *Proc. Inst. Radio Engrs, N.Y.*, **26**, 137. Ch. VIII; X.
SCHAFFERNICHT, W. (1948). *Fiat Rev. German Science Electronics*, pt. 1, p. 74. §12.5.
SCHERZER, O. (1933). *Z. Phys.* **80**, 193. Ch. III; VI.
SCHERZER, O. (1936). *Z. Phys.* **101**, 23, 593. Ch. VI.
SCHERZER, O. (1939). *Z. Phys.* **114**, 427. Ch. VII.
SCHERZER, O. (1941). *Z. Phys.* **118**, 461. Ch. VI.
SCHERZER, O. (1947). *Optik*, **2**, 114. Ch. VI; X.
SCHERZER, O. (1949*a*). *Optik*, **5**, 497. Ch. VI.
SCHERZER, O. (1949*b*). *J. Appl. Phys.* **20**, 20. Ch. VI.
SCHIFF, L. I. (1942). *Phys. Rev.* **61**, 721. Ch. VII.
SCHLESINGER, K. (1949). *Electronics*, **22** (Oct.), 102. Ch. XI.
SCHOTTKY, W. (1919). *Arch. Elektrotech.* **8**, 1 and 299. Ch. IX.
SCHWARTZ, E. (1938*a*). *Z. Tech. Phys.* **19**, 454. Ch. IX.
SCHWARTZ, E. (1938*b*). *Fernseh Mitt.* **1**, no. 2, p. 19. §12.2.
SCHWARTZ, E. (1943). *Phys. Z.* **44**, 348. Ch. VIII.
SCHWARZ, E., STRÜBIG, H. and PAEHR, W. (1938). *Z. Fernseh A.G.* **1**, 5. Ch. IX.

SCHWARZSCHILD, K. (1903). *Nachr. Ges. Wiss. Göttingen, Math. Phys. Kl.* **3**, 126. Ch. I.
SEELIGER, R. (1948). *Optik*, **4**, 258. Ch. VI.
SEELIGER, R. (1949). *Optik*, **5**, 490. Ch. VI.
SEELIGER, R. (1951). *Optik*, **8**, 311. Ch. VI.
SHOENBERG, I., BULL, C. S. and RODDA, S. (1933). Brit. Pat. 423,932. Ch. X.
SHORTLEY, G. H. and WELLER, R. (1938). *J. Appl. Phys.* **9**, 334. Ch. X.
SHULL, F. G. and DENNISON, D. M. (1947). *Phys. Rev.* **71**, 681. Ch. XI; §12.7.
SHUTT, R. P. and WHITTEMORE, W. L. (1951). *Rev. Sci. Instrum.* **22**, 73. Ch. XI.
SIDAY, R. E. (1942). *Proc. Phys. Soc.* **54**, 266. Ch. V; VII.
SIDAY, R. E. (1947). *Proc. Phys. Soc.* **59**, 905. Ch. XI.
SIDAY, R. E. and SILVERSTON, D. A. (1952). *Proc. Phys. Soc.* A, **65**, 328. §12.7.
SIEGBAHN, K. (1942). *Ark. Mat. Astr. Fys.* A, **28**, no. 17. Ch. V; §12.7.
SIEGBAHN, K. (1943). *Ark. Mat. Astr. Fys.* A, **30**, no. 1. Ch. V.
SIEGBAHN, K. (1944). *Ark. Mat. Astr. Fys.* A, **30**, no. 20. Ch. V; XI; §12.7.
SIEGBAHN, K. (1946). *Phil. Mag.* **37**, 162. Ch. VI; §12.7.
SIEGBAHN, K. and SWARTHOLM, N. (1946*a*). *Nature, Lond.*, **157**, 872. Ch. XI.
SIEGBAHN, K. and SWARTHOLM, N. (1946*b*). *Ark. Mat. Astr. Fys.* A, **33**, no. 21. Ch. XI; §12.7.
SKELLETT, A. M. (1944). *J. Appl. Phys.* **15**, 704. §12.10.
SKELLETT, A. M. (1946). *Rev. Mod. Phys.* **18**, 379. §12.10.
SLÄTIS, H. and SIEGBAHN, K. (1949). *Ark. Mat. Astr. Fys.* **1**, 339. Ch. VII; §12.7.
SMITH, L. P. and HARTMAN, P. L. (1940). *J. Appl. Phys.* **11**, 220. Ch. VIII.
SMYTHE, W. R. (1939). *Static and Dynamic Electricity*. New York. Ch. V.
SOMMER, A. and TURK, W. E. (1950). *J. Sci. Instrum.* **27**, 113. §12.4.
SOUTHWELL, R. V. (1946). *Relaxation Methods in Theoretical Physics*. Oxford. Ch. III.
SPANGENBERG, K. R. (1948). *Vacuum Tubes*. New York. Ch. VIII; XII.
SPANGENBERG, K. R. and FIELD, L. M. (1942*a*). *Elect. Commun.* **20**, 305. Ch. II; III; VI.
SPANGENBERG, K. R. and FIELD, L. M. (1942*b*). *Proc. Inst. Radio Engrs, N.Y.*, **30**, 138. Ch. II; III; VI.
SPANGENBERG, K. R. and FIELD, L. M. (1943). *Elect. Commun.* **21**, 194. Ch. IV.
STABENOW, G. (1935). *Z. Phys.* **96**, 634. Ch. V.
'Steels for permanent magnets' (1940). *Philips Tech. Rev.* **5**, 29. Ch. V.
'Steels for permanent magnets' (1945). *J. Sci. Instrum.* **22**, 56. Ch. V.
'Steels for permanent magnets' (1947). *Rev. Mod. Phys.* **19**, 29. Ch. V.
STEIGERWALD, K. H. (1949). *Optik*, **5**, 469. Ch. IX.
STEPHENS, W. E. (1934). *Phys. Rev.* **45**, 513. Ch. XI.

STÖRMER, C. (1933). *Ann. Phys., Lpz.*, **16**, 685. Ch. V; XI.
STRASHKEVITCH, A. (1940). *J. Tech. Phys. U.S.S.R.* **10**, 91. Ch. X.
SWARTHOLM, N. (1942). *Ark. Mat. Astr. Fys.* B, **28**, no. 16. Ch. V.
SWARTHOLM, N. (1946). *Ark. Mat. Astr. Fys.* A, **33**, no. 24. Ch. XI.
SWARTHOLM, N. (1948). *Phys. Rev.* **74**, 108. Ch. XI.
SWARTHOLM, N. (1950). *Ark. Mat. Astr. Fys.* A, **2**, no. 14. Ch. XI.
SWEDLUND, L. E. (1945). *Electronics*, **18** (March), p. 122. Ch. IX.
SWEDLUND, L. E. and SAUNDERS, R. (1951). *Electronics*, **24** (April), 118. §12.3.
SWEDLUND, L. E. and THIERFELDER, C. W. (1951). *J. Soc. Mot. Pict. Engrs*, **56**, 332. §12.3.
SYNGE, J. L. (1937). *Geometrical Optics*. Cambridge. Ch. VI.
TERRILL, H. M. and SWEENY, L. (1944*a*). *J. Franklin Inst.* **237**, 495. Ch. VIII.
TERRILL, H. M. and SWEENY, L. (1944*b*). *J. Franklin Inst.* **238**, 220. Ch. VIII.
THODE, H. G. and SHIELDS, R. B. (1949). *Rep. Progr. Phys.* **12**, 1. §12.10.
THOMPSON, B. J. and HEADRICK, L. B. (1940). *Proc. Inst. Radio Engrs, N.Y.*, **28**, 319. Ch. VIII; X.
THOMPSON, F. C. (1947). Ch. V of *Electronics*, ed. Lovell. London. §12.9.
THOMSON, G. P. and COCHRANE, W. (1939). *Theory and Practice of Electron Diffraction*. London. §12.10.
THOMSON, J. J. (1897). *Phil. Mag.* **4**, 293. Ch. XI.
THORP, J. S. (1949). *J. Sci. Instrum.* **26**, 203. Ch. X.
THORP, J. S. (1950). *Brit. J. Appl. Phys.* **1**, 144. Ch. X.
TRICKER, R. A. (1924). *Proc. Camb. Phil. Soc.* **22**, 454. Ch. VII.
VARIAN, R. H. and VARIAN, S. F. (1939). *J. Appl. Phys.* **10**, 321. §12.9.
VAUTHIER, M. R. (1952). *J. Phys. Radium*, **13**, 107. Ch. X.
VEKSLER, V. (1945). *J. Phys. U.S.S.R.* **9**, 153. §12.8.
VERSTER, N. F. (1950). *Appl. Sci. Res. Netherlands*, B, **1**, 363. Ch. VII.
VOGES, H. and RUTHEMANN, G. (1939). *Z. Phys.* **114**, 709. Ch. XI.
VOIT, H. (1939). *Z. Instrumkde*, **59**, 71. Ch. VI.
WAGNER, H. M. and FERRIS, W. R. (1941). *Proc. Inst. Radio Engrs, N.Y.*, **29**, 598. §12.9.
WALCHER, W. (1949). *Nucleonics*, **5** (Oct.), 42. Ch. XI.
WALCHER, W. (1951). *Z. angew. Phys.* **3**, 189. Ch. VIII.
WALDMANN, L. (1937). *Phys. Z.* **38**, 654. Ch. IX.
WALKER, G. B. (1949). *J. Instn Elect. Engrs*, pt. II, **96**, 319. Ch. X.
WALLAUSCHEK, R. and BERGMANN, P. (1935). *Z. Phys.* **94**, 329. Ch. V.
WALLMARK, J. T. (1952). *Proc. Inst. Rad. Engrs, N.Y.*, **40**, 41. §12.9.
WALLRAFF, A. (1935). *Arch. Elektrotech.* **29**. 351. Ch. XI.
WATSON, E. E. (1927). *Phil. Mag.* **3**, 849. Ch. VIII.
WEBER, E. (1950). *Electromagnetic Fields*, vol. **1**. 'Mapping of fields'. New York. Ch. III.
WEHNELT, A. (1903). *Ber. dtsch. phys. Ges.* **5**, 29, Ch. IX; §12.2. (A proper description of the Wehnelt cylinder has been given very much later only. See for instance: Wehnelt, A. and Jentsch, F. (1909). *Ann. Phys., Lpz.*, **28**, 541.)

WENDT, G. (1933). *Ann. Phys., Lpz.*, **17**, 445. Ch. IX.
WENDT, G. (1938). *Telefunkenröhre*, no. 15, p. 100. Ch. XI.
WENDT, G. (1942). *Z. Phys.* **119**, 423. Ch. XI.
WENDT, G. (1943). *Z. Phys.* **120**, 720. Ch. XI.
WESTENDORP, W. E. (1945). *J. Appl. Phys.* **16**. 581, 657. §12.8.
WIDEROE, R. (1928). *Arch. Electrotech.* **21**, 387. §12.8.
WIECHERT, E. (1899). *Ann. Phys., Lpz.*, **69**, 739. Ch. IX; §12.2.
WIEN, W. (1898). *Ann. Phys., Lpz.*, **65**, 440. Ch. XI.
WILKINS, J. J. (1950). *Proc. Phys. Soc.* A, **63**, 177. Ch. X.
WILLIAMS, F. C. and KILBURN, T. (1949). *J. Instn Elect. Engrs*, pt. II, **96**, 183. §12.10.
WILLIAMSON, K. I. (1947). *J. Sci. Instrum.* **24**, 242. Ch. V.
WILLOUGHBY, E. O. (1946). *J. Instn Elect. Engrs*, p. III, **93**, 275. Ch. III.
WILSON, W. (1948). *The Cathode Ray Oscillograph in Industry*, 3rd ed. London. §12.2.
WITCHER, C. M. (1941). *Phys. Rev.* **60**, 32. Ch. V; VII; §12.7.
WOOSTER, W. A. (1927). *Proc. Roy. Soc.* **114**, 729. Ch. XI.
WORONCOW, A. (1946). *J. Instn Elect. Engrs*, pt. III*a*, **93**, 1564. Ch. XI.
WRIGHT, D. A. (1949). *Proc. Phys. Soc.* **62**, 188. Ch. IX.
WYCOFF, R. W. G. (1949). *Electron Microscopy, Technique and Applications.* New York. §12.6.
YARNOLD, G. D. and BOLTON, H. C. (1949). *J. Sci. Instrum.* **26**, 38. Ch. XI.
ZWORYKIN, V. K. (1933*a*). *J. Franklin Inst.* **215**, 535. Ch. VIII; IX.
ZWORYKIN, V. K. (1933*b*). *J. Instn Elect. Engrs*, **73**, 437. Ch. IX; §12.3.
ZWORYKIN, V. K. (1945). *See* Bibliography A.
ZWORYKIN, V. K. and MORTON, G. A. (1940). *Television.* New York. Ch. III; X; XI; §12.3.
ZWORYKIN, V. K., MORTON, G. A. and MALTER, L. (1936). *Proc. Inst. Radio Engrs, N.Y.*, **24**, 351.
ZWORYKIN, V. K. and RAJCHMAN, J. A. (1939). *Proc. Inst. Radio Engrs, N.Y.*, **27**, 558. Ch. X.
ZWORYKIN, V. K. and RAMBERG, E. G. (1949). *Photoelectricity and its Application.* New York. §§12.4; 12.10.

INDEX

Abbe's sine law, 12–14, 156, 176, 250
Aberration invariant, 133
Aberrations,
  anisotropic, 169
  chromatic, 174–89
  classification of, 122
  combination of, 196
  electronic, 172–98
  in emission systems, 251–9
  field, 155–71, 251–2
  geometrical, 121–71
  relativistic, 189
  spherical, *see* Spherical aberration
  see also Deflexion error *and* Distortion
Acceleration of emitted electrons, 237
Accelerator,
  electron, 418–26
  induction, 420
  linear, 419
Accelerator electrode, 275
Acceptance, solid angle of, 179
Action, 3, 45, 234
Addition of spherical aberrations, 136
  see also Combination of aberrations
Adjustment error, 125 ff.
Air lock, 402
Alignment of valve grids, 309–11
Alignment errors, 125 ff.
Alnico, 111, 335
Aluminium surface micrograph, 408
Ampere-turns of magnetic lens, 88, 96, 103
Amplification factor, 260
Analyser, micro-, 434
  velocity, *see* Lens spectrometer *and* Deflexion spectrometer
Angular aperture, 193
Angular distribution of emission current, 267, 304
Angular velocity of meridional plane, 82, 86
Anisotropic aberrations, 169
Annular focus, 184, 187
Aperture, numerical, 193
  position of, affecting distortion, 167
  single, 60
  see also Three-aperture lens, Two-aperture lens *and* Penetration
Application of electron optics, 380–43
Astigmatic deflexion error, 366
Astigmatic intermediate image, 344
Astigmatism, 159–64
  anisotropic, 170
  see also Asymmetry error
Attraction between electron rays, 200
Auto-electronic emission, *see* Field emission
Automatic biasing of emission system, 272
Automatic ray tracing machine, 46
Axial electrodes, 152

Baffle, 179, 182
Baffle coil, paraxial, 94, 153
Balancing of space charge pressure, 222
Barrel, *see* Distortion
Beam intensity modulation, 259
Beam power valve, 310
Beam spread coefficient, 206–20, 256
Beam spread curve, 203
  relativistically correct, 215
Beam spread equation, 202
Beam tubes, 230
Bell-shaped magnetic field distribution curve, 91, 98, 105, 151, 169
Beta-ray spectra, 409, 417
Betatron, 352, 420–2
  2:1 rule, 421
Betatron start for synchrotron, 425
Black-out voltage, 244, 259, 263, 266, 304
Bounded fields for spectrometer, 378
  see also Field sector
Box lenses, 293 ff.
Brightness of electron source, 249
Brightness of fluorescent screen, 386
Broglie, *see* De Broglie wave
Buncher-resonator, 429
Bunching of electrons, 425, 437
Busch's formula, 87, 89, 164, 315

Candles per watt, 387
Cardinal points of deflecting fields, 342, 346
Cardinal points of lenses, 10, 15
  location of, 21
Catcher-resonator, 429

Cathode,
concave, 167, 241, 270, 280, 398, 429
filament, 272–5, 291, 306, 404
hair pin, 271, 306
oxide, 249
ray tracing near the, 36
Cathode loading, 260
Cathode-ray oscillograph, 381–5
Cathode-ray tube 176, 217, 263, 335
see also Cathode ray oscillograph *and* Television
Cathode surface and field plotting, 228
Cathode system, *see* Emission system
Cavity cathode, 274
Cavity magnetron, 431
Cee-electrode in synchrotron, 426
Centrifugal force, 79, 223
C.g.s. units, 438, 439
Charge storage, 392, 434, 435
Chief trajectory in emission system, 242
Child's law, 231, 262, 265, 303
Chromatic aberration, 174–89
in emission systems, 252
Circle method for ray tracing, 34
Circular symmetry, deviations from, 124–9
Coaxial lenses,
electrostatic, 152
magnetic, 94, 153
Coaxial slotted cylinders, 291
Cobweb thread as object, 140
Coil form factor, 88, 103
Coils,
air, 88–98
bent-head type of, 127
dimensions, 94, 95
iron-shielded, 98–107
saddle, 335, 367, 392
Cold emission, *see* Field emission
Collecting power, 178, 185–6, 409
of focusing deflexion field, 377–8
of lens, 94
of spectrometers, 412–13
Collector current, 415
Collinear projection, 10
Coma, 155–8
anisotropic, 170
Combination of aberrations, 136, 196
Combined electrostatic and magnetic lenses, 120
Comparison of spectrometers, 412–13
Compensating screws for magnetic field correction, 128
Compound spectrometer, 411
Computational mapping, 283
Computational method for ray tracing, 116
Concave cathode, 167, 241, 270, 280, 398, 429
Condenser, deflexion, 326–7
Condenser lens, 195, 402
Conical anode, 240
Conjugate points, 11, 18
Conservation of angular momentum, 83
Conservation of energy, 4
Conservation of flux, 25, 353
Conservative forces, 2
Continuum theory of space charge, 199 ff.
breakdown of, 213
Contrast in electron microscope image, 175
Cooling of coil, 95
Coulomb field, *see* Spherical condenser
Coulomb forces, 9, 200
Counting tubes, 436
C.P.S. tubes, 390
Crossed electrostatic and magnetic field, 357–62, 378
Cross-over, 213
Cross-over formation, 241–7
ring, 184–6
Cross-over shift, 264
Current density, high value, 274
maximum in coils, 96, 103
in spot, 386
Current efficiency, 305
Current loop, *see* Single wire loop
Curvature of image field, 162
Curvature of line focus, 293
Curvature of lips in line-focus lenses, 299
Curved cathode, *see* Concave cathode
Curved strip cathode, 308
Curvilinear coordinates for deflexion, 341, 346
'Cut-off parabola', 360
Cut-off voltage, *see* Black-out voltage
Cycloidal orbits, 358, 432
Cyclotron, 423
Cyclotron frequency, *see* Larmor frequency
Cylinder lens, *see* Tube lenses
Cylindrical condenser, 339
with superimposed magnetic field, 361, 373

D-electrode in cyclotron, 423
Damping of orbital oscillations, 422, 426

Davisson-Calbick formula, 63, 247, 291
Dawson function, 202, 206
De Broglie wave-length, 192
Deflecting fields, 320–79
Deflecting plates, 327–30
  tilted, 329
Deflecting power, 326, 328
Deflexion, electrostatic, 321–32, 378, 412
  by fringing field, 326
  magnetic, 323, 332–6, 375–8
Deflexion errors, 363–7
Deflexion field correction, 370
Deflexion focussing, 336 ff.
  errors of, 367–73
Deflexion grid, 330
Deflexion magnet, 333–5, 354
Deflexion mirror, 332
Deflexion plates, 325
  curved, 329
Deflexion prism, *see* Prism
Deflexion sensitivity, 382
Deflexion spectrometers, comparison of, 412
Deflexion valves, 427
Degaussing coils, 126–7
Density of emission current, 272
Depth of focus, 168, 389, 405
Design of triode systems, 264
Deviations from circular symmetry, 124–8
Diaphragm lenses, 56, 65
Differential analyser, 47
Diffraction camera, 434
Diffraction error, 192–8
Diffraction fringes, 196
Diffusion pump, 402
Diode, 262
Dip-field with no spherical aberration, 151, 187
Dipole, magnetic,
  with equal polarity, 316
  with opposite polarity, 352
Disk of confusion, 175, 178, 183, 194, 196, 207
Disk of least confusion, 134, 159
Dispersion of focusing deflexion field, 374
Dissector tube, *see* Image dissector
Distortion coefficient, 165
Distortion due to spherical aberration, 139
Distortion error, 164–8
  in electron microscope, 405
Distortion factor, 164
Distortion of spot, 124
  in deflecting fields, 365
Diverging lens, 52, 63, 73, 209, 226
Double-curved condenser, 343
Double-lens spectrometer, 188
Double-lipped box-lenses, 296
Double-lipped two-tube lenses, 297
Drift space, 270
Drift tube, 427

Earth-magnetic field, compensation of, 126
Einzel lens, 64, 188
  in emission system, 277
  and space charge, 219
  spectrometer, 413
Elastic-membrane model, 287
Electrokinetic force, 9
Electrolytic trough, 29, 31, 225–8, 244, 286, 308
  for magnetic field plotting, 114
Electromagnet design, 334
  see also Steels for magnets
Electron accelerators, 418–26
Electron beam, *see* Beam-spread coefficient, Beam-spread curve *and* Beam-spread equation
Electron beam voltmeter, 236, 436
Electron charge ($-e$), 4, 440
Electron diffraction, 434
  and refractive index, 5
  and spherical aberration, 137
Electron energy, 4, 440–2
Electron gun, 226, 276–7, 280, 382, 389, 421, 422
Electron mass, change of, with velocity, 441–2
Electron microscope, 249, 273–5
  image formation in, 195
  ultimate resolving power, 408
  see also Microscope lenses
Electron mirror, 74, 152, 174, 405
  deflecting, 332
  in klystron, 430
  semiconducting, 400
Electron momentum ($B_e r_e$), 6, 440–2
Electron multiplier, *see* Multiplier orthicon, Photo-multiplier *and* Thermionic multiplier
Electron orbits in emission systems, 245
Electron pencil, 245–6
Electron phase optics, 436
Electron ray, *see* Ray tracing

Electron spectrometer, *see* Deflexion spectrometer *and* Lens spectrometer
Electron velocity, 4, 440–2
Electron volt, 4, 440–2
Electron wave-length, 192
Electronic aberrations, 172–98
Electronic commutator, 436
Electronic valves, 230
Electrostatic electron lenses, 49
  aberrations of, 142 ff., 148 ff., 158, 166
Electrotonic force, 9
Elliptical saddle-coils, 336
Emission density, 250, 260, 386
  from cold cathodes, 274
Emission microscope, 402
Emission systems, 237–81, 302–13
  with line-focus, 302
  with magnetic fields, 279
Emission velocities, 172, 175, 262
Emitting area of cathode, 259, 261
Energy equation, 83, 440
Energy levels, calculated from momentum distribution, 417
Energy losses of electrons, 175, 434
Equations of motion, 43, 116, 120, 420
Equipotentials,
  in emission systems, 258, 307
  intersections of, 61, 66, 292
  in lenses, 32, 61, 67, 382
Equivalent diode voltage, 262
Equivalent length of homogeneous deflecting field, 337
Erect images, 77, 93
Error, *see* Aberrations
Error function, *see* Gaussian distribution
Excitation parameter of magnetic lens, 92
Exit pupil, 248

Faraday cage, 255
Fermat's principle, 3
Field aberrations, 155–71, 251–2
Field curvature, 159–64
  in emission systems, 251
Field distribution in electrostatic lenses, *see* Equipotentials
Field distribution in magnetic lenses, 98–108
  radial, 100
Field emission, 274, 396, 406
Field emission microscope, 406
Field-form factor, 242, 253
Field penetration,
  through aperture, 61
  in emission systems, 260
Field plotting,
  conjugate, 318
  electrolytic, 28, 286
  for magnetic lenses, 317
  in presence of space charges, 225–9
Field sector,
  electrostatic, 341
  magnetic, 346
  two-directional in, 355
Filament cathode, 272–5, 291, 306, 404
Film,
  metal, in electron lens, 152
  replica, for microscope, 408
  see also Photographic plate (film)
Fine focus, 274
First-order and third-order theory, 14, 123
Flooding gun, 435
Fluctuation of lens current, 402
  see also Noise, Voltage fluctuation
Fluorescent target, 245
Flux, conservation of, 25, 353
Flux ball, 112
Flux density, contour lines of, 101; *see also* Field distribution
Flying spot, 383
Focal length, definition, 11, 17
  effective, 105
  of emission system, 248
  periodical, 70
  minimum, 70, 103–5, 145, 166
Focus shift, 207–10
Focus spread, 207–9
Focusing by fringing field, 337
Focusing deflexion,
  by coaxial solenoids, 351, 372
  by cylindrical pole-pieces, 350, 372, 412
  in cylinder condenser, 339, 378, 412
  in homogeneous electrostatic field, 337
  in homogeneous magnetic field, 345, 378, 412
  in inhomogeneous fields, 351–6
  in spherical condenser, 341, 378, 412
Focusing efficiency, 97
Focusing errors in spectrometers, 368–73
Form factor, *see* Coil form factor
Four-plate lens, electrostatic, 290
  magnetic, 314

Four-pole magnet, 315
Four-pole spectrometer, 351
Fresnel diffraction, 196
Fringing fields, 325, 326, 337, 354, 356, 360, 365, 371
Fundamental principles of electron optics, 2–15

Gap-to-bore ratio in magnetic lenses, 106
Gap width of iron-shielded lens, 103 ff.
  and distortion, 165
  and spherical aberration, 147
Gap width of two-tube lens, 55–6
Gas discharge, 381
Gathering power, 178
Gauss's law, 63, 200, 203
Gaussian distribution, 254
Gaussian optics, 14
Gauze lenses, 72
Geometric factor of Child's law, 265
Geometrical aberration, 122–71
Gravitational model,
  of electrostatic lens, 60
  of magnetic lens, 84
  of two-dimensional field, 287
Grid, deflexion, 330
Grid bias, 259
Grid drive, 259
Grid electrode, 238 ff.
Grid modulation of emission system, 259 ff.
Grid-controlled image tubes, 397

Hair-pin cathode, 271, 306
Half-maximum width of current density in spot, 254
Half-maximum width of flux density distribution, 91, 93
Half-maximum width of spectrometer transmission curve, 181
Halo, 279, 307
  test for spherical aberration, 141
Hamilton's principle, 3
Hamiltonian characteristic function, 123
Hartmann test, 136
Heath's theorem, 38
Helmholtz coils, 126
Helmholtz-Lagrange principle, *see* Abbe's sine law
High frequency,
  for correcting lenses, 152
  in electron tubes, 427–33
Historical development, 1, 2, 291, 238, 380
Homogeneous electrostatic deflexion field, 321
Homogeneous electrostatic field for electron projection, 64, 177
Homogeneous magnetic deflexion field, 323
Homogeneous magnetic field for longitudinal focusing, 78
Horse-shoe magnets, 315
Hysteresis loop of space current, 234

Iconoscope, 388
Illuminating system for electron microscope, 272–4
Image amplifier, 399
Image converter, 101, 121, 177, 397–8
Image dissector, 396
Image formation in electron microscope, 195
Image formation theory, 10–15
Image iconoscope, *see* Superemitron
Image projection, 10 ff., 18 ff.
Image rotation, 86, 93, 169, 172, 189
Image surfaces, tangential and sagittal, 160
Image tubes, 396–401
Immersion lenses, *see* Two-electrode lenses
Immersion light-microscope, 195
Immersion objective, 402, 406
Immersion system, *see* Emission system
Index, *see* Magnetic field index *and* Refractive index
Induction accelerator, 420
Infra red, 397, 401
Injection of current into space charges, 233–6
Injection of electrons into betatron, 422
Intensity of emission, 249, 267, 274
Intermediate image,
  in microscope, 402
  in oscillograph, 381
Intermediate projection lens, 405
Ion acceleration, 423
Ion bombardment, 275
Ion microscope, 436
Ion optics, 436
Ion trapping, 220, 385
Ions,
  in electron space charges, 219
  negative, 385

Iris effect, 260
Iron shielding, 89 ff., 98 ff., 103–7, 402; *see also* Gap width of iron-shielded lens
Iron yoke, 333, 334

Klystron, 211, 270, 306, 428–31
Knife-edge test, 138

Labelling of equipotentials, 31
Lagrange's law, 14, 19, 23, 133, 156, 164, 388
Lambert's law, 13, 249
Laplace's equation, 26, 48, 227, 283, 287, 292
Larmor frequency, 79, 353, 357, 423
  in relativistic region, 79
Least action principle, *see* Maupertuis's principle
Least-time principle, *see* Fermat's principle
Lens chain, 64
Lens design, magnetic, 94
Lens errors, *see* Aberrations
Lens spectrometers, 177–89, 368, 378, 408–18
  comparison of, 413
Lens-strength parameter, 92
Lenses, *see* Box lenses, Diaphragm lenses, Einzel lenses, *etc.*
Light intensity,
  for orthicons, 393
  for photo-multiplier, 394
  of spectrometer, 178
  in television receiving tubes, 387
Limitation in spot-current density, 176
Line-focus,
  in deflexion fields, 340 ff., 345 ff., 369 ff.
  emission systems, 302–13
  length of, 300
Line-focus lenses,
  electrostatic, 282–302
  magnetic, 314–19
Line-width, monochromatic, 370
Linear accelerator, 419
Lines of force,
  electrostatic, 25
  magnetic, 107
Lipped lenses, 295
Lips for synchrotron magnet, 426
Loading, specific, of X-ray tubes, 433
Location of cardinal points, 16 ff.
'Lock-in' action in synchrotron, 425
Longitudinal aberration, 132
Lorentz contraction, 215
Lorentz equation, 9
Lorentz force, 9, 353
Luminance, 250
Luminosity, 411

M.k.s. units, 438–9
Magnetic field balance, 113
Magnetic field index, 352, 376, 421, 426
Magnetic lenses, 79–121
  aberrations of, 128, 145 ff., 148 ff., 162, 169 ff.
  with line-focus, 314–19
Magnetic potential difference, 86, 89, 115, 334
Magnetic potentiometer, 114
Magnetic prism, 345–51, 371, 378, 412
Magnetic rigidity of electron ray, 6
Magnetic saturation, 105
Magnetic scalar potential, 84
Magnetic shunts, 109
Magnetic vector potential, 8, 82, 94, 113, 325
Magnetomotive force, *see* Magnetic potential difference
Magnetron, 360, 431–2
Magnification, measurement of, 119
  zonal difference of, 158
Mass spectrometer, 345, 350, 436
Maupertuis's principle, 3, 8, 234
Maximum current density in space charges, 232
Maximum density of emission current, 274
Maximum space-charge density in electron guns, 258
Maxwellian distribution, 175, 253
Memory tubes, 434
Meridional foci, 159
Meridional plane in lenses, 30, 81, 85
Meridional potential, 9, 83
Meridional refractive index, *see* Refractive index
Metal vapour shadowing, 407
Metallographic research, 406
Micro-analyser, 435
Micro-focus X-ray tubes, 433
Microscope, electron mirror, 153, 404
Microscope lenses,
  electrostatic, 70, 145, 166, 173, 404
  magnetic, 92, 103–6, 128, 147, 151, 168, 173, 197, 403
  permanent magnetic, 110
Microscope objective, *see* Objective lenses

Microscope projection lens, *see* Projector lenses
Microtron, 424
Mid-focal length, 16 ff., 50 ff., 68, 93
Mid-object distance, 53, 54, 85, 346
Mid-plane of field sector, 348
Mid-plane of lens, 16, 32, 56, 66, 295
Mid-surface of lipped lens, 296
Mirror, *see* Electron mirror *and* Microscope
Mirror action of magnetic fields, 316
Misalignment, 124
Modulation, *see* Velocity modulation valves *and* Virtual cathode modulation
Modulation of beam intensity, 259–64
Modulator, *see* Grid electrode
Molecular structure from electron micrograph, 407
Momentum,
  conservation of angular, 83
  electron, 6, 440–2
  and energy distribution, 416
  energy resolving power, 418
Mosaic screen, 388, 434
Multielectrode emission systems, 275–9
Multielectrode lenses, 63
Multiple source, 272
Multiplier,
  photo-, 311–13
  thermionic electron, 313, 427
Multiplier orthicon, 392
Multiplier valves, *see* Multiplier, thermionic electron
Mutual repulsion, *see* Space charge

Negative ions, *see* Ions
Negative spherical aberration, 299
Neutralization of space charge, 221
Newton's lens equation, 11, 18
Nodal points, 11, 17, 53, 161
Noise,
  in multipliers, 395
  in valves, 427
Numerical aperture, 193
Numerical ray tracing, 44

Object, *see* Specimen
Object distance, 19 ff., 24, 195, 346
Object- and image-space, geometrical relations between, 18 ff.
Objective lenses, 69, 103 ff., 110, 128, 137, 140, 161, 168, 193 ff., 252, 401 ff.
Oblique illumination, 194
Open anode emission system, 239, 303
Optical approach to deflexion problem, 320
Optical approach to electron motion, 10
Optical approach to emission systems, 247
Orbital oscillations, 421
Orthicon, 280, 360
Oscillation of electron orbits, 340, 352, 421
Oscillograph, cathode-ray, 381–5
Oxide cathode, 249

Parabola method for ray tracing, 41
Paraxial baffle coil, 94, 153
Paraxial rays,
  in electrostatic lenses, 12, 43 ff.
  in magnetic lenses, 84 ff.
Paraxial ray equation, electrostatic, 43
  magnetic, 87
Particle velocity, 3
Peak loading of cathode, 260, 265
Pencil tracing, 245–6
Penetration of field through aperture, 61
Penetration factor, 260, 266, 303
Penetration shield, 126
Pepperpot diaphragm, 136, 160, 213, 245
Permanent magnet for deflexion, 334–5
Permanent magnetic lenses, 107–11
Perveance, 270–1, 304
Petzval curvature, 162
Phase focusing, 437
Phase velocity, 3
Photo-cathode, 161
Photographic plate (film), 403, 408
Photo-multiplier, 311–13, 359, 393–5
Pick-up tubes, 101, 388–93
Picture element, 435
Picture frame and picture points, 387
Pierce emission system, 269, 306
Pincushion *see* Distortion
Pin-hole radiographs, 306
Plate lens, electrostatic, 290
  magnetic, 314
Plotting, *see* Field-plotting
Plotting of spectral distribution curves, 415
Point cathode, 271–5
Point projector (field emission) microscope, 274, 406–7
Point projector (shadow) microscope, 404
Poisson's equation, 222, 224, 227, 231

Pole-pieces,
correction of asymmetries of, 125–6
of deflexion magnets, 354–55, 371
with double gap, 168
of microscope lenses, 103–106, 110
Positive ions, 219
Post-acceleration, 217, 384
Potential decay in lenses, 289
Potential depression, 221
Potential distribution,
axial, 28
computation of, 26
in emission systems, 243, 247
measurement of, 29
Potential minimum along beam, 230
Power consumption,
of magnetic lenses, 97
of scanning coils, 336
Power series,
for flux density, 84
for potential, 27
Preconcentration, 381
Predistortion, 364
'Preference spacings' in emission systems, 256–7, 275, 306
Pressure in vacuum tube, *see* Vacuum
Primary foci, 159
Principal planes,
definition of, 11, 19
in deflexion fields, 346, 355
in electrostatic lenses, 51, 55 ff., 69, 73
in magnetic lenses, 90–3, 104
methods for location of, 22 ff.
Principal surface, 156
Prism deflector, 331
Prism, magnetic, 345–51, 371, 378, 412
optical, 10, 320, 331, 336
Projection of photo-electric image, 390, 393; *see also* Image converter
Projection coil, *see* Projector lenses
Projection television, 387
Projector lenses, 69, 103 ff., 110, 168, 401 ff.
Pupil, 247

Radiation losses, 426
Range of emission velocities, 176
Rationalized m.k.s. system, 438 ff.
Ray equation, *see* Paraxial ray equation
Ray-tracing,
near the cathode, 36
through electrostatic lenses, 16, 34–47
through magnetic lenses, 115–20
Reflex klystron, 431
Reflexion of electrons, 74, 399, 400, 431
Refraction of an electron beam, 5, 81
Refractive index,
dimensionless, 4
in electron diffraction theory, 5
in electrostatic field, 4, 324
in emission systems, 237
in magnetic field, 8, 81, 324
meridional, 83, 115
and numerical aperture, 193
and variation principles, 2 ff., 7 ff.
Relativistic aberration, 189
Relativistic correction for beam spread, 215
Relativistic increase of electron mass, 6, 440–1
Relativistic region,
acceleration in, 422
in spectrometry, 418
Relativistic trajectories in Coulomb field, 341
Relativistic velocities,
in einzel lenses, 72
and Larmor frequency, 79
in two-tube lens, 55
Relativistically corrected electron voltage, 6, 88
Relaxation method 27, 111, 283–6
Replica technique for microscope, 408
Residual gas, *see* Vacuum
Resistor network, 33, 229
for magnetic field plotting, 113
Resolution, *see* Resolving power *and* Time resolution
Resolution of a picture, 'geometric', 387
Resolving power,
of electron microscope, 196 ff., 408
of spectrometer, 181, 183, 373–8, 412–13
Rest mass, *see* Voltage equivalent of electronic rest mass
Retarding voltage, 263, 415
Ribbon-shaped beams, 300–2
Ring collector, 184, 413
Rotation of image, *see* Image rotation
Rotation of meridional plane, 108
Rotation-free magnetic lenses, 93
Rubber-sheet model, 287

Saddle coils, 335, 367, 392
Saddle-field lenses, 64, 278
and space charge, 219
two-dimensional, 292

Saddle point, *see* Equipotentials, intersection of
Sagittal foci, 159
Sagittal surface, 160
Saturation current of emission, 262
Saturation of iron shield, 92
Saturation of pole pieces, 103
Scanning coils, 332, 335–6
Scanning of an electron beam, 363, 385
Scattering of electrons, 172, 175
Scherzer's thin-lens formula, 44
Schwarzschild's principle, 7
Scintillation, 395
Screen, *see* Grid electrode *and* Fluorescent target
Screen-grid emission systems, 275
Screen-grid tetrode valve, 309
Search coil, 111
Search coil oscillator, 112
Secondary emission, 391, 393, 434
Secondary foci, 159
Segmented coils, *see* Spaced coils
Seidel term, 123, 133
Semicircular focusing, 345, 370, 378, 412
  correction of, 370
Semi-conductor, 400
Semi-lenses, 52
Shadow method for lens investigation, 23
Shadow methods for measuring spherical aberration, 137–40
Shadow microscope, 404
Shadowgraph, 433
Shadowing technique for microscope, 407
Shield, *see* Screen-grid
Shield plates in line focus lenses, 293
Shielding, *see* Iron shielding
Side spots, 272
Signal plate, 388
Sine-expansion, 14, 123
Sine law, *see* Abbe's sine law *and* Snell's law
Single aperture, 60
Single-lipped box-lens, 295
Single wire loop, 89, 92, 94, 97
Sliding target, 16, 117, 185, 213, 245
  from gauze, 75
Slit scanning method, 255
Slope of modulation characteristic, 260, 262
Slope-to-capacity ratio of valves, 427
Slot lenses, 294
Slotted diaphragm lens, 294
Snell's law, 5, 34, 83, 229, 286, 324, 325
Solenoid, 91, 93, 177, 181, 413
Solenoidal spectrometer, 185, 410
Solid angle,
  of emission, 254
  of rays, 179
  see also Collecting power
Sound-recording electron tubes, 306, 315, 436
Source, electron-optical, 231
Source area, 179
Source diameter, 186
Source dimensions in electron spectrometers, 370, 412–13
Space charge, 199–236
  in deflecting fields, 338
  in electron lenses, 218
  in emission systems, 258
  for increasing slope of valves, 427
  interacting with electrodes, 216
  in klystrons, 429
  in magnetrons, 432
  in ribbon-shaped beams, 300
  in television tubes, 387
Space-charge control, 236
Space-charge density, 200
  maximum, 258
Space-charge equivalent lens, 207–9, 256
Space-charge error, 144, 191, 210
Space-charge factor, 203–5, 212, 256
  critical, in ribbon-shaped beams, 302
Spaced coils, dipfield between, 151
Spaced-coil spectrometer, 413
Specific charge (e/m) determination, 359, 408
Specimen in electron microscope, 175
Specimen techniques in electron microscopy, 407
Spectral distribution curves, 415
Spectrometer, *see* Lens spectrometer *and* Mass spectrometer
Spherical aberration, 129–55, 183, 188, 191, 273, 437
  coefficients, 132
  correction of, 150–5
  dimensionless coefficient of, 134
  distortion, 168
  in emission systems, 252
  of homogeneous magnetic field, 146
  of line-focus lenses, 294, 300
  of magnetic lenses, 145
  measuring methods, 136
  negative, 211

Spherical aberration (*cont.*)
of saddle-field lenses, 144
of space-charge equivalent lens, 210
of two-tube lens, 129–32, 143
variation with gap of iron shield, 147
Spiral distortion, 169
Spot diameter,
minimum in cathode ray tubes, 386
real and visual, 246
Spreading of a homogeneous beam, 199–206
Spurious fields, 124–7, 283
Stabilization, *see* Voltage stabilization
Steels for magnets, 105, 106, 457; *see also* Alnico
Steradian, 179
Stigmator, 128, 154
Stokes's equation, 82, 84, 115
Stored charge, *see* Charge storage
Stray field, *see* Fringing field
Strip cathode, 303, 310
Superemitron, 389
Superposition of electrostatic and magnetic field, 177, 279, 356–62
Surface tension, 30
Synchro-cyclotron, 424
Synchrotron, 426
Synchrotron magnet, 318

Tangential emission, 242, 248
Tangential foci, 159
Tangential surface, 160
Target, *see* Sliding target
Telefocus emission system, 274
Telescopic system, 80
Television, 1, 110, 241, 264, 332, 336, 385–93
projection tube, 215
Tetrode emission systems, 275
Tetrode valves, 230
Thermionic electron multiplier, 313, 427
Thermionic valves, 308–10, 313, 427–33
Thermodynamical discussion, *see* Abbe's sine law
Thick electrostatic lenses, 50 ff.
Thick lens spectrometer, 413
Thick magnetic lenses, 88
Thin electrostatic lens, 44
Thin equivalent lens, 21, 244
Thin films, *see* Film
Thin lens spectrometer, 413
Thin magnetic lens, 84
Third-order aberrations, 14, 123
Three-aperture lens, *see* Three-diaphragm lens
Three-diaphragm lens, 65
aberration of, 142 ff., 166
Three-stage electron microscope, 405
Three-tube einzel lens, 67, 161
aberrations of, 144, 161
Tilt of lens, 125
Tilt method for measuring aberration, 140, 145
Time resolution, 384
Tobacco mosic virus micrograph, 407
Toroidal coils, 367
Toroidal ring condenser, 344
Total emission current, 253
Tracing of cross-over radius, 246
Transition temperature of iron, 406
'Translational' symmetry, 282
Transmission of current through space charge, 235
Transmission of electrons through matter, 175, 434
Transmission of a spectrometer, 178
Transmission curve, 181
Transverse aberration, 133
Travelling wave, 420
Travelling-wave tube, 432
Trigonometrical ray-tracing, 36
Triode emission systems, 238, 264–75
Triode valves, 309
Trochoidal orbits, 355, 358
Trochotron, 436
Tube lenses, 56 ff.; *see also* Three-tube einzel lens, Two-tube lens *and* Saddle-field lens
Tungsten cathode, 269, 272
Tungsten helix, 306, 308
Tungsten-point cathode, 274, 406
Two-aperture lenses
see Two-diaphragm lenses
Two-diaphragm emission system, 238, 303
Two-diaphragm lenses, 56, 59
'Two-dimensional' line-focus lenses, 289, 314
Two-directional focusing deflexion, 341, 352, 362, 412
Two-electrode lenses, 50–60
Two-stream tube, 432
Two-tube lens, 16
asymmetrical, 57
symmetrical, 16, 32, 50

Ultrafocal field,
electrostatic, 70
magnetic, 89
of projection lens, 104
Ultrafocal refraction, 70
Unbounded space-charge flow, 230–5, 270
Uniform fields, *see* Homogeneous electrostatic field *and* Homogeneous magnetic field
Univoltage lens, 65
Unstable potential distribution, 232, 234
Unsymmetrical lenses, 56, 105

Vacuum, 220, 221, 268, 275
Valves, *see* Electronic valves
Variation principles, 2, 3
Vector potential, *see* Magnetic vector potential
Velocity analyser, *see* Lens spectrometers *and* Deflexion spectrometers
Velocity distributions, transformation of, 414
Velocity filter, Wien's, 357, 362
Velocity modulation valves, 428
Velocity selector, 179, 338 ff.
Virtual cathode (optical virtual object), 247
Virtual cathode (space charge), 232
Virtual cathode modulation, 277–9
Virus, 407
Voltage equivalent of electronic rest mass, 79, 423, 424, 441
Voltage fluctuations, 173, 174, 190, 197
Voltage ratio, 6, 35, 49
Voltage stabilization, 402
Voltmeter,
electron beam, 236, 436
electron-optical, 263, 436

Waist of circular beam, 202, 205, 207, 429
Waist of strip-beam, 301
Water cooling, 95, 101
Wave guide, 419
Wave-length of electron, *see* De Broglie wave-length
Wave velocity, 3
Weak deflecting fields, 321
Weak lens,
electrostatic, 43, 50 ff.
magnetic, 84 ff.
Wedge gauge, 124
Wedge-shaped field plotting trough, 30, 226, 317
Willemite, 22
Window area of spectrometer, 180
Writing speed of oscillograph, 381

X-ray tube, 274, 306–8, 433

Yield of secondary electrons, 393
Yoke, magnetic, 101

Zero voltage level, 4